Investigating the impact of applying different grid resolutions of NWP data in atmospheric dispersion modelling

C. Hood[1], D. Carruthers[1], J. O'Neill[1], R. Jackson[1], D. Jinks[1], M. Seaton[1], J. Mickech[1], J. Stocker[1], S. Strickland[1], P. Bedwell[2], J. Wellings[2]

[1] Cambridge Environmental Research Consultants Ltd (CERC)

[2] UK Health Security Agency (UKHSA)

ABSTRACT

Meteorological (met) data from Numerical Weather Prediction (NWP) models is increasingly used to drive dispersion models. Different NWP models/configurations provide met data at varying grid resolutions, this report describes investigations into how changes in NWP resolution affect both regulatory local dispersion modelling and probabilistic accident consequence modelling.

Following a literature review of NWP models and exploration of available datasets, NWP data was evaluated at eight locations across Great Britain. This included data from two different NWP models (WRF and UM) at three (1, 3 and 9 km) and two (1.5 and 10 km) different grid resolutions respectively. In general the models capture most of the variations of wind speed, wind direction and temperature well at all sites. For most metrics and datasets considered, the influence of model and configuration used is greater than the influence of the model resolution. There is greater uncertainty in the modelled variation of precipitation and cloud cover relative to observations, especially for the model dataset with lower temporal resolution and using parameterised convection. All models tend to overpredict the incidence of low-intensity precipitation and underestimate the variation of precipitation between sites.

The effects of differing input meteorology on local regulatory dispersion modelling outputs have been analysed for four sites, six NWP datasets and two local dispersion models (ADMS and AERMOD), using near-ground and elevated idealised sources. There is relatively little sensitivity in the modelled value and location of

This study was funded by the UK Atmospheric Dispersion Modelling Liaison Committee.

maximum annual average concentrations from near-ground or elevated sources to the use of different NWP datasets for flat terrain sites. The variation in model outputs increases for more complex locations (coastal and complex terrain) and for high percentiles of hourly concentrations and/or wet deposition values. Changes in NWP spatial resolution have relatively little effect on most concentration outputs, compared to differences between NWP models or the choice of NWP variables supplied to the local model.

The potential for "double-counting" terrain effects was investigated by comparing ADMS outputs when FLOWSTAR local terrain modelling is driven by NWP data with a resolution significantly finer than the FLOWSTAR domain size against equivalent outputs when the NWP resolution and FLOWSTAR domain size are similar. At both complex terrain sites considered, this double-counting leads to increased wind and concentration channelling along the valleys containing the source, although differences in maximum annual average concentration remained fairly small at typically no more than 10%. A modification made to FLOWSTAR to remove terrain scales greater than the NWP resolution can help to mitigate double-counting terrain effects in the region of the NWP grid cell used for input met data.

The impact of changing NWP resolution on probabilistic accident consequence modelling outputs was investigated. Differences in precipitation predictions between different NWP resolutions drive the variation in model outputs, particularly those influenced by the highest wet deposition rates. Differences in the parameterisation of relatively large scales of motion was secondary, but notable. In general finer-resolution NWP data led to longer, narrower plumes than coarser resolution NWP, with increased protective action maximum distances. The NWP dataset resulting in greater numbers of people and areas affected as a result of the implementation of protective actions varied, depending primarily on the magnitude of the source term and the magnitude of the dose thresholds applied.

EXECUTIVE SUMMARY

The use of meteorological data from Numerical Weather Prediction (NWP) models to drive dispersion models is becoming increasingly common. Specifically, the use of NWP data as input to regulatory models, for environmental permitting and planning assessments, is growing. The use of NWP data as input to probabilistic accident consequence models, for example for the assessment of the consequences of accidental release of radioactive material into the environment and the subsequent impact on public health, is also growing. This report details investigations into the impacts that NWP model grid resolution can have on dispersion model outputs, for both regulatory models and probabilistic accident consequence models. In particular:

- Concern has arisen about double-counting of terrain effects between local observations or fine-scale NWP meteorological data and local terrain modelling in regulatory dispersion modelling; and
- NWP model outputs are increasingly used for accident consequence modelling, but the influence of NWP resolution on probabilistic accident consequence model outcomes has not previously been investigated.

A new evaluation of NWP data from different models, resolutions and providers was carried out at eight meteorological observation locations. The evaluation used analysis NWP data, with some influence from observed data via data assimilation. Independent wind speed and direction data, not used for data assimilation in any of the NWP datasets, was available for one site. The analysis showed generally good matching of wind and temperature data between NWP and observations, although some underestimation of the variability of both wind speed and temperature with time and location. For most variables and locations, the differences between the NWP models were more significant than those due to resolution of the same NWP model. There is greater uncertainty in both measurements and model predictions of cloud cover and precipitation. All models overestimate the prevalence of low-intensity precipitation, predicting this to occur over wider ranges of wind speed and direction than observed, leading to more uniform predictions of precipitation than are observed. This difference in the modelled precipitation distribution may lead to long-term wet deposition predictions which are greater in magnitude than observed precipitation. Some models underestimate the prevalence of moderate to high intensity precipitation, which may lead to wet deposition predictions which are smaller in magnitude when compared to observations, particularly when considering short-term wet deposition.

In addition to the primary measured meteorological variables of wind speed and direction, temperature, cloud cover and precipitation, dispersion models use secondary variables including heat flux, boundary layer height and stability to define atmospheric mixing. A comparison of secondary variables calculated by the ADMS pre-processor showed relatively similar values of these dispersion parameters with differing input cloud cover values from observed or NWP data. In

contrast, the NWP predictions of heat flux, boundary layer height and stability show both very different distributions to the ADMS calculations and substantial variation between NWP datasets. The secondary meteorological variables are not routinely measured so it was not possible to assess the relative accuracy of the different distributions from ADMS and each NWP dataset within the current study.

Two distinct applications of atmospheric dispersion models were considered in this study: regulatory atmospheric dispersion modelling and probabilistic accident consequence atmospheric dispersion modelling. Regulatory dispersion models perform impact assessments of routine discharges into the environment; in this study the ADMS and AERMOD models were applied, performing deterministic type model runs, for the assessment of air quality. In contrast, probabilistic accident consequence models perform impact assessments of accidental discharges into the environment; in this study the NAME model was applied, performing probabilistic type model runs, for radiological assessments.

A comparison of regulatory dispersion modelling outcomes at distances up to 1 km from a near-ground source or up to 10 km from an elevated source was carried out with observed and NWP meteorological data from two models at two horizontal resolutions (1 and 9 km from WRF; 1.5 and 10 km from UM). The dispersion modelling was carried out using both ADMS (Carruthers *et al.* 1994, CERC 2023) and AERMOD (Cimorelli *et al.* 2004) and led to the following conclusions.

- The value and location of the maximum annual average concentrations from a near-ground source in flat terrain showed low sensitivity to the choice of input meteorological data within the tested set. More difference was found between results from different local models with observed meteorology than between results from the same local model using different resolution NWP data.
- There is greater sensitivity of dispersion model outputs to differing input meteorological data in complex terrain. In most cases, there was more difference between different NWP models and the combination of input variables provided from NWP to the local dispersion model than due to the NWP resolution alone.
- There is greater sensitivity of dispersion model outputs to input meteorological data for high percentiles of hourly concentration, especially 100^{th} percentile (maximum), than for annual average, due to the dependence of high percentile predictions on individual and unusual meteorological conditions.
- There is greater variability of local model predictions of wet deposition than concentration due to the use of NWP data in comparison to observed meteorological data, as a result of the dependence on the modelling of precipitation as well as dispersion variables. There were consistently higher predictions of wet deposition using UM than WRF NWP data but no consistent trend with resolution.

The FLOWSTAR complex terrain flow model in ADMS assumes that the input meteorological data is representative of the conditions 'upwind' of the FLOWSTAR domain, i.e. the conditions that would exist in the absence of the complex terrain in the FLOWSTAR domain. The risk of "double-counting" the impact of terrain on flow and dispersion thus exists if using NWP data with a resolution that is significantly finer than the size of the FLOWSTAR domain and thus already includes influences of the same terrain. The key findings of the investigation into double-counting are:

- Wind roses of input (NWP) and output (FLOWSTAR) wind data demonstrated that using NWP data with a resolution significantly finer than the FLOWSTAR domain size led to a clear over-emphasis of wind channelling within the large-scale valley at Sennybridge (and a smaller over-channelling effect at Drumalbin). In contrast, using NWP data with a resolution similar to the FLOWSTAR domain size showed minimal double-counting issues due to the fact that the scales modelled by FLOWSTAR and the NWP model did not significantly overlap.

- Long-term average flow fields generated by FLOWSTAR when using a FLOWSTAR domain similar in size to, and driven by, the coarsest resolution NWP data (to minimise double-counting) were broadly consistent with the long-term average flow fields from the finest resolution NWP models over the FLOWSTAR domain, but provided significantly more detail around smaller-scale terrain features. FLOWSTAR flow fields for specific hours often showed more notable differences with those from the finest resolution NWP models.

- For the two complex terrain sites and idealised source types considered (elevated and near-ground), maximum long-term average concentrations from ADMS/FLOWSTAR runs in which terrain effects were double-counted (i.e. driven by NWP data with resolution significantly finer than the FLOWSTAR domain size) typically differed by less than 10% when compared with equivalent runs driven by NWP data with resolution similar to the FLOWSTAR domain size. The location of the maximum long-term average concentration was often more significantly affected. Long-term concentration differences at individual receptors could also be significantly higher (up to 179% seen) due to differences in the direction of the dispersing plume when terrain effects are double-counted, which lead to greater predicted along-valley channelling at the sites considered.

- Using NWP data with resolution that is significantly coarser than the FLOWSTAR domain means that terrain effects associated with scales between the FLOWSTAR domain size and the NWP model resolution are not accounted for – in the case considered, this "half-counting" of terrain effects lead to concentration contours with a stronger across-valley component, though the predicted maximum long-term average concentrations were not significantly altered (2% difference).

- A modification was made to FLOWSTAR to remove terrain scales greater than the NWP model resolution. Using this modified FLOWSTAR in cases where the NWP model resolution was significantly finer than the FLOWSTAR domain reduced double-counting effects in the region of the NWP grid cell from which the data was extracted, but lacked the effect of the removed terrain scales on the plume at greater distances from this region. Application of this modification is most appropriate for near-ground sources where the maximum concentrations are typically within the region of the NWP grid cell, but is less appropriate for elevated sources where maximum impacts are further from the source. For the near-ground source case considered, the modified FLOWSTAR improved the orientation of the near-source concentration contours but the maximum annual average concentration was around 10% further away from the value obtained with an equivalent standard FLOWSTAR run that did not include significant double-counting effects.

- AERMOD's treatment of plumes in complex terrain is highly idealised with no specific flow field model used and so it is not possible to extend the above conclusions about ADMS/FLOWSTAR to AERMOD.

A comparison of accident consequence modelling outcomes with two resolutions of NWP data was carried out for a number of accidental release scenarios of radioactive material. Probabilistic accident consequence modelling simulates the dispersion of a release under many different sequences of meteorological conditions. The transfer of radionuclides through the environment was subsequently modelled, to predict radiation doses and protective action impacts. The comparison of outcomes had the following conclusions.

- In almost all scenarios considered, estimated peak environmental concentrations modelled using finer resolution NWP data were greater than respective values using coarser NWP data.

- For all scenarios considered, estimated environmental concentrations as a function of NWP data resolution agreed within a factor of three.

- Plumes tend to be longer and narrower with NWP data at finer grid resolution compared to coarser grid resolution.

- Differences in modelled high percentile radiation doses using different NWP resolution are driven by predicted precipitation differences, particularly the highest precipitation rates.

- Protective actions are predicted at larger distances from the release with finer-scale NWP than a coarser grid resolution.

- The greatest numbers of people and areas affected as a result of the implementation of protective actions varied with NWP grid resolution.

- Greater protective action impacts as a function of NWP dataset resolution were largely determined by the magnitude of the source term and the

magnitude of the dose thresholds applied, in addition to differences in the description of meteorological parameters.

- Future work assessing whether finer or coarser resolution NWP data as input to atmospheric dispersion models results in better representation of observations from field studies or real events would be beneficial, adding to studies already undertaken and building a stronger evidence base for the use of NWP data. The sparsity of radiological accidents would likely require the consideration of alternative scenarios. The tendency for finer scale NWP data to only be generated in limited area modelling domains makes identifying a suitable scenario more challenging.

Recommendations:

- NWP data providers are recommended to supply supporting information about the NWP model configuration alongside the meteorological data for dispersion modelling, to allow assessment of the quality of the NWP modelling approach. Configuration information should include information about the input datasets used for the NWP model, the spatial and temporal resolution of the NWP model, and any non-standard model options implemented. Comparisons between NWP output data and observations presented here showed that the NWP model configuration often has a greater impact than the resolution.

- NWP data providers are recommended to publish routine model evaluation data to allow dispersion modellers to assess the quality of meteorological data available.

- High quality NWP data at horizontal grid resolutions of 1 - 9 km and hourly temporal resolution can be an adequate substitute for observed meteorological data for use in regulatory dispersion modelling, where locally representative observed data are not available.

- The use of 'base' input variables (wind speed and direction, temperature, cloud cover and precipitation only) from NWP data is recommended for local dispersion modelling, in order to maintain consistency with modelling using observed meteorological data. The use of 'base' input variables allows the local model pre-processor to calculate secondary variables, such as the heat flux and boundary layer height. Values for these secondary variables should not be taken from NWP data, due to the additional uncertainty caused by differences in the heat flux, boundary layer height and thus atmospheric stability variations between NWP and local model pre-processors.

- When using a dispersion model that generates 3-dimensional flow fields over complex terrain from a single upwind condition, such as FLOWSTAR in ADMS, best practice is to drive the model with NWP data with a resolution similar to the modelling domain size to avoid double-counting terrain effects (when the NWP model resolution is finer than the modelling domain) or half-counting (when it is coarser than the modelling domain). This

typically means using the finest available NWP resolution for near-ground sources but potentially coarser resolution for elevated sources.

- If the magnitude of the maximum long-term average concentration is more important than its location, the issue of double-counting terrain effects is unlikely to be significant given the relatively small percentage differences seen in this study. Conversely, if the location of the maximum is more important, greater care should be taken in avoiding double-counting terrain effects.

- If the only NWP data available has finer resolution than the modelling domain, but gridded NWP data is available, the risk of double-counting can be mitigated by spatially averaging the NWP wind data over the grid cells covering the domain and using this as input to the complex terrain model. Other variables (e.g. temperature, cloud cover, precipitation) may still be taken from a single NWP grid cell. If no gridded NWP data is available but the modeller has a choice of single NWP grid cells, the NWP grid cell containing the source may not always be the most appropriate choice; if another grid cell within the modelling domain is less likely to be affected by terrain features within the domain that are larger than the NWP grid cell size this could avoid double-counting their effects.

- This study has considered regulatory dispersion modelling domains with sizes between 1-10 km, suitable for modelling individual or closely-spaced near-ground or elevated sources. For significantly larger modelling domains (e.g. > 50 km) containing multiple spread-out sources, spatial variations in the synoptic meteorology can become important. It may be necessary to use gridded NWP data even at coarse (~10 km) spatial resolution to cover a domain of this size. The use of NWP data with grid resolution coarser than ~10 km is not recommended, as the temporal resolution often becomes coarser than hourly. Further investigation into the use of a regulatory dispersion model that allows for spatially varying input meteorology from NWP models is recommended. This approach is already used in regional-to-local coupled systems that split a larger domain into smaller sub-domains. However, further development of these models would be required to include the effects of complex terrain within each sub-domain.

- For probabilistic accident consequence assessments, the importance of spatial and temporal resolution of NWP data is determined by the acceptable level of uncertainty in the results. The findings of this study suggest that NWP data grid resolutions in the range considered lead to differences of less than a factor of three in the majority of model endpoints calculated. However, the importance of NWP data grid resolution will be greater if any of the following are relevant to an assessment: model endpoints dictated by contributions from deposition onto surfaces; statistical endpoints in the extreme tail of the distribution, for example the 100^{th} percentile; scenarios with a focus on precipitation events. Literature suggests finer scale NWP data tends to result in better agreement between

atmospheric dispersion modelling and observations; therefore it is recommended that finer spatial and temporal resolution NWP data is used where practical.

CONTENTS

1 Overview of project aims and scope 1

2 Introduction to NWP models 3
2.1 Unified Model 5
2.2 WRF 5
2.3 ECMWF IFS and ERA reanalyses 6
2.4 GFS 6
2.5 Other models 7
2.6 Providers 7

3 Review of meteorological models and atmospheric dispersion modelling 9
3.1 Review of Meteorological Models 9
3.1.1 WRF 10
3.1.2 Unified Model 18
3.1.3 ERA and GFS 19
3.2 Review of Atmospheric Dispersion Modelling 19

4 NWP datasets for evaluation 23
4.1 Providers 23
4.2 Locations 24
4.3 Evaluated parameters 30
4.4 Evaluation approach 32

5 Meteorological Evaluation results 35
5.1 Overview of evaluated models 35
5.1.1 APS WRF 35
5.1.2 Lakes WRF 36
5.1.3 Met Office Unified Model 36
5.2 Resolution evaluation 37
5.2.1 Wind speed 38
5.2.2 Wind direction 42
5.2.3 Temperature 46
5.2.4 Precipitation 51
5.2.5 Cloud cover 57
5.3 WRF configuration evaluation 60
5.3.1 Wind speed 61
5.3.2 Wind direction 64
5.3.3 Temperature 67
5.3.4 Precipitation 71
5.3.5 Cloud cover 76
5.4 Comparison of secondary meteorological variables 79
5.4.1 Solar radiation 80
5.4.2 Surface sensible heat flux 83
5.4.3 Boundary layer height 88
5.4.4 Stability 94
5.5 Conclusions from NWP evaluation 96

6 Regulatory Dispersion evaluation 100
6.1 Dispersion study description 100
6.2 Concentration comparison – near-ground source 103
6.2.1 Annual average concentrations 103

6.2.2 98th percentile hourly average concentrations 108
6.2.3 Maximum hourly average concentrations 111
6.3 Concentration comparison – elevated source 114
6.3.1 Annual average concentrations 114
6.3.2 98th percentile hourly average concentrations 120
6.3.3 Maximum hourly average concentrations 124
6.4 Wet deposition comparison 127
6.4.1 Near-ground source 127
6.4.2 Elevated source 131
6.5 Conclusions from dispersion study 134

7 Double-counting terrain effects 140
7.1 Introduction 140
7.2 Comparing finest resolution NWP flow fields with FLOWSTAR 148
7.2.1 Gridded NWP data 148
7.2.2 FLOWSTAR flow fields 148
7.2.3 Long-term flow field plots 149
7.2.4 Short-term flow field plots 155
7.3 Spatially averaged vs single cell NWP data: effect on dispersion and airflow 161
7.3.1 Wind roses 161
7.3.2 Long-term dispersion results 167
7.3.3 Short-term dispersion results 176
7.3.4 Half-counting 179
7.4 Assessing the influence of using only fine scale terrain variations in FLOWSTAR 182
7.4.1 Sennybridge terrain 182
7.4.2 Sennybridge results – quantifying the double-counting of terrain effects 186
7.4.3 Sennybridge results – mitigating the double-counting of terrain effects 189
7.5 Conclusions from terrain effects study 192

8 Use of NWP data for probabilistic accident consequence assessments 194
8.1 Introduction 194
8.2 Methodology 194
8.2.1 Source terms 195
8.2.2 Atmospheric dispersion modelling 196
.2.3 Numerical Weather Prediction data 197
8.2.4 PACE Modelling 197
8.3 Results and Analysis 200
8.3.1 Comparison of environmental concentrations across all scenarios 200
8.3.2 Comparison of environmental concentrations across considered statistical endpoints 207
8.3.3 Comparison of environmental concentrations across statistical endpoints and sensitivity to release location 211
8.3.4 Comparison of environmental concentrations across statistical endpoints and sensitivity to release scenarios and year of meteorological data 213
8.3.5 Comparison of radiological protective actions across considered statistical endpoints 216
8.3.6 Comparison of NAME in PACE model run times when using UKV and global NWP datasets 223

9 Further work 225

References 228

APPENDIX A NWP Extraction Processes 238
A1 APS WRF 238
A2 MO UM 238

APPENDIX B Meteorological Evaluation results per site 240
B1 Resolution evaluation 240
B1.1 Wind speed 240
B1.2 Wind direction 243
B1.3 Temperature 249
B1.4 Precipitation 253
B1.5 Cloud Cover 259
B2 WRF configuration evaluation 265
B2.1 Wind speed 265
B2.2 Wind direction 267
B2.3 Temperature 271
B2.4 Precipitation 275
B2.5 Cloud cover 279
B3 Secondary meteorological variables 284
B3.1 Solar radiation 284
B3.2 Surface sensible heat flux 285
B3.3 Boundary layer height 291
B3.4 Stability 297

APPENDIX C Dispersion comparison 301
C1 Concentration comparison 301
C2 Wet deposition comparison 356

APPENDIX D Double-counting terrain effects 366
D1 Conversion of gridded NWP data 366
D2 Short-term flow field plots for other wind sectors 366
D3 Spatially averaged gridded NWP data 373
D4 Long-term 98th percentile plots 373
D5 FLOWSTAR code modifications 378

1 OVERVIEW OF PROJECT AIMS AND SCOPE

Atmospheric dispersion models require meteorological (met) data as input. Short-range regulatory dispersion models, which are appropriate for source-receptor distances of up to around 50 km, typically require a single set of hourly met data representative of the atmospheric conditions at the dispersion site. Historically, this data has been obtained from measurements taken at nearby met observational stations. More recently, however, the use of data from Numerical Weather Prediction (NWP) models has become increasingly common, due to improvements in resolution, accuracy and availability of this data, along with reduced availability of local observed data due to the closure of some observational stations. Furthermore, the use of data from NWP models in probabilistic accident consequence modelling has become increasingly common because of a shift from short-range to long-range dispersion models, benefiting the assessment of long-range model endpoints, such as the impacts of implementing restrictions on the sale of marketed foods. The current study was commissioned to investigate the influence of NWP horizontal grid resolution on dispersion model outcomes, through:

- Review of literature relating to NWP performance, focusing on grid resolution effects (Task 1, summarised in Sections 2 and 3 of this report);
- Evaluation of NWP data from different models and resolutions, in comparison with measurement data from multiple UK sites (Task 2, presented in Sections 4 and 5);
- Comparison of regulatory dispersion model outcomes using measured and NWP input meteorological data from different models and resolutions, at multiple UK sites (Task 3, results given in Section 6);
- Quantification of the possible 'double-counting' of terrain effects on flow between fine-scale NWP data and regulatory local modelling including complex terrain effects (Task 4, described in Section 7); and
- Investigation of the effect of different NWP grid resolutions on probabilistic accident consequence modelling outcomes (Task 5, presented in Section 8).

The project aimed to develop guidance for modellers about best practice for using NWP data in dispersion modelling, including the significance of grid resolution. It also aimed to quantify uncertainties in modelling outputs derived from differing choices of meteorological data. Some remaining queries and possibilities for further investigations are outlined in Section 9 of this report.

Two previous ADMLC projects, both published in 2002, investigated meteorological data sources for dispersion modelling and the likely effects of uncertainties in input meteorological data on dispersion model outputs. The "Sources of meteorological data for use in dispersion modelling" report (Nelson *et al.*, ADMLC/2002/1) describes both measurement methods and NWP data, though limited to UK Met

Office (MO) NWP with finest horizontal grid resolution at the time of around 11 km. The report also discusses but did not test the likely resulting impacts of differing input meteorological data on dispersion outputs. The "Uncertainty in deriving dispersion parameters from meteorological data" report (Auld *et al.*, ADMLC/2002/2) considered probabilistic effects of uncertainties in input meteorological data on regulatory dispersion model outputs. The majority of work related to uncertainties in measured meteorological parameters and the differing meteorological pre-processing algorithms implemented in ADMS and AERMOD. Differences in calculations of surface heat flux were identified as a key driver in differences in dispersion parameters between different input meteorological datasets and local models. Comparison of wind roses for a single coastal site showed better matching to on-site measurements from NWP data than from a relatively distant meteorological measurement site.

The current study is focused on archived rather than forecast NWP data, in the context of both regulatory dispersion modelling and probabilistic accident consequence modelling. Regulatory modelling applications typically use at least one year of hourly meteorological data from a single, continuously operating site and consider concentration and/or deposition impacts over distances of up to a few kilometres for near-ground sources or tens of kilometres for elevated sources. In contrast, probabilistic accident consequence modelling typically uses gridded meteorological data and considers repeated scenarios of relatively short-term releases, with dispersion typically calculated over a period of a few days post release, with outputs up to hundreds of kilometres from the source. Annual average concentration values are sensitive to mean wind speeds and dominant wind directions from input meteorology, while high percentile outputs are sensitive to specific short-term meteorological conditions, such as low wind speeds and/or high precipitation rates.

Smith (2018) argued that when using the dispersion model itself to account for complex terrain effects, e.g. FLOWSTAR in ADMS or AERMAP in AERMOD, it is best to drive the model with coarser NWP data with a resolution similar to that of the dispersion modelling domain (typically 10-20 km). Finer resolution (e.g. 1 km) NWP data (or indeed observational data) will already contain very localised signals and would therefore lead to "double-counting" by the complex terrain algorithm, amplifying the dominant wind patterns and attenuating the others. Examples from complex terrain sites were presented showing corresponding wind roses from weather station data, from 0.25° (28 km) resolution GFS data and finally from GFS-driven FLOWSTAR at the location of the weather station, and demonstrated that FLOWSTAR is broadly able to reproduce the local terrain effects that are apparent in the observational data but not in the GFS data. Section 7 of this report assesses the impact of potential double-counting of terrain effects between mesoscale and local modelling.

Modelled precipitation for a single grid cell may not be representative of conditions beyond neighbouring grid cells, particularly in complex terrain. However, observed data from a single site may also be unrepresentative of conditions throughout larger scale plume dispersion modelling domains. This uncertainty has not been investigated in the current study.

2 INTRODUCTION TO NWP MODELS

This section gives an introduction to the principles of Numerical Weather Prediction (NWP) models, followed by brief introductions to the models which are commonly used to generate data for dispersion modelling and an overview of organisations providing NWP data for UK dispersion modelling. This provides context to the more detailed review of published literature assessing the effects of NWP model grid scale which is reported in Section 3 of this report.

NWP models predict past, current and future states of the atmosphere by solving mathematical equations derived from physical laws of fluid dynamics and thermodynamics, including the conservation of mass and momentum (Navier-Stokes) and energy (first law of thermodynamics). These equations are solved on a discrete grid that typically divides the atmosphere into columns of grid cells of increasing depth with distance from the surface. The spacing between adjacent surface grid cells determines the (horizontal) resolution of the NWP simulation.

This discretisation of the atmosphere means that any important physical processes that occur on scales smaller than the numerical grid ('sub-grid scales') must be parameterised. Most operational NWP models include parameterisations for the following:

- A planetary boundary layer (PBL) scheme to describe the vertical fluxes of momentum, heat and moisture within the atmosphere due to sub-grid-scale turbulent motions. The PBL scheme is critical for accurate dispersion modelling within the boundary layer (Hu *et al*., 2010), particularly due to its strong effect on the simulated lower-level winds. Different PBL schemes are broadly divided into two categories; local schemes, in which fluxes are calculated via local gradients between adjacent grid cells, and non-local schemes, in which vertical exchanges can also occur between non-adjacent grid cells in a column (Stull, 1988).
- A land surface model (LSM) to calculate land-surface fluxes of heat and moisture based on input land-use data, to provide lower boundary conditions for the PBL scheme.
- A surface layer scheme to calculate the friction velocities and exchange coefficients required to estimate surface heat and moisture fluxes within the LSM and lower-boundary momentum fluxes within the PBL scheme. Surface layer scheme choices and calculations are also dependent on land-use data.
- Shortwave and longwave radiation schemes to estimate surface radiative fluxes and atmospheric temperature trends.
- A cloud microphysics scheme to describe resolved-scale cloud formation and precipitation, which is important for wet deposition estimates in dispersion modelling. At resolutions coarser than around 10 km, a separate cumulus parameterisation may also be required to represent the unresolved updrafts and downdrafts and also the compensating motion outside the clouds in convective regions (Borge *et al*., 2008).

- A turbulence scheme to account for horizontal and vertical diffusion due to sub-grid-scale eddy mixing. This complements the PBL scheme or replaces it in very high-resolution (sub-kilometre) simulations, in which the three-dimensional turbulence spectrum is partly resolved.

Another key technique used by NWP models is data assimilation, or 'nudging', in which observational data are used to update the state of the system, thereby limiting error growth in the simulation. For a forecast, observational data are only available at/around time zero; these data are assimilated into a previous short-range forecast of the atmospheric state at time zero to create a best-guess initial condition for the new forecast. This best-guess state is known as an analysis. Archives of analyses can be used for regulatory dispersion modelling. If the time between consecutive analysis fields is multiple hours, supplementary short-range forecast fields can be used in the intermediate hours if available.

A number of reanalysis datasets are also available. A reanalysis is essentially a hindcast generated from a fixed (optimal) model version and data assimilation system and could therefore be considered a more consistent product. Reanalysis simulations have observational data available throughout the simulation period for the data assimilation system.

Global NWP model simulations cover the Earth's full surface and therefore require no lateral boundary conditions. Due to the significant computational costs of running such a large domain, horizontal resolutions are typically limited to tens of kilometres. If finer resolutions are required, for example to capture local flow field patterns caused by sub-grid variations in terrain or to improve the representation of a coastline, a second limited-area NWP model or modelling domain can be used over the region of interest to downscale the coarse-resolution global model to finer resolutions. Limited-area models (LAMs) therefore often take their initial and boundary conditions from global NWP model outputs.

Models may initially be run for some hours as 'spin-up' from idealised initial conditions to stabilise outputs before the output data are used (Ma *et al.*, 2021). This approach can avoid calculation artefacts due to inaccuracies in initial conditions being included in output meteorological parameters. Models which are initialised from previous runs of the same model generally have lower requirements for spin-up.

Depending on the target resolution, the LAM may require several 'nested' domains to increase the resolution in stages; ratios of 3:1 or 5:1 between parent and nested domain resolutions are commonly used, but larger ratios are occasionally reported (Liang *et al.* 2019). For models using 'staggered' grid approaches, where scalar quantities are defined at grid cell centres and vector quantities at cell boundaries, odd-valued integer resolution ratios are strongly preferred in order to match cell centre and boundary locations between the domains (Skamarock *et al.* 2021). If the exchange of information is only from the parent to the nest, this is known as one-way nesting. In two-way nesting, information exchange is bi-directional, allowing for feedbacks from the finer to coarser domain.

Sections 2.1 to 2.5 provide more details on specific NWP models and reanalyses that are commonly used for dispersion modelling in the UK. Section 2.6 gives a list of some of the current providers of NWP data for dispersion modelling in the UK.

2.1 Unified Model

The Unified Model (UM) is developed and maintained by the UK Met Office (MO). As well as being used for numerical weather prediction, it can also be configured for longer-range climate forecasting using the same dynamical core. This core solves the fully compressible non-hydrostatic equations of motion. The UM is typically run, and its data distributed, by the MO, though some research and other organisations are able to run the model through licensing agreements.

The UM has a number of configurations that are used for operational deterministic numerical weather prediction. These include a global configuration with a current spatial resolution of approximately 10 km, archived at 3-hourly temporal resolution (Walters *et al*., 2019) and a nested higher-resolution configuration over the UK with an inner spatial resolution of 1.5 km, archived at hourly temporal resolution (Bush *et al*., 2020), known as the UKV configuration, that provides more detailed regional weather forecasts.

MO in collaboration with the University of Reading are working on further developments to the UM to enable modelling at 100 m scale, aiming to improve forecasting of small-scale events such as flooding and urban heat. This work may also lead to improvements of the representation of convective processes in kilometre-scale modelling.

2.2 WRF

The Weather Research and Forecasting (WRF) model (Skamarock *et al*., 2020) is an open-source mesoscale NWP system. It is primarily developed and maintained by the US National Center for Atmospheric Research (NCAR). It has a large worldwide community base and is used for both academic research and operational forecasting applications. Although global implementations of WRF have been tested (Zhang *et al*., 2012), it is typically used as a limited area model and is commonly used to downscale (re)analysis or forecast data from coarser-resolution (e.g. global) NWP models.

The WRF system originally comprised two dynamical cores referred to as ARW (Advanced Research WRF) and NMM (Nonhydrostatic Mesoscale Model); further development of the NMM core has been discontinued. It also features a data assimilation system and a system architecture that facilitates the use of parallel computation. WRF-ARW solves the fully compressible nonhydrostatic equations of motion (with a hydrostatic option) and uses a terrain-following vertical coordinate. It allows for one-way or two-way nesting with multiple nests.

WRF features a number of different atmospheric physics options, for example multiple PBL schemes, LSMs, microphysics and radiation schemes. While this provides the user with greater flexibility in terms of determining the optimal configuration for their particular study area, it adds complexity to questions such as "how does WRF performance change with horizontal resolution?", as model performance for a set resolution will also change with different configurations. Different studies on WRF configuration have focused on differing key output variables and used differing versions of WRF, which leads to difficulty in defining a single optimised configuration. Each released version of WRF includes updated atmospheric physics options so recommended configurations can quickly become outdated. When WRF data is provided by third parties, information about the configuration settings should be provided alongside the data.

Because of its highly configurable nature, WRF can be run at resolutions ranging from hundreds of metres to hundreds of kilometres.

2.3 ECMWF IFS and ERA reanalyses

The European Centre for Medium-Range Weather Forecasts (ECMWF) is a research institute which provides an operational NWP forecast service. The comprehensive Earth system model that forms the basis for all ECMWF data assimilation and forecasting activities is known as the Integrated Forecasting System (IFS) (ECMWF, 2021a-b).

ERA5 (ECMWF Re-Analysis, fifth generation) is a publicly available reanalysis dataset that provides hourly fields of meteorological variables from 1950 to the present day (Hersbach *et al*., 2020). It was generated using version CY41R2 of the IFS. The dataset covers the entire globe on a grid with a base resolution of around 30 km. It replaces the ERA-Interim reanalysis, which had a spatial and temporal resolution of around 80 km and 6 hours respectively.

ERA5 data can be downloaded from the Copernicus Climate Change Service (C3S) Climate Data Store (CDS, 2022) either through a web interface or using a Python-based API (Application Programming Interface). Data are in GRIdded Binary (GRIB) format, though free tools are also available to convert to network Common Data Format (netCDF).

2.4 GFS

The Global Forecast System (GFS, 2022) is the NWP modelling system run by the US National Centres for Environmental Prediction (NCEP), an arm of the National Oceanic and Atmospheric Administration's (NOAA) National Weather Service (NWS). Gridded forecast and analysis data are freely available, making GFS one of the world's most widely-used NWP models.

As well as generating the analyses used for the GFS forecasts, NCEP also generate FNL (final) analyses which lag behind the forecasts slightly so that they can include more observational data in the Global Data Assimilation System (GDAS).

GFS is run globally at a resolution of 0.125°, though data are currently only available at half this resolution (0.25° or 28 km at the equator) or coarser. Historical FNL analysis GRIB data at the finest (0.25°) resolution are available at 6-hourly intervals from 2015 to present via the Research Data Archive at the National Center for Atmospheric Research (NCAR, 2022).

GFS data are commonly used as the initial and boundary conditions for finer-resolution limited-area models such as WRF.

2.5 Other models

The MM5 (Fifth-Generation Penn State/NCAR Mesoscale Model) is another limited area model that is often viewed as the precursor to WRF. While active development of MM5 ended in 2005, the model is still used by some organisations to downscale global atmospheric analyses or forecasts, or provide inputs to air quality models. Like WRF, MM5 uses a terrain-following sigma coordinate system, allows for 4D data assimilation, can be configured as either hydrostatic or non-hydrostatic, and allows for one-way or two-way nesting.

NEMS (NOAA Environmental Modelling System) is a modelling framework used by NCEP. The NEMS-NMMB (Nonhydrostatic Multiscale Model on B-Grid) is the NWP model used for the NAM (North American Mesoscale) forecast system in order to generate forecasts over North America, but has also been used by other organisations to simulate in other regions of the globe. It can be run globally or regionally with embedded nests. Within NAM, four one-way nested domains are used, down to around 4 km resolution.

2.6 Providers

Table 1 gives a list of providers of NWP met data for UK dispersion modelling purposes, typically supplying time-series of data at a single site extracted and reformatted from NWP model outputs into appropriate format(s) for commonly used local dispersion models. Some providers may also be able to supply raw NWP outputs of spatially gridded and time-varying data and/or processed gridded meteorological data, for example for the CALPUFF dispersion model. Providers' approaches to data extraction from NWP model output to single site data files for a required location may use data from the nearest available grid cell or interpolation between data from nearby grid cells. This list is accurate as of the time of writing (summer 2023) and is not necessarily exhaustive. The order is alphabetical.

Table 1 Overview of providers of NWP data for UK dispersion modelling

Provider	NWP model(s) used	NWP model grid resolution(s) available	Single site dispersion model format(s) available	Notes, including availability of gridded data for dispersion modelling
ADM Ltd*		"less than 5 km"	ADMS, ISC (for BREEZE Roads), AERMOD, GasSim, AUSTAL, EDMS, STAR	- Data available worldwide from 2010 onwards - Listed within the Defra's LAQM TG(09) guidance as a supplier
Air Pollution Services†	WRF	3 km	ADMS, AERMOD, ISC (for BREEZE Roads), GasSim, AUSTAL, EDMS, STAR	- Data are available for multiple years, pre-processed for every 3 km x 3 km grid square in the UK - WRF is run with domains at 27 km and 9 km resolution; nested 1 km domains can be set up on request
AS Modelling & Data Ltd‡	GFS	Underlying operational GFS resolution (base 0.125°≈14 km)	ADMS (other formats may be available on request)	- Gridded and site-specific data available. - Standard ADMS variables pre-extracted but all GFS variables available
Enviroware§	WRF	9, 3 km	AERMET / AERMOD	- Data available worldwide from 2012 onwards - 3D gridded data for CALMET/CALPUFF also available
Lakes Environmental**	WRF	12, 9, 4, 3 km	AERMET / AERMOD	- Data available worldwide from 2006 onwards - 3D gridded data for CALMET/CALPUFF model (WRF or MM5) also available at 1, 4, 12 km resolutions
MeteoSim††	WRF	9, 3, 1 km	ADMS AERMET / AERMOD	- Data available worldwide from 1995 onwards - Online automated pricing tool - 3D gridded data for CALMET/CALPUFF also available
Met Office‡‡	Unified Model	10 km (Global) 1.5 km (UKV)	ADMS Possibly others (contact)	- Contact Met Office directly via email / phone to order ADMS-format data

* https://www.aboutair.com/data-purchase/
† https://www.airpollutionservices.co.uk/meteorological-nwp-data/
‡ https://asmodata.co.uk/
§ https://www.enviroware.com/portfolio/meteodata/
** https://www.weblakes.com/met-data/order-met-data/ and https://weblakes.myshopify.com/collections/meteorological-data

3 REVIEW OF METEOROLOGICAL MODELS AND ATMOSPHERIC DISPERSION MODELLING

This section reports the findings of the Task 1 literature review of the effects of NWP model grid resolution on the quality of model outputs (Section 3.1). Some additional literature relating to the effects of NWP model grid resolution on large scale dispersion model outputs is outlined in Section 3.2.

3.1 Review of Meteorological Models

The following section reviews the performance of the NWP models identified in Section 2 as being regularly used for UK dispersion modelling. The focus of the review is on the accuracy of predictions for meteorological variables particularly relevant to dispersion modelling (near-surface wind speed and direction, near-surface temperature, cloud cover and precipitation) and how the accuracy of predictions varies with model grid resolution. NWP predictions of boundary layer height have also been reviewed, as while this is not a routinely measured parameter, it can optionally be input into some local dispersion models. For NWP models that provide flexibility in terms of the model physics options used in the simulation, e.g. WRF, the effect of model configuration on prediction accuracy is also explored.

The scope of this study focuses on historical NWP data taken from (or driven by) (re)analysis fields, possibly supplemented by short-range forecast fields in the intermediate hours, in order to minimise the effects of forecast error when comparing model outputs with observational met data.

When comparing NWP model outputs against observational data, it is important to remember that observational data are derived from single-point measurements whereas NWP data represent grid-cell averages. NWP data may be extracted from the nearest grid cell or interpolated between the grid-cell values surrounding a required output location. The approaches of single grid cell extraction or interpolation between surrounding cells are expected to give similar results in most cases, as NWP variables are likely to vary smoothly between neighbouring grid cells. However, there may be greater differences between these approaches at coastal locations where there can be a substantial change in parameters between neighbouring cells over land and sea.

[††] https://metdata.meteosim.com/en/
[‡‡] https://www.metoffice.gov.uk/services/data/business-data

Temporally, observational data are usually reported as time-averaged values and are typically compared against instantaneous NWP data (noting also that there is an implied averaging time associated with the NWP model's spatial resolution). There are also differences in the measurement uncertainties for different meteorological parameters (WMO, 2018), with notably higher uncertainties for precipitation rates and cloud cover compared to wind speed, direction and temperature. Thus, even for a 'perfect' model, differences between modelled and observed values are expected due to the fact that the data represent different spatial and temporal scales (Hanna and Yang, 2001), as well as inherent uncertainties in both modelled and observed data. Furthermore, even if model outputs tend towards observational data as the grid resolution increases, this does not necessarily imply that finer resolution is always better for dispersion modelling purposes. Localised terrain effects may mean that the fine-resolution/observational data is less representative of the entire modelling domain than more spatially-averaged data that better describes the synoptic-scale flow (Smith, 2018), particularly when modelling elevated pollution sources (Kumar *et al*., 2021).

3.1.1 WRF

3.1.1.1 Configuration

Due to WRF's highly configurable nature and the fact that it is open source, there have been numerous WRF configuration studies published, e.g. Borge *et al*. (2008), Hu *et al*. (2010), Carvalho *et al*. (2012), Beevers *et al*. (2013), Santos-Alamillos *et al*. (2013), Xie *et al*. (2013), Shrivastava *et al*. (2015), Arasa *et al*. (2016), Siuta *et al*., (2017), and Fernández-González *et al*. (2018). While some common findings can be identified across these studies, it is also clear that there is no consensus on what is considered the 'best' configuration. Different physics options bring their own strengths and weaknesses, and the best combination will depend on the particular location being modelled and the intended application of the model; there is no 'one size fits all' (Shrivastava *et al*., 2015). In addition, the available configuration options change with each release of WRF, so 'optimal' configurations can rapidly become outdated. There is some advice available about best practice from the WRF developers[§§], for example that simpler microphysics schemes are more appropriate for coarser resolution model grids. Some configuration options are recommended for specific grid resolution ranges, for example convection parameterisations are required for coarser resolution modelling (≥10 km), but not for finer resolution modelling (≤ 4 km), with a 'grey area' for intermediate resolutions of 4 – 10 km where convection is neither well resolved nor appropriately parameterised. However, some recently developed 'scale-aware' convective parameterisations can adapt to the grid resolution.

Kumar *et al*. (2017) provide a summary of studies that have utilised WRF for air quality modelling applications, including discussions of optimal configuration,

[§§] https://www2.mmm.ucar.edu/wrf/users/namelist_best_prac_wrf.html

though this differs between studies. Some additional studies are summarised below, beginning with those that focus on simulations within the UK.

Beevers *et al*. (2013) conducted a WRF optimisation study for the purposes of improving the CMAQ-UK regional dispersion modelling system. Using a fixed horizontal grid resolution of 10 km over the UK with a surface layer depth of around 15 m, they tested various WRF PBL schemes, LSMs and surface layer schemes. They compared model output against observational data from 169 UK weather stations and 8 radiosonde sites over two separate months (January and July 2006). While there was no clear-cut 'best' configuration for all locations, the most consistent combination of physics options was the Asymmetric Convective Model version 2 (ACM2) PBL scheme, the Rapid Update Cycle (RUC) LSM and the Pleim-Xiu (P-X) surface layer scheme. They demonstrated that the simulated near-surface wind speed is particularly sensitive to the choice of PBL scheme (Figure 1), with some schemes (YSU and BouLac) giving significantly higher over-prediction (of up to around 0.75 m/s) during the evening/overnight period as a result of predicting a shallower diurnal stability range (insufficiently stable at night). Temperature, relative humidity and wind direction showed more consistent agreement with the observed average diurnal profiles across the different schemes. All configurations led to large under-predictions in surface observations of cloud cover (50-60%) and precipitation. This could be due to the relatively simple microphysics scheme which was tested and the fairly coarse 10 km resolution where convective effects are parameterised rather than resolved. The distribution of boundary layer heights predicted by the optimal configuration was qualitatively similar to other published data. The WRF simulation was driven by GFS analyses, and it was found that nudging all model layers using the shortest nudging time interval (6 hours) throughout the simulation was optimal. It was also concluded that increasing the number of vertical layers from 23 to 35 did not improve simulation accuracy enough to warrant the large (roughly doubled) computational time cost.

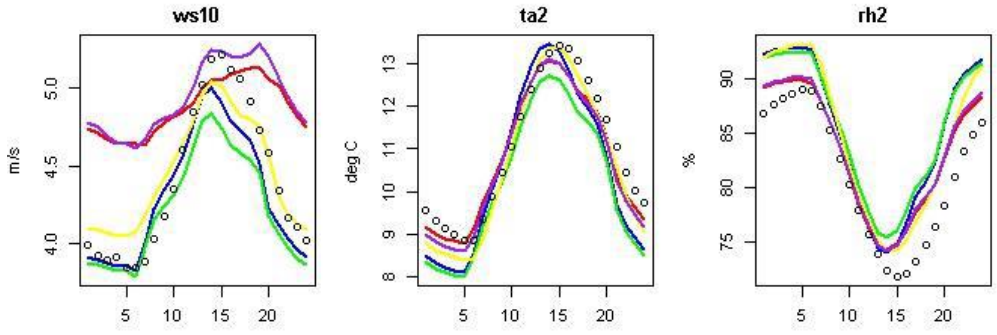

Figure 1 – Taken from Figure 3 of Beevers *et al*. (2013). All sites and the Jan 06 and Jul 06 period average of diurnal profiles of wind speed at 10 m (ws10), temperature at 2 m (ta2) and relative humidity at 2 m (rh2) for various different tested PBL schemes (blue = MYNN3.3.1, red = YSU, green = MYNN3.4, yellow = ACM2, purple = BouLac, black circles = observations)

Xie et al. (2013) tested various WRF PBL schemes in simulations over Southeast England, including two non-local schemes (ACM2 and YSU) and two local schemes (MYJ and MYNN2). As well as validating the model against measured data from eight weather stations, boundary layer heights determined from Doppler LiDAR (Light Detection and Ranging) data were also compared against simulated boundary layer heights. Initial and boundary conditions were taken from GFS FNL analyses at 1° spatial and 6 hourly temporal resolution, and three nested domains with horizontal resolutions of 27, 9 and 3 km were used. 50 vertical layers were used, with a surface layer depth of approximately 17.5 m. The radiation schemes (RRTM for longwave, Dudhia for shortwave), microphysics scheme (WSM 3-class scheme), LSM (Noah) and cumulus scheme (Grell-Devenyi; applied in the 27 and 9 km domains only) were fixed for all simulations. Two full months (June and November 2007) were simulated, each broken down into consecutive 4-day simulations with one day overlap to allow for model spin-up. As suggested by Carvalho *et al*. (2012), when using WRF to downscale analyses, it is better to limit individual simulation times to a few days in order to avoid large divergence errors from the analyses. It was shown that the local PBL schemes struggled to model the convective PBL accurately. Boundary layer heights obtained with ACM2, which uses the bulk Richardson number method, were generally in better agreement with the observations during both stable and unstable conditions. The ACM2 PBL scheme also led to generally better statistics (index of agreement, RMSE and mean bias) for predicting 2 m temperature and 10 m wind speed in both June and November.

Cai *et al*. (2019) looked specifically at the effect of different WRF physics options and downscaling options on rainfall estimates over part of Northwest England. A range of different types of rainfall events were simulated, including convective, frontal and orographic events, and model outputs compared against data from 50 rain gauges within the modelling region. Only those schemes that were thought to have a significant effect on simulated rainfall, namely the microphysics, cumulus and PBL schemes, were altered, with a total of 24 configurations. The shortwave/longwave radiation schemes (Dudhia/RRTM) and LSM (Noah) remained fixed. ERA-Interim reanalyses were used to drive the model. Three downscaling configurations were tested, each with three nested domains. The resolution of the innermost domain in each case was 10, 5 and 1 km, respectively. 28 vertical layers were used in the simulations but no information about the surface layer depth is available. While statistics of individual physics combinations were not presented, ensemble spread showed that, for the 1 km resolution downscaling configuration, results were most sensitive to changes in the cumulus scheme (applied in the coarsest nest only) for intense convective rainfall events but most sensitive to the PBL scheme for light rainfall events. Light rainfall events were best simulated with the 5 km resolution downscaling configuration (overestimated with the 1 km resolution configuration) whereas intense rainfall events that exhibit sharp spatial variations were only adequately simulated with the 1 km resolution configuration. The 10 km resolution configuration was the least accurate, and varying the physics options made little difference to this.

WRF is typically used to downscale global (re)analyses. When evaluating model performance, it is therefore important to remember that total errors will be a combination of those associated with the driving met data as well as those associated with WRF itself. Fernández-González *et al*. (2018) tested driving their WRF simulations with two different sets of initial and boundary conditions – GFS and ERA-Interim – downscaling to 1 km resolution over an area of complex terrain in Spain. They used 61 vertical layers in total, with eight layers within 120 m above ground. They found that while overall performance was similar, each dataset had its own set of (dis)advantages. GFS tended to be more accurate under weak wind conditions, while ERA-Interim performed better under strong wind conditions. The overall mean absolute error for wind speed was slightly lower with GFS. Carvalho *et al*. (2014) determined that ERA-Interim provided better initial and boundary conditions than GFS in their WRF simulations in Portugal but that both were viable options for accurate near-surface wind modelling.

The tendency of WRF to over-predict surface wind speeds is seemingly common (Borge *et al*., 2008; Beevers *et al*., 2012; Horvath *et al*., 2012; Kumar *et al*., 2021). Beevers *et al*. (2012) compared WRF-modelled 10 m above ground wind speeds (at 3 km resolution) with observational data from 147 UK weather stations located in a variety of settings (rural, urban, coastal) over a full year. They found that, on average across all met stations, WRF tended to over-predict wind speed by around 1 m/s at night (~+22% bias) falling to around 0.5 m/s (~+9% bias) in daylight hours, despite the use of observational nudging. Conversely, across the 14 urban sites, wind speed was slightly under-predicted at night with larger under-predictions during the day. Jiménez and Dudhia (2012) acknowledged WRF's positive wind speed bias over plains and valleys, and negative bias over hills and mountains, and proposed a new parameterisation that better accounts for the momentum sink effects of unresolved topographic features. They demonstrated the new scheme's effectiveness in simulations over complex terrain in northern Spain, in which the Mean Absolute Error (MAE) of the mean wind speed was reduced from 1.85 to 0.72 m/s and systematic error was not apparent. This was added to the YSU PBL scheme as an option in WRF version 4 (Skamarock *et al*., 2020).

3.1.1.2 Resolution

Again, due to its large user base, there are a substantial number of WRF studies that investigate the effect of resolution on model performance, e.g. Heikkilä *et al*. (2011), Carvalho *et al*. (2012), Horvath *et al*. (2012), Santos-Alamillos (2013), Arasa *et al*. (2016), Siuta *et al*., (2017), Fernández-González *et al*. (2018), Cai *et al*. (2019), Solbakken *et al*. (2021), Squitieri and Gallus (2020).

Solbakken *et al*. (2021) used WRF to evaluate the impact of grid resolution on simulated near-surface winds in a region of complex terrain in coastal Norway. Four nested domains with resolutions of 27, 9, 3 and 1 km were compared. 50 vertical layers were used, no information is available for the surface layer depth. The largest domain was driven by ERA5 reanalyses. In terms of traditional evaluation metrics including mean bias, MAE and RMSE, increasing the resolution from 27, through 9, down to 3 km led to significant improvements in simulated wind speeds, while increasing the resolution further to 1 km led to no further

reductions (and in many cases increases) in these error metrics. This trend of improved model statistics with increasing resolution until a 'saturation point' is also reported in other similar studies (Mass *et al*., 2002; Siuta *et al*., 2017). Conversely, metrics that analyse data spread and mean wind features, including standard deviation, frequency histograms and wind roses, indicated that there was benefit to increasing the resolution from 3 to 1 km, in which local topographic features are better resolved. One set of wind roses from this report are reproduced in Figure 2, in which it can be seen that the ERA5 data and coarsest resolution WRF domains are unable to capture the strong south-easterly wind patterns, and only the finest resolution domain predicts a significant frequency of wind speeds above 15 m/s, as seen in the observations. It was suggested that while the 1 km resolution is able to simulate smaller-scale wind patterns more accurately, these features are more susceptible to positional errors (in both space and time) which are penalised by traditional evaluation metrics like bias and RMSE.

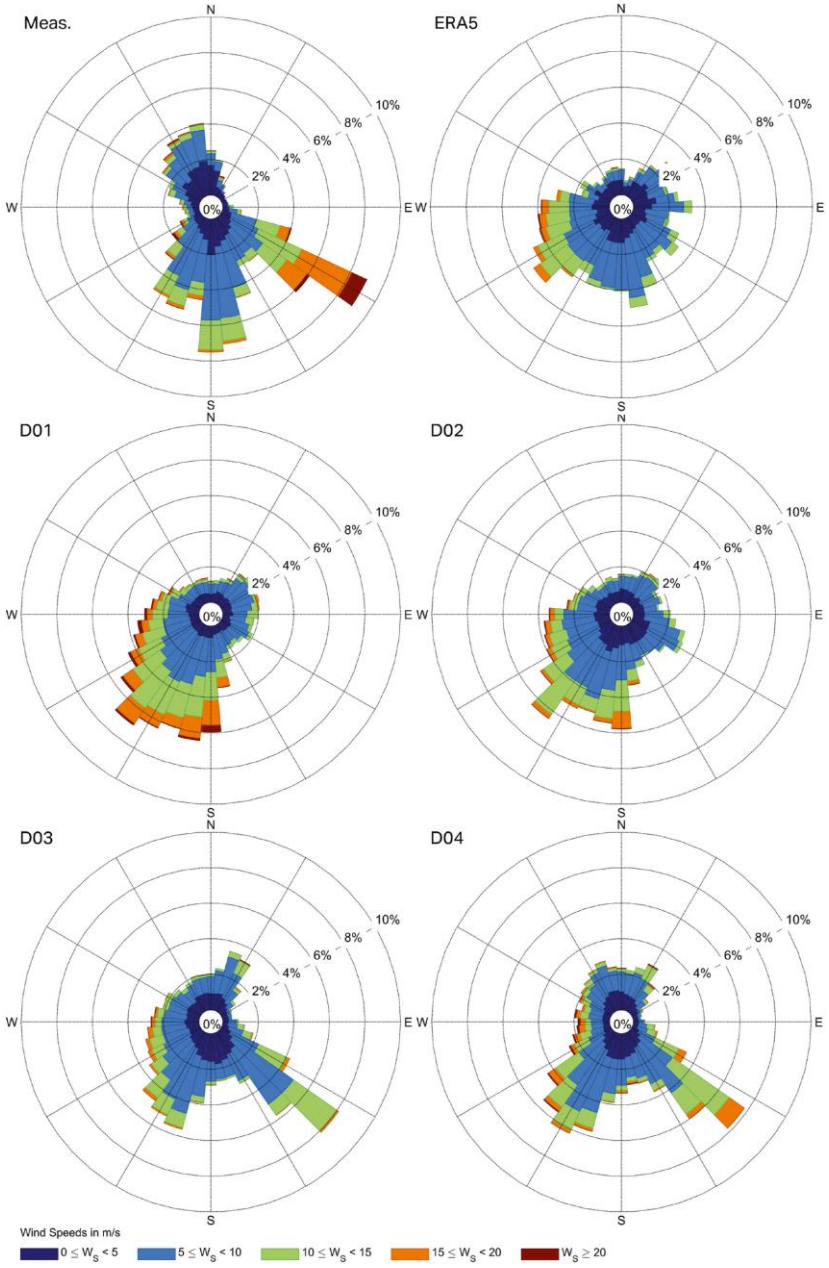

Figure 2 – Taken from Fig. 7 in Solbakken *et al*. (2021), showing measured and modelled wind roses at a location situated in complex terrain in coastal Norway (location C in their paper). Modelled wind roses correspond to ERA5 reanalysis data (used to drive WRF) and the four nested WRF domains D01-D04, with resolutions of 27, 9, 3 and 1 km respectively.

In contrast to the previous set of studies, some have reported improvements in traditional error metrics even at fine resolutions (Carvalho *et al*., 2012; Arasa *et al*., 2016; Fernández-González *et al*., 2018), indicating that other factors such as site characteristics and model configuration can be important. Fernández-González *et al*. (2018) observed noticeable improvements in near-surface wind speed bias and mean absolute error in their 1 km domain compared with their 9 and 3 km domains in their simulations over complex terrain in northern Spain.

Correlation, however, did not increase with resolution, again possibly due to phase errors. Carvalho *et al*. (2012) found that increasing the resolution from 3.6 to 1.2 km produced a lower RMSE, bias and standard deviation error for wind speed and direction in their WRF simulations over an area of complex terrain in Portugal. Arasa *et al*. (2016) conducted a validation of their optimally-configured operational WRF forecast system over Huelva (Spain) using two years of observational met data. At one met station, WRF output from two different grid resolutions (1 km and 0.333 km) was analysed. The finer resolution data showed an improvement in wind speed simulation accuracy, with the magnitude of mean bias reducing from -1.5 to 0.3 m/s and the percentage of hours where the wind speed was within 2 m/s of observed increasing from 61 to 84 %. Improvements were also seen for relative humidity. Conversely, temperature and wind direction were less accurately predicted at the finer resolution, with the percentage of hours where the temperature (wind direction) was within 2°C (30°) of observed decreasing from 79% (64%) to 57% (47%). It should be noted that the sub-kilometre resolution domain employed a LES (Large-Eddy Simulation) approach rather than using a PBL scheme.

Heikkilä *et al*. (2011) used WRF to downscale ERA-40 reanalysis data (a predecessor to ERA5 with a base resolution of 111 km) to horizontal resolutions of 30 and 10 km over Norway over a 30-year period. 40 vertical grid layers were used in this model configuration. Comparisons with surface observational data showed that WRF provided significant benefit compared with the ERA-40 data in predicting precipitation, particularly in relation to extreme values, due to the better representation of complex terrain and the associated orographic lifting. The finest resolution domain was judged to provide the highest overall model skill based on its improved ability to predict the intensity and frequency of individual precipitation events compared to the coarser resolutions. Mean temperature bias was also reduced as the resolution increased. Conversely, 10 m above ground wind speed predictions did not show significant improvements between the three model resolutions, indicating that resolutions finer than 10 km may be needed to capture the complex surface flow patterns in this mountainous region, along with finer-detail land use data. The 10 km simulation did however improve the wind speed bias at coastal sites, likely due to the better representation of the coastline.

The benefit of employing finer WRF model resolution in a region of complex terrain for simulating accumulated precipitation was also demonstrated by Moya-Álvarez *et al*. (2019), who found that their coarsest resolution of 18 km gave the lowest skill while their 3 and 0.75 km domains were able to better reproduce observed rainfall data over central Peru. All domains used 28 vertical grid layers. Similarly, Soares *et al*. (2012) observed significant improvements in simulated orographic precipitation over Portugal, particularly in relation to extreme rainfall events, when downscaling ERA-Interim (111 km resolution) reanalysis fields to 27 and 9 km using WRF. They used 49 vertical grid layers, with a surface layer depth of approximately 10 m and ten layers within around 425 m above ground.

Clearly, resolving finer-scale geographical features as the model grid resolution increases can only be achieved if the input geographical data is itself fine enough. Zhang *et al*. (2014) demonstrated the importance of increasing the resolution of

the topographical data in line with that of the model grid by running WRF over Hong Kong at four different horizontal grid resolutions (27, 9, 3 and 1 km, no information about vertical grid) with four different resolutions of DEM (Digital Elevation Model) data (10′ ≈ 18 km, 2′ ≈ 3.7 km, 30″ ≈ 900 m and 3″ ≈ 90 m). WRF automatically reprocesses DEM data that are finer than the model resolution to the representative grid scale. As shown in Figure 3, for the 1 km grid simulations, using the finest resolution DEM data led to a 38 % reduction in MAE for temperature compared with using the coarsest DEM data. This will partly be due to the reduced differences between real and simulated elevation at the output locations with finer DEM resolution. Similar reductions are seen for relative humidity, while wind speed and direction both show a sharp initial reduction as the DEM resolution increases before levelling off at finer resolutions. The effect of increasing the model resolution itself has little effect on the MAE in this study, except for temperature where the MAE is reduced from 2°C at 27 km resolution to 1.2°C at 1 km resolution (using the finest resolution DEM data). Similarly, Horvath *et al*. (2012) found that reduced grid spacing (below 1 km) did not generally improve simulation bias and RMSE of 10 m wind speeds at their study site in Nevada. They used 37 vertical layers with a surface layer depth of approximately 10 m above ground.

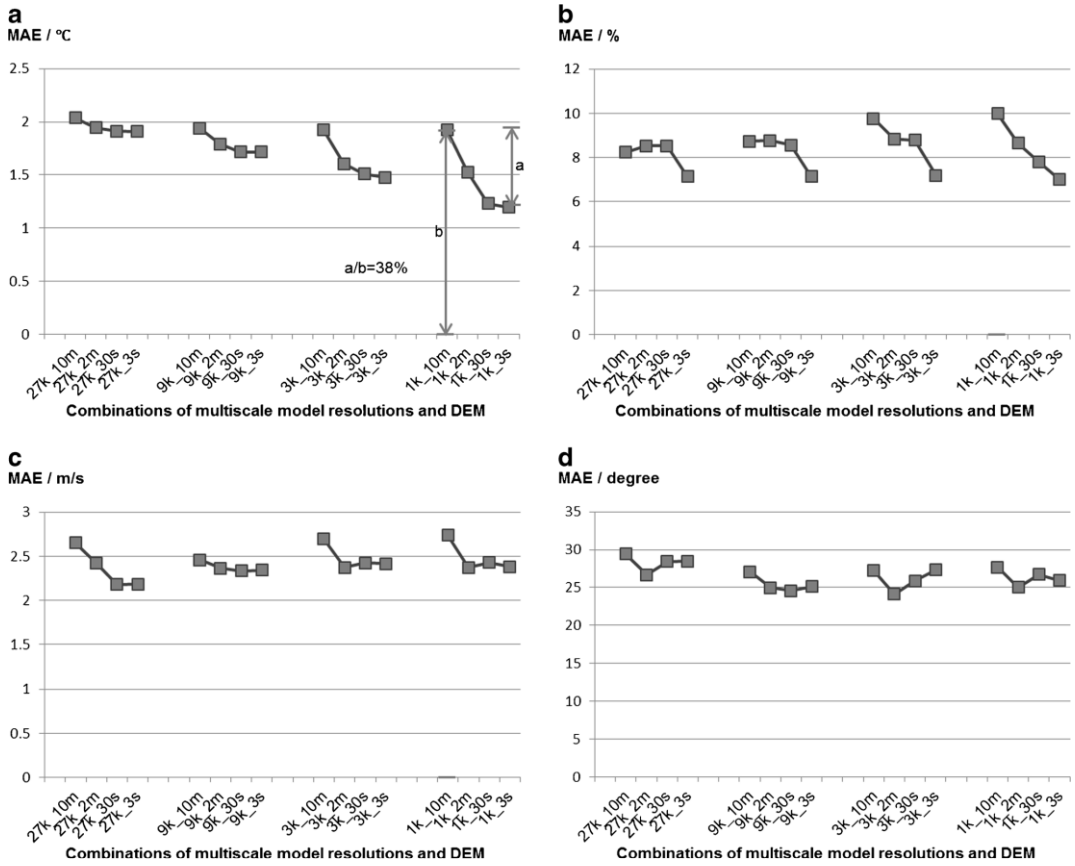

Figure 3 – Taken from Fig 5 in Zhang *et al*. (2014). Shows the separate effects of increasing the resolution of the model grid and the resolution of the input geographical data on mean absolute error (MAE) for (a) temperature, (b) relative humidity, (c) wind velocity and (d) wind direction.

Squitieri and Gallus (2020) used WRF to model 14 'Mesoscale Convective Storms' in the US Great Plains region of flat terrain. They found slight improvements of a forecast skill metric and in the representation of the locations of precipitation for 1 km grid resolution compared to 3 km, but limited additional benefit from 333 m grid resolution. This study highlights that the simulation of some meteorological features in flat terrain can also be sensitive to grid resolution. Intense convective rainfall is significant for accident consequence modelling where short-term wet deposition can influence peak deposition concentrations. However, for regulatory modelling of long-term wet deposition the impact of peak precipitation events is more limited.

3.1.2 Unified Model

Middleton (2008) analysed UM data at two different resolutions (40 and 12 km) in terms of the model's ability to reproduce the stability distribution derived from UK observational data. Both resolutions were found to give an adequate representation of the distribution at inland sites, while at coastal sites the 40 km resolution data significantly over-predicted the occurrence of neutral stability hours (at the expense of predicting too few hours in the stable regime) compared with the 12 km resolution data and conditions derived from observed data. The 40 km distribution was strongly affected by the marine boundary layer, in which the higher specific heat capacity of the sea leads to a narrower stability range. This highlights the importance of adequately resolving the coastline in order to prevent the heat flux on land from being excessively influenced by marine conditions.

Hanley *et al*. (2019) notes that the 1.5 km resolution UKV configuration of the UM, with 70 vertical levels, has a tendency to over-predict heavy convective rain and thus domain-average precipitation, but demonstrated that a change to the sub-grid mixing scheme used by UKV improves this.

Bush *et al.* (2020) describe separate fine-scale configurations of the UM suitable for mid-latitudes and for tropical regions, with an assessment method which allows for some spatial uncertainty in model predictions. This paper also describes modifications to cloud fraction calculations and modelling of convective cloud and precipitation between the global and fine-scale configurations of the UM.

Roberts and Lean (2008) ran the UM with grid resolutions of 12, 4 and 1 km over southern UK for two 10-day summer periods in which convective rainfall occurred. The 12 km and 4 km resolutions use 38 vertical grid layers whereas the 1 km resolution uses 76 grid layers. The 1 km resolution does not use any convective parameterisation, the 12 km resolution uses full convective parameterisation. The authors note that convective parameterisations are required at the 4 km grid scale but are not designed for this scale, a modified convective parameterisation was implemented at this resolution as a partial solution. They compared simulated rainfall estimates against radar data, using a fractional coverage approach over various spatial scales. The finest resolution simulation was shown to be the most skilful at all but the smallest scales as a result of a more accurate distribution of rainfall. The authors point out that if the model had only been evaluated at the grid scale, e.g. using fixed-point observational data, the improvement of the 1 km

resolution simulation would not have been detected or may even have appeared worse. This is due to small discrepancies in the location and timing of predicted precipitation from fine-scale modelling, which are penalised by single-point comparisons but may still lead to better representations of fractional coverage over a wider area from the finer resolution modelling than coarser grid resolutions.

3.1.3 ERA and GFS

Ramon *et al*. (2019) recently compared five global reanalysis datasets, including ERA5 and its predecessor ERA-Interim, in terms of their ability to simulate low-level wind fields, using observational data from 77 land-based measurement sites around the globe. The horizontal spatial resolutions of the global datasets range from 0.3°x0.3° (approximately 800 m, ERA5, with 137 vertical layers) to 1.875°x2°, with associated 1 to 6 hour temporal resolution and 28 – 137 vertical layers. ERA5 was shown to provide the most accurate near-surface wind characteristics in terms of correlation and variability. ERA5 was also shown to outperform four other reanalysis datasets in simulating temperature, wind speed and specific humidity over the Arctic (Graham *et al*., 2019).

Olauson (2018) demonstrated that ERA5 reanalysis data was able to produce effective near-surface wind fields for the purpose of wind energy modelling.

3.2 Review of Atmospheric Dispersion Modelling

The following section reviews the effects of applying different grid resolutions of NWP data as input to atmospheric dispersion models. The focus of the review is on (i) whether or not more finely resolved NWP data typically results in model results which differ compared with the respective model results derived using more coarsely resolved NWP data and (ii) whether or not more finely resolved NWP data typically results in model results which are in better agreement with observations. The studies are considered in chronological order.

Nasstrom and Pace (1998) evaluated the effect of different temporal and spatial resolutions of NWP data on Lagrangian particle long range dispersion simulations using the European Tracer Experiment (ETEX). The US Department of Energy's Atmospheric Release Advisory Capability (ARAC) program was applied. Higher resolution European Centre for Medium-Range Weather Forecasts (ECMWF) and lower resolution Navy Operational Global Atmospheric Prediction System (NOGAPS) NWP forecast and analysis data was used. The NOGAPS data had a horizontal resolution (latitude and longitude) of 2.5°, 4 vertical levels below 500 mb and a temporal resolution of 12 hours. The ECMWF data had a horizontal resolution of 0.5°, 7 vertical levels below 500 mb and a temporal resolution of 6 hours. An ECMWF dataset with decreased horizontal (2.5°), vertical (4 levels) and temporal (12 hours) resolution was also considered. A real time study applying forecast NWP data and a post experimental study applying analysis NWP data was conducted. Model results were compared with measured tracer concentrations in ground level air. The use of higher resolution ECMWF data produced significantly better agreement between concentrations predicted with the dispersion model and ETEX measurements than the use of lower resolution NOGAPS data. Degrading

the horizontal and temporal resolution of ECMWF data resulted in decreased accuracy of the dispersion simulations. Previous studies by Brost *et al.* (1988), McNider *et al.* (1988), Moran and Pielke (1996) and Gupta *et al.* (1997) supported the conclusions of Nasstrom and Pace (1998) that time and space resolution of NWP data are important to long-range (20-2000 km) dispersion modelling.

Hort and Athanassiadou (2005) compared environmental concentrations, derived using the UK Met Office's NAME model, across three NWP analysis datasets: 4 km high resolution hourly data, 12 km mesoscale hourly data, and 60 km global 3 hourly data. 38 vertical levels were applied across all three datasets. This study was purely an intercomparison of modelled results; no observations were included in the analysis. A single scenario was considered, with a release duration of 24 hours. Maximum time averaged air concentrations and total wet deposition concentrations were estimated over two timesteps (5 and 17 hours after the start of the release). Time integrated air concentrations (TIAC) were estimated over one timestep (17 hours after the start of the release). At both timesteps the application of global NWP data resulted in the lowest estimated maximum time averaged air concentrations. For one timestep, the application of high resolution NWP data resulted in the largest estimated maximum time averaged air concentrations. For the other timestep, the application of mesoscale NWP data resulted in the largest estimated maximum time averaged air concentrations. Analysis of TIACs revealed that with increasing NWP resolution, the integrated plume widened. Hort and Athanassiadou (2005) propose that this was likely due to higher resolution models capturing a greater amount of orographically induced spread that the equivalent scale parameterisations in more coarsely resolved models struggled to represent. At both timesteps considered, the application of mesoscale NWP data resulted in the smallest, and the application of high resolution NWP data resulted in the largest, estimated maximum wet deposition concentrations.

Davis and Dacre (2009) ran the NAME model for a single scenario (the European Tracer Experiment) across a range of temporal resolutions (15 minutes to 3 hours) and two spatial resolutions (12 x 12 km and 50 x 50 km). The goal of the study was to determine if improving the representation of a front that passed over the source location during the release, through increasing the temporal and spatial resolution of the meteorological input to NAME, would lead to improvements in model predictions of plume location and average air concentrations. Only minor qualitative differences were observed when varying the temporal resolution, although there was a tendency for peak concentrations to be reduced as the temporal resolution increased from 3 hours to 15 minutes. When spatial resolution was increased, considerable differences were observed. Throughout the simulation the plume was narrower when using the higher (12 km) spatial resolution NWP data. The 12 x 12 km NWP model captured the change in wind speed and direction due to the passage of a (cold) front significantly better than the 50 x 50 km model. Overall, when comparing individual stations, the spatial distribution of the surface tracer plume appeared to agree better with observations for the higher spatial resolution meteorological data simulation. To quantify changes in predicted plumes caused by changing temporal and spatial resolutions, a statistical analysis

was performed. Two statistical performance metrics were used: (i) the Pearson's correlation coefficient, which determines how well modelled and observed tracer concentrations agree spatially; (ii) fractional bias (FB), which is a measure of mean bias, indicating systematic errors which lead to consistent underestimates or overestimates of measured values. For the first 24 hours of the simulation, increases in spatial and temporal resolution of NWP data had no significant effect on either statistical metric. Estimates of the Pearson's correlation coefficient demonstrated that increased spatial resolution led to a significant improvement in the correlation (with observations) for the second half of the simulation. In the second 24 hours the FB indicated better agreement (than the first 24 hours) between modelling and observations, with a stronger agreement for model results derived on the basis of the lower spatial resolution data. This counter-intuitive finding can be explained as follows. The plumes were displaced for both datasets, but the more coarsely resolved spatial NWP data resulted in a more spread out plume, hence peak concentrations were lower than for the higher spatial resolution and generated an artificially lower FB for the more coarsely resolved spatial NWP data. There was good agreement between observations and modelling for the higher spatial and temporal resolution results, and this appeared to be a more genuine result.

Maurer *et al*. (2018) described a multi-model exercise. Seventeen participants modelled the long-range transport of radioactive xenon (^{133}Xe) in the southern hemisphere and compared model results to measurements at six monitoring stations. The atmospheric transport models applied included five Lagrangian models (including the NAME model) as well as one Eulerian model and one mixed model. A range of NWP models were used, mostly ECMWF's model and the US National Oceanic and Atmospheric Administration's (NOAA) National Weather Service's National Centers for Environmental Prediction (NCEP) model, but also the Weather Research and Forecasting (WRF) model, the Action de Recherche Petit Echelle Grand Echelle (ARPEGE) model, the Met Office's Unified Model-Global (UM) and the Canadian Meteorological Centre (CMC) Global Deterministic Prediction System (GPDS). NWP data horizontal resolutions ranged from 0.125-2.5 degrees, 7-19 vertical levels below 2.5 km and temporal resolutions between 1-6 hours. The use of highly resolved meteorological input fields was found to have no significant advantage compared to using lower resolved ones.

Selvaratnam *et al.* (2021) explored utilising higher temporal resolution NWP data as input to the Met Office's atmospheric dispersion model, NAME. Model runs were performed comparing particle trajectories calculated from ambient mean winds using 15 minute and hourly UKV NWP data (with a spatial resolution of 1.5 x 1.5 km). For the case considered there were notable differences in two of the three particle trajectories. Model runs were also performed predicting air concentrations and resulting plume shapes from hourly and 3 hourly global NWP data (with a spatial resolution of approximately 10 x 10 km at mid-latitudes). For both cases considered, the plume shape differed notably. In the case described by a constant wind direction, the more finely resolved NWP data resulted in a narrower plume. A time series of horizontal winds at 10 m above ground were extracted from the global model at both temporal resolutions and compared with observations. Model

results and observations were in good agreement for relatively large scales of motion. Model results and observations diverged for relatively small scales of motion, with the largest disagreement for lower temporal resolution NWP data. It was noted that model run times increased by a factor of three when moving from 3 hourly to hourly global NWP data, and a factor of four when moving from hourly to 15 minute UKV NWP data.

4 NWP DATASETS FOR EVALUATION

This section introduces the NWP datasets, measurement site locations, meteorological parameters and evaluation approach used in the evaluation of NWP meteorological data (Task 2, results presented in Section 5 of this report). A subset of the datasets and locations described in this section were also used for the regulatory dispersion model testing (Task 3, Section 6) and the investigation into possible double-counting of terrain effects between fine resolution NWP data and local flowfield modelling (Task 4, Section 7).

4.1 Providers

CERC identified and approached a number of providers of Numerical Weather Prediction (NWP) data for dispersion modelling purposes as summarised in Table 2. Following considerations of cost, the NWP model used and the availability of data at different horizontal grid resolutions, three providers were identified as viable options for supplying the data required for Task 2 evaluation, as summarised below:

- The Met Office Unified Model (UM) has two configurations over the UK with archived output data suitable for this project: a global configuration (referred to as UMG) with 10 km spatial resolution and 3-hourly archived temporal resolution, and a UK regional configuration (referred to as UKV) with 1.5 km spatial resolution and hourly temporal resolution. The Met Office provided this data free of charge for this project, allowing CERC to gain access to this data as well as the utility used to convert the raw NWP data file to ADMS .met file format, via the JASMIN data analysis platform. UKHSA also accessed this data for their investigations of the effects of NWP data resolution for probabilistic accident consequence modelling, as described in Section 8.
- Air Pollution Services (APS) provide NWP data formatted for use with ADMS, AERMOD and other standard air quality models. They run the WRF model over the UK using a set of nested domains with horizontal resolutions of 9, 3 and 1 km spatial resolution and hourly output resolution. APS also provided NWP data at adjacent grid cells to the evaluation locations, for use in Task 4 (investigation of double-counting terrain effects).
- Lakes Environmental Software provide AERMET-ready WRF data at four separate spatial resolutions, 3, 4, 9 and 12 km, for any location across the globe, with hourly output data. Due to their large user base, and given the fact that WRF is highly configurable and thus different providers will use different setups, CERC considered it necessary to obtain data at one resolution (3 km) in order to analyse how it compares with the other WRF dataset. It was not possible to obtain data at adjacent NWP grid cells from Lakes, only at the specified location.

Table 2 – Summary of NWP datasets selected for use in the Task 2 evaluation exercise

Provider	Model	Resolution(s)
Met Office	Unified Model	10, 1.5 km
Air Pollution Services	WRF	9, 3, 1 km
Lakes	WRF	3 km

4.2 Locations

After discussions between CERC, ADMLC and the project stakeholders, eight locations were chosen at which to compare the different NWP datasets against observational data (and each other), as summarised in Table 3. These locations cover a range of different geographical types, including flat terrain, complex terrain, coastal and urban. The inclusion of three complex terrain and three coastal locations reflects the fact that NWP model performance is likely to be more variable over these geographical settings, and will therefore provide an indication of the variation of NWP data between locations of the same site type as well as across different site types. The eight locations have also been chosen to form a wide spread across the island of Great Britain in order to broaden the applicability of the study findings. The 'Site code' is used in the analysis figures as a compact indicator of site type and to ensure that sites of the same type are grouped together.

Table 3 – Summary of locations

Type	Site name	Region, nation	Lat, lon	Site code
Flat terrain	Waddington	Lincolnshire, England	53.175, -0.522	1_Flat_W
Urban	Northolt	Greater London, England	51,548, -0.415	2_Urban_N
Complex terrain	Drumalbin	Lanarkshire, Scotland	55.627, -3.735	3_Complex_D
	Leek, Thorncliffe	Staffordshire, England	53.128, -1.980	3_Complex_L
	Sennybridge	Powys, Wales	52.063, -3.613	3_Complex_S
Coastal	Leuchars	Fife, Scotland	56.377, -2.861	4_Coastal_L
	Mumbles Head	Swansea, Wales	51.565, -3.981	4_Coastal_M
	Newhaven	Sussex, England	50.776, 0.058	4_Coastal_N

At each location except Newhaven, Met Office-operated automatic weather station data for recent years is freely available via the MIDAS-Open database[1] for all required variables (temperature, wind speed, wind direction, cloud cover, precipitation). 2019 was chosen as the analysis year and all of these locations have good data availability for this year.

[1] https://catalogue.ceda.ac.uk/uuid/dbd451271eb04662beade68da43546e1

At the Newhaven site, hourly measured anemometer data (wind speed and direction) for 2019 have been provided to CERC by Newhaven Port specifically for use in this project. This wind data has been supplemented with corresponding temperature and precipitation data from the nearby and similarly coastal Met Office-operated weather station at Shoreham. Cloud cover data were not available from Shoreham so these were substituted from the Herstmonceux measurement site. One interesting aspect about the Newhaven site is that we can be sure that it does not form part of the network of met stations used in the NWP data assimilation/nudging process for wind speed and direction, which is not the case for the other seven sites. However, for all parameters except wind speed and direction, the observed and modelled locations for the 'Newhaven' site are not the same.

There was poor availability of valid cloud cover data at Mumbles Head, so observed cloud cover values from the St Athan site were used instead. Figure 4 shows a map of the eight selected measurement sites used in the evaluation, along with the supplementary Shoreham and St Athan sites.

For budgetary reasons, Lakes WRF (3 km resolution) data was only purchased at four of these eight sites. The four sites chosen were Waddington, Sennybridge, Leuchars and Northolt, due to the fact that they cover the four site types as well as three countries within Great Britain.

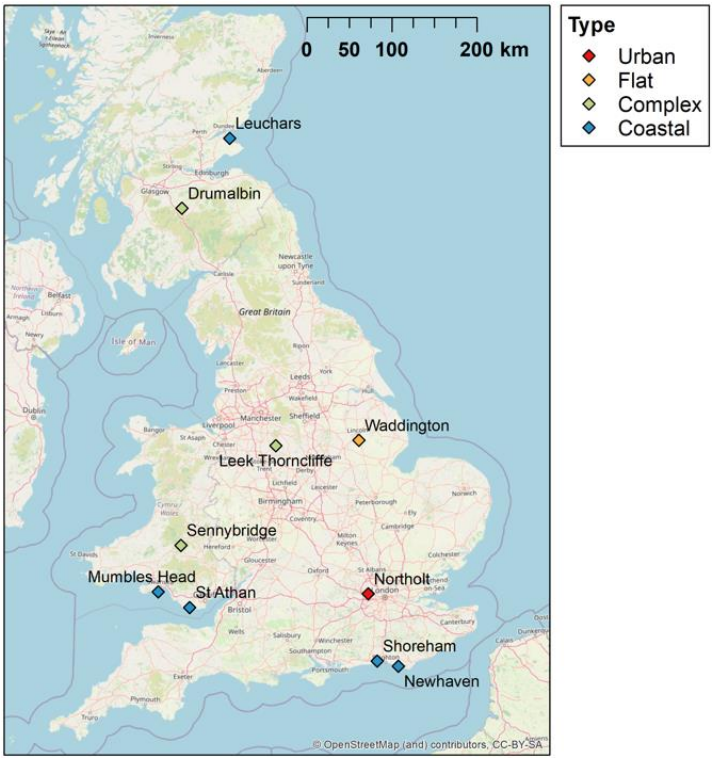

Figure 4 – Overview map of the eight core meteorological sites across GB included in the study, also showing the Shoreham site used to supplement Newhaven wind measurements and the St Athan site used to provide valid cloud cover for Mumbles Head.

Figures 5 and 6 show more details of the 8 meteorological measurement sites (shown by red diamonds) with background maps and overlaid terrain contours, derived from OS open terrain data at 50 m resolution. Each plot shows an area of approximately 15 x 15 km, centred on the meteorological measurement site for inland sites. The supplementary Shoreham and St Athan sites are shown in wider views of Newhaven and Mumbles Head in Figure 7.

The Newhaven monitor is located on a lighthouse at the end of a sea wall, approximately 650 m offshore, and is at a non-standard height of 18.5 m above mean sea level, while the Shoreham site used for supplementary temperature and precipitation data is located around 20 km along the coast from Newhaven and 1.25 km inland. The Herstmonceux site used for supplementary cloud cover is located around 22 km to the northeast of Newhaven and around 9 km inland. The St Athan site used for supplementary cloud cover data at Mumbles Head is around 41.5 km along the coast from Mumbles Head and 2 km inland. Of the three complex terrain sites, Sennybridge has the steepest gradients close to the measurement site. Both Sennybridge and Leek Thorncliffe are located on the sides of valleys, whereas Drumalbin is surrounded by more open terrain. Sennybridge also has areas of forest nearby which may affect the local airflow, in particular a substantial stand of trees around around 50-100 m from the measurement site to the north and west. Of the three coastal sites, Leuchars is the furthest inland, around 1 km from inland water and 2 km from open sea, and also has the flattest surrounding terrain, while the Mumbles Head site has the most complex surrounding terrain. The Northolt 'urban' site is located in outer London, around 20 km from the city centre. The airfield on which the measurement site is located is surrounded with open grassland in the immediate surroundings and suburban housing beyond.

Waddington, England – **Flat**

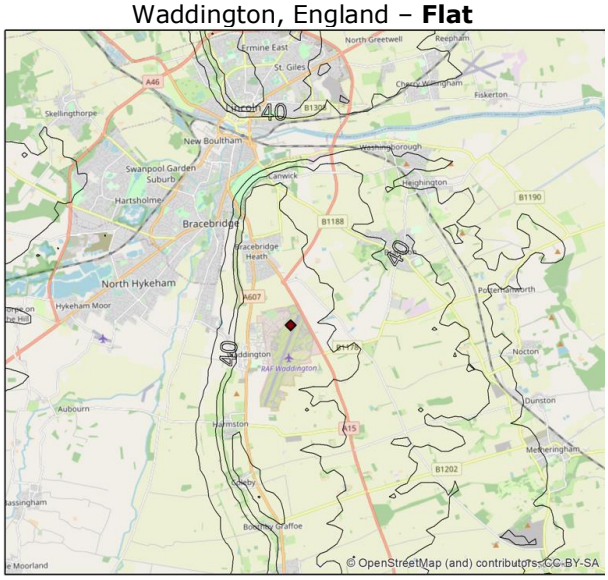

Northolt, England – **Urban**

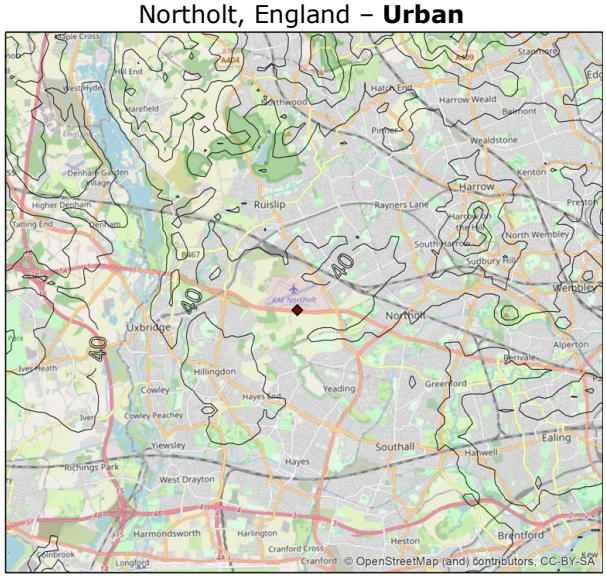

Drumalbin, Scotland – **Complex terrain**

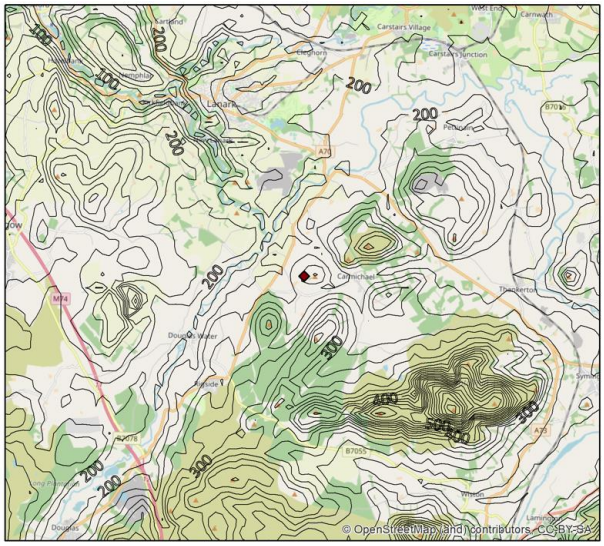

Leek Thorncliffe, England – **Complex terrain**

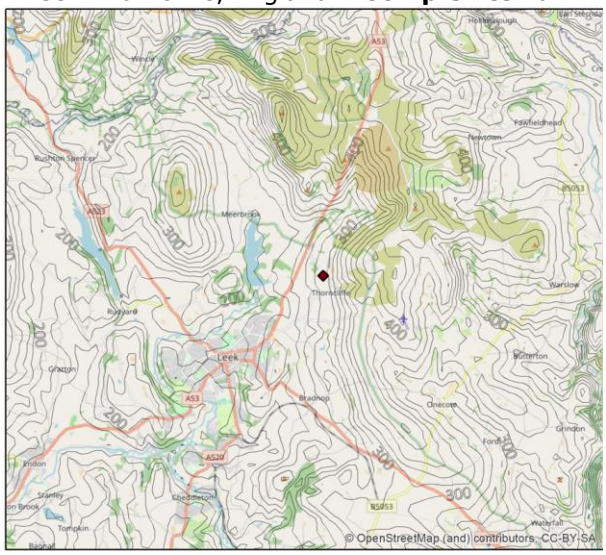

Sennybridge, Wales – **Complex terrain**

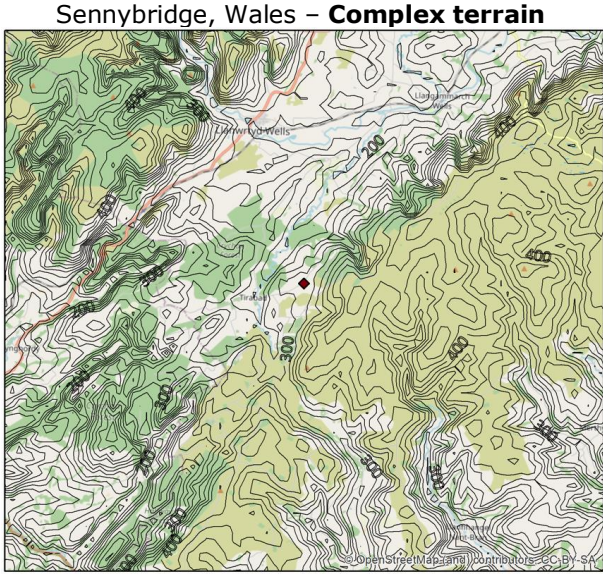

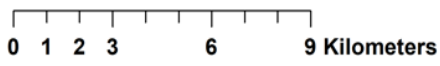

Figure 5 – Terrain contour levels, showing elevation in meters, in the ~15 x 15 km square area around each of the flat, urban and complex terrain sites.

Leuchars, Scotland – **Coastal**

Mumbles Head, Wales – **Coastal**

Newhaven, England – **Coastal**

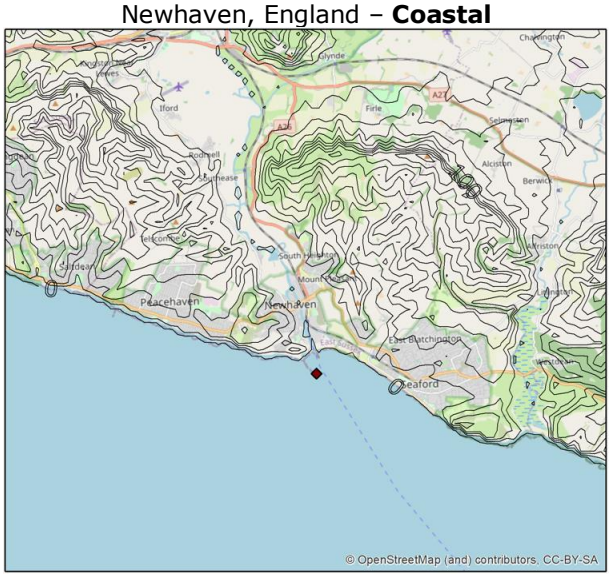

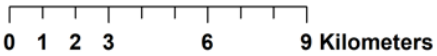

Figure 6 – Terrain contours levels, showing elevation in meters, in the ~15 km square area around each of the coastal sites.

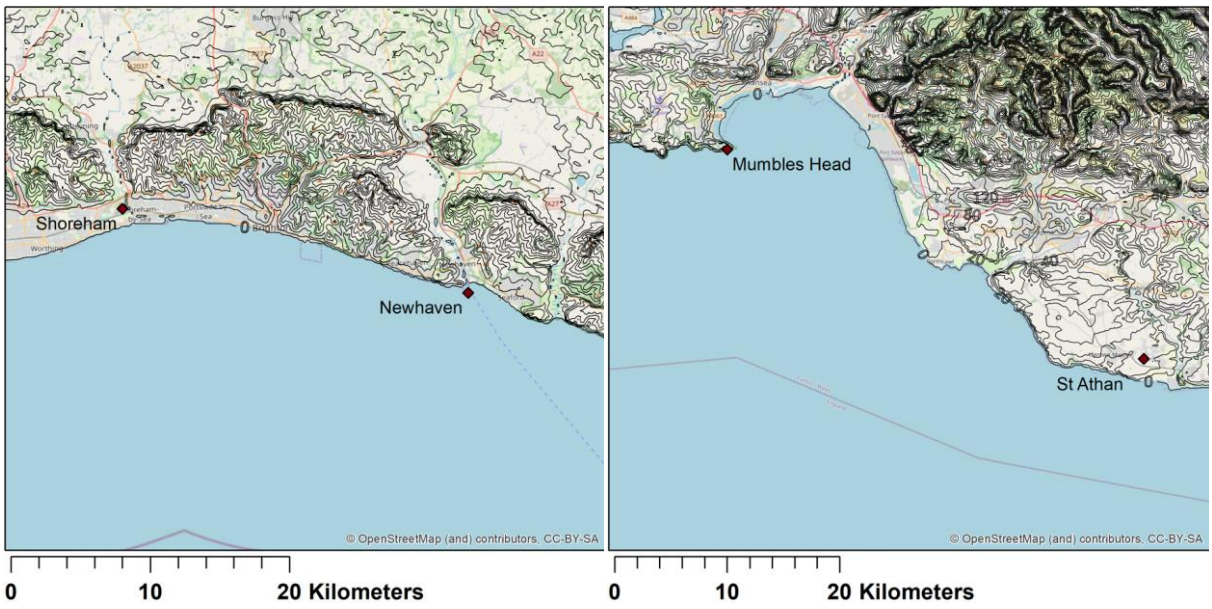

Figure 7 – Wider views of terrain around Newhaven and Mumbles Head, showing the supplementary Shoreham and St Athan sites respectively. Note different scales for each map.

The dominant land use in a model grid cell covering a specific location can vary due to the input land use dataset, grid resolution and/or detailed alignment of the grid. A schematic illustration of this issue for a site close to an eastern coastline is shown in Figure 8. In this diagram, the cell covering the output site in Grid A would be predominantly land, whereas in Grid B it would be predominantly sea, with different surface properties and meteorological behaviour. Similar issues of changing dominant surface conditions occur around other boundaries between land use types, such as the edges of urban areas. This is relevant to the three coastal sites and also to Northolt, located in outer London.

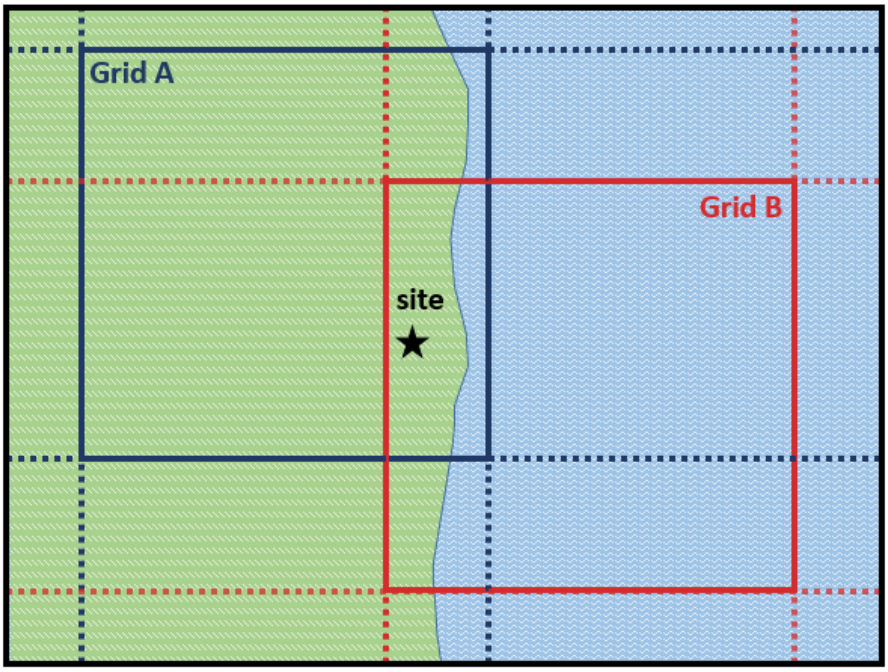

Figure 8 – Schematic showing different dominant land use in grid cells covering the same output location from two non-aligned grids at the same grid resolution.

4.3 Evaluated parameters

The primary meteorological variables routinely measured and used for dispersion modelling which have been considered in the evaluation are listed in Table 4, with associated units. The World Meteorological Organisation (WMO) have published a Guide to Instruments and Methods of Observation (WMO 2018) which gives useful information about the expected uncertainties in the observed meteorological data.

Wind speed and direction have a controlling influence on dispersion calculations, for instance a systematic inaccuracy in NWP wind direction would lead to an inaccurate prediction of the location of maximum concentration from an individual source, with possible effects on maximum concentration magnitudes if more complex dispersion effects such as buildings are considered. Systematic over- or under-estimates of wind speed can lead to under- or over-prediction of concentrations. The combined distribution of wind speed and direction are critical in relation to determining the spatial distribution of modelled concentrations. The relative measurement uncertainty in the lowest wind speeds (absolute uncertainty 0.5 m/s) can be greater than in high wind speeds (relative uncertainty 10%, WMO 2018). Low measured wind speeds are often reported as discrete values, with increments of around 0.5 m/s, whereas NWP values are reported as continuous values. At low wind speeds there can also be greater uncertainty in mean wind direction, as local effects such as buoyancy-induced flows can become similar in magnitude or greater than the geostrophic wind. There can be differences in the averaging periods represented by observed and NWP wind speed: observed wind speeds are based on averages over two and/or 10 minutes, whereas NWP wind

speed is calculated in short time-steps throughout an hour and may either be instantaneous or hourly average for output.

Cloud cover and temperature data are used in dispersion modelling as part of defining atmospheric stability, so will have a secondary effect on the results of dispersion calculations. Temperature measurements have low uncertainty from the measurement equipment, estimated as 0.2 K for typical UK air temperatures (WMO 2018).

Local dispersion models such as ADMS and AERMOD were developed to use observed cloud cover values as part of stability calculations, as these observations were more readily available than heat flux or solar radiation values. NWP modelled cloud cover values may not be used in dispersion model calculations if other variables such as heat flux, solar radiation and/or boundary layer height are available. The possibilities and impacts of using different combinations of NWP variables as input to dispersion models are investigated in Sections 5.4 and 6. The observed values of cloud cover include substantial uncertainty, with 'achievable measurement uncertainty' of two oktas within the range of 0 – 8 oktas (WMO, 2018). Automatic cloud cover observations are based on measurements directly above a single point, whereas manual observations are based on total sky cover visible from the measurement site. NWP cloud cover values will represent a whole grid cell, which is likely to be larger than the visible area. It is also challenging to derive overall cloud cover values from NWP outputs of cloud fractions in multiple vertical layers.

Precipitation data are used in model calculations of wet deposition and have a primary influence on this aspect of dispersion modelling, with a non-linear relationship between precipitation rate and wet deposition rate leading to strong sensitivity to predictions of this variable. In addition, associations between non-zero precipitation and particular combinations of wind speed and direction may alter the spatial pattern of wet deposition relative to concentration. However, there are challenges in the accurate measurement of precipitation, with greater uncertainties associated with higher wind speeds and/or low precipitation rates (Pollock *et al.* 2018). The WMO state a required measurement uncertainty of 0.1 mm/h for precipitation intensity values 0.2 – 2 mm/h, or 5% for values > 2 mm/h, also noting additional uncertainty due to wind (WMO 2018). NWP data may predict smaller increments of precipitation which cannot be measured. Routine regulatory modelling applications focus on annual total wet deposition, whereas short-term wet deposition can be important in emergency response modelling.

The standard height for wind speed and direction measurements is 10 m, wind speeds at 10 m above ground are also standard output variables for WRF and have been extracted from UM. At the Newhaven site the measurements are made at 18.5 m above sea level; the UM modelled wind variables have been extracted at the measurement height for comparison but the WRF data are still at 10 m. The standard height for temperature measurements is 1.2 m (screen height), while the modelled temperatures from WRF are at 2 m above ground, this height

difference is insignificant. Precipitation rates are measured and modelled at ground level, while cloud cover is considered as seen from ground level.

Table 4 – Primary variables considered in the evaluation.

Variable	Short name	Unit
Wind speed	ws	m/s
Wind direction	wd	degrees
Temperature	temp	degrees Celsius
Precipitation rate	p	mm/h
Cloud cover	cl	oktas

Within dispersion models, the primary measured meteorological variables are processed to calculate secondary variables such as surface sensible heat flux, boundary layer height and Monin-Obukhov length, which represents atmospheric mixing and is used to determine atmospheric stability. When NWP meteorological data are used in models, some of these secondary variables (heat flux, solar radiation, boundary layer heights) may also be available in the input meteorological data, and this may override the effect of cloud cover in the meteorological pre-processing. Secondary meteorological variables calculated by the model from measured primary variables or extracted from NWP data have been compared, in order to explore the effects on dispersion characteristics, with results presented in Section 5.4.

4.4 Evaluation approach

The core meteorological data evaluation statistics used in this project are defined and described in Table 5. Evaluation has been carried out over all sites and for each individual site. Evaluation has been carried out both for temporally matched model and observed data, for example using frequency scatter plots and correlation of hourly values, and temporally independent data, for example using annual mean bias, quantile-quantile plots and comparing total 'washout factor' for precipitation.

The Forum for Air Quality Modelling in Europe (Fairmode) has issued a technical reference guide to "The application of models under the European Union's Air Quality Directive" (European Environment Agency 2011), which includes some suggested benchmarks for evaluation of meteorological model output wind speed, wind direction, temperature and humidity. The Fairmode benchmarks were derived from suggestions in US EPA 2009 draft recommendations, re-issued in 2016 (US EPA 2016). These benchmark values are not yet well-established and are included in the current evaluation as a broad indication of model performance, they should not be considered as pass/fail criteria.

Some of the evaluated variables have particular features which require specific analysis approaches. For wind direction, calculations of bias were carried out with angular differences between modelled and measured, limited to be within ±180°.

Mean wind directions were calculated using vector averaging, whereas mean bias (MB) of wind directions was calculated from numeric averages of angular wind direction differences. This can lead to differences between the MB and the difference between mean observed and modelled wind directions, as illustrated in Figure 9. Evaluation was carried out for wind direction at all wind speeds and also for wind speeds above 1.5 m/s only, due to the greater measurement uncertainty for wind direction at low wind speeds.

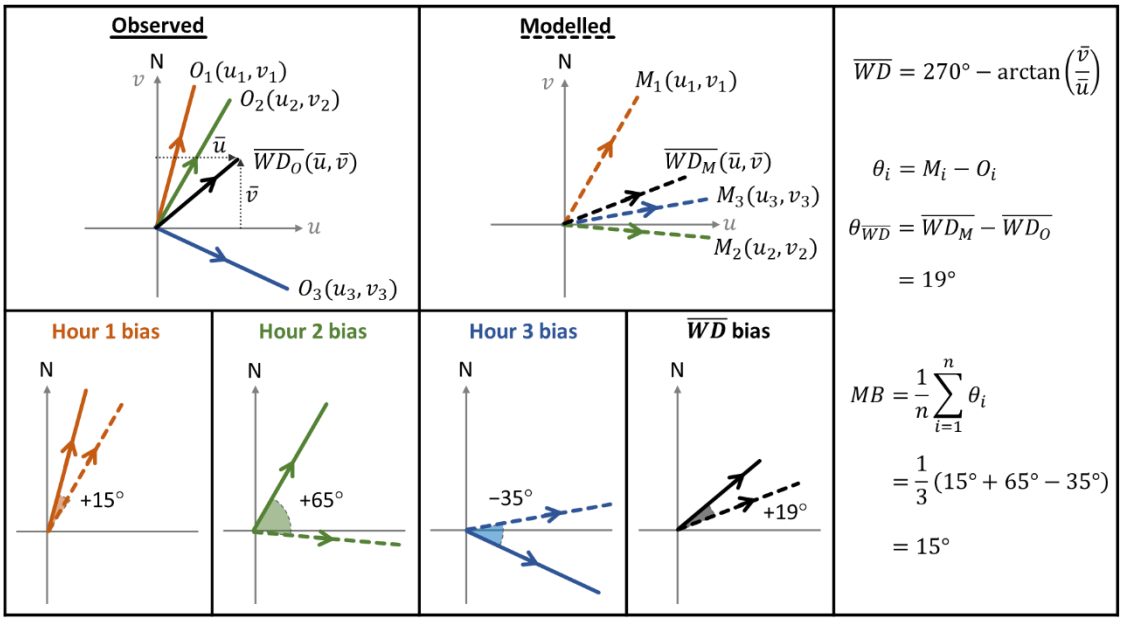

Figure 9 – Illustration of differences between numerical mean bias and differences in vector average mean wind directions

For precipitation, many of the modelled and measured values are zero, so an additional comparison has been made between the number of modelled and measured hours with zero/non-zero precipitation (using a threshold for 'zero precipitation' of 0.01 mm/h, the minimum non-zero observed precipitation rate), which is relevant to the modelling of wet deposition. The sum of hourly precipitation to the power of 0.64 ('washout factor') has also been calculated, which is the precipitation-dependent part of the washout coefficient and thus linearly related to wet deposition. For cloud cover, the measured data comprise integer values between 0 and 8, so an additional calculation has been made of the proportion of modelled data within ±1 of the measured values.

Table 5 – Evaluation statistics definitions. n is the number of valid pairs of modelled and observed values; M_i and O_i represent modelled and observed values for the i^{th} data point respectively; $\bar{M}$ and $\bar{O}$ represent the mean modelled and observed values respectively; and σ_M and σ_O represent the standard deviation of the modelled and observed values respectively.

Statistic	Title	Definition	Description
RMSE	Root Mean Square Error	$\sqrt{\frac{1}{n}\sum_{i=1}^{n}(M_i - O_i)^2}$	Provides an indication of the average error or how close modelled values are in comparison to measurements. Ideal value is zero.
R	Correlation coefficient	$\frac{1}{n-1}\sum_{i=1}^{n}\left(\frac{M_i - \bar{M}}{\sigma_M}\right)\left(\frac{O_i - \bar{O}}{\sigma_O}\right)$	Measures the strength of the linear relationship between two variables. 1 indicates perfect linear relationship with positive slope; -1 indicates perfect linear relationship with negative slope and 0 as no linear relationship between the variables.
MB	Mean Bias	$\frac{1}{n}\sum_{i=1}^{n}(M_i - O_i)$	Provides an indication of whether a model has a systemic favouring of either over- or under-estimation of values. The magnitude is representative of the physical quantity being evaluated. Ideal value is zero.
MGE	Mean Gross Error	$\frac{1}{n}\sum_{i=1}^{n}\lvert M_i - O_i\rvert$	Provides an indication of the magnitude of the model error, irrespective of the direction of the bias. The magnitude is representative of the physical quantity being evaluated. Ideal value is zero.
IOA	Index of Agreement	$1.0 - \frac{\sum_{i=1}^{n}\lvert M_i - O_i\rvert}{c\sum_{i=1}^{n}\lvert O_i - \bar{O}\rvert}$, $when \sum_{1=1}^{n}\lvert M_i - O_i\rvert \le c\sum_{i=1}^{n}\lvert O_i - \bar{O}\rvert$ $\frac{c\sum_{i=1}^{n}\lvert O_i - \bar{O}\rvert}{\sum_{1=1}^{n}\lvert M_i - O_i\rvert} - 1.0$, $when \sum_{1=1}^{n}\lvert M_i - O_i\rvert > c\sum_{i=1}^{n}\lvert O_i - \bar{O}\rvert$	This is an overview metric which compares the model bias to the observed variability. IOA can take values from -1 to +1, with values approaching +1 representing better model performance.
FRAC1	Fraction within ± 1	$\frac{n_{(\lvert M_i - O_i\rvert \le 1)}}{n}$	[Used for cloud cover only] The fraction of modelled values with a difference less than ±1 of the corresponding measurement. A value of 1 means that all modelled values are within ±1 of the measured values; a value of 0 means that none of the modelled values are within ±1.
ZNUM	Zero number	n_0	[Used for precipitation only] The number of modelled or observed hourly precipitation rate values that are zero, n_0. 'Zero' is defined as < 0.01 mm/h, to avoid rounding error.
Washout	Washout factor	$\sum_{i=1}^{n} {p_i}^B$	[Used for precipitation only] Where p_i is the hourly precipitation and $B = 0.64$. This is the precipitation-dependent component of the washout coefficient, linearly related to wet deposition.

5 METEOROLOGICAL EVALUATION RESULTS

This section presents results from an evaluation of NWP meteorological data in comparison with measurements. The evaluated datasets, measurement locations, meteorological parameters and evaluation approach followed are described in Section 4. The meteorological data evaluation has been divided into comparisons between models at matching sets of measurement sites. An overview of the evaluated models including information about spatial and temporal resolution, model inputs, configuration and assimilation of observed data is given in Section 5.1. Section 5.2 assesses the effects of model resolution using data from the APS WRF modelling at three resolutions alongside MO UM modelling at two resolutions, at all eight sites. Section 5.3 investigates the relative effect of differing WRF configurations and resolution by comparing data from APS and Lakes, for a subset of four sites. An inter-comparison of secondary meteorological variables derived from measurements and models is presented in Section 5.4. Conclusions from the meteorological variable evaluation are summarised in Section 5.5. The results of this meteorological data evaluation are used to aid interpretation of the regulatory dispersion modelling outcomes presented in Section 6 and the probabilistic accident consequence modelling outcomes reported in Section 8.

5.1 Overview of evaluated models

The model data under evaluation come from three different organisations and use different models and inputs. A summary of key model and configuration details is given below, to provide context to the evaluation results.

5.1.1 APS WRF

APS have provided data from WRF version 4.3.3 (Skamarock *et al.*, 2021) from nested domains at 9 km, 3 km and 1 km spatial resolutions. Data has been extracted from the nearest grid cell centre to the measurement site. CERC's WRFtoMet tool was used to extract wind speed, direction, temperature, incoming solar radiation, surface heat flux and boundary layer depth, while custom code was developed to extract cloud cover (based on relative humidity) and precipitation. More information about the procedure for extracting ADMS format data from WRF is given in Appendix Section A1. Outputs are given at hourly resolution. The model surface layer depth is approximately 50 m.

The driving meteorological data are taken from the ECMWF ERA5 reanalysis (Hersbach *et al.*, 2020), at hourly temporal resolution and 0.25 degree (approximately 30 km) spatial resolution. Surface properties are derived from MODIS land use data at 30 s (approximately 1 km) resolution, in 20 categories (Broxton *et al.*, 2014). Terrain data are obtained from the United States Geological Survey (USGS) Global Multi-resolution Terrain Elevation Data 2010 (GMTED-2010) dataset at 30" resolution (approximately 1 km, Danielson and Gesch 2011).

APS have adopted the 'CONUS' suite of physics configuration options[1], developed for convection-focussed forecasting across the USA. The physics suite includes: the Mellor Yamada-Janjic (MYJ) boundary layer and surface layer schemes; the Noah Land Surface Model; and the complex Thompson microphysics scheme for precipitation formation (Thompson *et al.*, 2008). While this set of configuration options may not be fully optimised for UK conditions, they were selected as a well-tested set of compatible configuration options which will be updated with newer versions of WRF.

Observed wind data from around 350 UK sites are assimilated in the WRF model. Other UK observation data are likely to be included in the ERA5 reanalysis forcing data.

5.1.2 Lakes WRF

The Lakes WRF data was supplied from WRF version 4.2, from calculations at 3 km spatial resolution and hourly temporal resolution. The WRF grid uses 35 vertical levels while the surface layer depth is unknown. Data from WRF were extracted by Lakes into formats suitable for AERMET and AERMOD using version 3.4 of the US EPA Mesoscale Model Interface Program (MMIF, Karamchandani *et al.*, 2022), applying settings according to US EPA guidance (US EPA, 2022). Data are extracted from the cell centre closest to the output location.

NCEP GFS forecast data are used to drive the WRF model, at 0.5 degree (approximately 50 km) spatial resolution and 6-hourly temporal resolution. MODIS land use data in 21 categories is used to define surface properties. No information was available about the underlying terrain data source used for WRF.

Lakes configure WRF to use the Yonsei University boundary layer scheme (Hong *et al.*, 2006) and Noah land surface model. Cumulus convection is parameterised for grid sizes greater than 10 km but resolved for smaller grid sizes. A relatively simple microphysics scheme is applied (WRF Single-moment 3-class scheme, Hong *et al.*, 2004).

No observed data assimilation is used in the local WRF modelling, and the only observed data incorporated in the GFS modelling system are for surface pressure.

CERC converted the supplied AERMOD input files into ADMS format for consistency with the other suppliers, using the ADMS Meteorological Data File Converter utility. This utility converts AERMOD input variables into the correct units for ADMS and creates a file in the appropriate format for ADMS.

5.1.3 Met Office Unified Model

Data from both the Global (10 km resolution, UMG, Walters *et al.*, 2019) and UK (1.5 km, UKV, Bush *et al.*, 2020) configurations of the Met Office Unified Model (MO UM) have been extracted for analysis. The UMG output is archived at 3-hourly temporal resolution, although the original forecast data is generated at hourly

[1] https://www2.mmm.ucar.edu/wrf/users/physics/ncar_convection_suite.php

resolution. The UKV data is archived at hourly resolution. The surface layer of the UMG has a depth of 10 m while the UKV has a surface layer depth of 2.5 m.

ADMS-format meteorological data files were extracted from the MO archives using the Numerical Atmospheric-dispersion Modelling Environment (NAME) model (Jones *et al.*, 2007). The extraction method, described further in Appendix A2, matches the process used by the MO when supplying NWP data to ADMS users. NAME applies linear temporal interpolation to archived UMG data for wind speed, wind direction, boundary layer depth and temperature to represent hourly resolution variations. However, cloud cover, surface sensible heat flux and precipitation values from UMG are treated as 3-hourly averages to avoid discontinuities. The extraction process for both UMG and UKV configurations applies a bilinear spatial interpolation from grid cell centres to the required output location.

As a global model the UMG does not need external driving meteorological data, it is initialised using an 'analysis' dataset derived from observed data, at approximately 40 km resolution. The fine scale UKV configuration obtains initial and driving boundary conditions from the global UMG at hourly resolution.

UMG uses the recently developed MO GL8.1 land surface representation. UKV uses the JULES (Joint UK Land Environment Simulator, Best *et al.* 2011) land surface model, with a tile approach to represent different land uses within each grid cell. Five different vegetation land use and four non-vegetation land use categories are used to characterise the land surface, including specific alterations to heat properties for urban areas. The land use data is obtained from IGBP-DISCover (International Geosphere-Biosphere Programme, Data and Information Systems, Loveland *et al.*, 2000). Boundary layer mixing uses a first-order turbulence closure scheme, with both ground surface and cloud-top turbulence sources in unstable conditions (Walters *et al.* 2019). The UMG parameterises convective transport, clouds and precipitation whereas the UKV resolves these effects.

The UMG uses terrain data from The Global Land One-kilometer Base Elevation dataset (GLOBE, Hastings *et al.* 1999), with an original resolution of 30" (around 1 km). This data is filtered to generate mean terrain height and sub-grid orographic characteristics for each grid cell. The UKV also uses GLOBE, supplemented by DTED 1 km resolution data (Bush *et al.* 2020).

The UMG uses a 'hybrid incremental' 4D-Var approach to assimilating observed data, at around 40 km resolution. The UKV uses a similar approach at around 4.5 km resolution for all commonly observed surface parameters, with additional nudging towards rainfall rates derived from radar data.

5.2 Resolution evaluation

This section compares hourly modelled UM from MO at 1.5 and 10 km resolution with WRF from APS at 1, 3 and 9 km resolution, with the aim of assessing the effect of changing model resolution on model performance. The evaluation is

presented for data over all eight sites and for individual sites separately, in order to assess the variation between different locations and site types. Supplementary evaluation results are presented in Appendix Section B1.

5.2.1 Wind speed

Table 6 presents the summary statistics comparing modelled and observed wind speed over all eight sites. The models show a tendency for a slight underprediction of observed wind speeds, by less than 10% of the observed mean. The differences between models and measurements are generally within the expected measurement uncertainty. There are noticeable improvements in mean bias (MB), mean gross error (MGE) and root mean square error (RMSE) with finer model resolution. Both models at all resolutions meet the suggested Fairmode benchmarks for RMSE and IOA, while the APS WRF also meets the MB benchmark. The MO UM data at 1.5 km resolution almost meet the benchmark for MB. The correlation (R) and index of agreement (IoA) values are similarly good for all model datasets, with very slightly higher values for MO UM and a small improvement with 1.5 km compared to 10 km resolution. Both MO UM and APS WRF assimilate local observations of wind speed from all of the evaluation sites except Newhaven.

Figure 10 shows frequency scatter plots comparing hourly modelled and observed wind speeds at all eight sites for each model and resolution. These show similarly good model performance for most of the lower observed wind speeds (< 5 m/s), with some tendency for WRF to overpredict at the finer resolutions, but a tendency to underestimate the highest observed wind speeds (> 15 m/s), most noticeably for the coarser resolution models.

Table 6 – Summary of meteorological model performance evaluation of wind speed at 10 m, or the recorded height. Statistics calculated over all eight sites (69857 total valid hours), compared against statistical benchmarks as suggested by Fairmode[1], and ideal model values, where applicable.

Model	Resolution (km)	Observed Mean (m/s)	Modelled Mean (m/s)	MB	MGE	RMSE	R	IOA
				Fairmode benchmark				
				-0.5 — 0.5	n/a	< 2	n/a	≥ 0.6
				Ideal model value				
				0	0	0	1	1
APS_WRF	1	5.09	4.99	-0.09	1.30	1.74	0.85	0.74
APS_WRF	3		4.75	-0.34	1.32	1.78	0.85	0.74
APS_WRF	9		4.63	-0.45	1.35	1.80	0.85	0.73
MO_UM	1.5		4.53	-0.55	1.22	1.62	0.89	0.76
MO_UM	10		4.40	-0.69	1.31	1.77	0.87	0.74

[1] https://www.eea.europa.eu/publications/fairmode

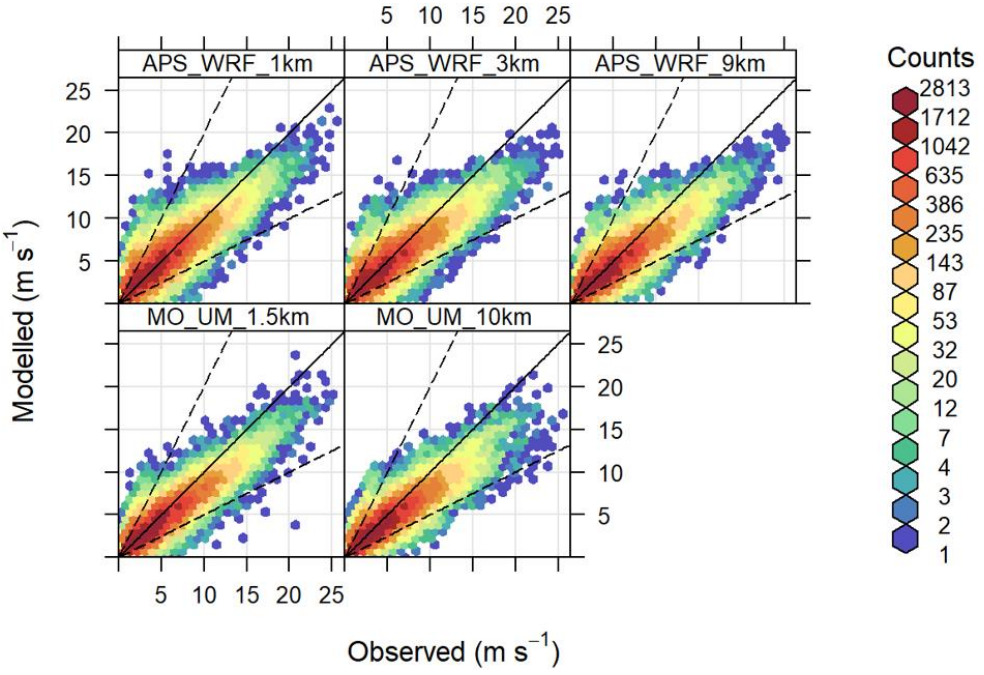

Figure 10 – Frequency scatter plots comparing modelled and observed wind speed in m/s over all eight sites. Colours indicate the number of data points in each area of the graph. The dashed lines show factor of two relationships between modelled and observed wind speeds.

Model evaluation statistics for wind speed have been calculated for each site. Numerical values are shown in Appendix B1.1 Table 48, while graphical comparisons are presented in Figure 11 for mean bias and Figure 12 for correlation. The mean bias plot confirms the general underprediction of mean wind speed, although at one site (Sennybridge), both models overpredict mean wind speed at all resolutions. In general the finer resolutions show smaller magnitudes of mean bias, though there is more variation for the sites in complex or coastal terrain. The APS WRF modelling at 1 km resolution meets the suggested Fairmode benchmark at four sites, while the MO UM modelling at 1.5 km meets the benchmark at three sites.

It appears that the models underestimate the variation in mean wind speed between sites, as the sites with higher mean wind speeds show greater underestimates, and the site with the lowest mean wind speed (Sennybridge) shows a tendency for model overestimates. However, the Northolt site also has a relatively low mean wind speed and shows a small underestimate from most model configurations, so the overestimates at Sennybridge may be associated with specific local conditions at this site. Drumalbin has more open terrain and shows higher observed mean wind speed than the other complex terrain sites, with underestimates of mean wind speed from all models. Leuchars is located both substantially further inland and on a different orientation of coastline than Mumbles Head and Newhaven; the lower mean wind speed at Leuchars compared to the other coastal sites may be due to sheltering by terrain from the south-west sector usually associated with high wind speeds in the UK.

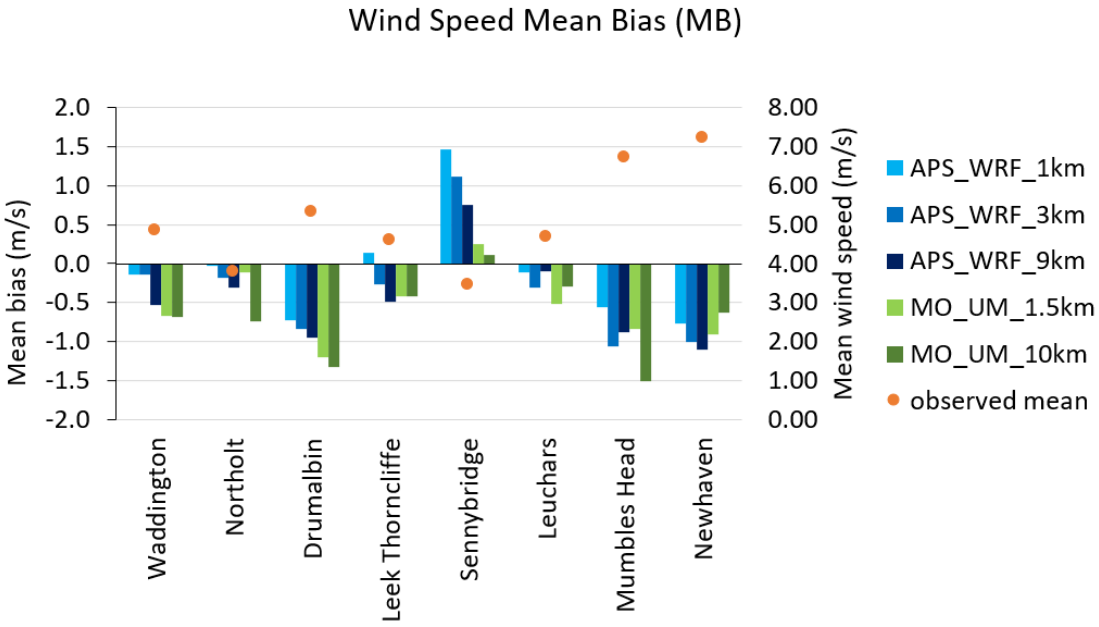

Figure 11 – Graphical summary of mean bias between modelled and observed wind speeds at each site, (bars and left-hand vertical axis scale). The corresponding observed mean wind speed for each site is indicated by the orange circles, using the right-hand vertical axis scale.

For correlation (Figure 12), there is less variation between models and resolutions and a less clear relationship between model resolution and performance, though all values show good model performance (correlation > 0.7). The complex terrain sites Leek Thorncliffe and Sennybridge show generally lower correlation than the other sites, but also a greater improvement in correlation at finer resolution. Frequency scatter plots for modelled and measured wind speed at each site are shown in Appendix B1.1 Figure 111. These show that the flat Waddington and urban Northolt sites have the narrowest range of observed wind speeds and the smallest scatter of modelled wind speeds. All three complex terrain sites show a broader scatter in wind speed, particularly Leek Thorncliffe and Sennybridge, where there are notable overestimates of lower wind speeds. At Drumalbin and the coastal Mumbles Head and Newhaven sites, there is a noticeable model underestimate of the highest observed wind speeds. Only Mumbles Head and Newhaven show substantial numbers of hours with observed wind speed above 15 m/s. The sheltering effect of terrain in the south-west sector at Leuchars may explain why this site does not show any of the very high observed wind speeds seen at Mumbles Head and Newhaven, though there is still a greater scatter of modelled wind speeds at Leuchars compared to the inland flat terrain Waddington site.

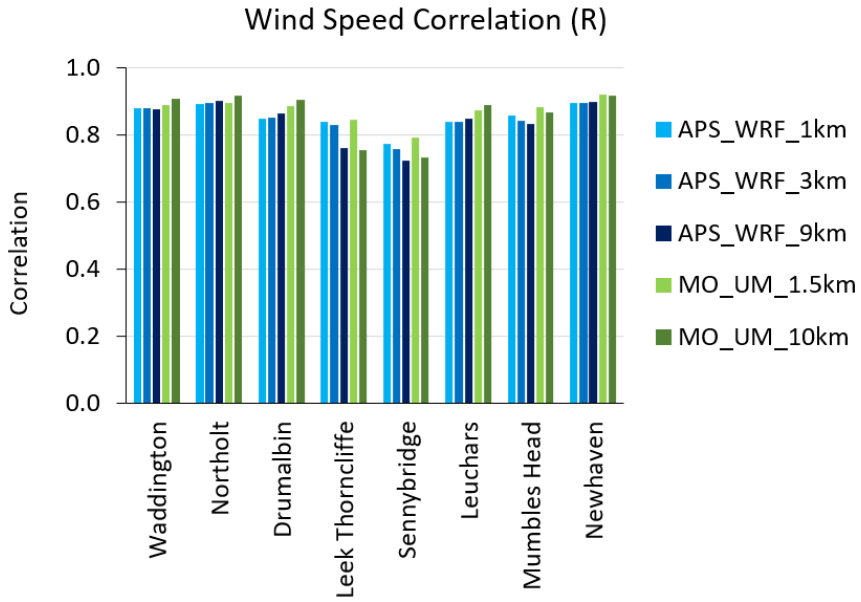

Figure 12 – Graphical summary of correlation between hourly modelled and observed wind speeds at each site.

Quantile-quantile plots of modelled and observed wind speeds, which remove the temporal pairing of modelled and observed data, are shown in Appendix B1.1 Figure 112. These show that the models are predicting the overall distribution of hourly wind speeds accurately for most sites, in addition to the good representation of temporally matched conditions shown by the strong correlation values. There are overall model underestimates of observed wind speed for Drumalbin, Mumbles Head and Newhaven, though for the coastal sites there is a noticeable improvement with finer model resolution. The lower resolution APS WRF models and both resolutions from MO UM show an underestimate of the highest observed wind speeds, most clearly visible for Leek Thorncliffe and Leuchars. The 1 km resolution APS WRF shows a greater overestimate of moderate wind speeds than the lower resolutions for the Sennybridge site.

There is no clear difference in model performance at Newhaven where the observed data is not assimilated in the models and the measurements are made at a non-standard height (18.5 m). In general for this report the APS WRF wind data for Newhaven remains at 10 m whereas the MO UM data were extracted at the measurement height. As an additional sensitivity test, MO UM data were evaluated at both 10 m and 18.5 m for this location. Figure 13 shows frequency scatter plots of modelled and observed wind speed at the Newhaven site from MO UM at both 1.5 km and 10 km resolution (rows), extracted at 10 m and 18.5 m height (columns). There is a stronger underprediction of observed wind speeds by model data extracted at 10 m than at the measurement height of 18.5 m, especially for hours with higher observed wind speeds and at 1.5 km horizontal model resolution. This might be expected due to the typical increase in wind speeds with height above ground. However the APS WRF 1 km resolution data for Newhaven, with modelled wind speed at 10 m, shows similar negative bias to the Drumalbin site (Figure 11), so the uncertainty due to the height difference of the

Newhaven measurements is not significantly greater than other uncertainties in the evaluation.

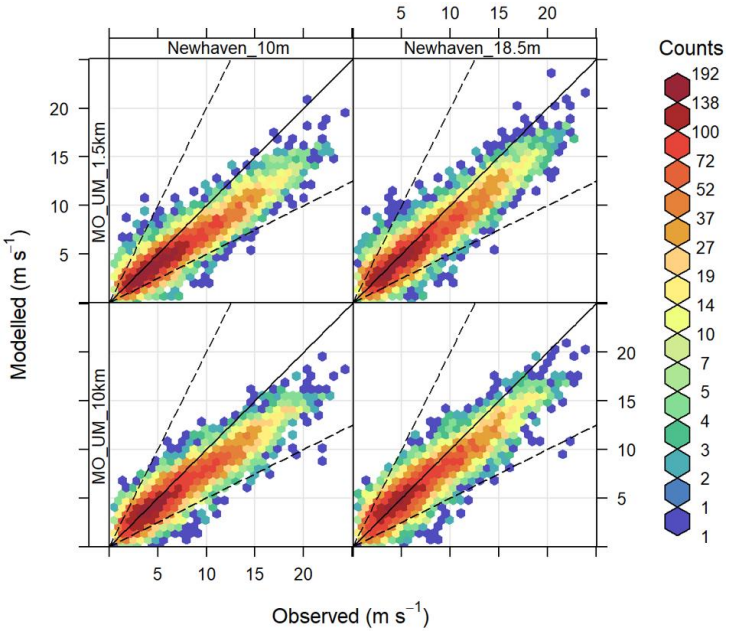

Figure 13 – Comparison between hourly wind speeds modelled by UM (1.5 km and 10 km resolution) at the Newhaven site, at model output heights of 10 m and 18.5 m (columns), against the observed wind speeds measured at 18.5 m.

5.2.2 Wind direction

Summary statistics comparing modelled and observed wind direction for all wind speeds are shown in Table 7. The mean bias and mean gross error values for all models and resolutions are smaller than or comparable in magnitude to the 10° sectors in which observed wind directions are reported, suggesting good model performance. The statistic values meet the suggested Fairmode benchmarks, with little difference between models and resolutions. Corresponding frequency scatter plots are shown in Figure 14, which show a strong cluster of points along the 1:1 line but also a broad scatter away from the line with a lower density of data. Note that points in the upper left and lower right corners of these plots are associated with low bias values, due to the circularity of wind directions. There are no clear visual differences between the frequency scatter plots for each model and resolution.

Table 7 – Summary of meteorological model performance evaluation of wind direction at 10 m, or the recorded height. Statistics calculated over all eight sites, compared against statistical benchmarks as suggested by Fairmode. Note that mean values are calculated by vector averaging whereas MB and MGE are calculated as numerical averages of angular difference, as shown in Figure 9.

Model	Resolution (km)	Number valid	Observed Mean (°)	Modelled Mean (°)	MB	MGE
					Fairmode benchmark	
					-10 — 10	< 30
					Ideal model value	
					0	0
APS_WRF	1	69803	243	229	-3.9	23.6
APS_WRF	3			230	-4.2	23.8
APS_WRF	9			230	-4.4	24.0
MO_UM	1.5			233	-5.0	20.8
MO_UM	10			234	-2.6	20.1

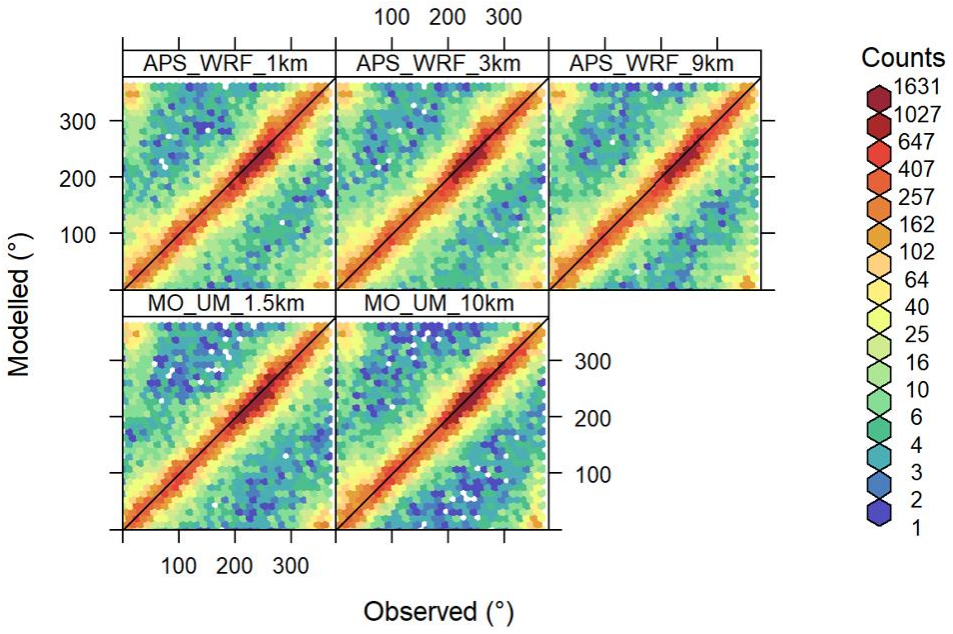

Figure 14 – Frequency scatter plots comparing modelled and observed wind direction in degrees. Wind direction data corresponding to all wind speeds and including all eight sites. Note that points in the upper left and lower right corners are associated with small bias values due to circularity of wind directions.

Figure 15 compares the mean gross error in wind direction for each site, for all wind speeds. The MO UM values tend to be smaller than APS WRF for all resolutions. Both models show the smallest MGE values for the flat terrain Waddington site. For most sites the MO UM 10 km resolution has lower MGE in wind direction than the 1.5 km resolution, whereas there are smaller and less consistent differences in MGE with model resolution for APS WRF.

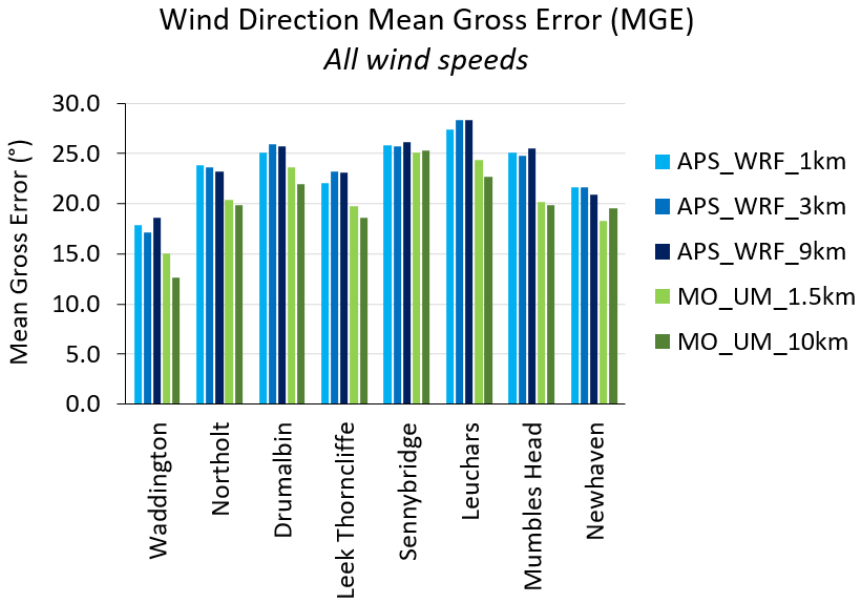

Figure 15 – Bar chart of mean gross error (MGE) for wind direction in degrees at each site, for all wind speeds.

Frequency scatter plots for wind direction at all sites for all wind speeds are shown in Appendix B1.2 Figure 113. These plots show strong clustering of data around the 1:1 line for most sites, with greater scatter for Drumalbin, Sennybridge, Leuchars and Mumbles Head. These sites also show signals of wind 'channelling' through local terrain features, with wind direction data clustered in a relatively narrow range of wind directions. The models generally capture this channelling and there is no clear difference between model resolutions.

There is greater uncertainty in measured wind direction data at low wind speeds, so the evaluation of modelled wind direction has been repeated, excluding hours with measured wind speed below 1.5 m/s, in order to investigate whether there is a clearer signal for model performance. Note that this threshold excludes different proportions of hours for each site, with 2-3% of hours at Waddington, Mumbles Head and Newhaven with wind speeds < 1.5 m/s, 6-7% at Drumalbin, Leek Thorncliffe and Leuchars, but 12% of hours at Northolt and 19% of hours at Sennybridge. The summary statistics in Table 8 show lower values of mean gross error in wind direction for this subset of wind speeds, particularly for the MO UM at 10 km resolution, but little change in mean bias. The corresponding frequency scatter plots are shown in Figure 16 and show a reduced density of points away from the 1:1 line, again most noticeably for the MO UM at 10 km resolution.

Table 8 – Summary of meteorological model performance evaluation of wind direction at 10 m, or the recorded height, for wind speeds of 1.5 m/s and above. Statistics calculated over all eight sites, compared against statistical benchmarks as suggested by Fairmode. Note that mean values are calculated by vector averaging whereas MB and MGE are calculated as numerical averages of angular difference.

Model	Resolution (km)	Number valid	Observed Mean (°)	Modelled Mean (°)	MB	MGE
					Fairmode benchmark	
					-10 — 10	< 30
					Ideal model value	
					0	0
APS_WRF	1	64691	241	227	-4.4	20.8
APS_WRF	3			228	-4.6	20.9
APS_WRF	9			229	-4.9	20.9
MO_UM	1.5			232	-5.1	18.0
MO_UM	10			232	-3.0	16.9

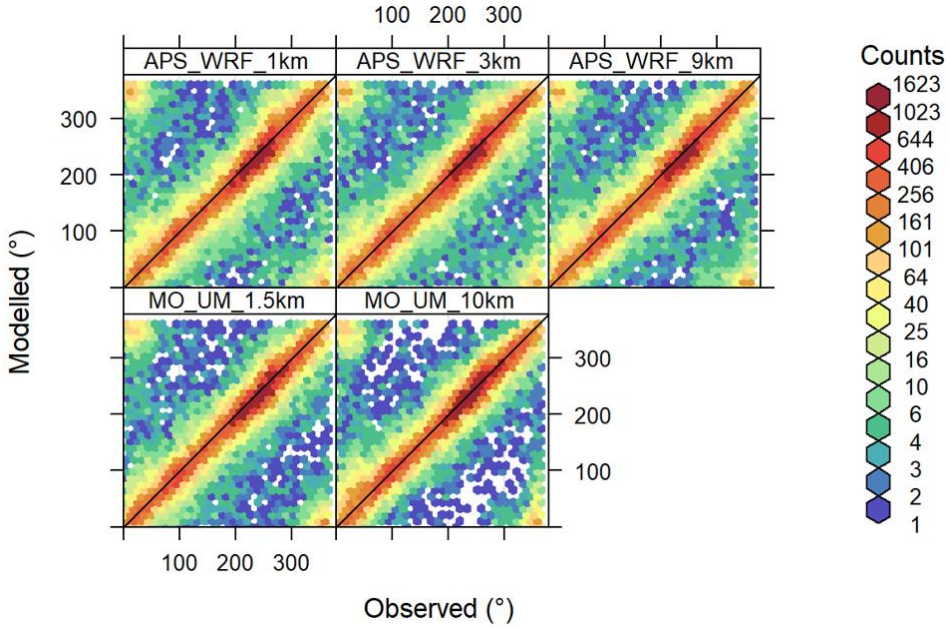

Figure 16 – Frequency scatter plots comparing modelled and observed wind direction in degrees, for all eight sites. Hours with wind speeds below 1.5 m/s excluded.

Comparing the plot of mean gross error in wind direction for each site excluding hours with wind speed below 1.5 m/s (Figure 17) with the corresponding plot for all wind speeds (Figure 15), the most substantial improvements are for Northolt and Sennybridge. This outcome might be expected as these sites also have the largest percentages of hours with wind speeds below 1.5 m/s. For the other sites, the small proportions of hours with very low wind speeds suggests that the assessment of modelled wind direction performance is not substantially affected by the increased uncertainty in measured wind directions at low wind speeds.

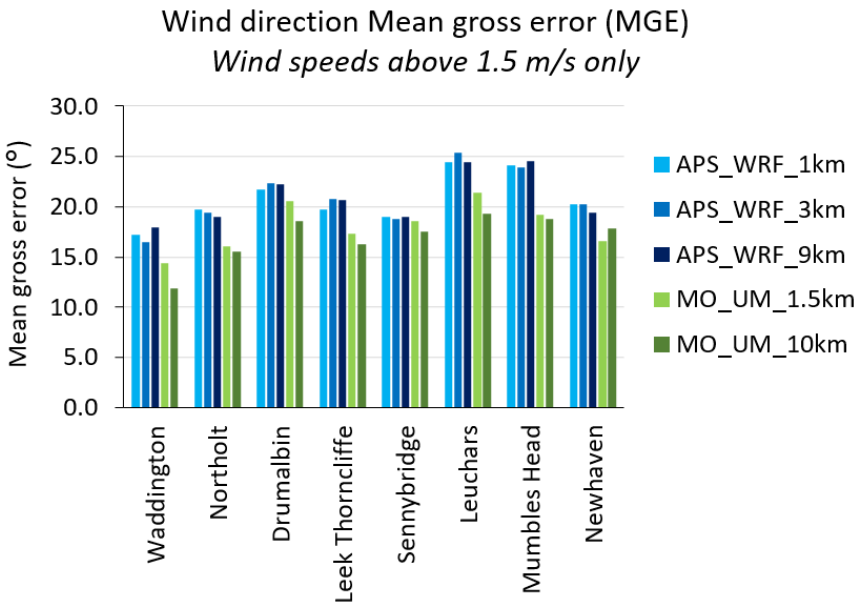

Figure 17 - Bar chart of mean gross error (MGE) for wind direction in degrees at each site, excluding hours with wind speed less than 1.5 m/s.

Polar frequency plots showing the distribution of combined wind speed and direction from observations and models are shown for example sites in Appendix B1.2 Figures 115 (Waddington), 116 (Sennybridge) and 117 (Leuchars). These comparisons show generally good matching between the observed and modelled distributions for the Waddington flat terrain site, with both models and all resolutions capturing the most common wind speed and direction combinations. There is a slightly stronger concentration of data in the dominant wind speed and direction sector from APS WRF than observed, especially at 1 km resolution, while MO UM predicts a slightly broader spread of wind speeds and directions than observed. At the more challenging Sennybridge complex terrain site, APS WRF is overestimating higher wind speed conditions and underestimating lower wind speed conditions for northerly winds, with an overestimate of the dominance of southwesterly winds at 9 km resolution. In contrast, MO UM better captures the lower wind speeds at a range of northerly wind directions, but misses the highest wind speeds at southwesterly wind directions and at 1.5 km resolution overpredicts the frequency of moderate southwesterly winds. It is possible that some of the reduced wind speeds observed in the northwesterly quadrant at Sennybridge are due to very local effects of trees sheltering the monitoring site, which will not be captured by the models. At Leuchars, both UM MO and APS WRF are predicting a slightly more southerly predominant wind direction than observed, with a particularly strong overestimate of the frequency of this sector from APS WRF at 1 and 3 km resolutions. MO UM at both resolutions predicts a slightly broader spread of wind directions at this site than observed.

5.2.3 Temperature

Model evaluation statistics for screen height temperature over all eight sites are presented in Table 9. All models and resolutions meet the suggested Fairmode benchmark thresholds, with very good model performance (correlation > 0.94).

The MO UM bias values are smaller in magnitude than the APS WRF, with associated lower MGE and RMSE. However the mean differences between all models and observations are comparable to the 0.2 K estimated measurement uncertainty. Frequency scatter plots over all sites are shown in Figure 18 and show narrower scatter for MO UM than APS WRF. There is very slightly poorer performance at fine resolution for WRF APS, but slightly better for MO UM at 1.5 km than 10 km. MO UM uses data assimilation for temperature at both resolutions, so the observed data will be contributing substantially to the model outputs, with a reduced effect at 'Newhaven' where the model output location is not co-located with the Shoreham measurement site. Temperature was reported as the 'most improved variable' due to the implementation of observed data assimilation in MO UM (Bush *et al.*, 2020). There is no assimilation of observed temperature data in the fine scale APS WRF modelling, but UK observed temperatures may contribute to the ERA5 reanalysis data used to drive the outermost WRF domain. The WRF APS results show a slight model tendency to underpredict the observed variation at finer scales, with a broader scatter towards positive bias at low temperatures and negative bias at high temperatures.

Table 9 – Summary of meteorological model performance evaluation of temperature at screen height. Statistics calculated over all eight sites (69914 total valid hours), compared against statistical benchmarks as suggested by Fairmode.

Model	Resolution (km)	Observed Mean (°C)	Modelled Mean (°C)	MB	MGE	RMSE	R	IOA
				Fairmode benchmark				
				-0.5 — 0.5	< 2	n/a	n/a	≥ 0.8
				Ideal model value				
				0	0	0	1	1
APS_WRF	1	9.92	9.58	-0.34	1.41	1.89	0.94	0.84
APS_WRF	3		9.68	-0.24	1.32	1.75	0.95	0.85
APS_WRF	9		9.71	-0.21	1.34	1.77	0.95	0.85
MO_UM	1.5		10.01	0.08	0.69	1.04	0.98	0.92
MO_UM	10		9.87	-0.05	0.84	1.26	0.97	0.91

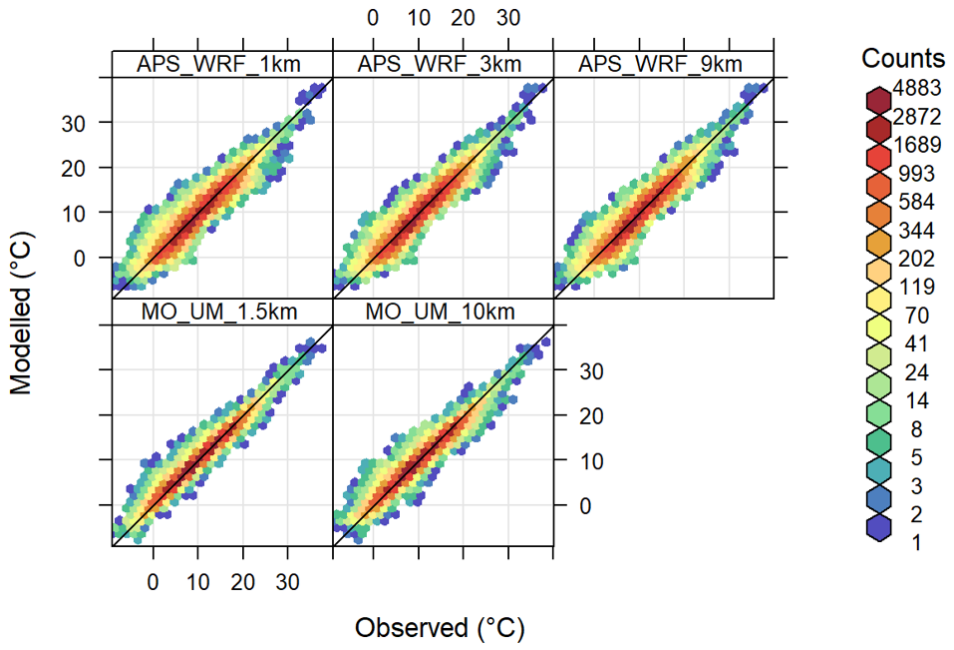

Figure 18 – Frequency scatter plots comparing modelled and observed temperature in degrees Celsius at screen height, over all eight sites.

A graphical comparison of mean bias for each model and site is shown in Figure 19, alongside the observed mean temperature at each site. There is no clear relationship between observed mean temperature and model bias, suggesting that the models are capturing variations between sites. The highest observed mean temperatures are found at Northolt, Mumbles Head and Newhaven, which may reflect some urban and coastal effects as well as their southerly and easterly locations. As for wind speed, Leuchars appears to show less of a marine influence than the other coastal sites. The 'Newhaven' temperature measurements are taken from Shoreham, 1.25 km further inland than the Newhaven anemometer site where the model results have been extracted, so the modelled data are more likely to reflect a maritime temperature than the observed data. MO UM model results meet the suggested Fairmode benchmark for all sites except Newhaven, reflecting the use of data assimilation. APS WRF shows smaller mean bias at 3 km than 1 km resolution for all sites except Drumalbin and Leuchars. However these relatively small differences in modelled mean temperature are unlikely to have substantial influences on dispersion modelling.

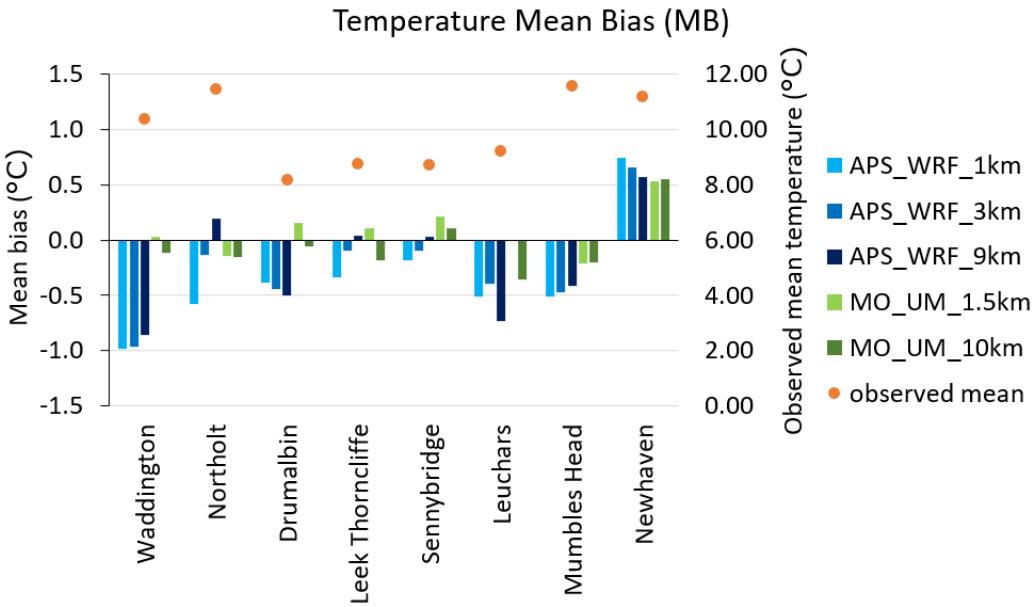

Figure 19 – Graphical summary of mean bias between modelled and observed temperatures at each site, (bars and left-hand vertical axis scale). The corresponding observed mean temperature for each site is indicated by the orange circles, using the right-hand vertical axis scale.

The graphical summary of correlation for each model and site shown in Figure 20 confirms the very strong model performance at all sites, with a minimum correlation value of 0.92 for all models and sites except Newhaven. There are slightly lower correlation values for Newhaven, where the model output location does not correspond as closely to the measurement location, but the minimum correlation of 0.86 remains high.

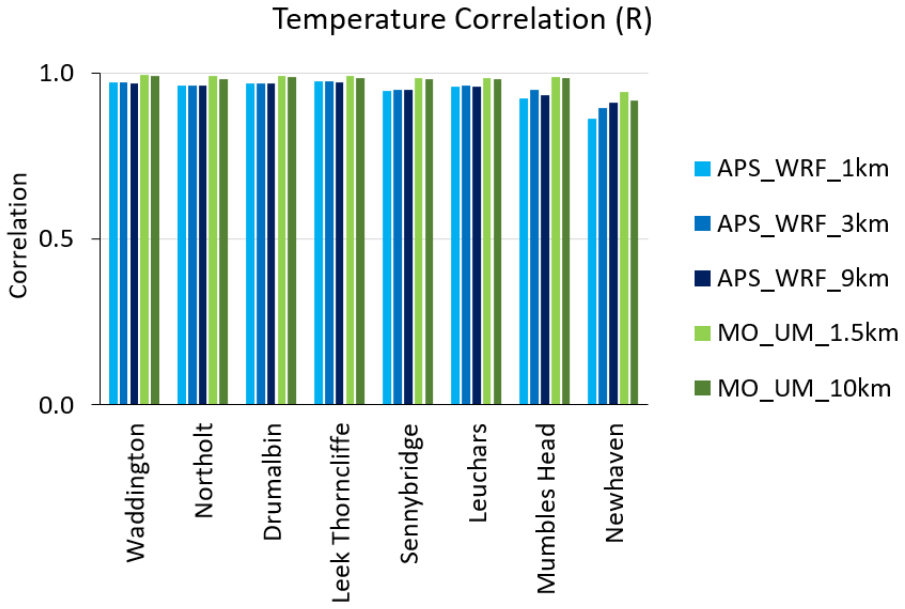

Figure 20 – Graphical summary of correlation between modelled and observed temperatures at each site.

Appendix B1.3 Figures 118 and 119 show the frequency scatter plots and quantile-quantile plots respectively, for modelled and observed temperature at individual sites. The MO UM data shows noticeably narrower scatter than APS WRF for all sites except Newhaven. There is little difference between model resolutions. The quantile-quantile plots demonstrate that there is a tendency for all of the model configurations to overestimate the lowest observed temperatures at several sites, especially Waddington, Drumalbin, Sennybridge and Newhaven. This is relevant to dispersion modelling because very cold conditions can be associated with reduced atmospheric mixing and thus high concentrations from local near-ground sources.

The pattern at Newhaven showing model overprediction of low observed temperatures and underprediction of high observed temperatures suggests that the modelled temperatures have a stronger marine influence than the observations, most clearly for the MO UM 10 km and APS WRF 1 km models. This will partly reflect the location discrepancy between the Newhaven modelled location and the Shoreham temperature observations, which are further inland, and also differing resolutions of coastline representation changing the dominant land use characteristic of a model cell between land and sea. The MO UM modelling includes stronger urban effects on heat transfer at Northolt at 10 km resolution, where the urban land use fraction is taken as 0.75 (including more urban areas to the south and east of the airfield), than at 1.5 km resolution, where the urban land use fraction is only 0.1 (airfield and parkland). There is slightly broader scatter in the 10 km than 1.5 km MO UM results, which may suggest that the urban effects in the 10 km modelling are not representative of the local surroundings of the measurement site. However, the APS WRF modelling does not include any urban effects and also shows broader scatter than the UM 1.5 km output. The APS distribution of hourly temperatures at Northolt has an unusual pattern of flat modelled temperatures for the highest observed temperatures, particularly at 9 km resolution.

Polar plots showing the variation of average observed and modelled temperatures with wind speed and direction are shown in Appendix B1.3 Figures 120 (Waddington, flat terrain), 121 (Sennybridge, complex terrain) and 122 (Leuchars, coastal). Observed temperatures are plotted with observed wind direction and wind speed while modelled temperatures are plotted with the associated modelled wind data. The plot for Waddington shows few observed low wind speeds. The lowest observed temperatures are associated with the highest northwesterly wind speeds, this feature is mostly captured by the models though less clearly by the 1.5 km MO UM. The maximum mean temperature is associated with strong southeasterly winds, this is not captured by APS WRF and not fully by MO UM. At Sennybridge the lowest observed temperatures are associated with the lowest observed wind speeds, suggesting stable dispersion conditions, this combination is not well captured by any of the models. The rest of the distribution of temperatures with wind speed and direction is reasonably well matched between models and observations. Similarly at Leuchars there is a signature of low observed temperatures associated with weak northeasterly winds which is poorly captured by most models, which tend to predict the lowest temperatures

at higher wind speeds. The higher temperatures associated with southerly winds are generally better captured by the models, with some underestimate from APS WRF at 9 km and overestimate at 1 km.

5.2.4 Precipitation

Summary evaluation statistics comparing modelled and observed precipitation data for all sites are presented in Table 10. The MO UM overpredicts mean precipitation at both resolutions, by a larger margin at 1.5 km than 10 km resolution, while APS WRF has very low mean bias values at all resolutions. The correlation values are substantially smaller for precipitation than for wind speed or temperature for all models. The mean precipitation rates may be distorted by a large proportion of hours with zero precipitation, it is notable that both the MGE and RMSE values for all models are greater than the mean observed precipitation. The mean annual precipitation rates are close to the expected uncertainty of 0.1 mm/h for low precipitation rates, such that the differences between modelled and observed values of mean precipitation are smaller than this uncertainty.

Supplementary statistics specific to precipitation, calculated over all sites, are shown in Table 11. All models underestimate the number of hours with zero precipitation, which in combination with a small model bias (APS WRF) suggests that the general intensity of rainfall rates may be underestimated. It also suggests that the prevalence of low-intensity precipitation is overestimated. The precipitation metric most relevant to regulatory dispersion model long-term wet deposition calculations is the non-linear component of the washout coefficient, calculated as the total of hourly precipitation rates raised to the power 0.64. All models overpredict this metric compared to observed data, APS WRF by around 17% and MO UM by at least 41%. The MO UM performance at 1.5 km resolution is better than at 10 km, but shows a bigger overestimate than the APS WRF at all resolutions. APS WRF shows the smallest overestimate at 1 km resolution but very small differences between the three resolutions.

Table 10 – Summary of meteorological model performance evaluation of hourly precipitation. Statistics calculated over all eight sites (69939 total valid hours). There are no suggested Fairmode benchmark values for precipitation.

Model	Resolution (km)	Observed Mean (mm/h)	Modelled Mean (mm/h)	MB	MGE	RMSE	R	IOA
				Ideal model value				
				0	0	0	1	1
APS_WRF	1	0.11	0.12	0.01	0.13	0.50	0.47	0.66
APS_WRF	3		0.11	0.00	0.13	0.48	0.48	0.67
APS_WRF	9		0.11	0.00	0.12	0.46	0.51	0.68
MO_UM	1.5		0.16	0.05	0.14	0.49	0.58	0.65
MO_UM	10		0.14	0.03	0.13	0.41	0.58	0.67

Table 11 – Additional precipitation-specific summary statistics, including the washout factor (sum of $p^{0.64}$) and the number of hours with zero precipitation (ZNUM), calculated over all eight sites (69939 total valid hours).

Model	Resolution (km)	Observed washout factor	Modelled washout factor	Observed ZNUM	Modelled ZNUM
APS_WRF	1	7264	8465	61075	53509
APS_WRF	3		8469		53005
APS_WRF	9		8638		51903
MO_UM	1.5		10241		54776
MO_UM	10		11265		41704

Frequency scatter plots comparing modelled and observed hourly precipitation over all sites are shown in Figure 21. While the models correctly capture a substantial proportion of the observed hours with low precipitation rates, there is a broad scatter in the prediction of higher rainfall rates for all models and resolutions. It is challenging for models to predict intense rainfall events correctly in both time and space, so the quantile-quantile plots shown in Figure 22 allow an examination of the distribution of rainfall rates allowing for differences in timing of specific events. These plots show generally good prediction of the overall distribution of precipitation rates by APS WRF at all resolutions, while the MO UM shows an overprediction of low rainfall rates at 1.5 km resolution and a pronounced underprediction of high rainfall rates at 10 km resolution. Some of the lower accuracy of MO UM 10 km rainfall may result from the three-hourly archive resolution of this data.

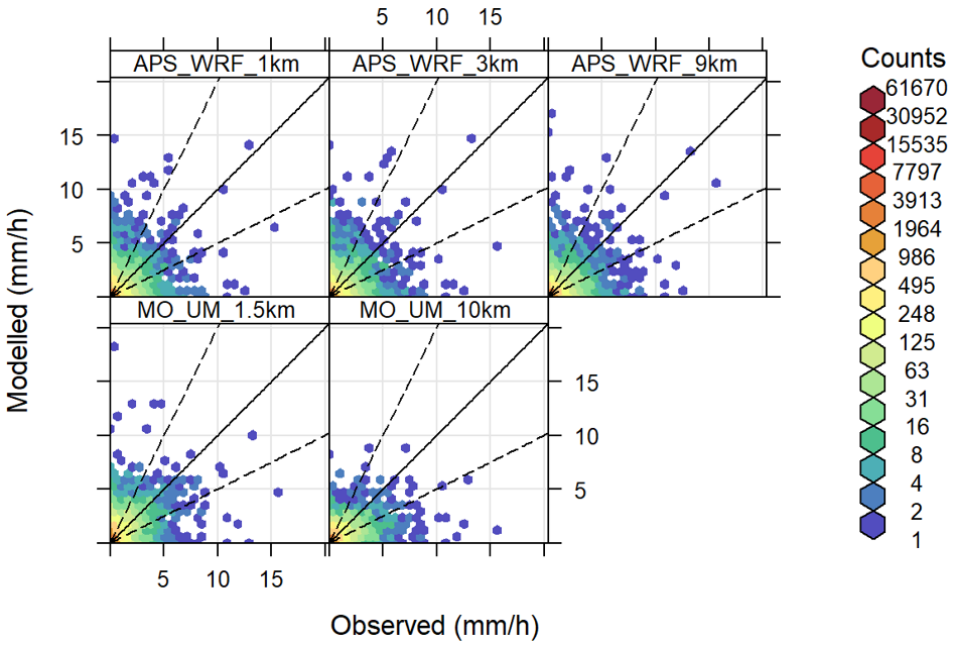

Figure 21 – Frequency scatter plots comparing modelled and observed precipitation rate in mm/h, over all eight sites.

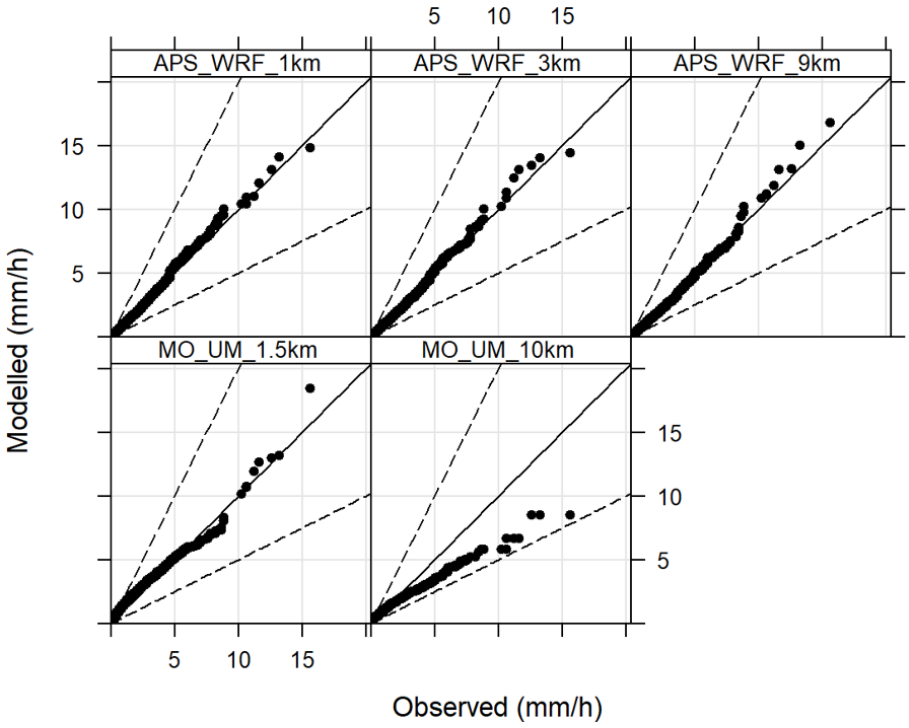

Figure 22 – Quantile-quantile plots comparing modelled and observed precipitation rate in mm/h, over all eight sites.

Model evaluation statistics have been calculated for each site and model (Appendix B1.4 Tables 52 and 53). A graphical summary of correlation values between modelled and observed hourly precipitation rates is shown in Figure 23, with notably lower correlation values for all sites and models than seen for wind speed or temperature. The highest correlation values are at the Sennybridge and Waddington sites, with no clear relationship to site type. In general the difference between correlation values for the different APS WRF resolutions is fairly small, though there is a tendency for the 9 km to have slightly higher correlation values at the complex terrain and coastal sites. MO UM at both resolutions shows higher correlation values than APS WRF at Waddington, Northolt, Leek Thorncliffe and Leuchars. There is variation between sites in relation to the difference between 1.5 km and 10 km resolution correlation values - some sites such as Leek Thorncliffe and Leuchars show small differences between resolutions, whereas Drumalbin and Mumbles Head both show increased correlation from the 10 km resolution.

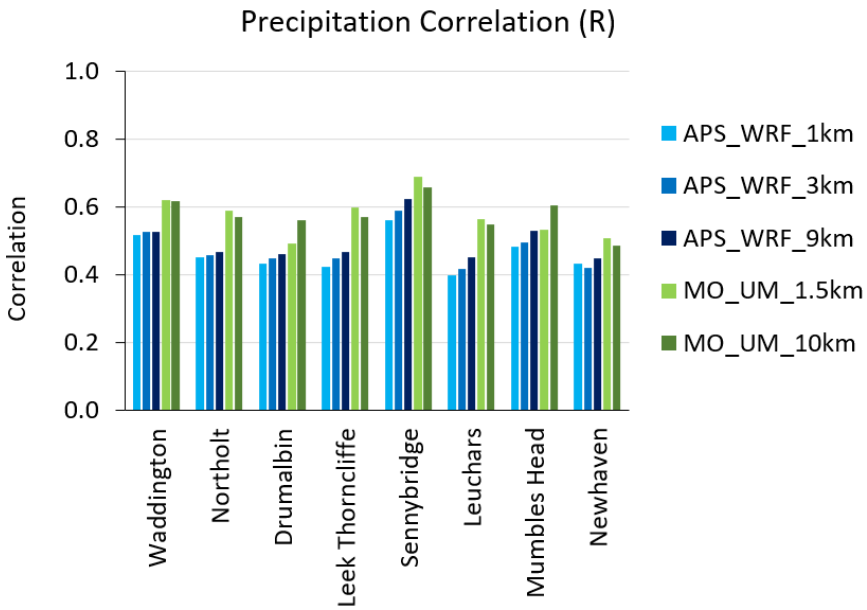

Figure 23 – Graphical summary of correlation between modelled and observed hourly precipitation at each site.

The number of hours with zero precipitation has been compared between observations and models in Figure 24. All models underestimate the number of hours with zero precipitation compared to observations. The values for all three APS WRF resolutions are similar and close to the MO UM 1.5 km resolution values, whereas the MO UM 10 km resolution underpredicts this metric very substantially, this may be partly due to the three-hourly archive resolution of the MO UM 10 km data. The equivalent plot of washout factor values for each model and site (Figure 25) shows a substantial overestimate from all models at most sites, with the exception of APS WRF which matches the observed values relatively closely at Sennybridge and Mumbles Head. The MO UM 10 km values show particularly strong overestimates of washout factor for Northolt, Mumbles Head and Newhaven. The variation of washout factor between sites is generally poorly captured by the models, for example similar modelled values are shown for Leek Thorncliffe and Sennybridge where the observed values differ by almost a factor of 2.

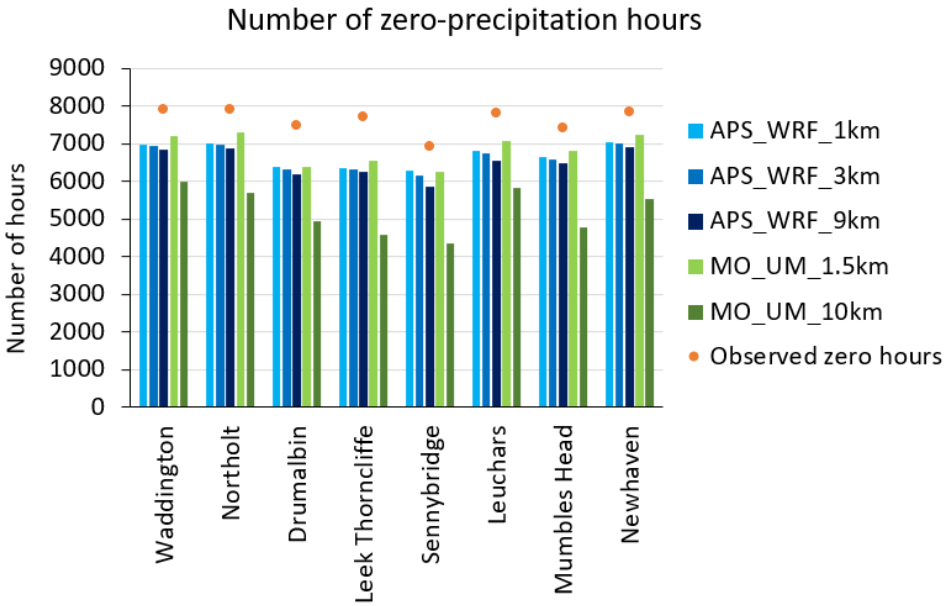

Figure 24 – Graphical summary of the modelled and observed number of hours with a precipitation of zero, at each site.

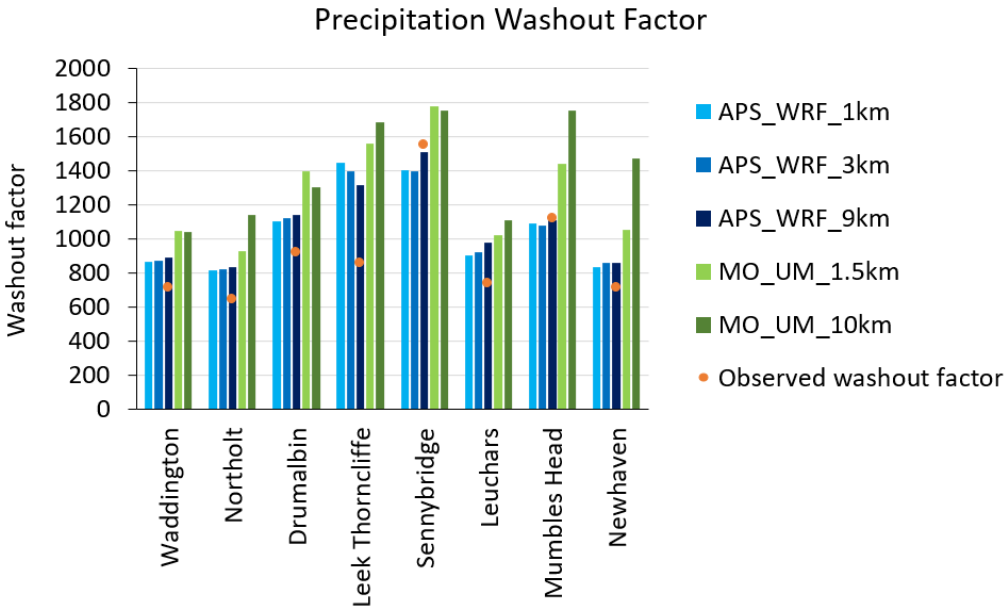

Figure 25 – Graphical summary of washout factor calculated from modelled and observed hourly precipitation at each site.

Model evaluation statistics have been calculated between observed data from pairs of sites used in the current exercise and are reported in Appendix B1.4 Table 54. The paired sites were grouped regionally, with separations of 40 – 100 km, and are not matched by type, except for St Athan and Mumbles Head which are both coastal and are also the pair with the smallest distance between sites. Using the observed precipitation data from Waddington at the Leek Thorncliffe site leads to

comparable statistics to the modelled precipitation data for all statistics except correlation, which is poorer than from the modelled datasets, likely to be due to temporal mismatches between rainfall at the two sites. Observed precipitation data from St Athan used at Mumbles Head have a lower mean bias but comparable values of other model evaluation statistics to the modelled datasets. However, all of the other site combinations considered (including using Leek Thorncliffe observations at Waddington) lead to poorer model evaluation statistics than from the modelled datasets. A more systematic evaluation of the relative performance of modelled data and observed data from alternative sites would be needed to investigate the length scale on which modelled data may better represent local conditions than observed data from a remote measurement site.

Frequency scatter plots comparing hourly modelled and observed precipitation data at each site are shown in Appendix B1.4 Figure 123. As with the plots over all sites, these are distorted by a small number of hours with very high precipitation rates, with a broad scatter of model results and no clear trends between models, resolutions or site types. The corresponding quantile-quantile plots (B1.4 Figure 124) are somewhat clearer, with a tendency for MO UM at 1.5 km and particularly 10 km resolution to overestimate the lowest precipitation rates and underestimate higher precipitation rates. This fits with the underestimation of the number of hours with zero precipitation predicted by this model. The APS WRF precipitation seems to capture the observed distribution more successfully, with points lying closer to the 1:1 line, and few substantial differences between resolutions. However, the APS WRF at all resolutions predicts a few hours with very high precipitation rates for the Northolt site, which are not present in the observations.

Polar plots of the variation of washout factor with wind speed and direction are shown in Appendix B1.4 Figures 125 (Waddington), 126 (Sennybridge) and 127 (Leuchars). At Waddington, the observed variation with wind speed and direction shows low washout factors for the lowest wind speeds and also for the strongest northwesterly winds, with a more uniform distribution for other combinations of wind speed and direction. Both MO UM resolutions show noticeable overestimates of washout factor, especially for moderate southerly winds. APS WRF shows a broader distribution of substantial washout factor values to higher wind speeds than observed. At Sennybridge, the observations show washout factors concentrated in a small range of wind speeds and directions in moderate southwesterly winds. This combination of conditions is captured by all of the models to differing extents, with slightly better matching from the coarser resolution models (MO UM 10 km and APS WRF 9 km). All of the models overpredict washout factor for easterly wind directions at this site. At Leuchars, the observed variation of washout factor shows the highest values for easterly winds, from the direction of the coastline, with low washout for the weakest and strongest northerly and westerly winds. Again the models predict moderate washout factor spread over wider ranges of wind speed and direction than observed. At all sites, the broader distribution of washout factor from models relative to observations confirms the tendency of the models to overpredict the number of hours with low intensity rainfall.

5.2.5 Cloud cover

The observed cloud cover values are recorded as integer values from 0 to 8 in units of oktas (eighths of the sky covered with cloud). APS WRF values were also supplied as integers while MO UM generated non-integer cloud cover values. Converting from modelled cloud representations, which may include different types of cloud and different proportional cloud cover in each vertical layer of the model grid, to overall cloud cover in oktas is a non-trivial task. The approach taken by APS to generating overall cloud cover values from WRF is described in Appendix A1.

Model evaluation statistics comparing modelled and observed cloud cover over all sites are given in Table 12. These show a small underestimate of mean cloud cover from APS WRF at all resolutions and MO UM at 1.5 km resolution, but a small overestimate from MO UM at 10 km resolution. However, the differences between models and observations are all within the measurement uncertainty of ±2 oktas. The correlation value for MO UM at 10 km resolution is poorer than the other four model configurations. This performance difference may be due to either the parameterised convection or 3-hourly resolution of the underlying archive data. The APS WRF statistics are similar at all resolutions, with smaller bias at 1 km but slightly better RMSE at 9 km. The MO UM at 1.5 km shows the best performance across all statistics, possibly due to the combination of explicitly modelled convection and the assimilation of observed cloud cover data in this model.

Table 12 – Summary of meteorological model performance evaluation of cloud cover. Statistics calculated over all eight sites (69911 total valid hours).

Model	Resolution (km)	Observed Mean (oktas)	Modelled Mean (oktas)	MB	MGE	RMSE	R	IOA	FRAC1
				Ideal model value					
				0	0	0	1	1	1
APS_WRF	1	5.36	5.15	-0.21	1.79	2.63	0.61	0.68	0.57
APS_WRF	3		5.13	-0.23	1.78	2.60	0.61	0.68	0.58
APS_WRF	9		5.08	-0.28	1.77	2.57	0.62	0.68	0.57
MO_UM	1.5		5.23	-0.13	1.65	2.51	0.65	0.70	0.55
MO_UM	10		5.45	0.09	1.90	2.80	0.54	0.66	0.50

Frequency scatter plots comparing modelled and observed hourly cloud cover over all sites for each model and resolution (Figure 26) show a preponderance of observed data with the highest and lowest values of cloud cover (0 or 8), with some matching of modelled values to these extremes but no clear relationship between modelled and observed data at intermediate observed values. There is little obvious variation between different models and resolutions in these plots.

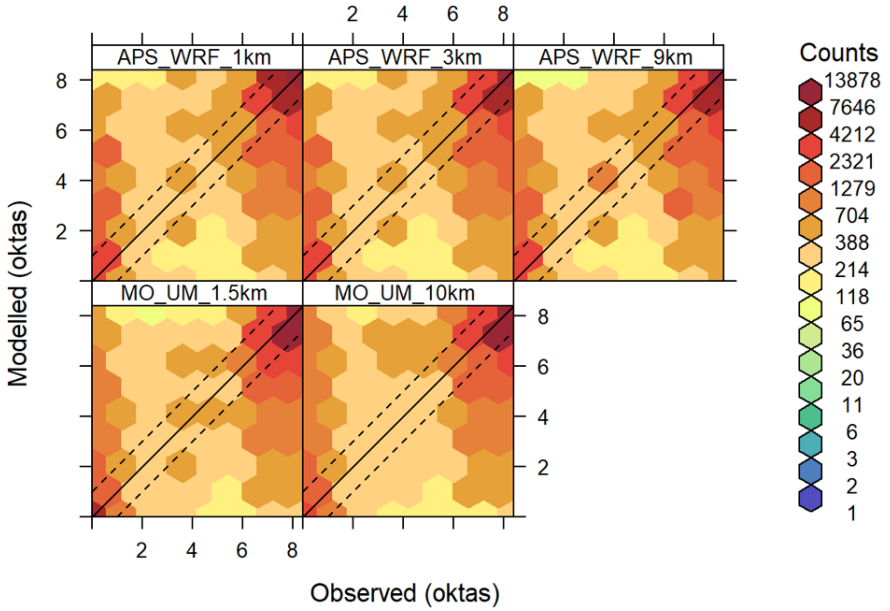

Figure 26 – Frequency scatter plots comparing modelled and observed cloud cover in oktas, over all eight sites. Dashed lines indicate values within ±1 okta.

Model evaluation statistics for cloud cover have been calculated for each site and are reported in Appendix B1.5 Table 55. The mean bias for each site is shown graphically in Figure 27. Cloud cover values are slightly underestimated at most sites by all models except MO UM at 10 km resolution, which tends to slightly overestimate cloud cover. There is a more substantial underestimate by all models at Sennybridge while all models overpredict observed cloud cover at Mumbles Head. There are relatively small differences between the observed mean cloud cover values at all sites, with a range from 5 to 6 oktas. The corresponding correlation plot (Figure 28) shows relatively little difference between the different APS WRF resolutions but a substantial difference between the two MO UM resolutions. The MO UM 10 km results tend to show notably lower correlation (and fraction of hours within ±1 okta of observed cloud cover) than the other modelled datasets. The APS WRF correlation values are relatively consistent between sites, with a small reduction at Sennybridge. The MO UM 1.5 km resolution correlation is slightly higher than APS WRF at most sites, but lower at Mumbles Head and similar at Newhaven. For both Mumbles Head and Newhaven, there are discrepancies between the model and measurement locations, but there is no clear trend in model performance at these sites. The cloud cover correlation values are slightly higher than for precipitation but substantially lower than for wind speed or temperature for all models and sites.

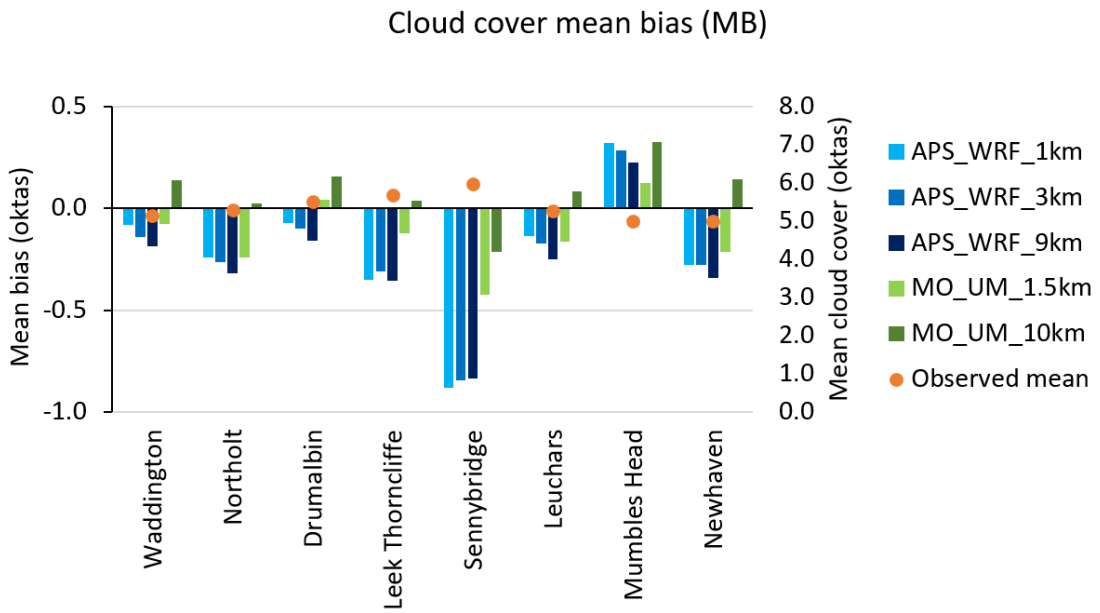

Figure 27 – Graphical summary of mean bias between modelled and observed cloud cover at each site, (bars and left-hand vertical axis scale). The corresponding observed mean cloud cover for each site is indicated by the orange circles, using the right-hand vertical axis scale.

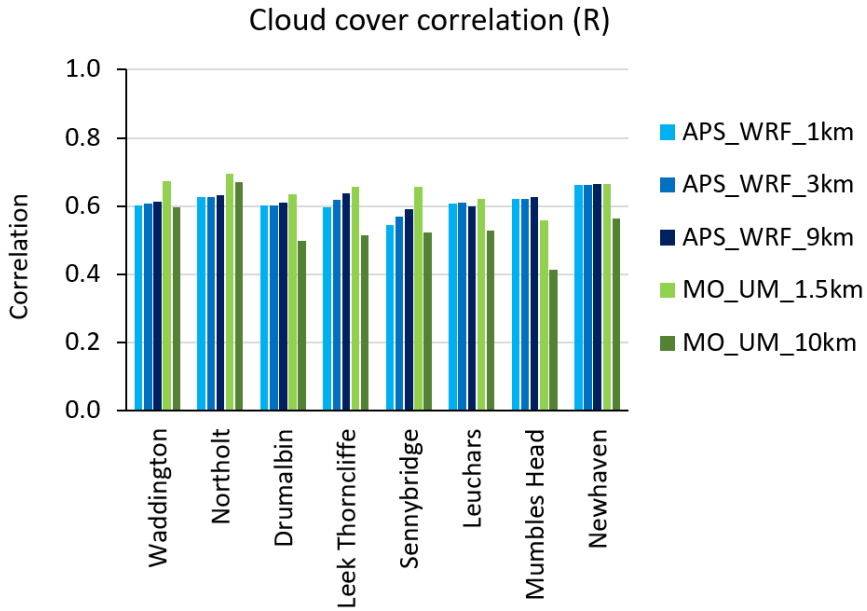

Figure 28 – Graphical summary of correlation between modelled and observed cloud cover at each site.

Frequency scatter plots comparing modelled and observed cloud cover from each model and site are shown in Appendix B1.5 Figure 128. There are no clear differences between models or resolutions in these plots. Histograms displaying the distribution of modelled and observed cloud cover values are shown in Appendix B1.5 Figures 129 (Waddington), 130 (Northolt), 131 (Sennybridge) and 132 (Leuchars). The observed cloud cover distributions at all sites show a

predominance of 0, 7 and 8 okta values. The models also show 8 oktas as the most common value, but tend to predict a more even distribution of values between 0-7 oktas than observed, particularly at Sennybridge and Leuchars. APS WRF predicts more intermediate cloud cover values than MO UM, while there is little difference between the predicted cloud cover distributions at different resolutions for either model. The APS algorithm for calculating integer cloud cover values may lead to underestimates of the frequency of clear sky (0 okta) conditions by around 25%. Model underpredictions of clear sky conditions in the daytime may lead to underestimates of convective stability conditions, associated with increased atmospheric mixing and thus low concentrations from local near-ground sources. Conversely, model underpredictions of night-time clear sky conditions may be associated with underestimates of stable conditions with reduced atmospheric mixing. Additional comparisons of observed and modelled cloud cover separated into day and night hours would be required to investigate the impacts on stability further.

Polar plots of the variation of mean cloud cover with wind speed and direction are shown in Appendix B1.5 Figures 133 (Waddington), 134 (Sennybridge) and 135 (Leuchars). The observed variation for Waddington shows very few combinations of wind speed and direction with mean cloud cover below 4, with the highest mean cloud cover values associated with high wind speeds, particularly from southwesterly and northeasterly directions. The models broadly capture this pattern, though the highest cloud cover values are spread over a broader range of wind directions for APS WRF. At Sennybridge the observations show very high cloud cover values for almost all westerly wind directions and lower for easterly wind directions, this pattern is not well captured by any of the models. APS WRF tends to predict lower mean cloud cover values at all wind directions and at all but the highest wind speeds. MO UM predicts high cloud cover values for high wind speeds and lower at lower wind speeds for all wind directions. In contrast, at Leuchars the observations show higher observed cloud cover values for easterly and southerly wind directions, coming from the coastline, and this pattern is broadly captured by all the models. There is no trend in behaviour with model resolution.

5.3 WRF configuration evaluation

Comparing data from WRF generated by APS at 1, 3 and 9 km resolution and by Lakes at 3 km resolution will enable a more direct evaluation of the relative importance of model resolution and configuration. Differences between APS and Lakes WRF at the same 3 km resolution may arise from: different model parameterisation options, for example MYJ (APS) or Yonsei University (Lakes) boundary layer schemes; different model input data, for example forcing by hourly ECMWF ERA 5 reanalysis (APS) or 6-hourly NCEP Global Forecast System (GFS) data (Lakes); and/or differences in grid definition, such that the same extracted location may lie in cells with different dominant land use, as illustrated and discussed in Section 4.2. Lakes do not use data assimilation of local observed data

in WRF, although there will be some use of UK observed data in the GFS, while APS assimilate local observations of wind speed and direction in WRF.

In this section, data from four sites (Waddington, Northolt, Sennybridge and Leuchars) are evaluated. The reduced number of sites included in this comparison leads to changes in both the observed and modelled statistics, compared to equivalent statistics and plots in Section 5.2.

5.3.1 Wind speed

Model performance statistics for wind speed across the four sites with Lakes data are summarised in Table 13. Both models meet the suggested Fairmode benchmark for all parameters, with APS showing slightly better overall performance than Lakes for the same resolution, possibly due to the use of observed data assimilation in the APS configuration. The differences in all evaluation statistics between APS and Lakes WRF at 3 km resolution are larger than between the different APS resolutions, though within the expected measurement uncertainty.

Figure 29 shows frequency scatter plots comparing modelled and observed wind speeds at all sites with Lakes data. There are no clear differences in these plots due to either model resolution or configuration. Note that these plots use reduced axis extents compared to the equivalent plots in Sections 4.2.1 and A1.1, due to the exclusion of coastal sites with the highest observed values.

Table 13 – Summary of meteorological model performance evaluation of wind speed at 10 m. Statistics calculated over the four sites with Lakes data, compared against statistical benchmarks as suggested by Fairmode. 34956 total valid hours.

Model	Resolution (km)	Observed Mean (m/s)	Modelled Mean (m/s)	MB	MGE	RMSE	R	IOA
				Fairmode benchmark				
				-0.5 — 0.5		< 2		≥ 0.6
				Ideal model value				
				0	0	0	1	1
APS_WRF	1	4.20	4.49	0.29	1.14	1.57	0.81	0.72
APS_WRF	3		4.32	0.12	1.09	1.49	0.81	0.73
APS_WRF	9		4.15	-0.05	1.09	1.46	0.82	0.73
Lakes_WRF	3		4.52	0.32	1.27	1.73	0.76	0.68

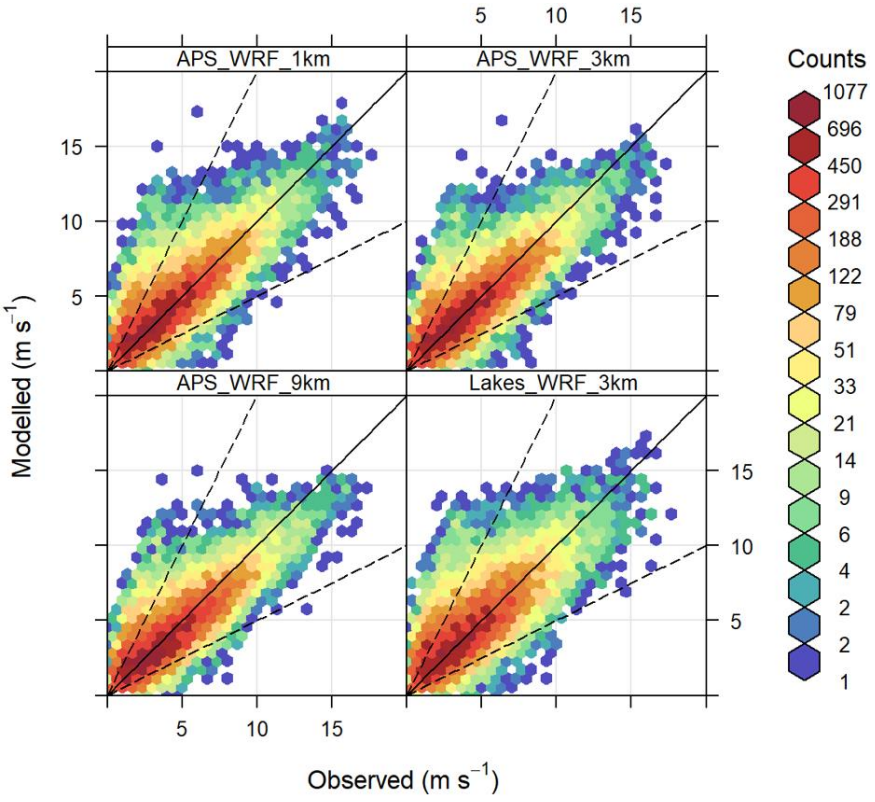

Figure 29 – Frequency scatter plots comparing observed wind speed in m/s over the four sites with modelled Lakes data and APS data at all resolutions. Note reduced axis extents compared to Figures 10 and 111. Dashed lines indicate factor of two relationships between modelled and observed wind speed.

Model evaluation statistics for wind speed have been calculated for each site. Numerical values are shown in Appendix B2.1 Table 56, while graphical comparisons are presented in Figure 30 for mean bias and Figure 31 for correlation. At Waddington, Northolt and Leuchars the mean bias shows a small underestimate for all models, with little difference between APS and Lakes results at 3 km resolution. At Sennybridge all models overestimate mean wind speed and there is a bigger difference in mean bias due to model configuration than

resolution, with a greater overestimate of mean wind speeds by Lakes than any of the APS resolutions. The suggested Fairmode benchmark for mean bias is met by all models at Waddington, Northolt and Leuchars but not by any model at Sennybridge. This may reflect the local sheltering effects in the observed wind data from Sennybridge. In contrast, the correlation values show more variation due to model configuration than resolution, with bigger differences at the complex terrain and coastal sites. The lower correlation values from Lakes than APS at all sites except Sennybridge may partly be due to the lower temporal resolution of the forcing data used – 6-hourly GFS for Lakes in contrast with hourly ERA5 for APS – as well as the assimilation of observed wind data in APS.

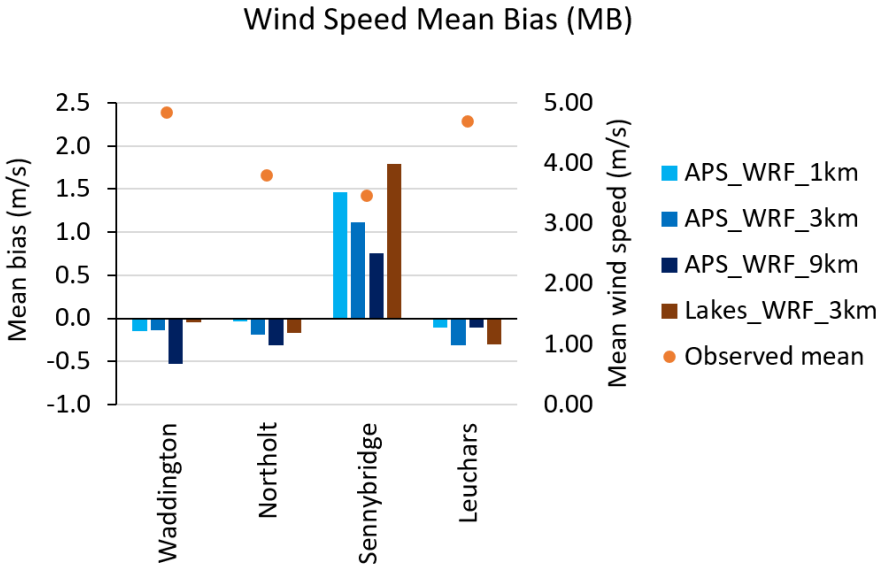

Figure 30 – Graphical summary of mean bias between modelled and observed wind speeds at each site, (bars and left-hand vertical axis scale). The corresponding observed mean wind speed for each site is indicated by the orange circles, using the right-hand vertical axis scale.

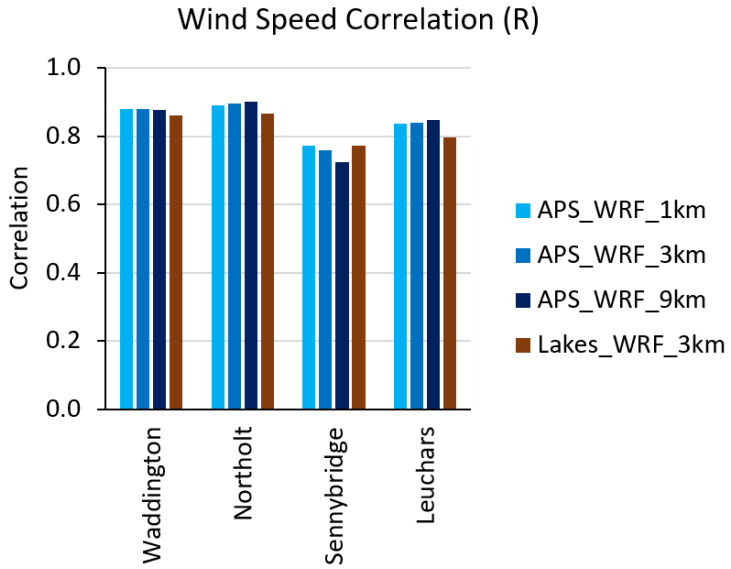

Figure 31 – Graphical summary of correlation between modelled and observed wind speeds at each site.

The frequency scatter plots comparing modelled and observed wind speeds at each site presented in Appendix B2.1 Figure 136 show relatively small differences between the four model datasets evaluated at Waddington and Northolt, but a stronger tendency for model overestimate of low wind speeds from Lakes WRF relative to APS at Sennybridge and Leuchars. The corresponding quantile-quantile plots in Appendix B2.1 Figure 137 show a tendency for all four model datasets to underestimate the highest observed wind speeds at Northolt and Leuchars, as well as confirming the overestimate of the lowest wind speeds at Sennybridge and Leuchars.

5.3.2 Wind direction

Summary model evaluation statistics comparing modelled and observed hourly wind directions across all four sites with Lakes data are given in Table 14. There are relatively small differences across the four modelled datasets under evaluation, with some indications of more influence from model configuration than resolution. The mean gross error values are comparable to the 10° sector size for wind direction measurements. All models meet the suggested Fairmode benchmarks for both mean bias and mean gross error.

Table 14 – Summary of meteorological model performance evaluation of wind direction at 10 m. Statistics calculated over the four sites with Lakes data, compared against statistical benchmarks as suggested by Fairmode.

Model	Resolution (km)	Number of valid points	Observed Mean (°)	Modelled Mean (°)	MB	MGE
					Fairmode benchmark	
					-10 — 10	< 30
					Ideal model value	
					0	0
APS_WRF	1	34917	244	231	-5.1	23.7
APS_WRF	3			234	-5.0	23.7
APS_WRF	9			230	-5.0	24.1
Lakes_WRF	3			228	-2.4	24.5

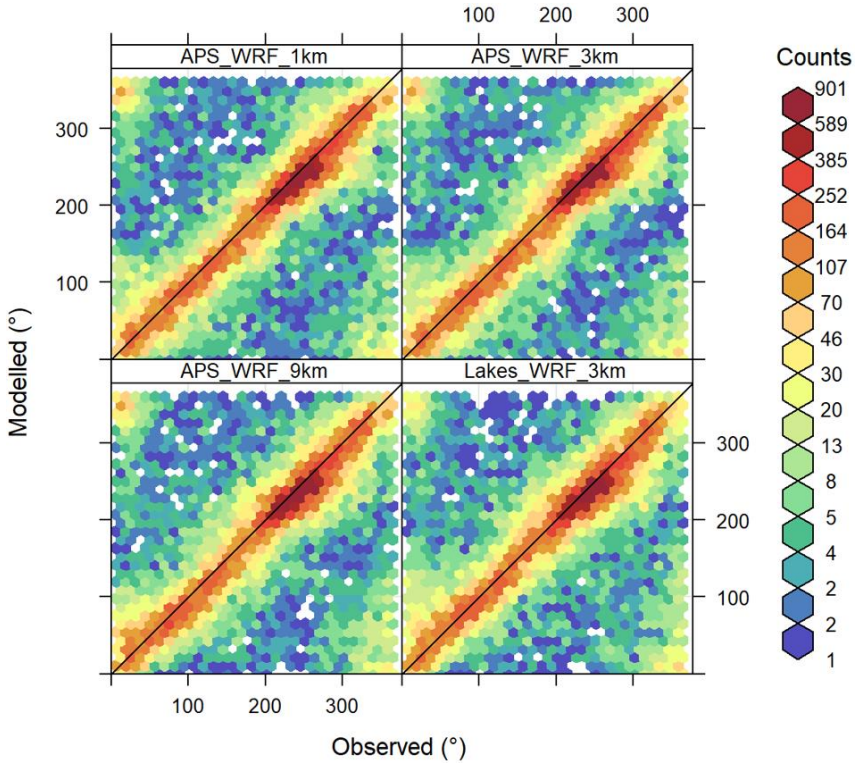

Figure 32 – Frequency scatter plots comparing modelled and observed wind direction in degrees. Wind directions included at all wind speeds. Including only four sites with modelled Lakes and APS WRF data.

Model evaluation statistics for wind direction at each site are reported in Appendix B2.2 Table 55. A graphical summary of MGE at each site is shown in Figure 33, with the lowest MGE values at Waddington for all models. There is also more difference from WRF configuration than resolution at all sites except Waddington.

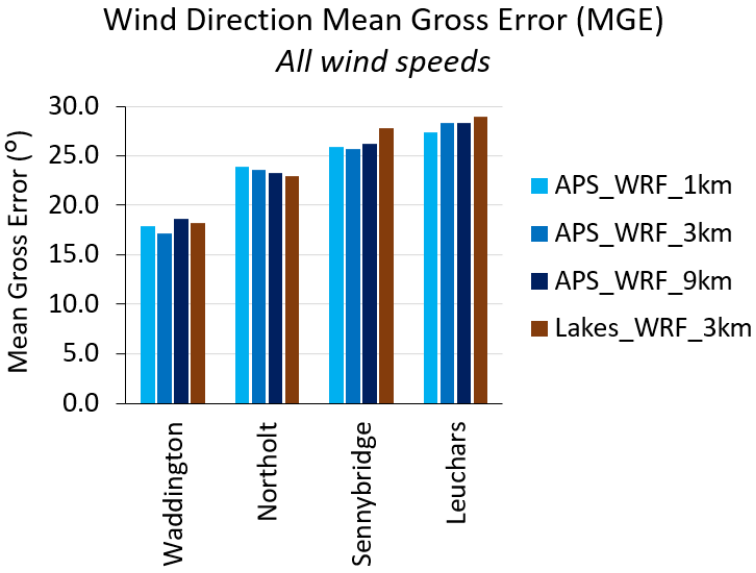

Figure 33 – Bar chart of mean gross error (MGE) for wind direction in degrees at four sites for Lakes and APS WRF data, for all wind speeds.

Table 15 presents summary model evaluation statistics comparing hourly modelled and observed wind direction data, excluding hours with measured wind speed values below 1.5 m/s in order to take account of the increased uncertainty of measured wind direction at very low wind speeds. All four model datasets considered meet the suggested Fairmode benchmarks for both MB and MGE, with relatively little difference due to either model resolution or configuration. Corresponding frequency scatter plots over all sites (Figure 34) also show no discernible difference between the modelled datasets.

Table 15 – Summary of meteorological model performance evaluation of wind direction at 10 m, for wind speeds of 1.5 m/s and above. Statistics calculated over the four sites with Lakes data, compared against statistical benchmarks as suggested by Fairmode.

Model	Resolution (km)	Number of valid points	Observed Mean (°)	Modelled Mean (°)	MB	MGE
					Fairmode benchmark	
					-10 — 10	< 30
					Ideal model value	
					0	0
APS_WRF	1	31402	240	229	-6.0	20.1
APS_WRF	3			231	-5.9	20.0
APS_WRF	9			229	-6.0	20.1
Lakes_WRF	3			227	-3.5	20.4

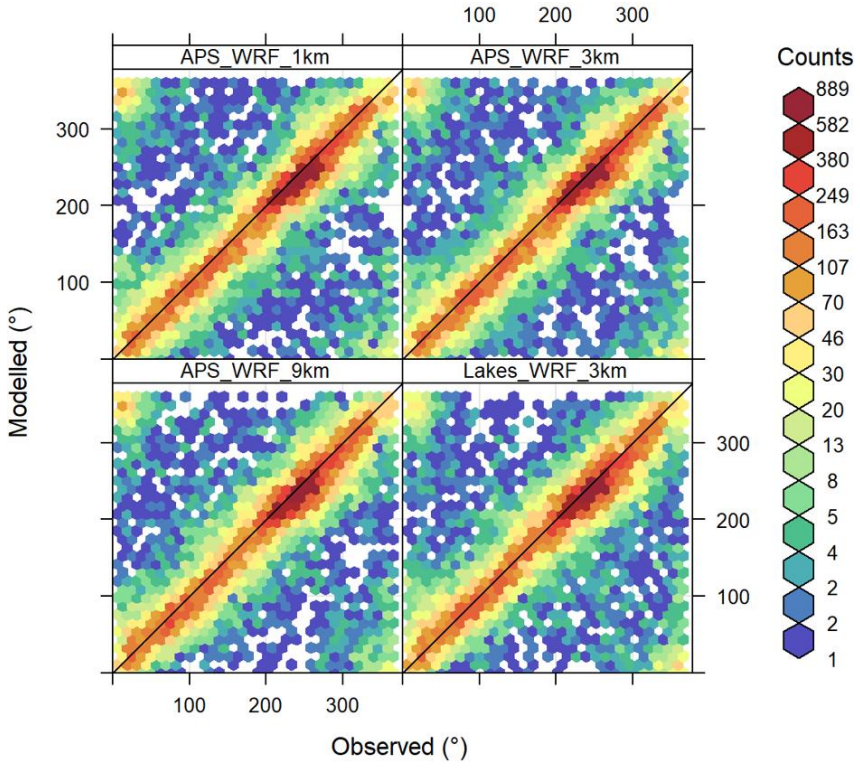

Figure 34 – Frequency scatter plots comparing modelled and observed wind direction in degrees. Wind directions excluded at wind speeds below 1.5 m/s. Including only the four sites with modelled Lakes and APS data.

Mean gross error (MGE) for each model dataset and site, excluding hours with observed wind speed below 1.5 m/s, is shown graphically in Figure 35. In comparison to the equivalent plot for all wind speeds (Figure 33), the MGE for higher wind speeds is reduced for Northolt and Sennybridge, making the model performance more similar between all sites except Leuchars. There is slightly more difference between wind direction MGE due to model configuration than resolution for Northolt and Sennybridge in this plot.

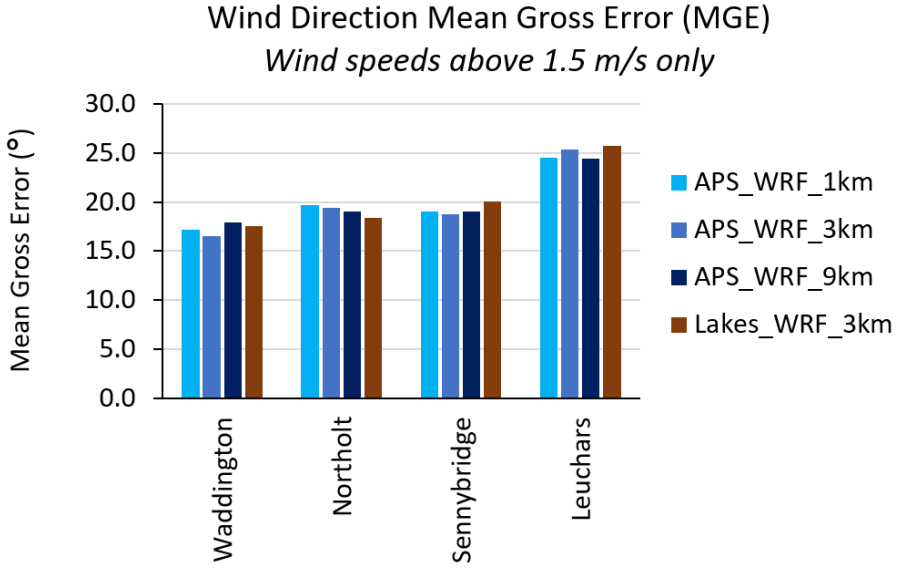

Figure 35 – Bar chart of mean gross error (MGE) for wind direction in degrees at the four sites with Lakes and APS WRF data. Wind directions excluded at wind speeds below 1.5 m/s.

Frequency scatter plots of hourly modelled and observed wind direction at each site, excluding hours with measured wind speed below 1.5 m/s are shown in Appendix B2.2 Figure 139. The Lakes plots are visually similar to those for APS at 3 km resolution, with slightly greater differences due to resolution at the Sennybridge site only.

Polar plots showing the distribution of observed and modelled wind speed and direction are presented in Appendix B2.2 Figures 140 (Waddington), 141 (Sennybridge) and 142 (Leuchars). At Waddington the dominance of moderate southwesterly winds is captured by both APS and Lakes (but slightly less so in the latter). At Sennybridge the observed low wind speeds for northerly wind directions are not well captured by any of the model configurations, this may be due to very local conditions at this observation site. Moderate southwesterly winds are overpredicted by Lakes and the APS WRF 9 km resolution, revealing influence of both resolution and configuration for this feature. At Leuchars the finer resolution (1 and 3 km) APS WRF datasets overpredict the frequency of moderate southwesterly winds, with slightly better matching by the 9 km resolution and Lakes datasets, again showing similar influence from resolution and configuration.

5.3.3 Temperature

Summary model evaluation statistics for temperature calculated over the four sites where Lakes data are available are shown in Table 16, compared with suggested

Fairmode benchmarks. All modelled datasets meet the suggested benchmark values, except for APS at 1 km resolution which just misses the mean bias threshold. All correlation values are very good (> 0.96). There are bigger differences in mean bias, mean gross error and RMSE due to WRF configuration than resolution. APS WRF shows a larger underestimate of mean temperature over this subset of four sites than the full set of eight sites in Table 9. The differences between models and observations are somewhat larger than the expected measurement uncertainty, but still small relative to daily and seasonal temperature variations.

Table 16 – Summary of meteorological model performance evaluation of temperature at screen height. Statistics calculated over the four sites with Lakes data. 34980 total valid hours.

Model	Resolution (km)	Observed Mean (°C)	Modelled Mean (°C)	MB	MGE	RMSE	R	IOA
				Fairmode benchmark				
				-0.5 — 0.5	< 2			≥ 0.8
				Ideal model value				
				0	0	0	1	1
APS_WRF	1	9.94	9.37	-0.56	1.36	1.76	0.96	0.85
APS_WRF	3		9.54	-0.40	1.30	1.70	0.96	0.86
APS_WRF	9		9.59	-0.34	1.35	1.75	0.96	0.85
Lakes_WRF	3		9.89	-0.04	1.13	1.52	0.97	0.88

Frequency scatter plots comparing modelled and observed hourly temperature values across all four sites with Lakes data are shown in Figure 36. All plots show a good model representation of the majority of observed temperatures, though a tendency to overpredict the lowest temperatures. There is a slightly narrower scatter in Lakes than APS at 3 km, again suggesting a stronger influence of configuration than resolution.

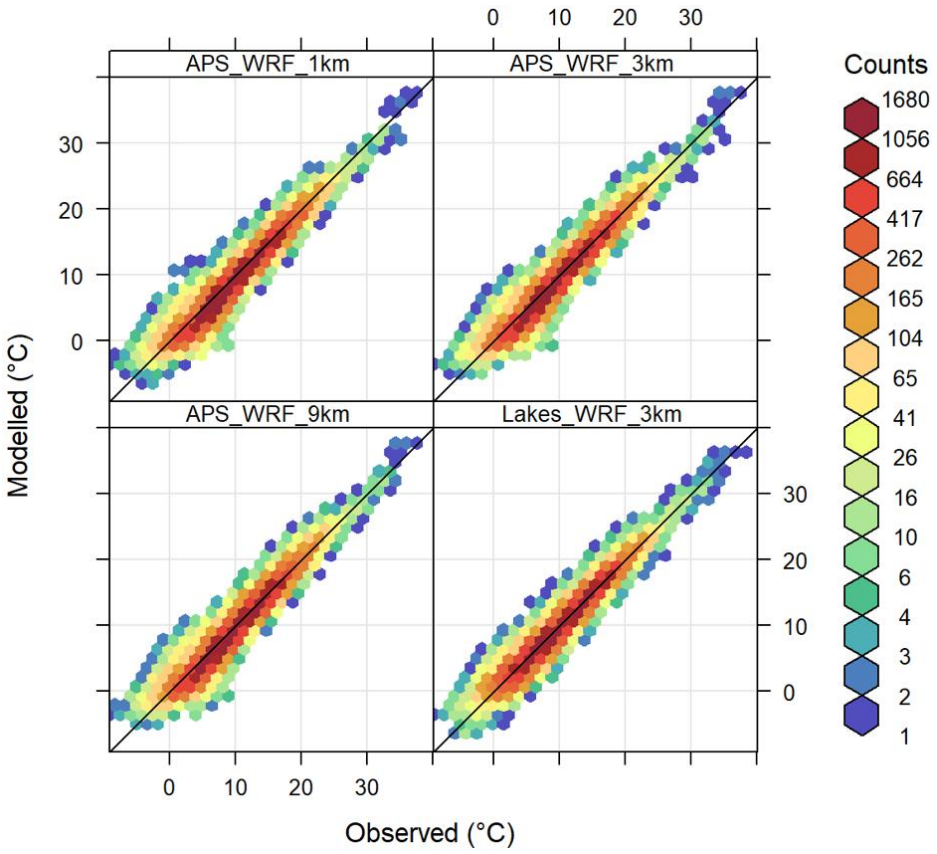

Figure 36 – Frequency scatter plots comparing modelled and observed temperature in degrees Celsius at screen height. Including only the four sites with Lakes and APS WRF modelling at all resolutions.

Figure 37 gives a graphical summary of temperature mean bias at the four sites with Lakes data. This plot shows more difference due to model configuration than resolution, however most values are small. Lakes WRF output meets the suggested Fairmode bias benchmark for all four sites. All of the compared results notably underestimate mean temperature at Waddington, and underestimate to a smaller extent at Leuchars. Figure 38 shows the corresponding plot for correlation, with all models having very high values and no clear difference from either model resolution or configuration at these sites.

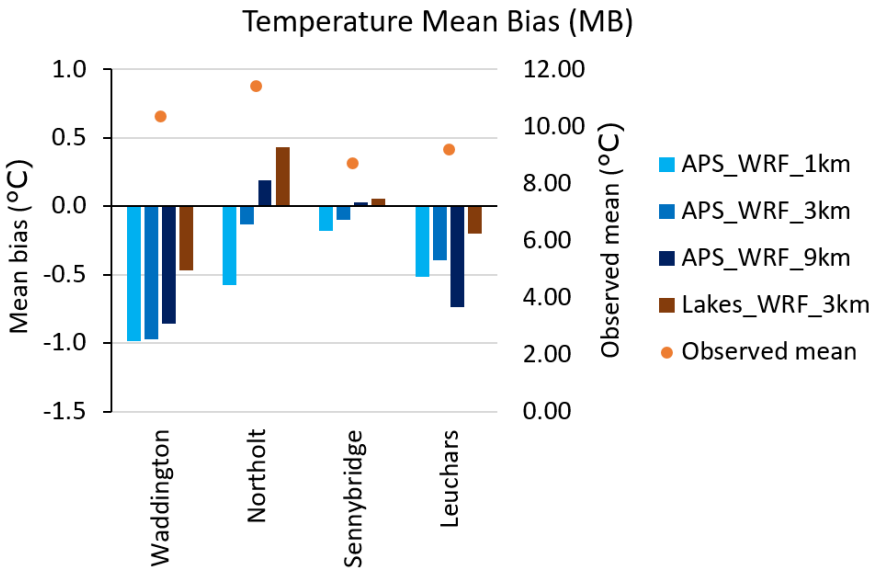

Figure 37 – Graphical summary of mean bias between modelled and observed temperatures at each site (bars and left-hand vertical axis scale). The corresponding observed mean temperature for each site is indicated by the orange circles, using the right-hand vertical axis scale.

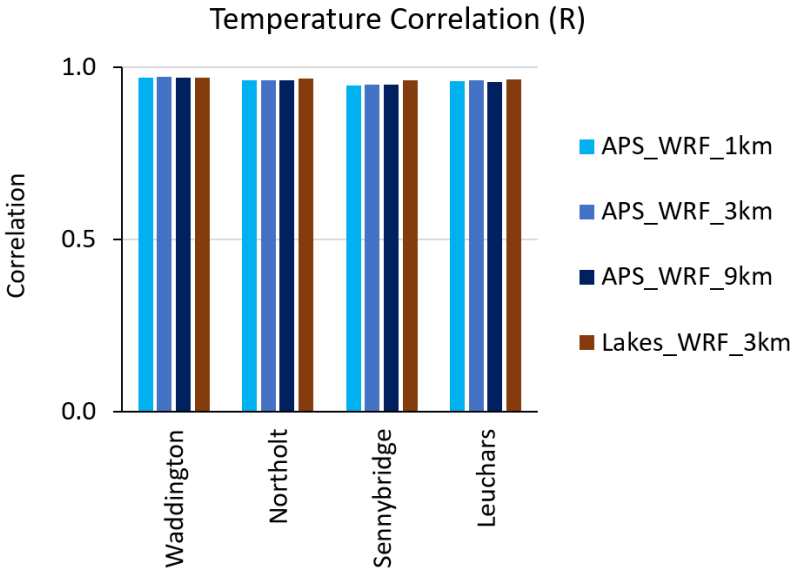

Figure 38 – Graphical summary of correlation between modelled and observed temperatures at each site, for the four sites with Lakes and APS WRF data.

Frequency scatter plots of modelled and observed hourly temperature values are shown in Appendix B2.3 Figure 143. There is a more pronounced overestimate of the lowest observed temperatures by APS than Lakes at Waddington and Sennybridge, while the Lakes data shows this most at Northolt. A stronger influence of model configuration than resolution is shown in these plots. The corresponding quantile-quantile plots in Appendix B2.3 Figure 144 show smaller differences between the different model configurations, with only a greater overestimate of low observed temperatures by Lakes at Northolt and underestimate of low observed temperatures by Lakes at Leuchars discernible.

Polar plots of the variation of modelled and observed mean temperature with wind speed and direction are shown in Appendix B2.3 Figures 145 (Waddington), 146 (Sennybridge) and 147 (Leuchars). For Waddington, Lakes captures the higher temperatures associated with strong southerly winds slightly better than APS but also overestimates mean temperatures for weak southerly winds. At Sennybridge, Lakes captures some observed low wind speed and temperature conditions but also predicts low temperatures for strong northeasterly winds which are not shown in the observations. At Leuchars both Lakes and the two finer resolution APS WRF configurations (1 and 3 km) predict the highest temperatures in a narrow band of southerly wind directions whereas the observations show high temperatures in a wider range of southerly and westerly wind directions. None of the models capture the observed lowest temperatures for weak northwesterly winds at Leuchars. There is slightly more difference visible in the plots due to configuration than resolution for Waddington and Sennybridge, with more difference due to resolution than configuration for Leuchars.

5.3.4 Precipitation

Summary model evaluation statistics comparing hourly modelled and observed precipitation rates over the four sites with Lakes data are presented in Table 17. There is more difference between the statistic values due to configuration than resolution, with poorer performance from the Lakes configuration. The precipitation-specific statistics shown in Table 18 show more comparable performance between APS and Lakes, with underestimates of the number of hours with zero precipitation and overestimates of washout factor. The differences in modelled precipitation between APS and Lakes may be a consequence of the different boundary layer and microphysics schemes adopted in the different WRF configurations.

Table 17 – Summary of meteorological model performance evaluation of hourly precipitation. Statistics calculated over the four sites with Lakes data. 34989 total valid hours.

Model	Resolution (km)	Observed Mean (mm/h)	Modelled Mean (mm/h)	MB	MGE	RMSE	R	IOA
				Ideal model value				
				0	0	0	1	1
APS_WRF	1	0.11	0.11	0.00	0.12	0.48	0.50	0.69
APS_WRF	3		0.11	0.00	0.12	0.47	0.52	0.69
APS_WRF	9		0.11	0.00	0.12	0.45	0.54	0.70
Lakes_WRF	3		0.13	0.02	0.15	0.63	0.34	0.61

Table 18 – Additional precipitation-specific summary statistics, including the washout factor (sum of $p^{0.64}$) and the number of hours with zero precipitation, calculated over the four sites with Lakes data (34989 total valid hours).

Model	Resolution (km)	Observed washout factor	Modelled washout factor	Observed ZNUM	Modelled ZNUM
APS_WRF	1	3653	3992	30587	27103
APS_WRF	3		4013		26806
APS_WRF	9		4212		26094
Lakes_WRF	3		4222		27432

Frequency scatter plots showing modelled and observed hourly precipitation rates for all four sites with Lakes data are shown in Figure 39 for each model and resolution. The Lakes data shows a few very high modelled precipitation rates (> 15 mm/h) for hours with zero observed precipitation rates. There is little difference visible between the different APS resolutions, again reflecting a greater influence from model configuration than resolution. The corresponding quantile-quantile plots shown in Figure 40 confirm that the Lakes configuration is overpredicting the highest observed precipitation rates, while APS show a better representation of the overall distribution of precipitation rates with little difference between resolutions.

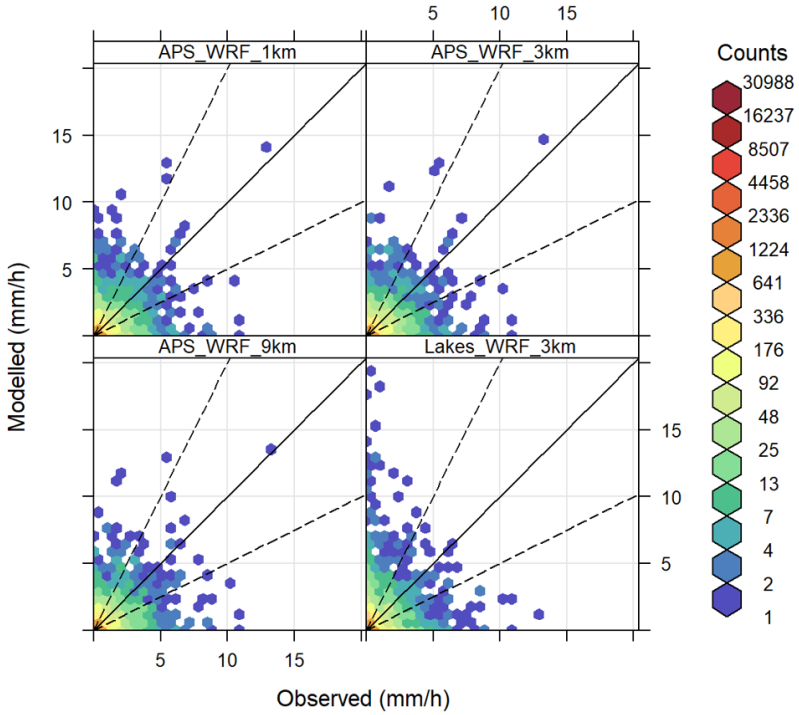

Figure 39 – Frequency scatter plots comparing modelled and observed precipitation rate in mm/h. Including only the four sites with Lakes and APS WRF modelling.

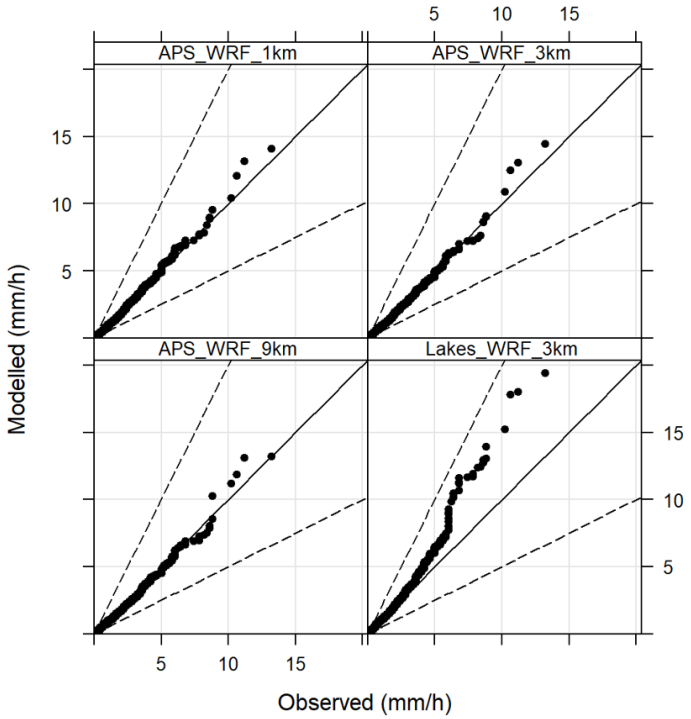

Figure 40 – Quantile-quantile plots comparing modelled and observed precipitation rate in mm/h. Including only the four sites with Lakes and APS WRF modelled data.

Model evaluation statistics comparing hourly modelled and observed precipitation rates at each site are reported in Appendix B2.4 Table 60, with supplementary precipitation-specific statistics in Appendix B2.4 Table 61. A graphical summary of correlation values between modelled and observed hourly precipitation rates is shown in Figure 41, with consistently lower correlation values from Lakes than APS in another demonstration of a greater influence of model configuration than resolution.

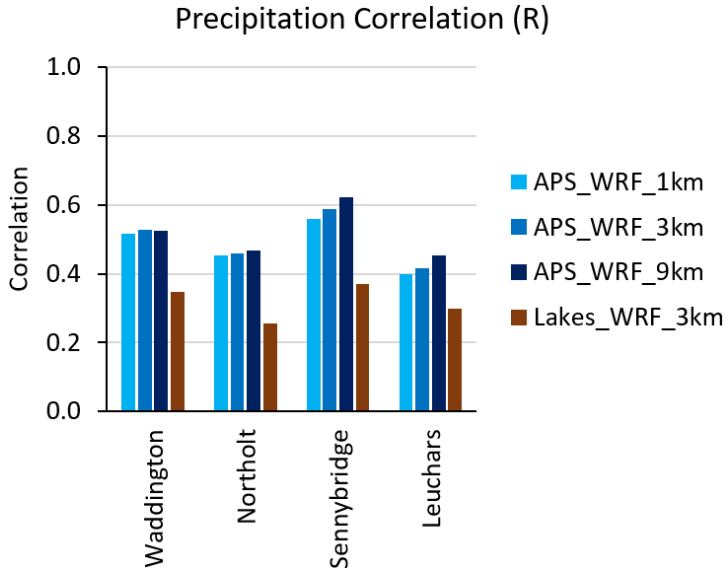

Figure 41 – Graphical summary of correlation between modelled and observed hourly precipitation at each site.

The comparison of the number of zero precipitation hours in observed and modelled datasets presented in Figure 42 shows much smaller differences between Lakes and APS. All models underpredict the number of hours with zero precipitation at all sites, with only slightly greater difference due to model configuration than resolution. Lakes show slightly less underprediction of hours with zero precipitation than APS at all sites except Sennybridge. The corresponding plot of washout factor (Figure 43) shows overestimate of this wet deposition indicator by all models at all sites except Sennybridge. All models capture the higher observed washout factor at Sennybridge but underestimate the magnitude of the difference in washout factor between sites. There are small differences in washout factor values due to APS resolution at all sites and slightly more difference due to configuration.

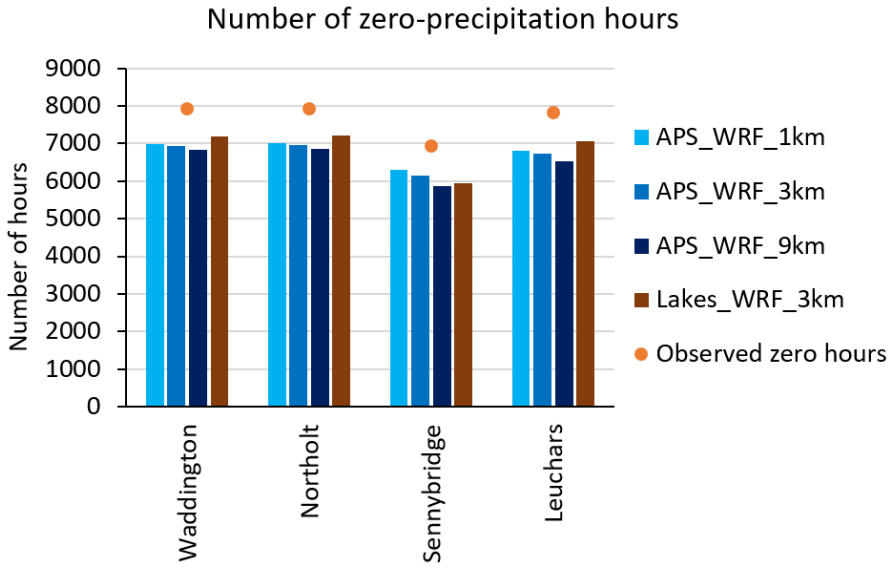

Figure 42 – Graphical summary of the modelled and observed number of hours with a precipitation of zero, at each site.

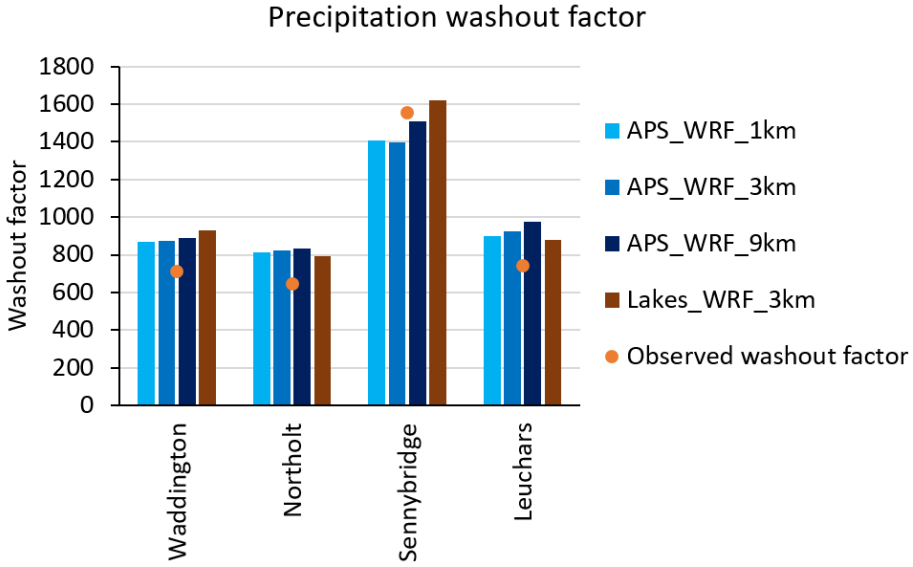

Figure 43 – Graphical summary of washout factor calculated from modelled and observed hourly precipitation at each site.

The frequency scatter plots for hourly precipitation rates shown in Appendix B2.4 Figure 148 demonstrate that the highest Lakes precipitation rates are predicted for the Northolt and Sennybridge sites, which have substantially lower maximum observed precipitation rates. The corresponding quantile-quantile plots (Appendix B2.4 Figure 149) also show an overestimate of higher precipitation rates by the Lakes modelling at Waddington and a few hours of excessively intense precipitation predicted by APS at Northolt.

Polar plots of the variation of washout factor with wind speed and direction, which would strongly influence the spatial distribution of modelled wet deposition, are shown in Appendix B2.4 Figures 150 (Waddington), 151 (Sennybridge) and 152 (Leuchars). At Waddington the observed washout is low for the lowest wind

speeds and the strongest northwesterly winds; the models do not fully capture either of these features. The matching of washout factor values for moderate wind speeds is reasonable. There is a stronger difference in results due to model configuration than resolution. At Sennybridge the observed washout is strongly concentrated in a narrow band of moderate southwesterly winds, while the Lakes results are spread over a wider range of wind speeds and the APS over a broader range of wind directions, especially at 1 and 3 km resolutions. Influences of both model resolution and configuration are visible in the results at this site. At Leuchars, all models capture the increased washout for easterly wind directions and reduced washout for northwesterly winds, but overpredict washout for southwesterly winds. There is a stronger difference between results due to model configuration than resolution at this site.

5.3.5 Cloud cover

Model evaluation statistics comparing modelled and observed hourly cloud cover values are presented in Table 19. While the Lakes mean bias value is similar to the APS values at all resolutions, the Lakes mean gross error and root mean square error values are higher and correlation much lower than APS, showing poorer capture of the variation of observed values. However, the proportion of hours with modelled value within ±1 oktas of the observed value (FRAC1) is similar between Lakes and APS.

Table 19 – Summary of meteorological model performance evaluation of cloud cover. Statistics calculated over the four sites with Lakes data. 34977 total valid hours.

Model	Resolution (km)	Observed Mean (oktas)	Modelled Mean (oktas)	MB	MGE	RMSE	R	IOA	FRAC1
				Ideal model value					
				0	0	0	1	1	1
APS_WRF	1	5.42	5.09	-0.33	1.81	2.62	0.59	0.66	0.57
APS_WRF	3		5.07	-0.36	1.79	2.59	0.60	0.66	0.57
APS_WRF	9		5.02	-0.40	1.78	2.57	0.61	0.66	0.57
Lakes_WRF	3		5.08	-0.34	2.40	3.61	0.36	0.55	0.55

Frequency scatter plots for hourly modelled and observed cloud cover at all four sites with Lakes data are shown in Figure 44. These show similar patterns for all APS resolutions, but a tendency for Lakes to predict a greater dominance of cloud cover values of 0 and 8 than found in the observations, with a substantial underprediction of observed cloud cover values 1-4.

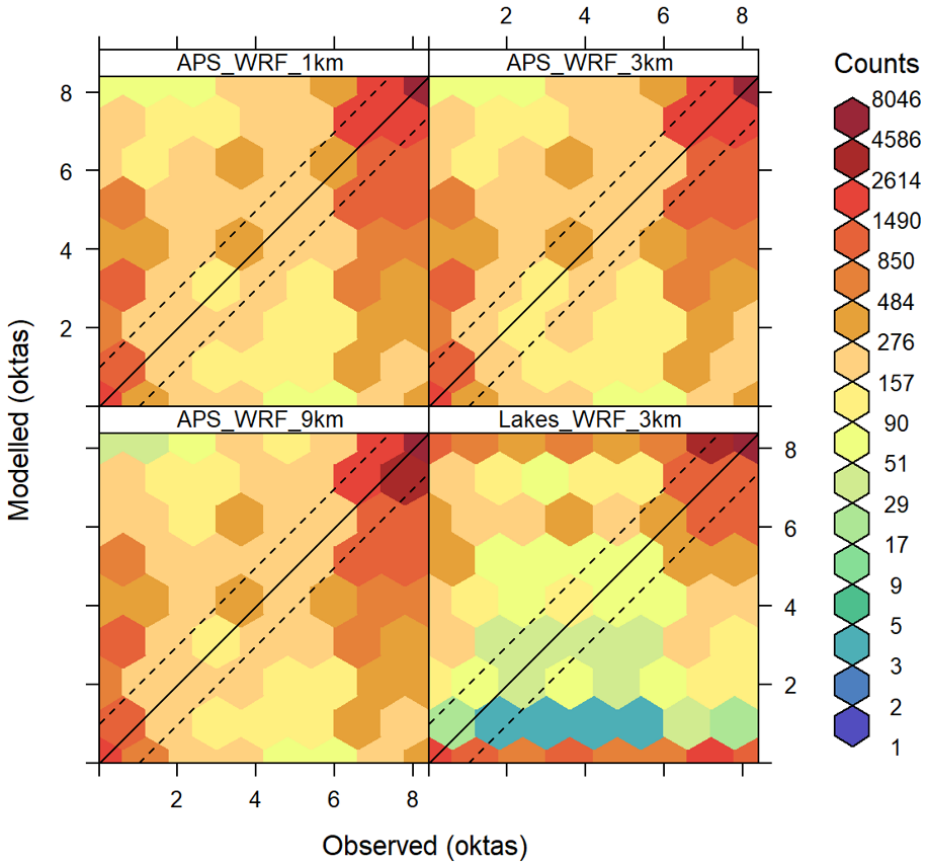

Figure 44 – Frequency scatter plots comparing modelled and observed cloud cover in oktas. Including only the four sites with Lakes and APS WRF modelled data. Dashed lines indicate values within ±1 okta.

Model evaluation statistics for each site are reported in Appendix B2.5 Table 62. A graphical summary of mean bias values is shown in Figure 45, with much larger magnitudes of mean bias from Lakes than APS at all sites except Sennybridge. All models and sites show model underprediction of observed mean cloud cover except Lakes at Northolt. All sites show a stronger influence of model configuration than resolution for this metric. The graphical summary of correlation values for each site in Figure 46 confirms the poorer performance of the Lakes dataset and strong influence of model configuration on this metric.

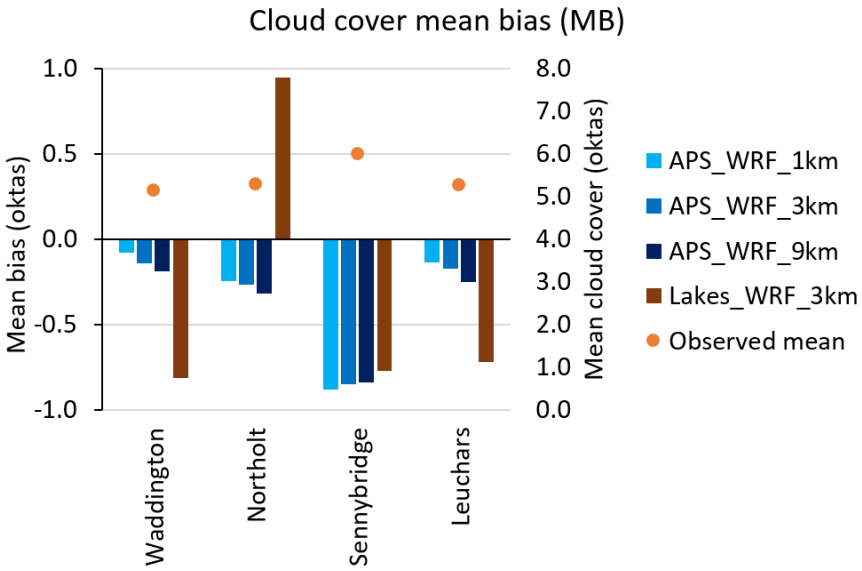

Figure 45 – Graphical summary of mean bias between modelled and observed cloud cover at each site (bars and left-hand vertical axis scale). The corresponding observed mean cloud cover for each site is indicated by the orange circles, using the right-hand vertical axis scale.

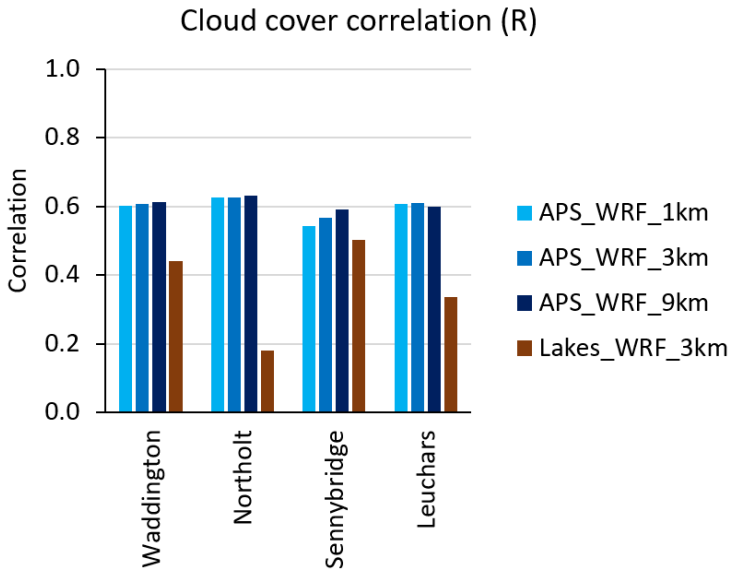

Figure 46 – Graphical summary of correlation between modelled and observed cloud cover at each site.

The frequency scatter plots for each site displayed in Appendix B2.5 Figure 153 show that the Lakes predictions of very few cloud cover values of 1 okta are replicated across all sites, with a particularly pronounced effect at Northolt. This is also confirmed by the histograms shown in Appendix B2.5 Figures 154 to 157. Lakes used version 3.4 of the MMIF tool to extract WRF data into AERMET and AERMOD formats for this study. This version of MMIF initially calculated cloud fraction in each vertical grid layer from the relative humidity value in that layer, then derived overall AERMOD cloud cover from the maximum clud fraction value across all layers. The use of maximum cloud fraction tends to lead to cloud cover

values which are either zero or high, as seen in the Lakes histograms. There is a slight distortion in the Lakes histograms due to the unit conversion from AERMOD cloud cover in integer tenths to ADMS cloud cover in oktas, this tends to artificially increase the proportion of hours with cloud cover values of 2 oktas and 6 oktas, but does not influence the low proportion of hours with 1 okta.

Polar plots showing the variation of mean cloud cover with wind speed and direction are given in Appendix B2.5 Figures 158 (Waddington), 159 (Sennybridge) and 160 (Leuchars). At Waddington the Lakes configuration underpredicts observed cloud cover for moderate wind speeds over all wind directions. At Sennybridge Lakes captures more of the observed dominance of high cloud cover values for all southwesterly winds than APS, but tends to underpredict observed cloud cover values for light easterly winds and overpredict for strong easterly winds. APS predicts a similar distribution of cloud cover with wind speed for all wind directions, with little variation between resolutions. At Leuchars all models capture the reduced mean cloud cover for northwesterly winds, while Lakes underpredicts cloud cover for moderate southerly winds. There are greater differences between plots due to configuration than resolution at all sites.

5.4 Comparison of secondary meteorological variables

Secondary meteorological variables which determine atmospheric stability, such as boundary layer height and surface heat flux, are not routinely observed but are often available in NWP datasets. ADMS can either use measured or modelled primary meteorological variables to generate secondary variables, or use secondary variables from NWP as input data. This section describes an inter-comparison of secondary variables calculated by ADMS from measured and NWP primary variables, alongside secondary variables directly extracted from NWP data. The comparisons have been carried out at Waddington (flat), Northolt (urban), Sennybridge (complex terrain) and Leuchars (coastal) sites.

ADMS can use multiple combinations of input meteorological variables to generate secondary variables. The combinations used in this study are summarised in Table 20. NWP data from APS WRF modelling at 1 km and 9 km resolutions and Met Office UM data at 1.5 km and 10 km resolutions were used in this comparison.

Table 20 Summary of meteorological configurations for secondary variable evaluation * Cloud cover data will not be used in ADMS when surface heat flux and/or boundary layer height data are input. ** Solar radiation data were not available from the Met Office UM data.

Variable	Units	Configuration		
		Base	Heat	Heat BLH
Wind speed	m/s	✓	✓	✓
Wind direction	°	✓	✓	✓
Temperature	°C	✓	✓	✓
Cloud cover	Oktas	✓	(✓)*	(✓)*
Precipitation	mm/h	✓	✓	✓
Solar radiation	W/m^2		✓**	✓**
Surface heat flux	W/m^2		✓	✓
Boundary layer height	m			✓

Section 5.4.1 describes the comparison of solar radiation data, including evaluation of modelled data in relation to measurements at Waddington and Leuchars. Comparisons of surface heat flux are summarised in Section 5.4.2, boundary layer height values are presented in Section 5.4.3 and overall stability comparisons are described in Section 5.4.4.

5.4.1 Solar radiation

Measurements of incoming solar radiation are available at the Waddington and Leuchars sites only. Modelled solar radiation was available in the APS WRF data but not the Met Office UM data. Evaluation statistics comparing modelled and measured solar radiation from APS WRF at Waddington and Leuchars are shown in Table 21. The values show good correlation between modelled and observed solar radiation, but a tendency for the model to overestimate mean measured solar radiation. The correlation values may partly result from correct model predictions of zero values of solar radiation overnight and non-zero values in daytime. The magnitude of model bias is slightly lower for the 9 km than 1 km modelling at both sites, but the differences are not substantial.

Table 21 Summary of APS WRF model evaluation for primary solar radiation at Waddington (8749 valid hours) and Leuchars (8750 valid hours).

Model	Site	Resolution (km)	Observed Mean (W/m^2)	Modelled Mean (W/m^2)	MB	MGE	RMSE	R	IOA
					Ideal model value				
					0	0	0	1	1
APS_WRF	Waddington	1	120.9	149.0	28.2	56.2	112.4	0.88	0.81
		9		142.4	21.5	53.4	106.7	0.88	0.82
	Leuchars	1	111.5	137.0	25.5	52.3	107.6	0.88	0.81
		9		131.0	19.4	50.5	104.4	0.87	0.82

Frequency scatter plots comparing observed hourly solar radiation at Waddington from APS WRF model data at 1 km and 9 km resolution are shown in Figure 47.

The plots for Leuchars are similar and are shown in Appendix Figure 161 for completeness. These plots show a dominance of low solar radiation values in both observations and model outputs. The tendency for model predictions to overpredict observations is visible, though with considerable scatter. There is no substantial difference in results due to model resolution.

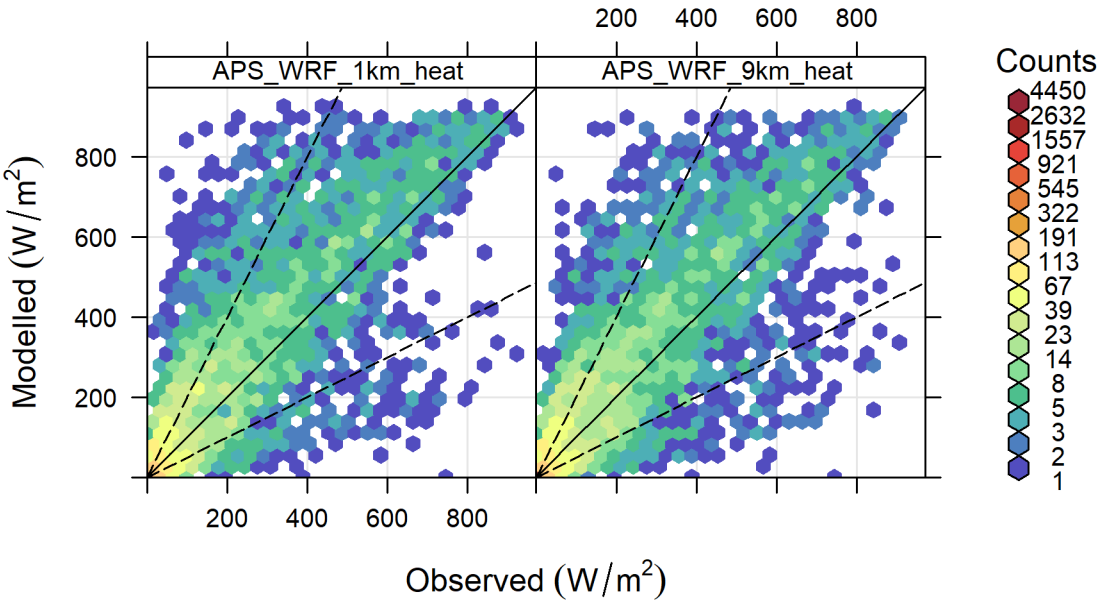

Figure 47 - Frequency scatter plots comparing hourly modelled and observed solar radiation in W/m² at Waddington. Dashed lines indicate modelled values within a factor of 2 of observed values.

ADMS can calculate solar radiation values from cloud cover, latitude, date and time data, if solar radiation is not included in the input meteorological data. These calculations have been carried out with measured and modelled 'base' configuration data, evaluated against measured solar radiation at Waddington and Leuchars. Statistics from this evaluation are given in Table 22. The secondary solar radiation calculated from measured cloud cover has higher correlation and lower RMSE values when compared to measured solar radiation at both sites than all of the NWP datasets. This may partly reflect the difficulty of deriving overall cloud cover fraction values from NWP cloud predictions. Secondary solar radiation values calculated from APS WRF cloud cover tend to slightly underestimate observed mean solar radiation while from MO UM tend to slightly overestimate, however the absolute differences are small (all within ±10%). APS WRF shows slightly better statistics at 9 km than 1 km resolution, whereas MO UM has consistently better performance at 1.5 km than 10 km resolution. There is a discrepancy between the primary solar radiation from APS WRF, which overestimates observed mean values, and the secondary solar radiation calculated by ADMS from APS WRF cloud cover values, which underestimates observed mean values. This may be due to the algorithm used by APS to derive cloud cover values from WRF output, based on relative humidity calculations, which tends to underestimate clear sky conditions as discussed in Section 5.2.5.

Table 22 Evaluation statistics for secondary solar radiation, calculated by ADMS meteorological pre-processor, at Waddington (8748 valid hours) and Leuchars (8697 valid hours). The 'Obs base' configuration uses input date-time, latitude and observed cloud cover values to calculate solar radiation.

Model	Site	Resolution (km)	Observed Mean (W/m^2)	Modelled Mean (W/m^2)	MB	MGE	RMSE	R	IOA
					Ideal model value				
					0	0	0	1	1
APS_WRF	Waddington	1	120.9	112.8	-8.03	40.3	88.8	0.89	0.86
		9		116.6	-4.26	38.8	84.8	0.90	0.87
MO_UM		1.5		122.7	1.83	32.7	69.6	0.93	0.89
		10		123.3	2.41	44.1	94.1	0.88	0.85
Obs base		n/a		119.3	-1.52	29.3	61.4	0.95	0.90
APS_WRF	Leuchars	1	111.4	104.8	-7.27	40.3	88.2	0.88	0.85
		9		108.8	-3.16	39.2	84.2	0.89	0.86
MO_UM		1.5		113.2	1.65	34.8	74.1	0.92	0.87
		10		114.6	3.05	42.8	90.9	0.88	0.84
Obs base		n/a		102.2	-9.37	31.3	67.9	0.93	0.89

Hourly values of secondary solar radiation calculated by ADMS from input base observed and NWP parameter values (primarily date-time, latitude and cloud cover) are compared to observed data in the frequency scatter plots in Figure 48 for Waddington. The equivalent plot for Leuchars (Appendix Figure 162) is similar. The comparison between directly observed solar radiation and the values derived from observed cloud cover shows narrower scatter than any of the NWP datasets. Discrete secondary solar radiation values are visible in the APS WRF and (to a lesser extent) observed datasets due to the integer values of cloud cover in these datasets. The MO UM data includes non-integer values of cloud cover, resulting in a more continuous variation of solar radiation values.

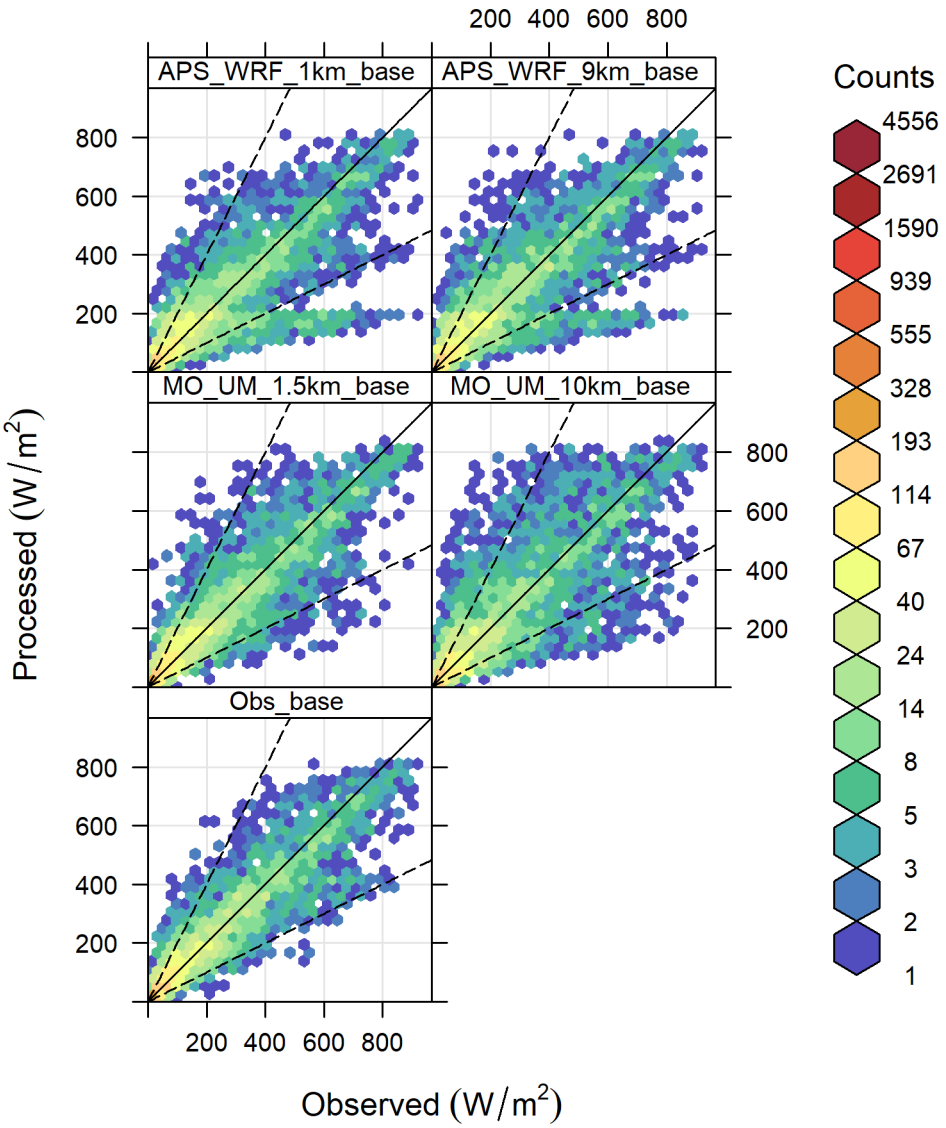

Figure 48 - Frequency scatter plots comparing hourly calculated (secondary) and observed (primary) solar radiation in W/m² at Waddington. Dashed lines indicate modelled values within a factor of 2 of observed values.

5.4.2 Surface sensible heat flux

No surface sensible heat flux measurements are available at the studied sites. This section describes a comparison of values calculated by the ADMS meteorological pre-processor from measured and modelled primary variables, also compared with heat flux values output directly from NWP.

The Priestley-Taylor parameter, representing surface moisture availability in ADMS heat flux calculations, was set to 1.0 for all sites. This value represents moist grassland, which is likely to be appropriate at all the studied sites in cooler weather but may overestimate moisture availability at sites other than Sennybridge in hot summer periods. It is possible to supply hourly varying values of this parameter to ADMS in the .met file, however this option has not been tested in the current study.

Surface sensible heat flux (F_{θ_0}) values show a diurnal cycle with positive values in daylight, when the ground surface is warmer than the air, and negative values at night, when the ground surface is colder than the air. Larger positive values of surface sensible heat flux are associated with increased intensity of vertical mixing in the atmosphere due to thermal instability. In contrast, larger negative surface sensible heat flux values are associated with thermal stratification and reduced vertical mixing.

Table 23 presents a statistical comparison between the hourly surface sensible heat flux values calculated by ADMS from the observed input variables to values calculated by ADMS from NWP 'base' input variables (wind speed, temperature and cloud cover), over four sites. The annual mean heat flux values are close to zero for all configurations and there are strong positive correlations between the values calculated by ADMS from all base input configurations. The corresponding statistics per site are given in Appendix Table 63. There is a trend to slightly higher mean surface heat flux values for the coarser resolution configuration of each model. There is also a trend for higher mean surface flux values from MO UM than APS WRF. There are higher correlations between the heat flux values derived from observations and NWP base variables at Waddington (flat) and Northolt (urban) than at the more complex Sennybridge (complex terrain) and Leuchars (coastal) sites. At Sennybridge this may partly reflect the discrepancies between modelled and observed wind speeds.

Table 23 – Statistics comparing surface sensible heat flux calculated by ADMS from observed 'base' input variables to surface sensible heat flux calculated from NWP 'base' input variables. Statistics calculated over four sites (34944 total valid hours).

Model	Resolution (km)	'Observed' mean (W/m^2)	Modelled Mean (W/m^2)	MB	MGE	RMSE	R	IOA
				Ideal model value				
				0	0	0	1	1
APS_WRF	1	-3.1	-5.4	-2.3	13.8	22.0	0.85	0.75
APS_WRF	9		-2.9	0.2	12.7	20.2	0.87	0.77
MO_UM	1.5		-0.7	2.4	11.5	18.8	0.89	0.79
MO_UM	10		0.3	3.4	13.0	21.7	0.86	0.76

Hourly values of surface sensible heat flux at all sites processed by ADMS from observed and NWP 'base' input variables are compared visually using frequency scatter plots in Figure 49. The near-zero values match well with all input 'base' datasets, but there is substantial scatter at larger magnitudes, particularly for the larger positive heat flux values. These may partly relate to uncertainties in discrete values of cloud cover for summer days, causing the lobed appearance of the scatter plots. The corresponding per-site plots shown in Appendix Figure 163 confirm a narrower spread of both positive and negative values for Waddington and Northolt compared to Leuchars and Sennybridge. There are no clear trends in the plots due to either NWP model resolution or configuration.

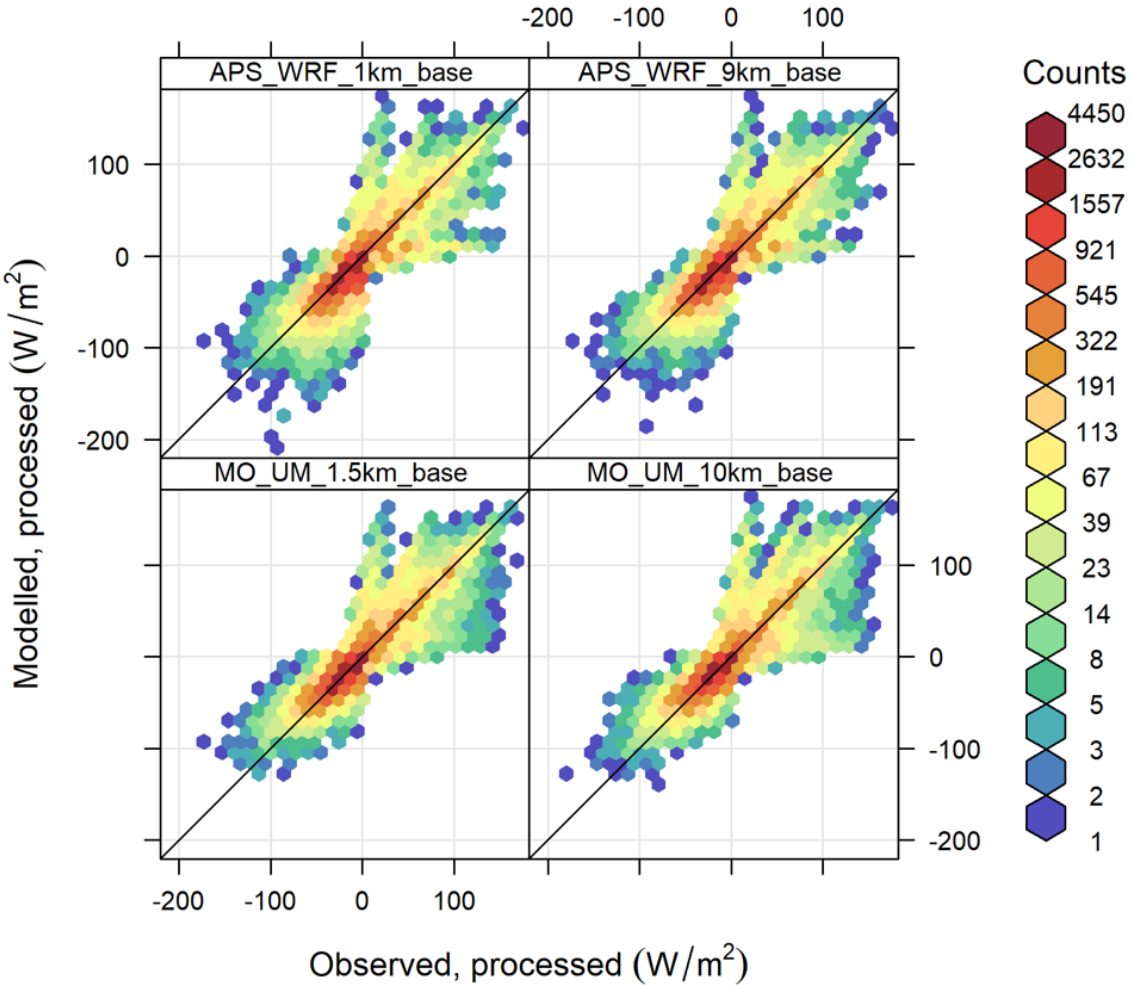

Figure 49 - Frequency scatter plots comparing hourly surface sensible heat flux in W/m², calculated by ADMS from base observations and model data at four sites. Colours indicate the density of points in each area of the graph.

Average diurnal variations of surface sensible heat flux calculated by ADMS from observed and NWP base input variables (wind speed, temperature and cloud cover) are plotted in Figure 50 for January and July at Waddington. In January there are only minor differences between the profiles for different input datasets, whereas in July there is slightly more difference in the daytime profiles. APS WRF data leads to slightly lower summer daytime heat flux while MO UM data leads to slightly higher peak values than calculated from observed input. Corresponding plots for the other sites are shown in Appendix Figure 164. At Northolt the sensible heat flux profiles calculated from observed or NWP input data show similar behaviour to Waddington. At Sennybridge notably smaller magnitudes of both positive and negative heat flux are calculated from observed base variables compared to NWP base variables for both months. At night this may be due to the lower observed than modelled wind speeds at this site. At Leuchars in January the APS WRF base variables lead to larger magnitudes of night-time negative heat flux than the observed base variables.

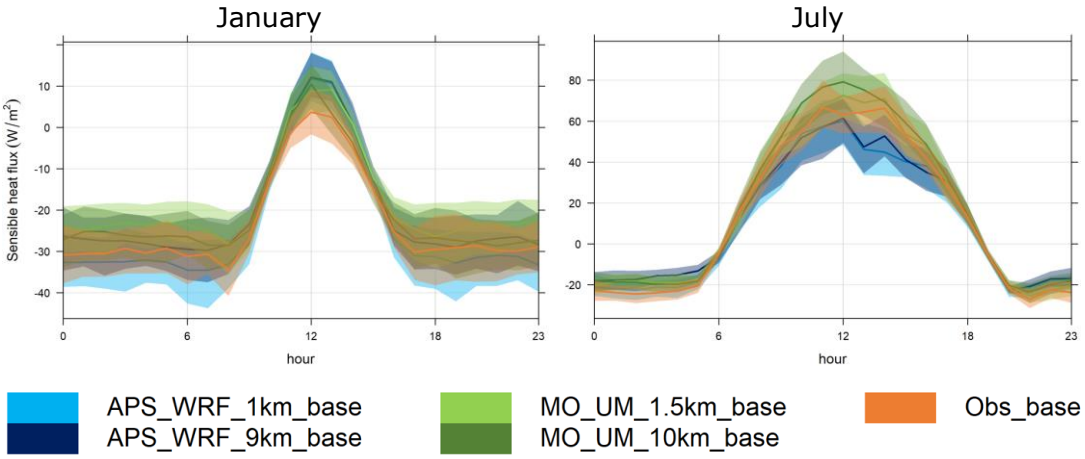

Figure 50 – Diurnal profiles of surface sensible heat flux in W/m² at Waddington, derived from observed and modelled base input variables, averaged for January (left) and July (right). The shaded areas show 95% confidence intervals around the mean.

The surface sensible heat flux values exported from the NWP models have been compared with values calculated by ADMS from the NWP base variables. Comparison statistics over all four sites are given in Table 24. Comparing the values in Tables 23 and 24 shows that the NWP surface sensible heat flux values give higher mean values than the values calculated by ADMS from NWP base variables. The correlation values between NWP heat flux and ADMS calculations from observed base variables are also lower than between the different base configurations, suggesting that the NWP heat flux variation with base variables differs from the ADMS calculations. Corresponding statistics for each site are given in Appendix Table 64. The values for APS WRF 9 km resolution at Northolt stand out with a much higher mean bias compared to the values calculated by ADMS from observed base variables at this site. Otherwise there are no consistent trends between the different models or resolutions.

Table 24 – Statistics comparing surface sensible heat flux calculated by ADMS from observed 'base' input variables to surface sensible heat flux extracted from NWP. Statistics calculated over four sites (34944 total valid hours).

Model	Resolution (km)	'Observed' mean (W/m²)	Modelled Mean (W/m²)	MB	MGE	RMSE	R	IOA
				Ideal model value				
				0	0	0	1	1
APS_WRF	1	-3.1	11.1	14.1	27.6	46.1	0.76	0.50
APS_WRF	9		19.8	22.9	34.2	58.6	0.74	0.37
MO_UM	1.5		7.7	10.8	21.3	32.6	0.80	0.61
MO_UM	10		8.6	11.7	21.2	32.7	0.81	0.61

Hourly surface sensible heat flux values calculated by ADMS from observed base values and extracted from NWP data are compared over the four sites in Figure 51. This figure shows much more scatter than the comparisons of ADMS calculated heat flux from observed and NWP base variables. The scatter for near-zero values will reflect discrepancies between the models in the assumed dawn/dusk timings.

The NWP maximum positive surface sensible heat flux magnitudes are higher than those calculated by ADMS for all sites, models and resolutions. There are particularly high positive heat flux values from APS WRF at both 1 km and 9 km resolution, not matched by ADMS calculations or MO UM predictions. The per-site frequency scatter plots in Appendix Figure 165 show that for the 9 km resolution these highest values are predicted for Northolt while for 1 km resolution the highest values are predicted at Leuchars. These sites may both be affected by changes in dominant land use between the different grid resolutions, with Northolt located on the edge of an urban area and Leuchars near the coast. Salvador *et al.* (2016) also showed WRF over-predictions of coastal daytime surface sensible heat flux compared to measurements for a short period.

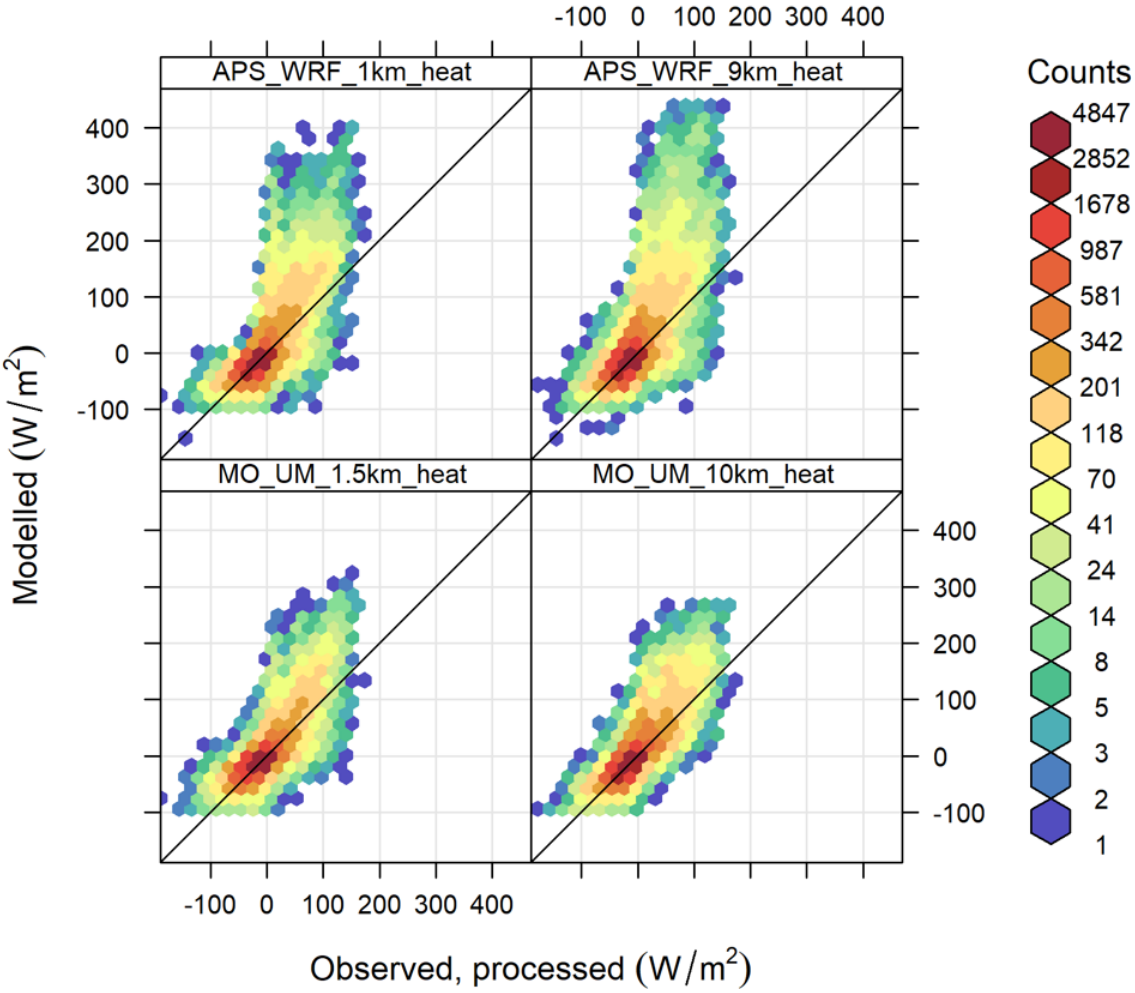

Figure 51 - Frequency scatter plots comparing hourly surface sensible heat flux in W/m², derived from base observations and extracted from NWP data at four sites.

Average winter and summer diurnal profiles of surface sensible heat flux calculated by ADMS from observed base variables and extracted from NWP at Waddington are shown in Figure 52. These show a temporal shift in the profiles between ADMS and NWP, with ADMS predicting both the morning increase and evening decrease in surface heat flux to occur later than the NWP data. The 3-hourly data archiving frequency of MO UM 10 km dataset is also visible in the profiles. At Waddington the surface heat flux values calculated by ADMS from observed data for these

months are generally lower than from NWP for both night and daytime. Corresponding profiles for other sites are shown in Appendix Figure 166. The dominant feature is large daytime summer heat flux values from the NWP datasets at all sites, with much lower predictions from ADMS. This could partly reflect the increased moisture availability in the ADMS calculations due to the uniform Priestley-Taylor parameter, leading to greater latent heat (evaporative) fluxes and lower surface sensible heat flux. The land surface models in the NWP data may allow for cumulative surface drying during hot weather and thus lower latent heat flux and higher surface sensible heat flux in this period.

The summer profiles from APS WRF 9 km at Northolt and APS WRF 1 km at Leuchars show particularly high peak flux values, as noted in the frequency scatter plots. The APS WRF 9 km at Northolt also shows positive summer overnight heat flux, which may be associated with urban land use or may be an artefact related to different land use categorisations at different grid resolutions. The winter profiles show smaller relative differences between the different models at all sites, with mostly overlapping confidence intervals.

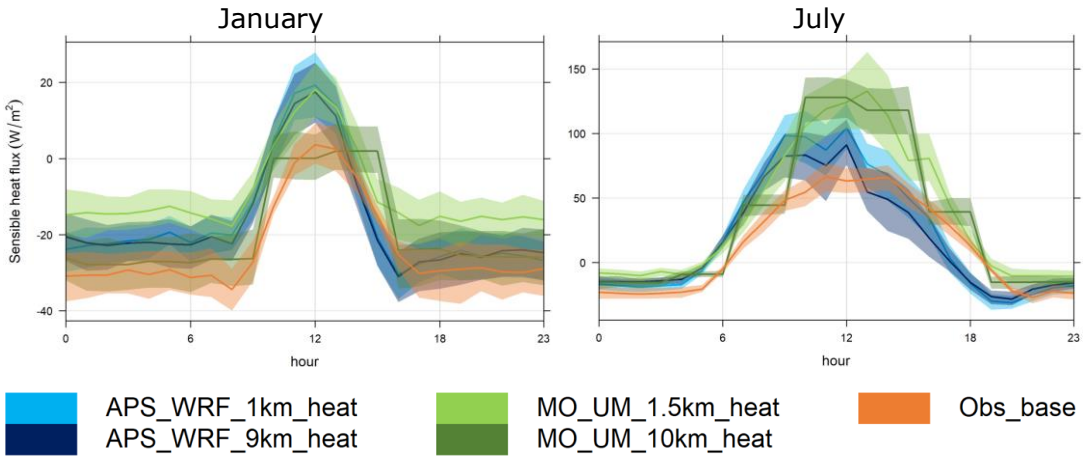

Figure 52 – Diurnal profiles of surface sensible heat flux in W/m^2 at Waddington, derived from base observations and extracted from NWP data, averaged for January (left) and July (right). The shaded areas show 95% confidence intervals around the mean.

5.4.3 Boundary layer height

No boundary layer height measurements are available at the studied sites. This section describes a comparison of values calculated by the ADMS meteorological pre-processor from measured and modelled primary variables, also compared with boundary layer heights output directly from NWP.

Statistics comparing ADMS calculated boundary layer height derived from observed base parameters or modelled base parameters are presented in Table 25. Mean boundary layer height values are higher for the finer resolution configuration of both models, with a bigger difference for APS WRF (higher than from observations for 1 km resolution, lower for 9 km). Otherwise, the statistics are similar for all four model configurations. Statistics for individual sites

(Appendix Table 65) show that mean boundary layer heights derived from APS WRF are lower than those derived from measurements at all sites except Sennybridge. The difference from measurements is bigger from the 9 km resolution configuration at Waddington and Northolt, with little difference at Leuchars. The biggest difference in mean boundary heights due to grid resolution for MO UM occurs at Northolt, where the boundary layer height derived from 10 km resolution inputs is smaller than from 1.5 km resolution. The correlation values between boundary layer heights derived from all base NWP datasets and those derived from observations are very high (> 0.9) for all sites except Sennybridge, which suggests that the ADMS meteorological pre-processor calculations of boundary layer height may be relatively insensitive to the differences in base input variables between NWP and observed data.

Table 25 – Statistics comparing boundary layer height calculated by ADMS from observed 'base' input variables to boundary layer height calculated from NWP 'base' input variables. Statistics calculated over four sites (34906 total valid hours).

Model	Resolution (km)	'Observed' mean (m)	Modelled Mean (m)	MB	MGE	RMSE	R	IOA
				Ideal model value				
				0	0	0	1	1
APS_WRF	1	491.5	522.7	31.2	148.9	246.8	0.87	0.80
APS_WRF	9		482.3	-9.2	143.0	231.6	0.87	0.80
MO_UM	1.5		460.7	-30.8	127.0	209.9	0.89	0.83
MO_UM	10		447.1	-44.4	141.7	233.6	0.87	0.81

Hourly boundary layer heights derived from basic observed and modelled variables at all four sites are compared in frequency scatter plots in Figure 53. There is a cluster of points along the 1:1 line, confirming the strong relationship between the boundary layer heights calculated from observed and modelled inputs indicated by the high correlation values. However, there is also a broad scatter, especially when low boundary layer heights are calculated from observed inputs and the boundary layer heights calculated from modelled inputs tend to be higher. The highest boundary layer heights derived from MO UM at 10 km resolution are notably lower than those derived from observations, this may be due to an underprediction of the frequency of clear sky conditions by the coarse (temporal and spatial) resolution MO UM, as shown in the cloud cover histograms in Appendix Figures 129 to 132. The frequency scatter plots for individual sites, shown in Appendix Figure 167, highlight that the broadest scatter between boundary layer heights derived from observed and modelled input variables occurs for the Sennybridge site, and may be associated with the observed wind speed anomalies at this location.

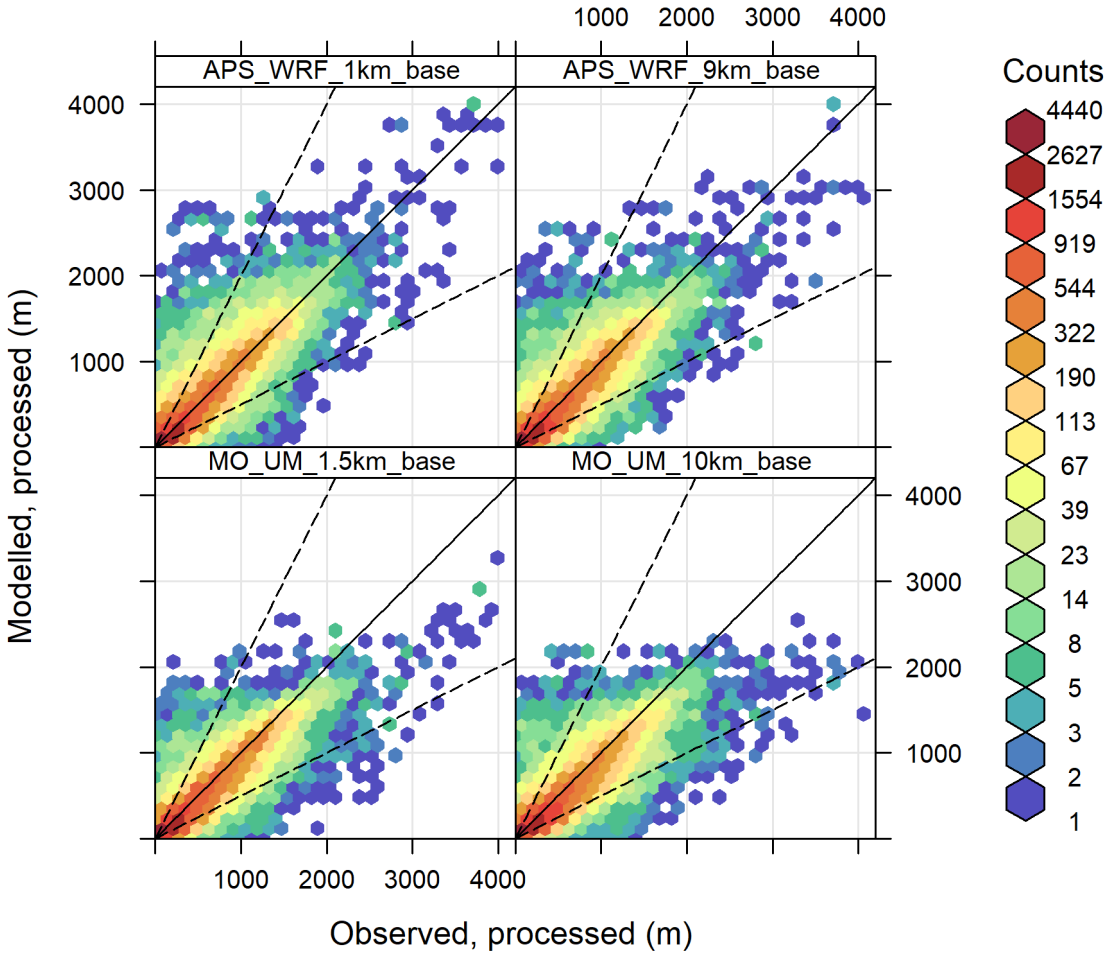

Figure 53 - Frequency scatter plots comparing hourly boundary layer heights in m, derived from base observations and model data at four sites. Dashed lines indicate modelled values within a factor of 2 of observed values.

Boundary layer heights vary through the day, with height increasing due to solar heating during the day and falling at night. The seasonal variation of day length and solar intensity also affects predicted boundary layer heights. Average diurnal cycles of boundary layer heights have been calculated separately for January and July, representing typical winter and summer conditions, and are plotted in Figure 54 for Waddington. Equivalent plots for other sites are shown in Appendix Figure 168. These plots show relatively consistent average profiles derived from observed and modelled inputs for most cases, with overlapping 95% confidence intervals. All the profiles show a higher maximum boundary layer height in July than January, as expected due to the increased duration and intensity of solar heating. Winter overnight boundary layer heights derived from modelled inputs tend to be lower than those calculated from observations at Waddington and Northolt, but higher at Sennybridge (possibly related to wind speed discrepancies at this site). At Leuchars, winter overnight boundary layer heights derived from APS WRF tend to be higher than those derived from observations whereas those derived from MO tend to be lower than observations. There is less difference between the datasets for the summer profiles except at Sennybridge where the boundary layer heights derived from observations are lower than those derived from model data.

The peak of the summer boundary layer height profiles derived from modelled input data for Leuchars and Northolt is slightly earlier than for the profiles derived from observed inputs. The differences due to model resolution are generally smaller than between the different models and observations.

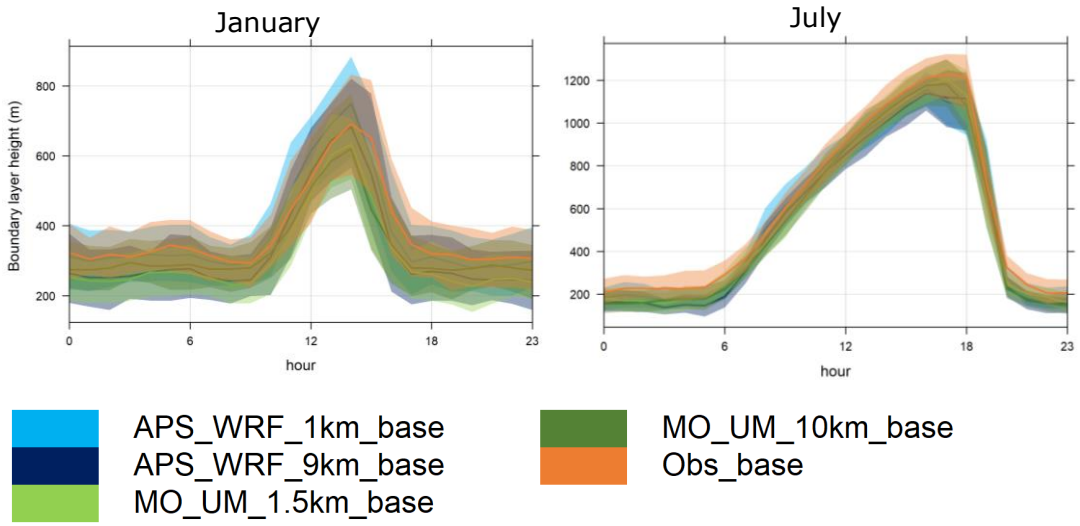

Figure 54 – Diurnal profiles of boundary layer height in m at Waddington, derived from observed and modelled base input variables, averaged for January (left) and July (right). The shaded areas show 95% confidence intervals around the mean.

Boundary layer height values can be extracted directly from the NWP models and used in ADMS. Statistics comparing NWP output boundary layer heights with those calculated by ADMS from observed input variables are shown in Table 26. The mean boundary layer height extracted from MO UM at 10 km resolution is substantially higher than that calculated from observed input data, whereas the other NWP datasets predict lower boundary layer heights than derived from observations. The correlation values of 0.55-0.59 are similar for all NWP datasets, suggesting differences in the calculated boundary layer height variation between NWP models and ADMS. Equivalent statistics for each site are presented in Appendix Table 66. These show a consistent trend for the MO UM at 10 km resolution to predict substantially higher mean boundary layer heights than the other NWP datasets or those derived by ADMS from observed inputs. At Northolt all the NWP datasets predict higher mean boundary layer heights than those derived from observations, while at the other sites APS WRF at both 1 km and 9 km resolution and MO UM at 1.5 km resolution give mean boundary layer heights lower than those derived from observations.

Table 26 – Statistics comparing boundary layer height calculated by ADMS from observed 'base' input variables to boundary layer height extracted from NWP. Statistics calculated over four sites (34906 total valid hours).

Model	Resolution (km)	'Observed' mean (m)	Modelled Mean (m)	MB	MGE	RMSE	R	IOA
				Ideal model value				
				0	0	0	1	1
APS_WRF	1	491.5	445.1	-46.4	261.3	393.8	0.57	0.64
APS_WRF	9		433.2	-58.3	260.1	388.7	0.57	0.64
MO_UM	1.5		415.9	-75.6	257.9	398.2	0.59	0.65
MO_UM	10		650.9	159.4	329.2	443.5	0.55	0.55

Hourly boundary layer heights extracted from NWP models and calculated by ADMS from observed input data are compared using frequency scatter plots in Figure 55. This shows broad scatter for all NWP datasets. The APS WRF plots look similar for both 1 km and 9 km resolution, while there is a clear difference between the MO UM 1.5 km and 10 km resolution outputs. The higher boundary layer height values predicted by the MO UM at 10 km resolution are clear, in particular for hours where the boundary layer height values calculated from observations are low. The APS WRF plots show discontinuities in the predicted boundary layer heights, this is due to the relationship between boundary layer height boundaries and vertical grid definition. Appendix Figure 169 shows equivalent plots for each site. Apart from MO UM at 1.5 km resolution, there is a strong tendency for the NWP boundary layer heights to be higher than the lowest values (less than around 300 m) derived from observations at all sites except Waddington.

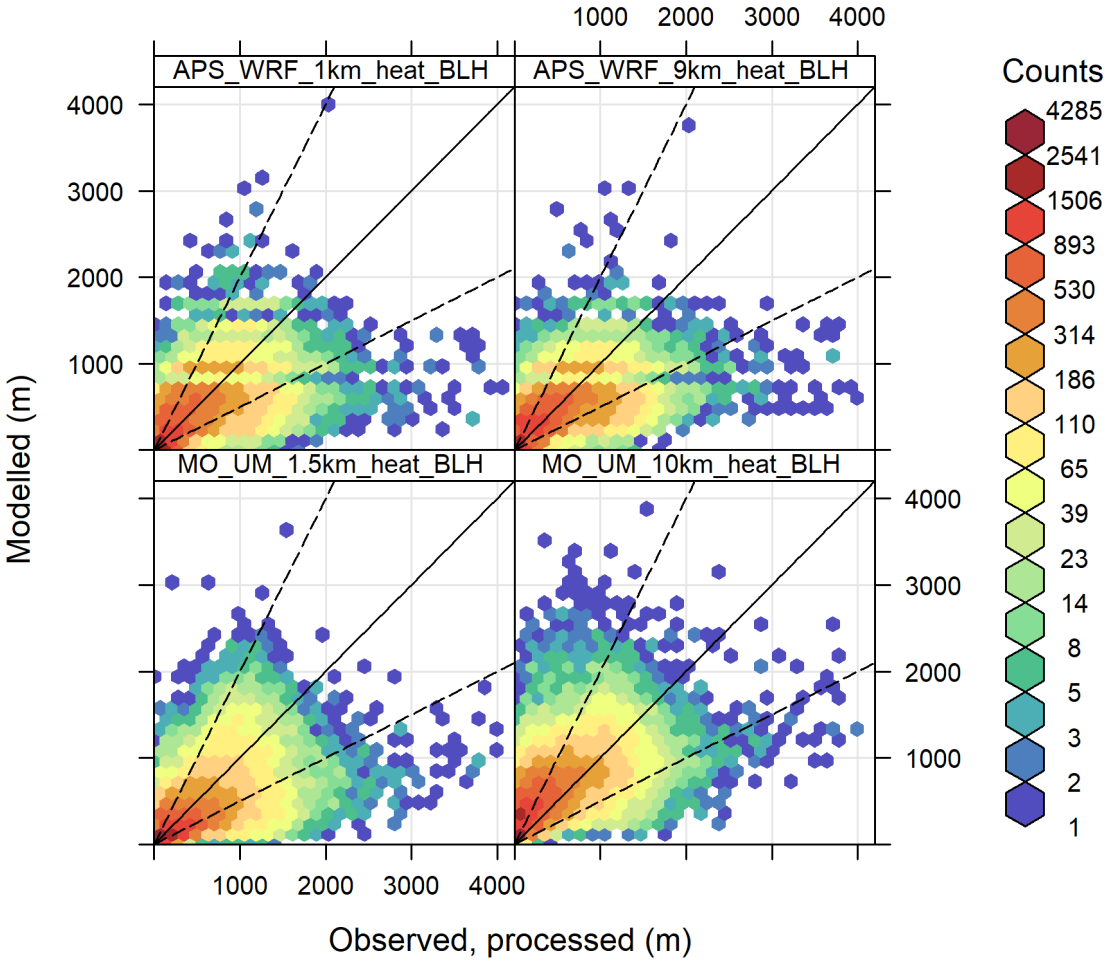

Figure 55 - Frequency scatter plots comparing hourly boundary layer heights in metres, derived from base observations and extracted from NWP data at four sites. Dashed lines indicate modelled values within a factor of 2 of observed values.

Average diurnal profiles of boundary layer heights extracted from NWP data and calculated by ADMS from observed input data have been calculated and plotted for January and July, representing typical winter and summer conditions. Figure 56 shows these plots for Waddington, while plots for other sites are provided in Appendix Figure 170. The MO UM at 10 km resolution consistently predicts higher boundary layer heights than the other datasets for winter conditions and also generally for summer night-time periods. The underlying 3-hourly temporal resolution of the MO UM at 10 km resolution is visible in the profiles. All of the NWP datasets show an earlier peak of summer boundary layer height than the ADMS calculations, with generally lower boundary layer heights from NWP data in late afternoon and early evening. The variability of boundary layer height values from NWP within the month is also higher than from the ADMS calculations, with less smooth average profiles and broader 95% confidence intervals for the NWP datasets. There is little difference between the APS WRF datasets at 1 km and 9 km in the winter profiles. There is a slight tendency for higher summer peak boundary layer height values from the APS WRF 1 km resolution dataset.

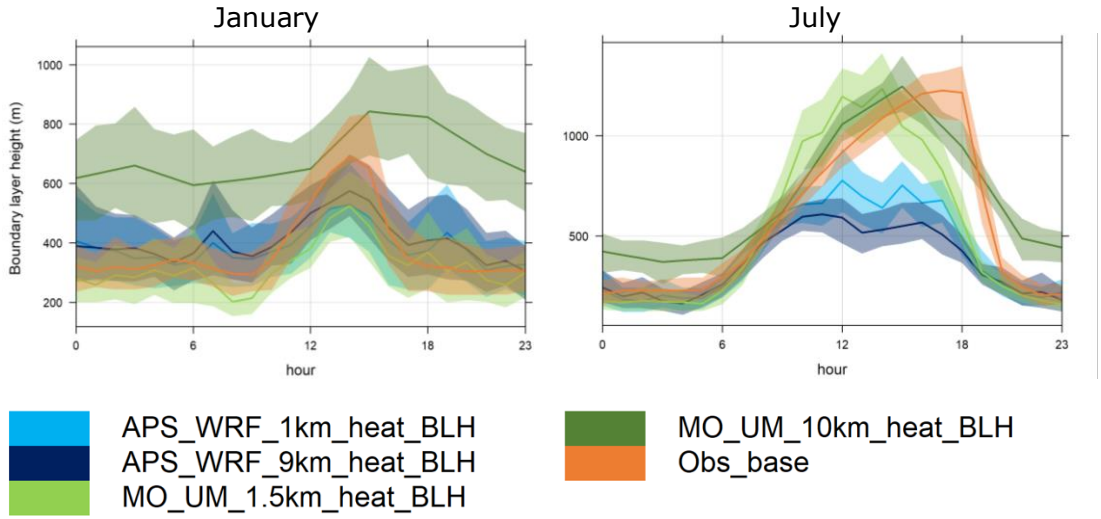

Figure 56 – Diurnal profiles of boundary layer height in m at Waddington, derived from base observations and extracted from NWP data, averaged for January (left) and July (right). The shaded areas show 95% confidence intervals around the mean.

5.4.4 Stability

Atmospheric stability is an important determinant of mixing within the boundary layer, which controls pollutant dispersion. ADMS defines stability using the ratio of boundary layer height (h) to Monin-Obukhov length (L_{MO}), representing the relative importance of thermal and mechanical mixing processes. Convective stability conditions are associated with strong sunshine, leading to high boundary layer heights and vigorous atmospheric mixing. In contrast, stable conditions are most likely to occur at night with ground surface cooling, but can persist throughout winter days. Stable conditions are linked to low boundary layer depths and little vertical mixing in the atmosphere. Neutral conditions are dominated by mechanical mixing processes, usually with strong winds. ADMS uses h/L_{MO} thresholds of -0.3 between convective and neutral conditions and 1.0 between neutral and stable. For the purposes of this study, additional categories of 'very convective' and 'very stable' have also been considered, as defined in Table 27.

Table 27 – Stability categories considered, with h/L_{MO} range values

Category	Minimum h/L_{MO}	Maximum h/L_{MO}
Very convective		-10.0
Convective	-10.0	-0.3
Neutral	-0.3	1.0
Stable	1.0	2.0
Very stable	2.0	

Histograms have been plotted to show the frequency of the different stability categories predicted by ADMS with changing input meteorological datasets. Plots

for Waddington are shown in Figure 57 while data for other sites are presented in Appendix Figures 171 to 173. The top row of panels shows the calculated stability using base modelled variables (wind speed, temperature and cloud cover), which generate stability distributions broadly consistent with those derived from observed base data (lower left panel).

Adding observed or modelled input heat variables (incoming solar radiation and/or surface heat flux as available) makes little difference to the stability distribution derived from observations, but tends to reduce the number of hours in the 'very stable' category for stabilities derived from modelled data.

When input boundary layer height values from NWP at Waddington, Sennybridge and (to a lesser extent) Leuchars are provided to ADMS, the proportion of hours in the neutral category increases substantially for both APS WRF datasets and the MO UM 1.5 km resolution configuration, with fewer hours in the (weakly) stable category. However, for MO UM at 10 km resolution at all sites, including the NWP boundary layer height data increases the number of hours in the 'very stable' category, reducing the frequency of both neutral and weakly stable conditions. This is a counter-intuitive consequence of the high winter overnight boundary layer height values seen in the MO UM 10 km data. At Northolt, the inclusion of heat variables from the APS WRF data at 9 km resolution increases the proportion of 'very convective' conditions, while further adding boundary layer height leads to a substantial increase in the number of hours in the weakly convective category. There are bigger differences in the stability distributions from the different resolutions of MO UM than APS WRF at most sites, this may be due to the effective temporal as well as spatial resolution difference between the two MO UM datasets.

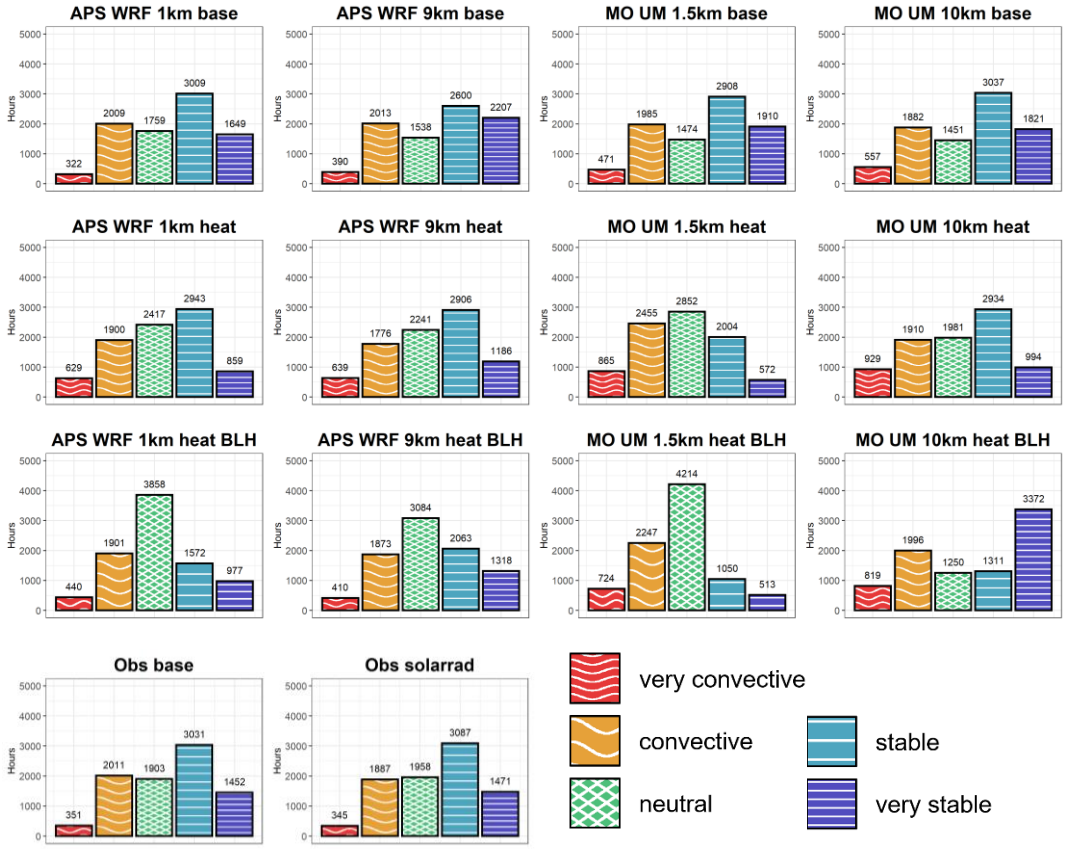

Figure 57 – Histograms showing number of hours in each stability category predicted by ADMS using observed and modelled input datasets with varying combinations of variables. Data for Waddington.

5.5 Conclusions from NWP evaluation

The NWP predictions of observed wind speed and direction data generally show a good match of overall distributions, but some underestimate of peak wind speeds especially at coastal locations. The models also show some overestimates of minimum wind speeds in complex terrain. The models capture most of the combined observed variation of wind speed and direction well in flat terrain but show more difference from observations in complex terrain and coastal locations. The assimilation of measured wind data is likely to improve model performance for both MO UM and APS WRF at all resolutions. There are bigger differences in modelled results between the different model configurations evaluated than between different resolutions of the same model in most cases. There is a stronger trend for small improvements in model performance statistics at complex terrain and coastal sites with finer grid resolution in the APS WRF results than MO UM.

The modelled hourly temperature values also generally match the observed values with good accuracy and little clear influence on performance from changing model resolution. However, there is some overestimate of the lowest hourly temperatures (notably for air temperatures below freezing), which suggests that

the models could underestimate the prevalence and/or intensity of very stable dispersion conditions, associated with high concentrations from local near-ground sources. This is supported by the variation of temperature with wind speed and direction, which shows that the models are not fully capturing the combination of low temperature and low wind speed, especially in complex terrain. However the comparison of stability distributions calculated by ADMS shows similar proportions of hours in 'very stable' conditions when modelled or measured 'base' variables (wind speed and direction, temperature, cloud cover and precipitation) are used as input. The similarity of stability distributions indicates that the ADMS stability calculations are not sensitive to the differences in ambient temperature values between observed and modelled data. When heat variables (incoming solar radiation and/or surface heat flux) from models are included as input to ADMS, there is a reduction in the number of hours of 'very stable' conditions predicted.

There is a small deterioration in the model performance statistics for temperature at 'Newhaven' where there is a 20 km location discrepancy between the observed and modelled data, but a different change in performance with resolution for each model.

The distribution of hourly precipitation rates is dominated by a large number of hours with zero observed rates, which may distort the annual mean precipitation rates. The correlation values for hourly precipitation are noticeably lower than for wind speed or temperature, reflecting both the challenge of modelling local precipitation events accurately in both space and time and the increased uncertainty in measurements of precipitation. The MO UM at 10 km resolution shows a very substantial overestimate of both the number of hours with non-zero precipitation rates and the washout factor (linearly related to total wet deposition). The poorer performance of this model configuration may result from the use of parameterisation for small-scale convective rain processes at this grid scale, and/or from the use of 3-hourly average values in the archiving and extraction process. The MO UM at 1.5 km, APS and Lakes WRF are able to resolve some convective processes, but still underpredict the number of hours with zero precipitation and overpredict the frequency of light precipitation compared to observed data. This leads to an overestimate of washout factors at most sites, which would result in overestimates of total wet deposition. Additional analysis of seasonal precipitation rates from modelled and observed datasets would be required to investigate the relative importance of convective rain events. Polar plots show a broader distribution of modelled washout factor with varying wind speed and direction than that observed, which will alter the spatial distribution of wet deposition. There is also a model tendency to underestimate the variation of washout factor between sites. However, comparing observed data between pairs of sites from the selection in this study, at distances of 40 – 100 km, shows better matching from modelled data than alternative observations. Further work would be needed to make a systematic comparison of the relative merits of modelled data or observations from alternative sites at varying distances. Investigations of the spatial variability of observed and modelled precipitation could also be useful for consideration of the validity of using single point precipitation data for larger scale plume modelling, particularly in complex terrain.

Cloud cover also shows poorer matching between modelled and observed hourly values than wind speed or temperature, partly due to challenges in deriving overall cloud cover in oktas from model representations of different cloud types in separate vertical layers, and also the substantial uncertainty in observed cloud cover values. There is little difference between APS WRF and MO UM 1.5 km resolution results. As for precipitation, there are poorer performance statistics for MO UM 10 km resolution, this may again be due either to the use of convective parameterisation in the MO UM global configuration or to the lower effective temporal resolution of this dataset. Observed cloud cover data are dominated by values of 0, 7 and 8, whereas the modelled data from both APS WRF and MO UM show a broader spread of values. The variation of observed cloud cover with wind speed and direction at Sennybridge is not well captured by any of the models. The Lakes approach of extracting cloud cover values from WRF via MMIF version 3.4 leads to an unusual distribution of values, with notably few values of 1 okta. However, the derived boundary layer height profiles and stability distributions calculated from ADMS from input observed and modelled base variables including cloud cover are very similar, suggesting that this variable does not have strong influence in the stability calculations and resulting dispersion predictions.

WRF output data from different configurations supplied by Lakes and APS was compared at a subset of four measurement sites. This comparison showed a more substantial effect from model configuration than grid resolution for wind speed, temperature, cloud cover and precipitation, while neither configuration nor resolution caused substantial differences in modelled wind direction, and configuration and resolution had similar levels of influence on the combined variation of wind speed and direction. It is not possible to isolate which difference in configuration between Lakes and APS is most affecting performance in the analysed datasets, for example the driving meteorology, boundary layer scheme and microphysics scheme may all influence the different model outputs for precipitation.

The comparison of modelled incoming solar radiation from APS WRF with measurements at Waddington and Leuchars shows good performance with little difference due to model resolution. The secondary solar radiation calculated by ADMS from latitude, cloud cover, date and time also compares well with measurements. More difference due to resolution was found in MO UM than APS WRF, possibly due to the lower effective temporal resolution of cloud cover data from the MO UM 10 km data. Boundary layer height variations calculated by ADMS from 'base' observed and modelled data variables are broadly similar and contribute to similar stability distributions for these datasets. However, the boundary layer heights extracted from the NWP models show different behaviour, particularly from the MO UM 10 km data. APS WRF has lower maximum boundary layer heights in the summer and more symmetric profiles around midday than those calculated by ADMS, with little difference due to model resolution. MO UM 10 km data show much higher boundary layer heights at night-time than any of the other datasets. Using NWP-extracted heat and boundary layer depth values as input to ADMS causes significant differences in the calculated stability distributions.

The key implications from this meteorological data comparison for dispersion modelling are:

- Models predict the general variation of wind speed, direction and temperature well for most sites and are likely to be suitable for general dispersion modelling;
- Model performance is broadly comparable between MO UM at 1.5 km resolution and APS WRF, though the MO UM modelling assimilation of a wider range of observed data than APS may contribute to slightly improved performance for temperature and cloud cover;
- Models may not fully capture reduced wind speeds observed in some complex terrain or the highest observed wind speeds at coastal sites, but there are small improvements at finer resolution for most sites;
- Models may not capture the observed combination of very low temperature and low wind speed conditions, but this does not significantly affect the overall stability distribution;
- Modelled precipitation should be used with caution for wet deposition modelling, as there is a general overestimate of total precipitation, differences in variation with wind speed and direction and also some underestimate of variation between sites compared to observations, though for the sites assessed the modelled local precipitation shows comparable or better performance than distant alternative observations;
- Convection-resolving model configuration and spatial resolution (< 10 km grid scale, ideally < 4 km), with hourly temporal resolution, should be used for local precipitation data if wet deposition modelling is required;
- Derived boundary layer height and stability conditions in ADMS are relatively insensitive to the differences between the observed and modelled 'base' input variables (wind speed, wind direction, temperature, cloud cover, precipitation); and
- There are substantial differences in the stability conditions calculated in ADMS when heat variables (solar radiation and/or surface heat flux) and boundary layer heights from NWP are used as input.

6 REGULATORY DISPERSION EVALUATION

This section presents the evaluation of the effects of NWP meteorological data on regulatory dispersion modelling outcomes (Task 3). The evaluation process used both ADMS and AERMOD as local models, with NWP data from both MO UM and APS WRF at two resolutions. These NWP datasets and the locations considered for the dispersion comparisons are a subset of those included in the meteorological evaluation (Task 2), described in Section 5. The study design is described in Section 6.1, with concentration results for near-ground sources in Section 6.2 and for elevated sources in Section 6.3. Results for wet deposition (from ADMS only) are presented in Section 6.4. Conclusions from these comparisons are summarised in Section 6.5.

6.1 Dispersion study description

The selection of sites for evaluation of the effects of NWP meteorological data on dispersion outcomes was discussed and agreed with ADMLC. Waddington was chosen as a flat rural baseline, where modelled and observed meteorology are generally well matched. Sennybridge was selected as an example complex terrain site, with greater differences between modelled and observed meteorology. Sennybridge has also been used as the baseline site for the probabilistic modelling investigation (Task 5, described in Section 8). Leuchars is included as a moderately coastal site, plausible for either industrial or agricultural sources. Drumalbin has been included as an additional complex terrain site in the base dispersion modelling comparison (Task 3, described in this Section) as it has also been used in the investigation of the interactions between NWP and local flow modelling (Task 4, described in Section 7).

The surface properties assumed for each site are shown in Table 28. Roughness length values were defined based on the land use around the sites.

Table 28 – Surface properties for each site, with descriptive land use

Site	Land use description	Roughness length (m)	Latitude (°)
Waddington	Airfield	0.2	53.2
Sennybridge	Agriculture	0.3	52.1
Drumalbin	Agriculture	0.2	55.6
Leuchars	Airfield	0.2	56.4

The core dispersion modelling case studies were carried out using the following model configuration.

- Waddington (flat), Sennybridge (complex terrain), Drumalbin (complex terrain) and Leuchars (coastal) locations. The sources were placed at the meteorological measurement site locations, as shown in Figures 4 to 6.

- Observed, APS WRF at 1 km and 9 km resolution and MO UM at 1.5 km and 10 km resolution meteorological datasets. While these datasets are not all routinely available to dispersion modellers, the range of horizontal NWP resolutions allows useful conclusions to be drawn. These resolutions are also relevant to the subsequent investigations of complex terrain effects at multiple scales, described in Section 7. All of the model and resolution combinations were used with 'base' variables - wind speed and direction, temperature, cloud cover and precipitation. 'Extra' configurations with additional NWP heat flux and boundary layer depth variables were also tested for the two fine resolution datasets (APS WRF 1 km and MO UM 1.5 km).

- Local dispersion models ADMS 5.9.0.1 (pre-release version of ADMS 6, Carruthers *et al.* 1994, CERC 2023) and AERMOD version 22112 (with AERMET 22112, Cimorelli *et al.* 2004) were used. AERMOD was run via the ADMS 6 interface, which aims to match the configuration of the two models as closely as possible, especially when the ADMS meteorological pre-processing is implemented. However, running AERMOD via ADMS 6 does not allow wet deposition calculations in AERMOD as they are not part of the standard regulatory configuration. ADMS 6 has been developed to use larger terrain files than were possible with ADMS 5, which had a limit of 66000 points in input terrain files. Otherwise the current study outcomes are likely to be consistent with ADMS 5 modelling.

- Idealised sources representing a typical intensive farming release, simplified as a near-ground point source, and an elevated point source, with source properties as summarised in Table 29. The near-ground source height has been increased from that used in Stocker *et al.* (2017) to reflect a more modern design of poultry shed. In addition, the near-ground source temperature was set to the maximum of the specified 17.4°C and the hourly ambient temperature, to avoid the unrealistic scenario of plumes denser than ambient air in summer months.

- Emission rates of 1 g/s of an inert pollutant for both elevated and near-ground sources.

- Complex terrain modelling inputs from OS terrain 50 elevation data for Sennybridge and Drumalbin at 50 m input resolution, with extents of approximately 13x13 km. Flowfield modelling was carried out with 256x256 points, such that the FLOWSTAR calculation resolution approximately matches the input terrain resolution.

- Default settings for minimum wind speed in each dispersion model, with no use of specialist modelling options for calm conditions. Hence, in AERMOD, the default use of 'random plume' at low wind speeds (when turbulent energy becomes a significant fraction of the total wind energy) was retained. In ADMS, hours with wind speed less than 0.75 m/s at 10 m above ground were not included in the modelling. The number of hours affected by this differs between sites, with the fewest observed low wind speed hours at Waddington (24) and the most at Sennybridge (673).

- No building effects included in the modelling. This is a reasonable assumption for the elevated source but a substantial simplification for the near-ground source which represents emissions from a livestock shed.
- No coastline effects included in the modelling for Leuchars. Coastline modelling in ADMS only occurs for hours when the wind blows from sea towards land, the land is warmer than the sea and the meteorological conditions on land are convective. It leads to an internal boundary layer which grows inland from the coastline, with convective conditions near the ground and stable conditions above. For elevated sources this leads to slow mixing when the plume is above the internal boundary layer, followed by rapid downwards mixing when the plume spreads through the internal boundary layer. The combination of conditions in which coastline effects would be considered by ADMS occurs for less than 7% of hours at Leuchars. The NWP meteorological data may include some coastal effects at Leuchars in the 'extra' variables (heat flux and boundary layer height). AERMOD does not yet include any coastline modelling options.

Table 29 - Summary of idealised source properties for dispersion modelling. *The near-ground source temperature was set to the maximum of 17.4°C and the ambient temperature for each hour.

Source property	Units	Value for near-ground source	Value for elevated source
Diameter	m	0.72	1.8
Height	m	5.5	90
Exit velocity	m/s	2.8	18
Exit temperature	°C	17.4*	140
Data source		Whitelees study, Stocker *et al.* (2017), increased height	Typical values for an industrial installation (NRW recommendation)

Concentration and wet deposition outputs were generated on polar grids of receptors, with a radius of 1 km for the near-ground source and 5 km for the elevated source. The angular point spacing is 30° for all runs. The radial (along-wind) point spacing is 10 m within 100 m of the near-ground sources, 25 m between 100 and 200 m from the source then 50 m from 200 m to 1 km from the source. For elevated sources the points are separated by 100 m up to 1 km from the source, then 200 m from 1 to 5 km from the source.

Post-processing was applied to the modelled concentration and deposition data, to calculate the magnitude of the maximum concentration and deposition and corresponding distance(s) from the source to the location of maximum concentration or deposition in a range of wind sectors, for both long-term mean concentrations, 98^{th} and 100^{th} percentile hourly concentrations and average wet deposition (proportional to total deposition). This analysis allows the differences in magnitude and location of maximum concentration and deposition values between modelling with observed and modelled meteorological data to be assessed.

When presenting results as downwind profiles, output points from the polar grid have been labelled according to the wind direction in which they are downwind of the central source. Each wind direction has been assigned a standard colour and symbol, as depicted in Figure 58.

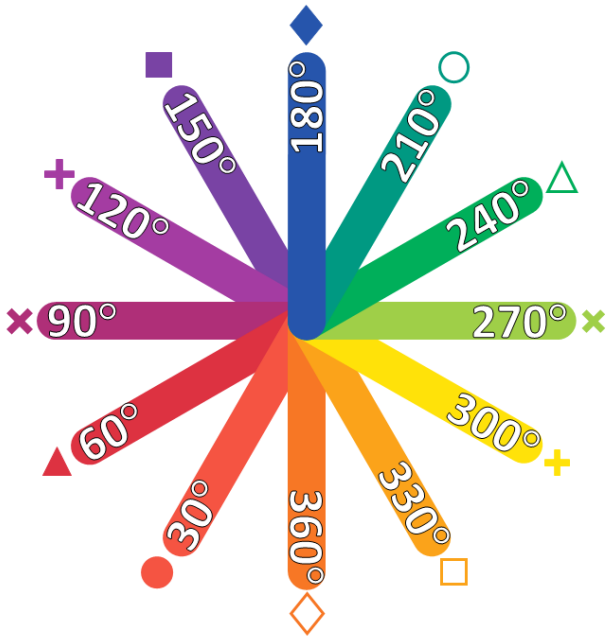

Figure 58 – Illustration of colour and symbol convention for output points relative to central source, labelled by the wind direction in which they are downwind.

6.2 Concentration comparison – near-ground source

The dispersion modelling results with a near-ground source, representative of intensive agriculture emissions, are presented in Section 6.2.1 for annual average concentrations, Section 6.2.2 for 98th percentile of hourly average concentrations and Section 6.2.3 for maximum hourly average concentrations.

6.2.1 Annual average concentrations

The annual average concentration results for a near-ground source at Waddington are shown as downwind profiles for each wind direction sector in Figures 59 and 60. All the profiles are qualitatively similar, with peak concentrations within 50 m of the source and in the most common wind direction sectors (210° and 240°). AERMOD predicts higher peak concentration values than ADMS with all meteorological datasets at this site. Tabulated values of peak concentrations and corresponding locations are given in Appendix Table 67. There is more difference in the magnitude of the peak annual average concentration between the two dispersion models than due to the different meteorological datasets with base variables. The runs using APS WRF meteorological data show more difference due to model resolution than the combination of input variables. In contrast, the runs using MO UM data show more difference due to the combination of input variables than model resolution, in both ADMS and AERMOD.

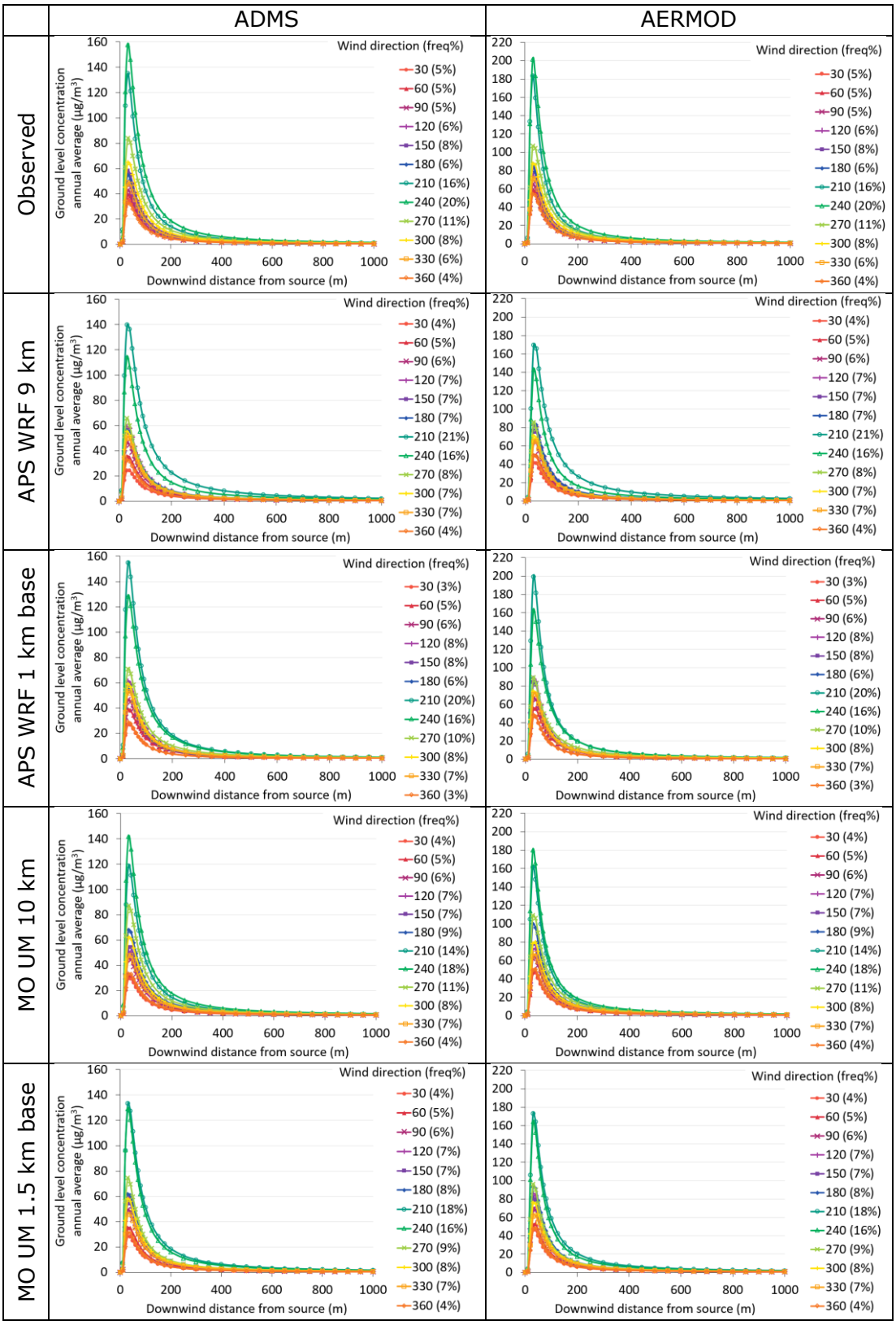

Figure 59 – Downwind profiles of annual average concentration for near-ground source at Waddington with varying wind direction, modelled with ADMS (left) and AERMOD (right), with observed or base NWP meteorological data. Note different vertical scale limits for ADMS and AERMOD plots.

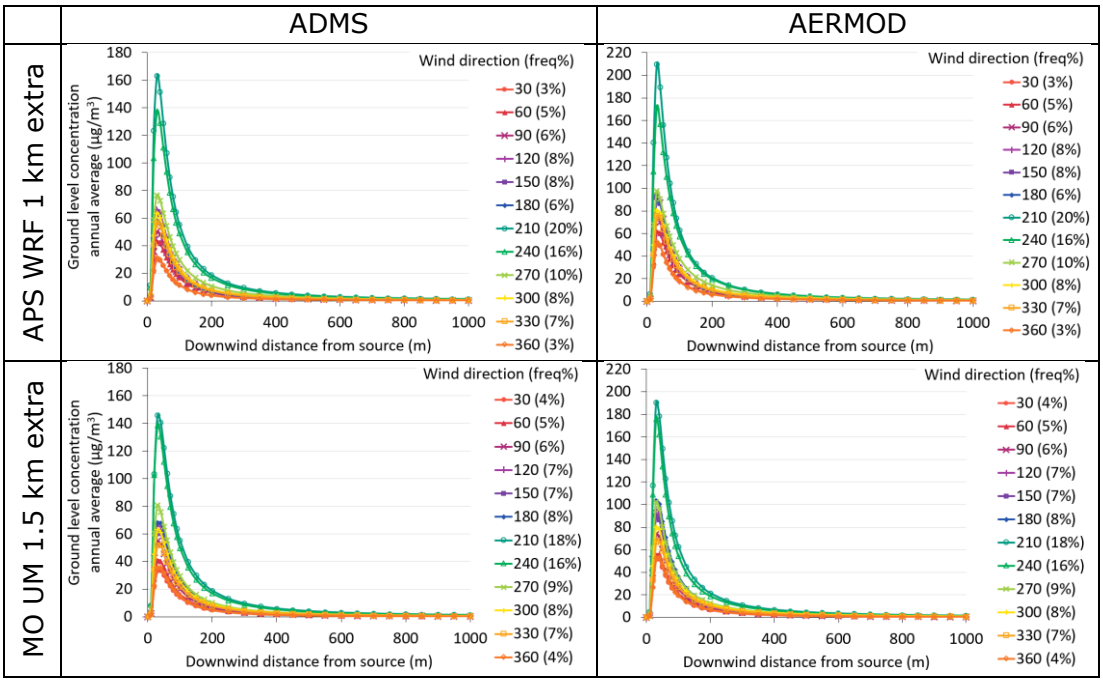

Figure 60 – Downwind profiles of annual average concentration for near-ground source at Waddington with varying wind direction, modelled with ADMS (left) and AERMOD (right), with NWP meteorological data including extra variables. Note different vertical scales are used for ADMS and AERMOD.

Equivalent annual average concentration results for near-ground sources at the other sites are shown in Appendix Figures 174 to 179 and Tables 68 to 70. All of the downwind concentration profiles show single near-source peaks for each wind direction. The magnitudes of peak annual average modelled concentrations with each meteorological dataset and local model are summarised in Figure 61. These plots show higher annual average concentrations predicted by AERMOD than ADMS at all sites except Sennybridge. The runs using observed meteorological data give higher maximum annual average concentrations than most NWP datasets at Waddington and Drumalbin, but lower at Sennybridge and Leuchars. The magnitude of the range of modelled peak annual average concentrations using the six NWP met datasets is around 20% of the peak values modelled using observed met for all sites except Leuchars. This range is similar in magnitude to the difference in values predicted by ADMS and AERMOD using the same observed meteorological data. At Leuchars there is a broader range in the modelled peak annual average concentrations, this is driven by the much higher modelled peak concentrations using the APS WRF 1 km 'extra' dataset, seen in both ADMS and AERMOD. The cause of this higher peak concentration may relate to the higher summer surface sensible heat flux from WRF at Leuchars (shown in Section 5.4.2), leading to increased mixing of the plume down to the surface.

The locations of the peak annual average modelled concentrations for each model and meteorological dataset are shown on maps in Figure 62. These show that the modelled locations of maximum annual average concentration from near-ground sources are predicted consistently with all meteorological datasets and both dispersion models at all four sites. The distance from the source to location of the

maximum annual average concentration is 30 – 40 m in all cases. The maximum angular difference in location is one wind direction sector (30°).

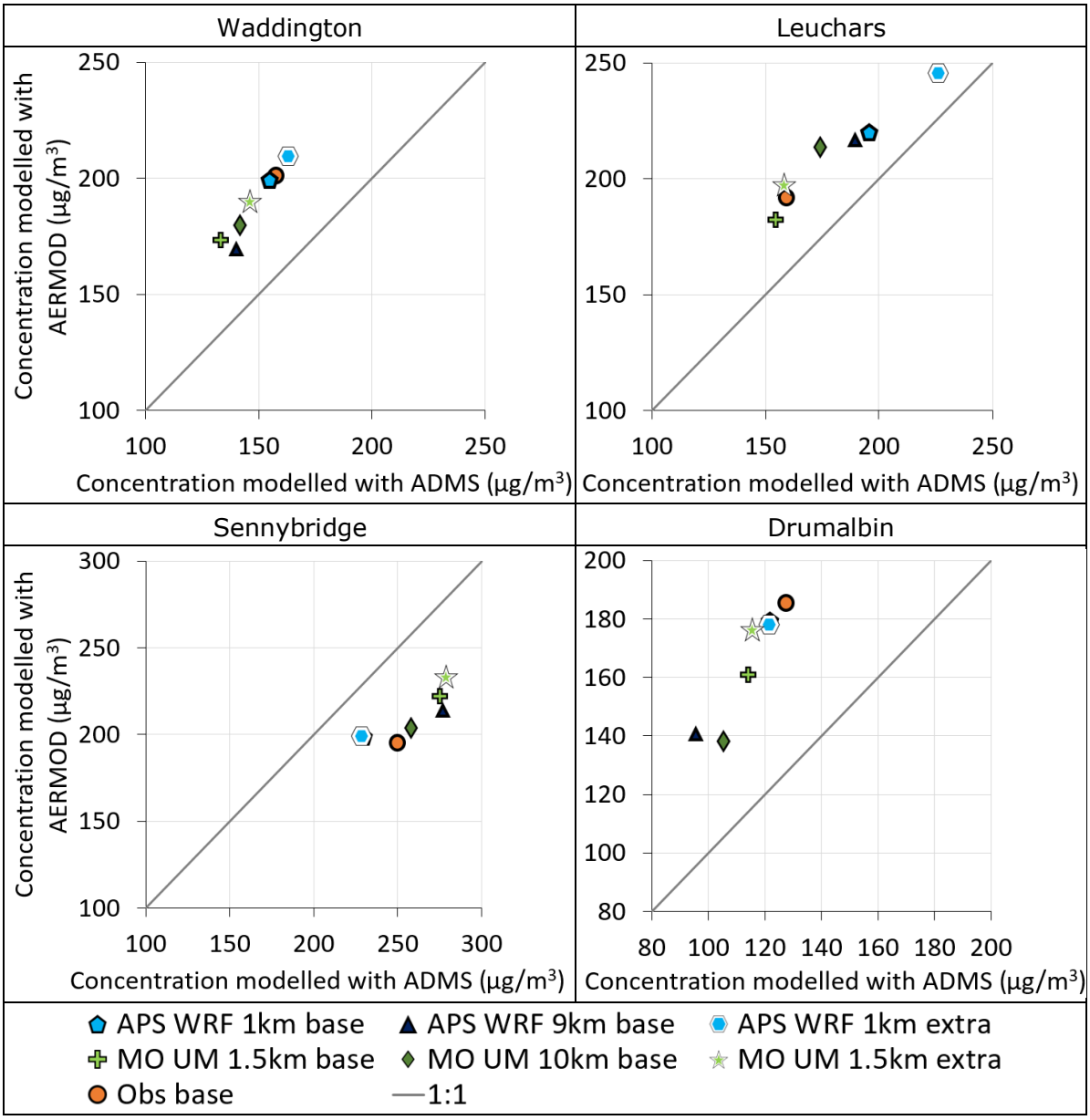

Figure 61 – Magnitudes of peak annual average concentrations for the near-ground source, as modelled with ADMS and AERMOD for each meteorological dataset and site.

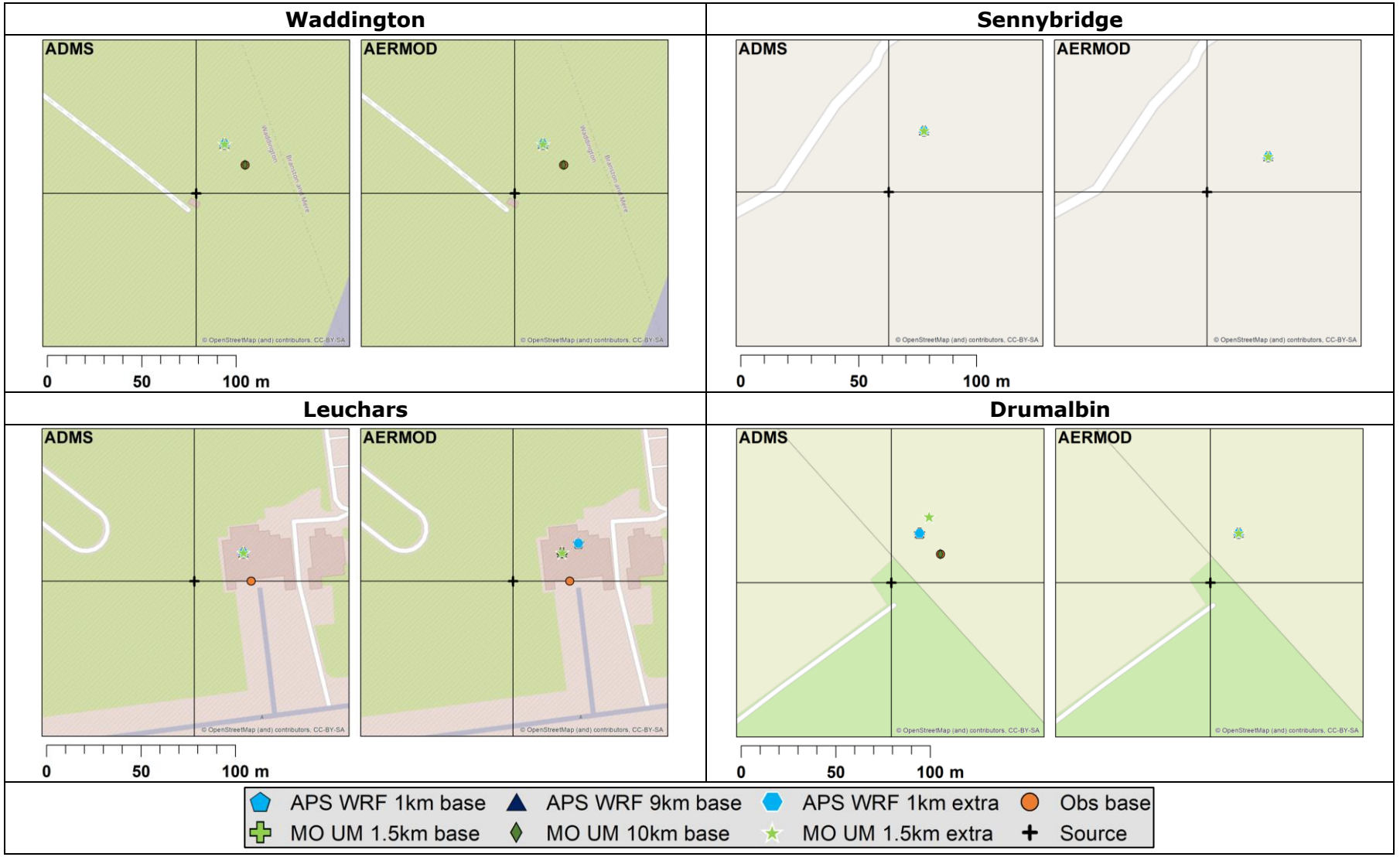

Figure 62 – Locations of peak annual average concentrations for the near-ground source, as modelled with ADMS (left) and AERMOD (right) for each meteorological dataset and site.

6.2.2 98th percentile hourly average concentrations

Downwind profiles of 98th percentile hourly concentrations from near-ground sources at each site are shown in Appendix Figures 186 to 193. Most of the profiles are qualitatively similar, with a single prominent near-source peak. At all sites except Sennybridge AERMOD predicts higher peak 98th percentile concentrations and a broader spread of 98th percentile concentrations with varying wind direction sectors than ADMS. At Sennybridge the modelled profiles are slightly more complex, with secondary peaks in the profiles further downstream, and ADMS predicts slightly higher peak concentrations than AERMOD with all met datasets.

Tabulated peak 98th percentile hourly concentrations and corresponding locations for near-ground sources at each site are given in Appendix Tables 67 to 70. These results are visualised using scatter plots in Figure 63 and maps in Figure 64. The scatter plots confirm that AERMOD predicts higher peak 98th percentile concentrations than ADMS with all meteorological datasets at all sites except Sennybridge. At all sites except Sennybridge, the difference in predicted peak 98th percentile hourly concentrations between the two dispersion models using observed meteorological data is bigger than the difference for each model using different NWP datasets. This suggests that the NWP tendency to miss cold, low wind speed conditions is not significantly affecting the predicted high percentile concentrations for these near-ground sources.

At Sennybridge, ADMS shows very strong sensitivity to the different NWP datasets for peak 98th percentile concentrations, whereas there is little variability in the AERMOD values for this metric. The effect of the 'extra' input meteorological variables is strongest at Leuchars, where all of the base configurations predict similar peak 98th percentile concentrations but the MO UM 1.5 km extra causes a strong increase in the AERMOD value, while APS WRF 1 km extra causes a strong increase in the ADMS value. This may relate to the variability of summer heat fluxes predicted by NWP at Leuchars.

The maps show that the peak 98th percentile hourly concentration location from the near-ground source is always predicted within 40 m of the source and in most cases very close to the location of maximum annual average concentration. Almost all the tested combinations of local dispersion model and input meteorological datasets predict consistent locations for the peak 98th percentile hourly concentration. There are exceptions for the MO UM 1.5 km 'extra' dataset in ADMS at Leuchars, where the peak 98th percentile hourly concentration is predicted to the west of the source, whereas all the other predictions are to the east. At Leuchars the downwind profile plots show that the peak 98th percentile concentration values calculated by ADMS are very similar for several non-adjacent wind direction sectors with both the MO UM 1.5 km base and extra datasets. Hence a relatively small change in 98th percentile concentration for one sector can alter the overall maximum location substantially. The greater spread of peak 98th percentile concentrations predicted by AERMOD for different wind directions leads to less sensitivity to the 'extra' input variables for the location of the overall maximum.

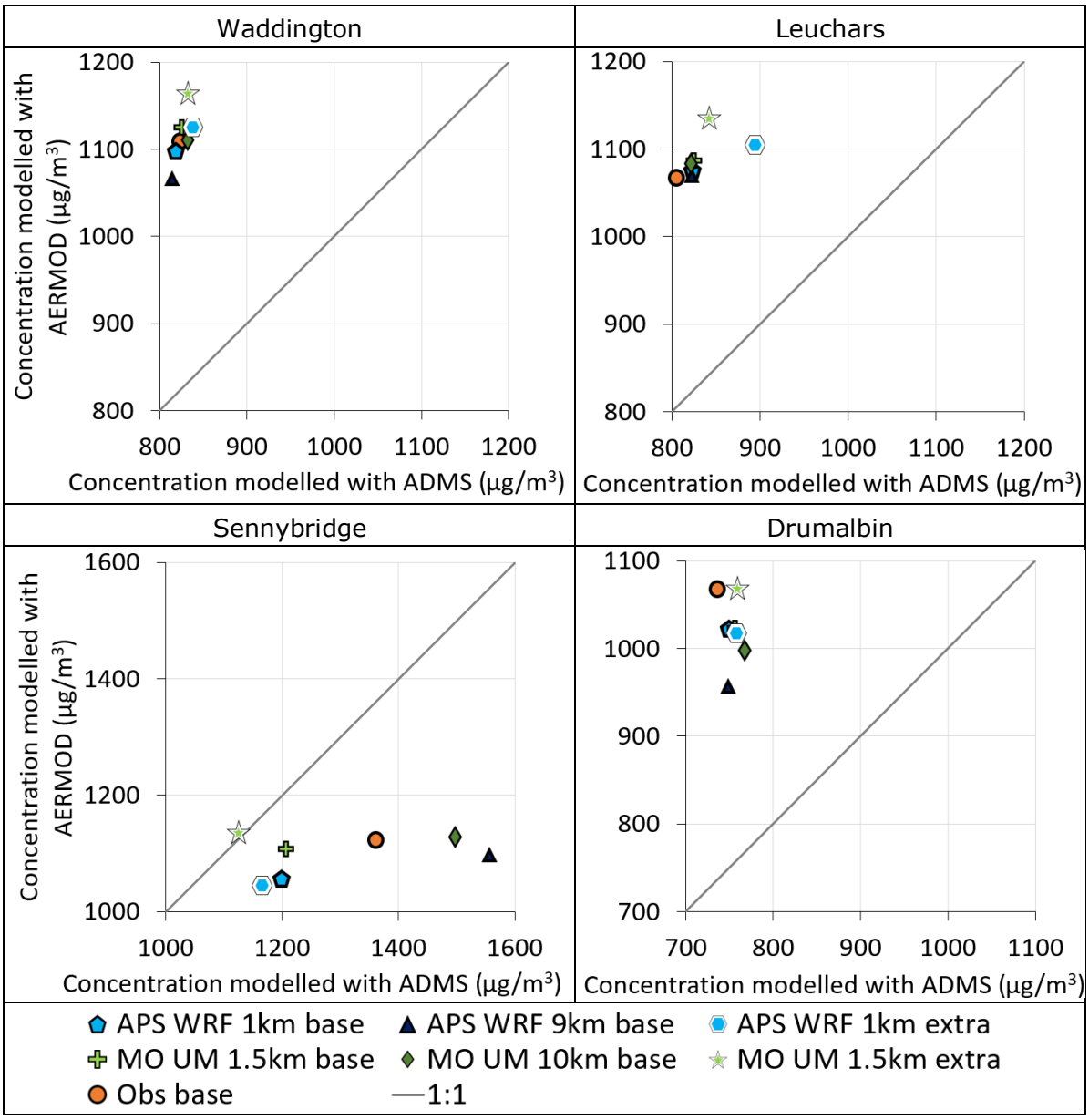

Figure 63 – Magnitudes of peak 98th percentile hourly concentrations for the near-ground source, as modelled with ADMS and AERMOD for each meteorological dataset and site.

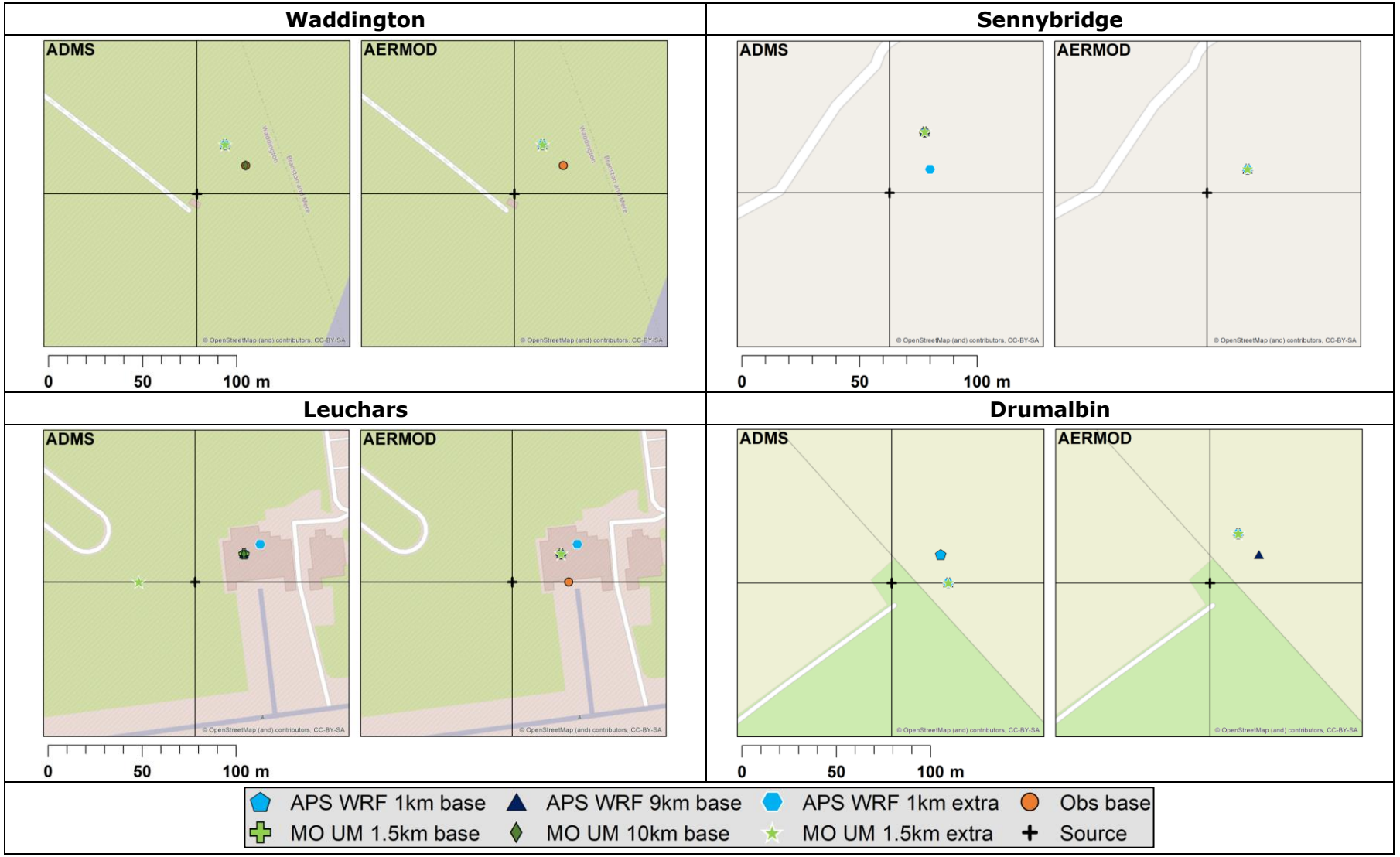

Figure 64 – Locations of peak 98th percentile hourly concentrations for the near-ground source, as modelled with ADMS (left) and AERMOD (right) for each meteorological dataset and site.

6.2.3 Maximum hourly average concentrations

Maximum hourly concentrations predicted by models are highly sensitive to small changes in meteorological inputs, as they depend on conditions for a single hour. Downwind profiles of maximum hourly average concentrations from the near-ground source are shown in Appendix Figures 202 to 209. The modelled maximum hourly concentrations from the local models are identified separately for each output point, so different parts of each downstream profile may reflect different meteorological conditions which cause locally increased concentrations. This leads to profiles with complex shapes. AERMOD predicts the most complex profiles at Drumalbin whereas ADMS predicts more complex profiles at Sennybridge. There are also substantial differences between the two local models and the different meteorological datasets in both the peak magnitude of maximum concentrations and the distribution of concentrations between different wind direction sectors.

The maximum hourly concentrations and corresponding locations predicted by each model for each site are tabulated in Appendix Tables 67 to 70. There is more variability in the locations of maximum hourly concentrations than maximum annual average or 98th percentile. However, all the predicted locations remain within 100 m of the near-ground source, except for AERMOD at Drumalbin with MO UM 10 km input meteorology (150 m) and ADMS at Sennybridge with MO UM 1.5 km 'extra' input meteorology (100 m).

Maximum hourly concentrations from each model and site are summarised using scatter plots in Figure 65. The two local models both show increased sensitivity to input meteorological datasets for this metric compared to annual average and 98th percentile. There are bigger differences in the predicted maximum hourly concentrations both between the two local models and for each local model with varying input meteorology than for maximum annual averages or 98th percentiles. In contrast to the other metrics, the largest relative range in maximum hourly concentrations is predicted at Waddington for both ADMS and AERMOD. AERMOD predicts a higher magnitude of maximum hourly concentrations than ADMS at all sites except Sennybridge.

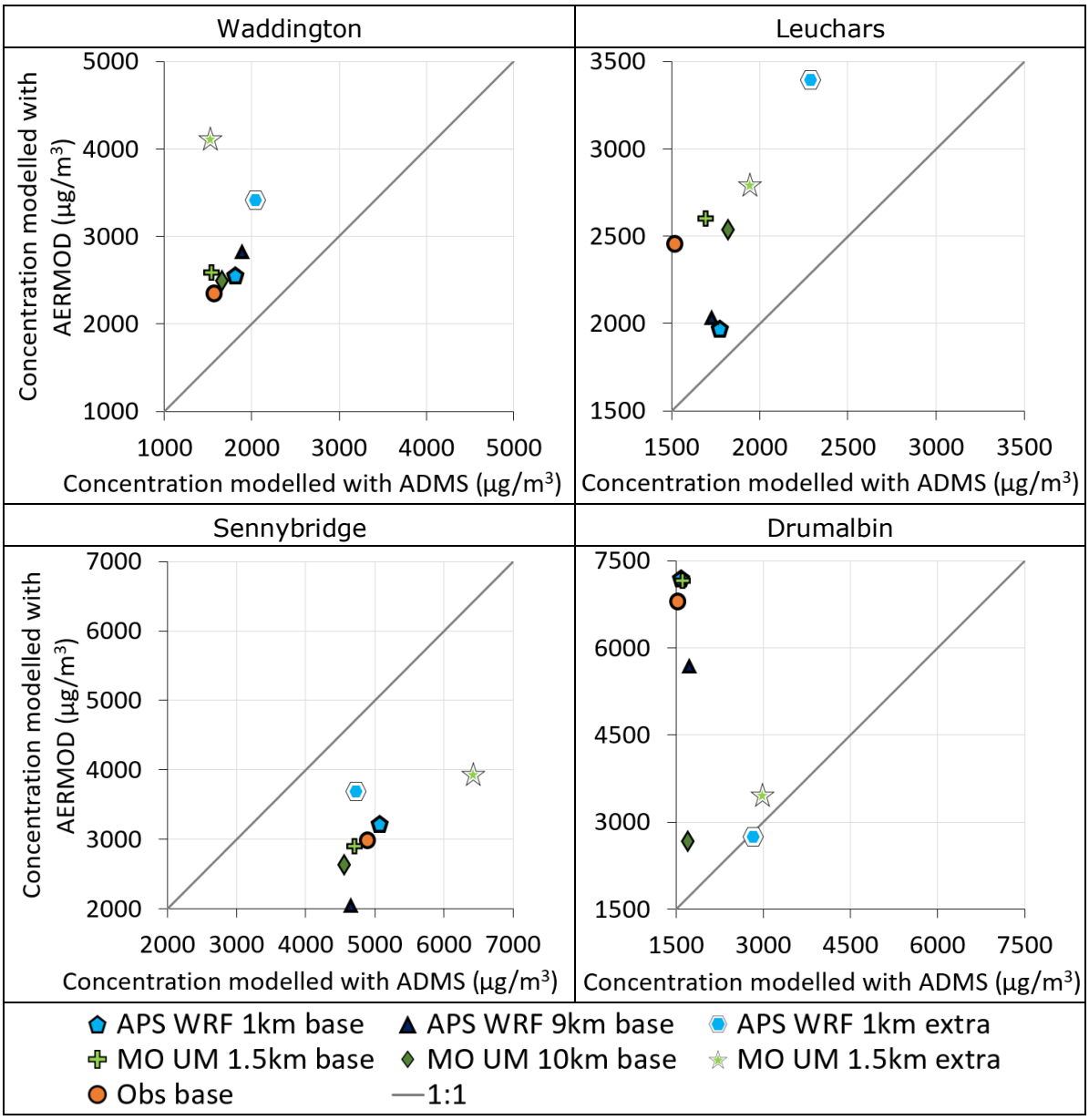

Figure 65 – Magnitudes of maximum hourly concentrations for the near-ground source, as modelled with ADMS and AERMOD for each meteorological dataset and site.

The locations of maximum hourly concentrations for each site are shown on maps in Figure 66. There is substantial variability in the predicted locations of maximum concentration between ADMS and AERMOD with observed meteorology at all sites, with substantial differences in wind direction and/or distance. ADMS predicts maximum hourly concentrations to occur closer to the site than AERMOD with most meteorological datasets at all sites except Sennybridge.

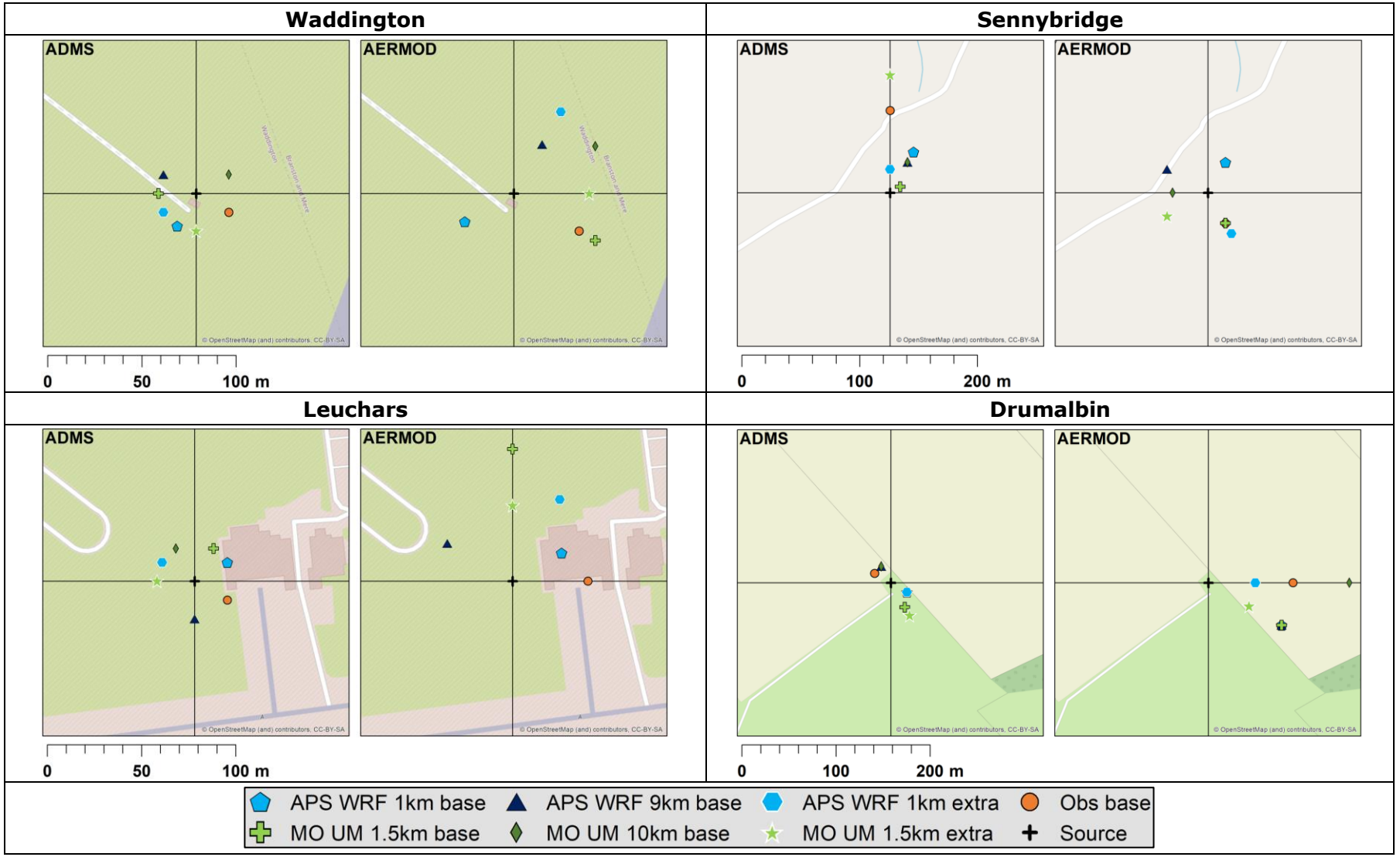

Figure 66 – Locations of maximum hourly concentrations for the near-ground source, as modelled with ADMS (left) and AERMOD (right) for each meteorological dataset and site.

6.3 Concentration comparison – elevated source

The modelled concentration outputs with differing input meteorology for an elevated source, representing a large combustion process exhaust stack, are presented in Section 6.3.1 for annual averages, Section 6.3.2 for 98th percentile of hourly values and Section 6.3.3 for maximum of hourly averages.

6.3.1 Annual average concentrations

Downwind profiles of annual average concentrations in each wind direction sector from an elevated source at Waddington are shown in Figure 67 for meteorological datasets with base input variables and Figure 68 for datasets with additional NWP variables. These graphs show a greater variation between meteorological datasets and local dispersion models than for the near-ground source (Figures 59 and 60). The peak concentrations modelled by AERMOD are slightly lower than those modelled by ADMS for all meteorological datasets. This is opposite to the behaviour for the near-ground source at Waddington, where the concentrations modelled by AERMOD are higher than ADMS. AERMOD also shows more difference in profile shapes for different wind directions than ADMS, most obviously for the 210° sector, where the AERMOD profile decays more slowly with increasing distance from the source than predicted by ADMS.

Numerical values of peak annual average concentration and associated location from an elevated source at Waddington are given in Appendix Table 71. The peak concentration is predicted to occur in the most common wind direction sectors (210° and 240°) with all meteorological datasets. ADMS predicts the peak concentration to occur 1200 m downwind of the source for all meteorological datasets, whereas the AERMOD predictions range from 900 to 1400 m. The variation in magnitude of peak concentrations between the different meteorological datasets is similar to the variation between ADMS and AERMOD. The AERMOD peak concentrations show very little variation due to either model resolution or the combination of input variables, but higher concentrations with MO UM than APS WRF data. In contrast, ADMS shows more variability between different model resolutions and input variable configurations, but no consistent difference between MO UM and APS WRF.

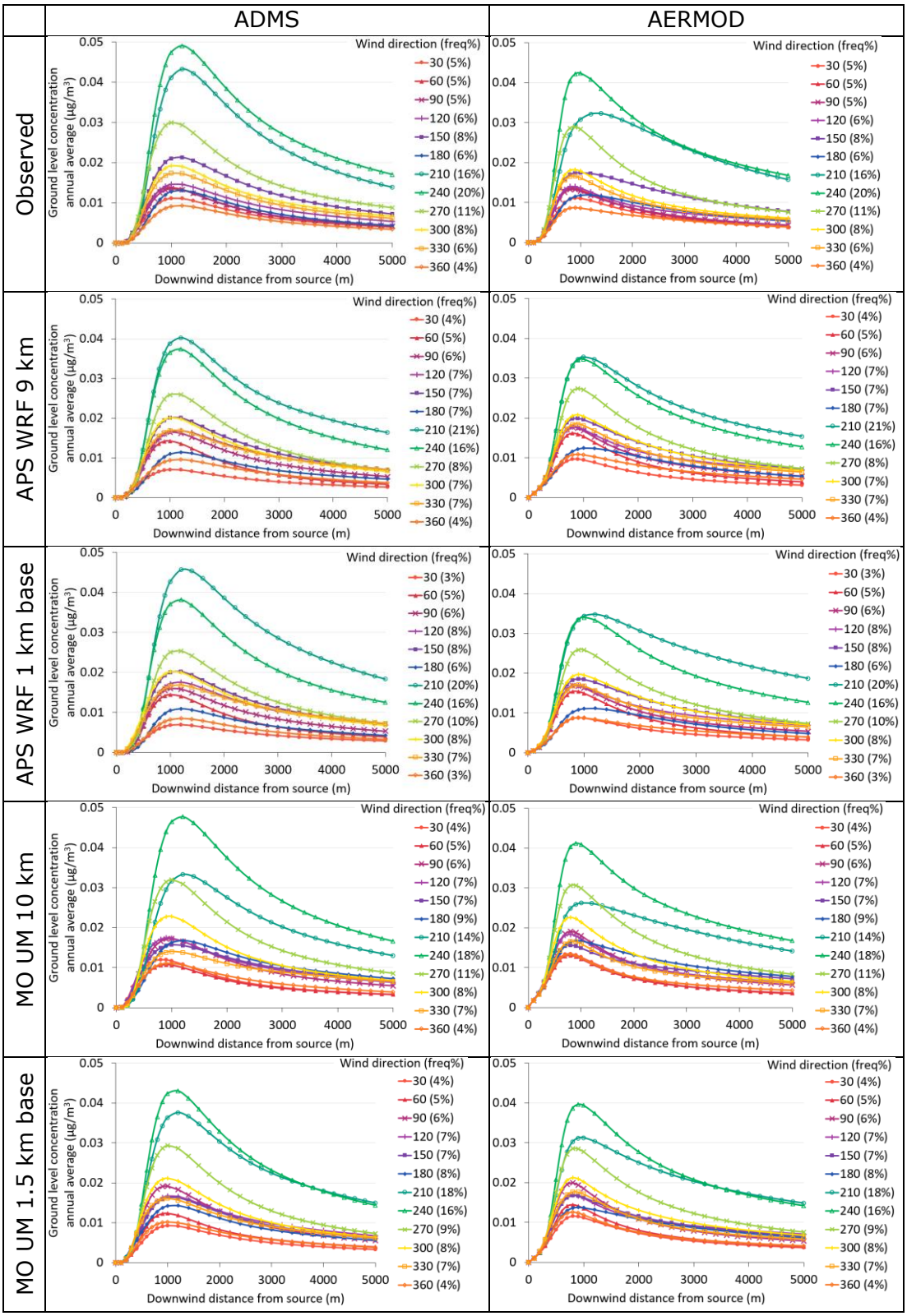

Figure 67 – Downwind profiles of annual average concentration for elevated source at Waddington with varying wind direction, modelled with ADMS (left) and AERMOD (right), using observed or NWP meteorological data with base variables.

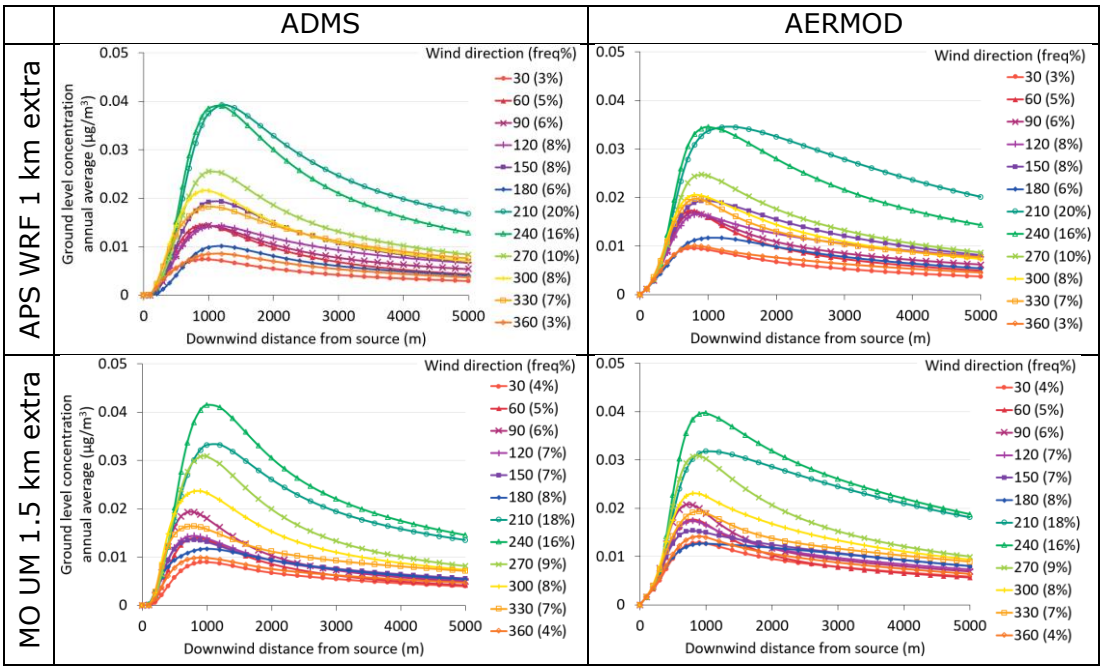

Figure 68 – Downwind profiles of annual average concentration for elevated source at Waddington with varying wind direction, modelled with ADMS (left) and AERMOD (right), with extra NWP meteorological data.

Downstream profile plots of annual average concentration for elevated sources at the other sites are shown in Appendix Figures 180 to 185. Tabulated maximum annual average concentrations and corresponding locations are shown in Appendix Tables 71 to 74. The shapes of the downstream profiles at the complex terrain sites, Sennybridge and Drumalbin, are more complex than at the flat terrain sites. There are also greater differences between the downstream profiles calculated by ADMS and AERMOD with all input meteorological datasets in complex terrain than flat terrain. This is due to different methods for complex terrain modelling in ADMS and AERMOD, as discussed in Carruthers *et al.* (2011). In particular, there are some unexpectedly high concentrations predicted by AERMOD at Drumalbin for large downstream distances (4 km) in relatively uncommon wind direction sectors.

Peak annual average concentration values predicted by ADMS and AERMOD with each meteorological dataset are compared using scatter plots for each site in Figure 69. In contrast to the results for the near-ground source, for this elevated source the concentrations from ADMS tend to be higher than those from AERMOD at all sites except Sennybridge. At Waddington (flat terrain), the differences between the peak annual average concentrations from the two local dispersion models with observed meteorological data are similar to the range of predictions with different input NWP datasets. At the other sites, there are larger ranges of predictions due to different input meteorology than between the two local models with observed meteorology, for at least one of the local models. At Leuchars the biggest differences are related to the 'extra' datasets in ADMS. At Drumalbin the coarser resolution datasets (APS WRF 9 km and MO UM 10 km) show different behaviour to the finer resolution datasets in AERMOD, while all of the NWP datasets lead to much lower peak annual average concentrations than observed meteorology in ADMS. At Sennybridge, the ADMS predictions have a relatively

narrow range for all meteorological datasets whereas the AERMOD predictions show a strong variation with the different datasets.

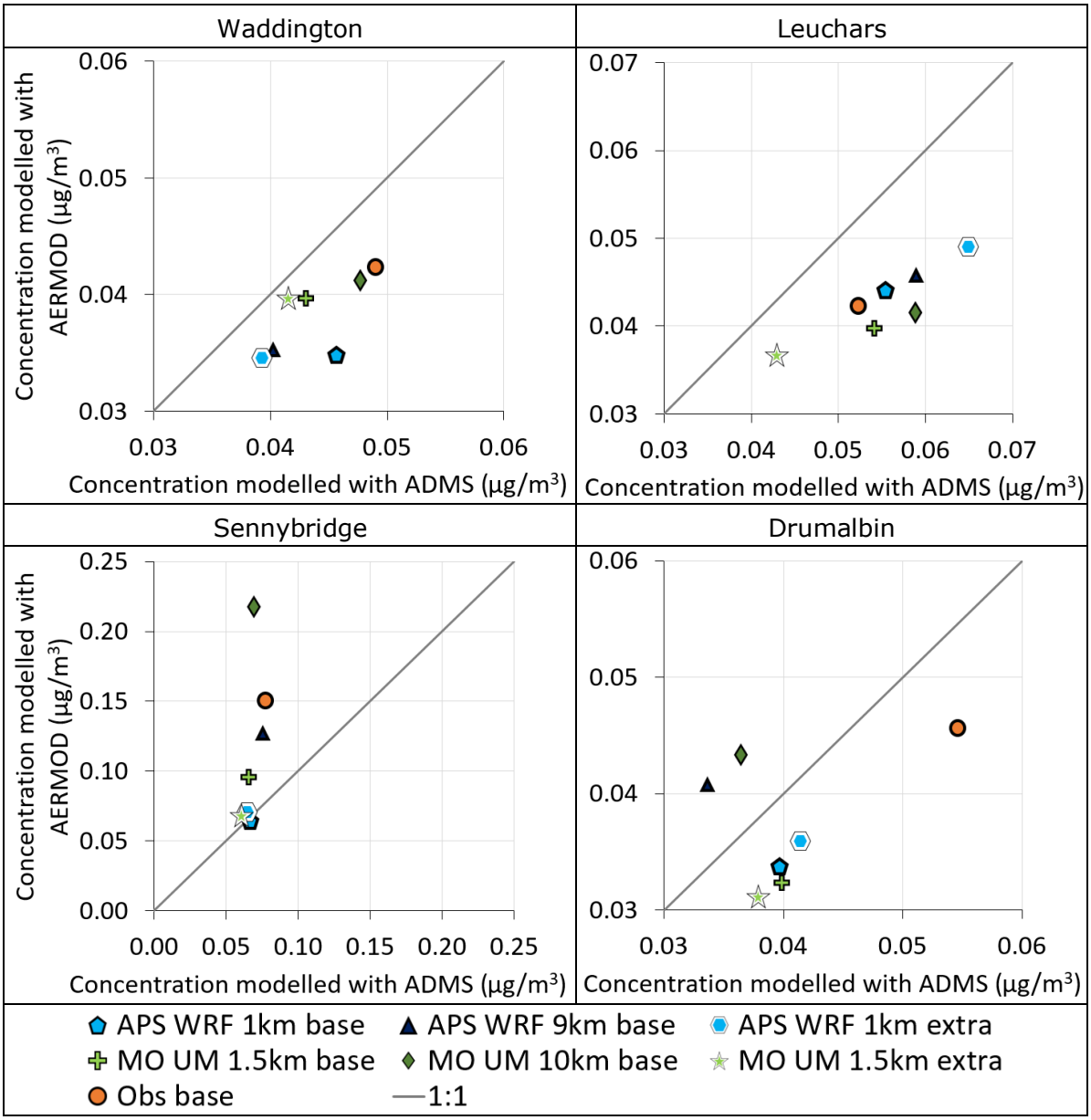

Figure 69 – Magnitudes of peak annual average concentrations for the elevated source, as modelled with ADMS and AERMOD for each meteorological dataset and site. Note different axis limits are used for each plot.

The locations of maximum annual average concentrations predicted by ADMS and AERMOD with each input meteorological dataset are shown on maps in Figure 70. The predicted locations are fairly consistent between the local dispersion models and input meteorological datasets for the two flat terrain sites (Waddington and Leuchars), with a maximum difference of one wind direction sector or two radial distance increments. The complex terrain site predictions from ADMS are also consistent between the different meteorological datasets, whereas AERMOD shows much more variation in the location of the predicted maximum annual average concentration with different meteorological datasets. In particular the coarser

resolution NWP datasets seem to affect the predicted location of peak annual average concentration very strongly in AERMOD.

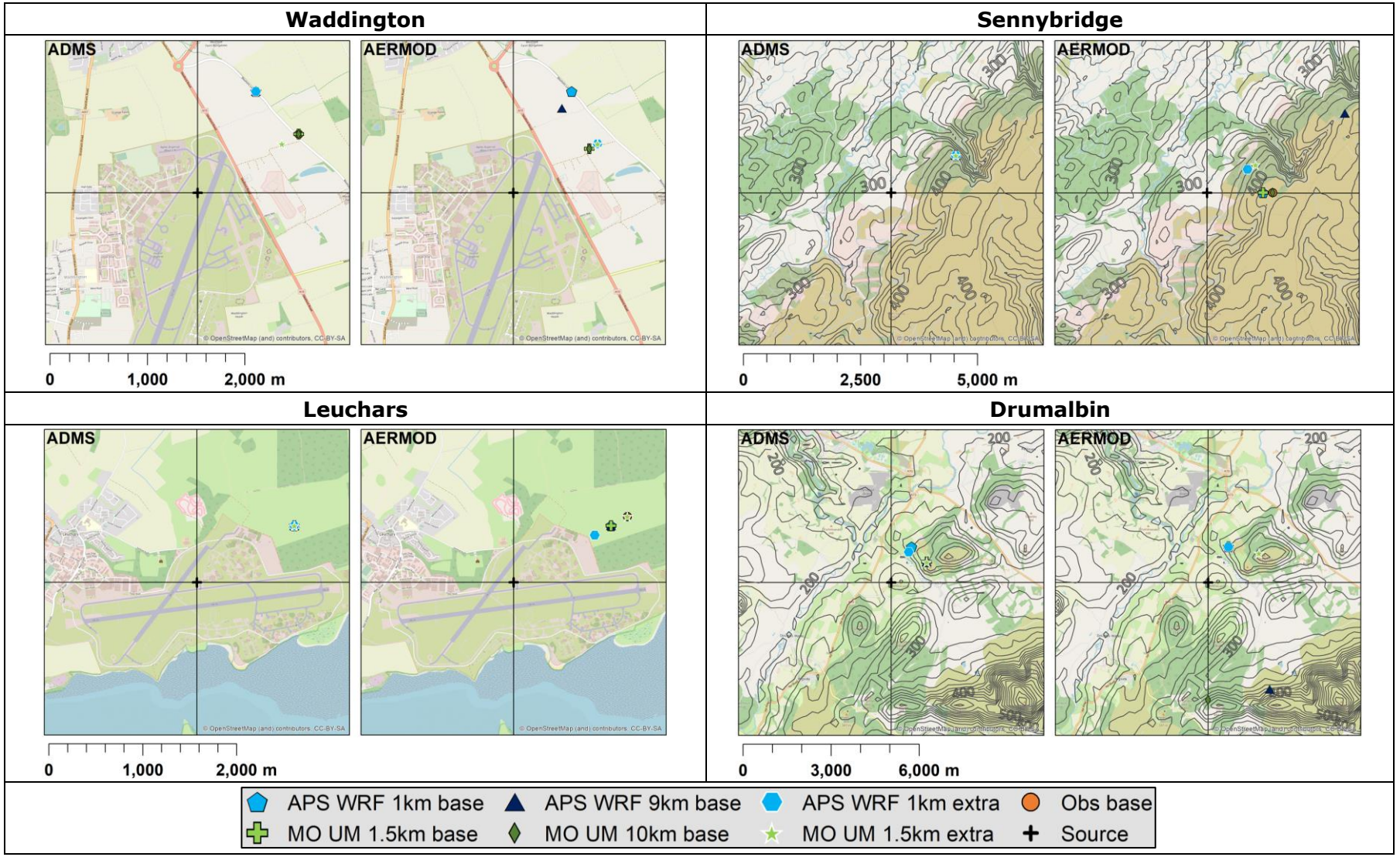

Figure 70 – Locations of peak annual average concentrations for the elevated source, as modelled with ADMS (left) and AERMOD (right) for each meteorological dataset and site. Complex terrain site results are presented over local terrain contours, showing elevation in metres.

6.3.2 98th percentile hourly average concentrations

Downwind profiles of 98th percentile hourly concentrations from elevated sources at each site are shown in Appendix Figures 194 to 201. As with the annual average concentrations, the elevated source profiles show more variability between different input meteorological datasets and more variability between the two local models than for the near-ground source. The profiles for flat terrain sites (Waddington and Leuchars) show a single peak at a downstream distance of approximately 1 km for the majority of wind direction sectors. In contrast the complex terrain sites have more complex profiles including subsidiary peaks further downstream for some wind directions. The modelled 98th percentile concentrations from the local models are identified separately for each output point, so different parts of each downstream profile may reflect different meteorological conditions which cause locally increased concentrations.

Numerical results for the magnitude and location of peak 98th percentile hourly concentrations at each site are shown in Appendix Tables 71 to 74. These show that AERMOD predicts peak 98th percentile concentrations to occur slightly closer to the elevated source than ADMS for most meteorological datasets at all sites except Sennybridge.

Maximum 98th percentile hourly concentration values for each site, calculated by ADMS and AERMOD with each meteorological dataset, are compared using scatter plots in Figure 71. These show fairly consistent predictions of 98th percentile concentrations between ADMS and AERMOD at Waddington and Leuchars, though with a greater variability from the different input meteorological datasets at Leuchars. At the complex terrain sites AERMOD shows a wider range of predicted 98th percentile concentrations than ADMS, with a particularly wide range for Sennybridge. The finer resolution NWP meteorological datasets lead to similar predictions from both ADMS and AERMOD at Sennybridge, whereas the coarse resolution NWP and observed datasets generate much higher concentrations in AERMOD than ADMS at this site.

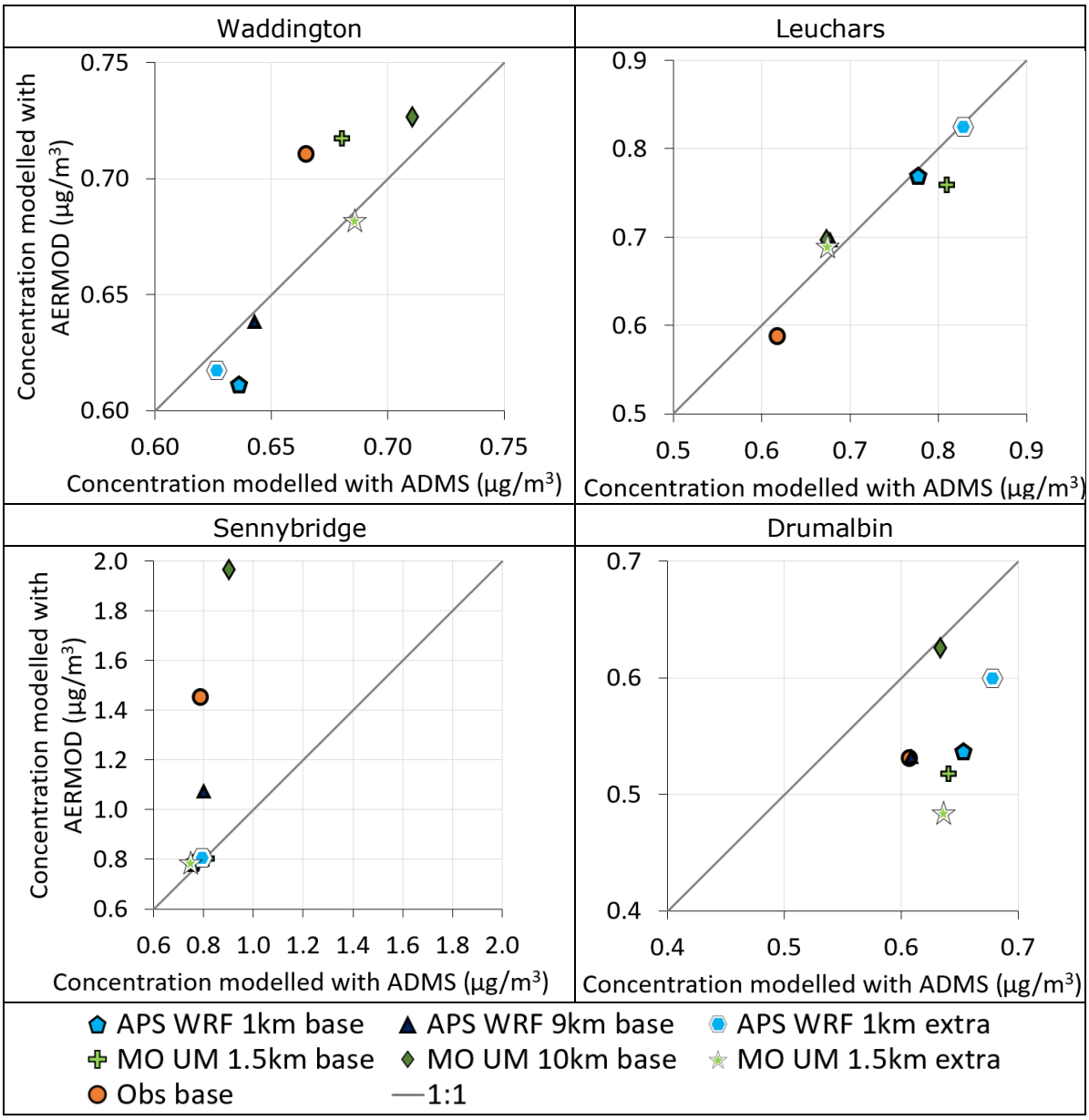

Figure 71 – Magnitudes of peak 98th percentile hourly concentrations for the elevated source, as modelled with ADMS and AERMOD for each meteorological dataset and site. Note different axis limits are used for each plot.

The locations of peak 98th percentile hourly concentrations from elevated sources predicted by ADMS and AERMOD with each input meteorological dataset are shown in Figure 72. At Waddington and Drumalbin the predicted locations are fairly consistent between both local models and all input meteorological datasets. At Sennybridge and Leuchars there is more variability in the distance of the maximum location from the source and/or the wind direction associated with maximum 98th percentile concentrations. At Leuchars ADMS and AERMOD predict maximum 98th percentile concentrations to occur in different wind direction sectors with the observed meteorological data. Referring to the downstream profiles in Appendix Figure 200 shows that the predicted peak 98th percentile concentrations for several non-adjacent wind direction sectors are very similar from both local

models at Leuchars with observed meteorological data. At Sennybridge AERMOD predicts a peak 98th percentile concentration far downstream with APS WRF 9 km input data only. There is also variation in both the wind direction sector and downstream distance for the remaining AERMOD and ADMS predictions of peak 98th percentile concentration locations for Sennybridge.

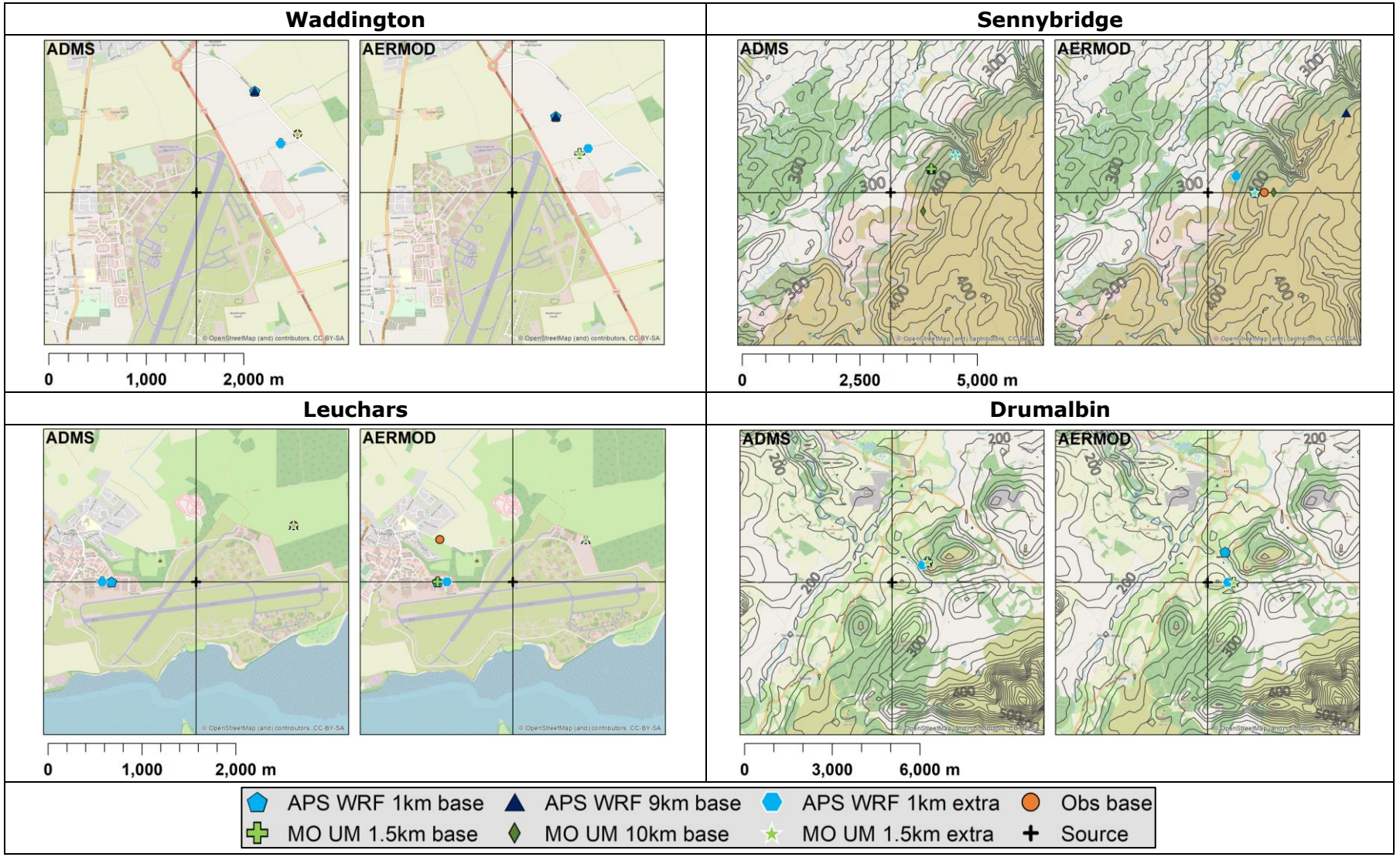

Figure 72 – Locations of peak 98th percentile hourly concentrations for the elevated source, as modelled with ADMS (left) and AERMOD (right) for each meteorological dataset and site. Complex terrain site results are presented over local terrain contours, showing elevation in metres.

6.3.3 Maximum hourly average concentrations

Downstream profiles of modelled maximum hourly average concentrations by wind direction sector from an elevated source are shown in Appendix Figures 210 to 219. As for near-ground sources, the profiles of maximum hourly concentrations are more complex than for annual average or 98th percentile hourly concentrations, due to influences of different individual meteorological conditions at different downstream distances. ADMS tends to predict a larger magnitude of near-source (<1 km) maximum concentrations than AERMOD, while AERMOD predicts some very high concentrations much further downstream for both complex terrain sites. AERMOD predicts uniform maximum concentrations across all wind directions close to the source with some meteorological datasets at Waddington and Leuchars. The standard configuration of AERMOD uses radial dispersion calculations for low wind speeds. In the AERMOD inputs this is referred to as a 'random plume' approach and accounts for the increased uncertainty in measured wind directions at low wind speeds. It is similar to the radial solution component of the ADMS module for modelling calm conditions. The uniform maximum concentrations close to the source for multiple wind directions with some meteorological datasets indicates that these maximum concentrations are derived from random plume modelling. There are substantial differences between the results for individual wind direction sectors using different input meteorological datasets in each model.

Values of maximum hourly concentrations and corresponding locations for each site and model are tabulated in Appendix Tables 71 to 74. These confirm that ADMS predicts maximum concentrations to occur within 500 m from the source for all sites and input meteorological datasets, except Sennybridge with observed and coarse-resolution NWP data. In contrast, AERMOD predicts maximum concentrations beyond 1 km from the source for all sites and meteorological datasets, with exceptions when the random plume modelling influences results and when running with APS WRF 1.5 km 'extra' data at Drumalbin. As for near-ground sources, there are bigger variations in the maximum hourly concentration predictions than the peak annual average or 98th percentile values, both between ADMS and AERMOD and between the different input meteorological datasets.

Magnitudes of predicted maximum hourly concentrations are compared between ADMS and AERMOD with different meteorological inputs for each site using scatter plots in Figure 73. For the flat terrain sites, ADMS predicts higher maximum concentrations and a wider variation with different meteorology than AERMOD. For the complex terrain sites, AERMOD predicts very high concentrations with all of the 'base' datasets, whereas the 'extra' datasets give relatively similar maximum concentrations between ADMS and AERMOD.

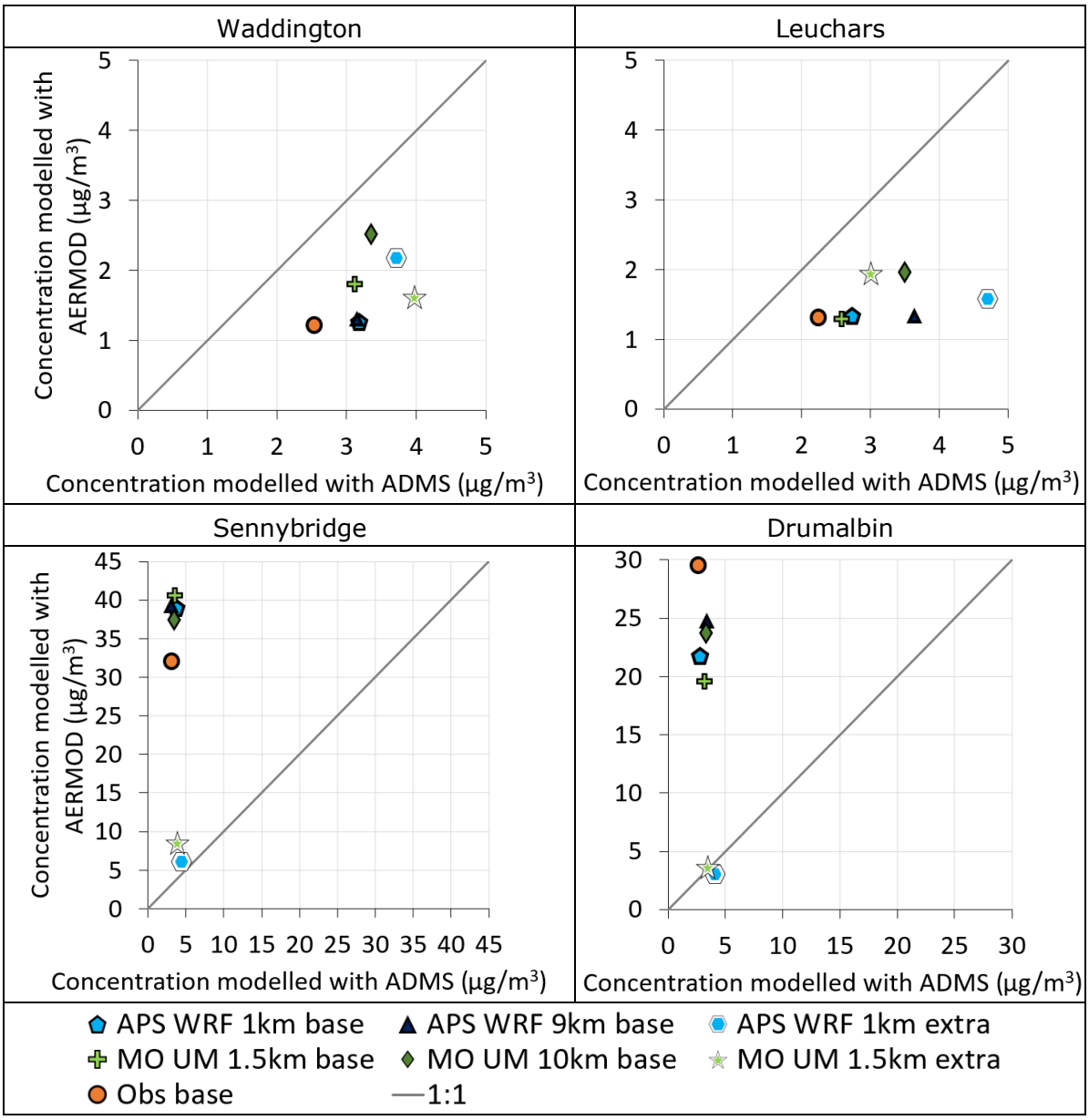

Figure 73 – Magnitudes of maximum hourly concentrations for the elevated source, as modelled with ADMS and AERMOD for each meteorological dataset and site. Note different axis limits are used for each plot.

Maps of the locations of maximum concentrations for each site, model and meteorological dataset are shown in Figure 74. ADMS predicts maximum concentration locations closer to the source than AERMOD with almost all meteorological datasets. There is also a wide scatter of wind direction sectors associated with maximum concentration locations at most sites. AERMOD predicts uniform maximum concentrations for all wind directions at Waddington and Leuchars when the 'random plume' low wind speed model is used. There is no clear trend in the location of maximum concentrations associated with the different NWP model resolutions.

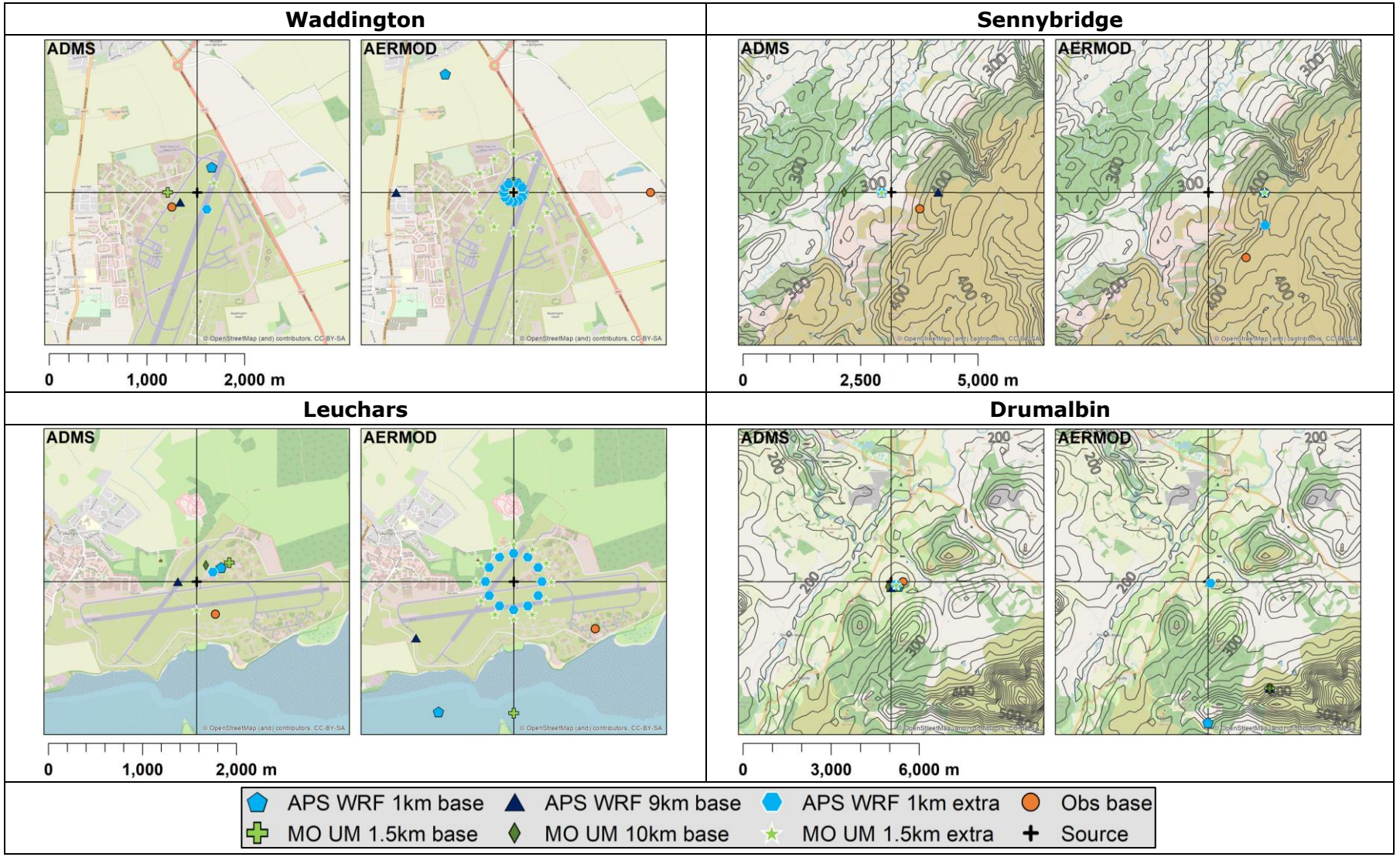

Figure 74 – Locations of maximum hourly concentrations for the elevated source, as modelled with ADMS (left) and AERMOD (right) for each meteorological dataset and site. Complex terrain site results are presented over local terrain contours, showing elevation in metres.

6.4 Wet deposition comparison

Annual average wet deposition is proportional to the total deposited mass resulting from wet deposition, the value of the conversion factor depends on the pollutant of interest. High percentile short-term wet deposition rates are not routinely required for regulatory modelling, although they can be important for accident consequence modelling, as discussed in Section 8. Hence this section focuses on annual average wet deposition rates as a proxy for total long-term deposited mass.

Additional uncertainty in modelled wet deposition is expected compared to concentration results, as modelled dispersion parameters are combined with modelled precipitation rates to calculate wet deposition. However, as wet deposition rates are calculated from concentrations through the full depth of the plume, they may be less sensitive to differences in vertical plume mixing and plume height than ground-level concentrations.

Wet deposition results from near-ground sources are discussed in Section 6.4.1 and from elevated sources in Section 6.4.2. Only ADMS results are presented as wet deposition is not part of the standard AERMOD modelling options.

The simplest ADMS wet deposition modelling approach has been adopted for this study, using a washout coefficient which varies only with precipitation rate. This matches the assessment of 'washout factor' in the meteorological model precipitation evaluation described in Sections 5.2.4 and 5.3.4. Wet deposition rates are calculated from the vertically integrated plume concentration and are inversely related to the wind speed at the mean plume height above ground. Precipitation is treated as spatially uniform throughout the modelling domain, affecting the whole horizontal and vertical extent of the plume.

6.4.1 Near-ground source

Downwind profiles of annual average wet deposition from near-ground sources at each site are shown in Appendix Figures 220 to 223. All the profiles are qualitatively similar, with a single near-source peak in wet deposition for all wind directions, sites and meteorological datasets. This is due to the use in the wet deposition calculations of vertically integrated concentrations, which are always highest near the source.

The maximum annual average wet deposition values over all wind directions are presented graphically in Figure 75 and tabulated in Appendix Tables 75 to 78. This shows that the modelled maximum wet deposition using MO UM NWP data is higher than with observed meteorological data at all sites, most substantially at Waddington and Drumalbin. This is consistent with the variation of modelled precipitation washout factor compared to observations, as shown in Figure 25. The APS WRF NWP data leads to consistently lower predictions of maximum wet deposition than MO UM NWP. In comparison with modelling using observed meteorology, the maximum wet deposition using APS WRF NWP data is higher at Waddington and Drumalbin, similar at Leuchars and lower at Sennybridge.

The pattern of maximum annual average wet deposition with NWP grid resolution varies between sites and between NWP models. In some cases, for example MO UM at Leuchars, the difference between maximum annual average wet deposition using fine and coarse resolution NWP shown in Figure 75 is opposite in sign to the difference in annual washout factor shown in Figure 25. This discrepancy may relate to the variation of precipitation with wind direction, as the maximum annual average wet deposition reflects a single wind direction whereas the annual washout factor is a total over all wind directions. At all sites except Sennybridge there is little difference in the maximum annual average washout factor due to resolution of APS WRF. There are bigger differences due to MO UM resolution at Sennybridge and Leuchars, in both cases with higher maximum annual average wet deposition using finer resolution NWP data.

The range of predicted maximum annual average wet deposition values using different NWP data is a substantially larger proportion of the value using observed meteorology than the equivalent metric for concentration at all sites except Leuchars. This highlights the contribution of increased uncertainties in precipitation rates between different NWP datasets to modelled wet deposition values.

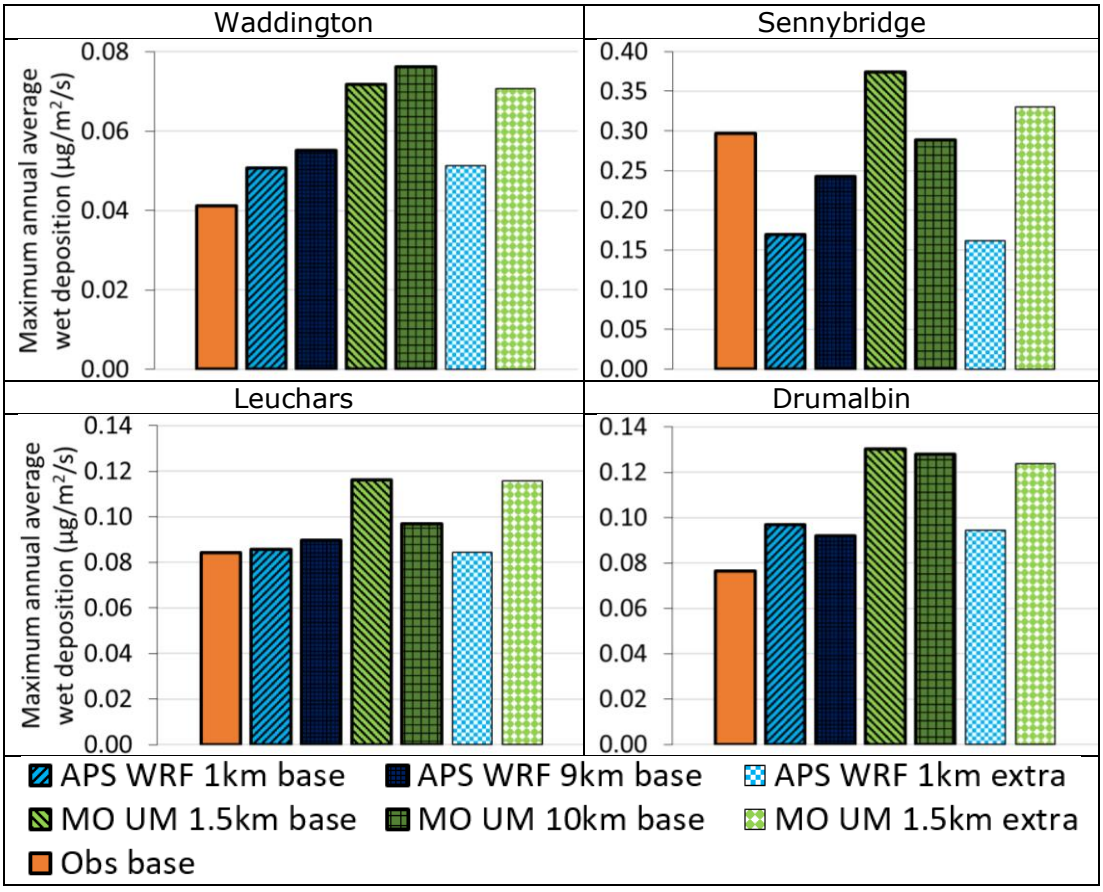

Figure 75 – Magnitudes of maximum annual average wet deposition for the near-ground source, as modelled with ADMS for each meteorological dataset and site. Note different axis limits are used for each plot.

The locations of the modelled maximum annual average wet deposition from a near-ground source with each meteorological dataset at each site are plotted on maps in Figure 76. All of the predicted locations are at the closest output grid point, 10 m from the source. This is a consequence of the calculation of wet deposition from vertically integrated concentrations in ADMS. For context, 10 m is around 14 source diameters downstream from the near-ground source, which has no or minimal buoyancy. While there may be some additional uncertainty in plume parameters very close to the source, a Gaussian plume representation is likely to be reasonable for hourly average properties. The spread of locations with wind direction is broader at Waddington and Leuchars than at the complex terrain sites (Sennybridge and Drumalbin).

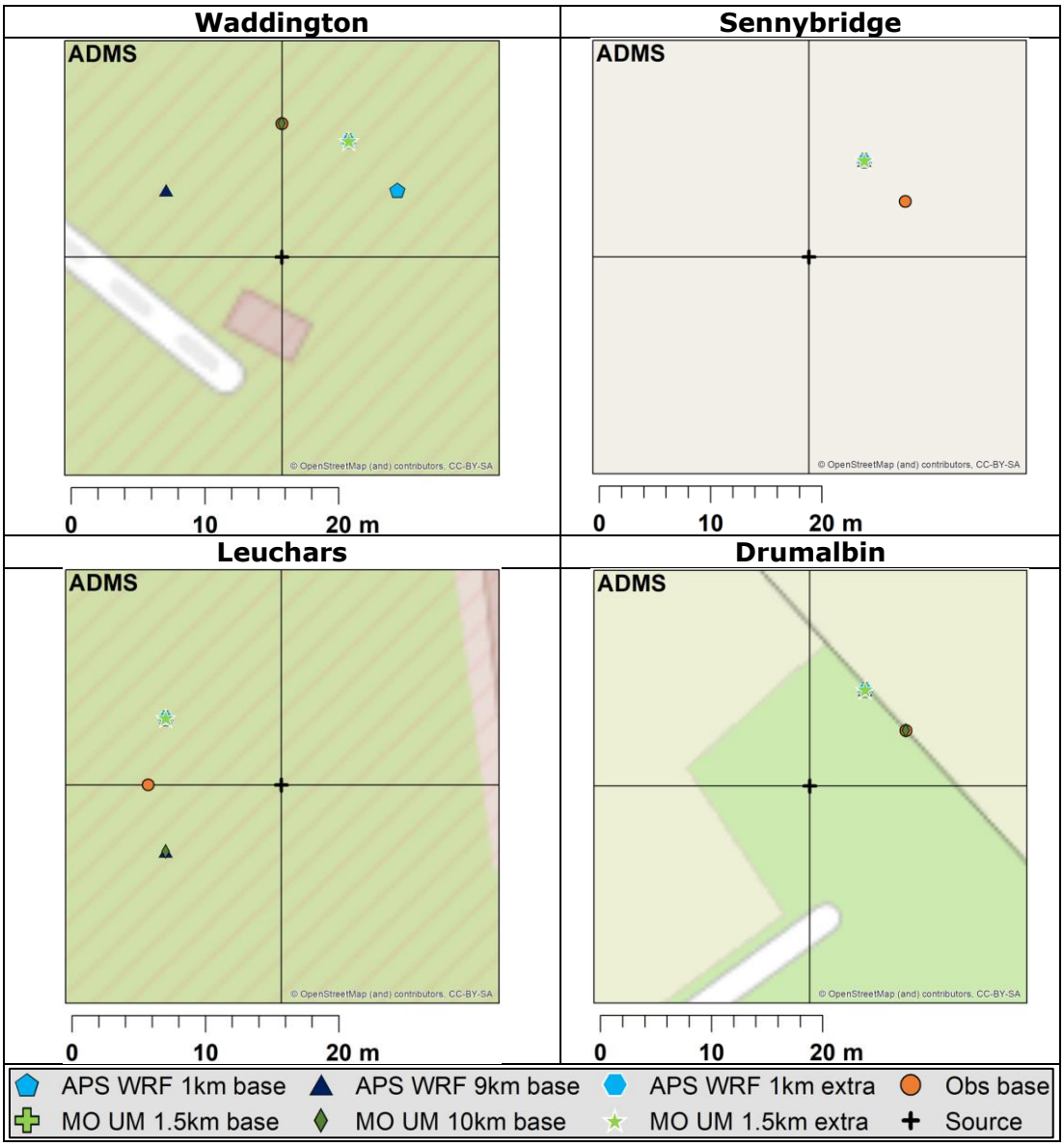

Figure 76 – Locations of maximum annual average wet deposition for the near-ground source, as modelled with ADMS for each meteorological dataset and site.

6.4.2 Elevated source

Downwind profiles of ADMS modelled annual average wet deposition from the elevated source look qualitatively similar at all sites and with all meteorological datasets, as shown in Appendix Figures 224 to 227.

Maximum annual average wet deposition values and corresponding locations are visualised in Figure 77 and tabulated in Appendix Tables 75 to 78. These show consistently higher maximum annual average wet deposition predictions when modelling with MO UM NWP data compared to modelling with either observations or APS WRF NWP data. This is likely to correspond to the overprediction of the prevalence of low-intensity precipitation by the MO UM noted in Section 5.2.4. The range of maximum annual average wet deposition values predicted with different NWP meteorological data, as a proportion of the value predicted with observed meteorological data, is greater than for maximum annual average concentrations at all sites.

The absolute magnitude of wet deposition due to elevated sources is predicted to be substantially lower than for near-ground sources with the same emission rate with all meteorological datasets, due to the inverse dependence of modelled deposition rate on the wind speed at the mean plume height. The change of maximum annual average wet deposition values with NWP data resolution varies between sites and NWP models. At all sites except Drumalbin, the dependence of maximum annual average wet deposition rate for the elevated source on NWP resolution is consistent with the results for the near-ground source. At Drumalbin, ADMS running with coarse resolution MO UM data generates slightly lower maximum annual average wet deposition than with fine resolution data for the near-ground source but higher annual average wet deposition for the elevated source. This may relate to differences in the stability distribution from the two resolutions, which would alter the vertical profiles of wind speed between the mean plume heights of the near-ground and elevated sources.

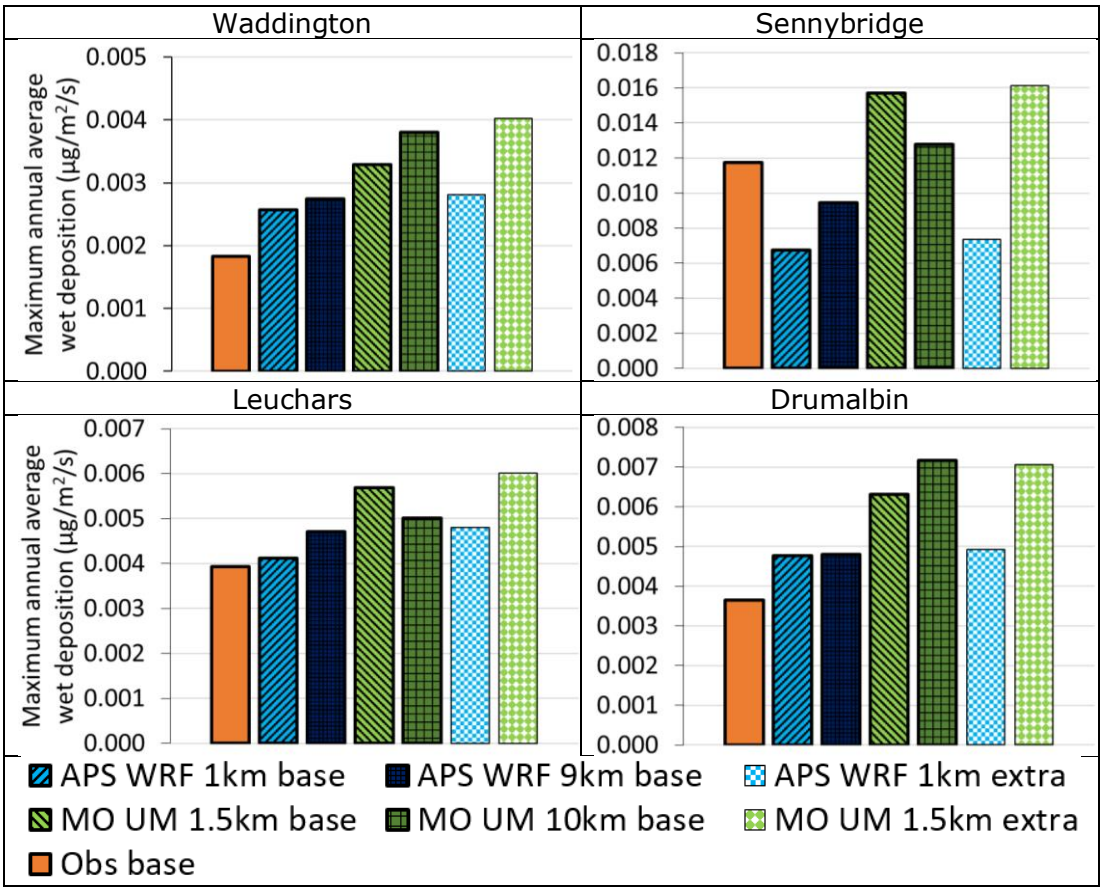

Figure 77 – Magnitudes of maximum annual average wet deposition for the elevated source, as modelled with ADMS for each meteorological dataset and site. Note different axis limits are used for each plot.

The locations of the modelled maximum annual average wet deposition from an elevated source with each meteorological dataset at each site are plotted on maps in Figure 78. The maximum wet deposition occurs very close to the source, at the first non-zero downstream distance for all configurations (100 m from the source for elevated sources). At Waddington, Sennybridge and Leuchars the locations are predicted in an angular range of up to two wind direction sectors, whereas at Drumalbin modelling with the MO UM 1.5 km 'extra' dataset leads to an anomalous location of maximum annual average wet deposition. The downstream profiles for different wind directions at each site do not show a clear cause for this difference.

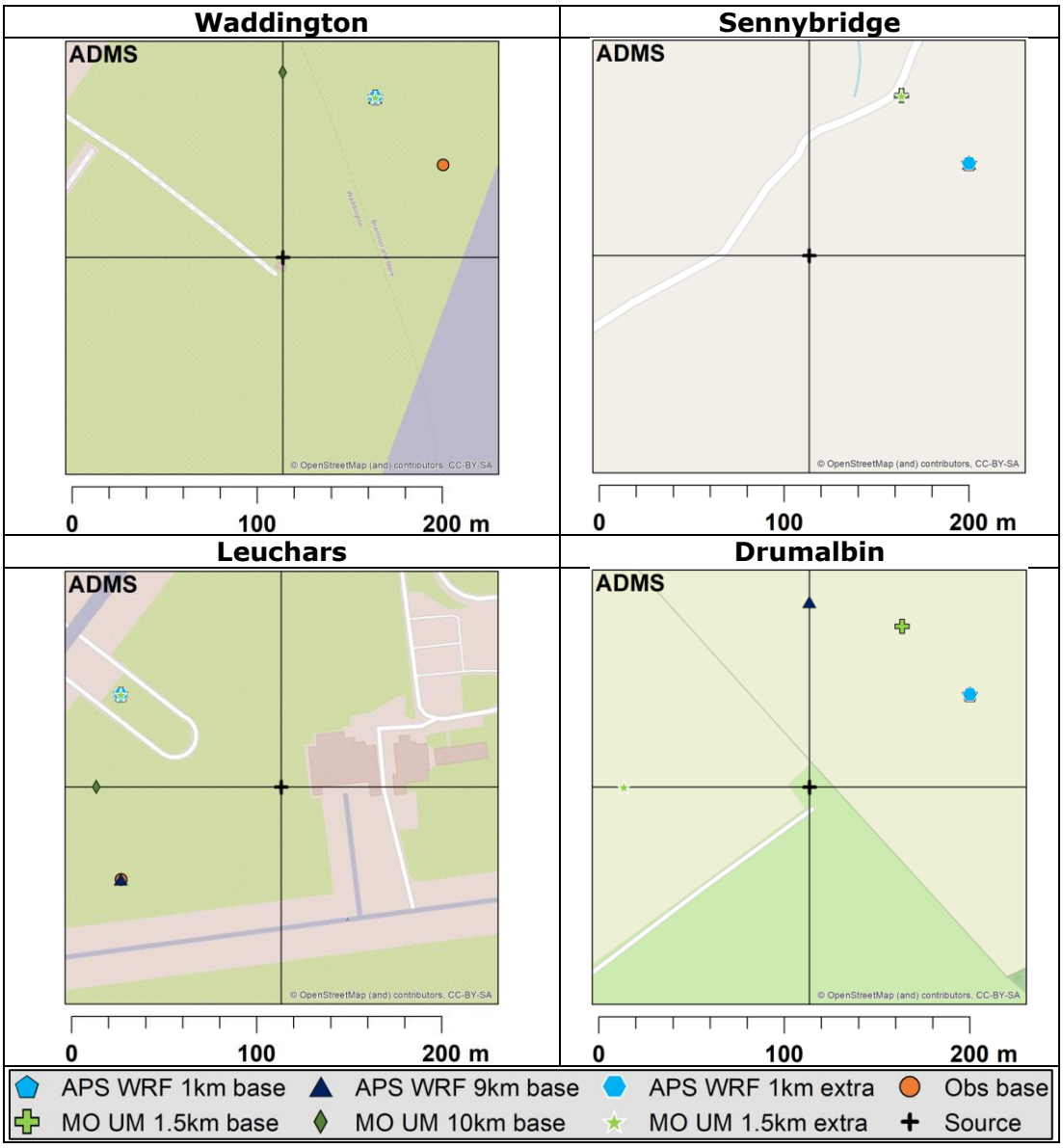

Figure 78 – Locations of maximum annual average wet deposition for the elevated source, as modelled with ADMS for each meteorological dataset and site.

6.5 Conclusions from dispersion study

The dispersion study examined differences between concentrations predicted by ADMS and AERMOD using both observed and NWP (MO UM and APS WRF at two different resolutions) meteorological datasets, for idealised near-ground and elevated sources. Different sensitivity to input meteorological data was found for different combinations of local model, source type, location and concentration metric. The value and location of the spatial maximum of annual average concentration and wet deposition, 98th percentile hourly average concentration and 100th percentile hourly average concentration have been used to summarise the variability of dispersion model results. The sensitivity of these dispersion model outputs to the choice of input meteorological data has been quantified using the ratio of the range of values with six different NWP datasets to the value with observed meteorological data. In Table 30 these sensitivity ratios have been classified by magnitude into Low (< 0.2, equivalent to an uncertainty of around 20%), Medium (0.2 – 0.4), High (0.4 – 1.0) and Very High (> 1.0).

Table 30 – Summary of sensitivity of ADMS 6 and AERMOD predictions of maximum annual average concentration (AAve), 98th percentile hourly concentration (P98), 100th percentile hourly concentration (P100) and annual average wet deposition (WetD). Sensitivity calculated as ratio of range of results with NWP meteorological data to result with observed meteorological data. Categories: Low < 0.2, Medium 0.2 – 0.4, High 0.4 – 1.0, Very High > 1.0.

Source type	Site type	ADMS 6 sensitivity				AERMOD sensitivity		
		AAve	P98	P100	WetD	AAve	P98	P100
Near-ground	Flat terrain	Low	Low	Medium	High	Low	Low	High
	Coastal	Medium	Low	Medium	Medium	Medium	Low	High
	Complex terrain	Medium	Medium	High	High	Medium	Low	High
Elevated	Flat terrain	Low	Low	Medium	High	Low	Low	Very high
	Coastal	Medium	Medium	High	High	Medium	Medium	High
	Complex terrain	Medium	Low	High	High	Very high	High	Very high

The modelled maximum annual average concentrations from near-ground sources at all sites showed more difference between AERMOD and ADMS with observed meteorological data than due to the use of differing NWP datasets/resolutions in each model. This suggests that the magnitude of uncertainty due to the differing NWP inputs tested is within the general modelling uncertainty for annual average concentrations from near-ground sources. The predicted locations of maximum annual average concentrations from near-ground sources also showed little sensitivity to the input meteorological dataset at all sites.

The variability in dispersion model outputs with differing meteorological inputs generally increases both for high percentiles of hourly averages and for concentrations from elevated sources, compared to annual averages from a near-ground source. For high percentiles of hourly averages (especially 100th

percentile), this is due to the greater uncertainty in meteorological model predictions of conditions for individual hours. For elevated sources, it reflects the longer time taken for plumes to spread towards the ground, with maximum concentrations predicted further from the source location, leading to increased sensitivity of model outputs to small differences in atmospheric stability, plume rise and dispersion parameters.

Figures 79 and 80 show downstream profiles for the most common observed wind direction sector at Waddington and Drumalbin respectively, modelled with observed and NWP meteorological data. At Waddington, the most common wind direction from the observed data is 240° (shown in Figure 59), whereas the APS WRF (both resolutions) and MO UM 1.5 km resolution have a most common wind direction of 210°. This leads to lower concentration predictions for the 240° wind direction sector from both ADMS and AERMOD with the NWP datasets than observed meteorology, for near-ground and elevated sources. However, there are also substantial differences between the ADMS and AERMOD predictions with observed meteorology for this wind direction sector.

At Drumalbin, the peak concentrations for the near-ground source are highest when modelling with observed data, but overall there is a larger difference between ADMS and AERMOD than due to the different meteorological data in each model. In contrast, there are bigger differences in the downwind profiles with different input meteorological data than local model for the elevated source. Modelling with observed meteorological data leads to the highest concentrations for this wind direction, and with coarse resolution NWP leads to the lowest concentrations. The observed and finer resolution NWP data predict the same most common wind direction sector (210°), whereas both coarser resolution NWP datasets predict a most common wind direction sector of 180°, with a broader distribution of hourly wind directions. The change of prevailing wind direction between coarse and fine NWP datasets may reflect finer scale terrain effects, which could be double-counted by the local terrain modelling, emphasising the concentration differences between the modelling using NWP datasets at different resolutions. This possibility for double-counting of terrain effects in local modelling is explored further in Section 7.

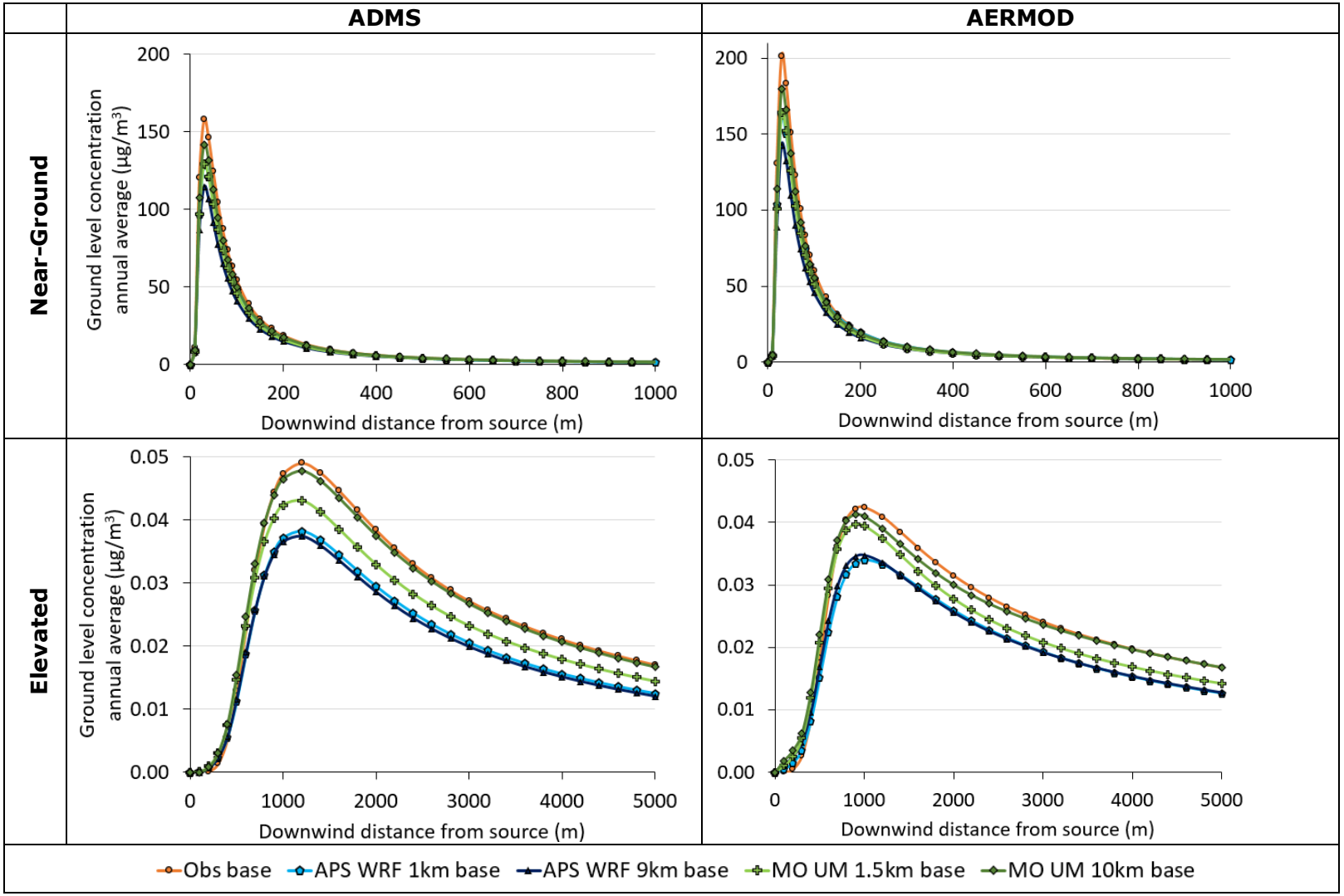

Figure 79 – Downstream annual average concentration profiles at Waddington for the most common observed wind direction sector (240°) with varying input meteorological data.

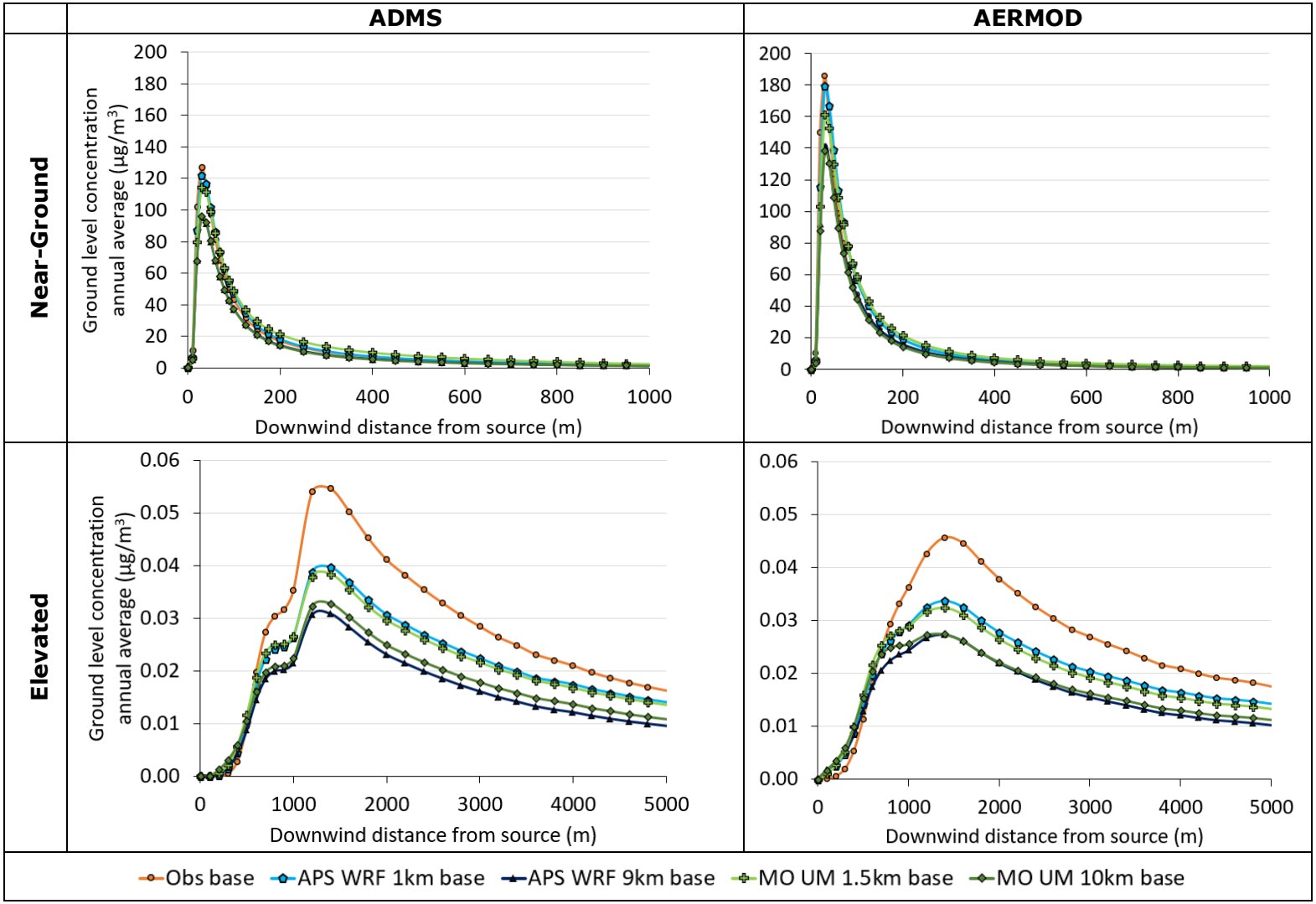

Figure 80 – Downstream annual average concentration profiles at Drumalbin for the most common observed wind direction sector (210°) with varying input meteorological data.

The modelled maximum annual average concentration values show more difference due to meteorological input data than between AERMOD and ADMS for elevated sources at all sites except Waddington (flat terrain). AERMOD shows greater sensitivity to input meteorological data than ADMS for this output at the complex terrain sites, while ADMS has a greater sensitivity at Leuchars (coastal). The ADMS predictions of the location of maximum annual average concentration from elevated sources are relatively insensitive to the input meteorological dataset, whereas the AERMOD predictions show more variation at all sites, and include anomalously far downstream maximum locations with the APS WRF 9 km dataset in complex terrain.

Higher maximum annual average concentrations are predicted by AERMOD than ADMS for near-ground sources whereas lower concentrations are predicted by AERMOD than ADMS for elevated sources, at all sites except Sennybridge in both cases. ADMS also predicts higher maximum values than AERMOD for high percentile hourly concentrations from near-ground sources at all sites except Sennybridge, while there is no clear trend between the different local dispersion models for the maximum high percentile concentrations from elevated sources. The different behaviour for varying source properties may reflect different plume rise and vertical plume spread algorithms in the two local dispersion models.

The ratio of predicted maximum values of annual average concentration from a near-ground source in flat terrain with fine resolution NWP to those with coarser resolution of the same NWP model show a range of 0.89 – 1.11 in ADMS (0.85 – 1.17 in AERMOD). This range of values is likely to be within the general uncertainty of model outputs. The NWP resolution has somewhat greater influence on this metric in complex terrain, with corresponding ranges of 0.83 – 1.27 in ADMS (0.93 – 1.27 in AERMOD). The high percentile concentrations from a near-ground source show less sensitivity than annual averages to NWP resolution in flat terrain but more sensitivity in complex terrain. The biggest influence of NWP resolution in ADMS occurs with APS WRF data at Sennybridge for 98th percentile (ratio of concentrations 0.77) while in AERMOD occurs with MO UM data at Drumalbin for maximum concentration (ratio 2.68). There is no consistent pattern of whether fine or coarse NWP data leads to higher or lower maximum concentration value predictions across different sites and metrics.

The use of 'extra' heat flux and boundary layer height variables from NWP data causes increased variability in the local dispersion model outputs compared to 'base' variables (wind speed and direction; temperature, cloud cover and precipitation only). This suggests that the ADMS meteorological pre-processing is relatively insensitive to the uncertainties in observed and NWP cloud cover values. In contrast, there are significant differences between the NWP predictions of heat flux and boundary layer height and the ADMS algorithms, which lead to discrepancies in atmospheric stability calculations and substantial differences in some concentration outputs. This is most apparent for the predictions of 100th percentile concentrations, which are dependent on individual meteorological conditions. Heat flux predictions at the coastal Leuchars site seem to have a particularly strong influence on dispersion modelling, this may relate to NWP

model difficulties with resolving coastal thermally-driven flows and associated uncertainties in heat fluxes.

Annual average wet deposition predictions from ADMS show greater sensitivity to the input meteorological data than concentrations, due to increased uncertainty between observed and modelled precipitation rates. Modelling using MO UM NWP data leads to higher predictions of maximum annual average wet deposition values than using APS WRF NWP data. There is no consistent pattern across sites and NWP models in the variation of predicted wet deposition between fine and coarser resolution NWP data.

7 DOUBLE-COUNTING TERRAIN EFFECTS

This section describes an investigation into the possibility of double-counting terrain effects between fine resolution NWP data and local flowfield modelling in ADMS. It uses a subset of the NWP datasets and locations described in Section 4 and evaluated in Section 5. The assessment of terrain effects on dispersion modelling outcomes uses regulatory model configurations shared with the dispersion modelling comparisons in Section 6.

7.1 Introduction

Dispersion models can vary markedly in their approaches to modelling the effects of complex terrain on plume dispersion. AERMOD (Cimorelli *et al.* 2004) employs a highly idealised approach in which the final plume concentration at a given receptor is a weighted average of the concentration from a horizontal (terrain-impacting) plume and a terrain-following plume, with the weighting dependant on the stability, wind speed and plume height relative to terrain. With this approach, the plume experiences no crosswind deviation. ADMS (Carruthers *et al.* 1994, CERC 2023) uses the in-built FLOWSTAR airflow model to generate a fully 3-dimensional flow field for each modelled meteorological hour, based on quasi-linear solutions of the momentum and continuity equations. Fourier transforms of the input terrain data are used to calculate the flow perturbations in Fourier space; the flow solution is then obtained by inverting the Fourier transformed solution. This spatially-varying flow field is then used to determine the plume trajectory and spread parameters during the dispersion calculations (Carruthers *et al.*, 2011).

FLOWSTAR is driven by the data from the ADMS meteorological (*.met*) file, i.e. by a single horizontal wind vector per hour (typically at 10 m above ground). This driving wind vector should ideally be *representative of the wind vector that would exist in the absence of the complex terrain within the FLOWSTAR domain*, which is often referred to as the 'upwind' vector. The FLOWSTAR domain is the region covered by FLOWSTAR's input terrain file, which is typically similar in size to (but necessarily slightly larger than) the dispersion modelling domain that covers all the sources and receptors. When the FLOWSTAR domain is similar in size to a single NWP grid cell, the wind vector from that NWP grid cell is likely to be a good representation of the upwind vector over the FLOWSTAR domain. In this scenario, FLOWSTAR can be thought of as further downscaling the NWP flow field within a single NWP grid cell, to account for the effects of terrain features with scales

between the FLOWSTAR grid resolution and the NWP grid cell size[1]. For high-resolution NWP data in which both the NWP grid cell and modelling domain are small, it may be that the terrain features within the NWP grid cell are sufficiently shallow that the use of FLOWSTAR is not necessary; it is usually advisable to include terrain height effects in ADMS only if gradients within the modelling domain exceed 1:10.

Conversely, when the NWP model resolution is significantly finer than the FLOWSTAR domain (i.e. multiple NWP grid cells cover the domain), and data from (say) the central NWP grid cell is used to drive FLOWSTAR, the wind vector from that NWP grid cell may no longer be a good representation of the upwind vector for the full FLOWSTAR domain. This will be the case if there are terrain features larger than the NWP grid cell size but within the FLOWSTAR domain that are likely to have significantly affected the wind field at that grid cell during the NWP simulation. This is often referred to as 'double-counting', as the influence of these terrain features will also be included in the FLOWSTAR model. On the other hand, the significance of double-counting is likely to be minor in cases where there is relatively little terrain variation at scales between the NWP grid cell size and the FLOWSTAR domain size (or these terrain features are located far enough away from the selected NWP grid cell for the data to be largely unaffected by them), in which case the use of finer resolution NWP data than the FLOWSTAR domain may be acceptable. It should be noted that while terrain features with scales coarser than the NWP grid cell size can influence the NWP wind vector, only those features with scales greater than a few NWP grid cell lengths are likely to be well resolved by the underlying topographic dataset.

Double-counting is also a potential issue when using measured meteorological data to drive FLOWSTAR, as the weather station may be located such that the recorded wind is itself significantly affected by prominent terrain features within the FLOWSTAR domain. Ideally, one would use data from a weather station that is either within the FLOWSTAR domain but not significantly affected by the prominent terrain features within it, or is located in an adjacent region of relatively flat terrain that is not so far away as to lead to significant changes in the synoptic wind vector or other (e.g., coastal) effects. When the weather station is within the FLOWSTAR domain, one can get an indication of whether double-counting terrain effects is a significant issue by comparing the wind rose of the input (measured) data against the wind rose of the output (FLOWSTAR) data extracted at the location of the weather station. This assumes that terrain features smaller than the FLOWSTAR grid resolution do not significantly affect the measured wind rose.

[1] NWP models that use nested domains to increase horizontal resolution in stages typically employ ratios no greater than 5:1 between the parent and child domain. This is in order to ensure a relatively smooth transition across each nested domain boundary, either side of which the same set of primitive equations are being used. The different (analytical) approach used by FLOWSTAR means that it is not necessary to ensure a similar ratio between the resolution associated with the NWP data supplied to FLOWSTAR and the FLOWSTAR grid resolution.

Examples are given in Figure 82 for the two complex terrain sites considered in Section 6: Drumalbin and Sennybridge. The output wind roses are the result of running FLOWSTAR using the met-site-centred ~13 x 13 km terrain file of OS Terrain® 50 data (shown in Figure 81) with a FLOWSTAR grid resolution of 50 m, as used in the regulatory dispersion modelling comparisons in Section 6, and extracting the hourly FLOWSTAR output wind vector at the met site location and height (10 m above ground level). At Drumalbin, the input and output wind roses are broadly similar, suggesting that this met site is reasonably located for driving FLOWSTAR within this domain without introducing significant double-counting effects. There is still a suggestion of some double-counting however, with a slightly higher frequeny of winds from the south-west and east and a slightly lower frequency of winds from the west in the output wind rose. The increased south-westerly winds in particular suggest a magnified chanelling effect caused by the broad south-west-to-north-east valley that runs through the domain. Conversely, the input and output wind roses at Sennybridge are more markedly different, suggesting more significant double-counting at this met site. The output wind rose shows a significantly higher frequency of winds from the north-north-east and south and a reduction of winds from the north-west quadrant. The cluster of south-westerly winds in the observational data also show a slightly more southerly component in the output wind rose. All this suggests a significant over-channelling effect in FLOWSTAR due to double-counting the influence of the comparatively steeper valley(s) within the Sennybridge domain.

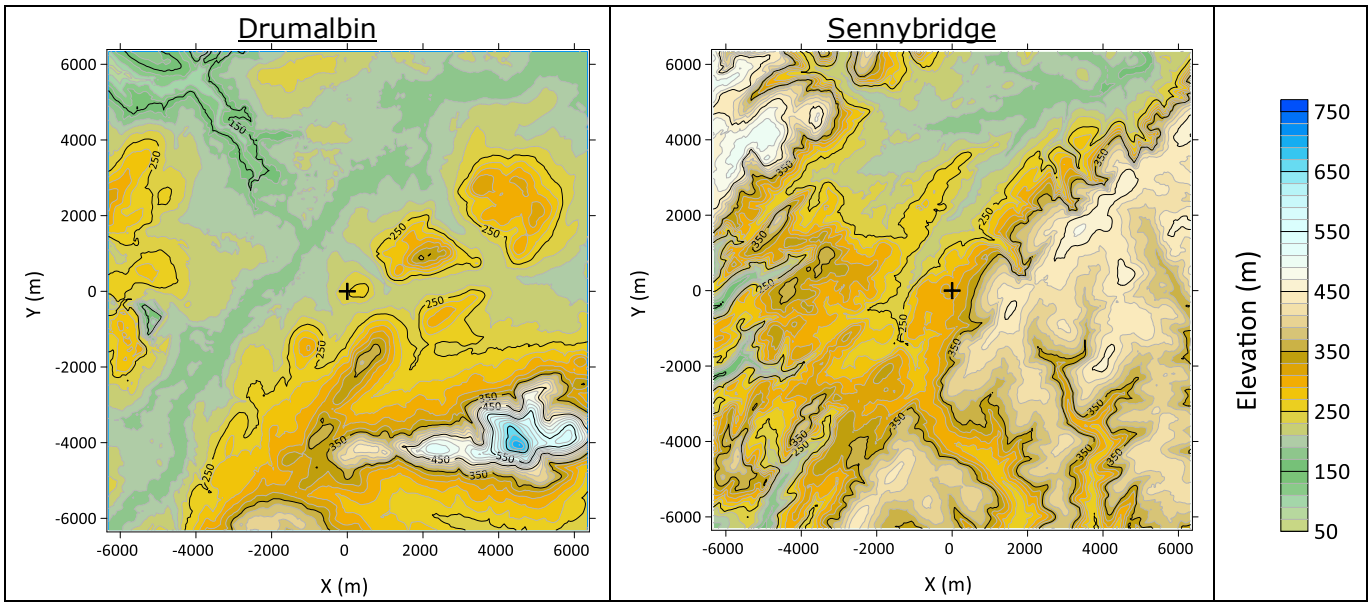

Figure 81 – Terrain elevation (m) within the ~13 x 13 km FLOWSTAR domain used for Drumalbin (left) and Sennybridge (right). Met site is at the domain centre, shown by the black cross.

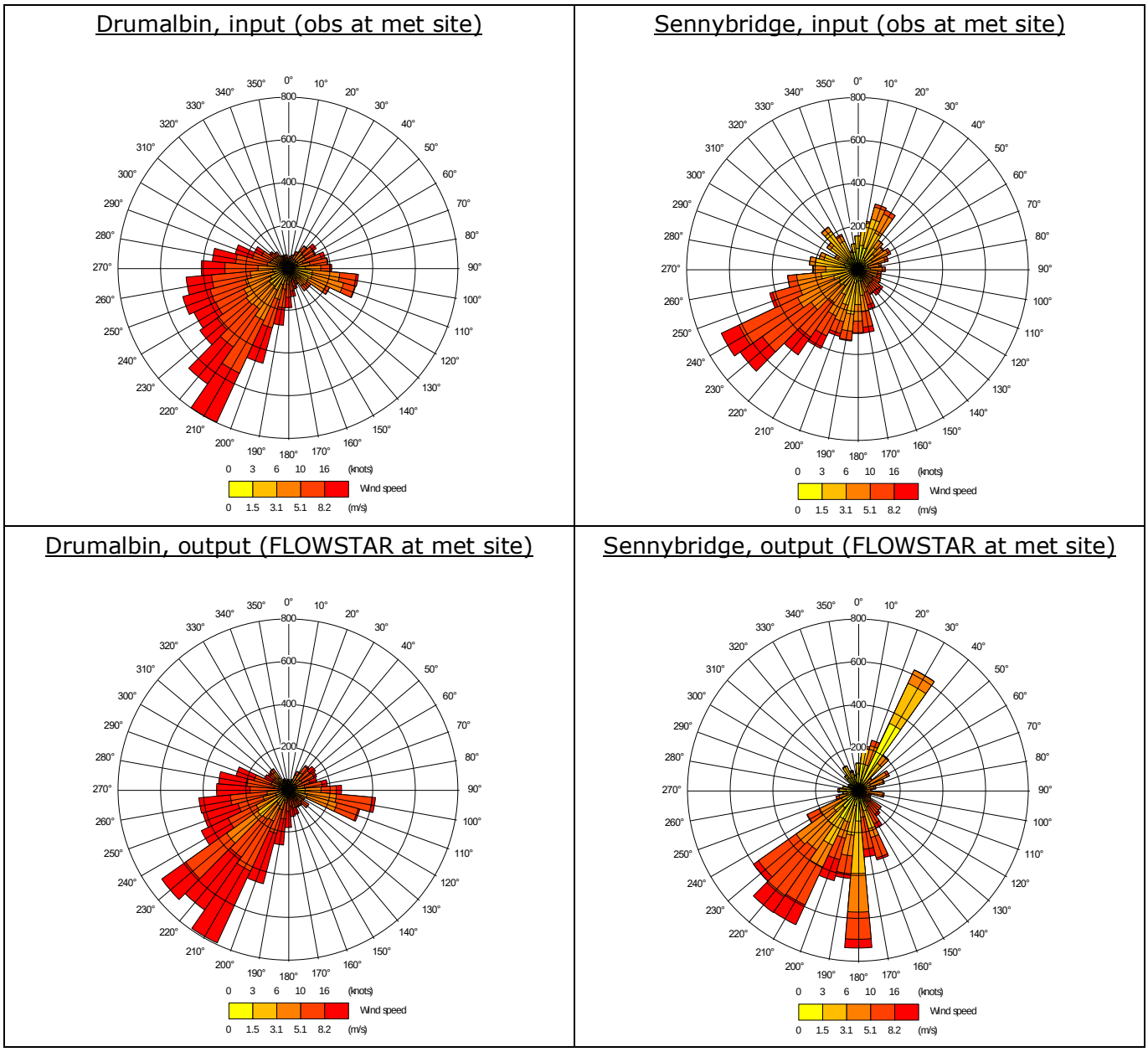

Figure 82 – Wind roses of the input data to FLOWSTAR (top), taken from met site observations, and the output data from FLOWSTAR extracted at the met site location (bottom) for Drumalbin (left) and Sennybridge (right).

In a similar way, it is possible to assess whether double-counting terrain effects is a significant issue when using NWP data to drive FLOWSTAR by comparing the wind rose of the input (NWP) data against the wind rose of the output (FLOWSTAR) data that has been spatially averaged over the NWP grid cell area. Figure 83 shows the input (top plots) and spatially averaged output (middle plots) wind roses for Drumablin and Sennybridge using the same FLOWSTAR domain as above but driving it using the 1.5 km resolution UM data extracted from the NWP grid cell containing the met site. Again, the wind roses are broadly similar at Drumalbin, with the output wind rose exhibiting a slightly stronger frequency of winds from

the south-west and east and a slightly lower frequency of winds from the west, indicating only a minor impact of double-counting. At Sennybridge, the output wind rose shows a clear over-prediction of winds from the north-east, and a more southerly component to winds within the south-west quadrant compared with the input wind rose, indicating a more significant impact from double-counting. For interest, Figure 83 (bottom plots) also shows wind roses of the output (FLOWSTAR) data extracted at the met site location when driven by the 1.5 km UM data. These should be compared with caution to the observational wind roses (top plots in Figure 82) as it is not possible to determine what proportion of the differences is due to double-counting issues and what proportion is due to inaccuracies in the models (NWP and FLOWSTAR) themselves. However, the comparison tentatively supports the suggestion that using 1.5 km UM data to drive FLOWSTAR within this domain would be reasonable at Drumalbin but lead to more significant double-counting issues at Sennybridge.

For completeness, Figure 84 shows the FLOWSTAR input (top plots) and spatially averaged output (middle plots) wind roses for Drumablin and Sennybridge when driven by the 10 km resolution UM data extracted from the NWP grid cell containing the met site. Given that the NWP grid cell is similar in size to the FLOWSTAR domain in this case, it is perhaps unsurprising that the wind rose of the FLOWSTAR output spatially averaged over the 10 km NWP grid cell area is very similar to the wind rose of the 10 km UM data itself, both at Drumalbin and now also at Sennybridge, confirming that double-counting is not a significant issue when using the 10 km UM data (because the scales modelled by FLOWSTAR and the NWP model do not significantly overlap). The bottom plots in Figure 84 show the wind roses of the 10 km-UM-driven FLOWSTAR output extracted at the met site. Again, these can be compared (with caution) to the observational data wind roses (top plots in Figure 82). At Sennybridge, while there are differences, the FLOWSTAR output wind rose at the met site is broadly consistent with the observational wind rose, indicating a relatively good level of accuracy in the (NWP and FLOWSTAR) model predictions. In this case, the 10 km UM dataset might reasonably be seen as the most appropriate dataset to drive FLOWSTAR within this domain, compared with the 1.5 km UM or observational datasets which both lead to fairly apparent double-counting issues. At Drumalbin, however, the FLOWSTAR output wind rose at the met site and the observational wind rose show more notable differences, with a more uniform distribution of winds within the south-west quadrant in the FLOWSTAR output in particular. In this case, the choice of whether to drive FLOWSTAR with the 10 km UM dataset or the 1.5 km UM (or observational) dataset is less clear, with the disadvantage of introducing (relatively minor) double-counting effects with the 1.5 km UM dataset possibly outweighed by the apparently better match to observations at the met site compared with the 10 km UM dataset. Of course, without the availability of observational wind data at the site of interest, it would be difficult to draw these conclusions.

The rest of this section is organised as follows. Firstly, qualitative comparisons are made between the finest resolution gridded NWP flow field data and equivalent FLOWSTAR flow fields to analyse the extra level of detail attained by using the

complex terrain option in ADMS (Section 7.2). Secondly, we attempt to quantify the impact of double-counting terrain effects on airflow and dispersion (Section 7.3). Thirdly, we assess the influence of using FLOWSTAR to model only terrain height variations with spatial scales smaller than those represented in the NWP model (Section 7.4).

Drumalbin, input (1.5 km UM data)

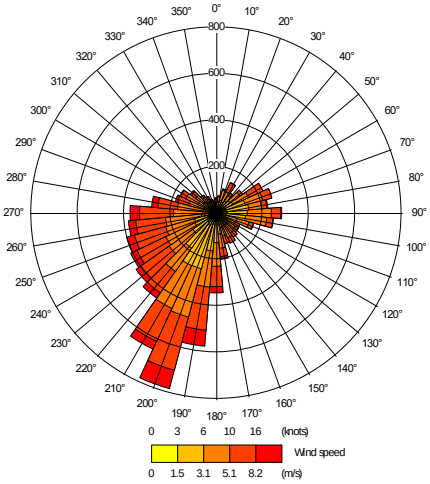

Sennybridge, input (1.5 km UM data)

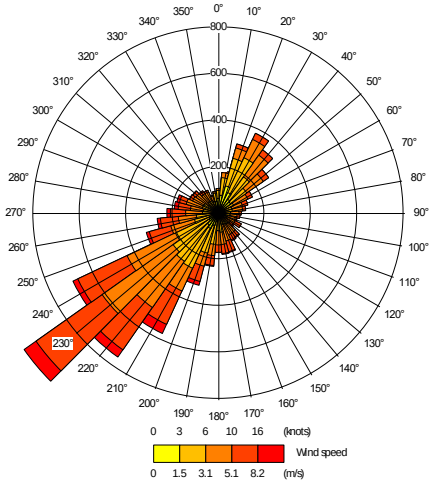

Drumalbin, output (1.5 km FLOWSTAR average)

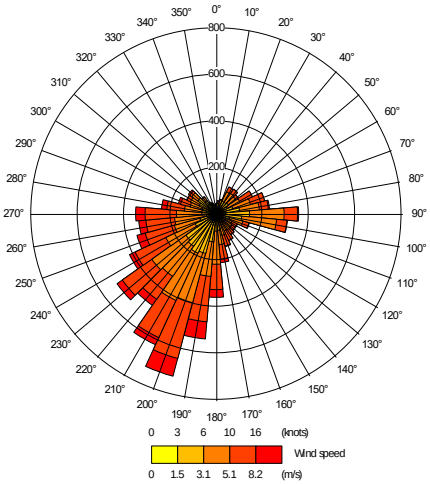

Sennybridge, output (1.5 km FLOWSTAR average)

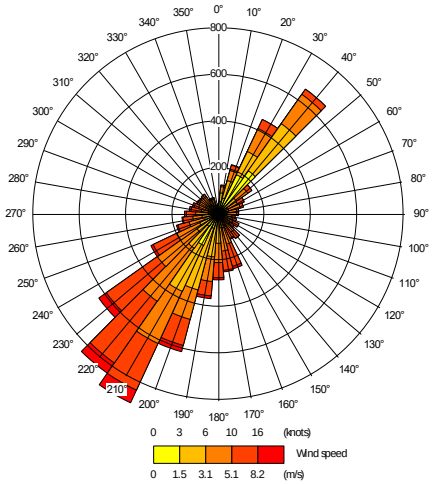

Drumalbin, output (FLOWSTAR at met site)

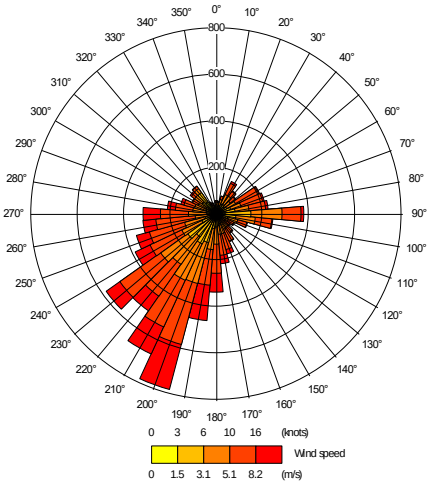

Sennybridge, output (FLOWSTAR at met site)

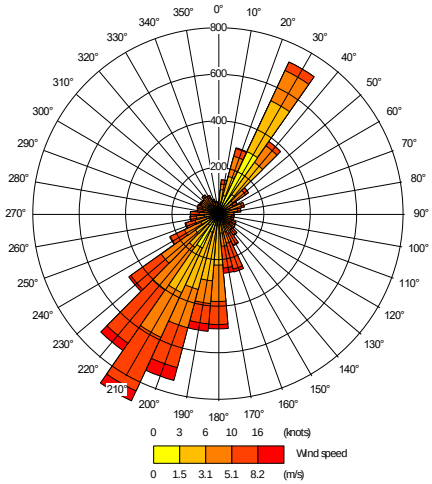

Figure 83 – Wind roses of the input data to FLOWSTAR (top), taken from the 1.5 km UM grid cell containing the met site, the output data from FLOWSTAR spatially averaged over the NWP grid cell area (middle) and the output data from FLOWSTAR extracted at the met site location (bottom) for Drumalbin (left) and Sennybridge (right)

Drumalbin, input (10 km UM data)

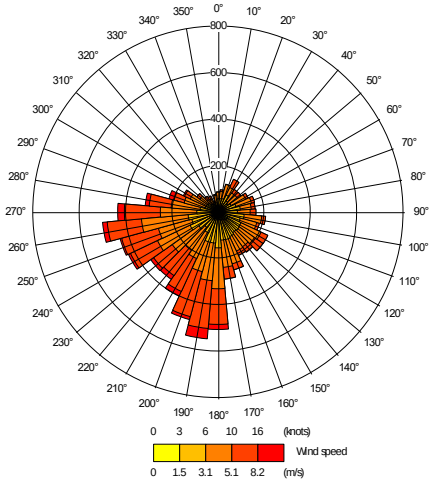

Sennybridge, input (10 km UM data)

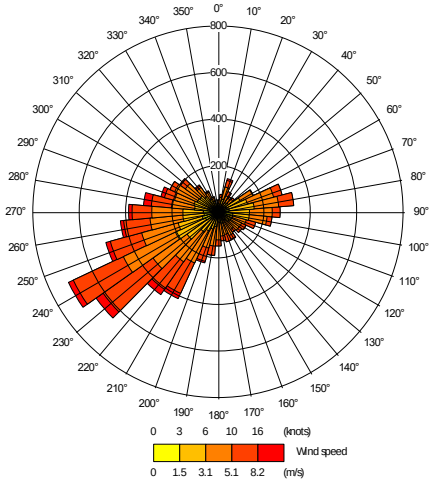

Drumalbin, output (10 km FLOWSTAR average)

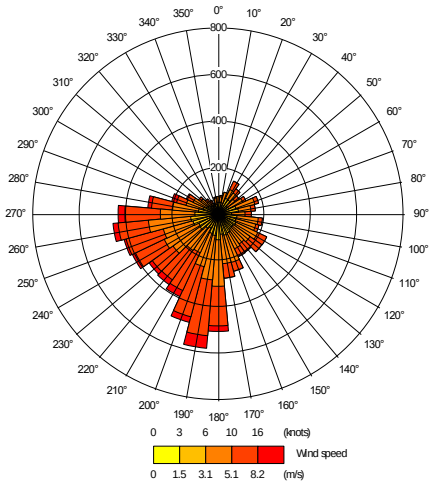

Sennybridge, output (10 km FLOWSTAR average)

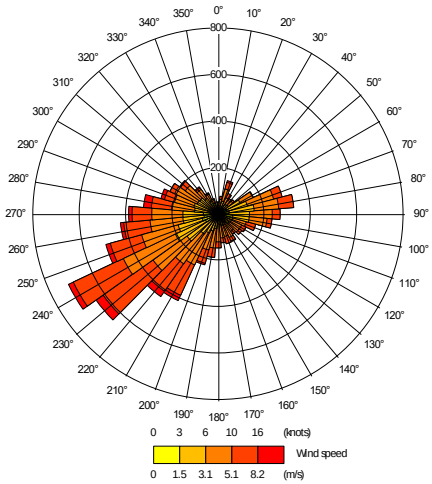

Drumalbin, output (FLOWSTAR at met site)

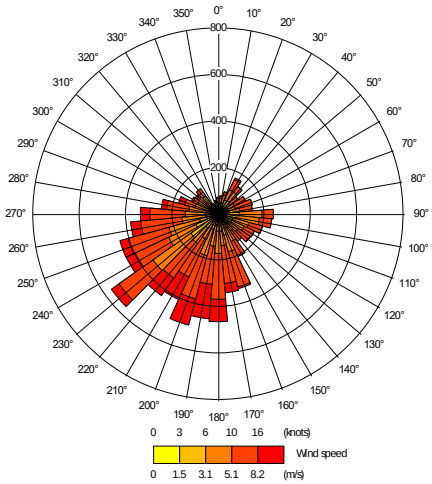

Sennybridge, output (FLOWSTAR at met site)

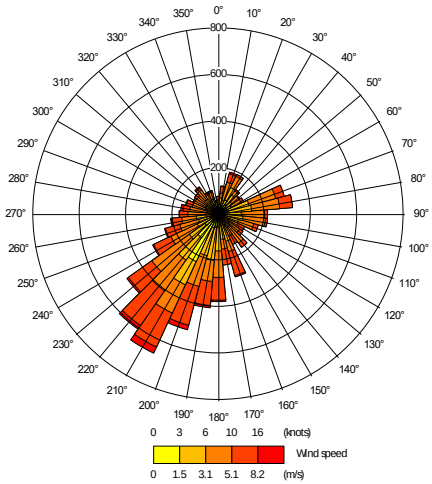

Figure 84 – Wind roses of the input data to FLOWSTAR (top), taken from the 10 km UM grid cell containing the met site, the output data from FLOWSTAR spatially averaged over the NWP grid cell area (middle) and the output data from FLOWSTAR extracted at the met site location (bottom) for Drumalbin (left) and Sennybridge (right).

7.2 Comparing finest resolution NWP flow fields with FLOWSTAR

In this section, gridded 10 m above-ground-level (agl) flow field data from the finest resolution NWP datasets are compared against equivalent FLOWSTAR flow fields.

7.2.1 Gridded NWP data

The gridded NWP datasets used in this evaluation exercise are summarised in Table 31. The gridded WRF data has a horizontal grid resolution of 1 km and the gridded UM data has a resolution of 1.5 km. Only data from the two complex terrain sites of Drumalbin and Sennybridge are considered. Each dataset is centred on the location of the weather station/idealised source at that site and has an extent large enough to cover the region of interest, which is taken to be the 10 × 10 km source-centred region used for the (elevated source) dispersion modelling exercise in Section 6.

Table 31 - Summary of gridded NWP datasets used in this evaluation exercise.

Provider	Model	Resolution	Extent	Site name	Lat, lon
Met Office	Unified Model	1.5 km	10.5 × 10.5 km (7 × 7 cells)	Drumalbin	55.627, -3.735
				Sennybridge	52.063, -3.613
Air Pollution Services	WRF	1 km	11 × 11 km (11 × 11 cells)	Drumalbin	55.627, -3.735
				Sennybridge	52.063, -3.613

The gridded NWP data were converted into a format expected by the ADMS Flow Field Plotter to aid plotting – further details are given in Appendix D1.

7.2.2 FLOWSTAR flow fields

The 10 m agl FLOWSTAR flow fields were generated by running ADMS with the 'Complex terrain' modelling option enabled and the option to 'Calculate flow field output' ticked. The terrain file (surface elevation) used at each site matches that used in Section 6, i.e. OS Terrain® 50 data with a resolution of 50 m and an extent of ~13 × 13 km, centred on the relevant site coordinates. The FLOWSTAR grid resolution was set to 256 × 256 points, equivalent to around 50 m and thus matching the terrain data resolution. An output grid was defined at 10 m agl, also with a horizontal resolution of 50 m, and an extent of 10 × 10 km centred on the relevant site coordinates. The dispersion (and met. measurement) site surface roughness was again set to 0.2 m for Drumalbin and 0.3 m for Sennybridge.

As explained in Section 7.1, FLOWSTAR must be driven by one set of hourly meteorological data. Given that we want to compare equivalent flow fields in this exercise, we drive FLOWSTAR using the coarsest resolution single-cell NWP data (9 km for WRF, 10 km for UM). As the results in Section 7.1 suggest, this should largely mitigate any double-counting effects that would occur if we instead used, for example, meteorological data from the centre cell of the highest resolution gridded NWP data to drive FLOWSTAR. The 'base' configuration of meteorological

variables (see Table 20) is used, i.e. wind speed, wind direction, temperature and cloud cover (and precipitation, which does not affect the FLOWSTAR solution).

7.2.3 Long-term flow field plots

We first compare the four long-term (annual) average gridded NWP and FLOWSTAR wind fields at 10 m agl. These are shown in Figures 85 – 88 for each site (Drumalbin, Sennybridge) and NWP model (UM, WRF) pairing. Each top plot shows the relevant surface elevation (filled contours), mean 10 m agl horizontal wind vector field from the finest-resolution gridded NWP data (large arrows) and mean 10 m agl horizontal wind vector field from an equivalent FLOWSTAR run driven by the coarsest resolution NWP data (small arrows). All arrows belonging to a particular wind vector field are given the same length. Arrow colours show the magnitude of the mean horizontal wind vector in m/s (given by $\sqrt{\bar{u}^2 + \bar{v}^2}$). For the gridded NWP data, the arrow frequency in X and Y is set to the underlying resolution of the gridded dataset. However, for the FLOWSTAR output, the arrow frequency in X and Y is set to four, i.e. three arrows are skipped for every one arrow shown (one arrow every 200 m). This is to improve plot clarity; non-overlapping arrows at the underlying FLOWSTAR resolution of 50 m are too small to easily interpret. Each pair of bottom plots shows the mean horizontal wind speed ($\overline{\sqrt{u^2 + v^2}}$) in m/s at 10 m agl from the gridded NWP data (left) and the FLOWSTAR run (right). To illustrate the difference between the magnitude of the mean wind vector and the mean wind speed, consider a 5 m/s vector pointing east and a 4 m/s vector pointing west – the magnitude of the mean wind vector (which points east) is 1 m/s, while the mean wind speed is 4.5 m/s.

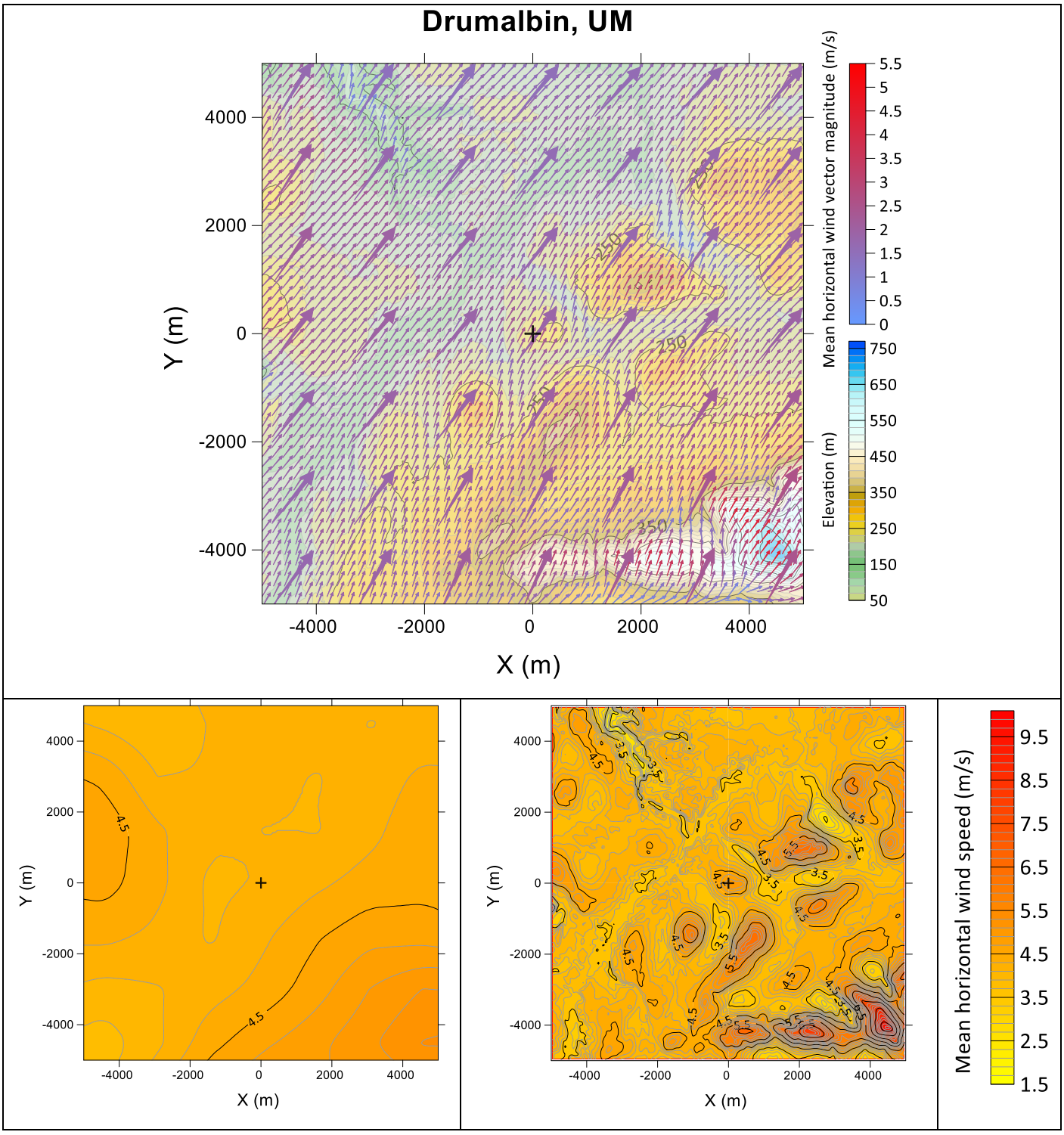

Figure 85 – Top: Drumalbin 10 m agl annual mean horizontal wind vector field from the gridded 1.5 km resolution UM data (large arrows) and from an equivalent FLOWSTAR run forced by the 10 km resolution UM data (small arrows). Centred on the source location (black cross). Surface elevation (m) shown by filled contours. Arrow colours show the magnitude of the mean horizontal wind vector (m/s). Bottom: 10 m agl annual mean horizontal wind speed (m/s) contours from the UM data (left) and the FLOWSTAR run (right).

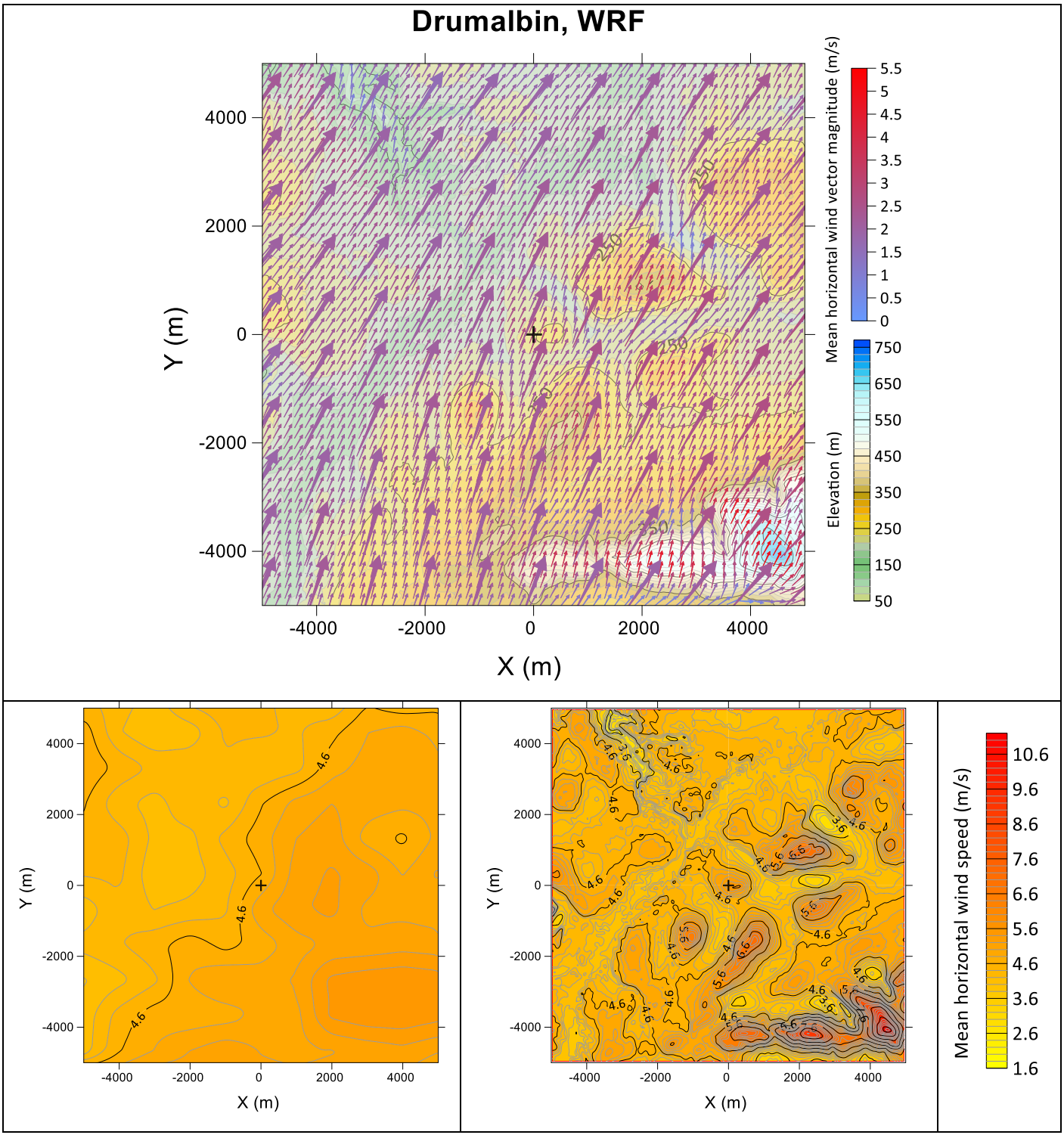

Figure 86 – As in Figure 85 but showing the mean horizontal wind vector field from the gridded 1 km resolution WRF data (Top: large arrows) and from an equivalent FLOWSTAR run forced by the 9 km resolution WRF data (Top: small arrows), and the mean horizontal wind speed contours from the WRF data (Bottom left) and the FLOWSTAR run (Bottom right).

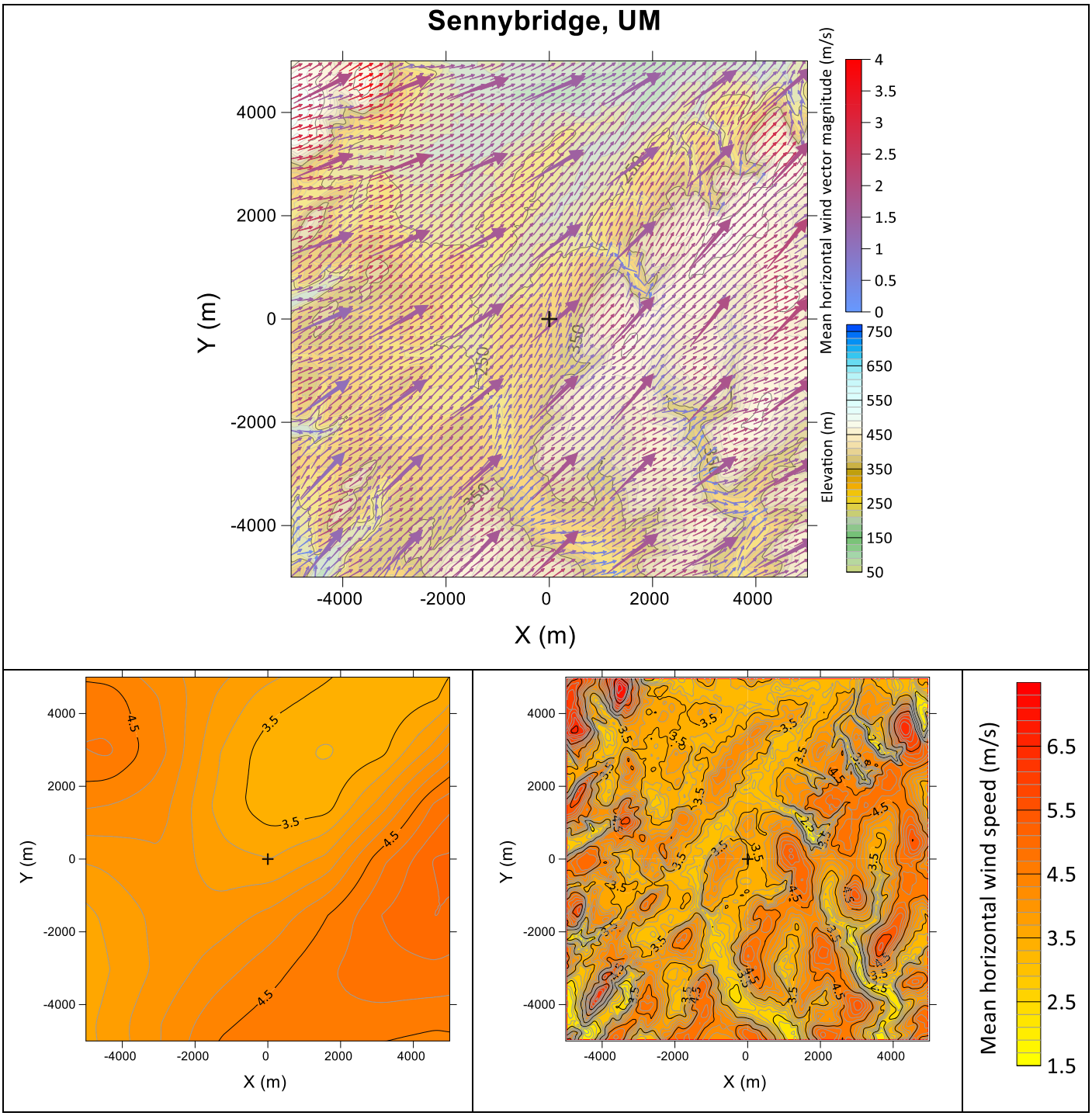

Figure 87 – As in Figure 85 but for Sennybridge.

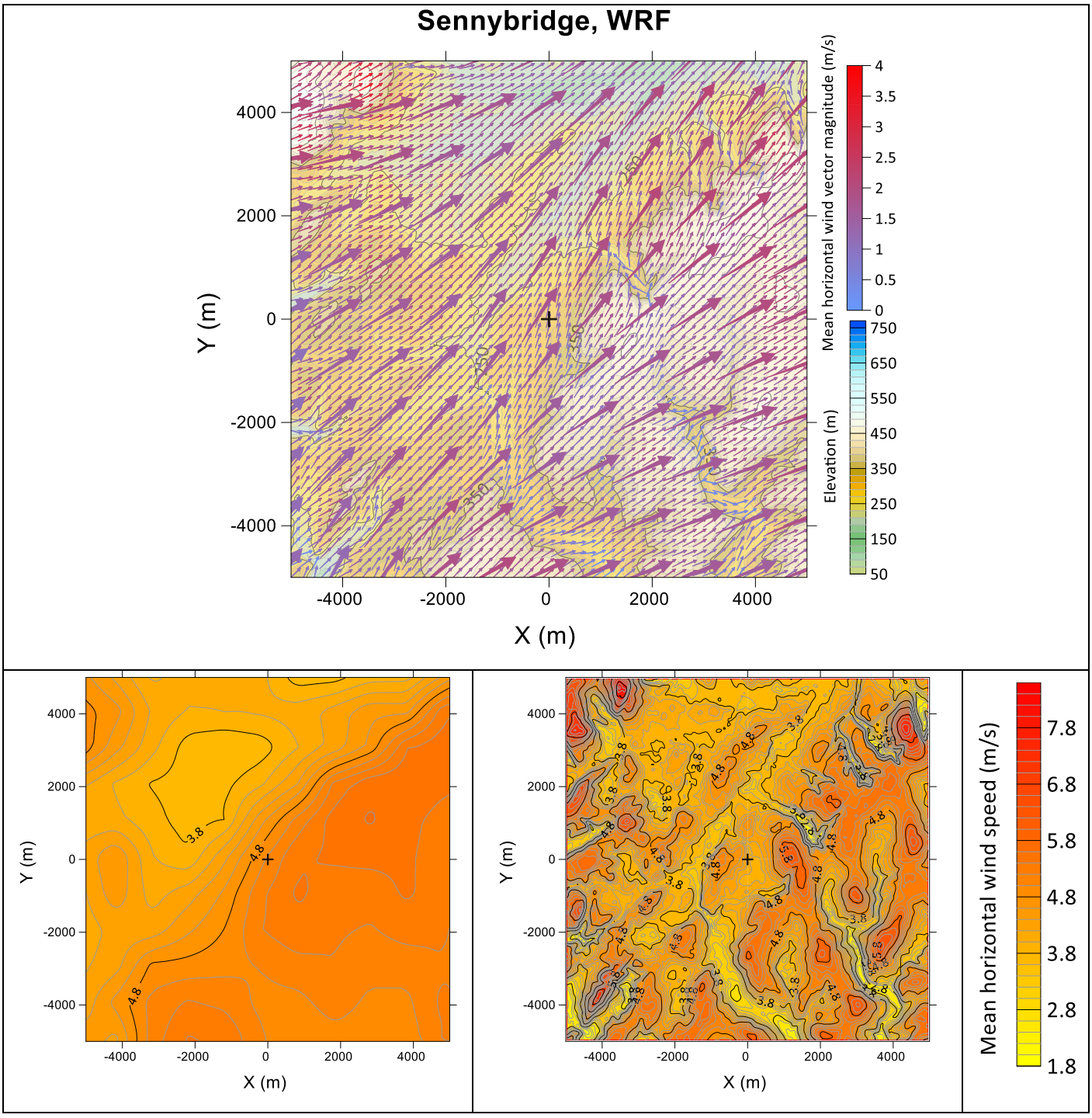

Figure 88 – As in Figure 86 but for Sennybridge

The FLOWSTAR mean wind vectors are broadly consistent with those from the NWP models but provide significantly greater detail around terrain features that are too small to be resolved by the NWP models. For instance, at Drumalbin, there is clear deviation around the isolated hill that lies approximately 2 km northeast of the source. The mean wind vector magnitudes over the steep hill in the SE corner of the domain are also much larger with FLOWSTAR compared with the NWP models. At Sennybridge, FLOWSTAR predicts highly localised flow patterns in many of the small valleys that are not identified by the NWP models.

At the domain scale, both sites are broadly characterised by a southwest-to-northeast-aligned valley. The Sennybridge vectors show a more obvious long-term 'channelling' flow pattern along this valley than the Drumalbin ones, with a more westerly flow above the higher elevation areas and a more south-westerly flow along the valley itself. This channelling is more obvious in the WRF vectors compared with the UM ones, which may be due to the slightly finer WRF grid resolution.

The mean wind speed contours output by FLOWSTAR again exhibit significantly greater detail around small terrain features than those from the gridded NWP data. The average, minimum and maximum wind speeds from the FLOWSTAR output and the gridded NWP data are given in Table 32 for each site/NWP model pair. The range of wind speeds are notably larger in the FLOWSTAR output. The average wind speed across the modelling domain remains similar between FLOWSTAR and the gridded NWP data, though the FLOWSTAR values are never larger than the NWP ones in the four cases presented.

Table 32 – Mean wind speed statistics of FLOWSTAR output and gridded NWP data.

Site	NWP model	Statistic of mean wind speeds (all m/s)	FLOWSTAR output	Gridded NWP data
Drumalbin	UM	Minimum	1.5	3.8
		Maximum	10.0	5.3
		Average	4.2	4.3
Drumalbin	WRF	Minimum	1.6	4.0
		Maximum	10.9	5.6
		Average	4.7	4.7
Sennybridge	UM	Minimum	1.5	3.3
		Maximum	7.3	5.1
		Average	3.9	4.1
Sennybridge	WRF	Minimum	1.8	3.6
		Maximum	8.2	5.6
		Average	4.4	4.7

7.2.4 Short-term flow field plots

It is also useful to compare gridded NWP and FLOWSTAR 10 m agl wind fields for specific hours. It is informative to consider hours covering each of the four different quadrants with regard to wind direction φ:

- Northerly ($315° < \varphi < 45°$)
- Easterly ($45° < \varphi < 135°$)
- Southerly ($135° < \varphi < 225°$)
- Westerly ($225° < \varphi < 315°$)

as well as hours covering each of the following stability/wind speed categories, defined using the ratio of boundary layer height to Monin-Obukhov length (h/L_{MO}) and the wind speed at 10 m agl (U_{10}):

- Convective ($h/L_{MO} < -0.3$) with low wind speed ($U_{10} < 3\ \mathrm{m/s}$)
- Neutral ($-0.3 \leq h/L_{MO} \leq 1$) with moderate-strong wind speed ($U_{10} > 5\ \mathrm{m/s}$)
- Stable ($h/L_{MO} > 1$) with low-moderate wind speed ($U_{10} < 5\ \mathrm{m/s}$)

A procedure was devised to identify, at each site, individual hours where both NWP models (UM and WRF) predict similar wind direction, stability and wind speed values for each combination of the categories listed above, thus giving 12 example hours per site. This procedure was based on data in the meteorological output (*.mop*) files from the four long-term ADMS/FLOWSTAR runs described in the previous subsection that were driven by the coarsest resolution single-cell NWP data (9 km for WRF, 10 km for UM). The hours identified are given in Table 33 below, along with the corresponding values of φ, h/L_{MO} and U_{10} for each NWP model as given in the relevant *.mop* file.

Table 33 – Individual hours identified for short-term flow field plots.

Site	Quadrant	Stability	Date, hour (all 2019)	φ UM (°)	φ WRF (°)	$\frac{h}{L_{MO}}$ UM	$\frac{h}{L_{MO}}$ WRF	U_{10} UM (m/s)	U_{10} WRF (m/s)
Drumalbin	Northerly	Convective	18 May, 11	24.0	29.3	-4.88	-4.15	2.55	2.44
		Neutral	04 Nov, 21	33.7	34.2	0.88	0.84	7.19	7.25
		Stable	28 Nov, 22	317.9	318.1	25.00	25.00	1.39	1.26
	Easterly	Convective	23 Apr, 07	90.9	91.8	-0.52	-0.72	1.93	2.26
		Neutral	09 Aug, 03	89.9	89.0	0.94	0.94	5.87	5.87
		Stable	03 Oct, 23	104.4	104.6	1.10	1.12	4.65	4.71
	Southerly	Convective	15 May, 10	160.3	164.1	-20.20	-20.56	1.76	1.90
		Neutral	27 Dec, 16	181.2	182.0	0.83	0.86	7.21	7.39
		Stable	24 Sep, 03	157.8	157.5	1.31	1.31	4.51	4.38
	Westerly	Convective	21 May, 06	255.4	259.3	-0.95	-0.97	1.88	2.13
		Neutral	06 Dec, 09	250.5	251.3	0.92	0.99	6.87	7.06
		Stable	19 Sep, 18	250.4	249.8	25.00	25.00	1.94	1.89
Sennybridge	Northerly	Convective	17 Sep, 09	16.4	32.9	-5.92	-5.55	2.20	2.27
		Neutral	27 Jan, 10	322.7	321.0	0.15	-0.09	9.15	9.69
		Stable	10 May, 24	330.6	331.2	16.66	16.66	0.78	0.87
	Easterly	Convective	09 Nov, 13	129.3	123.2	-6.60	-6.69	1.57	2.59
		Neutral	26 Jun, 20	68.0	66.6	0.55	0.55	6.58	7.31
		Stable	21 Apr, 03	94.7	93.0	16.66	16.66	1.27	1.25
	Southerly	Convective	23 Aug, 12	190.7	188.3	-14.08	-13.54	1.88	2.83
		Neutral	25 Oct, 18	214.5	215.3	0.63	0.65	9.72	9.93
		Stable	09 Sep, 05	190.7	192.1	1.29	1.29	3.51	3.43
	Westerly	Convective	14 Sep, 17	241.0	242.7	-3.29	-3.04	2.95	2.78
		Neutral	22 Aug, 08	225.5	225.8	0.08	0.18	5.71	5.67
		Stable	09 Aug, 24	239.8	239.7	1.85	1.85	3.11	3.19

The UM and WRF plots for Drumalbin for a westerly wind direction are shown in Figure 89. The Drumalbin plots for the remaining wind directions are given in Appendix D2. The plots are formatted similarly to the long-term ones, with surface elevation shown by filled contours, the 10 m agl NWP wind vector field shown by large arrows and the 10 m agl FLOWSTAR wind vector field shown by small arrows. In addition, the corresponding upwind wind direction used in the FLOWSTAR run is shown above each plot.

For the convective hour, the wind channelling within the large-scale diagonal valley is evident in both the FLOWSTAR and NWP flow fields, though it is a stronger feature of the WRF flow field compared with the UM. WRF agrees better with the FLOWSTAR flow field, including the faster wind speed predictions over higher ground to the south-east. WRF seems to identify the smaller valley flow in the north-west corner of the domain; this may be too small to be adequately resolved by the UM.

For the neutral met hour, the WRF and UM wind fields are largely uniform in direction and speed, though WRF again predicts larger wind speeds over the tall

hill in the south-east corner. FLOWSTAR still includes additional local deviations around smaller terrain features. It is interesting to note that the general wind direction in the UM wind field does not match with the input FLOWSTAR wind direction, indicating an inconsistency between the 1.5 km and 10 km UM wind fields for this hour.

For the stable hour, both NWP models predict large-scale convergence within the domain. This is particularly apparent in the UM, where north-westerly winds enter the north of the domain while south-westerly winds enter the south of it. By conservation of mass, this implies air is rising where it is converging. This large-scale convergence is not reproduced in the FLOWSTAR wind fields. It is worth noting that FLOWSTAR has no information about terrain features or synoptic weather patterns outside of the input terrain file region, whereas the NWP modelling domains extend significantly further than this and may therefore be better at describing the flow patterns entering the model domain. FLOWSTAR is however able to resolve very localised flow patterns within the valleys that lie south-east of the source. It should be noted that FLOWSTAR uses a different algorithm in stable flows, with air below a dividing streamline flowing around rather than over hills.

The plots for the other wind directions at Drumalbin in Appendix D2 show broadly similar patterns to those for a westerly wind direction presented here. Hours where differences between the NWP model and FLOWSTAR flow fields are particularly noticeable include the northerly stable hour, where both UM and WRF predict an area of southerly flow in the south-west region of the domain whereas the FLOWSTAR flow field remains largely north-westerly throughout. This may again be due to the lack of information of conditions outside the FLOWSTAR terrain extent and/or the fact that FLOWSTAR must be driven by a single upwind condition and so cannot account for synoptic meteorological variations within the domain. The southerly convective hour also shows a clear convergence to an easterly flow in the WRF flow field that is not seen in either the UM or FLOWSTAR flow fields. Note that FLOWSTAR does not currently consider thermally-driven flows, which may also contribute to some of the differences between FLOWSTAR output and NWP model flow fields.

The UM and WRF plots for Sennybridge for a westerly wind direction are shown in Figure 90. The Sennybridge plots for the remaining wind directions are given in Appendix D2. Again, FLOWSTAR can be seen to add significantly more detail than the NWP models are able to resolve in certain situations/regions. The WRF data is again slightly more consistent with the FLOWSTAR wind field compared with the UM, particularly for the stable met line in which a southerly wind is predicted by WRF and FLOWSTAR in the central region of the modelling domain while it remains largely westerly in the UM data.

Interesting plots from the other wind directions at Sennybridge in Appendix D2 include: the northerly stable hour, in which the UM predicts an easterly flow in the central region of the domain that is not apparent in either the WRF or FLOWSTAR flow fields (which broadly agree with each other apart from within a region north-east of the source); the easterly convective hour, where FLOWSTAR and WRF

again show fairly good agreement, other than in the north-west region of the domain, whereas the UM predicts a more southerly component to the wind across a larger area; the easterly stable hour, where the UM again predicts a southerly flow over a much larger area than either the WRF model or FLOWSTAR; and the southerly convective hour, where an inconsistency between the UM 1.5 km resolution general wind direction and the 10 km resolution wind direction (used to drive FLOWSTAR) is again evident.

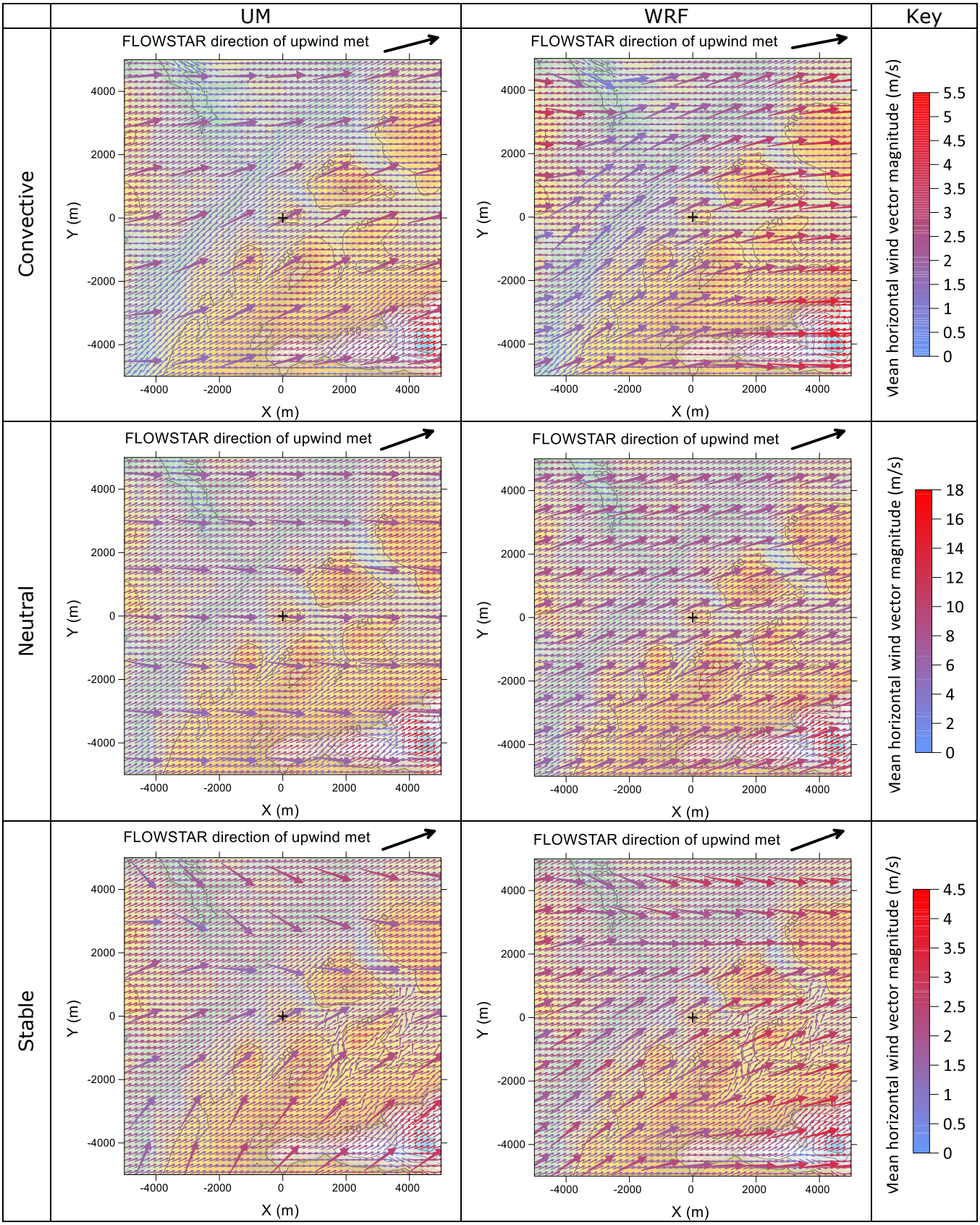

Figure 89 – Drumalbin 10 m agl horizontal wind vector fields for individual hours with a westerly wind direction and convective (top), neutral (middle) and stable (bottom) conditions. Large arrows show finest-resolution gridded NWP data, small arrows show equivalent FLOWSTAR run forced by coarsest-resolution NWP data; UM (left) and WRF (right).

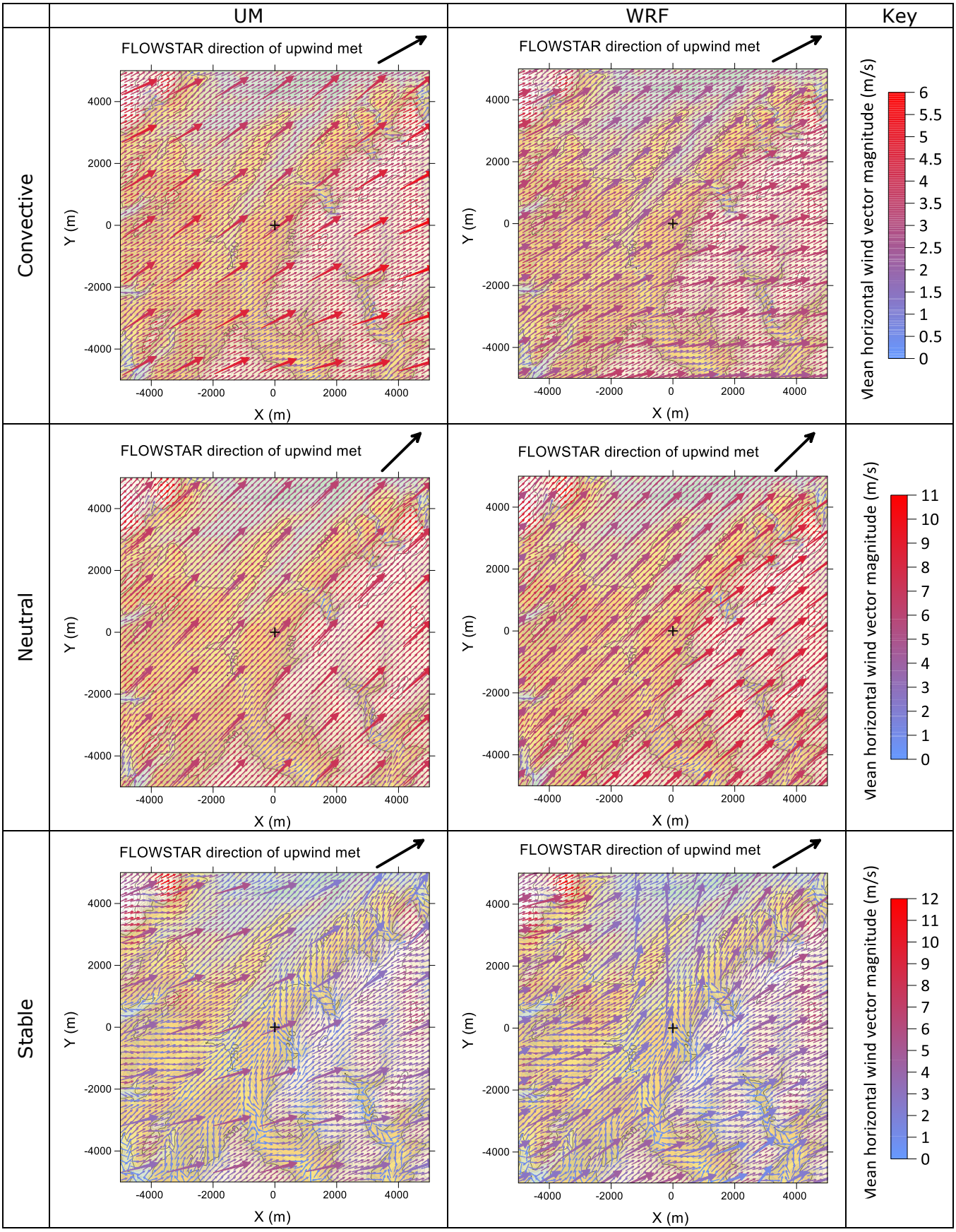

Figure 90 – As in Figure 89 but for Sennybridge (westerly wind direction).

7.3 Spatially averaged vs single cell NWP data: effect on dispersion and airflow

In this section, we assess the effect on dispersion and airflow of driving FLOWSTAR using two different NWP datasets in an attempt to quantify the impact of double-counting terrain effects. For brevity, only one NWP model (UM) has been considered in this analysis. The two NWP datasets considered are:

a) Single-cell fine-resolution (1.5 km) NWP data extracted at the source

b) Gridded fine-resolution (1.5 km) NWP data spatially averaged over a region covering most of the FLOWSTAR domain (10.5 x 10.5 km).

Details of how the gridded NWP data were spatially averaged are given in Appendix D3. For the single-cell met dataset, the 'base' configuration input files containing the 1.5 km resolution UM data extracted at the source were used without any further processing.

For the dispersion analysis, ADMS was configured as described in Section 7.2.2, with an additional output level at 0 m agl to obtain ground level concentrations. The two example sources ('Elevated' and 'Near-ground') used for the dispersion comparisons in Section 6 were also added. For the long-term runs, both long-term (annual) average and 98th percentile concentrations were output.

Using gridded fine-resolution NWP data spatially averaged over a region covering most of the FLOWSTAR domain should mitigate double-counting terrain effects, while FLOWSTAR will recreate the local wind flow patterns within the domain. Note that in this particular case we might alternatively have used the 10 km resolution UM data to drive FLOWSTAR, as this is also similar to the FLOWSTAR domain size, and Figure 84 indicates that double-counting impacts are minimal when using the 10 km UM data to drive this FLOWSTAR domain. However, some of the plots in Section 7.2 and Appendix D2 (e.g. the UM westerly neutral hour at Drumalbin and the UM southerly convective hour at Sennybridge) indicate that the spatial average of the finer resolution NWP flow field is not always consistent with the coarser resolution NWP flow field (in terms of general wind direction). For interest, however, some of the analysis below also shows equivalent results using the single-cell coarse-resolution (10 km) UM data extracted at the source, which again were taken from the 'base' configuration input files.

7.3.1 Wind roses

Wind roses for the spatially averaged (10.5 km) met datasets at Drumalbin and Sennybridge are shown in Figure 91 (top plots). For each site, the middle plot shows the result of driving FLOWSTAR with this met dataset (using the same FLOWSTAR domain described above) and spatially averaging the resulting FLOWSTAR output over the same 10.5 km region used to calculate the met data, while the bottom plot shows the FLOWSTAR output extracted at the met site location. The equivalent wind roses for the 1.5 km and 10 km UM met datasets were presented in Figures 83 and 84 respectively. The annual average 10 m agl wind speed and the direction of the annual average wind vector for each of the NWP met datasets are also given in Table 34.

Table 34 – Annual average 10 m agl wind speed and direction of annual average wind vector for each NWP met dataset

NWP met dataset	Annual Average wind speed (m/s)	Direction of annual average wind vector (°)
Drumalbin, spatially averaged (10.5 km) met	4.3	214
Drumalbin, single cell (1.5 km) met	4.1	216
Drumalbin, single cell (10 km) met	4.0	216
Sennybridge, spatially averaged (10.5 km) met	4.1	233
Sennybridge, single cell (1.5 km) met	3.7	229
Sennybridge, single cell (10 km) met	3.6	237

Figure 91 shows that, at both sites, the wind rose of the FLOWSTAR output spatially averaged over the 10.5 km region is very similar to the wind rose of the input spatially-averaged 10.5 km met data itself, indicating that double-counting is not a significant issue when using this input dataset. Again, this is unsurprising given that the scales modelled by FLOWSTAR do not significantly overlap with those represented in the input met dataset. The comparison of the FLOWSTAR output extracted at the met site (Figure 91, bottom plots) with the observational wind data (Figure 82) shows similar discrepancies to those seen when using the 10 km UM data to drive FLOWSTAR.

At Drumalbin, the most prevalent wind direction (to the nearest 10°) in the spatially-averaged 10.5 km and single-cell 10 km met datasets is 190°, compared with 200° in the single-cell 1.5 km met dataset. There is a significantly higher frequency of winds from this south-south-westerly direction (and comparatively lower frequencies of winds from westerly and south-easterly directions) in the 1.5 km dataset. This is likely the result of winds from this sector being channelled along the broad valley that runs southwest-to-northeast through the modelling domain. The spatially-averaged 10.5 km and single-cell 10 km met dataset wind roses are broadly consistent with each other (there are much clearer differences between these wind roses and the single-cell 1.5 km met dataset wind rose), however there is a tendency for a slightly higher frequency of westerly winds and slightly lower frequency of southerly and easterly winds in the single-cell 10 km met dataset.

At Sennybridge, the single-cell 1.5 km met dataset shows a narrowing of the range of wind directions from the south-west compared with the spatially averaged 10.5 km met dataset, with a greater frequency of winds from the 230° sector. Again, this is a signal of wind channelling along the southwest-to-northeast valley that also exists within this modelling domain. There is also a clear tendency for winds from the north-east sector to show a more northerly component in the 1.5 km met dataset compared with the spatially averaged 10.5 km met dataset. The spatially-averaged 10.5 km and single-cell 10 km met dataset wind roses are again broadly consistent with each other, though winds from the south-west quadrant show a broader distribution of wind directions in the single-cell 10 km met dataset.

At both Drumalbin and Sennybridge, the average wind speed is slightly higher for the single-cell 1.5 km met dataset compared with the single-cell 10 km dataset (4.1 vs 4.0 m/s at Drumalbin, 3.7 vs 3.6 m/s at Sennybridge). However, the average wind speed for the spatially averaged 10.5 km met dataset is higher than the single-cell 1.5 km met dataset value at both sites (4.3 m/s at Drumalbin, 4.1 m/s at Sennybridge). It is difficult to establish why spatially averaging the fine-resolution UM data up to the scale of the coarse resolution data leads to higher average wind speeds than the average wind speeds in the coarse resolution data itself, as there are multiple differences between the two associated UM configurations (UKV and UMG).

It is also informative to compare wind roses at different heights to see how quickly the differences between the UKV (1.5 km resolution) and UMG (10 km resolution) UM configurations decrease with height. Figures 92 and 93 show wind roses at 100, 200, 400, 700 and 1000 m agl extracted at the source from the UKV and UMG datasets for Drumalbin and Sennybridge respectively. At Drumalbin, the differences between the two UM configurations have largely disappeared by around 700 m agl. At Sennybridge, the increased frequency of south-westerly winds is still faintly apparent at this height.

Drumalbin, input (spatially averaged 10.5 km UM data)

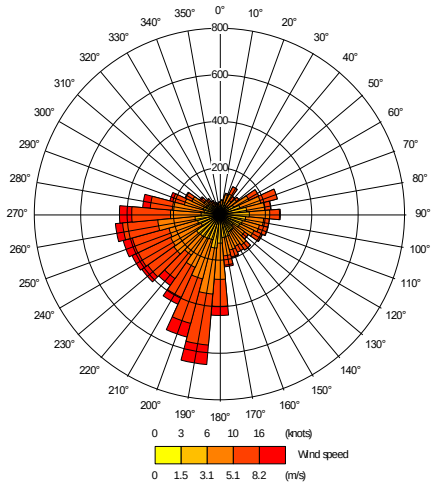

Sennybridge, input (spatially averaged 10.5 km UM data)

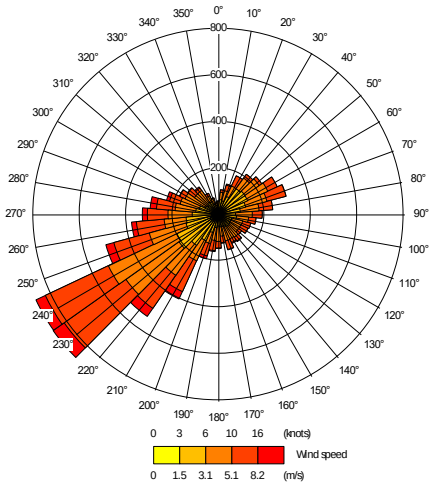

Drumalbin, output (10.5 km FLOWSTAR average)

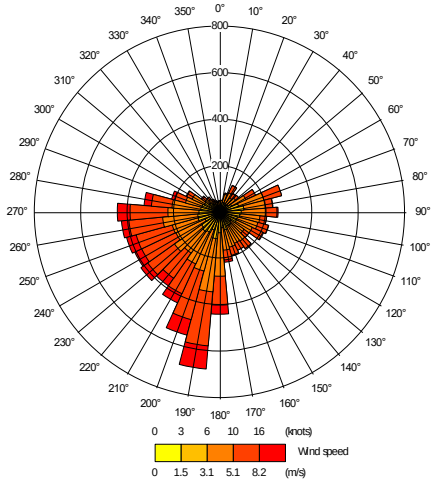

Sennybridge, output (10.5 km FLOWSTAR average)

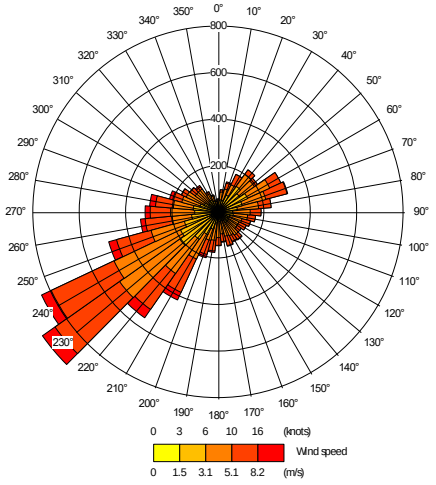

Drumalbin, output (FLOWSTAR at met site)

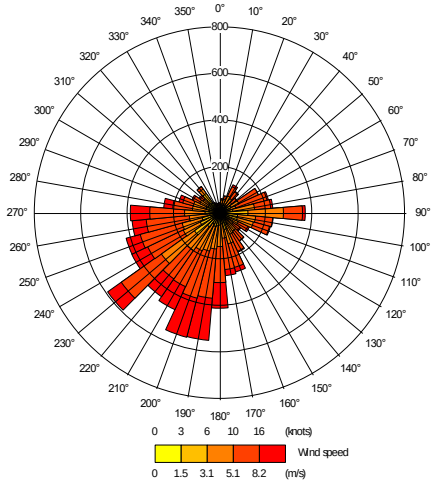

Sennybridge, output (FLOWSTAR at met site)

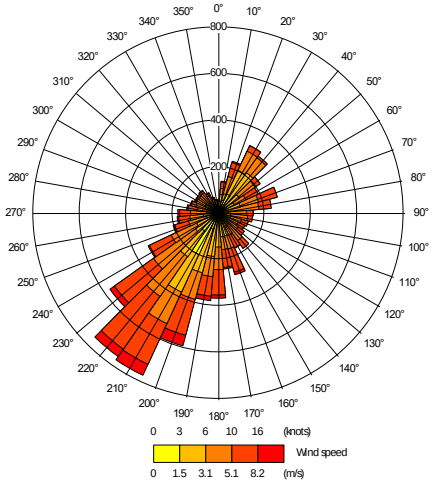

Figure 91 – Wind roses of the input data to FLOWSTAR (top), created by spatially averaging the 1.5 km UM data over a 10.5 km region (top), the output data from FLOWSTAR spatially averaged over the same 10.5 km region (middle) and the output data from FLOWSTAR extracted at the met site location (bottom) for Drumalbin (left) and Sennybridge (right).

Drumalbin	UKV (1.5 km) configuration	UMG (10 km) configuration
100 m agl	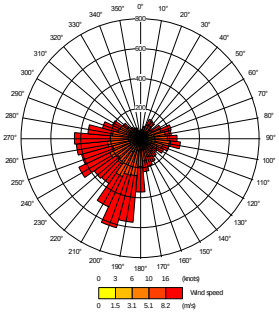	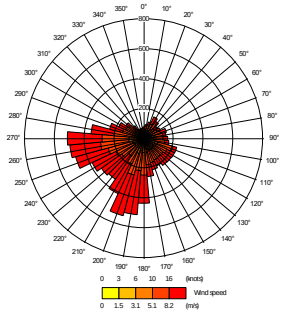
200 m agl	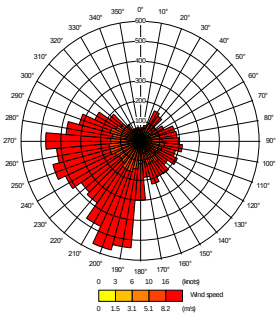	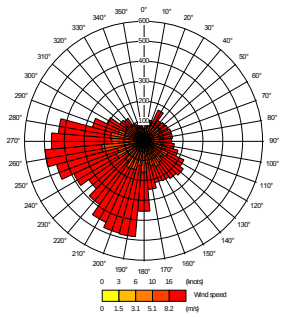
400 m agl	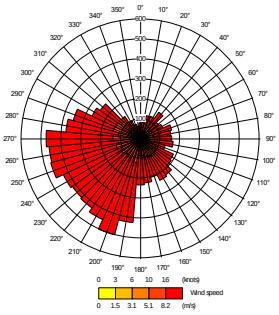	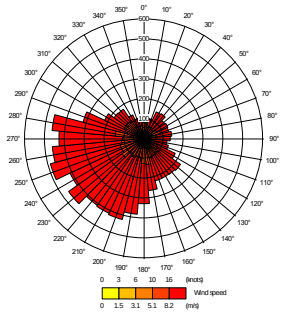
700 m agl	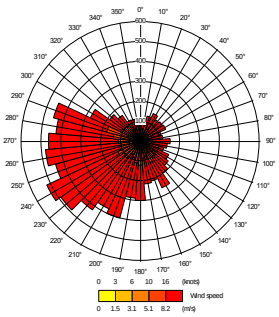	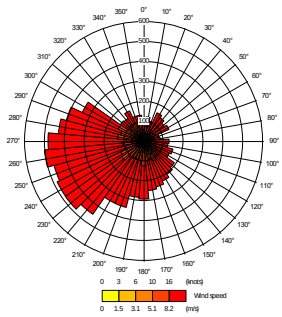
1000 m agl	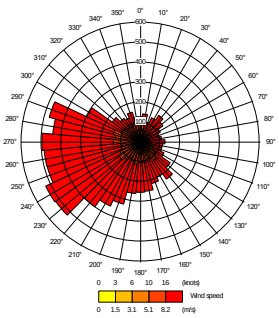	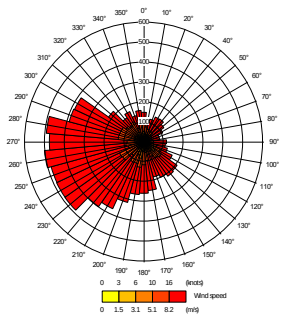

Figure 92 – Drumalbin annual wind roses at various heights agl based on data from the UKV (1.5 km resolution) and UMG (10 km resolution) UM configurations.

Sennybridge	UKV (1.5 km) configuration	UMG (10 km) configuration
100 m agl	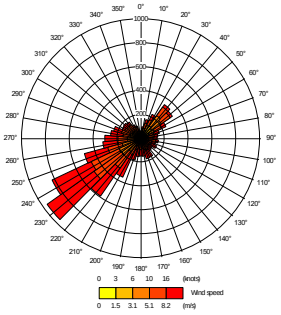	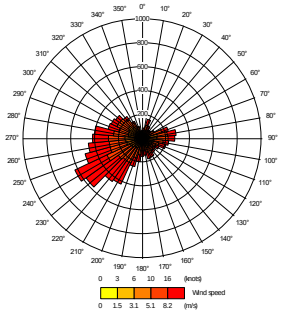
200 m agl	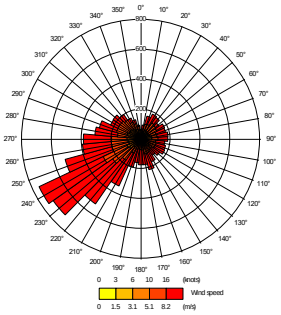	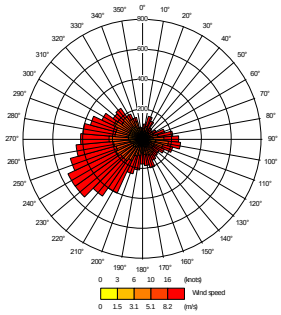
400 m agl	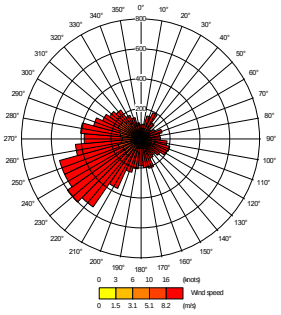	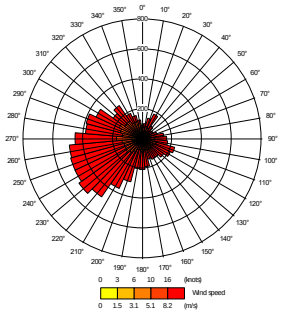
700 m agl	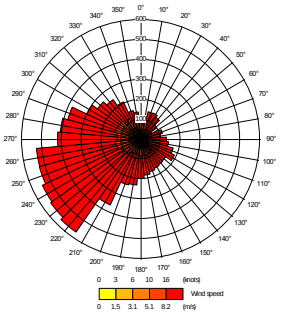	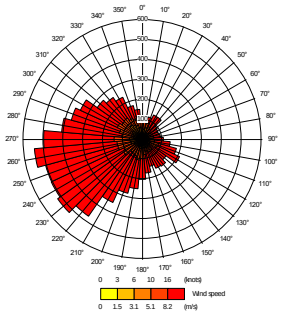
1000 m agl	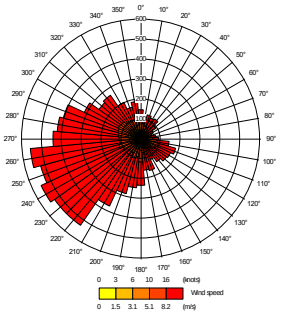	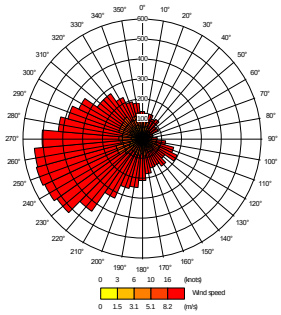

Figure 93 – As in Figure 92 but for Sennybridge.

7.3.2 Long-term dispersion results

We first compare the annual average concentration fields obtained using the spatially averaged 10.5 km and single-cell 1.5 km met datasets. These are shown in Figures 94 – 97 for each site (Drumalbin, Sennybridge) and source (elevated and near-ground) pairing. Each top plot shows the relevant concentration field (non-filled contours) and surface elevation (filled contours). Also shown (bottom left) are the differences between the two concentration fields in each case. *These difference plots can be interpreted as a measure of the impact of double-counting terrain effects on the long-term average concentrations*.

Figure 94 (Drumalbin, elevated source): The annual average concentration differences primarily reflect the differences seen in the annual wind roses for the two NWP datasets, with higher average concentrations to the north-east of the source and lower ones to the north/north-west and east of the source when using the single-cell 1.5 km UM data. This is consistent with the annual average concentration profiles for the elevated source shown in Figure 80 for the most common observed wind direction sector (210°), which showed higher concentrations with the finer resolution than with the coarser resolution NWP datasets.

At the receptor with the highest difference, which has coordinates relative to the source of (550 m, 1250 m), the concentration obtained with the 1.5 km met is 16% higher than that obtained with the spatially averaged 10.5 km met. At the receptor with the most negative difference, (50 m, 1500 m), the concentration obtained with the 1.5 km met is 13% lower than that obtained with the spatially averaged 10.5 km met.

The maximum annual average concentration obtained with the 1.5 km met, which occurs at (450 m, 1200 m), is 7.6% higher than the maximum annual average concentration obtained with the spatially averaged 10.5 km met, which occurs at (1250 m, 500 m), around 800 m away from the location of maximum concentration modelled with 1.5 km met. There are two distinct local maxima in the concentration field in this case and the location of the overall maximum changes between the different input met datasets. The higher maximum concentration predicted with the 1.5 km met is likely due to the increased frequency of the prevailing wind direction; this 'narrowing' of the distribution of wind directions leads to more hours when the plume disperses over that particular downwind sector, which can increase the long-term average concentrations within that sector. Note that this percentage difference is within the range of differences seen between ADMS and AERMOD using the same observed met data in Section 6, so is likely to be within the general uncertainty of modelling.

Figure 95 (Drumalbin, near-ground source): The annual average concentration differences for the near-ground source show a similar pattern to those seen with the elevated source but extend closer to the source, as the near-ground source has a stronger influence on ground level concentrations closer to the source. There is a clear tendency for the plume to travel north-east from the source more often, and east and north-west from the source less often, when using the 1.5 km data.

At the receptor with the highest concentration difference, (21 m, 36 m), the concentration obtained with the 1.5 km met is 17% higher than that obtained with the spatially averaged 10.5 km met. At the receptor with the most negative difference, (-27 m, 18 m), the concentration obtained with the 1.5 km met is 27% lower than that obtained with the spatially averaged 10.5 km met.

The maximum annual average concentration obtained with the 1.5 km met, which occurs at (14 m, 30 m), is 8.1% higher than the maximum annual average concentration obtained with the spatially averaged 10.5 km met, which occurs at (29 m, 11 m), around 24 m away from the location of maximum concentration with 1.5 km met. Again, this percentage difference in concentration is likely to be within the general uncertainty of modelling. The reason for the higher concentration value may again be due to the increased frequency of the prevailing wind direction, although the average wind speed at the source is also an important factor for maximum long-term concentrations from near-ground sources.

The 10 m agl average horizontal wind speed at the source as calculated by FLOWSTAR is 5.2 m/s for the run forced by the 1.5 km met compared with 5.3 m/s for the run forced by the spatially averaged 10.5 km met. This is consistent with the slightly higher average wind speed in the input spatially averaged met dataset (see Table 34). For near-ground sources, lower average wind speeds at the source typically lead to higher maximum long-term average concentrations, as seen in this case.

Figure 96 (Sennybridge, elevated source): Again, the annual average concentration differences for the elevated source at Sennybridge primarily reflect the differences seen in the annual wind roses for the two NWP datasets, with higher concentrations north-east of the source and lower concentrations further east when using the 1.5 km met due to the narrowing of winds within the south-west sector. The tendency for winds from the north-east sector to show a more northerly component in the 1.5 km met data is also clear in the difference plot. For these hours, the region of maximum difference occurs at the southern edge of the modelling domain where the elevated plume impacts the isolated hill in this region when travelling in a south-south-westerly direction.

At the location of the highest difference within the modelling domain, (-1800 m, -5000 m), which falls on this hill, the concentration obtained with the 1.5 km met is 179% higher than that obtained with the spatially averaged 10.5 km met, due to the increased frequency of plumes impacting the hill. At the location of the most negative difference, (1400 m, 700 m), the concentration obtained with the 1.5 km met is 20% lower than that obtained with the spatially averaged 10.5 km met.

The maximum annual average concentration obtained with the 1.5 km met, which occurs at (950 m, 900 m), is 2.3% higher than the maximum annual average concentration obtained with the spatially averaged 10.5 km met, which occurs at (1250 m, 900 m), 300 m away from the location of the maximum concentration with 1.5 km met. Again, this percentage difference in maximum concentration is likely to be within the general uncertainty of modelling while the reason for the

higher value may be due to the increased frequency of the prevailing wind direction.

Figure 97 (Sennybridge, near-ground source): There is a clear increased channelling effect on the annual average concentrations from the near-ground source when using the single-cell 1.5 km met data. The concentration contours closely follow the base of the valley edge to the south-east of the source, with relatively smaller concentrations to the east and west of the source.

At the receptor with the highest concentration difference, (-18 m, -35 m), the concentration obtained with the 1.5 km met is 43% higher than that obtained with the spatially averaged 10.5 km met. At the receptor with the most negative difference, (18 m, 9 m), the concentration obtained with the 1.5 km met is 22% lower than that obtained with the spatially averaged 10.5 km met.

The maximum annual average concentration obtained with the 1.5 km met, which occurs at (15 m, 21 m), is 4.8% lower than the maximum annual average concentration obtained with the spatially averaged 10.5 km met, which occurs at (16 m, 19 m), around 2 m away from the 1.5 km met maximum. Again, this percentage difference is likely to be within the general uncertainty of modelling.

The 10 m agl average horizontal wind speed at the source as calculated by FLOWSTAR is 3.7 m/s for the run forced by the 1.5 km met compared with 3.9 m/s for the run forced by the spatially averaged 10.5 km met and so does not explain the lower maximum annual average concentration obtained with the 1.5 km met. However, the distance from the source to the location of the maximum is slightly larger than the distance to the location of the maximum obtained with the spatially averaged met (25.8 m vs 24.8 m), which taken on its own is consistent with a lower concentration.

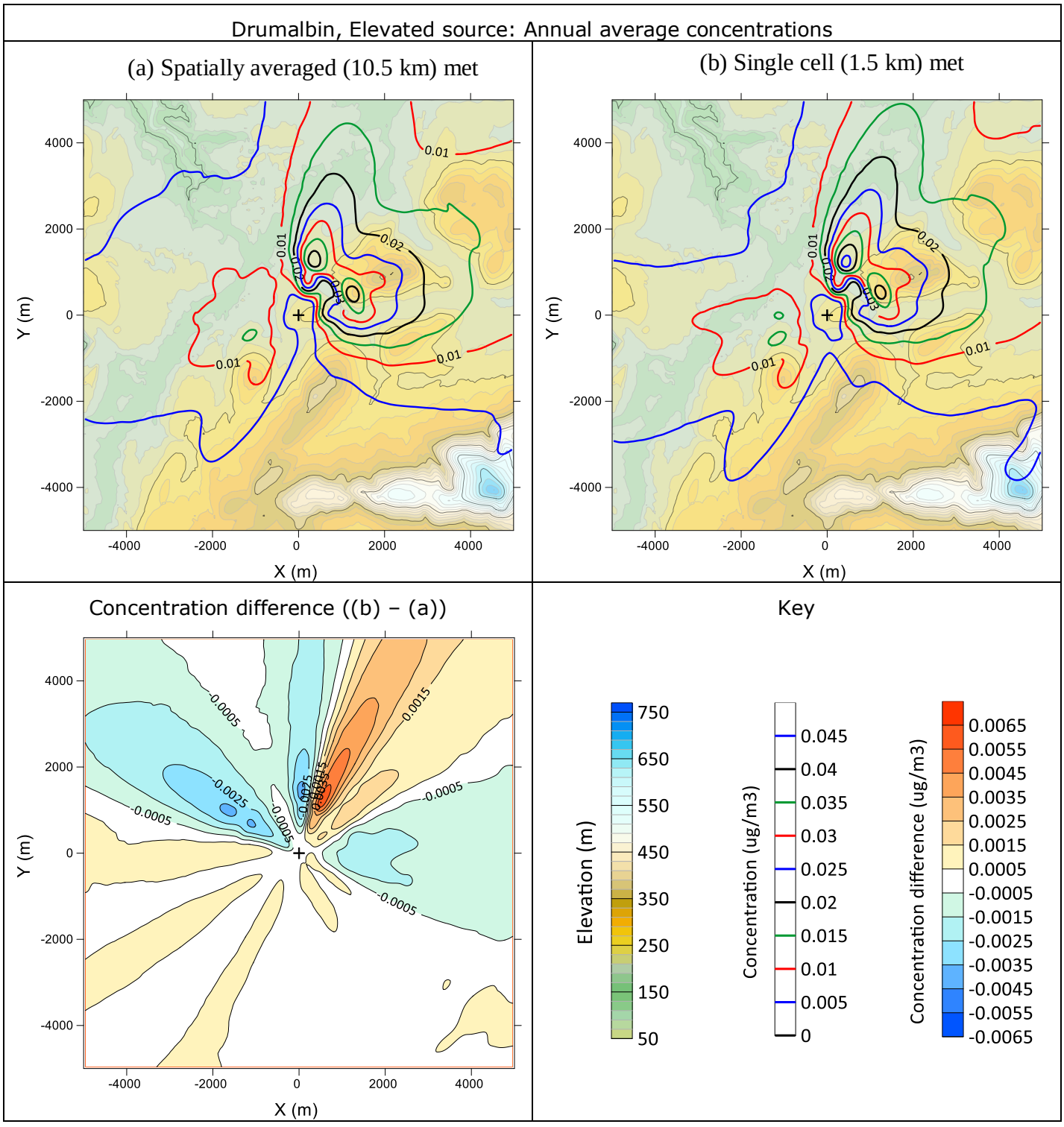

Figure 94 – Top: Drumalbin annual average ground level concentrations (non-filled contours) for the elevated source from an ADMS/FLOWSTAR run forced by (a) spatially averaged (10.5 km) met and (b) single cell (1.5 km) met. Surface elevation shown by filled contours. Bottom left: Concentration difference (b) – (a).

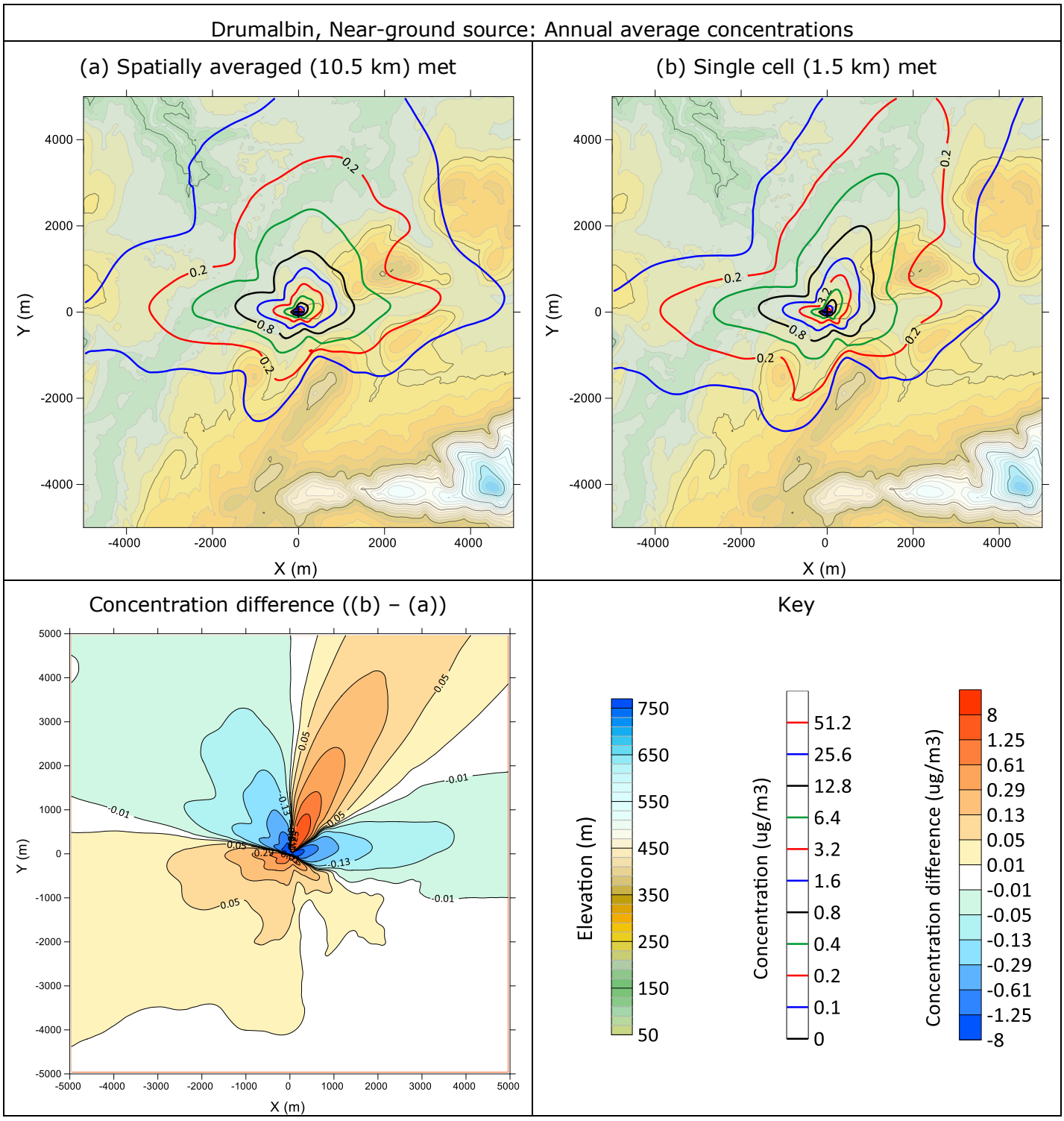

Figure 95 – As in Figure 94 but for the near-ground source at Drumalbin.

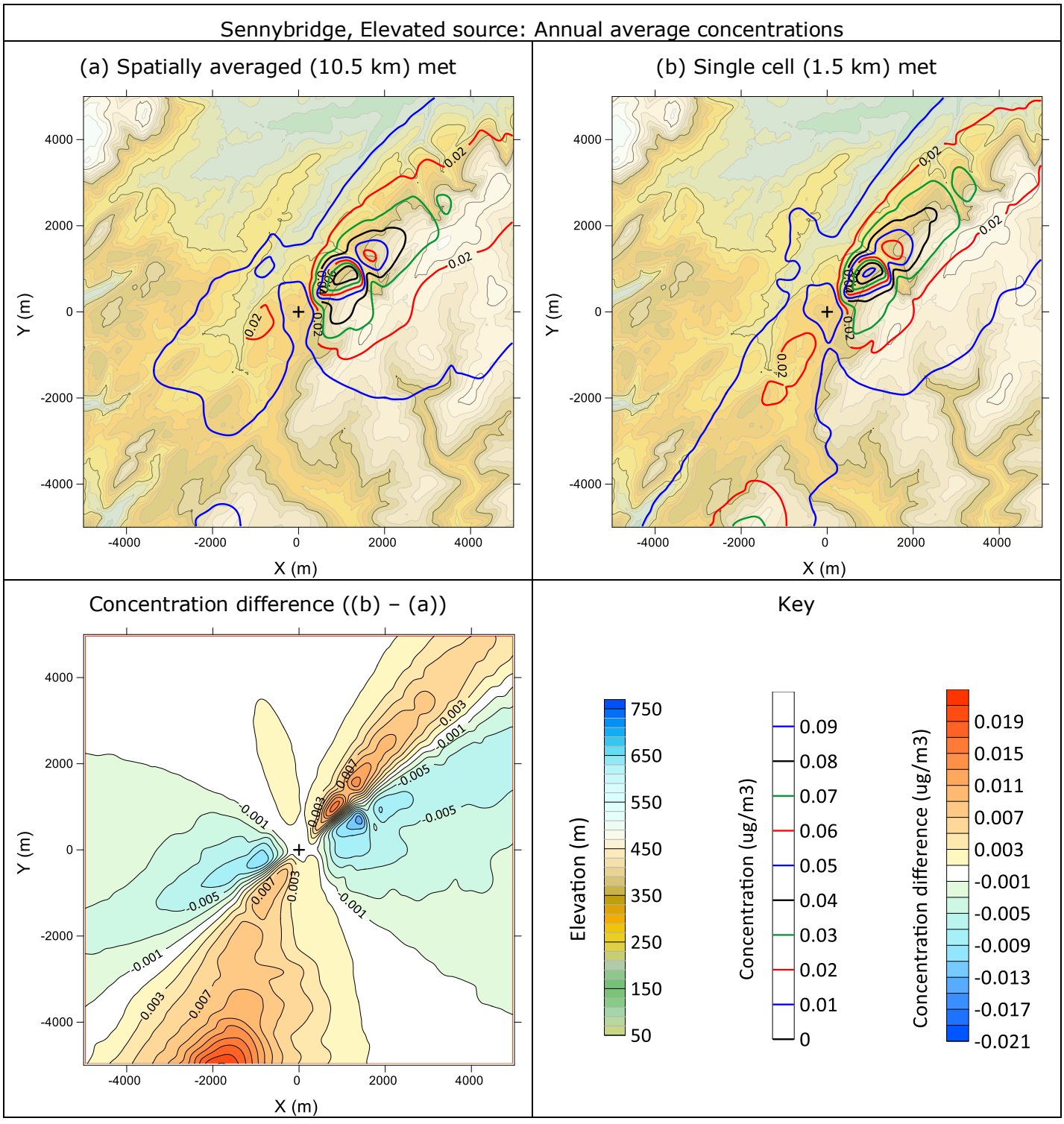

Figure 96 – As in Figure 94 but for the elevated source at Sennybridge.

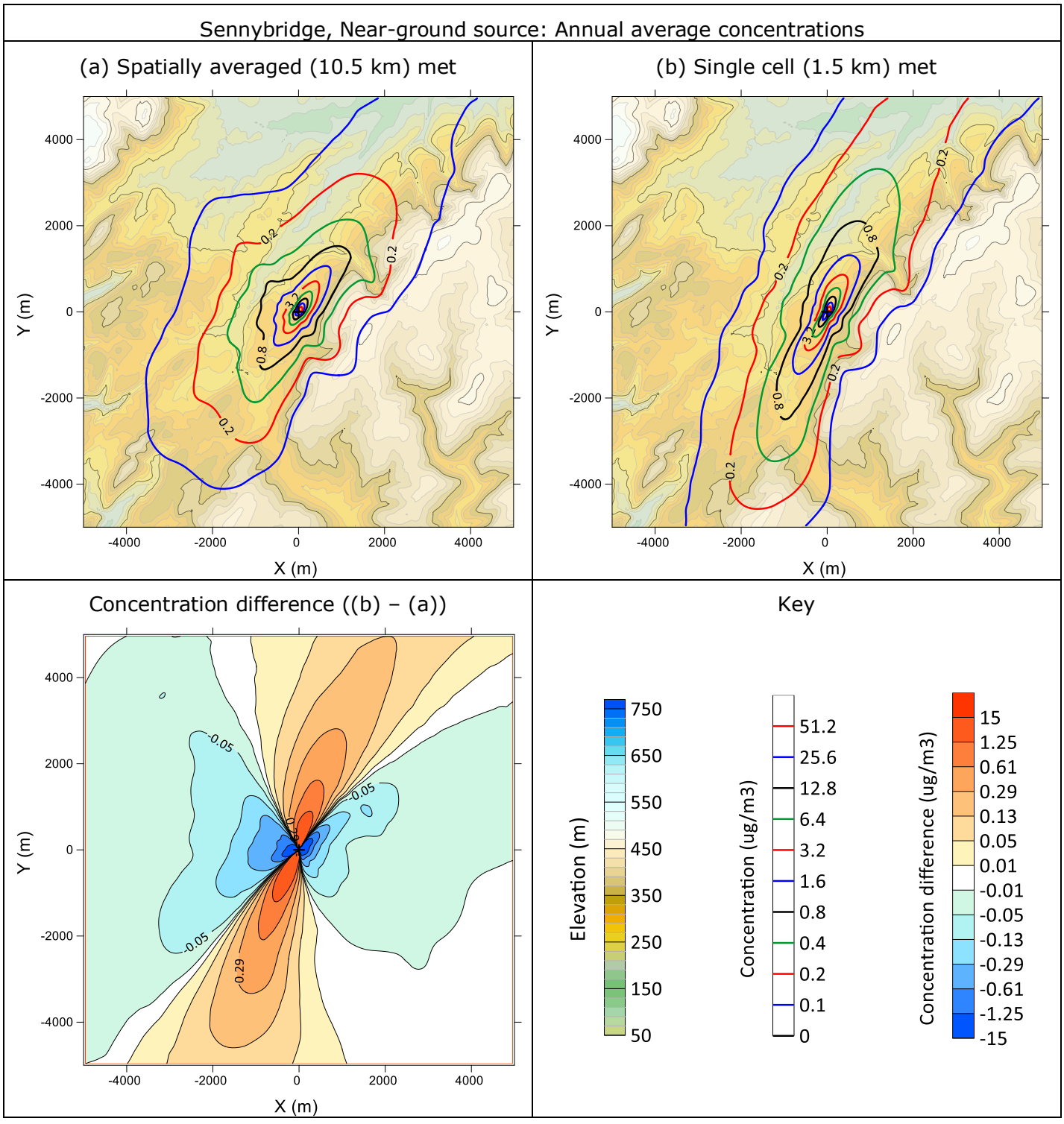

Figure 97 – As in Figure 94 but for the near-ground source at Sennybridge.

Figure 98 shows equivalent results to those presented in Figure 97 except that the first ADMS/FLOWSTAR run has been forced by the single-cell coarse-resolution 10 km met dataset rather than the spatially averaged 10.5 km met dataset. Although there are differences between the annual average concentration contours generated using these two met datasets (Figure 97(a) vs Figure 98(a)), the concentration differences between these contours and those generated using the single-cell fine-resolution 1.5 km met dataset (bottom left panels of Figure 97 and Figure 98) are largely consistent with each other in terms of the regions of positive and negative differences. This is also true for the equivalent plots to those presented in Figures 94 – 96 using the single-cell coarse-resolution 10 km met dataset rather than the spatially averaged 10.5 km met dataset, which are not shown for brevity. However, Table 35 shows that the maximum annual average concentrations obtained with the single-cell 10 km met dataset can be noticeably different from those obtained with the spatially averaged 10.5 km dataset, though the sign of the difference between the values obtained with the single-cell 1.5 km met dataset and each of these datasets is usually consistent. The 10 m agl average horizontal wind speed at the source as calculated by FLOWSTAR for the run forced by single-cell 10 km met is 5.0 m/s at Drumalbin and 3.5 m/s at Sennybridge, i.e. smaller than the value from the run forced by spatially averaged 10.5 km met in both cases (5.3 m/s and 3.9 m/s respectively).

Table 35 – Comparison of percentage differences in maximum annual average concentrations

Site	Source	% difference in maximum annual average concentration between run forced by single-cell 1.5 km met and run forced by...	
		spatially averaged 10.5 km met	single-cell 10 km met
Drumalbin	Elevated	+7.6%	+9.9%
Drumalbin	Near-ground	+8.1%	+4.8%
Sennybridge	Elevated	+2.3%	+26.0%
Sennybridge	Near-ground	-4.8%	+0.9%

Comparisons of the 98th percentile hourly average concentration fields obtained using the spatially averaged 10.5 km and single-cell 1.5 km NWP datasets are shown in Appendix D4. While the magnitude of the concentration differences are different to those seen for the annual average concentrations, the regions of positive and negative differences relative to the source location are again very similar for each site/source combination.

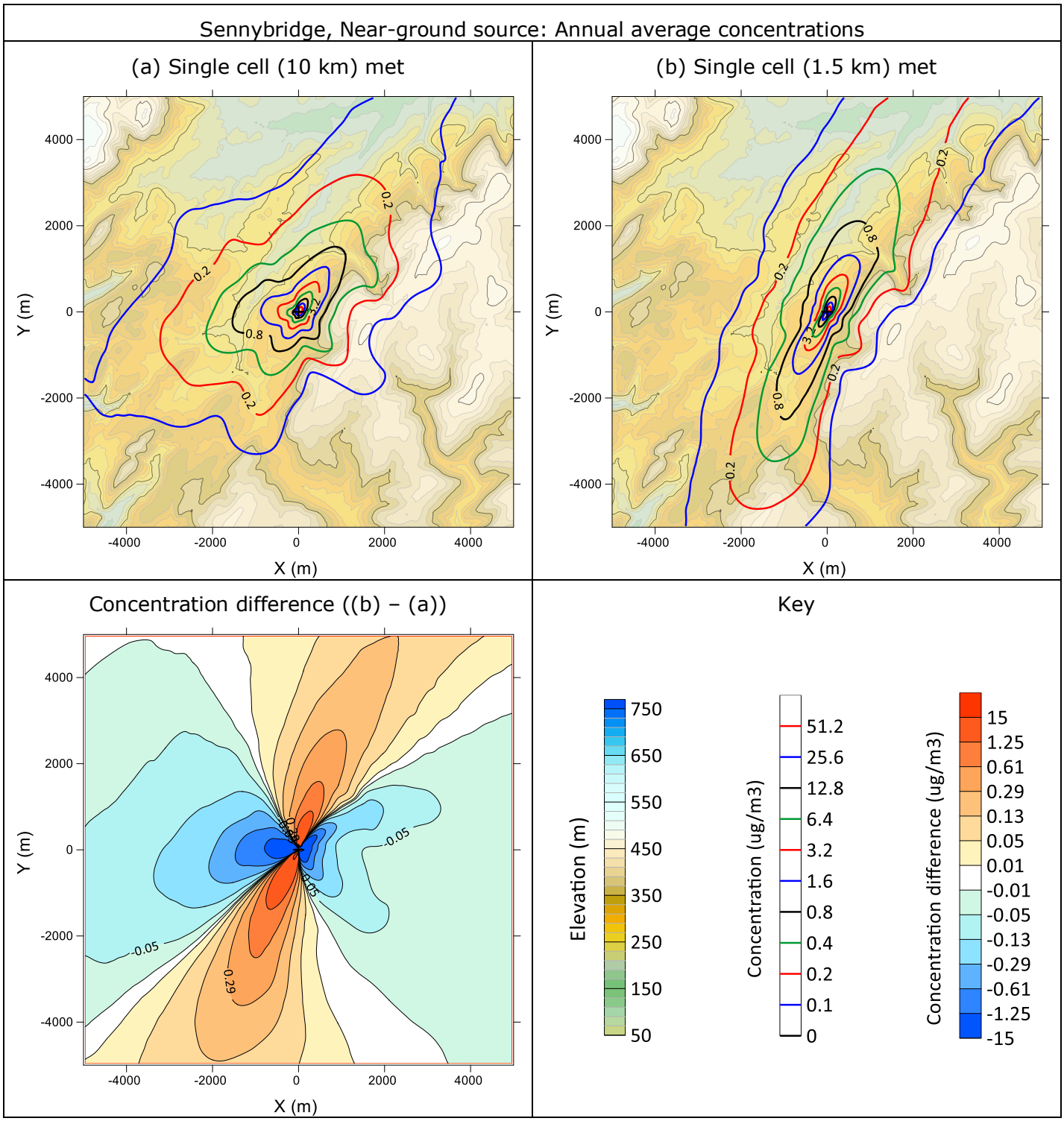

Figure 98 – As in Figure 97 but the first ADMS/FLOWSTAR run (a) is forced by single cell (10 km) met rather than spatially averaged (10.5 km) met.

7.3.3 Short-term dispersion results

It is informative to demonstrate how terrain effects can be double-counted when using finer-resolution NWP data than the FLOWSTAR domain through individual-hour examples. Two such examples are shown below, one for Drumalbin (Figure 99) and another for Sennybridge (Figure 100). For both hours, the plot of the 10 m agl horizontal wind vector field from the gridded 1.5 km UM data for that hour (top left) shows that the local wind flow near the source exhibits a moderate valley channelling effect in which the wind veers from a predominantly westerly direction to a more west-south-westerly direction. For each hour, ADMS was run with FLOWSTAR driven by the 1.5 km UM data and (separately) the spatially averaged 10.5 km UM data. At Drumalbin, the driving 10 m agl wind speed was 2.86 m/s and 2.94 m/s and h/L_{MO} was 2.4 and 2.3 (stable) for the 1.5 km- and 10.5 km-driven runs respectively. At Sennybridge, the driving 10 m agl wind speed was 2.6 m/s and 3.4 m/s and h/L_{MO} was 1.4 and -0.1 (stable/neutral) for the 1.5 km- and 10.5 km-driven runs respectively.

Table 36 shows that, for both hours, the wind direction at the source as predicted by the 1.5 km UM data is very similar to the wind direction at the source as predicted by FLOWSTAR when driven by the spatially averaged 10.5 km UM data. Thus FLOWSTAR is able to recreate the local wind flow pattern at the source when driven by met data whose scale is similar to the FLOWSTAR domain size. Conversely, when FLOWSTAR is driven by the 1.5 km UM data itself, the channelling effect is overemphasised (double-counted). This leads to a more south-westerly (almost southerly at Sennybridge) wind direction at the source that is significantly different from the wind direction at the source as seen in the original 1.5 km UM data. The difference is 20.7° at Drumalbin and 53.7° at Sennybridge. The plume is thus advected away from the source in a very different direction; the two contour patterns are almost completely non-overlapping, particularly in the Sennybridge case. At Drumalbin, the flow field exhibits bifurcation around the hill to the north-east of the source, which further magnifies the difference in plume direction. At both sites, for the FLOWSTAR runs driven by the spatially averaged 10.5 km UM data, the flow patterns further from the source eventually lead to a plume track that veers from west-south-westerly to a more westerly direction.

Table 36 – Wind directions at the source for an hour at each site that demonstrates double-counting

Site	Date, time	Wind direction at (0,0)		
		UM 1.5 km data	FLOWSTAR driven by spatially averaged (10.5 km) met	FLOWSTAR driven by single-cell (1.5 km) met
Drumalbin	30/12/2019, 21:00	245.0°	245.3°	224.3°
Sennybridge	19/10/2019, 16:00	242.6°	244.2°	188.9°

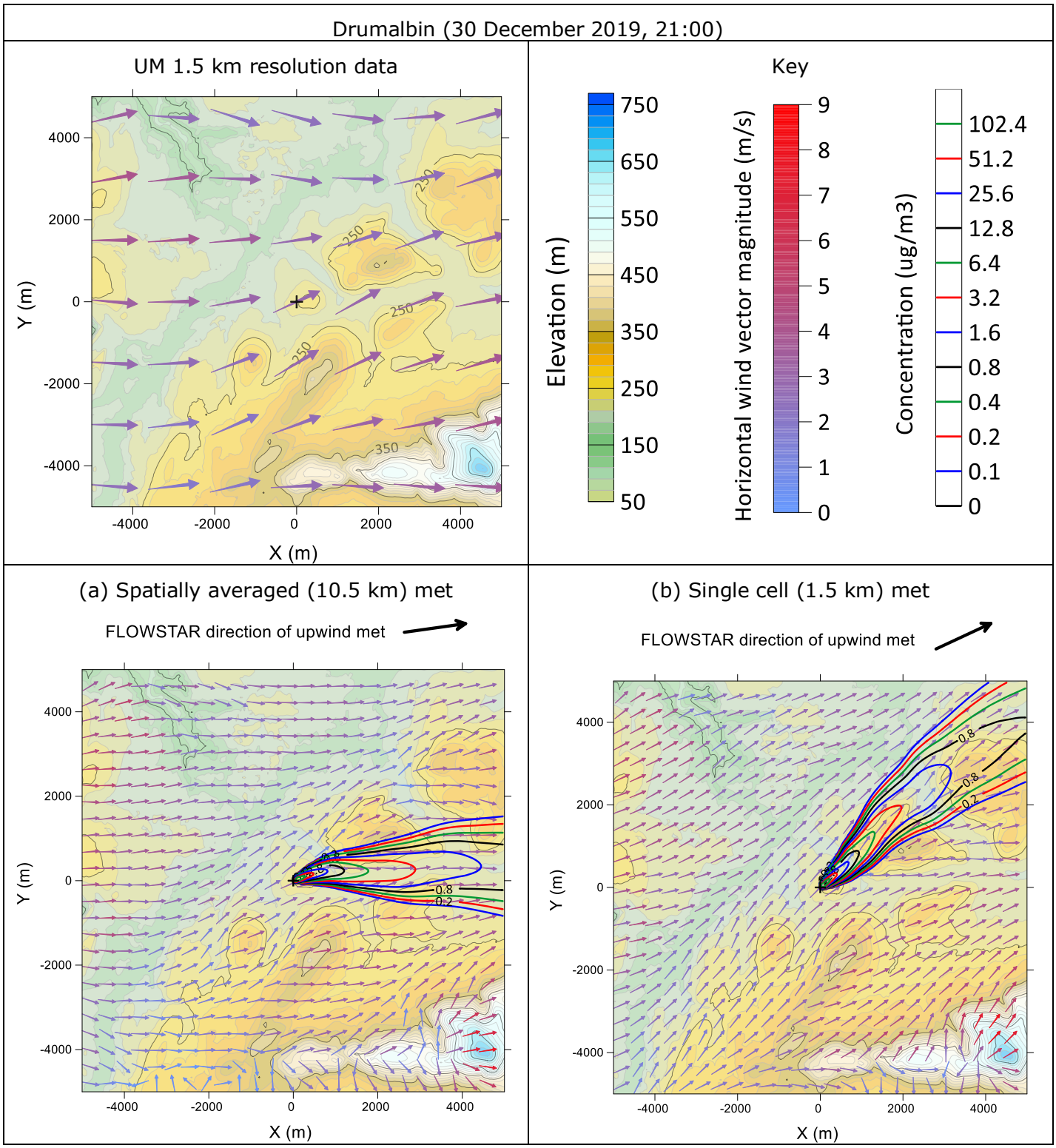

Figure 99 – An hour when double-counting is evident at Drumalbin (30 December 2019, 21:00). Top left: 10 m agl horizontal wind vector field from the gridded 1.5 km resolution UM data. Bottom: Concentrations (non-filled contours) for the near-ground source from an ADMS/FLOWSTAR run forced by (a) spatially averaged 10.5 km met and (b) single cell 1.5 km met, plus the FLOWSTAR-calculated horizontal wind vector field (arrows) and surface elevation (filled contours).

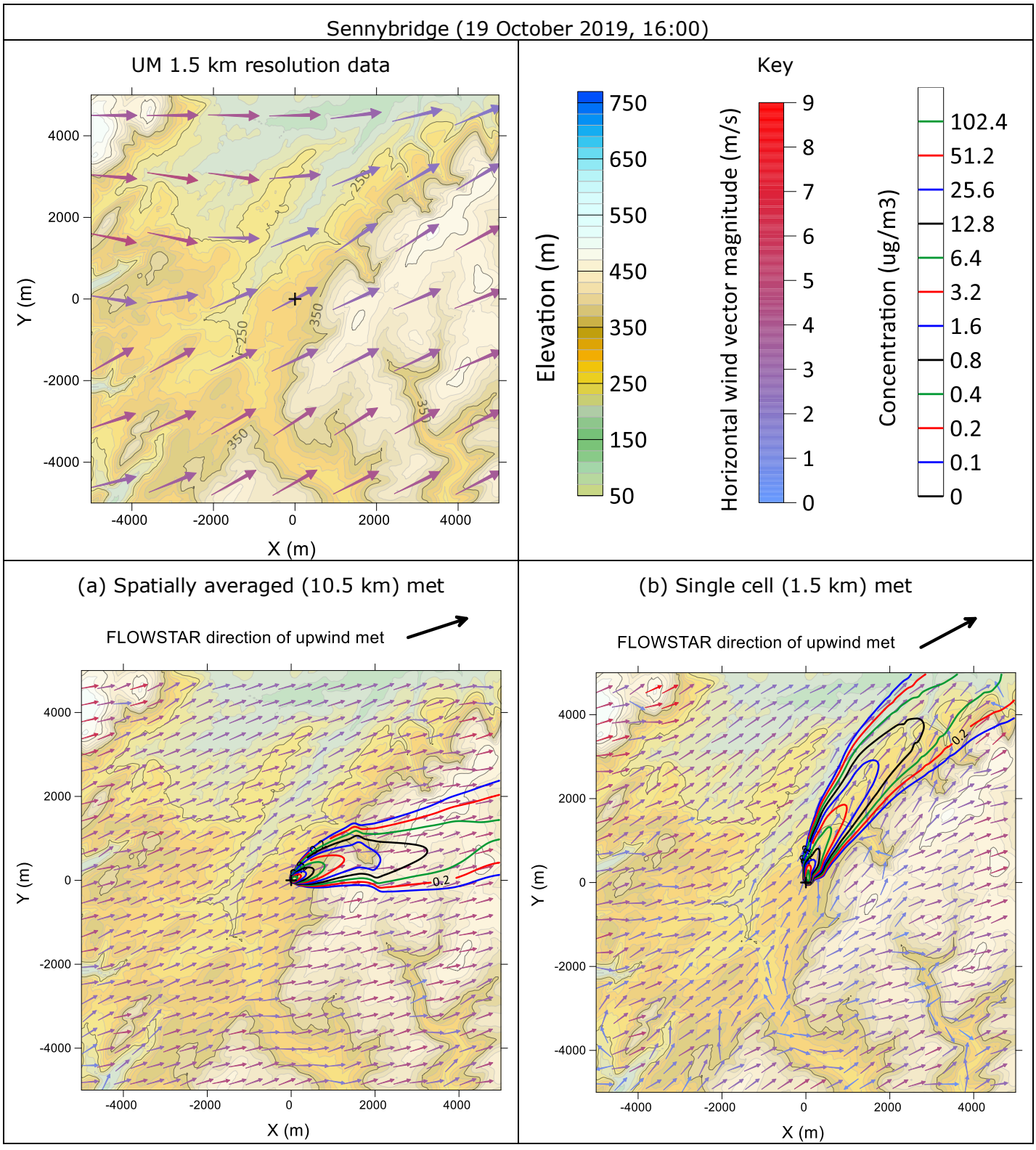

Figure 100 – As in Figure 99 but for an hour when double-counting is evident at Sennybridge (19 October 2019, 16:00).

7.3.4 Half-counting

So far we have considered a 10 × 10 km modelling domain. However, if we were only interested in concentrations closer to the source, say within a 1 × 1 km modelling domain, we might choose to use a terrain file with a much smaller extent. This is particularly relevant for near-ground sources where maximum ground level concentrations typically occur within 100 m of the source. In this scenario, it is more appropriate to drive FLOWTAR using the single cell 1.5 km UM data rather than the coarser 10 km data (or spatially averaged 10.5 km data), as the 1.5 km data should give a better representation of conditions upwind of the (smaller) FLOWSTAR domain. Using NWP data that is significantly coarser than the FLOWSTAR domain size will mean that terrain effects associated with scales between the FLOWSTAR domain size and the NWP model resolution are not accounted for – we might call this "half-counting".

We demonstrate half-counting by performing two additional ADMS/FLOWSTAR runs at Sennybridge using a 1 × 1 km modelling domain and the near-ground source. The minimum terrain file extent for this modelling domain size is 2 × 2 km, as a margin of at least 500 m around the modelling domain is required by FLOWSTAR, this is shown in Figure 101. The first run is driven by the single-cell 1.5 km met data and the second is driven by the spatially averaged 10.5 km met data. Panels (a) and (b) in Figure 102 show the resulting annual average concentrations from these two runs. Also shown in panel (c) is the annual average concentration field from the near-ground source at Sennybridge taken from the 10 × 10 km domain run using the spatially averaged 10.5 km met data (Figure 97(a)), but focused on the central 1 × 1 km region.

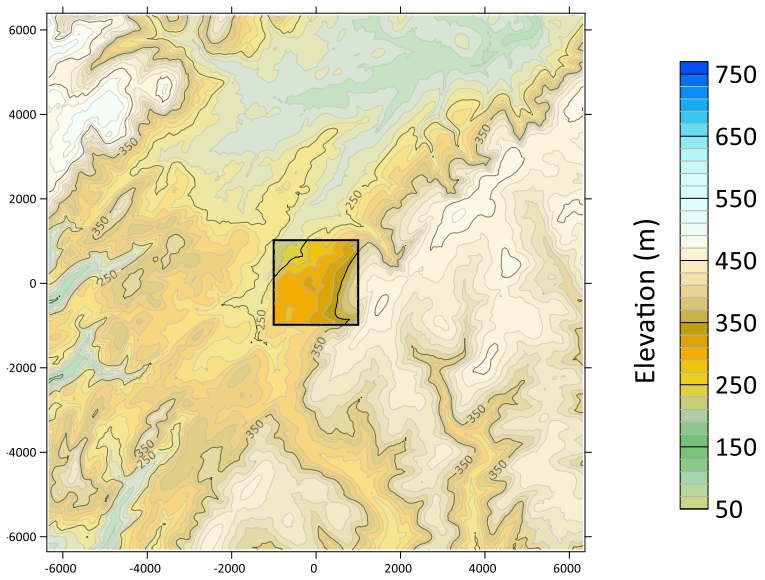

Figure 101 – Terrain file extent used for the 10 km modelling domain (outer square) and 1 km modelling domain (inner square) at Sennybridge.

The dominant orientation of the concentration contours from the 10 km modelling domain run forced by spatially averaged 10.5 km met is better matched by the 1 km modelling domain run forced by the single cell 1.5 km met than it is with the 1 km modelling domain run forced by the spatially averaged 10.5 km met. The dominant orientation of the concentration contours in Figure 102(b) is approximately 15° different to that in Figure 102(a) and (c), exhibiting a stronger across-valley component. It should be noted that there are still differences between Figure 102(a) and (c) despite the better matched orientation.

While the orientation of the contours is noticeably different between the two top panels in Figure 102, the maximum annual average concentrations are fairly similar: The value obtained with the 1 km modelling domain run forced by spatially averaged 10.5 km met, which occurs at (21 m, 16 m), is 2% lower than the value obtained with the 1 km modelling domain run forced by the single cell 1.5 km met, which occurs at (20 m, 19 m), around 3 m away from the 10.5 km met maximum. In contrast, the value obtained with the 1 km modelling domain run forced by the single cell 1.5 km met is 21% lower than the value obtained with the 10 km modelling domain run forced by spatially averaged 10.5 km met, which occurs at (15 m, 21 m), around 5 m away from the 1.5 km met maximum. Thus, in terms of maximum annual average concentration, the difference between the two runs driven by NWP data whose resolution is similar to the FLOWSTAR domain size (and should therefore not include any significant double- or half- counting effects) is significantly greater than the difference between the two runs in which one includes significant half-counting effects and the other doesn't. This suggests that the influence of the modelling/FLOWSTAR domain size is greater than the influence of half-counting terrain effects in this case.

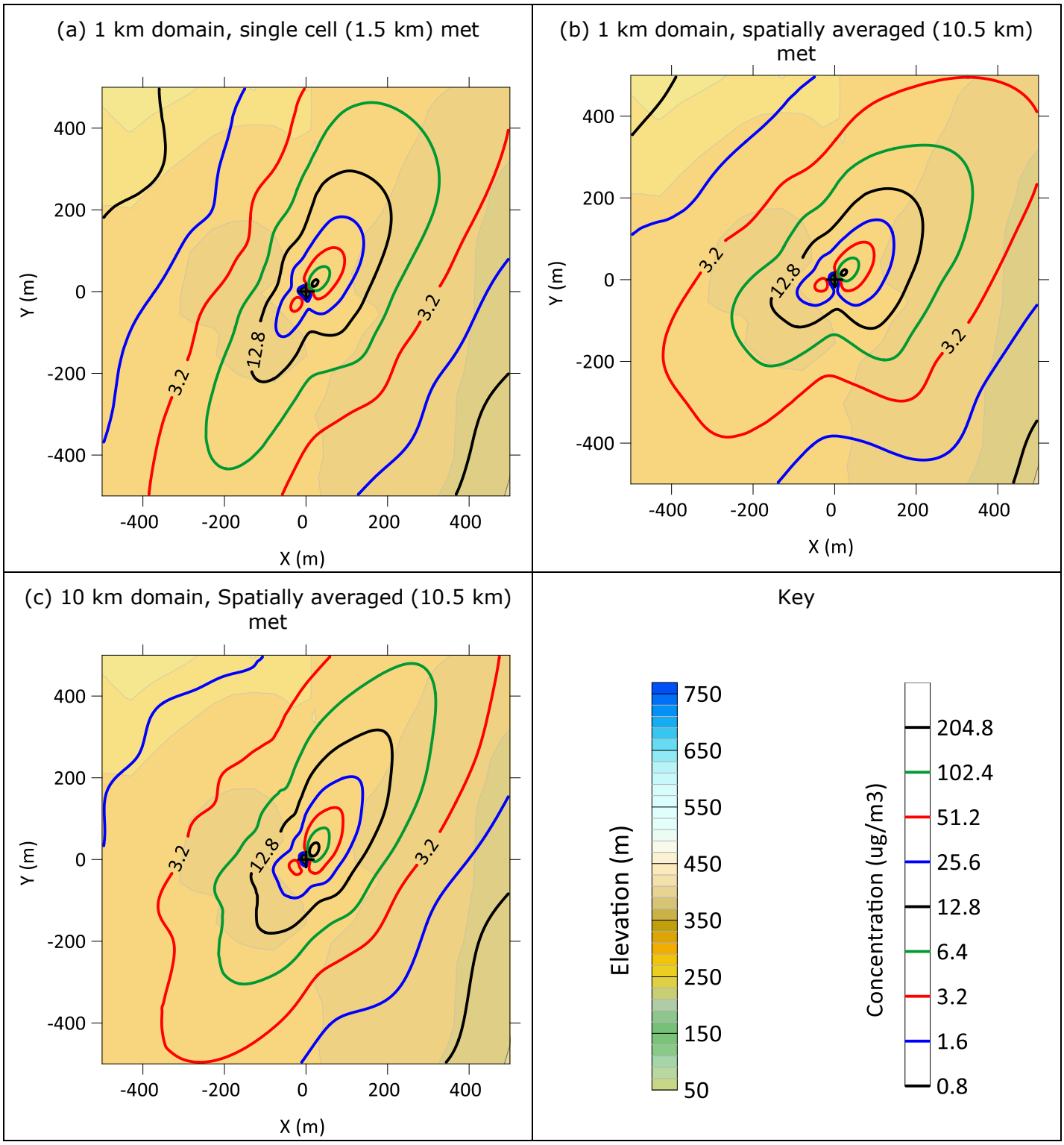

Figure 102 – Sennybridge annual average concentrations (non-filled contours) for the near-ground source from (a) the 1 km modelling domain run forced by single cell 1.5 km met, (b) the 1 km modelling domain run forced by spatially averaged 10.5 km met, and (c) the 10 km modelling domain run forced by spatially averaged 10.5 km met. Surface elevation shown by filled contours.

7.4 Assessing the influence of using only fine scale terrain variations in FLOWSTAR

A different way to quantify the impact of double-counting terrain effects is to compare standard FLOWSTAR runs that take account of changes in terrain elevation on all spatial scales (up to the FLOWSTAR domain size) with FLOWSTAR runs that only take account of spatial scales smaller than those included in the NWP model. If we assume that the effect on airflow of the smaller scale topography is largely independent of its general (large-scale) elevation, the differences between these two runs can be attributed to the influence of the spatial scales that lie between the NWP grid resolution and the FLOWSTAR domain size. It is these scales that are double-counted when data from an NWP model with finer resolution than the FLOWSTAR domain is used to drive FLOWSTAR.

Details about the FLOWSTAR code modifications required to allow certain spatial scales to be removed from the terrain are given in Appendix D5. Results from using the modified FLOWSTAR at Sennybridge are presented in Sections 7.4.1 – 7.4.3.

7.4.1 Sennybridge terrain

We use the modified FLOWSTAR code to remove certain wavelengths from the (Fourier representation of the) Sennybridge OS Terrain® 50 terrain data used in previous sections. A 3-D surface plot of the original terrain heights is shown in Figure 103.

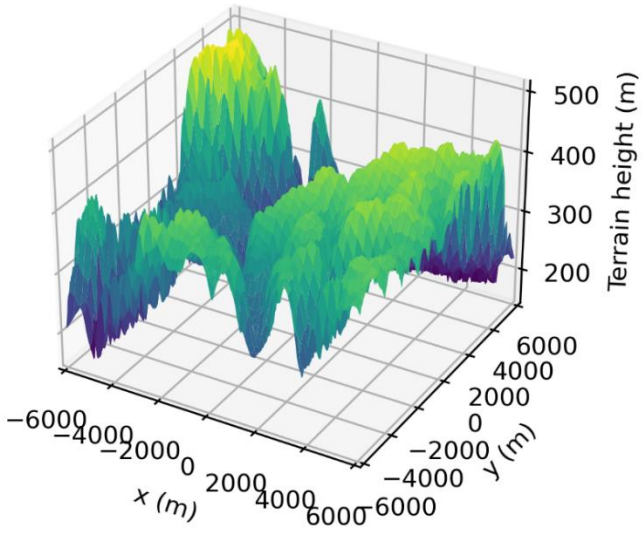

Figure 103 – 3D surface plot of Sennybridge input terrain heights. Note that the vertical length scale is different to the horizontal scales to make the variation more visible.

The following plots show the effect of removing long (Figure 104) or short (Figure 105) wavelengths from the original terrain data for a number of different cut-off wavelengths (L_c = 9 km, 3 km and 1 km). Removing long wavelengths from the terrain data preserves the localised height variations but 'flattens out' the wider-scale height variations. Removing short wavelengths removes the local height variations leaving only the smoother wider-scale height variations; note that this type of smoothing is similar to how terrain data is represented in the NWP models, which only includes those scales larger than the horizontal NWP grid resolution.

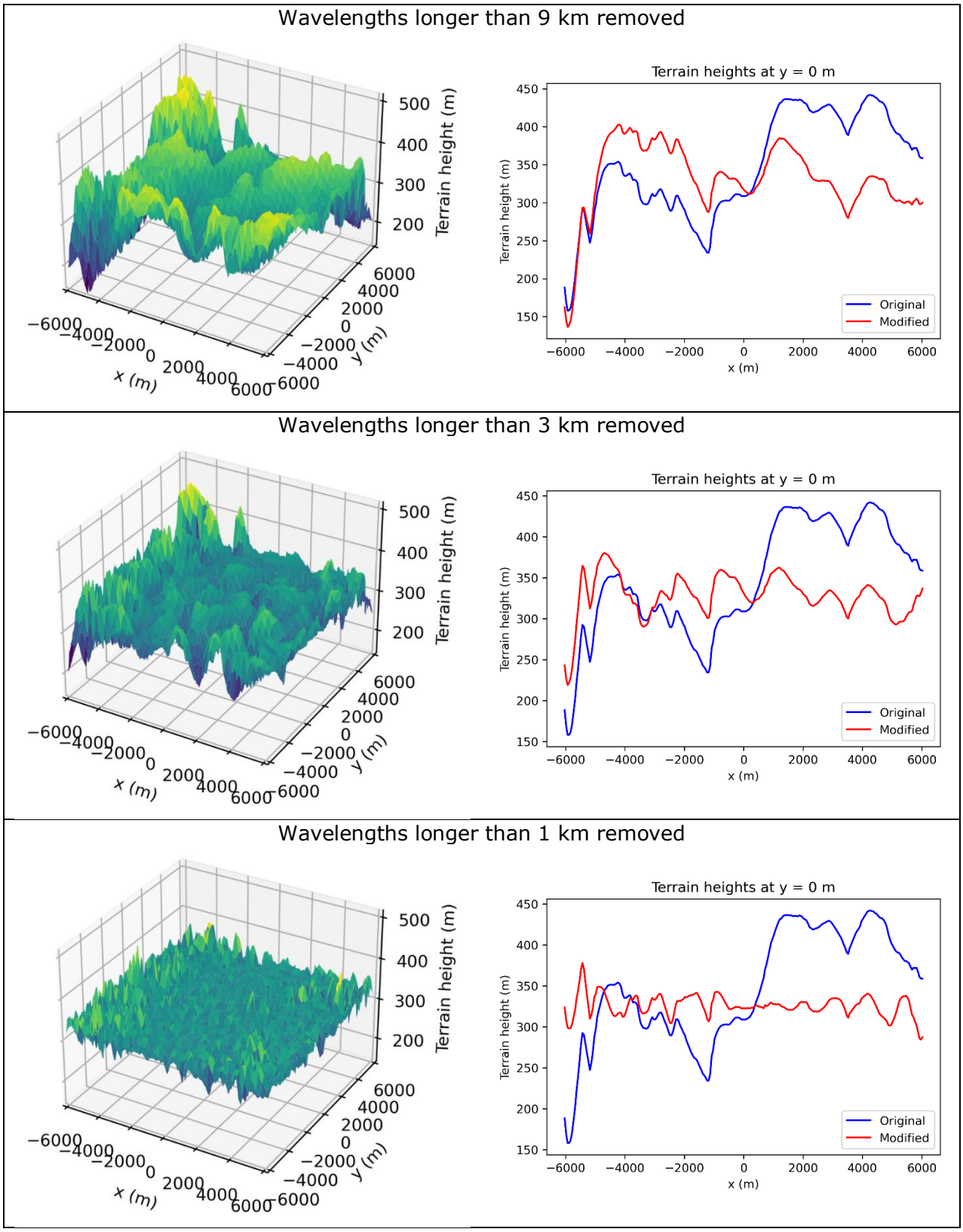

Figure 104 – 3D surface plots of terrain height with long wavelengths removed (left) and 2D plots showing terrain heights along the line y = 0 m before and after the removal of the long wavelengths (right) for three different cut-off wavelengths of 9 km (top), 3 km (middle) and 1 km (bottom).

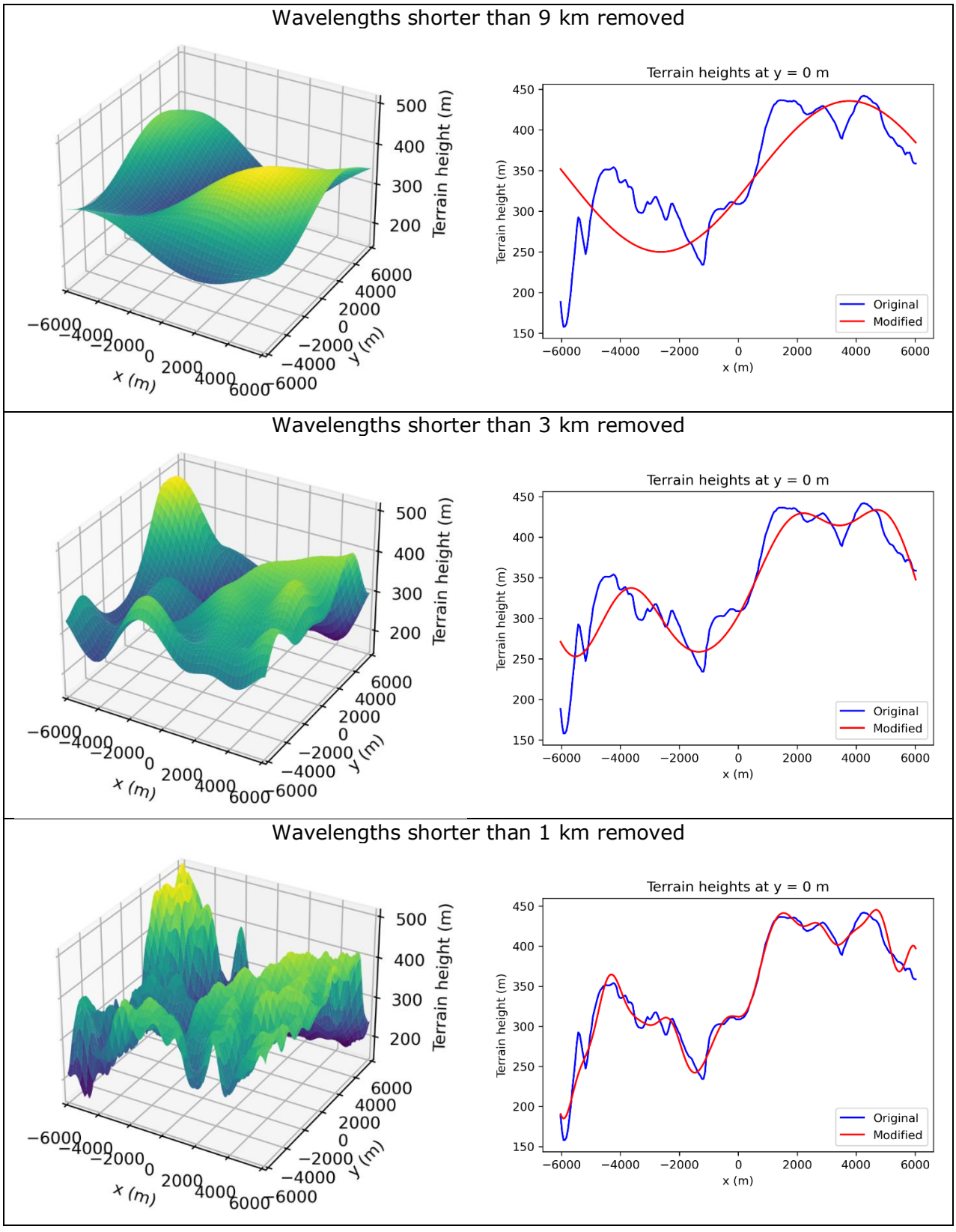

Figure 105 – As in Figure 104 but with short wavelengths removed.

7.4.2 Sennybridge results – quantifying the double-counting of terrain effects

We first analyse the effect of terrain scales between 1.5 km and the FLOWSTAR domain size for a run in which FLOWSTAR is driven by meteorological data that is representative of the conditions upwind of the FLOWSTAR domain. This provides information about the impact of the scales that would be double-counted if FLOWSTAR was instead driven by the 1.5 km resolution NWP data. Figure 106 shows annual average concentrations within the 10 km modelling domain for the near-ground source at Sennybridge when driven by the spatially averaged 10.5 km UM data. Panel (a) shows the concentrations obtained when all spatial scales up to the FLOWSTAR domain size are included (identical to Figure 97(a) but repeated here for convenience), panel (b) shows the concentrations obtained when all spatial scales greater than 1.5 km are removed from the terrain data, and panel (c) shows the concentration differences between these two fields ((a) – (b)). The difference plot shows that the main influence of the terrain scales that lie between 1.5 km and the FLOWSTAR domain size is to channel the plume along the broad valley (i.e., either north-east or south-west from the source) and thus reduce the occurrence of hours where the plume travels in a more across-valley direction. We should therefore expect to see enhanced concentrations along the valley and reduced concentrations across the valley from the source when these scales are double-counted. This is consistent with the annual average concentrations obtained within the 10 km modelling domain when FLOWSTAR is driven by the single cell 1.5 km UM data (see Figure 97(b)).

The above result should be largely invariant to the prevailing wind direction in terms of regions of positive and negative concentration difference. We can demonstrate this by instead comparing FLOWSTAR runs that are driven by a circular wind rose in which each 1° wind sector contains an equal frequency of met lines. We set the stability of each met line to be exactly neutral (i.e. a surface sensible heat flux of zero) and the wind speed at 10 m agl to 5 m/s. The resulting long-term average concentrations are shown in Figure 107. The difference plot confirms that, even when the driving conditions are given equal weighting across all wind directions, the changes in terrain elevation on spatial scales between 1.5 km and the FLOWSTAR domain size act to channel the plume along the broad valley more often than across it.

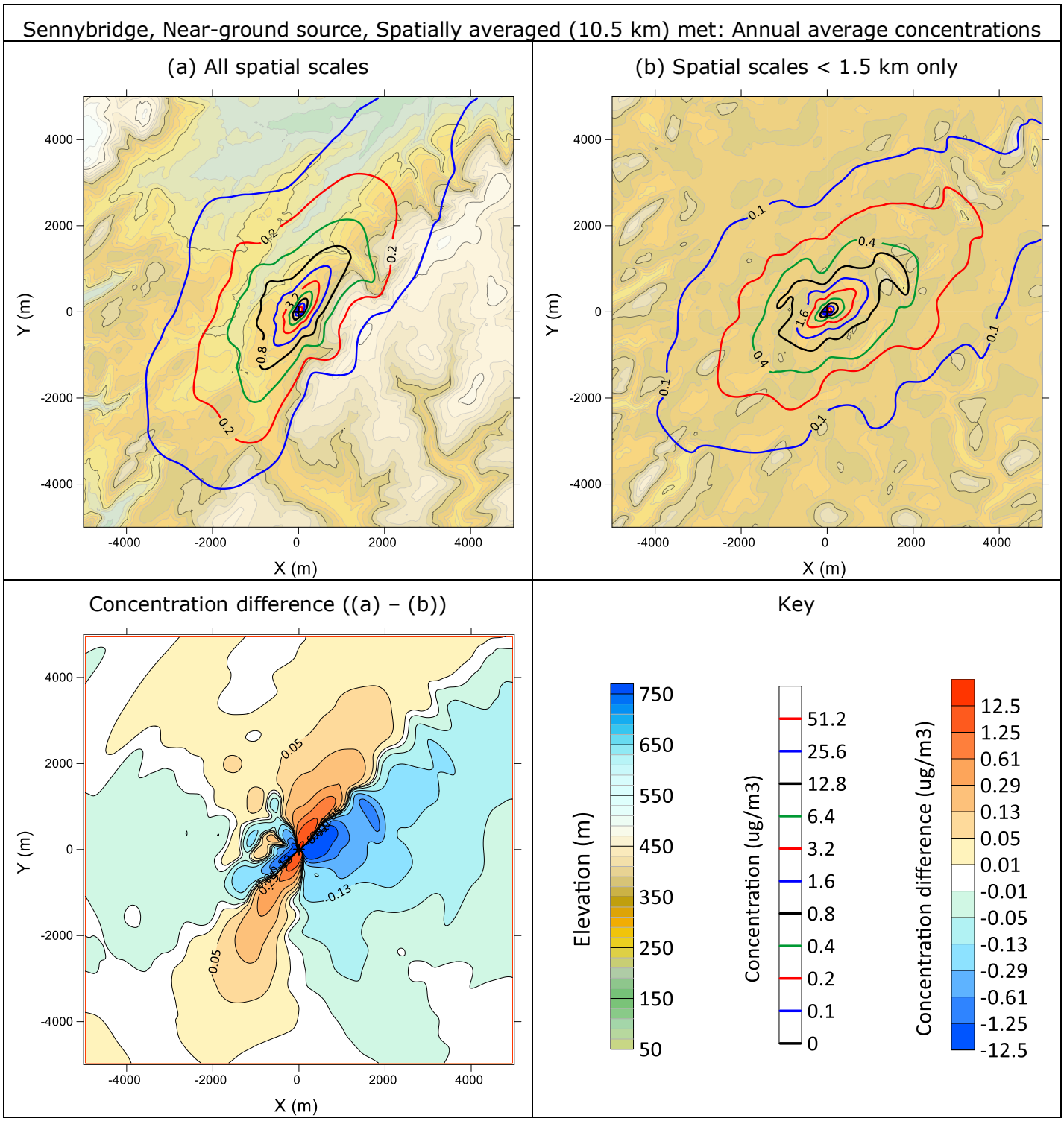

Figure 106 – Top: Sennybridge annual average concentrations (non-filled contours) for the near-ground source from an ADMS/FLOWSTAR run forced by spatially averaged 10.5 km met and using terrain data that contains (a) all spatial scales and (b) spatial scales < 1.5 km only. Also shown is the surface elevation after the removal of any spatial scales (filled contours). Bottom left: Concentration difference (a) – (b).

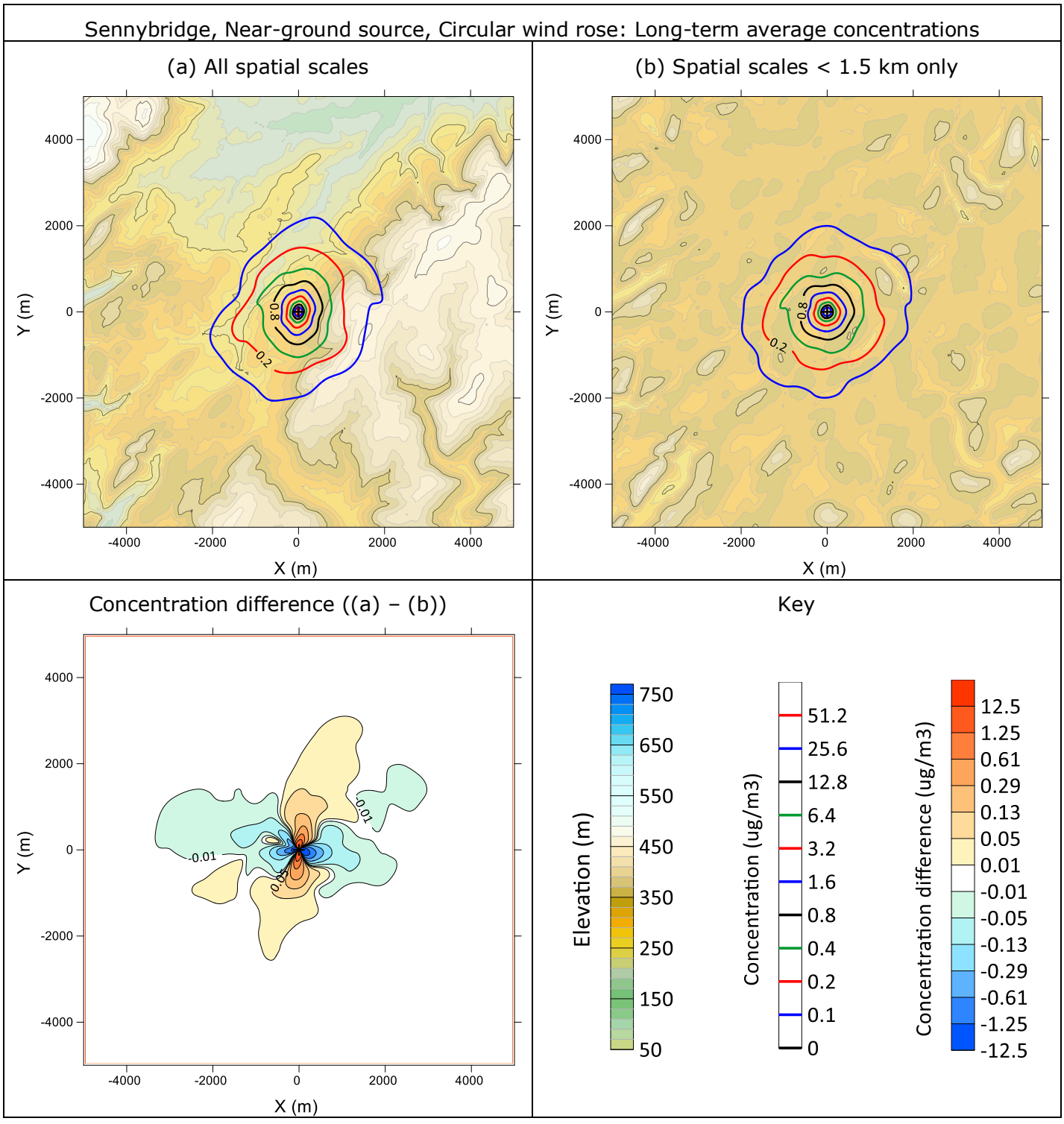

Figure 107 – As in Figure 106 but for a circular (exactly neutral) wind rose.

7.4.3 Sennybridge results – mitigating the double-counting of terrain effects

The results presented in the previous section help to understand the likely impacts of double-counting terrain effects at Sennybridge. We now consider whether the FLOWSTAR code modifications can be used to help to mitigate the effects of double-counting.

Consider the case where concentrations are required within a 10 km modelling domain, but only single-cell 1.5 km resolution UM data (extracted at the source) are available for the dispersion calculations. Removing scales greater than 1.5 km from the FLOWSTAR terrain data will ensure that the FLOWSTAR solution does not include the effects of these terrain scales. The resulting flow field should be appropriate in the ~1.5 km region close to the source, since the 1.5 km UM data is representative of the conditions upwind of this region and will not have been affected by the terrain scales greater than 1.5 km between the upwind FLOWSTAR domain edge and the source. At greater downwind distances from the source, however, the FLOWSTAR solution will lack the influence of the terrain scales that were removed. This will lead to modelled concentrations diverging from those expected as the distance from the source increases. For near-ground sources, it is often the case that we are primarily concerned with ground-level concentrations close to the source (where values are highest), and so this divergence is unimportant in this case. For elevated sources, however, this is not the case and the use of FLOWSTAR with scales greater than the NWP resolution removed may not be appropriate. This is demonstrated in the following analysis.

Figure 108 shows annual average concentrations within the 10 km modelling domain for the *near-ground* source at Sennybridge when driven by single-cell 1.5 km UM data. Panel (a) shows the concentrations obtained when all terrain scales up to the FLOWSTAR domain size are included (identical to Figure 97(b) but repeated here for convenience), while panel (b) shows the concentrations obtained when all spatial scales greater than 1.5 km are removed from the terrain data. Below each panel is a close-up of the central 1 × 1 km region, as indicated by the white square in the upper panels.

The near-source concentration contours from the run with terrain scales greater than 1.5 km removed are qualitatively similar in orientation to those from the run with the 1 km modelling domain forced by the single-cell 1.5 km met (Figure 102(a)) and the run with the 10 km modelling domain forced by spatially averaged 10.5 km met (Figure 102(c)), both of which do not include significant double-counting effects due to the NWP data resolution being similar to the FLOWSTAR domain size. The dominant orientation of the near-source concentration contours in Figure 108(a) (lower panel) is approximately 10° different to that in Figure 108(b) (lower panel), exhibiting a stronger along-valley component as a result of double-counting the valley channelling effect. Further from the source, the concentration contours in panel (b) diverge more significantly from those seen when the NWP data resolution is similar to the FLOWSTAR domain size (see Figure 106(a)).

The maximum annual average concentration obtained from the run driven by single-cell 1.5 km UM data with terrain scales greater than 1.5 km removed (Figure 108(b)), which occurs at (19 m, 20 m), is 10% lower than the value obtained from the equivalent standard FLOWSTAR run (Figure 108(a)), which occurs at (15 m, 21 m), and 14% lower than the value obtained from the standard FLOWSTAR run driven by spatially averaged 10.5 km met (Figure 106(a)), which occurs at (16 m, 19 m). Thus, while the near-source orientation of the concentration contours has improved as a result of using the modified FLOWSTAR to mitigate double-counting in this region, the calculated maximum annual average concentration is further away from the value obtained with the run that does not include significant double-counting effects.

The average horizontal wind speed at the source as calculated by FLOWSTAR is 3.6 m/s for the run driven by single-cell 1.5 km UM data with terrain scales greater than 1.5 km removed. This is lower than the value from the equivalent standard FLOWSTAR run (3.7 m/s) and the value from the standard FLOWSTAR run driven by spatially averaged 10.5 km met (3.9 m/s) and so does not explain the lower maximum annual average concentration. However, the distance from the source to the location of the maximum is 27.6 m for the run with terrain scales removed, which is larger than the distance to the location of the maximum in the equivalent standard FLOWSTAR run (25.8 m) and in the standard FLOWSTAR run driven by spatially averaged 10.5 km met (24.8 m), which taken on its own is consistent with a lower concentration.

Figure 109 shows annual average concentrations within the 10 km modelling domain for the *elevated* source at Sennybridge when driven by single-cell 1.5 km UM data. Panel (a) shows the concentrations obtained when all terrain scales up to the FLOWSTAR domain size are included (identical to Figure 96(b) but repeated here for convenience), while panel (b) shows the concentrations obtained when all spatial scales greater than 1.5 km are removed from the terrain data. There are some notable differences between the concentration contours in panel (b) and those seen when (standard) FLOWSTAR is driven by NWP data whose resolution is similar to the FLOWSTAR domain size (see Figure 96(a)), particularly at further distances from the source, as expected.

The maximum annual average concentration obtained from the run driven by single-cell 1.5 km UM data with terrain scales greater than 1.5 km removed (Figure 109(b)), which occurs at (1200 m, 950 m), is 17% higher than the maximum annual average concentration obtained from the standard FLOWSTAR run driven by spatially averaged 10.5 km met (Figure 96(a)), which occurs at (1250 m, 900 m).

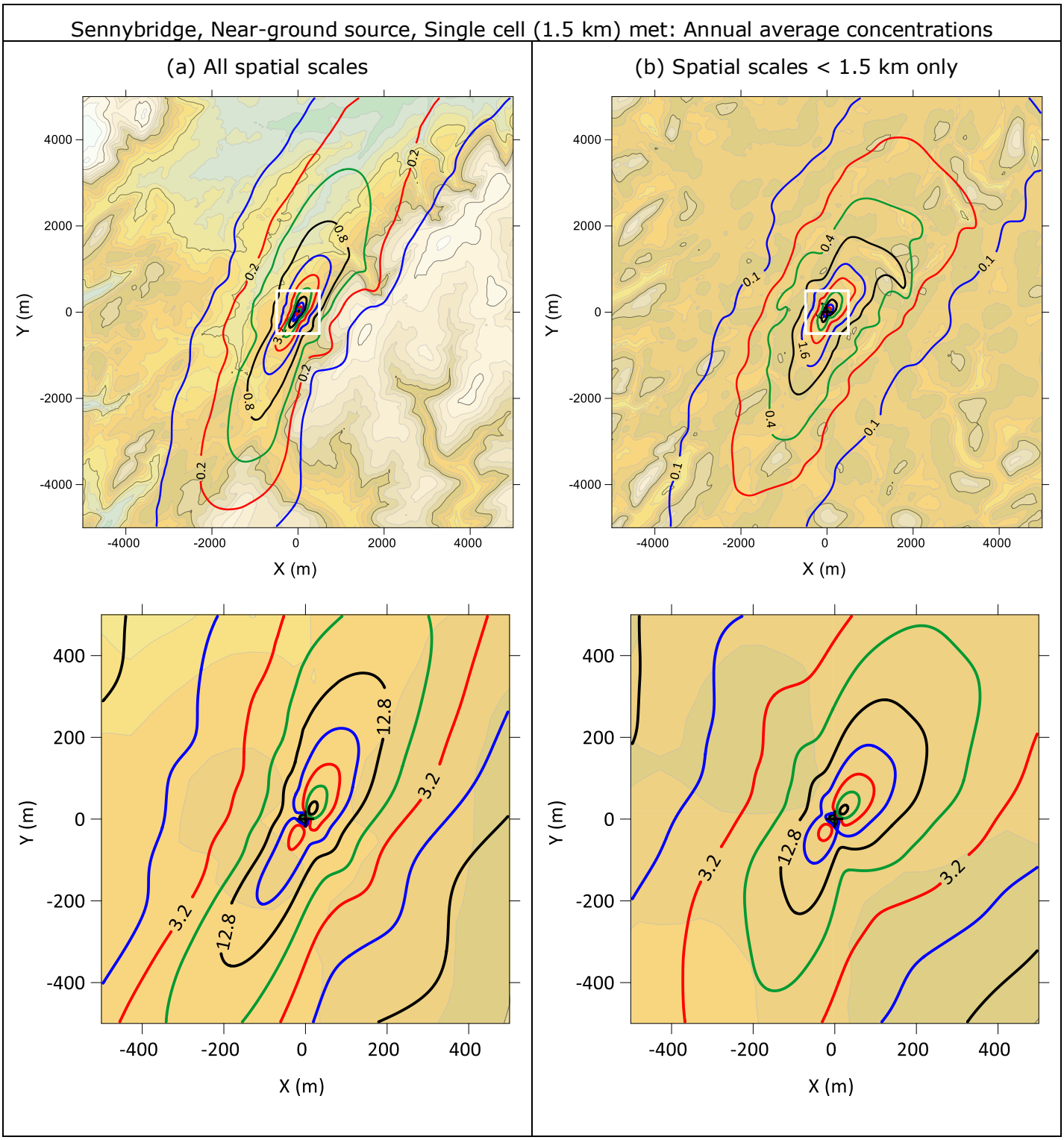

Figure 108 – Sennybridge annual average concentrations (non-filled contours) for the near-ground source from an ADMS/FLOWSTAR run forced by single-cell 1.5 km met and using terrain data that contains (a) all spatial scales and (b) spatial scales < 1.5 km only. Upper panels show concentrations within the full 10 × 10 km modelling domain, lower panels show a close-up of the central 1 × 1 km region, as indicated by the white square. Also shown is the surface elevation after the removal of any spatial scales (filled contours).

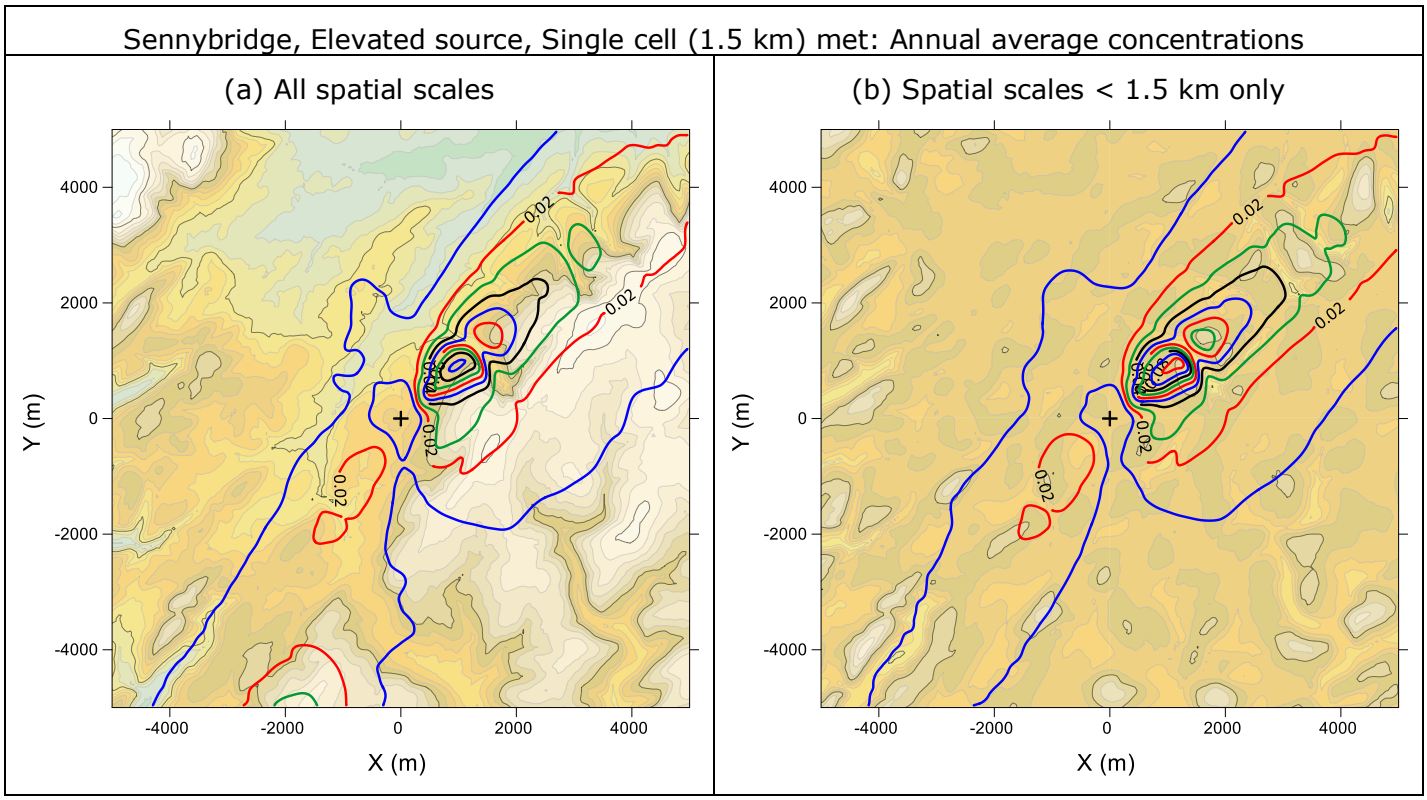

Figure 109 – As in Figure 108 (upper panels only) but for the elevated source at Sennybridge.

7.5 Conclusions from terrain effects study

The terrain effects study analysed the impact on airflow and dispersion of using significantly finer resolution NWP data than the domain size of the complex terrain module (in this case FLOWSTAR in ADMS), which introduces the risk of double-counting the influence of terrain scales between the NWP resolution and the FLOWSTAR domain size. Wind roses of input (NWP) and output (FLOWSTAR) wind data at Sennybridge demonstrated that using 1.5 km UM data to drive a FLOWSTAR domain of size ~13x13 km led to a clear over-emphasis of wind channelling along the large-scale southwest-to-northeast-aligned valley within the domain. In contrast, using the coarser 10 km UM dataset led to minimal double-counting as the scales modelled by FLOWSTAR and the NWP model did not significantly overlap. At Drumalbin, the impact from double-counting when using the 1.5 km UM dataset was more moderate, suggesting that the NWP grid cell from which the 1.5 km UM data were extracted was less affected by the terrain scales between the NWP resolution and the FLOWSTAR domain size.

Comparisons of the long-term (annual average) flow fields generated by FLOWSTAR when driven with the coarsest-resolution UM (10 km) or WRF (9 km) dataset (to avoid significant double-counting issues) against the gridded finest-resolution UM (1.5 km) or WRF (1 km) flow field data over the 10 km modelling domain at Drumalbin and Sennybridge showed that the FLOWSTAR output is

broadly consistent with the gridded NWP data but provides significantly more detail around smaller-scale terrain features, due to the wider range of scales resolved. More significant differences were observed for some short-term (hourly) flow fields, which may be due to the fact that FLOWSTAR is only driven by a single upwind vector so does not account for any domain-scale synoptic flow variations, nor does it currently model thermally-driven winds.

To analyse the impact of double-counting terrain effects on dispersion, two sets of ADMS/FLOWSTAR runs modelling emissions from a single near-ground or elevated point source were compared. The first set was driven by single-cell 1.5 km UM data and thus susceptible to double-counting issues, while the second was driven by spatially-averaged gridded 1.5 km UM data with an effective resolution (10.5 km) that was similar to the FLOWSTAR domain size and thus should largely mitigate any double-counting issues. Concentration difference plots of annual average ground-level concentration showed that at both sites double-counting tended to increase concentrations along the large-scale valley within the domain and reduce concentrations across it as a result of the magnified wind channelling effect. However, the maximum annual average concentration from the run with double-counting typically differed from the value from the run with minimal double-counting by no more than 10%, which is likely to be within the general uncertainty of modelling. Percentage differences at individual receptors and high percentile short-term concentrations could however be higher than this. Individual hour examples of concentration contour plots were also presented for cases where the impact of double-counting terrain effects was evident.

Results were also presented to demonstrate that using NWP data with a resolution significantly coarser than the FLOWSTAR domain size could lead to 'half-counting', in which the effect of terrain scales between the FLOWSTAR domain size and the NWP resolution are not represented in either model. At Sennybridge, this led to a stronger across-valley concentration footprint, though maximum annual average concentration was only 2% different from that obtained with an equivalent run forced by NWP data with a resolution similar to the FLWOSTAR domain size.

A code modification to remove the effect of terrain scales greater than the NWP resolution from the FLOWSTAR solution was presented and used for a run at Sennybridge with a ~13x13 km FLOWSTAR domain forced by 1.5 km UM data. While this improved the orientation of the annual average concentration contours within the region of the NWP grid cell used to drive FLOWSTAR (compared with a run forced by UM data with a resolution similar to the FLOWSTAR domain size), it did not improve the prediction of the maximum annual average concentration. As the FLOWSTAR solution lacked the influence of the terrain scales that were removed, this also led to modelled concentrations diverging from those expected as the distance from the region of the NWP grid cell used to drive FLOWSTAR increased. Application of this modification is thus only appropriate for near-ground sources within the region of the NWP grid cell used to drive FLOWSTAR, as the maximum concentrations typically occur within this region.

8 USE OF NWP DATA FOR PROBABILISTIC ACCIDENT CONSEQUENCE ASSESSMENTS

This section presents the outcome of investigations into the effect of NWP data resolution on probabilistic accident consequence assessment modelling outcomes. The core NWP datasets and locations used are described in Section 4.

8.1 Introduction

Higher resolution Numerical Weather Prediction (NWP) datasets are preferred (as part of the atmospheric dispersion modelling process) for near-real-time emergency response modelling. At the time of publishing this study the Met Office preferentially use UKV 1.5 km NWP data for emergency response applications when modelling boundary layer (including surface) releases in the UK. However, the most appropriate spatial and temporal resolution of NWP data in the context of emergency planning, and more specifically in the context of probabilistic assessments, is less clear and has not been investigated previously.

This study investigated the impact of applying different spatially and temporally resolved NWP data on modelled outcomes. The relative differences in model endpoints are analysed alongside other relevant considerations, such as model run time. The aim is to provide those undertaking probabilistic assessments with sufficient information to determine which (spatial and temporal) resolution of NWP data is likely to best meet their needs.

The investigation was performed by way of a range of probabilistic assessments using UKHSA's PACE suite of models, including the Met Office's atmospheric dispersion model, NAME. Gridded spatially varying NWP data derived from the Met Office's Unified Model was applied. This is a key difference from the regulatory dispersion modelling described in Section 6, which relies on input meteorological data from a single site. The analysis focuses on UKV (with spatial and temporal resolutions of approximately 1.5 km and one hour, respectively) and Global (with spatial and temporal resolutions of approximately 10 km and 3 hours, respectively) NWP datasets. Where model endpoints were found to differ as a result of the application of the two NWP datasets, reasons for such differences were explored.

8.2 Methodology

A range of simplified notional source terms across a number of different UK locations were considered (as described in Section 8.2.1). The UK Met Office's Lagrangian Particle NAME model was used to model the atmospheric dispersion and deposition of radioactivity and the calculation of external dose from the radioactive plume (as described in Section 8.2.2). Two types of NWP data were used as input to NAME as part of the dispersion modelling process (as described

in Section 8.2.3). All assessments in this study, including the estimation of dose for additional exposure pathways, were carried out using UKHSA's Probabilistic Accident Consequence Evaluation tool (PACE) (as described in Section 8.2.4). Depending on the nature of the scenario, model endpoints were determined separately within two distinct groups of model runs: non-food based and food based. Non-food based model endpoints include doses from direct inhalation of the dispersing plume and external exposure to gamma emitters deposited on a range of surfaces, as well as external dose from the radioactive plume. Furthermore, non-food based model endpoints include the impacts of implementing the protective actions: sheltering, evacuation and stable iodine prophylaxis. Food based model endpoints include doses from the ingestion of contaminated foods and the impacts of implementing restrictions on the sale of marketed foods.

8.2.1 Source terms

For the purposes of this study five simple notional source terms were considered (Table 37).

In all cases the release height was assumed to be 10 metres. A passive release was assumed (i.e. no momentum or buoyancy). The release rate was assumed to be constant. In most model runs a release duration of one hour was assumed. A separate release duration of 24 hours was also considered for the purposes of a sensitivity assessment. Table 37 details the total radioactivity assumed to be released for each considered source term.

Table 37 Source term description

Source Term ID	Radionuclide	Radioactivity (Bq)	Model endpoints
ST1	^{137}Cs	1.0×10^{16}	Non-food based
ST2	^{137}Cs	1.0×10^{13}	Food based
ST3	^{131}I	1.0×10^{15}	Non-food based
ST4	^{131}I	1.0×10^{13}	Food based
ST5	Pu (^{238}Pu & ^{239}Pu)	1.0×10^{12} (5.0×10^{11} & 5.0×10^{11})	Food based & non-food based

Source terms based on radioisotopes of caesium (Cs), iodine (I) and plutonium (Pu) were chosen as they tend to generate a broad range of exposure pathways and are frequently found to make significant contributions to total dose across a range of radiation emergency scenarios. Caesium-137 releases are frequently dominated by external exposure, ^{131}I dominated by ingestion exposure and $^{238/239}$Pu dominated by inhalation exposure pathways. This enables a thorough comparison of the model endpoints derived using the two NWP datasets to be made (see Section 8.2.3). The source term inventories were determined using scoping assessments; the inventory of each source term was iterated until protective actions (see explanation in Section 8.2.4) were estimated at a distance of a few kilometres to a few tens of kilometres from the release. For a given source term, food-based protective actions tend to extend over a much larger area than

other protective actions; for this reason two source terms of differing activities were considered for both caesium and iodine based scenarios.

Explicit modelling of the ingrowth of radioactive daughter products was typically not necessary in this study. However, the decay of ^{137}Cs to ^{137m}Ba was modelled. It was assumed that no ^{137m}Ba was released. Caesium-137 and $^{238/239}$Pu were assumed to be in particulate form. For particulates, a respirable particle size of 1 μm was assumed. Iodine-131 was assumed to be in elemental vapour form.

Table 38 – Summary of release locations

Type	Site name	Region, Nation	Lat, Lon	Site code
Urban	Northolt	Greater London, England	51.548, -0.415	2_Urban_N
	Canary Wharf	Central London, England	51.503, -0.018	2_Urban_C
Complex terrain	Drumalbin	Lanarkshire, Scotland	55.627, -3.735	3_Complex_D
	Sennybridge	Powys, Wales	52.063, -3.613	3_Complex_S
Coastal	Sizewell	Suffolk, England	56.377, -2.861	4_Coastal_S

Sennybridge was selected as the primary modelling release location because it is situated in a region of complex terrain and relatively high levels of precipitation; these characteristics were appealing because it was hypothesised that NWP datasets were likely to vary notably in their description of precipitation and thereby have the potential to result in meaningful differences in wet deposition concentrations. This is important as wet deposition can significantly impact radiological model endpoints.

Other sites (detailed in Table 38) were selected as part of a sensitivity assessment. Drumalbin was selected because it is situated in a region of complex terrain and relatively high precipitation, and modelled versus observed patterns identified in Figures 23 – 25 (in particular the correlation between modelled and observed hourly precipitation) were notably different from those described for Sennybridge. Northolt and Canary Wharf were selected to assess the impact of the two NWP datasets on estimated radiological model endpoints for releases in urban environments. A prevailing south-westerly wind is commonplace across the UK and results in releases from eastern coastal sites being advected out to sea. Sizewell was selected to investigate the potential impact of an eastern coastal site.

8.2.2 Atmospheric dispersion modelling

The UK Met Office's Numerical Atmospheric-dispersion Modelling Environment, NAME, is a Lagrangian particle-trajectory model designed to predict the atmospheric dispersion and deposition of gases and particulates (Jones *et al.*, 2007). The mean flow or advection of a particle is determined by the flow information, primarily the wind velocity, detailed in the required meteorological input data. Diffusion is described by random walk (Monte Carlo) processes, determined by the turbulent velocity. Each model particle carries the mass or radioactivity of one or more pollutant species and evolves by various physical and chemical processes during its lifespan. A box-averaging scheme is used to derive radioactivity concentrations in air from model particle activities.

The dry deposition scheme in NAME employs a deposition velocity, whereby the flux of a pollutant to the ground is proportional to the near surface concentration in air and the deposition velocity. The wet deposition scheme in NAME uses scavenging coefficients (a function of the precipitation rate, type of precipitation and type of deposition process). The radioactivity on a model particle in NAME is depleted and an equal activity contribution deposited as a result of wet deposition processes according to an exponential function. The exponent is the scavenging coefficient scaled by a timestep (a value of 30 seconds was assumed in this study). The exponential function is multiplied by the radioactivity on the model particle at the start of the timestep.

For radiological releases, NAME incorporates both radioactive decay processes and estimates of external dose from the radioactive plume (Bedwell *et al.*, 2010). NAME version 7.2 was applied in this study.

8.2.3 Numerical Weather Prediction data

The Met Office's Unified Model (UM) is a Numerical Weather Prediction (NWP) model which is used for both weather prediction and long-term climate modelling (Cullen, 1993; Staniforth and Wood, 2008). Analysis data from the Unified Model run in two configurations was obtained: the UKV configuration and the Global configuration. UKV NWP data has a horizontal resolution of approximately 1.5 km by 1.5 km and a temporal resolution of 1 hour. A total of 57 vertical levels are defined, up to a maximum height of 12 km. Global NWP data has a horizontal resolution of approximately 10 km by 10 km and a temporal resolution of 3 hours. The Global UM configuration is run at an hourly resolution, but the data is archived at a 3-hourly resolution. NAME then temporally interpolates within this 3-hourly resolution for some, but not all, meteorological variables. A total of 59 vertical levels are defined, up to a maximum height of 29 km. The effects of terrain and surface roughness at corresponding scales are included in both sets of NWP data.

The majority of model runs used 2019 NWP data. Data for 2020 was also considered for the purposes of sensitivity assessments.

8.2.4 PACE Modelling

PACE (Probabilistic Accident Consequence Evaluation) is a software tool developed by UKHSA for calculating the consequences of a short-term release of radionuclides to the atmosphere. It runs within a geographic information system (ESRI ArcGIS [TM]).

PACE models the transfer of radionuclides through the environment, the subsequent dose distributions in the population, the impact of protective actions which might be introduced to reduce doses, the health effects in the population, and the economic costs of health effects and urgent protective actions. In the present study, PACE has been used to estimate environmental concentrations, radiation dose and the impact of protective actions. Other endpoints have not been considered.

PACE allows the user to consider either deterministic model runs, simulating a release under a single set (or single sequence) of meteorological conditions, or probabilistic model runs, simulating a release under many different sequences of

meteorological conditions (Charnock *et al.*, 2013); the latter approach has been considered in this study. In general, sampling a larger number of meteorological sequences gives greater statistical accuracy when determining the distribution of modelling results; however, it is necessary to balance meteorological data considerations with the need for manageable run-times. In this study, for each model run, 194 different meteorological sequences were sampled, with each meteorological sequence having a duration of 36 hours (increased to 59 hours for the 24 hour release duration sensitivity model run) and a start-time 45 hours later than the start-time of the previous sequence. This results in suitable sampling of the seasonal and diurnal variability of meteorological conditions for each considered site.

A model run comprising of a one hour release of ^{131}I from the Sennybridge site under 2019 meteorological conditions was performed and used as a template for further model scenarios and runs. This original model scenario was iterated by way of four additional release sites (Northolt, Canary Wharf, Drumalbin and Sizewell), two additional radionuclide releases (^{137}Cs and $^{238/239}$Pu), one additional year of meteorological data (2020) and one additional release duration (24 hours). In total nine different model scenarios were considered.

The calculation of the dispersion of radionuclides in the atmosphere may be performed using either the NAME model or the ADEPT model in PACE; the former was used in this study (the ADEPT model cannot be run using NWP data). The NAME model estimates radioactivity concentrations in air, which are subsequently used by PACE to calculate doses from direct inhalation of the dispersing plume, and external exposure to gamma radiation from the plume. NAME also calculates concentrations of radioactivity deposited onto the ground which are used as input to PACE's calculation of dose from ingestion of contaminated foods and external exposure to gamma emitters deposited on a range of surfaces in the inhabited environment. These four routes of exposure were all considered in this study.

Committed effective[1] and thyroid doses (in units of mSv) from each of the four routes of exposure were assessed. Details of the dose assessment methodology are described by Charnock *et al.* (2020). In summary the dose assessments follow a multiplicative approach, using relevant environmental concentration data and relevant human habit and physiological data. Doses to a single age group (10 year old child) were modelled. Two dose integration periods (two days and one year) were assumed (but for individual ingestion doses only a one year integration period was considered). The full suite of foodstuffs considered in PACE were included in the assessment of total dose (summed over all exposure pathways). It was assumed that only cows' milk and (leafy) green vegetables were consumed from locally produced food; all other foods were assumed to be consumed from

[1] The committed effective dose is the sum of the products of the committed organ or tissue equivalent doses and the appropriate organ or tissue weighting factors over a specified time integration period. The integration time is 50 years for adults and up to age 70 years for children.

national supplies. Ingestion doses from cows' milk and (leafy) green vegetables only were output from the PACE model for analysis.

Doses were assessed with and without protective actions implemented (residual dose and projected dose, respectively). Protective actions include measures such as sheltering, evacuation, stable iodine prophylaxis and restrictions on the sale of marketed foods. Sheltering and evacuation can mitigate the dose from both the inhalation and the two external exposure pathways. Stable iodine prophylaxis can reduce the dose from internal exposure pathways, primarily inhalation. Food restrictions can lessen the dose from the ingestion exposure pathway.

Maximum environmental concentrations and radiological doses were modelled (for each sequence of the 194 different meteorological sequences) at radial distances greater than or equal to 1, 3, 5, 10, 30 and 50 km from the point of the release.

The numbers of people affected, the total area affected and the furthest distance affected by the implementation of sheltering and evacuation and the administration of stable iodine prophylaxis were assessed (for each sequence of the 194 different meteorological sequences). These model endpoints were determined by comparing approximated averted doses (the reduction in dose or dose avoided by the implementation of protective actions) with the Emergency Reference Levels (Nisbet, 2019). Regarding restrictions on marketed foods, the total area, the furthest distance and the maximum duration affected were also assessed (for each sequence of the 194 different meteorological sequences). These model endpoints were determined by comparing the radioactivity concentrations in foods with the Food and Feed (Maximum Permitted Levels of Radioactive Contamination) (Amendment) (EU Exit) Regulations (2019).

Each model run performed in this study was "probabilistic" in the sense that it sampled a large range of representative meteorological conditions, calculated results for each set of conditions, and then presented the results in the form of statistical measures, including mean, median, 90^{th} percentile, 95^{th} percentile, 97.5^{th} percentile and maximum values.

In the assessment of dose (and environmental concentrations), a single maximum dose (or environmental concentration) value was identified for each meteorological sequence. Therefore, 194 "maximum" values, one for each meteorological sequence, were modelled. Statistical analysis was then carried out on those 194 "maximum" values in order to identify the mean, median, and percentile values. When terms such as "mean", "median", and "percentiles", are applied to such endpoints, it must be remembered that they are referring to the mean, median, and percentiles, *of the 194 "maximum" values*. They are not referring to the mean, median, and percentiles, of *all* values.

In the assessment of impacts of protective actions, a single outcome was identified for each meteorological sequence. In total 194 values, one for each meteorological sequence, were modelled. Statistical analysis was then carried out on those 194 values in order to identify the mean, median and percentiles. When terms such as "mean", "median", and "percentiles", are applied to such endpoints, they are referring to the mean, median, and percentiles, of *all* values.

The analysis of the intercomparison of a UKV NWP data based model endpoint with the respective Global NWP data based model endpoint is presented here using relative differences (or ratios). Each result generated by a run using UKV NWP data was divided by the respective result generated by a run using Global NWP data.

PACE version 4.0.0 was used in this study.

8.3 Results and Analysis

Whilst six different statistical endpoints were modelled in the study, results of only three are presented here: the 95th percentile, median and mean. These statistical endpoints were selected because they represent typical values and cover a suitable level of variability, whilst not representing the extreme tails of the distribution. These statistical endpoints tend to be considered in UKHSA's radiological assessments (for example, Bexon *et al.*, 2019). It is recognised that considering alternative statistical endpoints may impact the results and analysis and this is discussed where appropriate.

8.3.1 Comparison of environmental concentrations across all scenarios

For almost all scenarios and model endpoints considered here, estimated values modelled using UKV NWP data were greater than the respective values modelled using global NWP data.

For example, radioactivity concentrations in air and radioactivity concentrations of deposition on the ground were assessed, at six different distances from the release location (ranging from 1 to 50 km), for nine different release scenarios (with variations of the radionuclide released, the release location and the year of the meteorological dataset considered), and for three statistical measures (95th percentile, median and mean). In 98.5% of cases the maximum radioactivity concentrations in air and maximum radioactivity concentrations of deposition on the ground were greater when modelled using UKV NWP data.

Table 39 details the differences in environmental concentrations estimated by runs using UKV NWP data and runs using global NWP data. Two types of environmental concentrations were considered: time integrated activity concentrations in air (TIACs) and activity concentrations of deposition on the ground (Dep Concs). Each result generated by a run that used UKV NWP data was divided by the respective result generated by a run that used global NWP data. Note that "respective results" are likely to reflect a similar radial distance but not necessarily a similar direction from the release location. Note that rounding effects mean that the values in each column in Table 39 do not necessarily sum to exactly 100.

A comparison of modelled radiation doses (with and without the implementation of protective actions) was performed using both UKV and global NWP datasets. The results are not presented here (for reasons of brevity), but the pattern

observed was akin to that detailed in Table 39; in almost all cases the maximum doses were greater when modelled using UKV NWP data.

Table 39 – Relative differences in environmental concentrations using UKV and global NWP data

Relative difference ranges	Percent of cases: TIACs	Percent of cases: Dep Concs
< 0.333	0	0
0.333 - 0.5	0	0
0.5 - 0.667	0	0
0.667 - 0.8	0	0
0.8 - 1.0	1.9	1.2
1.0 - 1.25	57	27
1.25 - 1.5	40	37
1.5 - 2.0	1.2	28
2.0 - 3.0	0	6.8
>= 3.0	0	0

8.3.1.1 TIACs modelled assuming UKV and Global NWP data

A literature review was performed to investigate why model endpoints estimated using UKV NWP data were greater in magnitude than those based on global NWP data.

Larger scales of motion are resolved by the NWP model, whilst the motions at sub grid scales are unresolved. The dispersion model parameterises the effects of unresolved motions, notably small-scale turbulence and unresolved mesoscale motions. The scale of the unresolved mesoscale motions depends on the spatial and temporal resolution of the NWP data. If the effects of scales of motion not captured by the NWP model are not parameterised by the dispersion model, then the dispersion plumes will be unrealistically narrow. The parameterisation provides a statistical representation of scales of motion. These parameterisations, for example the diffusivity value, K, tend to smooth the plume; thus the model will tend to overestimate the spread and underestimate peak concentrations (Selvaratnam *et al.*, 2021 and Bush *et al.*, 2020). As there exists a greater degree of parameterisation in the coarser global NWP model relative to the more finely resolved UKV NWP model, this issue of overestimating plume spread and underestimating peak concentrations tends to be more readily observed in dispersion model runs applying global NWP data. This is largely supported by the findings of Hort and Athanassiadou (2005) and Davis and Dacre (2009), these studies are described in Section 3.2.

The primary factors and impact due to the scales of motion in the horizontal plane are apparent; the factors and impact in the vertical plane less so. Specifically for an elevated release height (not considered in this study), would greater spread stemming from a coarser resolution NWP model result in higher ground level peak concentrations or would better resolved scales of motion from a finer resolution

NWP model result in higher ground level peak concentrations? This is perhaps an aspect for future work.

Turbulent motions in the atmosphere are not resolved by the UK Met Office's global NWP model; the parameterisation scheme applied is that of Lock *et al.* (2000) with the modifications described in Lock (2001) and Brown *et al.* (2008) (as discussed by Walters *et al.* (2019)).

The parameterisation of turbulent motions in kilometre-scale models (including the UKV NWP model) requires special treatment because, although most turbulent motions are still unresolved, the largest scales can be of a size similar to the grid length (Bush *et al.*, 2020). The model must therefore be able to parameterise the smaller scales, resolve the largest scales and not omit or double-count any scales of motion. A "blended" boundary layer parameterisation described by Boutle *et al.* (2014) is used to achieve this. This scheme transitions from the 1-D vertical turbulent mixing scheme of Lock *et al.* (2000), suitable for low-resolution simulations such as global configurations, to a 3-D turbulent mixing scheme based on Smagorinsky (1963) suitable for high-resolution simulations based on the ratio of the grid length to a turbulent length scale.

It is likely that the difference in the way the UKV and global models describe turbulence is a significant factor in determining the differences in the environmental concentrations observed in this study. However, the scale of the contribution to the relative differences is not known. Furthermore, the impact of additional differences in the UKV and Global models on atmospheric dispersion modelling and derived environmental concentrations is also unclear; such differences include the way the orography is defined, the way meteorological features such as cold and warm fronts are described, the impact of (lateral) boundary conditions on local area models, and the disparity in the characterisation of grids. Defining a suitable co-ordinate system is challenging in a Global NWP model whereby a "standard" grid at the equator tends to be impractical at the poles and vice versa.

The effect of local and mesoscale orographic features not resolved by the mean orography, from individual hills to small mountain ranges, must be parameterised in the Met Office's Global NWP model (Walters *et al.*, 2019); local area models, such as the UKV NWP model are able to better account for such orographic features and less parameterisation is required. The UKV model is likely to better represent the effects of valley flows and mesoscale features such as convergence and coastal effects. This is demonstrated by the work of Hort and Athanassiadou (2005). Their analysis of TIACs reveals that with increasing NWP resolution, the integrated plume widens; this is contrary to the impact of turbulent motions (where increasing NWP resolution typically results in a narrower plume). Hort and Athanassiadou (2005) propose that this is likely due to higher resolution models capturing a greater amount of orographically induced spread that the equivalent scale parameterisations in more coarsely resolved models struggle to represent. Note that this effect is very site specific, and depending on the nature of the terrain, orographic effects, such as channelling, could conversely act to reduce plume width.

Davis and Dacre (2009) observed that the 12 x 12 km NWP model captured the change in wind speed and direction due to the passage of a (cold) front significantly better than the 50 x 50 km model. As well as a visual comparison, the improvement in the dispersion modelling after the passage of the front when applying 12 km NWP data was demonstrated in the Pearson's correlation coefficients calculated, which were closer to (the optimal score of) 1. Davis and Dacre (2009) examined the vertical structure of the tracer plume and identified that (when assuming a relatively high spatial resolution) increasing the temporal resolution led to increased vertical lifting of the plume due to frontal ascent. This enhanced lifting resulted in less tracer advected at ground level, hence causing lower surface concentrations and a consequent reduction (and therefore improvement) in the FB (fractional bias).

8.3.1.2 Deposition concentrations modelled using UKV and global NWP data

It is apparent from Table 39 that estimates of deposition concentration based on UKV NWP data were almost always higher than the respective estimates based on global NWP data. This observation is supported by the work of Hort and Athanassiadou (2005) who compared estimated maximum wet deposition concentrations across three NWP datasets: 4 km High Resolution hourly data, 12 km mesoscale hourly data and 60 km global 3 hourly data. Hort and Athanassiadou (2005) found that the application of mesoscale NWP data resulted in the smallest, and the application of high resolution NWP data resulted in the largest, estimated maximum wet deposition concentrations.

This observed difference in modelled deposition concentrations can partially be explained by the differences observed in estimated TIACs (as explained in the Section 8.3.1.1) and the use of TIACs in the derivation of deposition concentrations. However, it is evident that the differences were more pronounced for deposition concentrations. For example, in only 1.2% of considered cases was the difference in modelled TIACs greater than 1.5 when applying UKV versus global NWP data; in contrast, in almost 35% of considered cases was the difference in modelled deposition concentrations greater than 1.5. Furthermore, 6.8% of considered cases resulted in modelled deposition concentrations differing by a factor of 2 or more when applying UKV versus global NWP data, compared to 0% of considered cases when evaluating TIACs. The more pronounced differences in modelled deposition concentrations suggests the existence of at least one further factor in addition to the factors that contribute to the observed differences in TIACs.

To understand why UKV NWP data based deposition concentration estimates were greater in magnitude than the respective global NWP data estimates, and furthermore, why the differences in deposition concentrations were more pronounced than the differences in TIACs, a literature review was performed.

Differences in dry deposition concentrations as a result of the application of UKV and global NWP models were similar in magnitude to the differences observed in estimated TIACs. This was expected because the derivation of dry deposition concentrations in this study was based upon a dry deposition velocity and was independent of the meteorological conditions.

The Met Office's Unified Model overpredicts mean precipitation (compared to observations) at both considered resolutions but by a larger margin for the 1.5 km than the 10 km resolution NWP dataset (Table 10). Furthermore, there was a greater tendency for overpredicting hourly observations when applying 1.5 km relative to 10 km resolution NWP data, and conversely a greater tendency for underpredicting hourly observations for 10 km relative to 1.5 km resolution data (Figure 21). The tendency to underpredict observations was most prominent for moderate to high precipitation rates for the 10 km resolution NWP data (Figure 22). These intercomparisons were based on meteorological data extracted in ADMS format for single sites from UM data using NAME's meteorological pre-processor. Where appropriate, spatial and temporal interpolation and unit conversions were applied in the process of extracting such data. These intercomparisons of single site meteorological data differ with the assessments considered here (in Section 8), in which spatially varying meteorological data taken directly from an NWP dataset (with no pre-processing) was used.

Roberts and Lean (2008) found that however widespread or localised the precipitation, the 1 km NWP model demonstrated greater skill in representing the precipitation than the 12 and 4 km NWP models. Furthermore, the 12 km forecasts tended to overpredict low precipitation rate values (or precipitation thresholds) and underpredict high precipitation thresholds; in contrast the 1 km model tended to overpredict the amount of precipitation for all thresholds. Hanley *et al.* (2019) undertook two case studies; one observed good estimates of the domain averaged precipitation rate (even though the distribution of precipitation rates was poorly represented) for the UKV model; the other observed overestimates of the domain averaged precipitation for the UKV model.

Roberts and Lean (2008) assessed the skill of the 1 x 1 km, 4 x 4 km and 12 x 12 km NWP models using a spatial verification metric termed "fractions skill score" (FSS). FSS is based on the derivation of the mean square error (MSE), which is used to compute a MSE skill score relative to a low-skill reference forecast. FSS curves were determined for accumulated precipitation thresholds of 0.2, 1.0, 4.0 and 16.0 mm over 4 hours of considered model forecasts. For the low thresholds of 0.2 and 1.0 mm, both the 1 and 12 km NWP models were significantly more skilful than the 4 km model. For the higher thresholds of 4.0 and 16.0 mm, the 1 and 4 km NWP models had comparable skill, but the 12 km model was considerably worse, especially for the 16.0 mm threshold. The lack of skill in the 12 km NWP model is at least partially related to a limitation in its ability to capture peak precipitation rates during relatively high precipitation rate events.

Hort and Athanassiadou (2005) recognise that at higher resolutions much more structure is observed in NWP precipitation fields, while lower resolution simulations tend to spread out the precipitation. Frontal precipitation is likely to be forecast to a similar level of precision irrespective of the resolution of model applied (Hort and Athanassiadou, 2005); that is not necessarily the case for convective precipitation. Much of the convection that was once parameterised in coarser resolution NWP models is explicitly resolved in a 1 km resolution model (Roberts and Lean, 2008).

Roberts and Lean (2008) derived FSS curves using percentile precipitation thresholds. The 75th percentile locates widespread precipitation accumulations that occupy a quarter of the domain. Increasingly higher percentiles sample less extensive precipitation areas. The 99th percentile threshold picks out localised features in the precipitation pattern that occupy only 1% of the domain. The 1 km model was the most skilful over all thresholds considered, and the gain was greatest for more localised precipitation. Greater improvement in skill at 1 km for more localised precipitation can be attributed to the transition to explicitly modelling convection (and also improvements in the representation of orography and local dynamics); whereas the distribution of more widespread precipitation is dependent on larger-scale mesoscale forcing, which should vary less between resolutions, especially when initial conditions are identical.

Roberts and Lean (2008) identified that for 12 km forecasts, overprediction of low precipitation thresholds and underprediction of high precipitation thresholds is characteristic of an NWP model that does not have sufficient resolution to represent most of the convection explicitly, and instead has to rely on a convection parameterisation scheme. Most of the convection was parameterised and large precipitation totals were underpredicted. However, on a few occasions the 12 km model attempted to resolve more intense storms, but inadequate convective parameterisation led to intense dynamical ascent, resulting in excessive resolved precipitation at small scales. As highlighted previously, the 1 km NWP model overpredicts the amount of precipitation for all thresholds. This behaviour is characteristic of a model that tries to represent the convection explicitly, but still lacks sufficient resolution. In general, it does not generate enough small showers, delays initiation and then generates larger, more intense, and well-separated storms.

Hanley *et al.* (2019) reported that a grid length of order 1 km is still not sufficient to fully resolve the individual convective elements (e.g. Bryan *et al.*, 2003), leading to convection still being under-resolved (hence such models are referred to as "convection-permitting" rather than "convection-resolving"). For example, convective initiation in the Met Office's 1.5 km UK NWP model tends to lag observations and the convective cells tend to be too large and too circular, with too much heavy precipitation and not enough light precipitation (e.g. McBeath *et al.*, 2013; Hanley *et al.*, 2015; Stein *et al.*, 2015), illustrating a lack of refinement of the nature of small-scale mixing and microphysical processes. There is notable room for improvement in the onset time of precipitation, a more realistic distribution of precipitation rates and better organisation of individual convective cells into larger complexes such as supercells (Hanley *et al.*, 2015; Hanley *et al.*, 2016).

In a case study performed by Hanley *et al.* (2019) the UKV NWP model captured the initiation time, main location, extent and decay of showers, however the cores of the showers were too intense and there was a lack of light precipitation. The simulation had more regions with high surface precipitation (above 4 mm/hr) and less light precipitation (below 1 mm/hr) than observed by the radar. Furthermore, the simulation overestimated the number of grid points with precipitation rates above 32 mm/hr by one order of magnitude. A further case study reported that

another simulation captured the general area and extent of the showers, however the cells in the model tended to be too circular compared to those observed by the radar, with too much heavy precipitation and not enough light precipitation between the convective cores. The simulation initiated daytime convection too early and overestimated domain-average precipitation.

Roberts and Lean (2008) suggested that much of the overprediction of precipitation when applying the 1 km NWP model may be a result of not including a moist turbulence parameterisation for cloud mixing outside the boundary layer. In addition, the 1 km forecasts were initialised from 12 km data (also used for lateral boundary conditions), which was detrimental to the first few hours of the forecast.

The differences in the way the UKV and global NWP models describe precipitation and convection are likely significant factors in determining the differences in the deposition concentrations observed in this study. However, the scale of the contribution to the differences is not known. The impact of other differences in the UKV and global NWP models on the nature of wet deposition and modelled deposition concentrations is also unclear; such differences include the modelling of soil hydrology (Bush *et al.*, 2020 and Walters *et al.*, 2019), description of cloud amounts, derivation of aerosol concentrations and determination of cloud droplet number.

There is evidence that more finely resolved NWP data is associated with higher domain averaged precipitation and strong evidence that more finely resolved NWP data is associated with higher peak precipitation rates during relatively high precipitation rate events. Both of these are understood to be significant factors in determining more pronounced differences between UKV and global NWP based modelled maximum radioactivity concentrations of deposition on the ground (relative to modelled TIACs).

Whilst it is widely recognised that NWP models approximating a grid resolution of 1 km tend to have more skill than models approximating a grid resolution of 10 km, it is also recognised that greater realism does not necessarily mean more accurate forecasts; for example, Done *et al.* (2004) found that, although precipitation was better represented, point specific forecasts were not necessarily improved. In summary, a 1 km NWP model is found to overpredict precipitation (including too much heavy rain and not enough light rain), lag observations in respect of precipitation onset times, not generate enough small showers and produce convective cells which tend to be too large and too circular.

Also, as is commonly the case, the location of showers is difficult to predict. This will result in additional uncertainty in estimated environmental concentrations. For many model runs over an extended period, errors in the timing and location of showers are likely to balance out. Therefore, because of the probabilistic nature of the assessments performed in this study, such errors are likely to be of relatively little importance (contrary to a deterministic assessment). However, errors in the intensity of showers are likely to be of more importance in probabilistic assessments.

8.3.1.3 Relative differences in environmental concentrations using UKV and Global NWP data

It is evident (from Table 39) that the differences between UKV and global NWP based modelled environmental concentrations tended to be relatively small (in a radiological protection context at least). Over 98% of TIACs modelled using global NWP data were within a factor of 1.5 of the respective UKV NWP based modelled values; and all TIACs modelled were within a factor of two. Over 65% of deposition concentrations modelled using global NWP data were within a factor of 1.5 of the respective UKV NWP based modelled values; and all deposition concentrations modelled were within a factor of three.

The magnitude of the differences detailed in Table 39 are typically smaller than the overall uncertainties expected when running an atmospheric dispersion model such as NAME, and are typically significantly smaller than the overall uncertainties expected when performing a radiological assessment of doses to members of the public resulting from a release to atmosphere (Smith *et al.*, 2022).

8.3.1.4 Summary

For almost all scenarios considered here, estimated environmental concentrations modelled using UKV NWP data were greater than the respective values modelled using global NWP data. All estimated TIACs agreed within a factor of two. All estimated deposition concentrations agreed within a factor of three. There exists a greater degree of parametrisations of larger scales of motion in the global NWP model and differences in the way the UKV and global NWP models describe convective precipitation. It is likely that these factors, whilst not comprehensive, are significant in determining the differences in environmental concentrations observed in this study, including relative overestimations of plume spread and underestimations of peak concentrations for dispersion model runs using global NWP data.

8.3.2 Comparison of environmental concentrations across considered statistical endpoints

It is evident from Table 40 that the relative differences in deposition concentration estimates (as a result of considering the two different NWP datasets) vary as a function of statistical endpoint whilst the relative differences in TIAC estimates were very similar across the statistical endpoints considered.

Table 40 – Proportion of values falling within given ranges of relative differences (x) in environmental concentrations as a function of statistical measure, using UKV and global NWP data

	0.8< x <1.25	0.666< x <1.5	0.5< x <2	0.333< x <3	Mean Ratio
95th %ile TIAC	54%	100%	100%	100%	1.23
50th %ile TIAC	58%	100%	100%	100%	1.23
Mean TIAC	65%	96%	100%	100%	1.21
95th %ile Dep Conc	7%	26%	80%	100%	1.71
50th %ile Dep Conc	65%	96%	100%	100%	1.22
Mean Dep Conc	13%	74%	100%	100%	1.44

Each cell in Table 40 was derived on the basis of 54 values, covering six different distances from the release location (ranging from 1 to 50 km) and nine different release scenarios (with variation of the radionuclide released, the release location and the year of the meteorological dataset considered). The "Mean Ratio" represents the average of all individual ratios of UKV NWP based modelled values divided by the respective global NWP based modelled values (and may include ratios less than 1 as well as greater than 1 in the assessment of an average value).

A literature review was used to investigate why greater variability was found for deposition concentration than TIAC estimates for varying statistical metrics, with differing input meteorology.

It is widely recognised that when it rains, deposition concentrations tend to be dominated by wet (rather than dry) deposition processes. For example, Bedwell *et al.* (2011) demonstrate that for light rainfall, at 1-40 km downwind, modelled deposition concentrations are 30-40 times greater than if no rain occurred and only dry deposition processes prevailed; the disparity is significantly larger for heavier rainfall events.

The total number of hours in which no precipitation occurs was estimated in Table 11 for a number of datasets, across a range of UK sites. The datasets included observations, UKV and global NWP data. The total number of hours was summed over all 8 UK sites considered in Section 8.3.2 (and detailed in Table 3). It was identified that over a total of 8 years of data, precipitation was observed to occur 13% of the time, and was modelled to occur 22% and 40% of the time, for UKV and global NWP models, respectively (reflective of the specific site locations of all considered sites and the grid cells within which the sites are located). It should be noted that precipitation is not likely to have occurred for the entirety of each hour that it was observed / modelled.

Accounting for the prevalence of precipitation at sites across the UK and the dominance of wet deposition in determining deposition concentrations, it is logical that the 95th percentile of estimated deposition concentrations will almost always, if not entirely, be associated with, and dominated by, precipitation events, and the 50th percentile of estimated deposition concentrations will almost always, if not entirely, be associated with dry conditions (no precipitation). Specifically, it is approximated that for UKV NWP based model runs precipitation events will be associated with the 100th to the 78th percentile of estimated (maximum) deposition concentrations, and for global NWP based model runs precipitation events will be associated with the 100th to the 60th percentile of estimated (maximum) deposition concentrations. This argument is sound for estimated maximum environmental concentrations for a release of duration one hour and nearby receptors (of the order of a few kilometres from the release).

For larger release durations (considering the same total activity released over a longer period of time) the coincidence of precipitation and a plume is likely to occur more often, although it is also more likely that precipitation will not occur for the entirety of the passage of the plume. Therefore, the number of model runs impacted by some precipitation will be greater, but the number of model runs

impacted by significant wet deposition will be smaller. As demonstrated by Table 42, a scenario with a 24 hour release duration is likely to "soften" the impact of the most influential hours of meteorological conditions, thus compressing the distribution of results, reducing the higher percentile values and increasing the lower percentile values. In essence a 24 hour release duration is likely to reduce the differences arising between the model output from a UKV and global NWP data based dispersion model run.

There will be instances whereby some but not all of the plume is impacted by a precipitation event. Therefore, 22% and 40% for UKV and Global NWP models, respectively, is unlikely to be an accurate estimate of the frequency of precipitation impacting at least some of a modelled plume. A plume at 50 km downstream (the largest distance from the release location considered in this study) is likely to have a greater chance of being intersected by a precipitation event than a plume at 1 km downstream (the smallest distance from the release location considered in this study), simply because the former covers a larger area than the latter. Bedwell *et al.* (2011) supports the notion that peak TIACs at 50 (or 40) km are likely to have a greater chance of being intersected by a precipitation event than peak TIACs at 1 km, because the former covers a larger area than the latter. The present study's assessment of deposition concentrations across all considered distances, ranging from 1 km to 50 km from the release, revealed no discernible pattern when comparing UKV NWP and global NWP data based results. One may have expected larger differences in UKV NWP and global NWP data based results for larger distances from the release and for 95^{th} percentile estimates of deposition concentrations; and no significant change in the differences in UKV NWP and global NWP data based results as a function of distance from the release and for 50^{th} percentile estimates of deposition concentrations. Whilst no discernible pattern provides little conclusive evidence, nor does it provide conflicting evidence that the 50^{th} percentile of estimated deposition concentrations is likely associated with (relatively) dry conditions, for a one hour release duration.

Precipitation rate frequency scatter plots detailed in Figure 21 indicate high precipitation rates modelled by UKV NWP datasets where relatively low precipitation rates were observed; this was not the case for global NWP datasets. Furthermore, the precipitation frequency scatter plots indicate more instances of lower precipitation rates modelled for global NWP datasets where moderately high precipitation rates were observed. Lastly, precipitation rate quantile-quantile plots detailed in Figure 22 indicate an underestimation of moderate and high precipitation rates for global NWP datasets, an underestimation of high precipitation rates for UKV NWP datasets, and an overestimation of very high precipitation rates for UKV NWP datasets. These findings largely concur with those detailed in Section 8.3.1.2 and presented by Roberts and Lean (2008).

Thus, as the precipitation rate associated with a precipitation event increases, wet deposition increases, and the percentile of the deposition concentration is likely to increase. In parallel, heavier precipitation events are more likely to be associated with more localised, sometimes showery, convective meteorological conditions, which are recognised as being described differently in the two NWP datasets considered, thereby resulting in somewhat diverse estimates of deposition. This is

thought to explain the relative differences in deposition concentration estimates (for UKV versus global NWP data) which vary as a function of statistical endpoint (Table 40).

Bedwell *et al.* (2011) investigated the impact of plume depletion on TIACs derived using NAME for a range of precipitation rates and distances from the release. Bedwell *et al.* (2011) indicates that plume depletion is only likely to have a significant impact (ie by a factor of two or more) on TIACs at distances of 10 km or greater from the release (in the range 1 – 50 km), and only for moderate or heavy precipitation rates (depending on the distance). The 50th percentile of estimated TIACs is likely to be associated with dry conditions given that at least 60% of the time it is understood to be dry. Any heavy precipitation rate event resulting in notable plume depletion will act to reduce TIACs, likely resulting in low percentile TIAC estimates. Therefore, if precipitation were associated with the 50th percentile of estimated TIACs, the precipitation rate will almost certainly be small and plume depletion negligible. The 95th percentile of estimated TIACs would most likely be associated with stable and dry conditions and is unlikely to be associated with precipitation. Therefore, the values of 95th and 50th percentile TIACs are thought to be unaffected by the differences in the descriptions of convection and convective precipitation in UKV and global NWP models. This strengthens the case for the relative differences in TIAC estimates (for UKV versus global NWP data) not varying as a function of the statistical endpoints considered in this study (Table 40).

The maximums (of the maximums) or 100th percentile of the maximum environmental concentrations were assessed, but have not been presented in detail here because they represent a value in the extreme tail of the range of estimated values and thereby tend not to be considered in radiation protection assessments. However, it is worth noting that the 100th percentile results follow a similar trend to the patterns previously identified when analysing the 50th and 95th percentile results (Table 40).

Calculations demonstrated that 47%, 93% and 100% of modelled 100th percentile of maximum TIACs based on UKV NWP data were within factors of 1.25, 1.5 and 2, respectively, of the corresponding global NWP based estimates. Middleton (2008) observed that the most stable atmospheric conditions occurred at greater frequencies for mesoscale (12 km) NWP data compared to global (40 km) data, for both an inland and a coastal site (noting that the difference was more pronounced for the coastal site). The 12 km NWP data was found to underestimate the observed frequency of the most stable conditions to a lesser degree. The most stable atmospheric conditions are likely to be associated with the 100th percentile of maximum TIACs. Middleton's (2008) observations fit with the findings of this study. Firstly, TIACs estimated on the basis of finer NWP data will be greater in magnitude than the respective TIACs estimated on the basis of coarser NWP data. Secondly, the disparity between TIACs modelled using two different forms of NWP data will be greatest in the tail of the distribution i.e. at the 100th percentile.

For the 100th percentile of the maximum deposition concentrations 17%, 37%, 74%, 94% and 96% of UKV NWP data based estimates were within factors of

1.25, 1.5, 2, 3 and 4, respectively, of the corresponding global NWP data based estimates; in one case the ratio was as high as 6. Thus, in the extreme tail of the distribution of estimates of deposition concentrations, likely associated with the heaviest precipitation events, the relative differences in deposition concentrations (as a result of applying different resolutions of NWP models) were observed to be greatest. This aligns with the findings of Roberts and Lean (2008) that, "the 1 km model is the most skilful over all of the thresholds, and the gain is greatest for more localised rainfall. The greater improvement in skill at 1 km for the more localised rainfall can be attributed to the transition to explicit modelling of convection".

8.3.2.1 Summary

The relative differences in deposition concentration estimates (as a result of using the two different NWP datasets) vary as a function of statistical endpoint whilst the relative differences in TIAC estimates were very similar across the statistical endpoints considered. This is thought to be primarily due to the significantly greater impact of precipitation on deposition concentrations compared to TIACs, and that convective precipitation is described differently in the two NWP datasets considered. In the extreme tail of the distribution of estimates of deposition concentrations, likely associated with the heaviest precipitation events, the relative differences in deposition concentrations (as a result of applying different resolutions of NWP models) were observed to be greatest (up to a factor of six).

8.3.3 Comparison of environmental concentrations across statistical endpoints and sensitivity to release location

Each cell in Table 41 was derived on the basis of 6 values, comprising six different distances from the release location (ranging from 1 to 50 km). The values in each cell represent the average of individual ratios of UKV NWP based modelled values divided by the respective global NWP based modelled values for each release location (and may include ratios less than 1 as well as greater than 1 in the assessment of an average value).

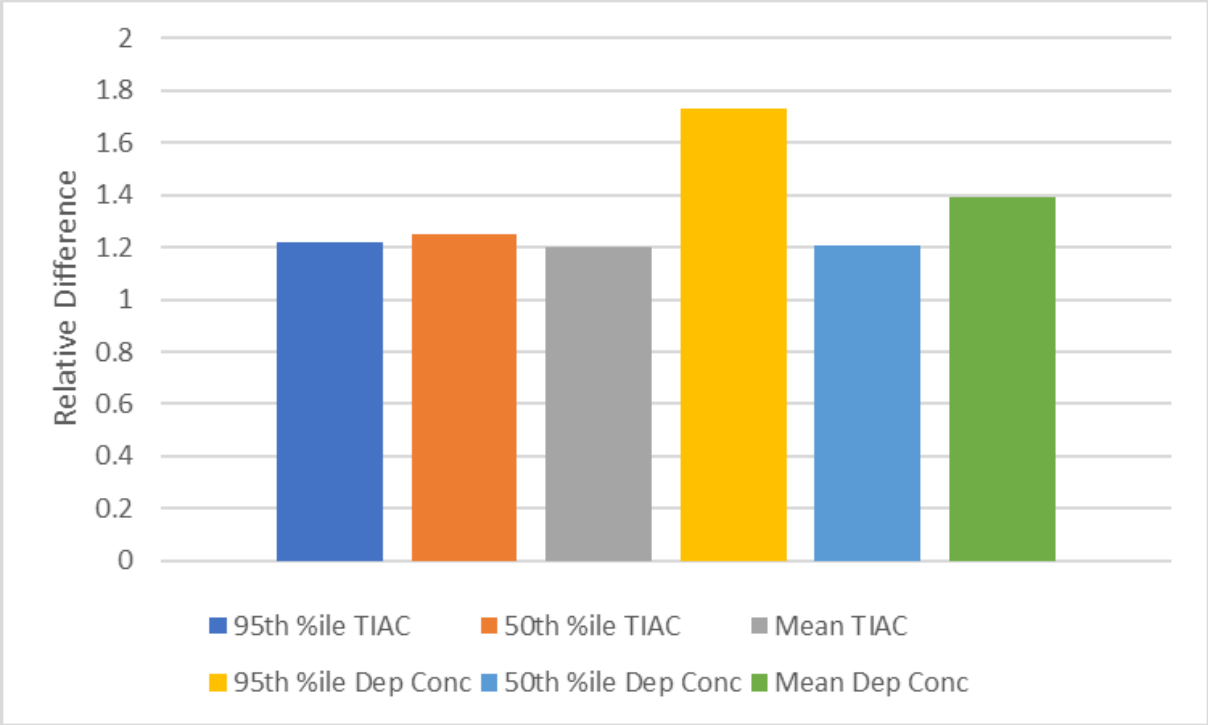

Figure 110 - Relative differences in environmental concentrations for Sennybridge as a function of the statistical measure using UKV and global NWP data

Table 41 – Relative differences in environmental concentrations as a function of the statistical measure and release location using UKV and global NWP data

	Sizewell	Sennybridge	Drumalbin	Northolt	Canary Wharf
95th %ile TIAC	1.20	1.22	1.32	1.45	1.26
50th %ile TIAC	1.20	1.25	1.28	1.36	1.09
Mean TIAC	1.17	1.20	1.28	1.41	1.12
95th %ile Dep Conc	1.41	1.73	1.65	1.72	1.88
50th %ile Dep Conc	1.20	1.21	1.27	1.40	1.17
Mean Dep Conc	1.27	1.39	1.38	1.47	1.37

It is evident from Table 41 that a similar pattern of relative differences was observed for each site. The relative differences in deposition concentration estimates (as a result of considering two different NWP datasets) varied, whilst the relative differences in TIAC estimates were very similar as a function of the statistical endpoint considered (as demonstrated in Figure 110 for the Sennybridge site). The relative differences in environmental concentrations were similar at Sennybridge and Drumalbin (inland sites situated in regions of relatively complex terrain and relatively high annual precipitation rates) across all statistical endpoints (Table 41). All other observations from Table 41 focus on differences rather than similarities. Notably that for Northolt (a suburban site) the relative differences in estimated TIACs were comparatively large, for Canary Wharf (a very

urban site) the relative differences in estimated 50th percentile environmental concentrations were comparatively small, and for Sizewell (a rural eastern coastal site) the relative difference in estimated 95th percentile of deposition concentrations was comparatively small.

Bush *et al.* (2020) reported that in the global NWP model, urban surfaces are represented by a single urban tile, but in the UKV NWP model, two separate tiles for street canyons and roofs are used (Porson *et al.*, 2010). Currently the two-tile scheme is limited to domains over the UK due to the availability of morphology data. Further differences in the description of urban land use are detailed in Section 5.2.3. Modelling in the UM at Northolt features more pronounced urban (surface sensible) heat transfer for global NWP data, where the urban land use fraction is defined as 0.75 (including urban areas to the south and east of the airfield), than for UKV NWP data, where the urban land use fraction is only 0.1 (the smaller cell covering mainly airfield and parkland). Such discrepancies in surface fluxes are likely to differentially impact turbulent motions. Differences in heat transfer between the global and UKV NWP datasets are expected to be most prominent during high solar heating daytime summer conditions, likely associated with relatively substantial turbulence and low percentile TIACs. Conversely, differences in heat transfer between the global and UKV NWP datasets are expected to be least prominent during low solar heating night-time conditions, likely associated with relatively limited turbulence and high percentile TIACs. This observation is consistent with the relative differences for Northolt presented in Table 41.

The notably smaller relative differences in estimated 95th percentile of deposition concentrations at Sizewell (Table 41) were likely a result of the coastal location, which is less conducive to land based convection scenarios because of the moderating effect of the sea; and likely a result of the UK's prevailing (south-westerly) wind direction, which will tend to advect oceanic based convectively driven precipitation events further out to sea rather than onto land. Thus, it appears that the primary reason for relative differences in estimated deposition concentrations when applying UKV versus global NWP data, i.e. the difference in the treatment of convection by the two NWP datasets, is somewhat moderated when considering an eastern coastal release location in the UK.

8.3.3.1 Summary

For each of the release locations considered in this study, the relative differences in deposition concentration estimates (as a result of considering two different NWP datasets) varied whilst the relative differences in TIAC estimates were similar, as a function of the statistical endpoint considered.

8.3.4 Comparison of environmental concentrations across statistical endpoints and sensitivity to release scenarios and year of meteorological data

Each cell in Table 42 was derived on the basis of 6 values, covering six distances from the release location (ranging from 1 to 50 km). The values in each cell represent the average of individual ratios of UKV NWP based modelled values divided by the respective global NWP based modelled values for each release

scenario (and may include ratios less than 1 as well as greater than 1 in the assessment of an average value). All data presented in Table 42 is representative of a release at the Sennybridge site. The table column titled "Default" represents a one hour release of iodine under 2019 meteorological conditions. Each subsequent column in the table represents a single edit made to the Default model run, where "Pu" represents a release of plutonium, "Cs" represents a release of caesium, "2020" represents a release assuming 2020 meteorological conditions and "24h" represents a release over a duration of 24 hours.

Table 42 – Relative differences in environmental concentrations as a function of statistical endpoint, radionuclide released, year of meteorological data and release duration, using UKV and global NWP data

	Default	Pu	Cs	2020	24h
95th %ile TIAC	1.22	1.13	1.13	1.20	1.14
50th %ile TIAC	1.25	1.21	1.21	1.36	1.10
Mean TIAC	1.20	1.17	1.17	1.26	1.12
95th %ile Dep Conc	1.73	2.03	2.03	1.56	1.36
50th %ile Dep Conc	1.21	1.17	1.17	1.23	1.19
Mean Dep Conc	1.39	1.70	1.70	1.41	1.24

A similar pattern was observed for each model scenario (in Table 42). The relative differences in deposition concentration estimates (as a result of considering two different NWP datasets) vary whilst the relative differences in TIAC estimates were similar as a function of the statistical endpoint considered. The reasons for such a pattern are discussed in detail in Section 8.3.2, but in summary arise due to differences in the descriptions of convection and convective precipitation in the UKV and global NWP models, and the relative impacts of precipitation on modelled TIACs and deposition concentrations.

The relative differences in TIAC and deposition concentration estimates were identical for plutonium and caesium release scenarios for all considered statistical endpoints (Table 42). This is to be expected as they were both treated as particulates and modelled in an identical way in respect of atmospheric dispersion and deposition processes (the only difference being the rate of radioactive decay).

Relative differences in environmental concentration estimates as a result of the use of differing input meteorology were the same for Pu and Cs model runs but distinct for I model runs (Table 42). A smaller relative difference was observed for the 95th percentile of deposition concentrations for the iodine release than for the plutonium and caesium releases. This was a result of the difference in dry deposition velocities (the process of modelling wet deposition was the same irrespective of the radionuclide considered). A 1 μm (aerodynamic diameter) particle, assumed to be representative for both plutonium and caesium release scenarios, was assumed to dry deposit at a rate of 10^{-3} m s^{-1}. In comparison iodine in elemental vapour form was assumed to dry deposit at a rate of 10^{-2} m s^{-1}, i.e. ten times greater. Bedwell *et al.* (2011) observed that for a rainfall rate of 0.5 mm h^{-1}, at a distance of 1 km from the release, dry deposition contributed to only a few percent of the total deposition when modelling a 1 μm particle size, but

contributed a few tens of percent to the total deposition when modelling iodine in elemental vapour form. This secondary but significant contribution from dry deposition to total deposition for iodine in elemental vapour form acts to moderate the notable differences in wet deposition seen between the UKV and global NWP datasets. It was not clear why a larger relative difference was observed for the 50th percentile of deposition concentrations and for both the 50th and 95th percentile of TIACs for the iodine release compared to the plutonium and caesium releases, but it is speculated that a relationship exists between the dry deposition rate, the magnitude of the dry deposition velocity and the degree of parameterisation of turbulent motions. The relative differences in TIAC and deposition concentration estimates were similar when considering meteorology covering the years 2019 and 2020 except for the 95th percentile of deposition concentrations, where there was a more notable difference as a result of the application of the two forms of NWP data (Table 42). The larger relative difference for the 95th percentile of deposition concentrations when applying 2019 meteorological data was likely due to the larger relative difference in UKV NWP modelled precipitation rates (compared to Global NWP modelled precipitation rates) at higher percentiles (Table 43).

Table 43 – Percentiles of precipitation rate (mm h^{-1}) modelled for Sennybridge using UKV and global NWP models

	UKV		Global	
	2019	2020	2019	2020
100th %ile	13	19	5.8	4.3
99th %ile	3.6	3.8	2.3	2.5
98th %ile	2.7	3.0	1.6	1.9
97th %ile	2.3	2.5	1.4	1.5
96th %ile	1.9	1.9	1.2	1.2
95th %ile	1.6	1.6	0.97	1.06
94th %ile	1.4	1.4	0.85	0.94
93rd %ile	1.2	1.1	0.71	0.82
92nd %ile	0.99	0.97	0.61	0.72
91st %ile	0.83	0.78	0.54	0.64
90th %ile	0.68	0.66	0.48	0.56

The relative differences in environmental concentration estimates were always less when considering a 24 hour release duration compared to a 1 hour release duration (Table 42). This was because over a 24 hour period a greater range of weather conditions will be considered, which will act to "soften" the impact of the most influential hours of meteorological conditions, thus compressing the distribution of results, reducing the higher percentile values and increasing the lower percentile values.

8.3.4.1 Summary

For the radionuclides, years of meteorological data and release durations considered in this study, the relative differences in deposition concentration estimates (as a result of considering two different NWP datasets) varied whilst the

relative differences in TIAC estimates were similar as a function of the statistical endpoint considered. The relative differences in environmental concentration estimates were always less when considering a longer release duration. A smaller relative difference was observed for the 95th percentile of deposition concentrations for iodine in elemental vapour form than for a 1 μm aerosol release. There were no standout differences when varying the year of meteorological data.

8.3.5 Comparison of radiological protective actions across considered statistical endpoints

Individual radiation doses were estimated but have not been presented here as they are directly correlated to either TIACs or deposition concentrations, depending on the exposure pathway considered. Therefore, the relative differences of doses are similar to the relative differences of environmental concentrations resulting from the application of the two different NWP datasets (presented and analysed in Sections 8.3.1-8.3.4). However, the impacts of radiological protective actions are not directly correlated to TIACs and deposition concentrations. Firstly, because of their dependency on the spatial (and temporal) variability of demographics and agricultural production. Secondly, because of threshold effects; the implementation of protective actions tends to be based on a number of factors, including the exceedance of dose thresholds. Thus, the relative differences of the impacts of radiological protective actions, as a result of the application of UKV versus global NWP datasets, are presented and analysed here.

Demographics and agricultural production are not uniform over the model domain. Errors in the timing and location of showers may thus have a disproportionate effect on estimated modelled impacts because protective action impacts are dependent on the interaction of the dispersing plume with the spatial and temporal distribution of the population and agricultural production. Whilst this may not impact statistical measures such as median and mean, there is a greater likelihood that statistical measures representative of the tail of the distribution will be impacted.

8.3.5.1 Differences in sheltering and evacuation due to the use of UKV and Global NWP data

The relative differences of the impacts of two protective actions (evacuation and sheltering) were considered in Table 44. Each cell in Table 44 was derived on the basis of 9 values, resulting from nine different release scenarios (varying as a function of radionuclide released, release location, release duration and year of the meteorological dataset considered). Results were presented for three statistical measures (95th percentile, median and mean). Table 44 details analysis of numbers of people affected, total area affected and furthest distance affected by the implementation of evacuation and sheltering (see Section 8.2.4 for further information describing the method used). The ratios were calculated from UKV NWP based modelled values divided by global NWP based modelled values. The mean ratio is the average over the nine scenarios. The range of ratios details the minimum and maximum value over the nine scenarios. The "No of ratios > 1" represents the number of scenarios (out of a total of nine) in which the ratio was

greater than 1, i.e. the UKV NWP based modelled value was greater than the respective Global NWP based modelled value.

Whilst relative differences of evacuation impacts predominantly follow a similar pattern to the environmental concentrations (for which the UKV NWP based value was typically greater than the respective global NWP based value), this was not the case for relative differences of the 95th percentile of sheltering impacts (Table 44), where the total number of people affected and total area affected by sheltering tended to be greater when applying global NWP data. Conversely, the 50th percentile of sheltering impacts (Table 44) tended to be greater when applying UKV NWP data.

The reason for the distinctions in the relative differences in the 95th percentile impacts for evacuation and sheltering can be explained as follows. Evacuation is deemed justifiable between the averted effective dose thresholds of 30 and 300 mSv (depending on the nature of the scenario); sheltering is deemed justifiable between the averted effective dose thresholds of 3 and 30 mSv (depending on the nature of the scenario). In the scenarios considered in this study dose thresholds of 30 and 3 mSv for implementing evacuation and sheltering, respectively, were applied. The size of the source term considered was important, tending to result in relatively small evacuation impacts and relatively large sheltering impacts. More finely resolved NWP data tends to act to increase peak environmental concentrations, and narrow and extend the plume, and more coarsely resolved NWP data tends to smooth the peaks, and broaden and reduce the extent of the plume (see Section 8.3.1.1). Consequently, calculations based on UKV NWP data lead to actions to evacuate and shelter at further distances from the release. In this study it was found that the use of UKV NWP data leads to more cases where doses are above the relatively high 30 mSv threshold which results in relatively large areas and numbers of people being affected by evacuation. Conversely, calculations based on global NWP data tended to predict a large geographical spread of doses above the relatively low 3 mSv threshold, and lead to relatively large areas and numbers of people being affected by sheltering. The same explanation can be applied to the distinctions in relative differences in the 50th percentile impacts for evacuation and sheltering. However, the value of the mean ratio of the 50th percentile relative differences (in Table 44) is always greater than the respective 95th percentile values. This is because all of the 50th percentile impacts are on a much smaller scale, and there is an even greater reliance on peak estimated doses exceeding thresholds over a very localised region. This favours the UKV NWP dataset. So much so, that for 50th and 95th percentiles of relative differences of numbers of people and areas of sheltering, the dominant NWP dataset is reversed.

The dose (averted) integration period was assumed to be two days. Over this integration period the inhalation exposure pathway tended to dominate. However, scenarios were identified whereby external exposure from deposition on surfaces contributed significantly to the total averted dose. For example, a caesium release combined with heavy rainfall resulted in the external exposure from deposition on surfaces dominating the contribution to total dose (however this was not necessarily the meteorological condition which resulted in the largest total dose

for this release). It was identified in Section 8.3.1 that larger relative differences tended to be associated with deposition concentrations rather than TIACs. But it was apparent for the caesium release scenario (for example) that the relative differences were at most only moderately greater than for other release scenarios. It was clear that precipitation was not the dominant process in determining the scale of the relative differences and hence the likely impact of NWP data resolution on the extent of protective actions.

Note that individuals impacted by evacuation cannot also be impacted by sheltering. This is reflected in the results presented in Table 44. Further model runs were performed, assessing the impacts of sheltering whilst assuming evacuation was not implemented. In these assessments the sheltering results differed marginally to those presented in Table 44, but the pattern of the results remained the same.

Table 44 – Relative differences of evacuation and sheltering impacts as a function of statistical endpoint, using UKV NWP and global NWP data

		Evacuation			Sheltering		
		Number of people	Area	Furthest distance	Number of people	Area	Furthest distance
Mean Ratio	95th %ile	1.02	1.05	1.19	0.83	0.87	1.11
	50th %ile	1.38	1.27	1.27	1.18	1.14	1.20
	Mean	1.17	1.14	1.22	0.92	0.96	1.16
Range of ratios	95th %ile	0.73 – 1.49	0.67 – 1.15	1.10 – 1.32	0.61 – 1.01	0.64 – 0.97	1.02 – 1.24
	50th %ile	0.76 – 2.33	0.80 – 1.63	0.95 – 1.48	0.82 – 1.73	0.79 – 1.43	1.04 – 1.33
	Mean	0.71 – 1.96	0.76 – 1.37	1.04 – 1.39	0.76 – 1.16	0.74 – 1.15	1.05 – 1.29
No of ratios > 1	95th %ile	4	8	9	1	0	9
	50th %ile	7	7	8	8	7	9
	Mean	7	8	9	1	3	9

It is noteworthy that a greater number of people evacuated can sometimes be associated with the application of UKV NWP data and sometimes be associated with the application of global NWP data (Table 44). This variability is likely caused by threshold effects and the inhomogeneous nature of the distribution of the UK population. The size and shape of the predicted zone for exceeding the threshold dose can intersect notably different population hubs.

A breakdown of the protective action impacts by release location was not presented here for purposes of brevity. However, it is noteworthy that anomalous results can be found for coastal sites. For example, at Sizewell (an eastern coastal

site), the estimated total number of people evacuated was greater when applying the global NWP dataset (for all statistical endpoints considered in the study bar one), contrary to the more generalised findings detailed in Table 44. It is thought that this is likely to be a result of a large proportion of modelled plumes being entirely or partially advected out to sea (due to the prevailing south westerly winds), alongside the broader global NWP based plumes increasing intersections with local populations compared to the longer but narrower UKV NWP based plumes.

8.3.5.2 Differences in the administration of stable iodine prophylaxis due to the use of UKV and Global NWP data

The description of Table 45 is very similar to that of Table 44. However, Table 45 applies to the protective action of administering stable iodine prophylaxis, and each cell was derived on the basis of 7 (rather than 9) values, comprising seven different release scenarios (varying as a function of release location, release duration and year of the meteorological dataset considered, comprising the nine scenarios described in Section 8.2.4 but excluding the Cs and Pu release scenarios). Note that administering stable iodine prophylaxis would only be considered if the source term included a release of radioiodine.

Table 45 – Relative differences of the administration of stable iodine as a function of statistical endpoint using UKV and global NWP data

		Number of people	Area	Furthest distance
Mean Ratio	95th %ile	1.25	0.85	1.13
	50th %ile	1.13	1.12	1.15
	Mean	1.09	0.95	1.14
Range of ratios	95th %ile	0.82 – 2.59	0.75 – 1.04	1.07 – 1.21
	50th %ile	0.79 – 1.36	0.91 – 1.36	1.04 – 1.25
	Mean	0.81 – 1.74	0.79 – 1.09	1.08 – 1.21
No of ratios > 1	95th %ile	3	1	7
	50th %ile	5	5	7
	Mean	3	3	7

The 95th percentile of the total area affected by the administration of stable iodine (Table 45) tended to be greater when applying global NWP data. This is similar to the pattern observed for sheltering, although not to the same extent. Conversely, the 50th percentile of all impacts of administering stable iodine and the 95th percentile of the furthest estimated distance that stable iodine would be administered tended to be greater when applying UKV NWP data. Again, this is similar to the pattern observed for sheltering. The 95th percentile of the total number of people affected by the administration of stable iodine varied between being greater when applying global NWP data and being greater when applying UKV NWP data. This is similar to the pattern observed for evacuation. The decision to implement the administration of stable iodine (and the associated impacts) are based in part upon modelled thyroid doses from the inhalation exposure pathway only and dose thresholds of 30 and 100 mSv. Visual representations of the impacts

of the administration of stable iodine for a number of modelled meteorological sequences demonstrated that whilst UKV NWP based impacts were associated with larger distances from the release (as a result of longer narrower plumes), global NWP based impacts were associated with notably broader plume footprints without significant reductions in "downwind" extent. For example, at the Drumalbin site, application of global NWP data resulted in an almost circular footprint of the maximum total area affected by the administration of stable iodine. Table 46 summarises the distribution of NWP wind speeds for the Sennybridge site, and reveals a propensity for lower wind speeds when applying the global NWP model. Lower wind speeds are commonly associated with broader plumes.

Table 46 – Percentiles of wind speed (m s^{-1}) at Sennybridge over 2019 from UKV and global NWP models

	UKV	Global
100th %ile	14	12
90th %ile	6.7	6.3
80th %ile	5.6	5.3
70th %ile	4.7	4.6
60th %ile	4.0	3.9
50th %ile	3.4	3.4
40th %ile	2.8	2.8
30rd %ile	2.3	2.2
20nd %ile	1.7	1.6
10st %ile	1.2	1.0

The relative differences of modelled administration of stable iodine impacts tend to be smaller than the respective relative differences of modelled evacuation impacts. This is likely due to threshold effects but may also be because the stable iodine administration impact is based solely on TIACs. In contrast, evacuation impacts include a contribution from deposition concentrations (see Section 8.2.4 for additional information). As previously discussed, relative differences of modelled TIACs were typically less than the respective relative differences of modelled deposition concentrations (see Section 8.3.1.2).

8.3.5.3 Differences between UKV and global NWP based impacts of the action to restrict the sale of contaminated foods

The relative differences of the impacts of restricting the sale of two foodstuffs were considered in Table 47: green vegetables and milk. Each cell relating to the foodstuff "Green Vegetables" in Table 47 was derived on the basis of 9 values, comprising nine different release scenarios (varying as a function of radionuclide released, release location, release duration and year of the meteorological dataset considered). Each cell relating to the foodstuff "Milk" in Table 47 was derived on the basis of 8 values (one fewer than green vegetables because concentrations of Pu in cow's milk tend to be very small), comprising eight different release scenarios (also varying as a function of radionuclide released, release location, release duration and year of the meteorological dataset considered). Results were presented for three statistical measures (95th percentile, median and mean). The

ratios calculated from UKV NWP based modelled values were divided by global NWP based modelled values. The mean ratio is the average over the total number of considered scenarios. The range of ratios details the minimum and maximum value over the total number of considered scenarios. The "No of ratios > 1" represents the number of scenarios in which the ratio was greater than 1, i.e. the UKV NWP based modelled value was greater than the respective global NWP based modelled value.

Impacts of the restrictions of the sale of contaminated foods are rarely represented by a uniform footprint and are frequently represented by multiple inhomogeneous footprints. This is because of the non-uniform nature of precipitation and the particularly non-uniform nature of agricultural production (upon which these impacts highly depend). The estimated distance (in Table 47) is the distance from the release location to the furthest extent of the most distant footprint for a given scenario and sequence of meteorological data. The estimated area (in Table 47) is the total area of all the footprints for a given scenario and sequence of meteorological data.

Table 47 – Differences in food restriction impacts as a function of statistical endpoint, assuming UKV and global NWP data

		Green Vegetables			Milk		
		Area	**Distance**	**Time**	**Area**	**Distance**	**Time**
Mean Ratio	95th %ile	1.07	1.23	1.11	1.15	1.44	1.13
	50th %ile	0.94	1.17	1.11	0.91	1.02	1.00
	Mean	1.03	1.19	1.04	1.11	1.26	1.06
Range of ratios	95th %ile	0.92 – 1.21	1.03 – 1.39	1.00 – 2.00	0.98 – 1.54	1.19 – 1.95	1.00 – 2.00
	50th %ile	0.62 – 1.16	1.09 – 1.29	1.00 – 2.00	0.67 – 1.08	0.94 – 1.08	1.00
	Mean	0.94 – 1.14	1.13 – 1.27	0.96 – 1.12	0.95 – 1.53	1.14 – 1.69	0.96 – 1.19
No of ratios > 1	95th %ile	8	9	1	7	8	1
	50th %ile	3	9	1	2	6	0
	Mean	7	9	8	6	8	6

The 95th percentile of all impacts of restrictions on the sale of green vegetables and milk (Table 47) tended to be greater when applying UKV NWP data. These model endpoints are modelled using radioactivity concentrations in foods, which in turn are modelled using deposition concentrations on the ground. Ground deposition concentrations are likely to be highest for scenarios in which there is (heavy) precipitation, and precipitation events are likely to contribute to the 95th percentile of deposition concentrations (see Section 8.3.2). It was found that the

UKV NWP model tended to be associated with higher precipitation rates and thus greater (wet and total) maximum deposition concentrations (see Section 8.3.1.2).

The 50th percentile of all impacts of restrictions on the sale of green vegetables and milk (Table 47) are likely to be impacted by dry conditions (and no precipitation), and therefore be dominated by dry (rather than wet) deposition processes (see Section 8.3.2). The 50th percentile of the total area of restrictions on the sale of green vegetables and milk (Table 47) tended to be greater when applying global NWP data. This is because although global NWP data based modelled plume footprints tended not to extend as far from the release as the respective UKV NWP footprints, this was outweighed by the fact that the global NWP footprints tended to be broader. Hence, the global NWP footprints generally covered a larger area. The 50th percentile of maximum distance of restrictions on the sale of green vegetables and milk (Table 47) tended to be greater when applying UKV NWP data. This is because UKV NWP data based modelled plume footprints tended to be longer (and narrower) than the respective global NWP plume footprints (see Sections 8.3.1.1 and 8.3.5.1); thus the former extended over a larger distance from the release. The 50th percentile of maximum length of time of restrictions on the sale of green vegetables and milk (Table 47) tended to be the same irrespective of the application of UKV or global NWP data. This is because the different times are presented using a discrete number of bins (e.g. 7, 30, 60, 90, 180, 270 days and 1, 2, 3, 5 years etc) rather than a continuous range of values. As the effect of using the two different NWP datasets is relatively small, the time duration bin tends to be the same (for each scenario and sequence of meteorological data considered).

8.3.5.4 Summary

Relative differences in maximum distances out to which a protective action extends predominantly follow a similar pattern to the environmental concentrations, for which the UKV NWP based value was typically greater than the respective global NWP based value. This would be expected due to the more finely resolved NWP data being associated with narrower plumes which extend further from the release.

UKV NWP based values were typically greater than the respective global NWP based values for evacuation impacts. However, for the protective actions of sheltering, administration of stable iodine and restriction of the sale of contaminated foodstuffs, and for the impacts of total number of people affected and total area affected, the NWP dataset resulting in the greater impact varied. It appears that the NWP dataset resulting in the greater impact is largely dictated by the magnitude of the source term and the magnitude of the dose thresholds applied. Where dose thresholds are relatively high, and only peak doses are large enough to exceed the threshold, the use of UKV NWP data tends to result in the greater impact. Where dose thresholds are relatively low, and the threshold is exceeded over a relatively large area, global NWP data tends to result in the greater impact. This reflects the finding that UKV NWP data tends to act to increase the peaks and result in relatively little lateral spread; global NWP data tends to act to smooth the peaks and result in relatively large lateral spread. It is hypothesised that for different magnitudes of source term and different

magnitudes of dose threshold, the results are likely to differ from those presented in this study.

8.3.6 Comparison of NAME in PACE model run times when using UKV and global NWP datasets

Probabilistic NAME model runs within the PACE system of models were performed, simulating a release under many (194) different sequences of meteorological conditions. For each probabilistic model run over all 194 meteorological sequences, the model run time was recorded.

Run time can be affected by many different factors; for example: how many runs are taking place concurrently, the extent to which a single model run is parallelised and the associated number of computational threads employed, and whether the same computational resources are being utilised by multiple users. Depending on the NWP dataset applied, the number of geographical sub-domains (commonly termed "cut-outs") being used also impacts model run time; there are 16 cut-outs (or parts) comprising the full UKV NWP dataset; either one or two UKV cut-outs were considered in a single model run, depending on the release location. For a larger model domain, a greater number of cut-outs may be required. A greater number of cut-outs would increase model run time. A single UKV NWP data file, representing a single cut-out and a single hour of data, ranged from 10,000 – 17,000 KB in size. There are 14 cut-outs (or parts) comprising the full global NWP dataset; only one global cut-out was necessary in all model runs applied here. This cut-out included data representative of the whole of Europe, and parts of Greenland, north Africa, and the Middle-East. Thus, the domain of the global NWP meteorological data was considerably larger than the atmospheric dispersion model domain. A single global NWP data file, representing a single cut-out and three hours of data, ranged from 163,000 – 180,000 KB in size.

Given all the other possible influences on run time, it is hard to isolate the difference that is being made solely by the choice of NWP data type. However, when comparing analogous runs carried out during the present study, the UKV NWP based model runs were sometimes quicker, and the global NWP based model runs were sometimes quicker. In either case, the difference was always less than a factor of two (usually very much less). For context, atmospheric dispersion model run times applying the NAME model were a few hours for a one hour release and of the order of one day for a 24 hour release. Selvaratnam *et al.* (2021) investigated the use of higher resolution NWP data alongside application of the NAME model. Selvaratnam *et al.* (2021) notes that in respect of model run times, only the part of the run time for reading and processing meteorology is affected, leading to model run time increasing by a factor of three when moving from Global NWP 3 hourly to hourly temporal resolution, and model run time increasing by a factor of four when moving from UKV NWP hourly to 15 minute temporal resolution. Selvaratnam *et al.* (2021) acknowledged that at the time of the study, the ability to parallelise the reading of the meteorological data had not yet been implemented in the NAME model run process, but it was thought that this would lead to significantly faster runs. It should be noted that the run time comparisons carried out by Selvaratnum *et al.* focused solely on changes in temporal resolution,

and so are not directly analogous to the comparison carried out in the present study.

9 FURTHER WORK

The investigations and analysis carried out in this study and reported in previous sections have suggested some additional areas of research relating to NWP data and dispersion modelling, which would require additional resources to carry out.

The following relatively minor extensions to the current analysis and modelling could be implemented using existing data, requiring up to a week of work for each task.

- Some of the uncertainty associated with NWP precipitation may be associated with the representation of convective processes in the different models and resolutions. An additional seasonal assessment of model performance for precipitation would help to evaluate the relative significance of convective processes, which are most common in summer.
- The analysis of cloud cover and precipitation highlighted possible model performance effects due to the three-hourly model archiving frequency in the MO UM 10 km (global) data. There may also be influence of different temporal resolution of the forcing data in the WRF configuration comparison. Additional analysis of temporal variations, for example diurnal cycles of temperature and wind speed, could be useful for identifying any specific recommendations for best practice in meteorological model configuration.
- The Sennybridge site shows differences between measured and modelled wind directions partly due to the effect of a stand of trees close to the measurement site. The use of spatially varying roughness modelling within ADMS to represent these very local variations could be tested.
- The regulatory dispersion modelling study used constant values of the Priestley-Taylor parameter in ADMS, representing ground surface moisture availability. It could be valuable to carry out a sensitivity test for the use of temporally varying values of this parameter to represent dryer ground conditions in summer. This would change the predicted variation of surface sensible heat flux, possibly reducing the discrepancies between NWP and ADMS summer heat flux, with associated changes to stability values and hence dispersion model outcomes.
- The regulatory dispersion modelling study did not implement the coastline modelling option in ADMS at the Leuchars site. A sensitivity test for the influence of this option on dispersion outcomes at this site would be of interest.

The following tasks are more substantial, requiring weeks to months of work and/or requirements for additional data.

- In this study NWP data from meteorological measurement site locations have been compared to measured data from the same locations. However, when a dispersion site is located further away from meteorological measurement locations, the relative performance of NWP and measurement data may

change. Modelling choices could be informed by a new systematic study comparing observed data from additional sites separated by varying distances, to assess the distance at which modelled meteorological data may become more representative of local conditions than observed data from an alternative measurement site. This would also be relevant to the selection of supplementary data from either an alternative measurement site or NWP where the nearest measurement site does not have sufficient data availability for all required variables. In this study supplementary data sites were used to provide non-wind data at Newhaven (Shoreham and Herstmonceux) and cloud cover at Mumbles Head (St Athan). A relatively minor extension of the current analysis would be to assess additional modelled data at these supplementary sites, to estimate the uncertainty associated with the location discrepancy between NWP and measurement locations in this case. The systematic study of observed data from sites at varying separation distances would be a substantial task.

- The prediction of locations of short time-scale and small length scale precipitation (showers) is highly uncertain. A 'Neighbourhood' comparison of modelled and observed precipitation, where precipitation rates are evaluated across a group of adjacent model grid cells in comparison with a single observation site, or fractional coverage of precipitation is compared with radar data as in Roberts and Lean (2008), can be used to assess model performance allowing for minor uncertainties in spatial predictions. This would require the extraction and processing of gridded NWP data around each measurement site, then implementation of a neighbourhood evaluation metric.

- The WRF configuration comparison highlighted differences in the approaches to calculation of overall cloud cover from WRF data, with resulting differences in the distribution of cloud cover values. Further investigation of methods for extracting overall cloud cover from WRF for local modelling would be required to establish a recommendation for best practice and potentially implement this within CERC's WRFtoMet utility.

- Surface heat flux and boundary layer height values are not included in routine meteorological measurements, but some short-term campaign measurement data have been generated. An evaluation of surface heat flux and boundary layer height from NWP and calculated by ADMS against campaign measurements would help to inform the choice of variables which should be supplied from NWP to ADMS.

- There is a desire for additional best practice guidance for WRF configuration options. However, the availability of different options in each released version of WRF means that this is not likely to be feasible to maintain. Further investigation would be required to illustrate any trends in performance of the various WRF configuration options for different types of scenarios.

- It would be interesting to explore alternative methods to mitigate double-counting terrain effects that might be more applicable throughout the entire modelling domain than the modified FLOWSTAR presented in this report. One

approach (that would require gridded NWP data) could be to run FLOWSTAR as many times as there are NWP grid cells within the FLOWSTAR domain, using the met data from the local NWP cell as the driving condition and cutting the terrain extent down to the NWP cell size in each run. Spatial smoothing between individual FLOWSTAR solutions would be required. The approach of splitting large domains into smaller runs and recombining the model output is already used in CERC's regional-to-local coupled system models (ADMS-Urban Regional Model Link and Multi-model Air Quality System - MAQS), though terrain effects are not currently considered within these models.

- This report has considered regulatory dispersion modelling domains with sizes between 1-10 km, suitable for modelling individual or closely-spaced near-ground or elevated sources. However, there is growing interest in using regulatory dispersion models over significantly larger modelling domains that contain multiple spread-out sources, for example with length scales greater than 50 km. In such cases, spatial variations in the synoptic meteorology can become important and so a dispersion modelling approach that allows for spatially varying input meteorology (i.e. gridded NWP data) should be investigated, for example those mentioned in the previous bullet. It would be interesting to explore the impact of spatial resolution of the gridded NWP data in such cases.

- It would be beneficial to assess whether finer or coarser resolution NWP data as input to probabilistic atmospheric dispersion models results in better representation of observations from field studies or real events, adding to studies already undertaken and building a stronger evidence base for the use of NWP data. The sparsity of radiological accidents would likely require the consideration of alternative scenarios. The tendency for finer scale NWP data to only be generated in limited area modelling domains makes identifying a suitable scenario more challenging.

REFERENCES

Arasa R, Porras I, Domingo-Dalmau A, Picanyol M, Codina B, González MÁ, Piñón J (2016) Defining a Standard Methodology to Obtain Optimum WRF Configuration for Operational Forecast: Application over the Port of Huelva (Southern Spain). Atmospheric and Climate Sciences, 6: 329-350. http://dx.doi.org/10.4236/acs.2016.62028

Auld V, Hill R, Taylor T J (2002) Uncertainty in deriving dispersion parameters from meteorological data. A report prepared for ADMLC, ADMLC/2002/2. Available from https://admlc.com/publications/ (accessed October 2023)

Bedwell P, Wellings J, Haywood SM, Hort MC, Jones AR, Thomson DJ (2011) Intercomparison of the 'R91' Gaussian Plume Model and the UK Met Office's Lagrangian Particle NAME III Model in the Context of a Short-duration Release. HPA-CRCE-029. ISBN: 978-0-85951-710-2. Available from https://assets.publishing.service.gov.uk/media/5a7eee7aed915d74e33f3534/HPA-CRCE-029_for_website.pdf (accessed October 2023)

Bedwell P, Wellings J, Haywood SM, Hort M (2010) Cloud gamma modelling in the UK Met Office's NAME III model. IN 13th International Conference on Harmonisation within Atmospheric Dispersion Modelling for Regulatory Purposes. Paris (France), ARIA Technologies. Available from https://www.researchgate.net/publication/311885800_Cloud_Gamma_Modelling_in_the_UK_Met_Office's_NAME_III_model (accessed October 2023)

Beevers SD, Kitwiroon N, Williams ML, Carslaw DC (2012) One way coupling of CMAQ and a road source dispersion model for fine scale air pollution predictions, Atmos Environ, 59: 47-58. https://doi.org/10.1016/j.atmosenv.2012.05.034

Beevers S, Kitwiroon N, Fraser A, Murrells T, Rose R, Chemel C, Francis X, Sokhi R, Derwent D (2013) CMAQ Development for UK National Modelling: WRF Optimisation, Defra report, available from https://uk-air.defra.gov.uk/library/reports?report_id=879 (accessed October 2023)

Best MJ, Pryor M, Clark DB, Rooney GG, Essery RLH, Ménard CB, Edwards JM, Hendry MA, Porson A, Gedney N, Mercado LM, Sitch S, Blyth E, Boucher O, Cox PM, Grimmond CSB, Harding RJ (2011) The Joint UK Land Environment Simulator (JULES), model description – Part 1: Energy and water fluxes. Geosci Model Dev 4: 677-699. https://doi.org/10.5194/gmd-4-677-2011

Bexon A, Haywood SM, Mortimer K and Bedwell P (2019) REPPIR 2019 consequence assessment methodology. PHE-CRCE-50. Available from https://www.gov.uk/government/publications/radiation-consequence-assessment-methodology-for-reppir-2019 (accessed October 2023)

Borge R, Alexandrov V, del Vas JJ, Lumbreras J, Rodríguez E (2008) A comprehensive sensitivity analysis of the WRF model for air quality applications

over the Iberian Peninsula. Atmos Environ, 42: 8560-8574. https://doi.org/10.1016/j.atmosenv.2008.08.032

Broxton PD, Zeng X, Sulla-Menashe D, Troch PA (2014) A Global Land Cover Climatology Using MODIS Data. J Appl Meteorol Climatol 53(6): 1593-1605. https://doi.org/10.1175/JAMC-D-13-0270.1

Boutle IA, Eyre JEJ, Lock AP (2014) Seamless stratocumulus simulation across the turbulent gray zone. Mon Weather Rev, 142, 1655–1668, https://doi.org/10.1175/MWR-D-13-00229.1.

Brown AR, Beare RJ, Edwards JM, Lock AP, Keogh SJ, Milton SF, Walters DN (2008) Upgrades to the boundary-layer scheme in the Met Office numerical weather prediction model. Bound-Lay Meteorol, 128, 117–132. https://doi.org/10.1007/s10546-008-9275-0.

Bryan GH, Wyngaard JC, Fritsch JM (2003) Resolution requirements for the simulation of deep convection. Mon Wea Rev, 131, 2394–2416. https://doi.org/10.1175/1520-0493(2003)131%3C2394:RRFTSO%3E2.0.CO;2

Bush M, Allen T, Bain C, Boutle I, Edwards J, Finnenkoetter A, Franklin C, Hanley K, Lean H, Lock A, Manners J, Mittermaier M, Morcrette C, North R, Petch J, Short C, Vosper S, Walters D, Webster S, Weeks M, Wilkinson J, Wood N, Zerroukat M (2020) The first Met Office Unified Model–JULES Regional Atmosphere and Land configuration, RAL1, Geosci Model Dev, 13: 1999–2029. https://doi.org/10.5194/gmd-13-1999-2020

Cai J, Zhu J, Dai Q, Yang Q, Zhang Shuliang (2019) Sensitivity of a weather research and forecasting model to downscaling schemes in ensemble rainfall estimation. Meteorol Appl, 27: 1-16. https://doi.org/10.1002/met.1806

Carruthers DJ, Holroyd RJ, Hunt JCR, Weng W-S, Robins AG, Apsley DD, Thompson DJ, Smith FB (1994) UK-ADMS: A new approach to modelling dispersion in the earth's atmospheric boundary layer. J Wind Eng. Ind. Aerodyn., 52:139-153, https://doi.org/10.1016/0167-6105(94)90044-2

Carruthers DJ, Seaton MD, McHugh CA, Sheng X, Solazzo E, Vanvyve E (2011) Comparison of the Complex Terrain Algorithms Incorporated into Two Commonly Used Local-Scale Air Pollution Dispersion Models (ADMS and AERMOD) Using a Hybrid Model. J Air & Waste Manage. Assoc., 61:1227-1235. https://doi.org/10.1080/10473289.2011.609750

Carvalho D, Rocha A, Gómez-Gesteira M, Santos C (2012) A sensitivity study of the WRF model in wind simulation for an area of high wind energy. Environ Model Softw, 33: 23-34. https://doi.org/10.1016/j.envsoft.2012.01.019

Carvalho D, Rocha A, Gómez-Gesteira M, Santos C (2014) WRF wind simulation and wind energy production estimates forced by different reanalyses: Comparison with observed data for Portugal. Appl Energy, 117: 116-126. https://doi.org/10.1016/j.apenergy.2013.12.001

CDS (2022) Climate Data Store. https://cds.climate.copernicus.eu/ (accessed October 2023)

CERC (2023) ADMS Technical Specification. Available from https://www.cerc.co.uk/TechSpec (accessed October 2023)

Charnock TW, Bexon A, Sherwood J, Higgins N, Field SJ (2013) PACE: A geographic information system based level 3 probabilistic accident consequence evaluation program. ANS PSA 2013 International Topical Meeting on Probabilistic Safety Assessment and Analysis. Columbia, SC. 22-26 September 2013. American Nuclear Society. Available from https://researchportal.ukhsa.gov.uk/en/publications/pace-a-geographic-information-system-based-level-3-probabilistic- (accessed October 2023)

Charnock TW, Bexon AP, Sherwood J, Higgins NA, Field S, Smith J, Brown IK (2020) The Probabilistic Accident Consequence Evaluation (PACE) Software Methodology for version 3.3.2. Public Health England, CRCE-RAD-006-2020. Available from https://www.ukhsa-protectionservices.org.uk/cms/assets/gfx/content/resource_5201csf50c7035e5.pdf (accessed October 2023)

Cimorelli AJ, Perry SG, Venkatram A, Weil JC, Paine RJ, Wilson RB, Lee RF, Peters WD, Brode RW, Paumier JO (2004) AERMOD: Description of Model Formulation; United States Environmental Protection Agency; EPA-454/R-03-004. Available from https://gaftp.epa.gov/Air/aqmg/SCRAM/models/preferred/aermod/aermod_mfd_454-R-03-004.pdf (accessed October 2023)

Cullen MJP (1993) The Unified Forecast/climate model. Meteorological Magazine (122), 81-94. Available from https://digital.nmla.metoffice.gov.uk/download/file/digitalFile_33af6d4a-7c25-4bbc-819a-be64312e783d (accessed October 2023)

Danielson JJ, Gesch DB (2011) Global multi-resolution terrain elevation data 2010 (GMTED2010). USGS Report series 2011-1073, ID ofr20111073. doi: https://doi.org/10.3133/ofr20111073

Davis LS, Dacre HF (2009) Can dispersion model predictions be improved by increasing the temporal and spatial resolution of the meteorological input data? Weather – September 2009, Vol 64, No 9. https://doi.org/10.1002/wea.421

Done J, Davis CA, Weisman M (2004) The next generation of NWP: Explicit forecasts of convection using the weather research and forecasting (WRF) model. Atmos Sci Lett, 5, 110–117. https://doi.org/10.1002/asl.72

ECMWF (2021a) IFS Documentation CY47R3 - Part II: Data assimilation. https://doi.org/10.21957/t445u8kna

ECMWF (2021b) IFS Documentation CY47R3 - Part IV Physical processes. https://doi.org/10.21957/eyrpir4vj

European Environment Agency (2011) The application of models under the European Union's Air Quality Directive: A technical reference guide. EEA Publications Office, Technical report No. 10/2011 ISSN 1725-2237 https://doi.org/10.2800/80600

Fernández-González S, Martín ML, García-Ortega E, Merino A, Lorenzana J, Sánchez JL, Valero F, Rodrigo JS (2018) Sensitivity Analysis of the WRF Model: Wind-Resource Assessment for Complex Terrain. J Appl Meteorol Climatol, 57: 733-753. https://doi.org/10.1175/JAMC-D-17-0121.1

The Food and Feed (Maximum Permitted Levels of Radioactive Contamination) (Amendment) (EU Exit) Regulations (2019) No 701. Available from https://www.legislation.gov.uk/ukdsi/2019/9780111180228/contents (accessed October 2023)

GFS (2022) Global Forecast System. https://www.ncei.noaa.gov/products/weather-climate-models/global-forecast (accessed October 2023)

Graham RM, Hudson SR, Maturilli M (2019) Improved Performance of ERA5 in Arctic Gateway Relative to Four Global Atmospheric Reanalyses. Geophys Res Lett, 46: 6138-6147. https://doi.org/10.1029/2019GL082781

Hanley K, Whitall M, Stirling A, Clark P (2019) Modifications to the representation of subgrid mixing in kilometre scale version of the Unified Model. University of Reading. Quarterly Journal of the Royal Meteorological Society, 145 (725), pp3361-3375. https://doi.org/10.1002/qj.3624.

Hanley KE, Barrett AI, Lean HW (2016) Simulating the 20 May 2013 Moore, Oklahoma tornado with a 100-meter grid-length NWP model. Atmos Sci Let, 17, 453–461. https://doi.org/10.1002/asl.678

Hanley KE, Plant RS, Stein THM, Hogan RJ, Nicol JC, Lean HW, Halliwell C, Clark PA (2015) Mixing length controls on high resolution simulations of convective storms. Q J R Meteorol Soc, 141, 272–184. https://doi.org/10.1002/qj.2356

Hanna SR, Yang R (2001) Evaluations of Mesoscale Models' Simulations of Near-Surface Winds, Temperature Gradients, and Mixing Depths. J Appl Meteorol Climatol, 40: 1095-1104. https://doi.org/10.1175/1520-0450(2001)040<1095:EOMMSO>2.0.CO;2

Hastings DA, Dunbar PK, Elphingstone GM, Bootz M, Murakami H, Maruyama H, Masaharu H, Holland P, Payne J, Bryant NA, Logan TL, Muller J-P, Schreier G, MacDonald JS (1999) The Global Land One-kilometer Base Elevation (GLOBE) Digital Elevation Model, Version 1.0, Digital online data base, available from https://www.ngdc.noaa.gov/mgg/topo/globe.html (accessed October 2023).

Heikkilä U, Sandvik A, Sorteberg A (2011) Dynamical downscaling of ERA-40 in complex terrain using the WRF regional climate model. Clim Dyn, 37: 1551-1564. https://doi.org/10.1007/s00382-010-0928-6

Hersbach H, Bell B, Berrisford P, Hirahara S, Horanyi A, Munoz-Sabater J, Nicolas J, Peubey C, Radu R, Schepers D, Simmons A, Soci C, Abdalla S, Abellan X, Balsamo G, Bechtold P, Biavati G, Bidlot J, Bonavita M, Chiara G, Dahlgren P, Dee D, Diamantakis M, Dragani R, Flemming J, Forbes R, Fuentes M, Geer A, Haimberger L, Healy S, Hogan RJ, Holm E, Janiskova M, Keeley S, Laloyaux P, Lopez P, Lupu C, Radnoti G, Rosnay P, Rozum I, Vamborg F, Villaume S, Thepaut J-N (2020) The ERA5 global reanalysis. Q J R Meteorol Soc, 146: 1999–2049. https://doi.org/10.1002/qj.3803

Hong S-Y, Dudhia J, Chen S-H (2004) A Revised Approach to Ice Microphysical Processes for the Bulk Parameterization of Clouds and Precipitation. Mon Wea Rev 132(1): 103-120. https://doi.org/10.1175/1520-0493(2004)132%3C0103:ARATIM%3E2.0.CO;2

Hong S-Y, Noh Y, Dudhia J (2006) A new vertical diffusion package with an explicit treatment of entrainment processes. Mon Wea Rev 134(9): 2318-2341. https://doi.org/10.1175/MWR3199.1

Hort M, Athanassiadou M (2005) High Resolution UM Data and NAME III. NAME III Document, MD13/6(version 1), 01/05/05.

Horvath K, Koracin D, Vellore R, Jiang J, Belu R (2012) Sub-kilometer dynamical downscaling of near-surface winds in complex terrain using WRF and MM5 mesoscale models. J Geophys Res Atmos, 117. https://doi.org/10.1029/2012JD017432

Hu X-M, Nielsen-Gammon JW, Zhang F (2010) Evaluation of three planetary boundary layer schemes in the WRF model. J Appl Meteorol Climatol, 49: 1831-1844. https://doi.org/10.1175/2010JAMC2432.1

ICRP (2012). Compendium of dose coefficients based on ICRP Publication 60. Publication 119. Annals of the ICRP 41 (Suppl.). Available from https://www.icrp.org/docs/P%20119%20JAICRP%2041(s)%20Compendium%20of%20Dose%20Coefficients%20based%20on%20ICRP%20Publication%2060.pdf (accessed October 2023)

Jiménez PA, Dudhia J (2012) Improving the Representation of Resolved and Unresolved Topographic Effects on Surface Wind in the WRF Model. J Appl Meteorol Climatol, 51: 300-316. https://doi.org/10.1175/JAMC-D-11-084.1

Jones AR, Thomson DJ, Hort M, Devenish B (2007) The U.K. Met Office's next-generation atmospheric dispersion model, NAME III. In Borrego C and Norman A-L (Eds) Air Pollution Modeling and its Application XVII (Proceedings of the 27th NATO/CCMS International Technical Meeting on Air Pollution Modelling and its Application), Springer, pp 580-589. Available from https://link.springer.com/chapter/10.1007/978-0-387-68854-1_62 (accessed October 2023).

Karamchandani P, Emery C, Brashers B (2022) The Mesoscale Model Interface (MMIF) Program Version 4.0 User's Manual. Report for US EPA. Available from

https://gaftp.epa.gov/Air/aqmg/SCRAM/models/related/mmif/MMIFv4.0_Users_Manual.pdf (accessed October 2023).

Kumar A, Patil RS, Dikshit AK, Kumar R (2017) Application of WRF model for air quality modelling and AERMOD – a survey. Aerosol Air Qual Res, 17: 1925-1937. https://doi.org/10.4209/aaqr.2016.06.0265

Kumar A, Dikshit AK, Patil RS (2020) Use of Simulated and Observed Meteorology for Air Quality Modeling and Source Ranking for an Industrial Region. Sustainability, 13: 4276. https://doi.org/10.3390/su13084276

Liang X-Z, Li Q, Mei H, Zeng M (2019) Multi-Grid Nesting Ability to Represent Convections Across the Gray Zone. J Adv Model Earth Syst 11: 4352-4376. https://doi.org/10.1029/2019MS001741

Lock AP (2001) The numerical representation of entrainment in parametrizations of boundary layer turbulent mixing. Mon Weather Rev, 129, 1148–1163. https://doi.org/10.1175/1520-0493(2001)129<1148:TNROEI>2.0.CO;2

Lock AP, Brown AR, Bush MR, Martin GM, Smith RNB (2000) A new boundary layer mixing scheme. Part I: Scheme description and single-column model tests. Mon Weather Rev, 128, 3187–3199. https://doi.org/10.1175/1520-0493(2000)128<3187:ANBLMS>2.0.CO;2.

Loveland TR, Reed BC, Brown JF, Ohlen DO, Zhu Z, Yang L, Merchant JW (2000) Development of a global land cover characteristics database and IGBP DISCover from 1 km AVHRR data. Int J Remote Sens 21: 1303-1330. https://doi.org/10.1080/014311600210191

Ma Z, Zhao C, Gong J, Zhang J, Li Z, Sun J, Liu Y, Chen J, Jiang Q (2021) Spin-up characteristics with three types of initial fields and the restart effects on forecast accuracy in the GRAPES global forecast system. Geosci Model Dev 14: 205-221. https://doi.org/10.5194/gmd-14-205-2021

Mass CF, Ovens D, Westrick K, Colle BA (2002) Does increasing horizontal resolution produce more skilful forecasts?: the results of two years of real-time numerical weather prediction over the pacific northwest. Bull Am Meteorol Soc, 83: 407-430. https://doi.org/10.1175/1520-0477(2002)083<0407:DIHRPM>2.3.CO;2

McBeath K, Field PR, Cotton RJ (2013) Using operational weather radar to assess high-resolution numerical weather prediction over the British Isles for a cold air outbreak case-study. Q J R Meteorol Soc. https://doi.org/10.1002/qj.2123

Middleton DR (2008) Dispersion model input parameters from numerical weather prediction or synoptic observations. Met Office. Available from https://hrcak.srce.hr/file/96107 (accessed October 2023)

Moya-Álvarez AS, Martínez-Castro D, Kumar S, Estevan R, Silva Y (2019) Response of the WRF model to different resolutions in the rainfall forecast over

the complex Peruvian orography. Theor Appl Climatol, 137: 2993–3007. https://doi.org/10.1007/s00704-019-02782-3

NCAR (2022) NCEP GDAS/FNL 0.25 Degree Global Tropospheric Analyses and Forecast Grids. Research Data Archive at the National Center for Atmospheric Research, Computational and Information Systems Laboratory. https://doi.org/10.5065/D65Q4T4Z

Nelson N, Mirza A K, Weaver K N (2002) An Assessment of Alternative Sources of Met Data for Use in Dispersion Modelling. A report prepared for ADMLC, ADMLC/2002/1. Available from https://admlc.com/publications/ (accessed October 2023)

Nisbet A (2019) Public Health Protection in Radiation Emergencies. PHE-CRCE-049. Available from https://www.gov.uk/government/publications/radiation-emergencies-public-health-protection-2019 (accessed October 2023)

Olauson J (2018) ERA5: The new champion of wind power modelling? Renew Energy, 126: 322-331. https://doi.org/10.1016/j.renene.2018.03.056

Pollock MD, O'Donnell G, Quinn P, Dutton M, Black A, Wilkinson ME, Colli M, Stagnaro M, Lanza LG, Lewis E, Kilsby CG, O'Connell PE (2018) Quantifying and mitigating wind-induced undercatch in rainfall measurements. Water Resour Res 54: 3863-3875. https://doi.org/10.1029/2017WR022421

Porson A, Clark P, Harman I, Best M, Belcher S (2010) Implementation of a new urban energy budget scheme in the Met UM. Part I: Description and idealized simulations. Q J Roy Meteor Soc, 136, 1514–1529, https://doi.org/10.1002/qj.668

Ramon J, Lledó L, Torralba V, Soret A, Doblas-Reyes FJ (2019) What global reanalysis best represents near-surface winds? Q J R Meteorol Soc, 145: 3236-3251. https://doi.org/10.1002/qj.3616

Roberts NM, Lean HW (2008) Scale-Selective Verification of Rainfall Accumulations from High-Resolution Forecasts of Convective Events. Mon Weather Rev, 136: 78-97. https://doi.org/10.1175/2007MWR2123.1

Salvador N, Reis J NC, Santos JM, Albuquerque TTdeA, Loriato AG, Delbarre H, Augustin P, Sokolov A, Moreira DM (2016) Evaluation of Weather Research and Forecasting Model Parameterizations under Sea-Breeze Conditions in a North Sea Coastal Environment. J Meteorol Res, 30(6): 998-1018. https://doi.org/10.1007/s13351-016-6019-9

Santos-Alamillos FJ, Pozo-Vázquez D, Ruiz-Arias JA, Lara-Fanego V, Tovar-Pescador J (2013) Analysis of WRF Model Wind Estimate Sensitivity to Physics Parameterization Choice and Terrain Representation in Andalusia (Southern Spain). J Appl Meteorol Climatol, 52: 1592-1609. https://doi.org/10.1175/JAMC-D-12-0204.1

Selvaratnam V, Webster H, Thomson D, Devenish B, Jones A (2021) Utilising higher temporal resolution NWP data with NAME. NAME User Workshop, Met Office, Exeter.

Shrivastava R, Dash SK, Oza RB, Hedge MN (2015) Evaluation of parameterization schemes in the Weather Research and Forecasting (WRF) model: A case study for the Kaiga nuclear power plant site. Ann Nucl Energy, 75: 693-702. https://doi.org/10.1016/j.anucene.2014.09.016

Siuta D, West G, Stull R (2017) WRF hub-height wind forecast sensitivity to PBL scheme, grid length and initial condition choice in complex terrain. Weather Forecast, 32: 493-509. https://doi.org/10.1175/WAF-D-16-0120.1

Skamarock WC, Klemp JB, Dudhia J, Gill DO, Liu Z, Berner J, Wang W, Powers JG, Duda MG, Barker DM, Huang X-Y (2021) A Description of the Advanced Research WRF Model Version 4.3, NCAR Technical Note NCAR/TN-556+STR. http://dx.doi.org/10.5065/1dfh-6p97

Smagorinsky, J (1963) General circulation experiments with the primitive equations: I. the basic experiment. Mon Weather Rev, 91, 99–164. https://doi.org/10.1175/1520-0493(1963)091<0099:GCEWTP>2.3.CO;2.

Smith JG, Bedwell P, Charnock T, Jones K, Wellings J (2022) Verification and validation of models used in radiological assessment tools PACE and PC CREAM 08. UKHSA-RCE-004. Available from https://www.gov.uk/government/publications/verification-and-validation-of-models-in-pace-and-pc-cream-08 (accessed October 2023)

Smith S (2018) The use and abuse of meteorological and terrain data. ADMS 5 User Group Meeting, available from http://www.cerc.co.uk/software-support/user-area/usergrouppresentations.html (accessed October 2023)

Soares PMM, Cardoso RM, Miranda PMA, de Medeiros J, Belo-Pereira M, Espirito-Santo F (2012) WRF high resolution dynamical downscaling of ERA-Interim for Portugal. Clim Dyn, 39: 2497–2522. https://doi.org/10.1007/s00382-012-1315-2

Solbakken K, Birkelund Y, Samuelsen EM (2021) Evaluation of surface wind using WRF in complex terrain: Atmospheric input data and grid spacing. Environ Model Softw, 145. https://doi.org/10.1016/j.envsoft.2021.105182

Squitieri BJ, Gallus WA (2020) On the forecast sensitivities of MCS Cold Pools and related features to horizontal grid spacing in Convection-Allowing WRF simulations. Weather and Forecasting (35) 325-346. https://doi.org/10.1175/WAF-D-19-0016.1

Staniforth A, Wood N (2008) Aspects of the dynamical core of a nonhydrostatic deep-atmosphere, unified weather and climate prediction model. Journal of Computational Physics (277), 3445-3464. https://doi.org/10.1016/j.jcp.2006.11.009

Stein THM, Hogan RJ, Clark PA, Halliwell C, Hanley KE, Lean HW, Nicol J, Plant RS (2015) The DYMECS project: A statistical approach for the evaluation of convective storms in high-resolution NWP models. Bull Amer Meteorol Soc, 96, 939–951. http://dx.doi.org/10.1175/BAMS–D–13–00279.1

Stocker J, Ellis A, Smith S, Carruthers D, Venkatram A, Dale W, Attree M (2017), A review of dispersion modelling of agricultural emissions with non-point sources. Int J Environ and Pollution, 62: 247-263. https://dx.doi.org/10.1504/IJEP.2017.089410

Stull RB (1988) An introduction to boundary layer meteorology. Kluwer publishers.

Thompson G, Field PR, Rasmussen RM, Hall WD (2008) Explicit Forecasts of Winter Precipitation Using an Improved Bulk Microphysics Scheme. Part II: Implementation of a new Snow Parameterization. Mon Wea Rev, 136: 5095-5115. https://doi.org/10.1175/2008MWR2387.1

US Environmental Protection Agency (2016) Reassessment of the Interagency Workgroup on Air Quality Modeling (IWAQM) Phase 2 Summary Report: Revisions to Phase 2 Recommendations. Report EPA-454/R-16-007 Available from https://www.epa.gov/sites/default/files/2021-01/documents/iwaqm_phase2_reassessment_2016.pdf (accessed October 2023)

US Environmental Protection Agency (2022) Guidance on the Use of the Mesoscale Model Interface Program (MMIF) for AERMOD applications. Report EPA-454/B-22-011 available from https://gaftp.epa.gov/Air/aqmg/SCRAM/models/related/mmif/MMIF_Guidance.pdf (accessed October 2023)

Walters D, Baran AJ, Boutle I, Brooks M, Earnshaw P, Edwards J, Furtado K, Hill P, Lock A, Manners J, Morcrette C, Mulcahy J, Sanchez C, Smith C, Stratton R, Tennant W, Tomassini L, Van Weverberg K, Vosper S, Willett M, Browse J, Bushell A, Carslaw K, Dalvi M, Essery R, Gedney N, Hardiman S, Johnson B, Johnson C, Jones A, Jones C, Mann G, Milton S, Rumbold H, Sellar A, Ujiie M, Whitall M, Williams K, Zerroukat M (2019) The Met Office Unified Model Global Atmosphere 7.0/7.1 and JULES Global Land 7.0 configurations, Geosci Model Dev, 12: 1909–1963. https://doi.org/10.5194/gmd-12-1909-2019

WMO [World Meteorological Organisation] (2018) Guide to Instruments and Methods of Observation (WMO-No. 8): 2018 edition Volume I – Measurement of Meteorological Variables. Report WMO No. 8, 2018 edition. Available from https://library.wmo.int/index.php?id=12407&lvl=notice_display#.YvV4CnbMKM_ (accessed October 2023)

Xie B, Hunt JCR, Carruthers DJ, Fung JCH, Barlow JF (2013) Structure of the planetary boundary layer over Southeast England: Modeling and measurements. J Geophys Res Atmos, 118: 1-20. https://doi.org/10.1002/jgrd.50621

Zhang C, Lin H, Chen H, Yang L (2014) Scale matching of multiscale digital elevation model (DEM) data and the Weather Research and Forecasting (WRF)

model: a case study of meteorological simulation in Hong Kong. Arab J Geosci, 7: 2215–2223. https://doi.org/10.1007/s12517-014-1273-6

Zhang Y, Hemperly J, Meskhidze N, Skamarock WC (2012) The Global Weather Research and Forecasting (GWRF) Model: Model Evaluation, Sensitivity Study, and Future Year Simulation. Atmospheric and Climate Sciences, 2: 231-253. https://doi.org/10.4236/acs.2012.23024

APPENDIX A NWP EXTRACTION PROCESSES

A1 APS WRF

APS use the WRFtoMet utility developed by CERC to extract hourly values of:

- Horizontal wind components at 10 m above ground;
- Air temperature at 2 m above ground;
- Incoming solar radiation;
- Surface heat flux; and
- Boundary layer depth

from WRF output files. The WRFtoMet utility:

- Extracts data from the WRF grid cell centre nearest to the specified output location;
- Calculates wind speed and direction from horizontal components;
- Converts units of temperature from Kelvin to Celsius; and
- Writes an ADMS-format meteorological data file (.met).

APS developed custom code to extract cloud cover and precipitation data from WRF and incorporate this into the .met files. Fractional cloud cover values are derived from maximum relative humidity values above a critical threshold in 'low' (excluding surface, humidity threshold 75%), 'medium' (humidity threshold 75%) and 'high' (humidity threshold 60%) layer ranges. The maximum cloud fraction across the three ranges is then converted to integer oktas using the mid-points of fraction ranges. This algorithm is based on recommendations from the WRF developers (NCAR).

A2 MO UM

Extracting ADMS-format data from MO UM was carried out as a two-stage process. Initially the NAME model was used to spatially interpolate the archived UM data to the specified output location. For the 10 km resolution global dataset NAME also temporally interpolates wind speed and direction, boundary layer depth and temperature variables from 3 hourly to hourly resolution. Cloud cover, surface sensible heat flux and precipitation values are not temporally interpolated. This step generated a text file with NAME format headers and date-time conventions. The second step reformats the NAME output data file to an ADMS input format data file. Standard settings were used for each step as recommended by the MO.

This process matches the method used by the MO to supply NWP data to ADMS modellers.

APPENDIX B METEOROLOGICAL EVALUATION RESULTS PER SITE

B1 Resolution evaluation

B1.1 Wind speed

This section gives per-site statistics and plots for 10 m wind speed, supplementing the results over all sites included in Section 5.2.1.

Table 48 – Meteorological model performance evaluation of wind speed at 10 m, by site.

Terrain type	Site	Model	Res. (km)	Observed Mean	MB	MGE	RMSE	R	IOA
					0	0	0	1	1
Flat	Waddington	APS_WRF	1	4.84	-0.15	0.84	1.10	0.88	0.76
		APS_WRF	3		-0.14	0.84	1.10	0.88	0.76
		APS_WRF	9		-0.53	0.96	1.22	0.88	0.73
		MO_UM	1.5		-0.67	0.97	1.23	0.89	0.73
		MO_UM	10		-0.69	0.92	1.17	0.91	0.74
Urban	Northolt	APS_WRF	1	3.80	-0.03	0.79	1.02	0.89	0.78
		APS_WRF	3		-0.18	0.78	1.01	0.90	0.78
		APS_WRF	9		-0.31	0.79	1.02	0.90	0.78
		MO_UM	1.5		-0.11	0.78	1.01	0.89	0.78
		MO_UM	10		-0.74	0.98	1.25	0.92	0.73
Complex	Drumalbin	APS_WRF	1	5.32	-0.73	1.47	1.85	0.85	0.71
		APS_WRF	3		-0.84	1.50	1.88	0.85	0.71
		APS_WRF	9		-0.95	1.50	1.88	0.86	0.71
		MO_UM	1.5		-1.20	1.52	1.96	0.89	0.70
		MO_UM	10		-1.33	1.61	2.07	0.90	0.69
	Leek Thorncliffe	APS_WRF	1	4.61	0.13	1.10	1.48	0.84	0.73
		APS_WRF	3		-0.26	1.14	1.49	0.83	0.72
		APS_WRF	9		-0.49	1.31	1.75	0.76	0.68
		MO_UM	1.5		-0.42	1.09	1.42	0.85	0.73
		MO_UM	10		-0.42	1.24	1.73	0.75	0.70
	Sennybridge	APS_WRF	1	3.47	1.46	1.73	2.29	0.77	0.56
		APS_WRF	3		1.12	1.55	2.07	0.76	0.61
		APS_WRF	9		0.76	1.47	1.96	0.72	0.63
		MO_UM	1.5		0.24	1.15	1.56	0.79	0.71
		MO_UM	10		0.11	1.30	1.72	0.73	0.67
Coastal	Leuchars	APS_WRF	1	4.69	-0.11	1.18	1.53	0.84	0.73
		APS_WRF	3		-0.31	1.19	1.53	0.84	0.73
		APS_WRF	9		-0.10	1.14	1.47	0.85	0.74
		MO_UM	1.5		-0.51	1.11	1.44	0.87	0.75
		MO_UM	10		-0.30	1.02	1.31	0.89	0.77
	Mumbles Head	APS_WRF	1	6.73	-0.56	1.65	2.12	0.86	0.74
		APS_WRF	3		-1.06	1.87	2.41	0.84	0.71
		APS_WRF	9		-0.88	1.85	2.38	0.83	0.71
		MO_UM	1.5		-0.84	1.60	2.09	0.88	0.75
		MO_UM	10		-1.51	1.99	2.58	0.87	0.69
	Newhaven	APS_WRF	1	7.24	-0.77	1.63	2.09	0.89	0.77
		APS_WRF	3		-1.01	1.71	2.19	0.90	0.75
		APS_WRF	9		-1.10	1.75	2.25	0.90	0.75
		MO_UM	1.5		-0.91	1.52	1.94	0.92	0.78
		MO_UM	10		-0.62	1.46	1.86	0.92	0.79

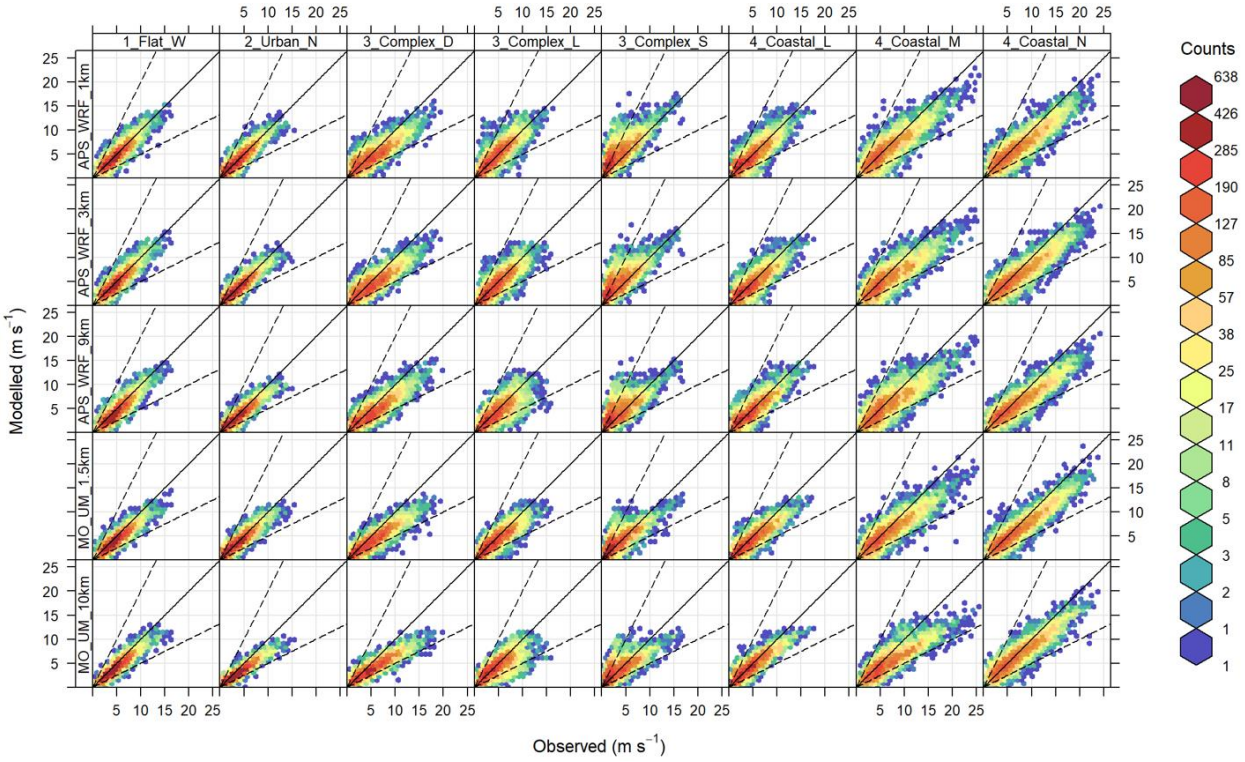

Figure 111 – Frequency scatter plots of modelled and observed wind speed (m/s) at each site, colours indicate the number of data points in each area of the plot.

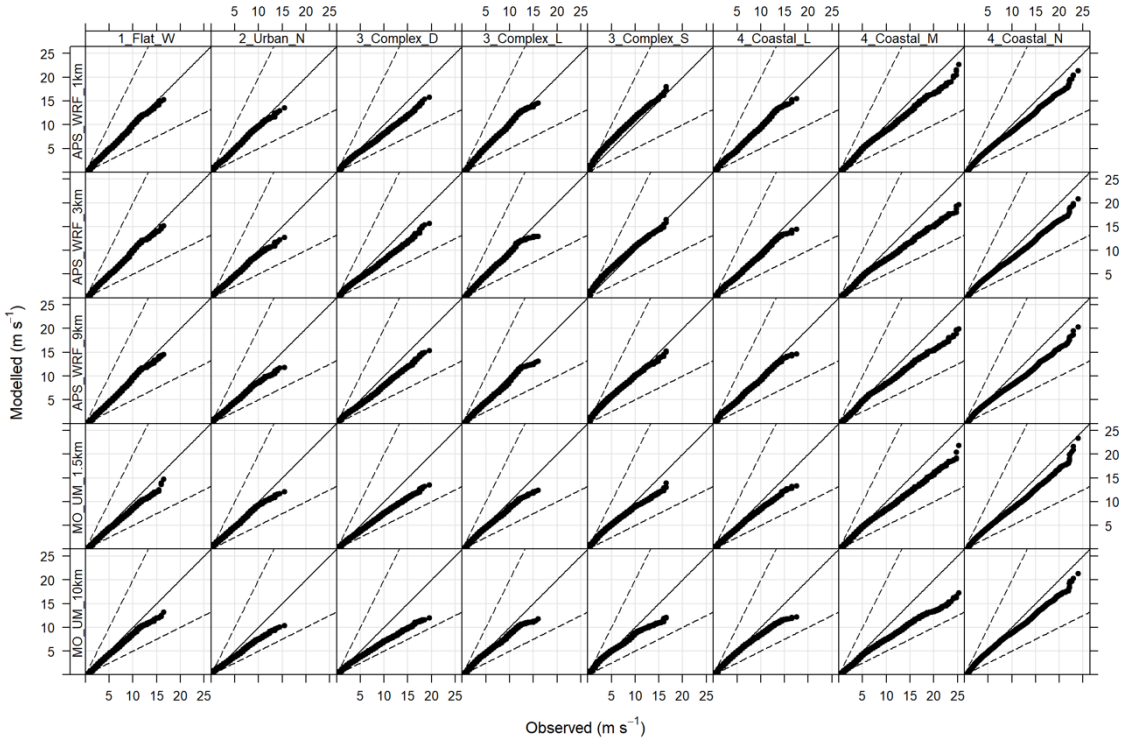

Figure 112 – Quantile-quantile plots of modelled and observed wind speed (m/s) at each site, ordered independently.

B1.2 Wind direction

This section gives per-site statistics and plots for 10 m wind direction, supplementing the results over all sites included in Section 5.2.2.

Table 49 – Meteorological model performance evaluation of wind direction at 10 m, by site, with no wind speed filtering applied.

Terrain type	Site	Model	Res. (km)	Observed Mean	Modelled Mean	MB	MGE
						0	0
Flat	Waddington	APS_WRF	1	231	224	-0.82	17.90
		APS_WRF	3		228	0.01	17.17
		APS_WRF	9		221	-3.47	18.60
		MO_UM	1.5		224	0.37	15.01
		MO_UM	10		230	1.21	12.60
Urban	Northolt	APS_WRF	1	255	249	-6.22	23.86
		APS_WRF	3		249	-5.90	23.62
		APS_WRF	9		245	-6.11	23.26
		MO_UM	1.5		234	-6.24	20.42
		MO_UM	10		236	-7.51	19.88
Complex	Drumalbin	APS_WRF	1	219	202	-8.95	25.10
		APS_WRF	3		200	-9.47	25.93
		APS_WRF	9		205	-8.71	25.77
		MO_UM	1.5		209	-11.20	23.68
		MO_UM	10		208	-7.01	21.99
	Leek Thorncliffe	APS_WRF	1	222	198	-9.66	22.07
		APS_WRF	3		197	-11.03	23.17
		APS_WRF	9		222	-13.07	23.07
		MO_UM	1.5		223	-10.56	19.74
		MO_UM	10		233	-10.60	18.63
	Sennybridge	APS_WRF	1	233	212	-0.97	25.87
		APS_WRF	3		222	-0.73	25.69
		APS_WRF	9		231	0.66	26.17
		MO_UM	1.5		232	-6.76	25.10
		MO_UM	10		233	1.92	25.33
Coastal	Leuchars	APS_WRF	1	259	240	-12.20	27.38
		APS_WRF	3		237	-13.47	28.34
		APS_WRF	9		229	-11.00	28.30
		MO_UM	1.5		235	-10.67	24.34
		MO_UM	10		234	-6.57	22.69
	Mumbles Head	APS_WRF	1	249	257	9.63	25.05
		APS_WRF	3		253	8.52	24.80
		APS_WRF	9		248	9.33	25.49
		MO_UM	1.5		255	8.44	20.15
		MO_UM	10		255	8.93	19.83
	Newhaven	APS_WRF	1	280	262	-2.34	21.63
		APS_WRF	3		263	-1.42	21.61
		APS_WRF	9		261	-2.55	20.91
		MO_UM	1.5		260	-3.66	18.32
		MO_UM	10		251	-1.05	19.59

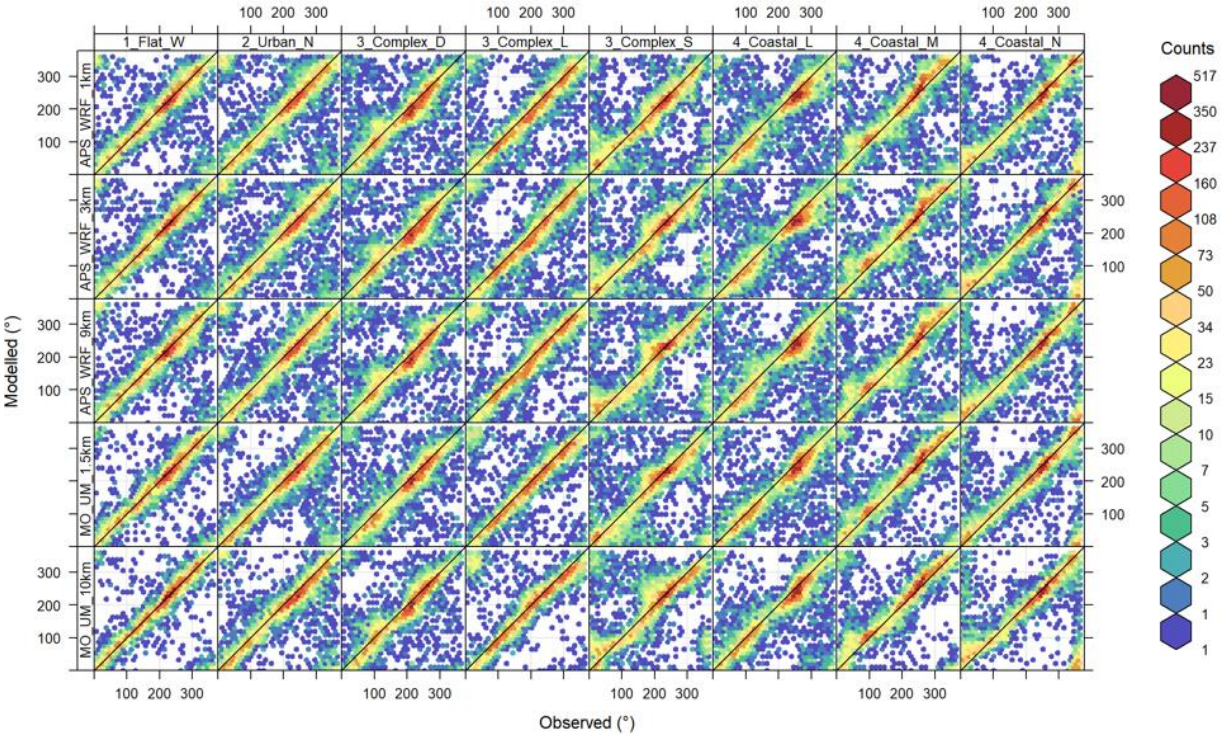

Figure 113 – Frequency scatter plots of modelled and observed wind direction (°) at each site, colours indicate the number of data points in each area of the plot.

Table 50 – Meteorological model performance evaluation of wind direction at 10 m, by site. Hours with wind speeds under 1.5 m/s have been filtered out.

Terrain type	Site	Model	Res. (km)	% Hours Filtered	Observed Mean	Modelled Mean	MB	MGE
							0	0
Flat	Waddington	APS_WRF	1	1.6	232	224	-0.77	17.20
		APS_WRF	3			229	0.04	16.50
		APS_WRF	9			221	-3.48	17.92
		MO_UM	1.5			224	0.39	14.37
		MO_UM	10			230	1.28	11.91
Urban	Northolt	APS_WRF	1	12.4	250	247	-8.28	19.73
		APS_WRF	3			246	-8.28	19.41
		APS_WRF	9			245	-8.48	19.03
		MO_UM	1.5			236	-7.79	16.03
		MO_UM	10			238	-9.16	15.50
Complex	Drumalbin	APS_WRF	1	7.0	220	203	-10.00	21.67
		APS_WRF	3			201	-10.39	22.33
		APS_WRF	9			205	-9.89	22.24
		MO_UM	1.5			210	-12.16	20.60
		MO_UM	10			210	-8.63	18.53
	Leek Thorncliffe	APS_WRF	1	6.1	218	197	-10.35	19.67
		APS_WRF	3			196	-11.53	20.74
		APS_WRF	9			214	-13.20	20.65
		MO_UM	1.5			219	-10.73	17.34
		MO_UM	10			227	-10.35	16.22
	Sennybridge	APS_WRF	1	18.8	225	211	-2.33	19.03
		APS_WRF	3			217	-1.71	18.76
		APS_WRF	9			224	-0.56	19.00
		MO_UM	1.5			224	-6.91	18.61
		MO_UM	10			222	0.05	17.50
Coastal	Leuchars	APS_WRF	1	7.4	255	239	-12.52	24.47
		APS_WRF	3			236	-13.54	25.38
		APS_WRF	9			231	-11.13	24.45
		MO_UM	1.5			235	-10.99	21.41
		MO_UM	10			235	-7.29	19.28
	Mumbles Head	APS_WRF	1	2.1	249	255	9.72	24.08
		APS_WRF	3			252	8.62	23.87
		APS_WRF	9			247	9.30	24.53
		MO_UM	1.5			254	8.61	19.20
		MO_UM	10			254	9.22	18.79
	Newhaven	APS_WRF	1	3.0	278	261	-2.00	20.24
		APS_WRF	3			261	-1.19	20.25
		APS_WRF	9			260	-2.20	19.41
		MO_UM	1.5			261	-2.99	16.53
		MO_UM	10			251	-0.31	17.78

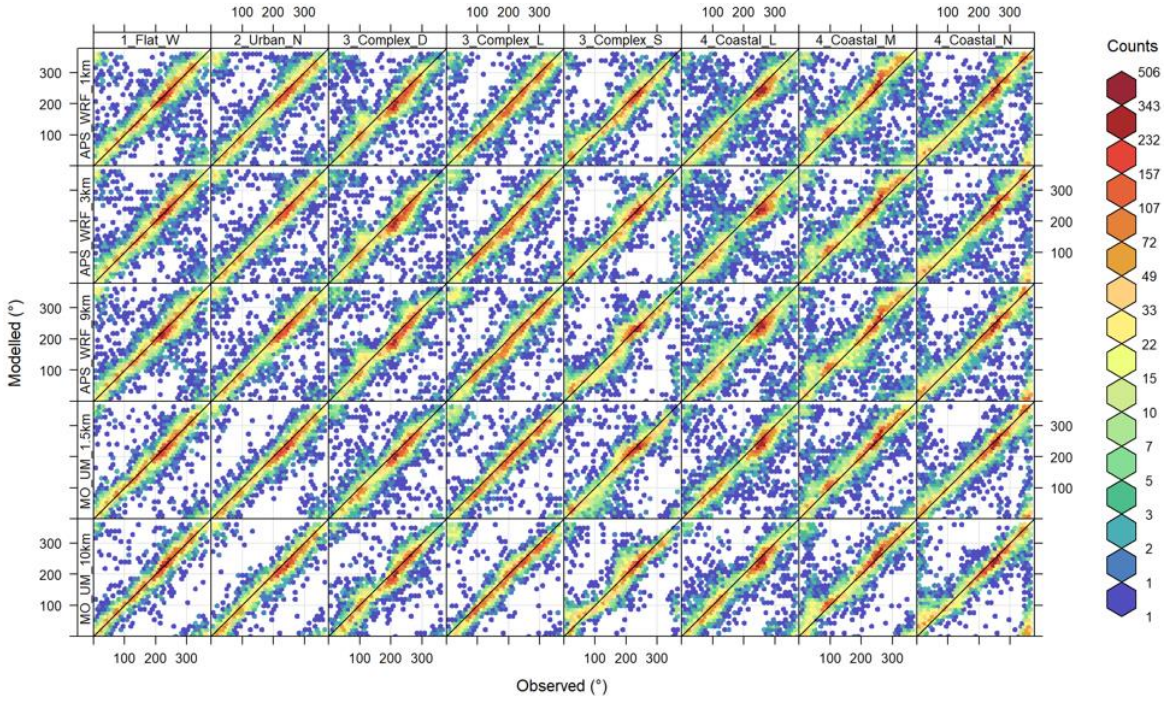

Figure 114 – Frequency scatter plots of modelled and observed wind direction (°) at each site, filtering out hours with wind speeds under 1.5 m/s. Colours indicate the number of data points in each area of the plot.

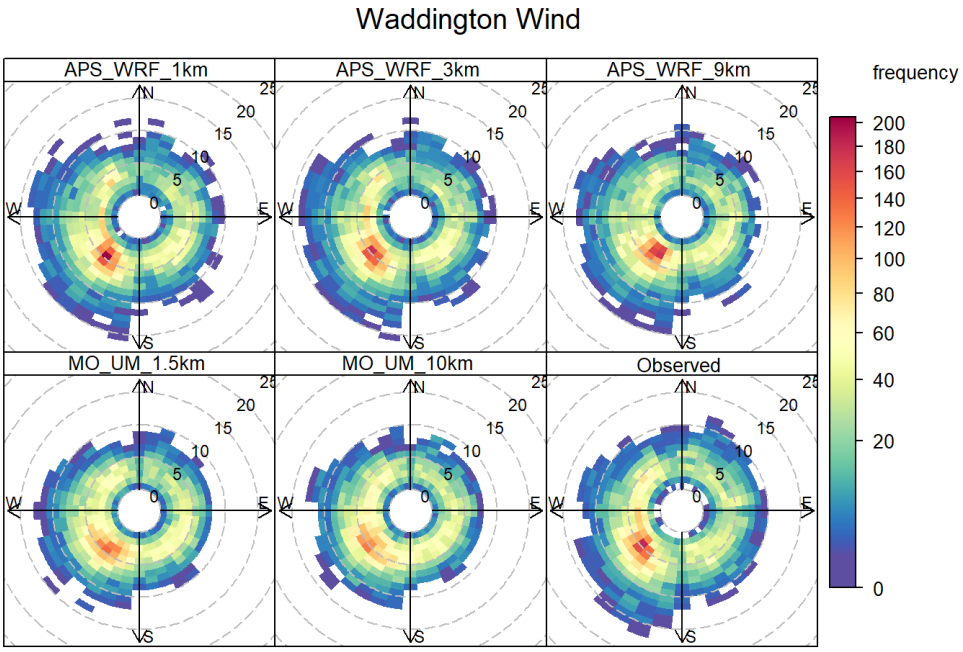

Figure 115 – Polar frequency plots showing the distribution of wind speed and direction at Waddington (flat terrain), colours indicate the number of hours with each combination of 10° wind direction and 1 m/s wind speed bins.

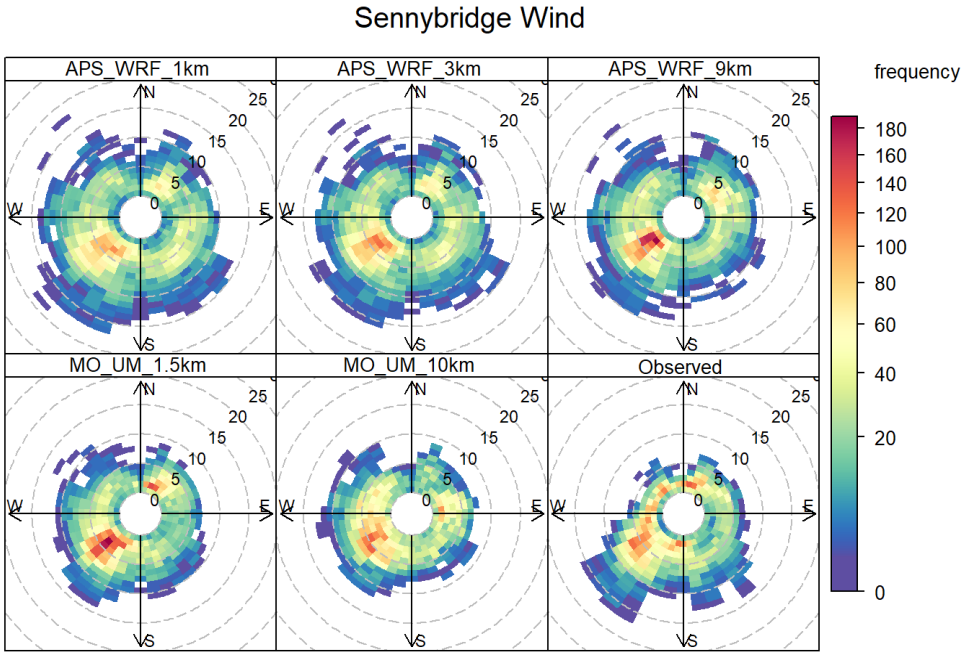

Figure 116 – Polar frequency plots showing the distribution of wind speed and direction at Sennybridge (complex terrain), colours indicate the number of hours with each combination of 10° wind direction and 1 m/s wind speed bins.

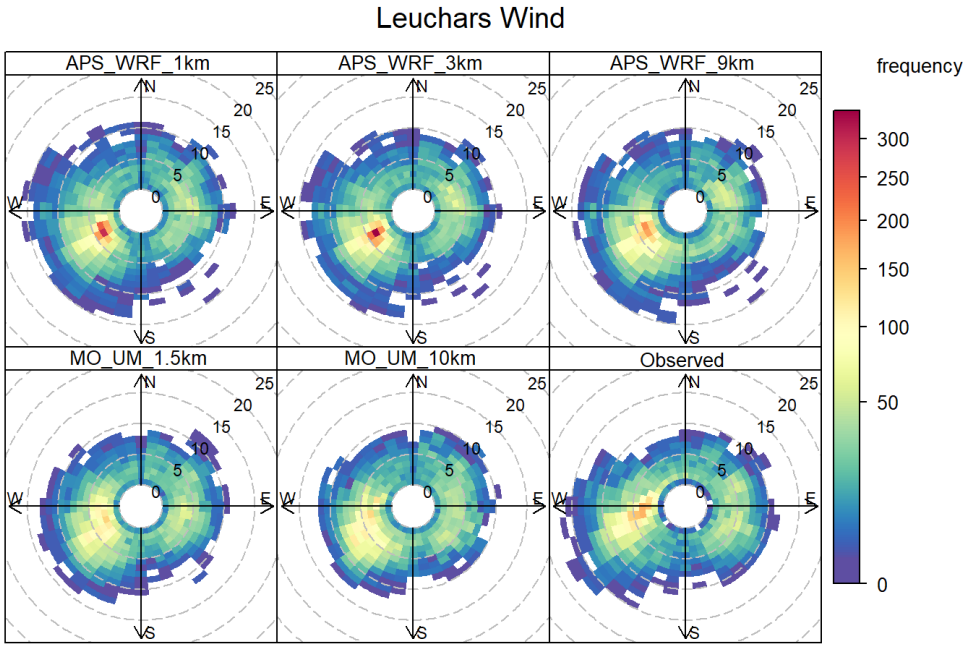

Figure 117 – Polar frequency plots showing the distribution of wind speed and direction at Leuchars (coastal), colours indicate the number of hours with each combination of 10° wind direction and 1 m/s wind speed bins.

B1.3 Temperature

This section gives per-site statistics and plots for screen height temperature, supplementing the results over all sites included in Section 5.2.3.

Table 51 – Meteorological model performance evaluation of temperature (°C) by site.

Terrain type	Site	Model	Res. (km)	Observed Mean	MB	MGE	RMSE	R	IOA
					0	0	0	1	1
Flat	Waddington	APS_WRF	1	10.37	-0.99	1.42	1.78	0.97	0.85
		APS_WRF	3		-0.97	1.40	1.74	0.97	0.85
		APS_WRF	9		-0.85	1.40	1.80	0.97	0.85
		MO_UM	1.5		0.03	0.50	0.68	0.99	0.95
		MO_UM	10		-0.12	0.61	0.82	0.99	0.93
Urban	Northolt	APS_WRF	1	11.44	-0.58	1.43	1.89	0.96	0.86
		APS_WRF	3		-0.13	1.34	1.81	0.96	0.87
		APS_WRF	9		0.19	1.36	1.83	0.96	0.86
		MO_UM	1.5		-0.14	0.68	0.95	0.99	0.93
		MO_UM	10		-0.15	0.90	1.26	0.98	0.91
Complex	Drumalbin	APS_WRF	1	8.16	-0.39	1.12	1.42	0.97	0.87
		APS_WRF	3		-0.44	1.14	1.44	0.97	0.87
		APS_WRF	9		-0.50	1.16	1.47	0.97	0.87
		MO_UM	1.5		0.16	0.56	0.76	0.99	0.93
		MO_UM	10		-0.05	0.63	0.86	0.99	0.93
	Leek Thorncliffe	APS_WRF	1	8.73	-0.33	1.06	1.36	0.97	0.88
		APS_WRF	3		-0.09	1.04	1.34	0.97	0.88
		APS_WRF	9		0.04	1.07	1.38	0.97	0.88
		MO_UM	1.5		0.11	0.51	0.69	0.99	0.94
		MO_UM	10		-0.18	0.64	0.99	0.98	0.93
	Sennybridge	APS_WRF	1	8.72	-0.18	1.32	1.74	0.95	0.85
		APS_WRF	3		-0.10	1.28	1.69	0.95	0.85
		APS_WRF	9		0.03	1.25	1.69	0.95	0.85
		MO_UM	1.5		0.22	0.65	0.97	0.98	0.92
		MO_UM	10		0.11	0.72	1.06	0.98	0.92
Coastal	Leuchars	APS_WRF	1	9.20	-0.51	1.27	1.62	0.96	0.85
		APS_WRF	3		-0.40	1.19	1.53	0.96	0.86
		APS_WRF	9		-0.74	1.38	1.70	0.96	0.84
		MO_UM	1.5		-0.01	0.64	0.89	0.99	0.92
		MO_UM	10		-0.35	0.87	1.12	0.98	0.90
	Mumbles Head	APS_WRF	1	11.56	-0.51	1.40	1.82	0.92	0.81
		APS_WRF	3		-0.47	1.15	1.49	0.95	0.85
		APS_WRF	9		-0.41	1.30	1.67	0.93	0.83
		MO_UM	1.5		-0.21	0.55	0.76	0.99	0.93
		MO_UM	10		-0.20	0.58	0.80	0.98	0.92
	Newhaven	APS_WRF	1	11.17	0.74	2.27	2.98	0.86	0.75
		APS_WRF	3		0.66	1.99	2.65	0.89	0.78
		APS_WRF	9		0.57	1.82	2.45	0.91	0.80
		MO_UM	1.5		0.53	1.40	1.98	0.94	0.84
		MO_UM	10		0.55	1.76	2.41	0.92	0.80

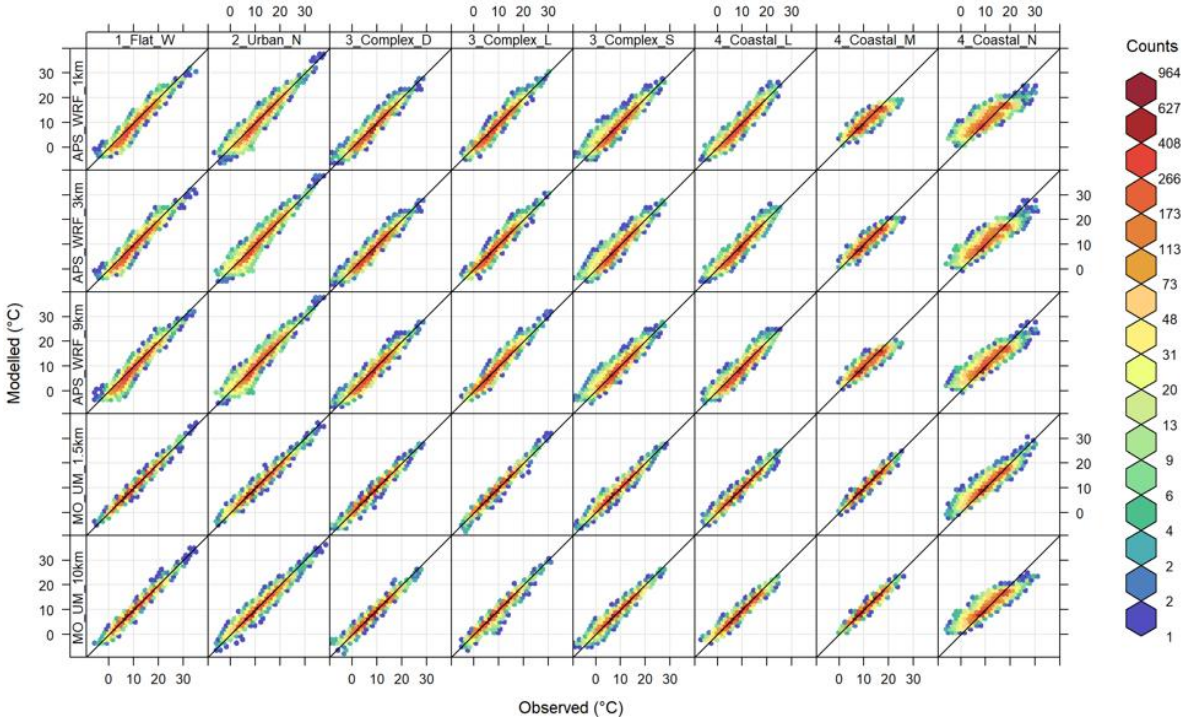

Figure 118 – Frequency scatter plots of modelled and observed temperature (°C) at each site. Colours indicate the number of data points in each area of the plot.

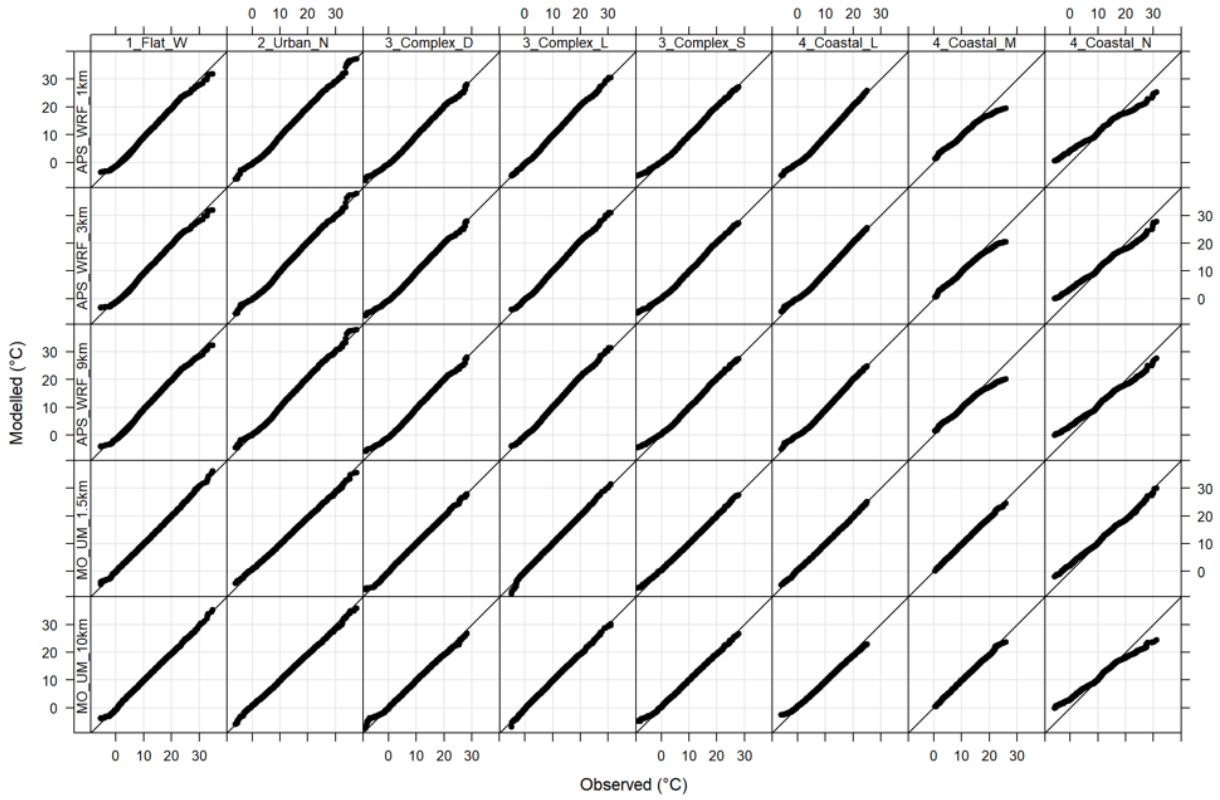

Figure 119 – Quantile-quantile plots of modelled and observed temperature (°C) at each site, ordered independently.

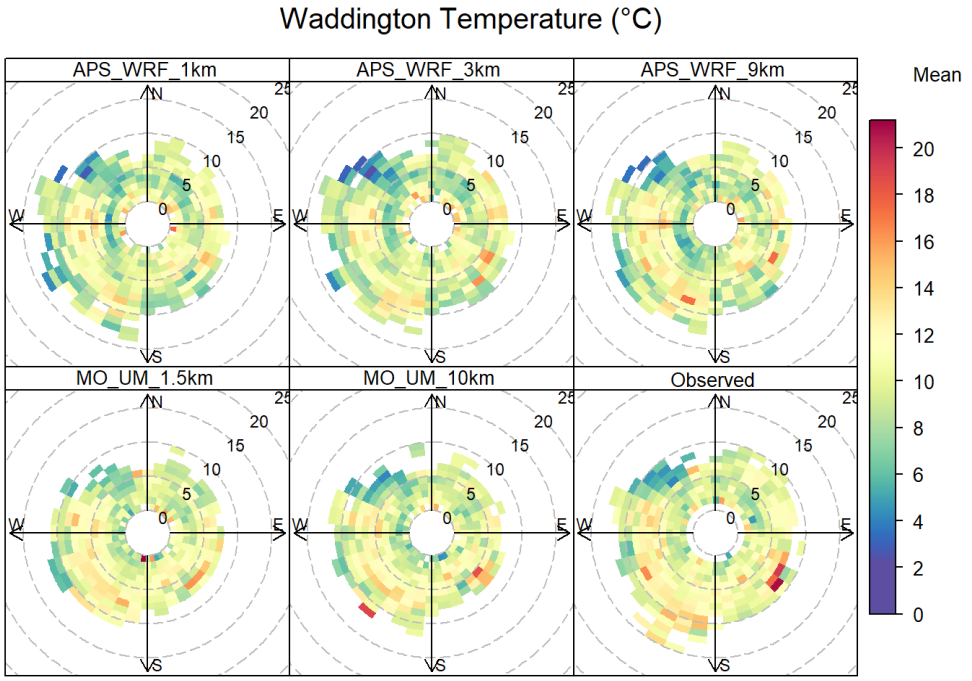

Figure 120 – Polar plots showing the average temperature (indicated by the colour scale) associated with variation of wind speed (radial scale) and wind direction at Waddington. Combinations of wind speed and direction which occur for fewer than 3 hours per year are not displayed. Observed temperatures are plotted with observed wind speed and temperature while modelled temperatures are plotted with the associated modelled wind data.

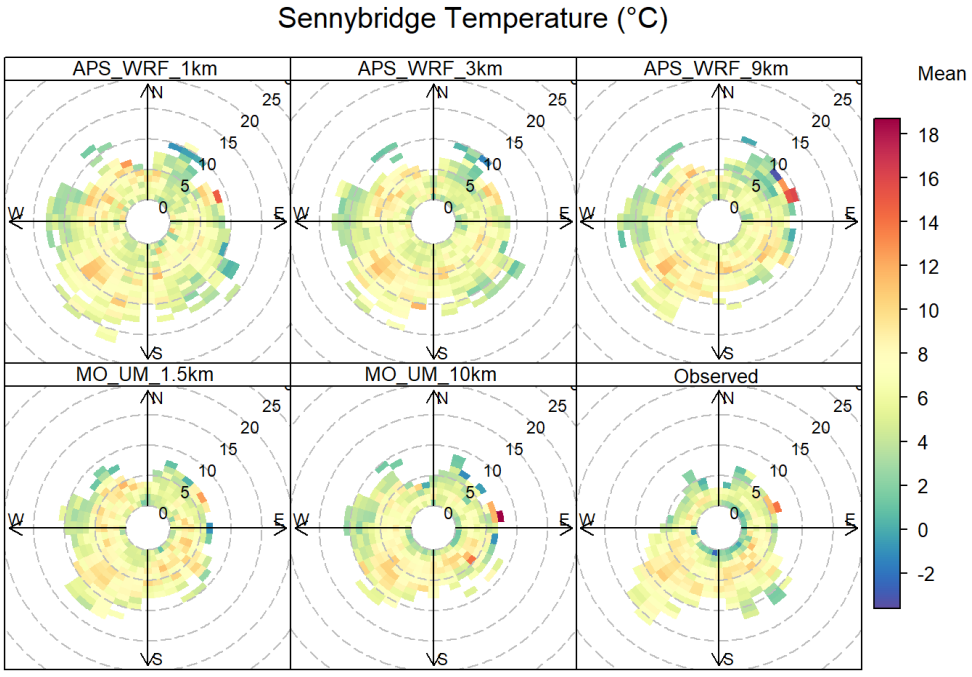

Figure 121 – Polar plots showing the average temperature (indicated by the colour scale) associated with variation of wind speed (radial scale) and wind direction at Sennybridge. Combinations of wind speed and direction which occur for fewer than 3 hours per year are not displayed.

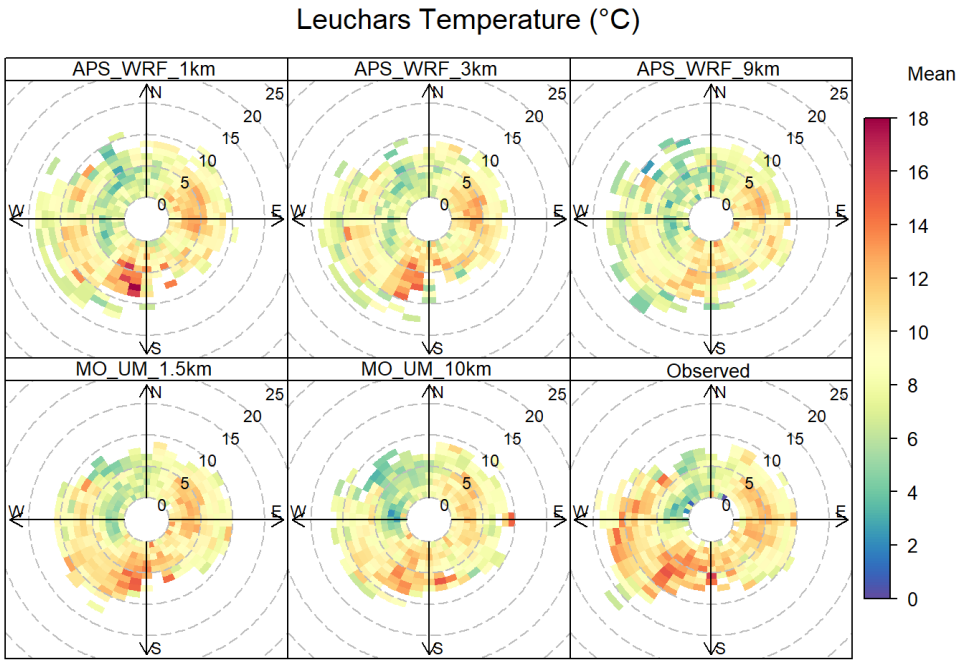

Figure 122 – Polar plots showing the average temperature (indicated by the colour scale) associated with variation of wind speed (radial scale) and wind direction at Leuchars. Combinations of wind speed and direction which occur for fewer than 3 hours per year are not displayed.

B1.4 Precipitation

This section gives per-site statistics and plots for hourly precipitation, supplementing the results over all sites included in Section 5.2.4.

Table 52 – Meteorological model performance evaluation of hourly precipitation (mm/h) by site.

Terrain type	Site	Model	Res. (km)	Observed Mean	MB	MGE	RMSE	R	IOA
					0	0	0	1	1
Flat	Waddington	APS_WRF	1	0.09	0.00	0.10	0.43	0.52	0.69
		APS_WRF	3		0.00	0.10	0.42	0.53	0.70
		APS_WRF	9		0.00	0.10	0.43	0.52	0.70
		MO_UM	1.5		0.04	0.11	0.42	0.62	0.68
		MO_UM	10		0.01	0.09	0.37	0.62	0.72
Urban	Northolt	APS_WRF	1	0.08	0.01	0.10	0.44	0.45	0.64
		APS_WRF	3		0.01	0.10	0.44	0.46	0.64
		APS_WRF	9		0.01	0.10	0.42	0.47	0.65
		MO_UM	1.5		0.03	0.09	0.38	0.59	0.66
		MO_UM	10		0.03	0.10	0.33	0.57	0.65
Complex	Drumalbin	APS_WRF	1	0.10	0.01	0.13	0.46	0.43	0.64
		APS_WRF	3		0.01	0.13	0.44	0.45	0.64
		APS_WRF	9		0.01	0.13	0.43	0.46	0.64
		MO_UM	1.5		0.06	0.15	0.51	0.49	0.59
		MO_UM	10		0.01	0.12	0.35	0.56	0.67
	Leek Thorncliffe	APS_WRF	1	0.11	0.07	0.17	0.59	0.42	0.54
		APS_WRF	3		0.06	0.17	0.56	0.45	0.56
		APS_WRF	9		0.04	0.15	0.51	0.47	0.60
		MO_UM	1.5		0.09	0.16	0.53	0.60	0.57
		MO_UM	10		0.06	0.15	0.42	0.57	0.61
	Sennybridge	APS_WRF	1	0.19	-0.03	0.19	0.58	0.56	0.70
		APS_WRF	3		-0.04	0.18	0.55	0.59	0.71
		APS_WRF	9		-0.03	0.18	0.52	0.62	0.71
		MO_UM	1.5		0.04	0.18	0.54	0.69	0.70
		MO_UM	10		-0.02	0.17	0.48	0.66	0.73
Coastal	Leuchars	APS_WRF	1	0.09	0.01	0.11	0.45	0.40	0.66
		APS_WRF	3		0.01	0.11	0.44	0.42	0.66
		APS_WRF	9		0.01	0.11	0.42	0.45	0.66
		MO_UM	1.5		0.03	0.11	0.41	0.56	0.66
		MO_UM	10		0.02	0.10	0.36	0.55	0.68
	Mumbles Head	APS_WRF	1	0.14	-0.02	0.14	0.55	0.48	0.70
		APS_WRF	3		-0.02	0.14	0.54	0.49	0.71
		APS_WRF	9		-0.02	0.14	0.51	0.53	0.72
		MO_UM	1.5		0.04	0.17	0.58	0.53	0.65
		MO_UM	10		0.04	0.16	0.47	0.60	0.67
	Newhaven	APS_WRF	1	0.09	0.00	0.10	0.45	0.43	0.66
		APS_WRF	3		0.01	0.11	0.46	0.42	0.65
		APS_WRF	9		0.00	0.10	0.46	0.45	0.67
		MO_UM	1.5		0.05	0.12	0.49	0.51	0.60
		MO_UM	10		0.07	0.14	0.46	0.49	0.56

Table 53 – Additional precipitation-specific summary statistics, by site.

Terrain type	Site	Model	Res. (km)	Observed washout factor	Modelled washout factor	Observed ZNUM	Modelled ZNUM
Flat	Waddington	APS_WRF	1	713	870	7925	6975
		APS_WRF	3		872		6942
		APS_WRF	9		892		6830
		MO_UM	1.5		1051		7206
		MO_UM	10		1042		6003
Urban	Northolt	APS_WRF	1	646	815	7923	7016
		APS_WRF	3		823		6972
		APS_WRF	9		835		6863
		MO_UM	1.5		932		7301
		MO_UM	10		1141		5706
Complex	Drumalbin	APS_WRF	1	922	1103	7472	6387
		APS_WRF	3		1121		6305
		APS_WRF	9		1143		6182
		MO_UM	1.5		1399		6394
		MO_UM	10		1305		4926
	Leek Thorncliffe	APS_WRF	1	855	1448	7725	6340
		APS_WRF	3		1396		6310
		APS_WRF	9		1315		6260
		MO_UM	1.5		1559		6536
		MO_UM	10		1685		4580
	Sennybridge	APS_WRF	1	1554	1405	6924	6294
		APS_WRF	3		1395		6156
		APS_WRF	9		1508		5862
		MO_UM	1.5		1781		6249
		MO_UM	10		1752		4348
Coastal	Leuchars	APS_WRF	1	740	902	7815	6818
		APS_WRF	3		923		6736
		APS_WRF	9		978		6539
		MO_UM	1.5		1024		7065
		MO_UM	10		1112		5836
	Mumbles Head	APS_WRF	1	1121	1089	7435	6647
		APS_WRF	3		1077		6590
		APS_WRF	9		1108		6467
		MO_UM	1.5		1439		6802
		MO_UM	10		1753		4760
	Newhaven	APS_WRF	1	712	833	7856	7032
		APS_WRF	3		862		6994
		APS_WRF	9		860		6900
		MO_UM	1.5		1056		7223
		MO_UM	10		1474		5545

Table 54 – Evaluation statistics of hourly precipitation (mm/h) between geographically paired measurement sites, using observed data at both sites.

Observed terrain	Observed site	Substitute site	Distance (km)	Obs. mean	MB	MGE	RMSE	R	IOA
					0	0	0	1	1
Complex	Leek Thorncliffe	Waddington	98	0.11	-0.02	0.15	0.59	0.19	0.61
Flat	Waddington	Leek Thorncliffe	98	0.09	0.02	0.15	0.59	0.19	0.55
Complex	Drumalbin	Leuchars	100	0.10	-0.02	0.14	0.52	0.20	0.59
Coastal	Leuchars	Drumalbin	100	0.09	0.02	0.14	0.52	0.20	0.54
Complex	Sennybridge	Mumbles Head	61	0.20	-0.05	0.21	0.67	0.39	0.66
Coastal	Mumbles Head	Sennybridge	61	0.14	0.05	0.21	0.67	0.39	0.56
Coastal	St Athan	Mumbles Head	42	0.14	0.00	0.16	0.58	0.47	0.67
Coastal	Mumbles Head	St Athan	42	0.14	0.00	0.16	0.58	0.47	0.66

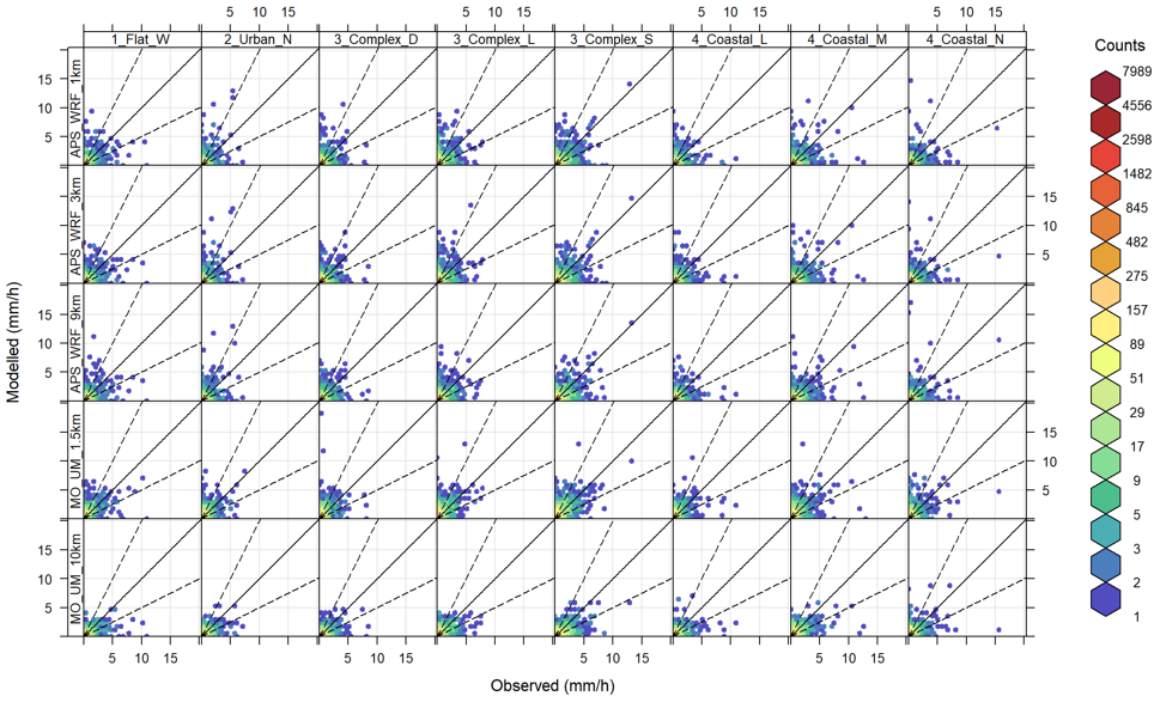

Figure 123 – Frequency scatter plots of modelled and observed hourly precipitation (mm/h) at each site. Colours indicate the number of data points in each area of the plot.

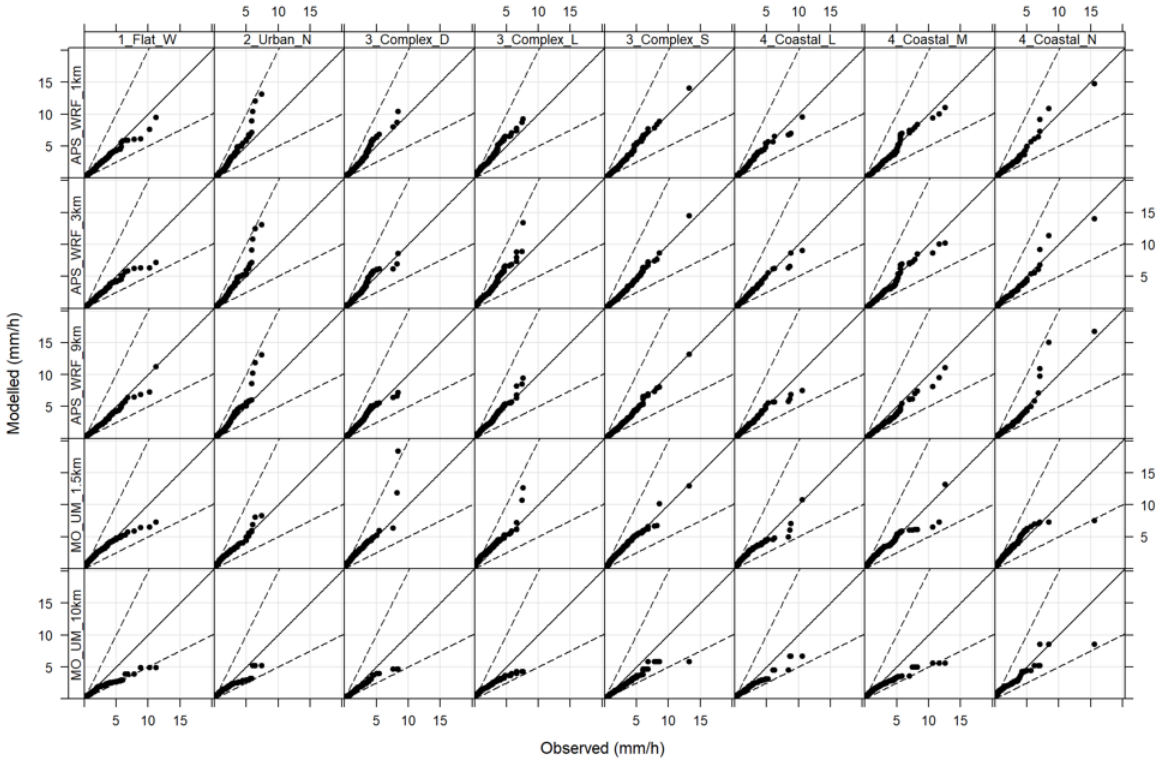

Figure 124 – Quantile-quantile plots of modelled and observed hourly precipitation (mm/h) at each site, ordered independently.

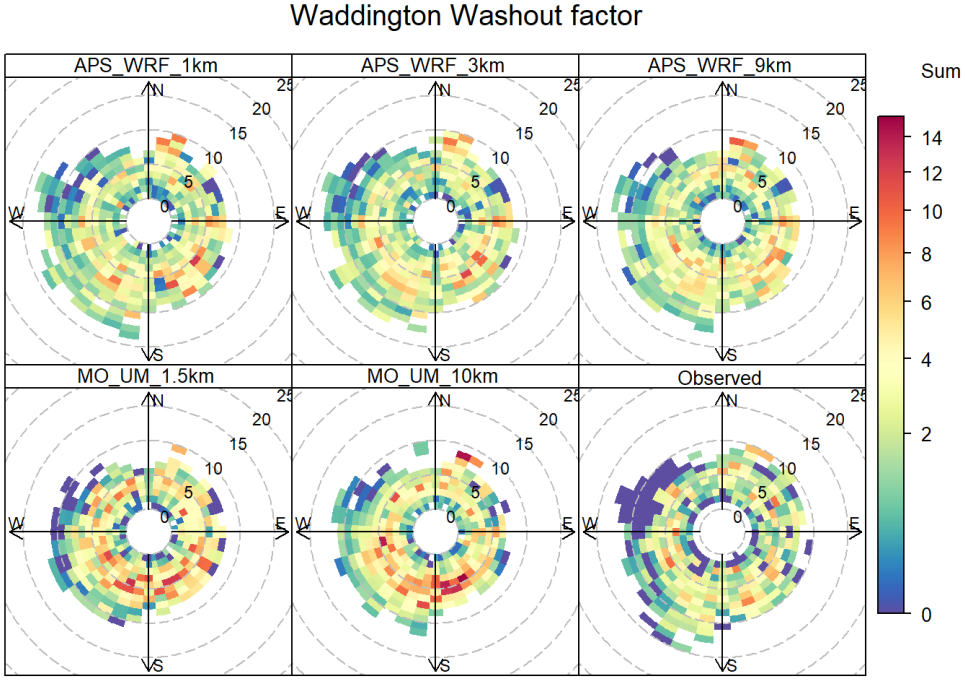

Figure 125 – Polar plots showing the total washout factor (indicated by the colour scale) associated with variation of wind speed (radial scale) and wind direction at Waddington. Combinations of wind speed and direction which occur for fewer than 3 hours per year are not displayed. Observed washout values are plotted with observed wind speed and direction while modelled washout values are plotted with the associated modelled wind data.

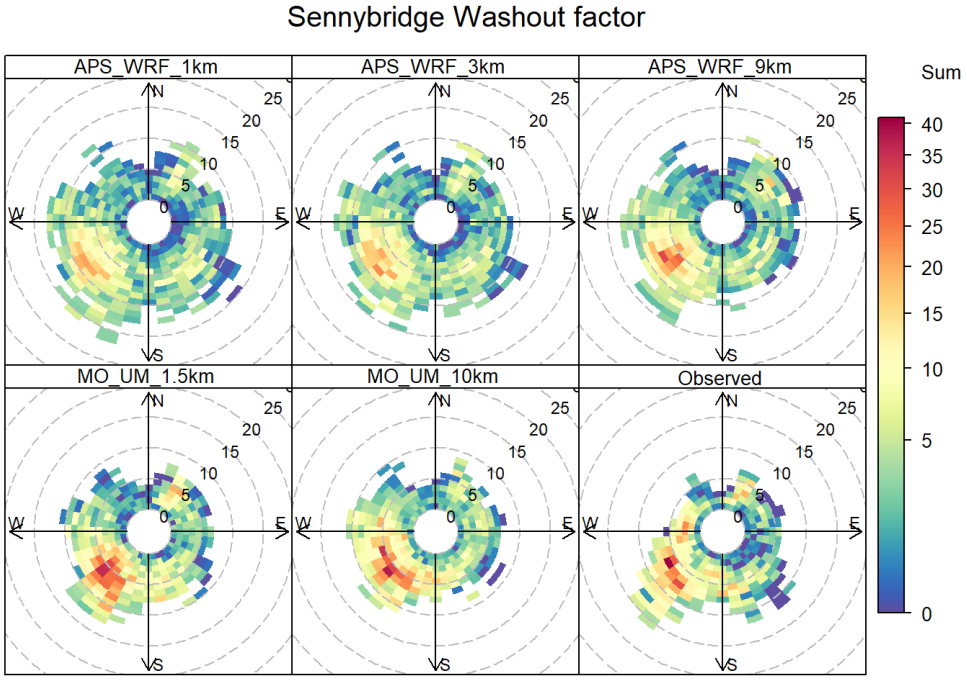

Figure 126 – Polar plots showing the total washout factor (indicated by the colour scale) associated with variation of wind speed (radial scale) and wind direction at Sennybridge. Combinations of wind speed and direction which occur for fewer than 3 hours per year are not displayed.

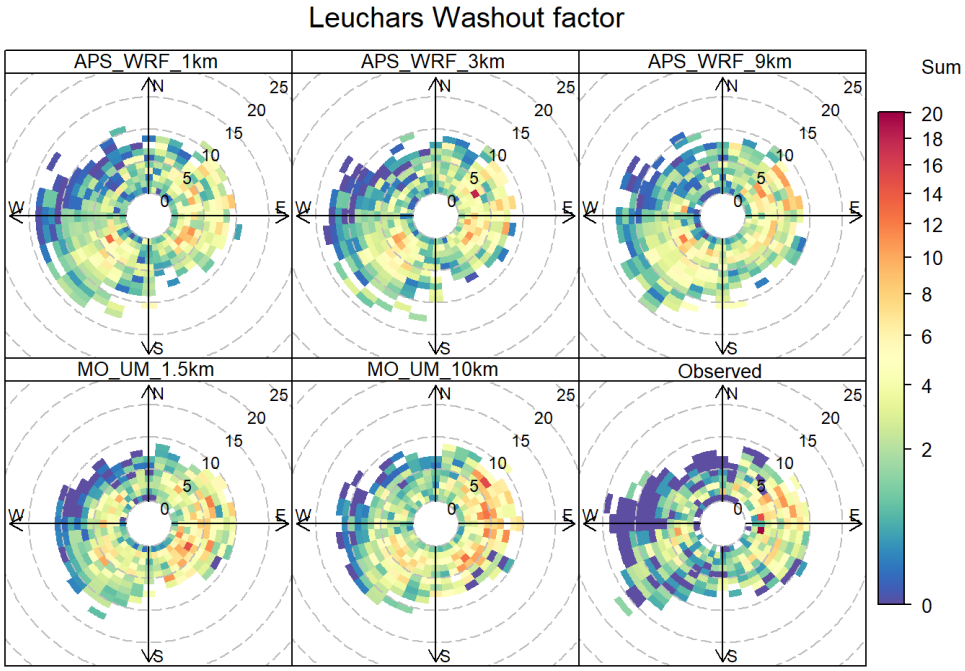

Figure 127 – Polar plots showing the total washout factor (indicated by the colour scale) associated with variation of wind speed (radial scale) and wind direction at Leuchars. Combinations of wind speed and direction which occur for fewer than 3 hours per year are not displayed.

B1.5 Cloud Cover

This section gives per-site statistics and plots for cloud cover, supplementing the results over all sites included in Section 5.2.5.

Table 55 – Meteorological model performance evaluation of cloud cover by site.

Terrain type	Site	Model	Res. (km)	Observed Mean	MB	MGE	RMSE	FRAC1	R	IOA
					0	0	0	1	1	1
Flat	Waddington	APS_WRF	1	5.15	-0.08	1.74	2.49	0.58	0.60	0.66
		APS_WRF	3		-0.14	1.73	2.48	0.57	0.61	0.66
		APS_WRF	9		-0.19	1.72	2.46	0.58	0.61	0.67
		MO_UM	1.5		-0.08	1.53	2.30	0.56	0.67	0.70
		MO_UM	10		0.14	1.72	2.52	0.53	0.60	0.66
Urban	Northolt	APS_WRF	1	5.29	-0.24	1.71	2.47	0.58	0.63	0.67
		APS_WRF	3		-0.27	1.71	2.46	0.58	0.63	0.67
		APS_WRF	9		-0.32	1.71	2.46	0.58	0.63	0.67
		MO_UM	1.5		-0.24	1.51	2.26	0.57	0.69	0.71
		MO_UM	10		0.02	1.54	2.30	0.56	0.67	0.70
Complex	Drumalbin	APS_WRF	1	5.51	-0.07	1.76	2.60	0.58	0.60	0.68
		APS_WRF	3		-0.10	1.77	2.60	0.58	0.60	0.68
		APS_WRF	9		-0.16	1.77	2.57	0.58	0.61	0.68
		MO_UM	1.5		0.05	1.62	2.49	0.56	0.64	0.70
		MO_UM	10		0.16	1.97	2.86	0.49	0.50	0.64
	Leek Thorncliffe	APS_WRF	1	5.68	-0.35	1.77	2.65	0.59	0.60	0.67
		APS_WRF	3		-0.31	1.71	2.56	0.60	0.62	0.68
		APS_WRF	9		-0.36	1.68	2.49	0.60	0.64	0.69
		MO_UM	1.5		-0.12	1.54	2.44	0.58	0.66	0.71
		MO_UM	10		0.04	1.88	2.81	0.52	0.52	0.65
	Sennybridge	APS_WRF	1	5.99	-0.88	1.95	2.86	0.55	0.54	0.60
		APS_WRF	3		-0.85	1.88	2.77	0.57	0.57	0.61
		APS_WRF	9		-0.84	1.83	2.69	0.57	0.59	0.63
		MO_UM	1.5		-0.42	1.53	2.38	0.56	0.66	0.69
		MO_UM	10		-0.22	1.79	2.71	0.53	0.52	0.63
Coastal	Leuchars	APS_WRF	1	5.27	-0.13	1.83	2.66	0.56	0.61	0.68
		APS_WRF	3		-0.17	1.82	2.65	0.56	0.61	0.68
		APS_WRF	9		-0.25	1.88	2.68	0.55	0.60	0.67
		MO_UM	1.5		-0.16	1.75	2.64	0.52	0.62	0.70
		MO_UM	10		0.08	1.99	2.89	0.48	0.53	0.65
	Mumbles Head	APS_WRF	1	5.00	0.32	1.81	2.66	0.57	0.62	0.70
		APS_WRF	3		0.29	1.82	2.65	0.57	0.62	0.70
		APS_WRF	9		0.22	1.81	2.63	0.57	0.63	0.70
		MO_UM	1.5		0.13	1.97	2.89	0.49	0.56	0.67
		MO_UM	10		0.33	2.33	3.29	0.44	0.41	0.61
	Newhaven	APS_WRF	1	5.01	-0.28	1.77	2.62	0.57	0.66	0.71
		APS_WRF	3		-0.28	1.78	2.62	0.57	0.66	0.71
		APS_WRF	9		-0.34	1.78	2.61	0.57	0.67	0.71
		MO_UM	1.5		-0.21	1.74	2.61	0.53	0.67	0.72
		MO_UM	10		0.14	2.00	2.94	0.49	0.56	0.68

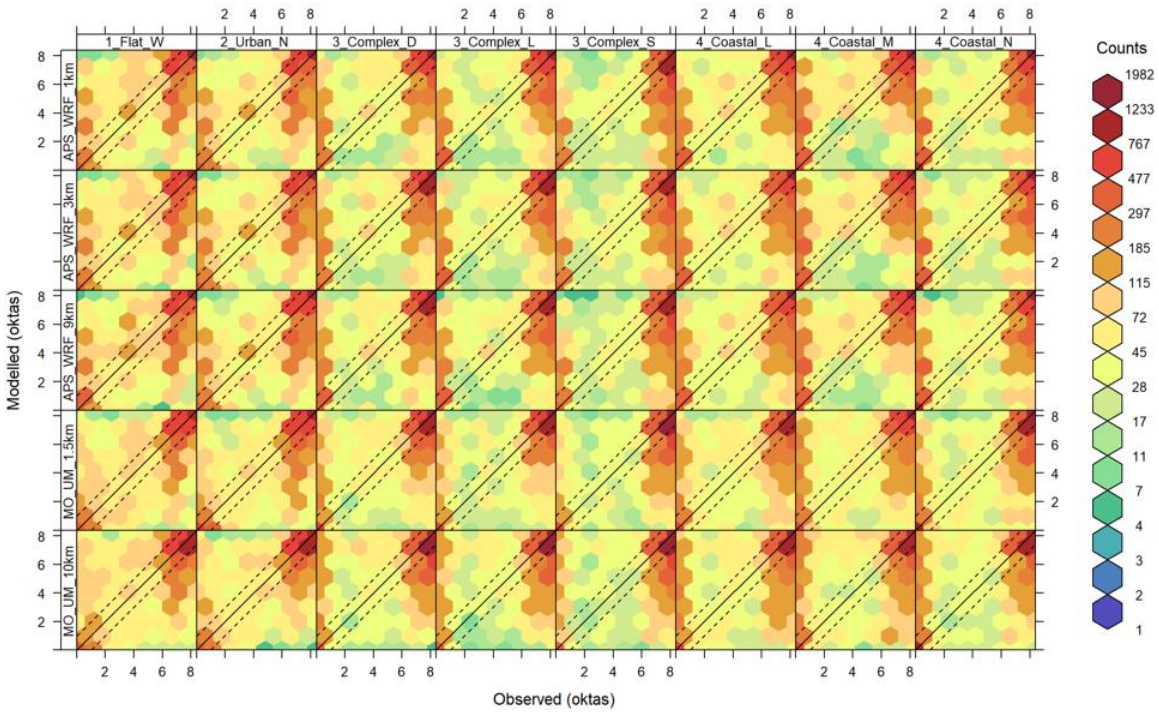

Figure 128 – Frequency scatter plots of modelled and observed cloud cover (oktas) at each site. Colours indicate the number of data points in each area of the plot. Dashed lines indicate values within ±1 okta.

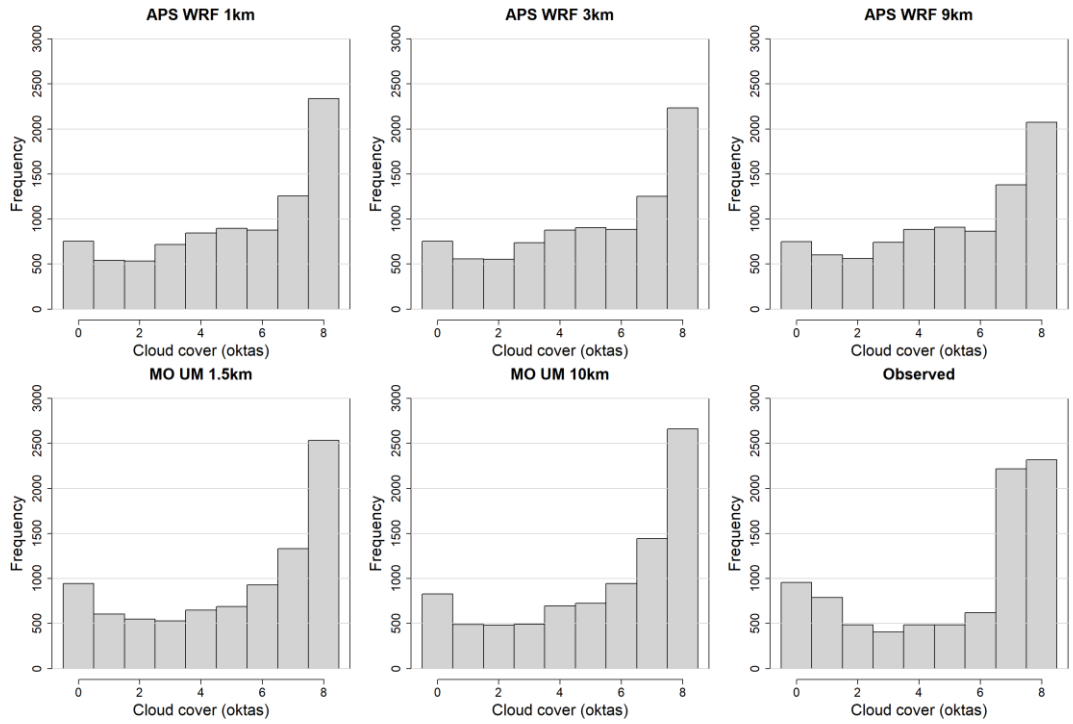

Figure 129 – Histogram charts of modelled and observed cloud cover (oktas) at Waddington (flat terrain site).

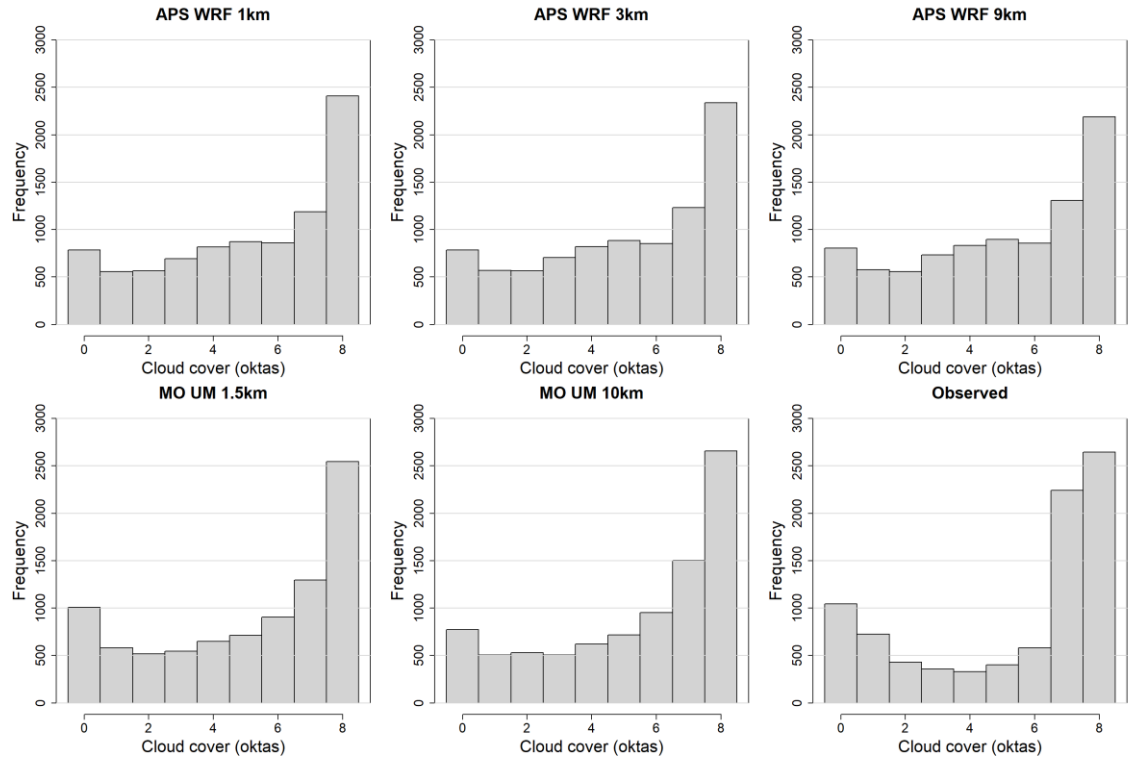

Figure 130 – Histogram charts of modelled and observed cloud cover (oktas) at Northolt (urban site).

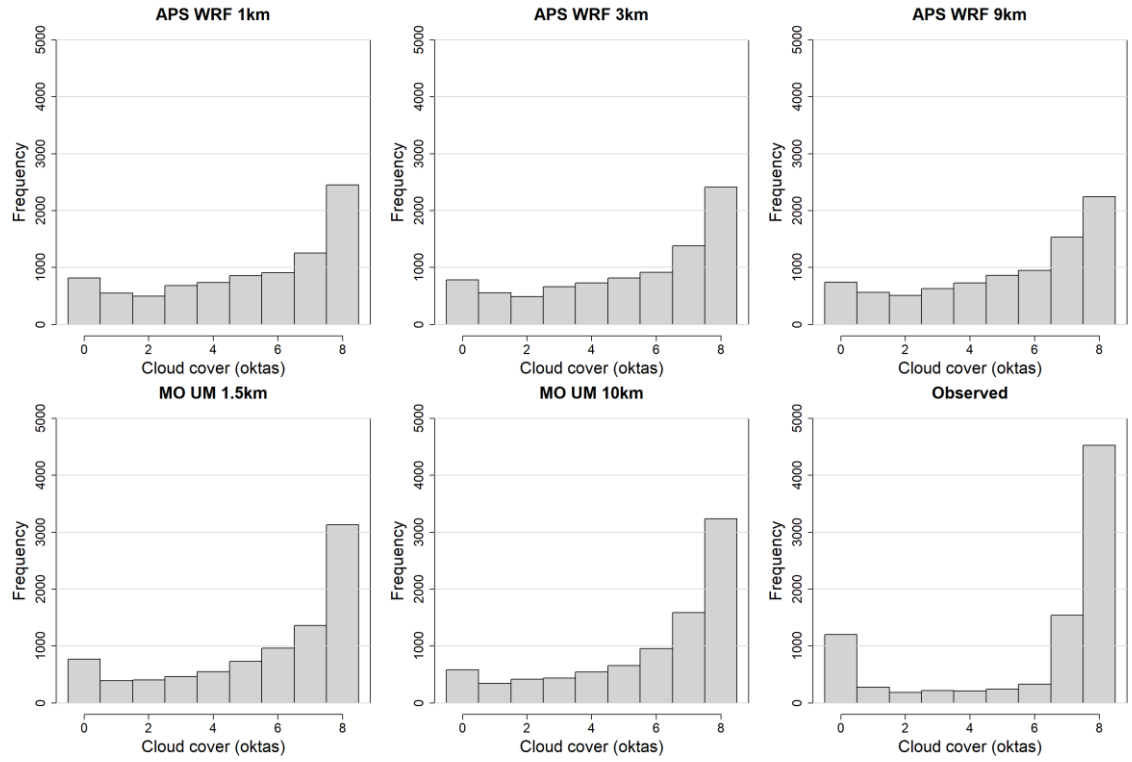

Figure 131 – Histogram charts of modelled and observed cloud cover (oktas) at Sennybridge (complex terrain site).

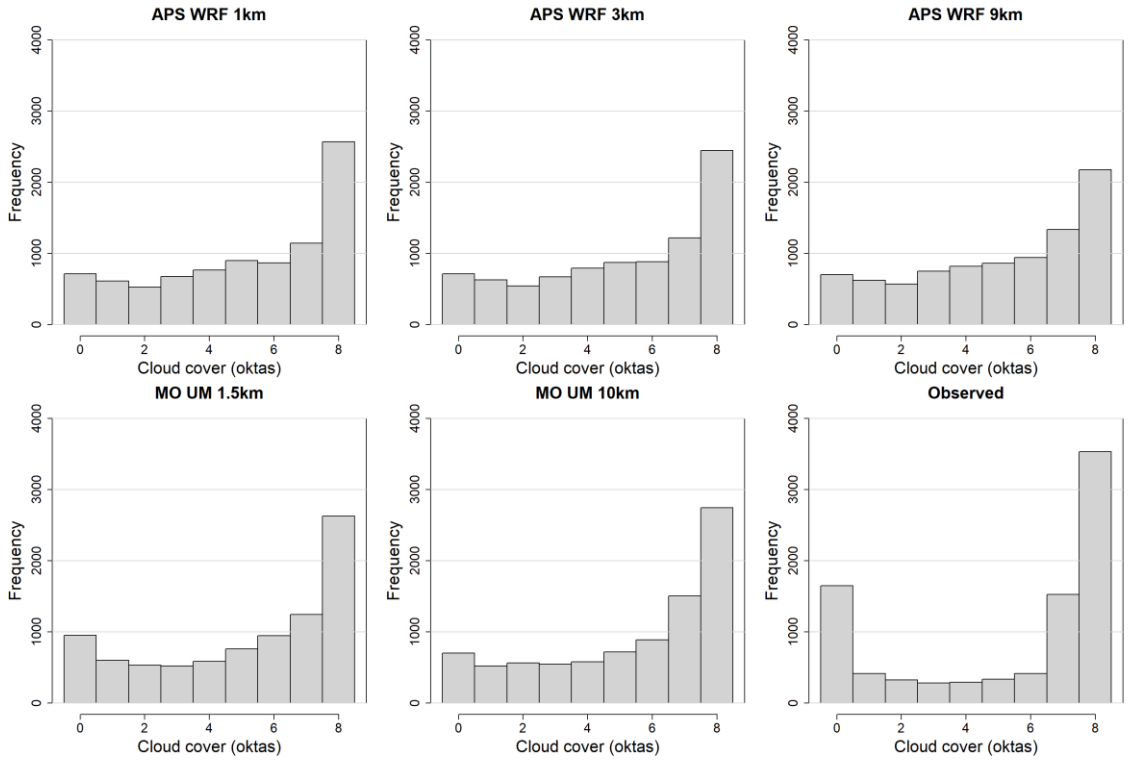

Figure 132 – Histogram charts of modelled and observed cloud cover (oktas) at Leuchars (coastal site).

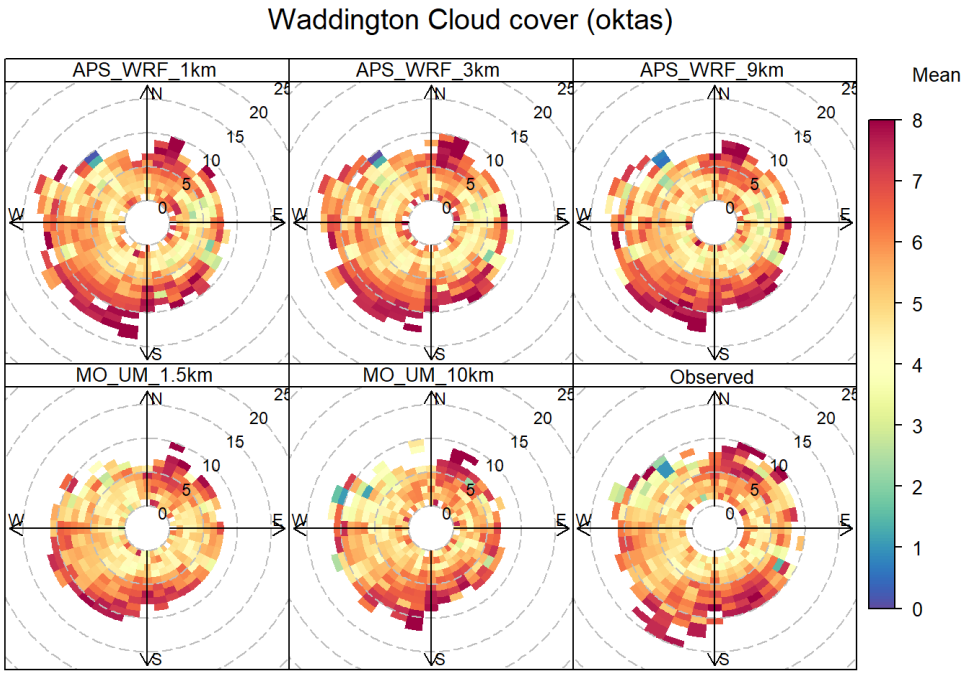

Figure 133 – Polar plots showing the mean cloud cover (indicated by the colour scale) associated with variation of wind speed (radial scale) and wind direction at Waddington. Combinations of wind speed and direction which occur for fewer than 3 hours per year are not displayed. Observed cloud cover values are plotted with observed wind speed and direction while modelled cloud cover values are plotted with the associated modelled wind data.

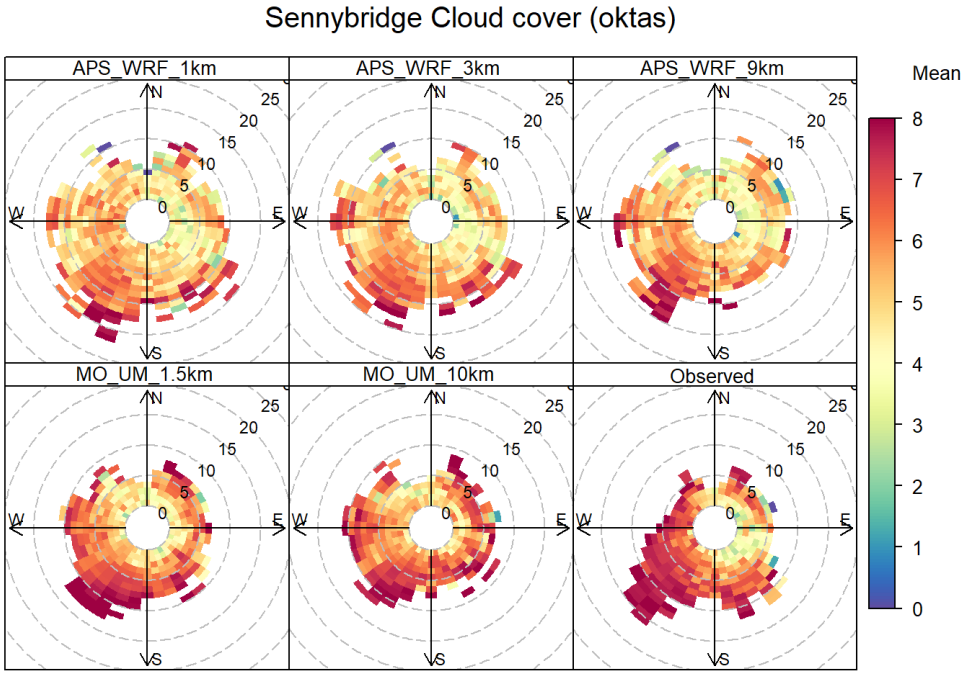

Figure 134 – Polar plots showing the mean cloud cover (indicated by the colour scale) associated with variation of wind speed (radial scale) and wind direction at Sennybridge. Combinations of wind speed and direction which occur for fewer than 3 hours per year are not displayed.

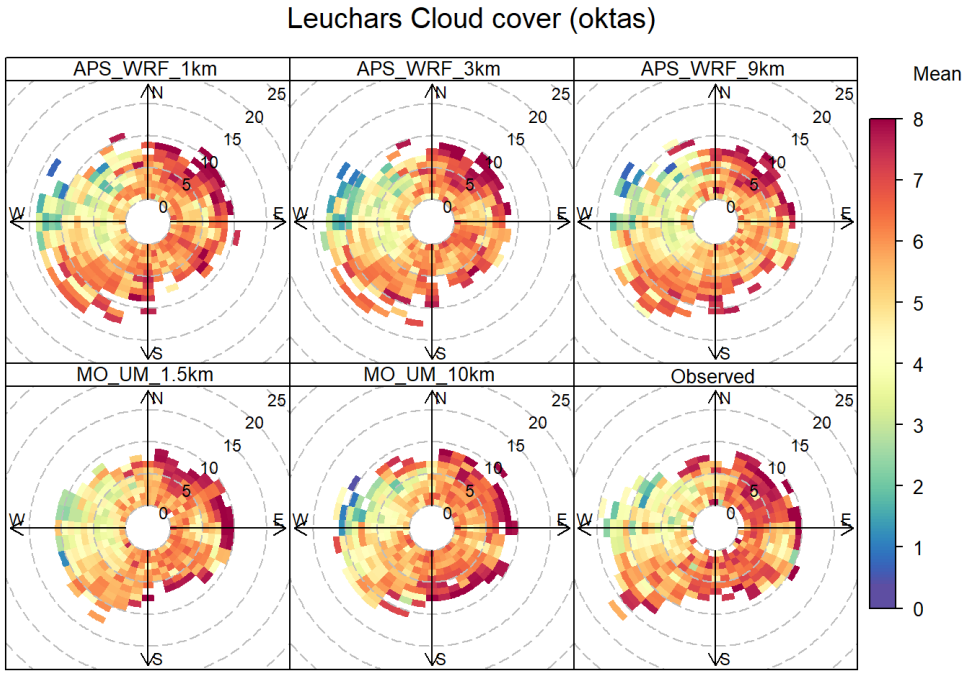

Figure 135 – Polar plots showing the mean cloud cover (indicated by the colour scale) associated with variation of wind speed (radial scale) and wind direction at Leuchars. Combinations of wind speed and direction which occur for fewer than 3 hours per year are not displayed.

B2 WRF configuration evaluation

Supplementary statistics and plots included in this section expand the evaluation of the relative importance of WRF configuration and resolution presented in Section 5.3.

B2.1 Wind speed

This section gives per-site statistics and plots for 10 m wind speed, supplementing the results over all sites included in Section 5.3.1.

Table 56 – Meteorological model performance evaluation of wind speed at 10 m by site, for the WRF models.

Terrain type	Site	Model	Res. (km)	Observed Mean	MB	MGE	RMSE	R	IOA
					0	0	0	1	1
Flat	Waddington	APS_WRF	1	4.84	-0.15	0.84	1.10	0.88	0.76
		APS_WRF	3		-0.14	0.84	1.10	0.88	0.76
		APS_WRF	9		-0.53	0.96	1.22	0.88	0.73
		Lakes_WRF	3		-0.04	0.92	1.20	0.86	0.74
Urban	Northolt	APS_WRF	1	3.80	-0.03	0.79	1.02	0.89	0.78
		APS_WRF	3		-0.18	0.78	1.01	0.90	0.78
		APS_WRF	9		-0.31	0.79	1.02	0.90	0.78
		Lakes_WRF	3		-0.16	0.87	1.13	0.87	0.76
Complex	Sennybridge	APS_WRF	1	3.47	1.46	1.73	2.29	0.77	0.56
		APS_WRF	3		1.12	1.55	2.07	0.76	0.61
		APS_WRF	9		0.76	1.47	1.96	0.72	0.63
		Lakes_WRF	3		1.79	1.98	2.52	0.77	0.50
Coastal	Leuchars	APS_WRF	1	4.69	-0.11	1.18	1.53	0.84	0.73
		APS_WRF	3		-0.31	1.19	1.53	0.84	0.73
		APS_WRF	9		-0.10	1.14	1.47	0.85	0.74
		Lakes_WRF	3		-0.31	1.31	1.70	0.80	0.70

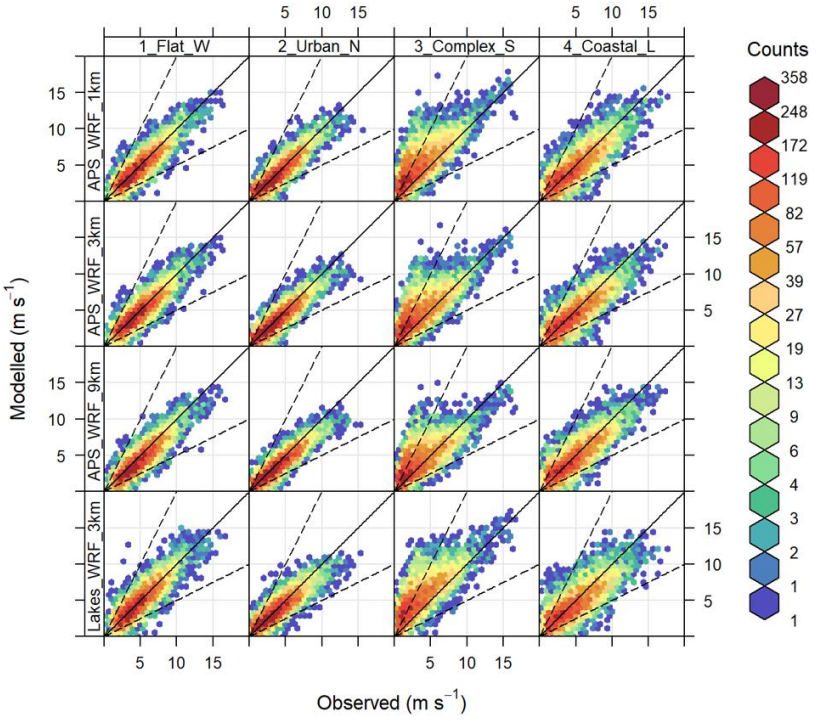

Figure 136 – Frequency scatter plots of modelled and observed wind speed (m/s) at each site. Colours indicate the number of data points in each area of the plot. These plots use reduced axis extents compared to the equivalent plots in Sections 5.2.1 and B1.1, due to the exclusion of coastal sites with the highest observed values. Dashed lines indicate factor of two relationships between modelled and observed wind speed.

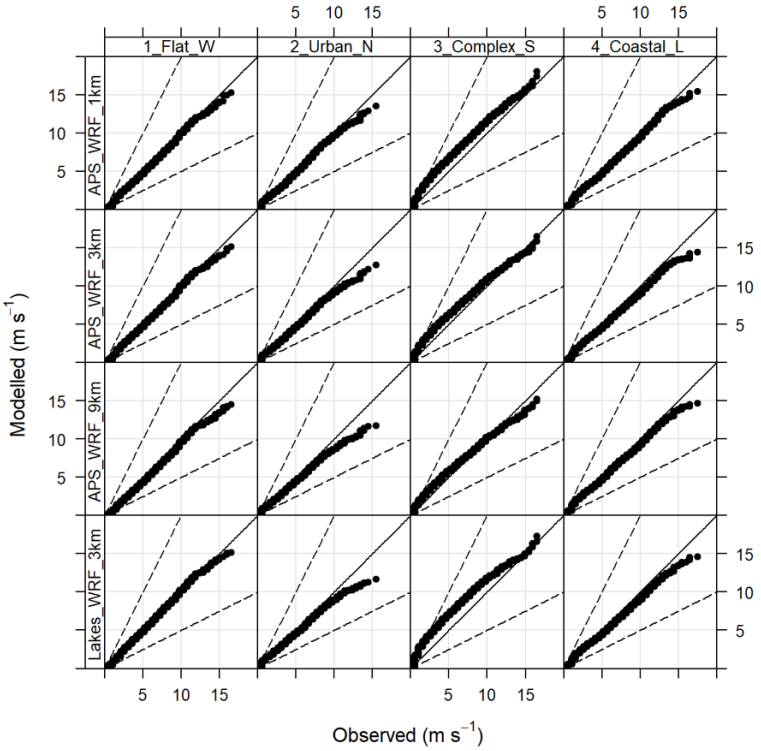

Figure 137 – Quantile-quantile plots of modelled and observed wind speed (m/s) at each site, ordered independently.

B2.2 Wind direction

This section gives per-site statistics and plots for 10 m wind direction, supplementing the results over all sites included in Section 5.3.2.

Table 57 – Meteorological model performance evaluation of wind direction at 10 m by site, for the WRF models. All wind speeds included in the evaluation.

Terrain type	Site	Model	Res. (km)	Observed Mean	Modelled Mean	MB	MGE
						0	0
Flat	Waddington	APS_WRF	1	231	224	-0.82	17.90
		APS_WRF	3		228	0.01	17.17
		APS_WRF	9		221	-3.47	18.60
		Lakes_WRF	3		224	2.04	18.20
Urban	Northolt	APS_WRF	1	255	249	-6.22	23.86
		APS_WRF	3		249	-5.90	23.62
		APS_WRF	9		245	-6.11	23.26
		Lakes_WRF	3		239	-3.88	22.97
Complex	Sennybridge	APS_WRF	1	233	212	-0.97	25.87
		APS_WRF	3		222	-0.73	25.69
		APS_WRF	9		231	0.66	26.17
		Lakes_WRF	3		220	2.73	27.77
Coastal	Leuchars	APS_WRF	1	259	240	-12.20	27.38
		APS_WRF	3		237	-13.47	28.34
		APS_WRF	9		229	-11.00	28.30
		Lakes_WRF	3		231	-10.30	28.99

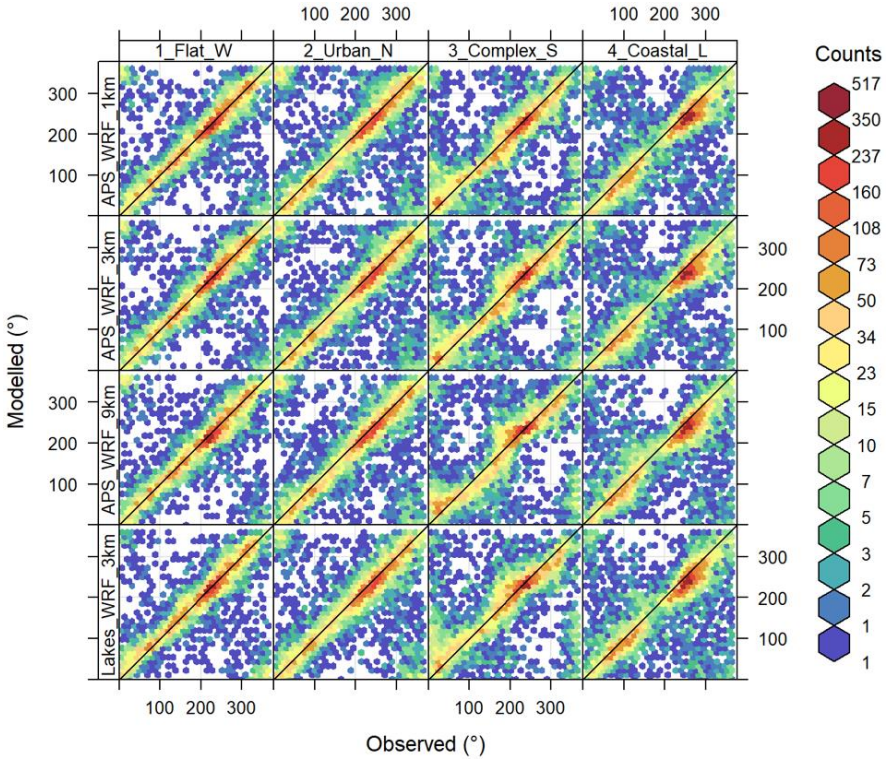

Figure 138 – Frequency scatter plots of modelled and observed wind direction (°) at each site. Colours indicate the number of data points in each area of the plot. Wind directions at all wind speeds are included.

Table 58 – Meteorological model performance evaluation of wind direction at 10 m by site, for the WRF models. Wind directions at wind speeds under 1.5 m/s have been filtered out of the evaluation.

Terrain type	Site	Model	Res. (km)	% Hours Filtered	Observed Mean	Modelled Mean	MB	MGE
							0	0
Flat	Waddington	APS_WRF	1	1.6	232	224	-0.77	17.20
		APS_WRF	3			229	0.04	16.50
		APS_WRF	9			221	-3.48	17.92
		Lakes_WRF	3			224	1.91	17.54
Urban	Northolt	APS_WRF	1	12.4	250	247	-8.28	19.73
		APS_WRF	3			246	-8.28	19.41
		APS_WRF	9			245	-8.48	19.03
		Lakes_WRF	3			239	-5.90	18.35
Complex	Sennybridge	APS_WRF	1	18.8	225	211	-2.33	19.03
		APS_WRF	3			217	-1.71	18.76
		APS_WRF	9			224	-0.56	19.00
		Lakes_WRF	3			218	1.14	20.10
Coastal	Leuchars	APS_WRF	1	7.4	255	239	-12.52	24.47
		APS_WRF	3			236	-13.54	25.38
		APS_WRF	9			231	-11.13	24.45
		Lakes_WRF	3			232	-10.96	25.77

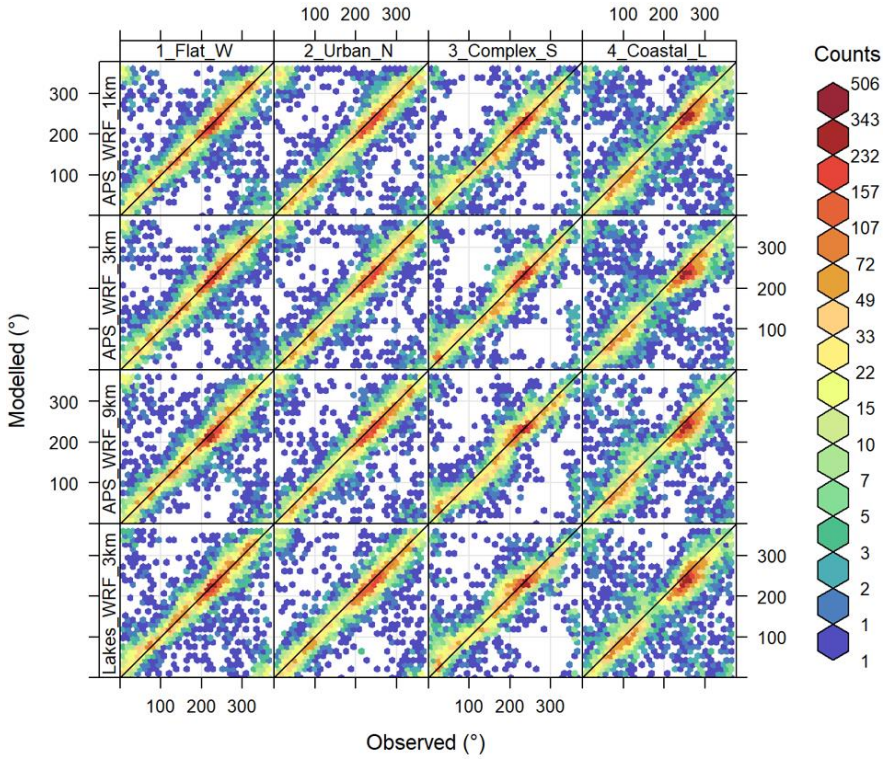

Figure 139 – Frequency scatter plots of modelled and observed wind direction (°) at each site. Colours indicate the number of data points in each area of the plot. Wind directions at wind speeds under 1.5 m/s have been filtered out of the evaluation.

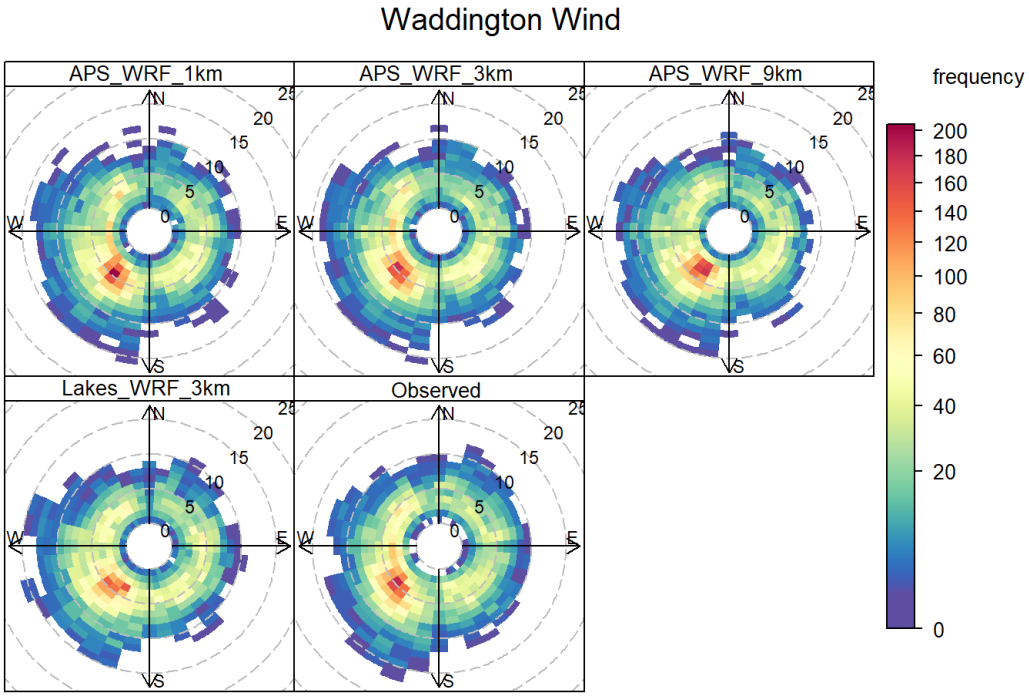

Figure 140 – Polar frequency plots showing the distribution of wind speed and direction at Waddington (flat terrain), colours indicate the number of hours with each combination of 10° wind direction and 1 m/s wind speed bins.

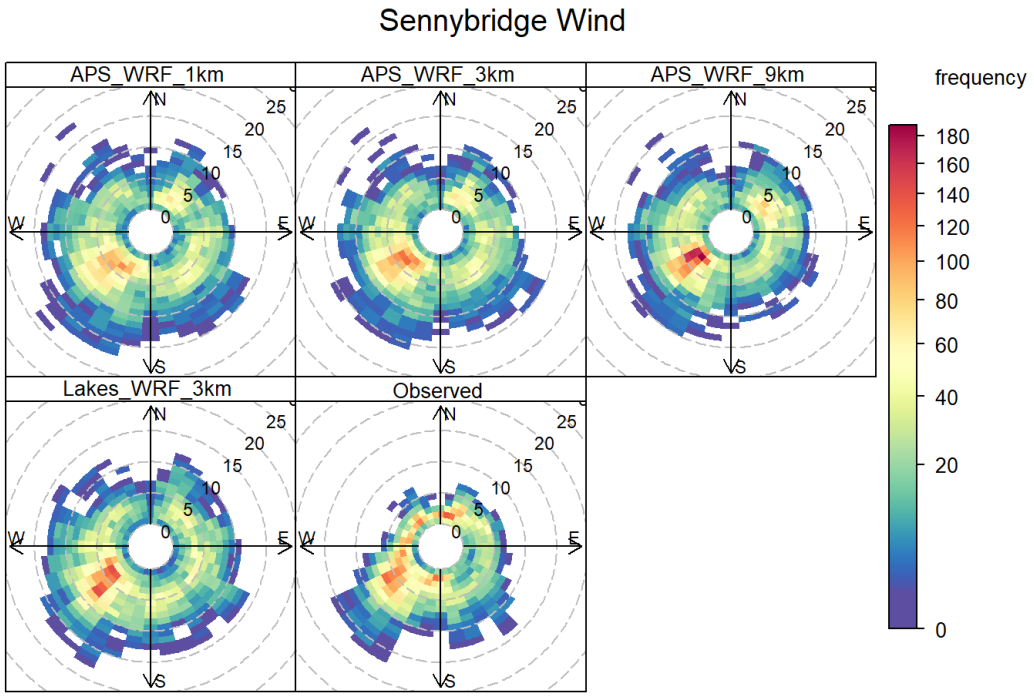

Figure 141 – Polar frequency plots showing the distribution of wind speed and direction at Sennybridge (complex terrain), colours indicate the number of hours with each combination of 10° wind direction and 1 m/s wind speed bins.

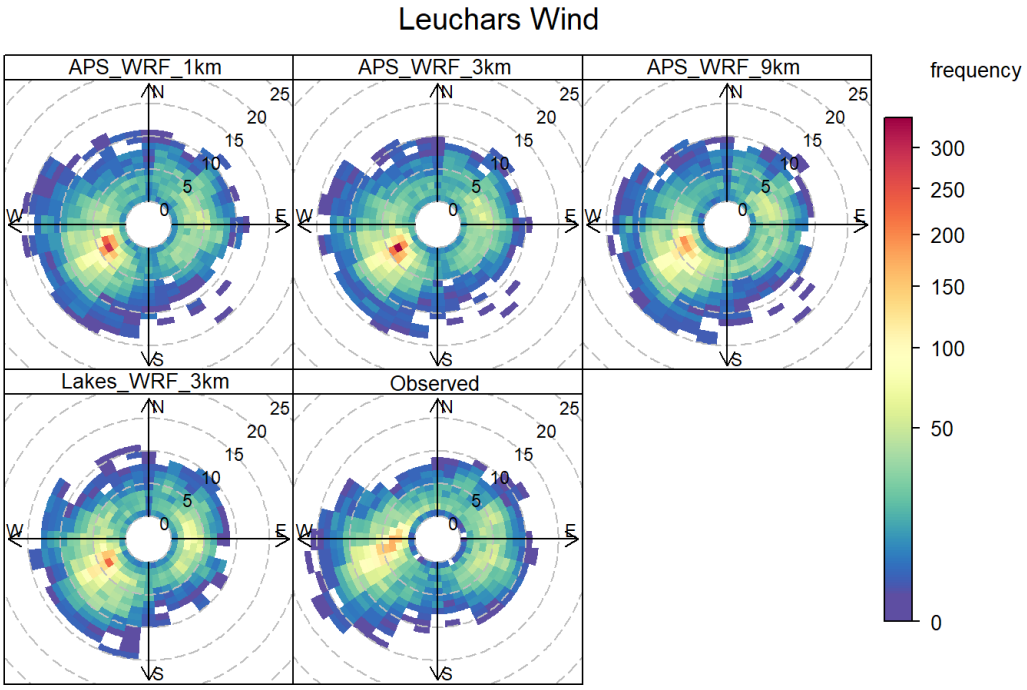

Figure 142 – Polar frequency plots showing the distribution of wind speed and direction at Leuchars (coastal), colours indicate the number of hours with each combination of 10° wind direction and 1 m/s wind speed bins.

B2.3 Temperature

This section gives per-site statistics and plots for screen height temperature, supplementing the results over all sites included in Section 5.3.3.

Table 59 – Meteorological model performance evaluation of temperature by site, for the WRF models.

Terrain type	Site	Model	Res. (km)	Observed Mean	MB	MGE	RMSE	R	IOA
					0	0	0	1	1
Flat	Waddington	APS_WRF	1	10.37	-0.99	1.42	1.78	0.97	0.85
		APS_WRF	3		-0.97	1.40	1.74	0.97	0.85
		APS_WRF	9		-0.85	1.40	1.80	0.97	0.85
		Lakes_WRF	3		-0.46	1.19	1.58	0.97	0.87
Urban	Northolt	APS_WRF	1	11.44	-0.58	1.43	1.89	0.96	0.86
		APS_WRF	3		-0.13	1.34	1.81	0.96	0.87
		APS_WRF	9		0.19	1.36	1.83	0.96	0.86
		Lakes_WRF	3		0.44	1.21	1.65	0.97	0.88
Complex	Sennybridge	APS_WRF	1	8.72	-0.18	1.32	1.74	0.95	0.85
		APS_WRF	3		-0.10	1.28	1.69	0.95	0.85
		APS_WRF	9		0.03	1.25	1.69	0.95	0.85
		Lakes_WRF	3		0.06	1.05	1.44	0.96	0.88
Coastal	Leuchars	APS_WRF	1	9.20	-0.51	1.27	1.62	0.96	0.85
		APS_WRF	3		-0.40	1.19	1.53	0.96	0.86
		APS_WRF	9		-0.74	1.38	1.70	0.96	0.84
		Lakes_WRF	3		-0.20	1.06	1.40	0.97	0.87

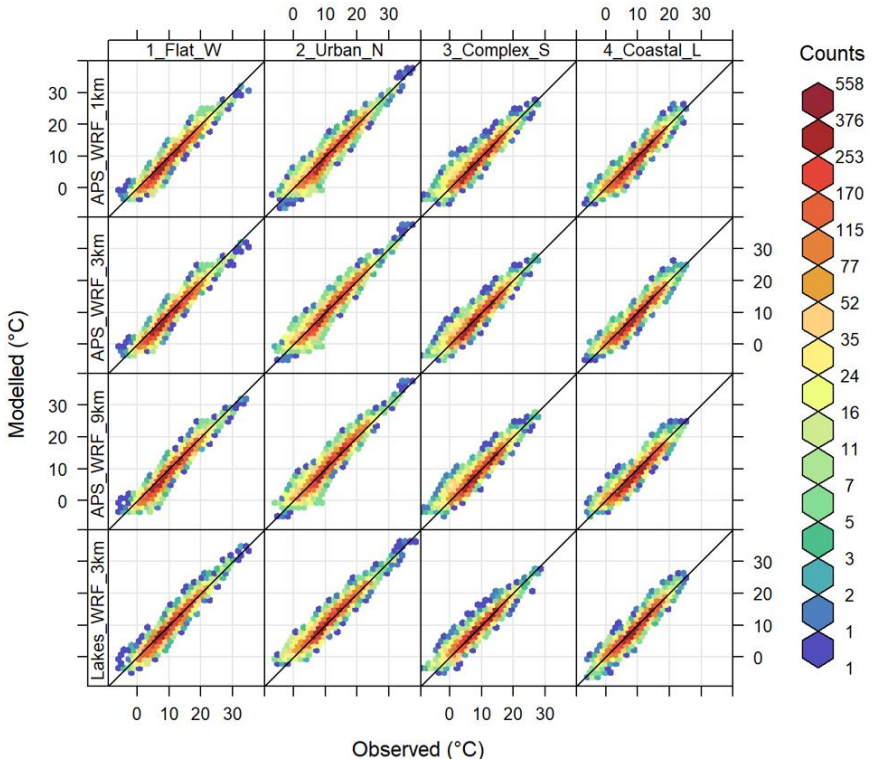

Figure 143 – Frequency scatter plots of modelled and observed temperature (°C) at each site. Colours indicate the number of data points in each area of the plot.

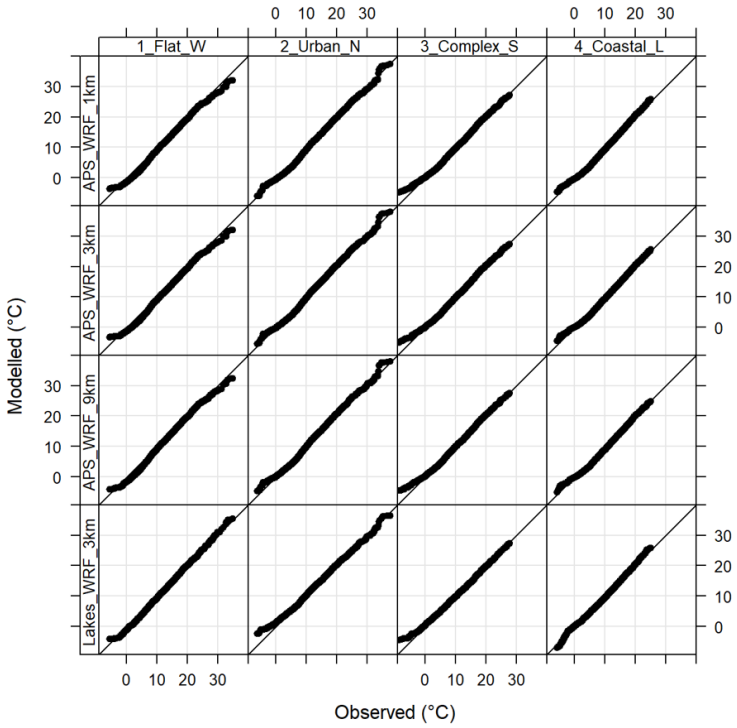

Figure 144 – Quantile-quantile plots of modelled and observed temperature (°C) at each site, ordered independently.

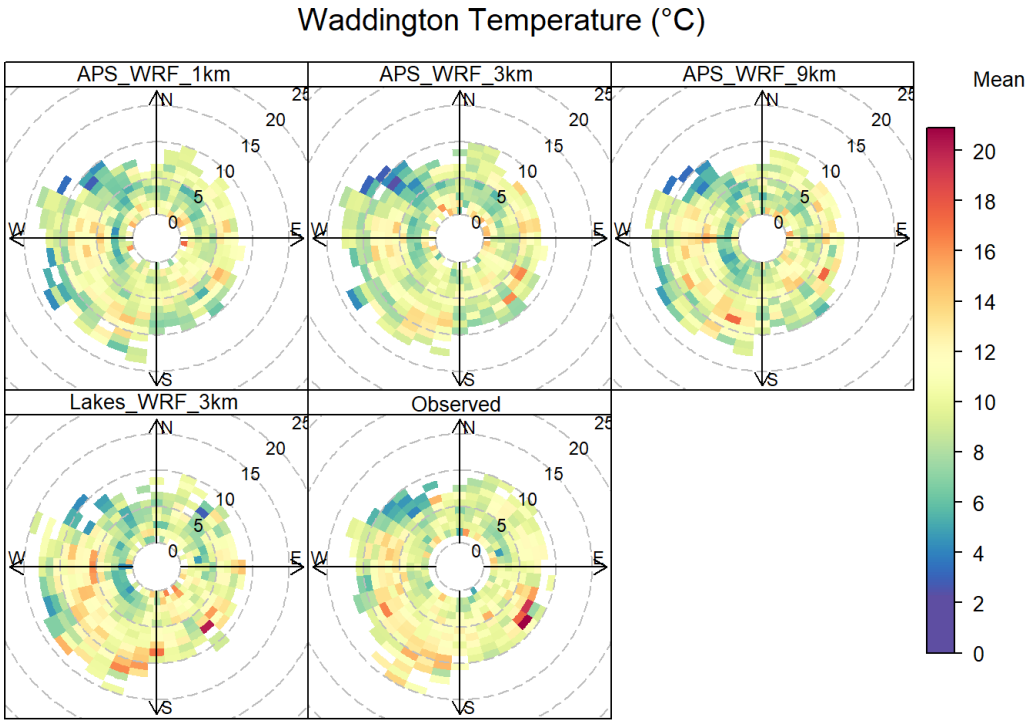

Figure 145 – Polar plots showing the mean temperature (indicated by the colour scale) associated with variation of wind speed (radial scale) and wind direction at Waddington. Combinations of wind speed and direction which occur for fewer than 3 hours per year are not displayed. Observed temperature values are plotted with observed wind speed and direction while modelled temperature values are plotted with the associated modelled wind data.

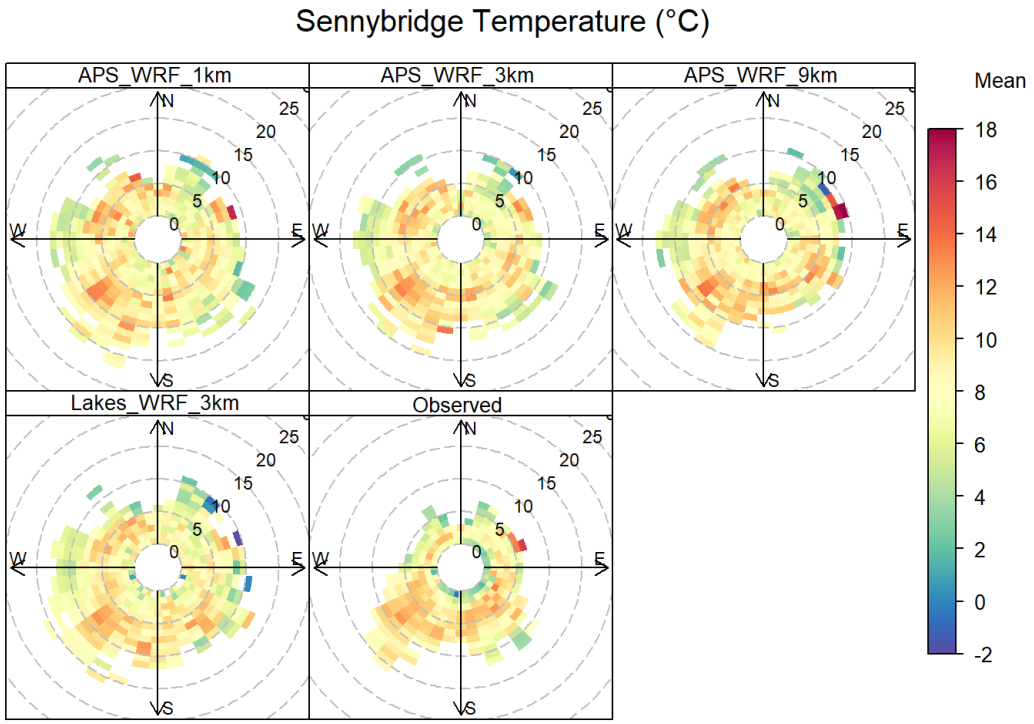

Figure 146 – Polar plots showing the mean temperature (indicated by the colour scale) associated with variation of wind speed (radial scale) and wind direction at Sennybridge. Combinations of wind speed and direction which occur for fewer than 3 hours per year are not displayed.

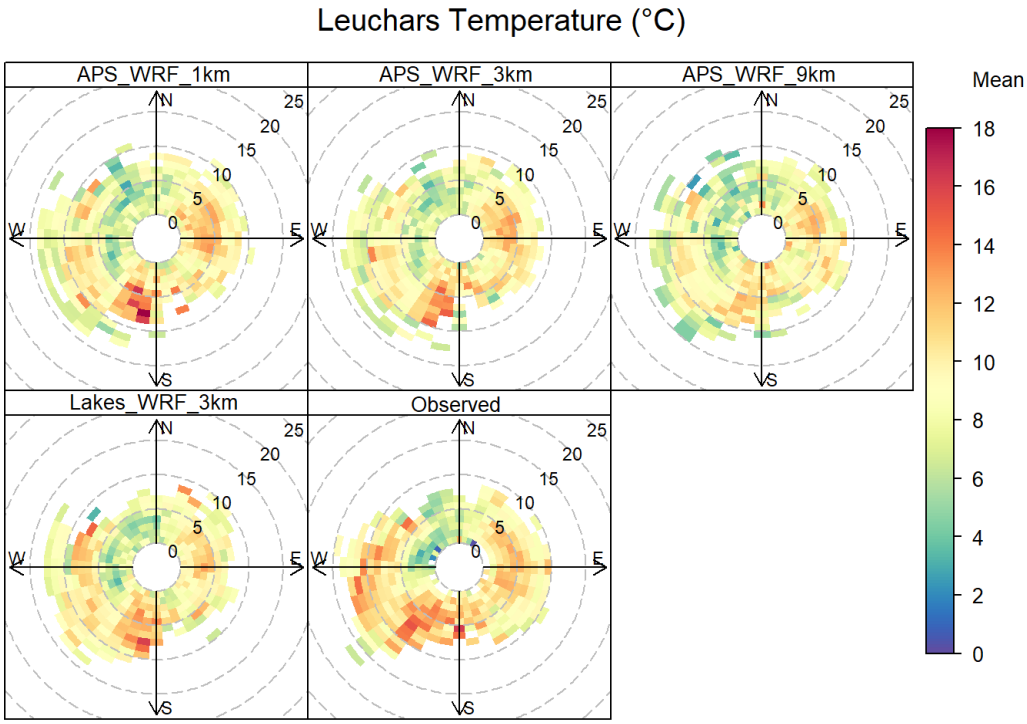

Figure 147 – Polar plots showing the mean temperature (indicated by the colour scale) associated with variation of wind speed (radial scale) and wind direction at Leuchars. Combinations of wind speed and direction which occur for fewer than 3 hours per year are not displayed.

B2.4 Precipitation

This section gives per-site statistics and plots for hourly precipitation, supplementing the results over all sites included in Section 5.3.4.

Table 60 – Meteorological model performance evaluation of hourly precipitation by site, for the WRF models.

Terrain type	Site	Model	Res. (km)	Observed Mean	MB	MGE	RMSE	R	IOA
					0	0	0	1	1
Flat	Waddington	APS_WRF	1	0.09	0.00	0.10	0.43	0.52	0.69
		APS_WRF	3		0.00	0.10	0.42	0.53	0.70
		APS_WRF	9		0.00	0.10	0.43	0.52	0.70
		Lakes_WRF	3		0.03	0.13	0.61	0.35	0.59
Urban	Northolt	APS_WRF	1	0.08	0.01	0.10	0.44	0.45	0.64
		APS_WRF	3		0.01	0.10	0.44	0.46	0.64
		APS_WRF	9		0.01	0.10	0.42	0.47	0.65
		Lakes_WRF	3		0.02	0.12	0.57	0.26	0.57
Complex	Sennybridge	APS_WRF	1	0.19	-0.03	0.19	0.58	0.56	0.70
		APS_WRF	3		-0.04	0.18	0.55	0.59	0.71
		APS_WRF	9		-0.03	0.18	0.52	0.62	0.71
		Lakes_WRF	3		0.00	0.23	0.79	0.37	0.63
Coastal	Leuchars	APS_WRF	1	0.09	0.01	0.11	0.45	0.40	0.66
		APS_WRF	3		0.01	0.11	0.44	0.42	0.66
		APS_WRF	9		0.01	0.11	0.42	0.45	0.66
		Lakes_WRF	3		0.01	0.12	0.50	0.30	0.61

Table 61 – Additional precipitation-specific summary statistics by site, for the WRF models.

Terrain type	Site	Model	Res. (km)	Observed sum washout factor	Modelled sum washout factor	Observed ZNUM	Modelled ZNUM
Flat	Waddington	APS_WRF	1	713	870	7925	6975
		APS_WRF	3		872		6942
		APS_WRF	9		892		6830
		Lakes_WRF	3		930		7201
Urban	Northolt	APS_WRF	1	646	815	7923	7016
		APS_WRF	3		823		6972
		APS_WRF	9		835		6863
		Lakes_WRF	3		792		7208
Complex	Sennybridge	APS_WRF	1	1554	1405	6924	6294
		APS_WRF	3		1395		6156
		APS_WRF	9		1508		5862
		Lakes_WRF	3		1621		5955
Coastal	Leuchars	APS_WRF	1	740	902	7815	6818
		APS_WRF	3		923		6736
		APS_WRF	9		978		6539
		Lakes_WRF	3		878		7068

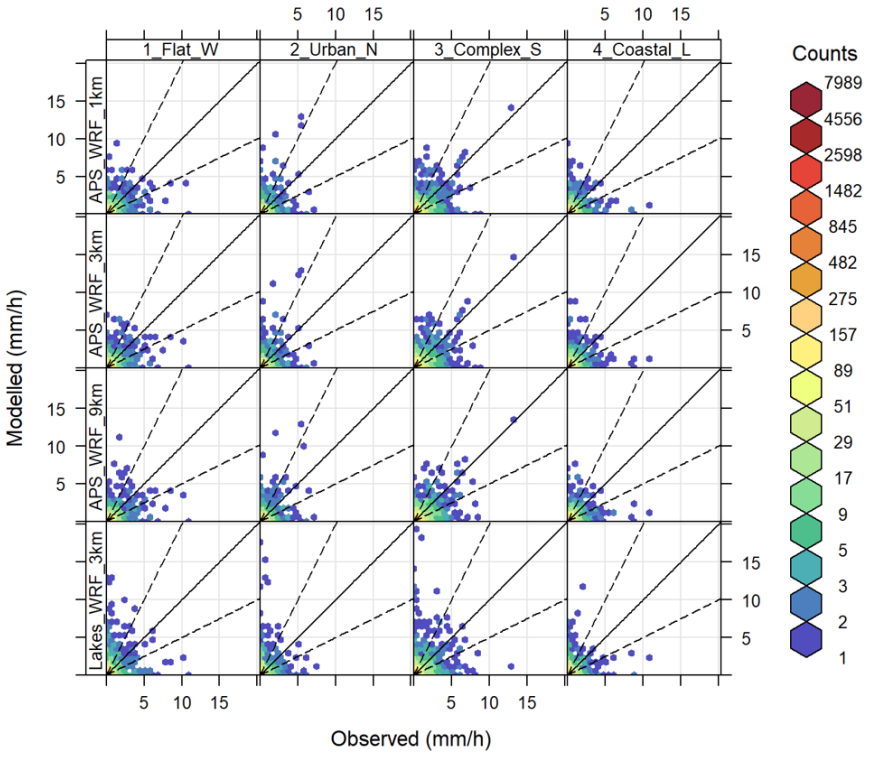

Figure 148 – Frequency scatter plots of modelled and observed hourly precipitation (mm/h) at each site. Colours indicate the number of data points in each area of the plot.

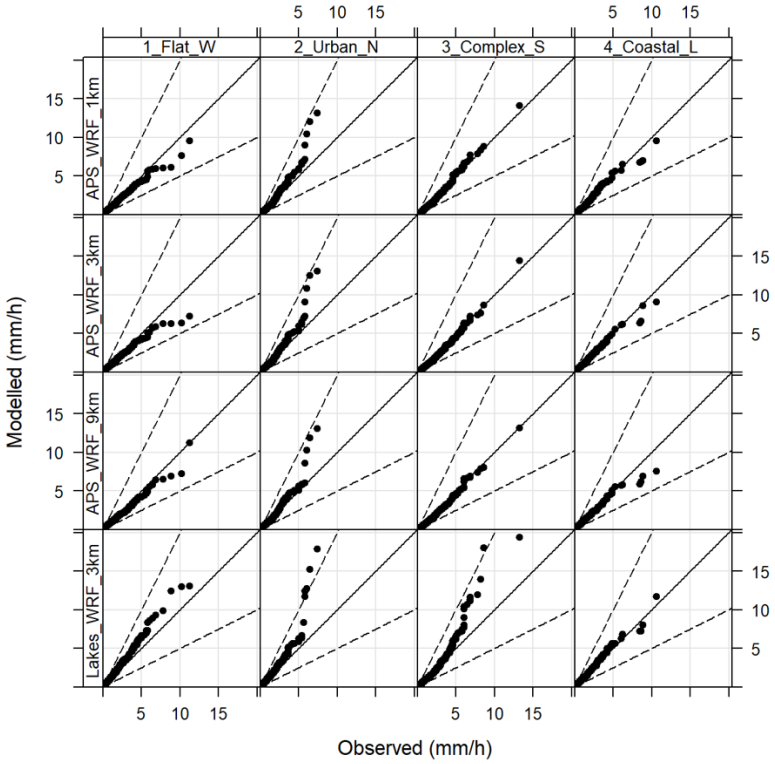

Figure 149 – Quantile-quantile plots of modelled and observed hourly precipitation (mm/h) at each site, ordered independently.

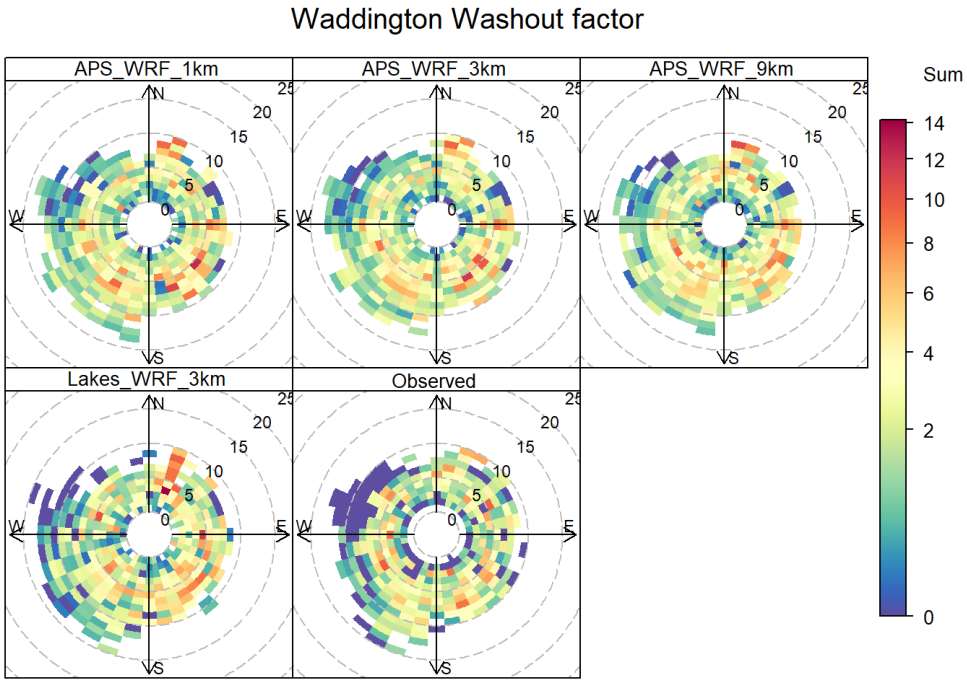

Figure 150 – Polar plots showing the total washout factor (indicated by the colour scale) associated with variation of wind speed (radial scale) and wind direction at Waddington. Combinations of wind speed and direction which occur for fewer than 3 hours per year are not displayed. Observed washout values are plotted with observed wind speed and direction while modelled washout values are plotted with the associated modelled wind data.

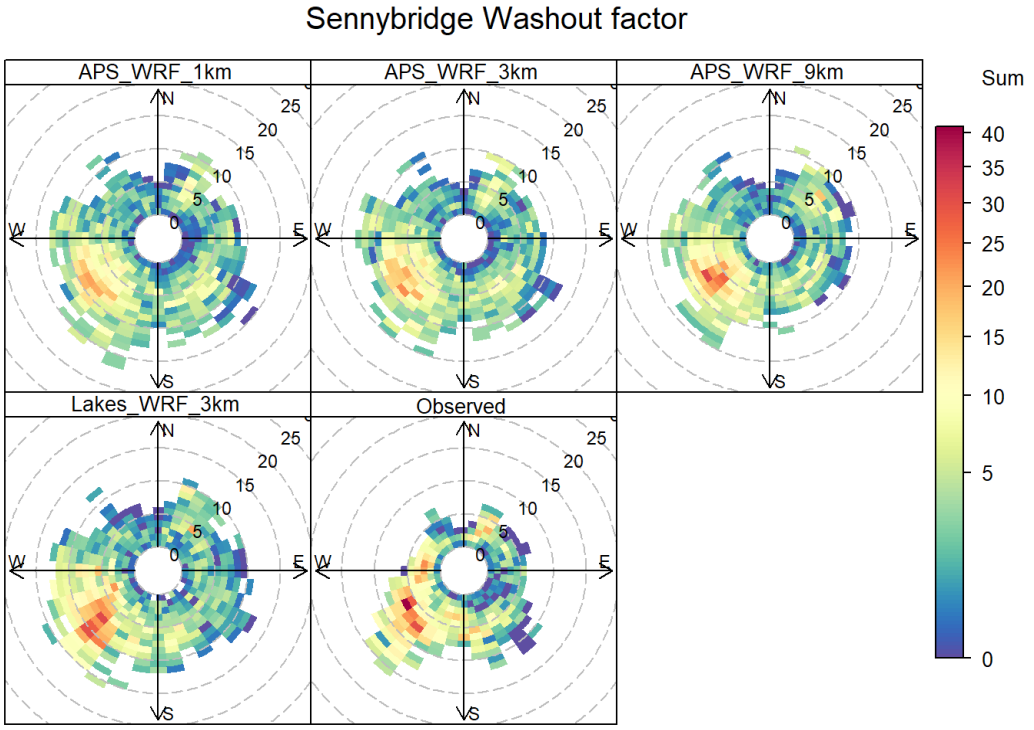

Figure 151 – Polar plots showing the total washout factor (indicated by the colour scale) associated with variation of wind speed (radial scale) and wind direction at Sennybridge. Combinations of wind speed and direction which occur for fewer than 3 hours per year are not displayed.

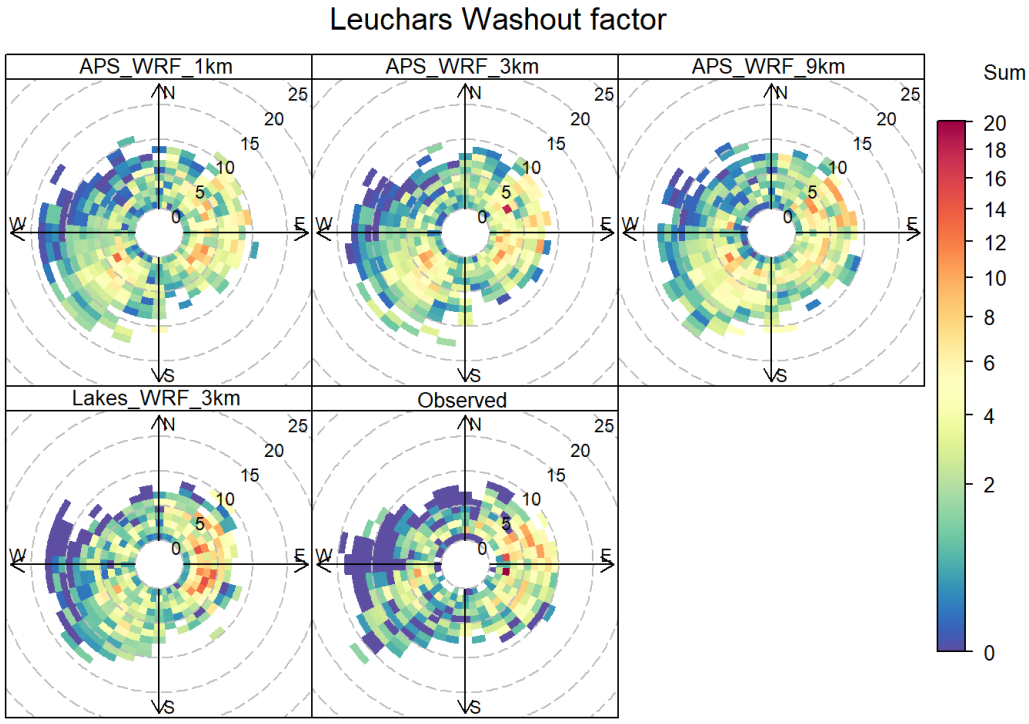

Figure 152 – Polar plots showing the total washout factor (indicated by the colour scale) associated with variation of wind speed (radial scale) and wind direction at Leuchars. Combinations of wind speed and direction which occur for fewer than 3 hours per year are not displayed.

B2.5 Cloud cover

This section gives per-site statistics and plots for cloud cover, supplementing the results over all sites included in Section 5.3.5.

Table 62 – Meteorological model performance evaluation of cloud cover (oktas) by site, for the WRF models.

Terrain type	Site	Model	Res. (km)	Observed Mean	MB	MGE	RMSE	FRAC1	R	IOA
					0	0	0	1	1	1
Flat	Waddington	APS_WRF	1	5.15	-0.08	1.74	2.49	0.58	0.60	0.66
		APS_WRF	3		-0.14	1.73	2.48	0.57	0.61	0.66
		APS_WRF	9		-0.19	1.72	2.46	0.58	0.61	0.67
		Lakes_WRF	3		-0.82	2.40	3.47	0.53	0.44	0.53
Urban	Northolt	APS_WRF	1	5.29	-0.24	1.71	2.47	0.58	0.63	0.67
		APS_WRF	3		-0.27	1.71	2.46	0.58	0.63	0.67
		APS_WRF	9		-0.32	1.71	2.46	0.58	0.63	0.67
		Lakes_WRF	3		0.95	2.60	3.84	0.54	0.18	0.50
Complex	Sennybridge	APS_WRF	1	5.99	-0.88	1.95	2.86	0.55	0.54	0.60
		APS_WRF	3		-0.85	1.88	2.77	0.57	0.57	0.61
		APS_WRF	9		-0.84	1.83	2.69	0.57	0.59	0.63
		Lakes_WRF	3		-0.77	1.95	3.25	0.63	0.50	0.60
Coastal	Leuchars	APS_WRF	1	5.27	-0.13	1.83	2.66	0.56	0.61	0.68
		APS_WRF	3		-0.17	1.82	2.65	0.56	0.61	0.68
		APS_WRF	9		-0.25	1.88	2.68	0.55	0.60	0.67
		Lakes_WRF	3		-0.72	2.64	3.85	0.50	0.34	0.54

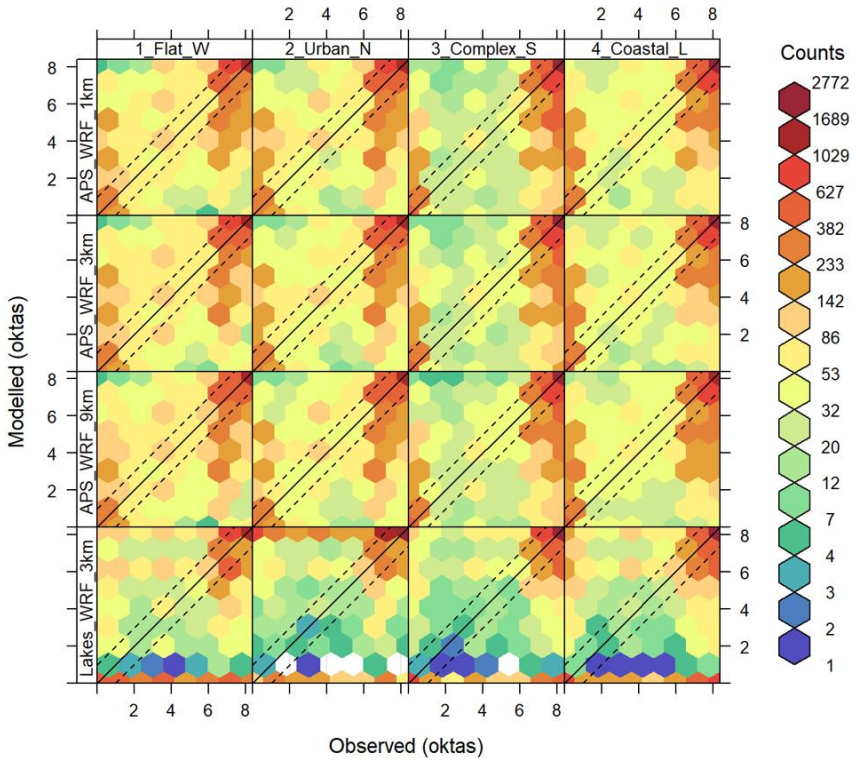

Figure 153 – Frequency scatter plots of modelled and observed cloud cover (oktas) at each site. Colours indicate the number of data points in each area of the plot. Dashed lines indicate values within ±1 okta.

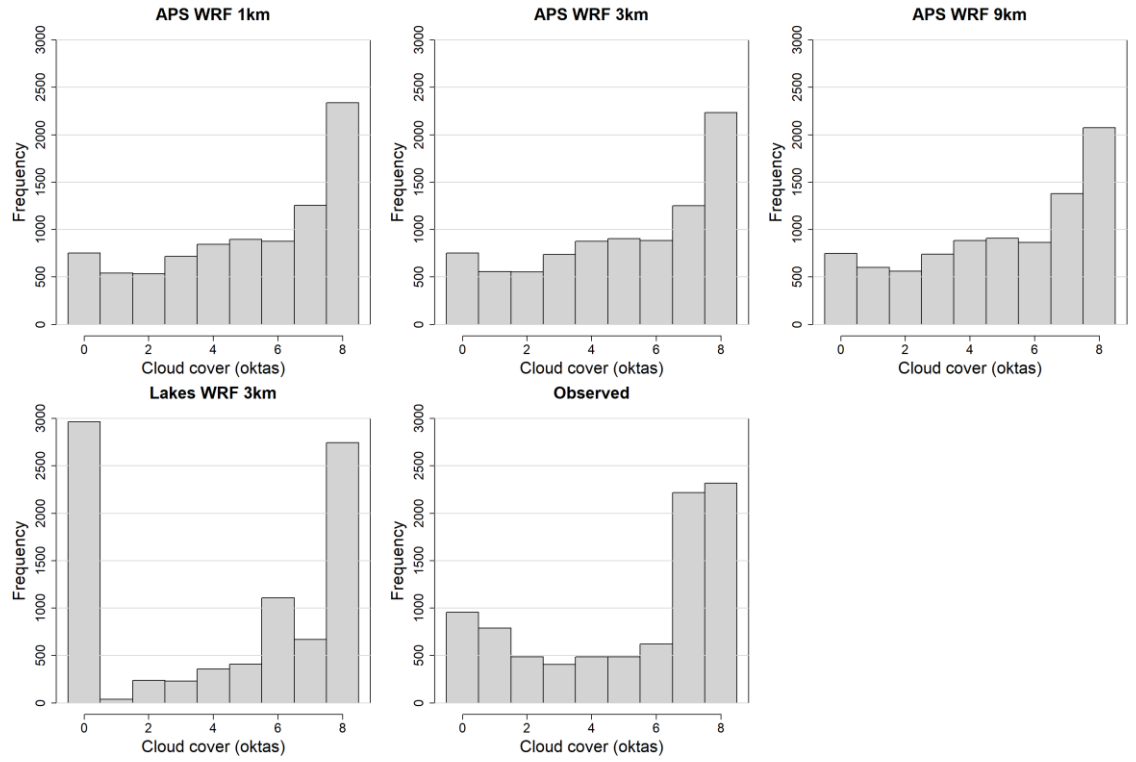

Figure 154 – Histogram charts of modelled and observed cloud cover (oktas) at Waddington (flat terrain site).

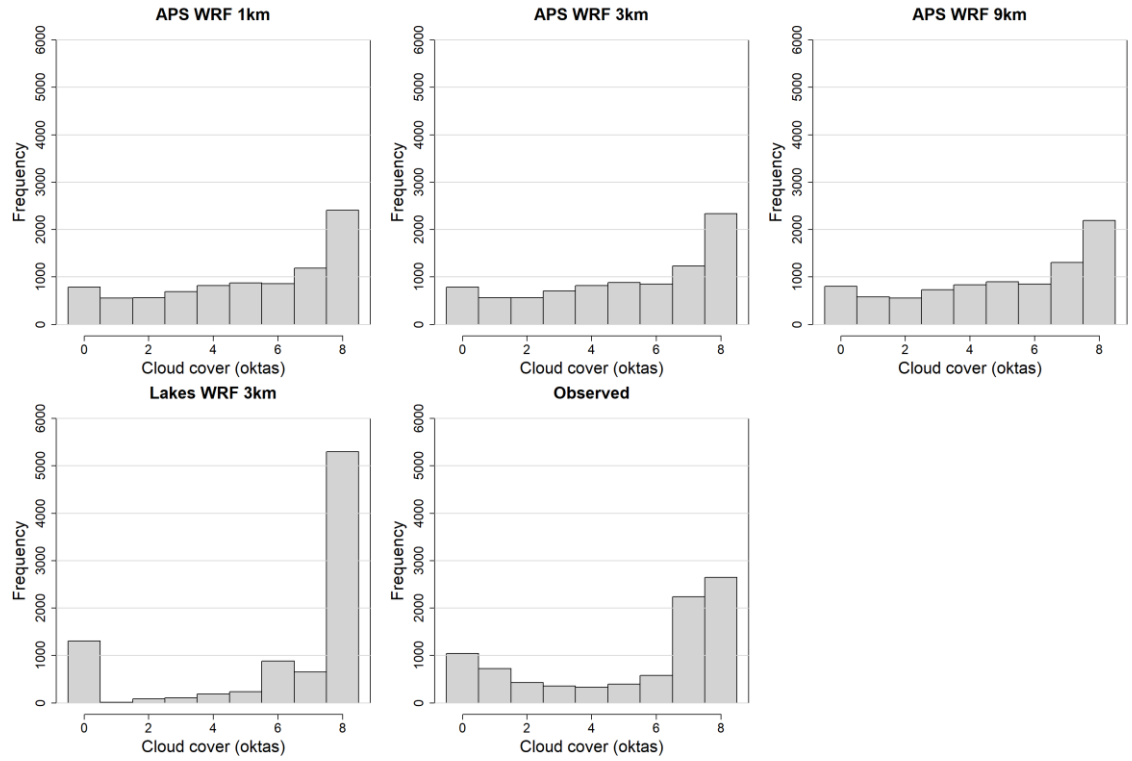

Figure 155 – Histogram charts of modelled and observed cloud cover (oktas) at Northolt (urban site).

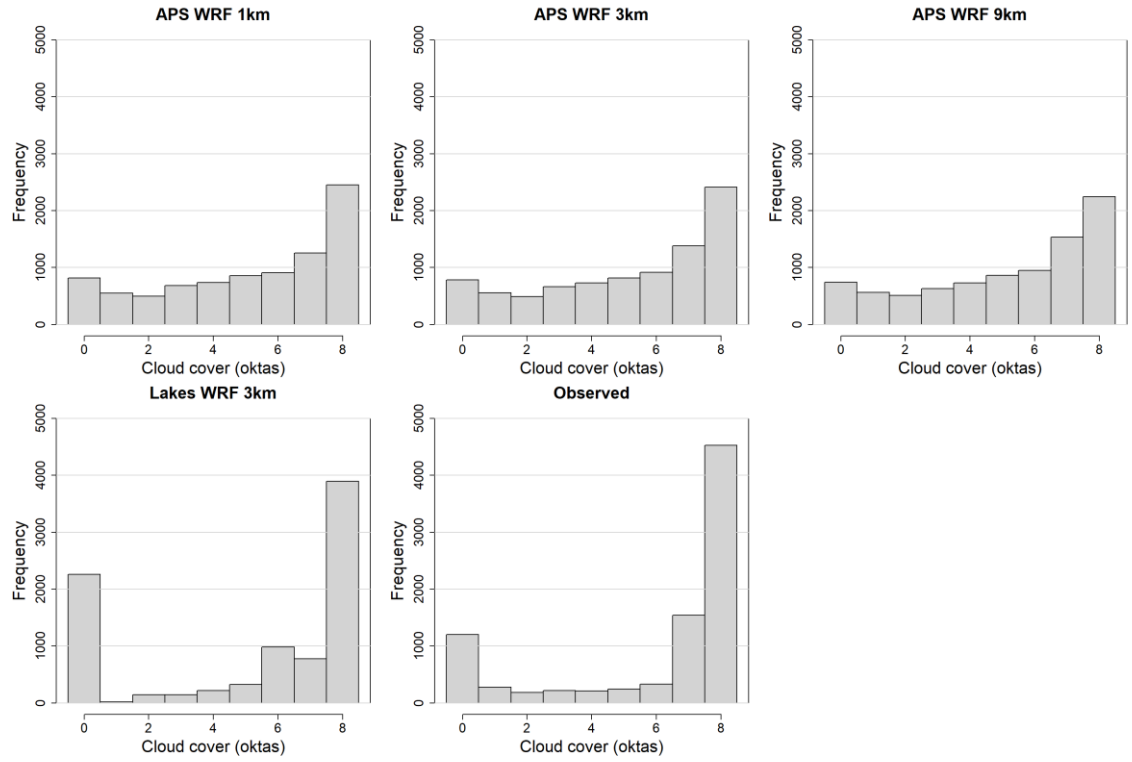

Figure 156 – Histogram charts of modelled and observed cloud cover (oktas) at Sennybridge (complex terrain site).

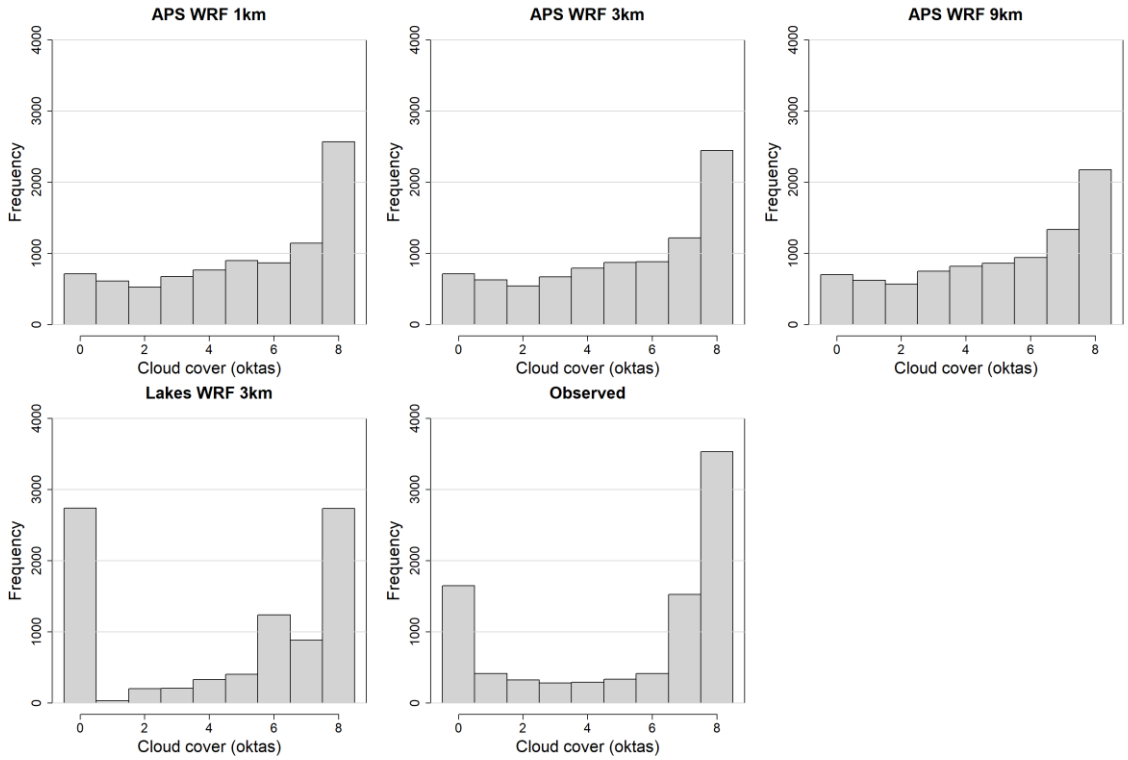

Figure 157 – Histogram charts of modelled and observed cloud cover (oktas) at Leuchars (coastal site).

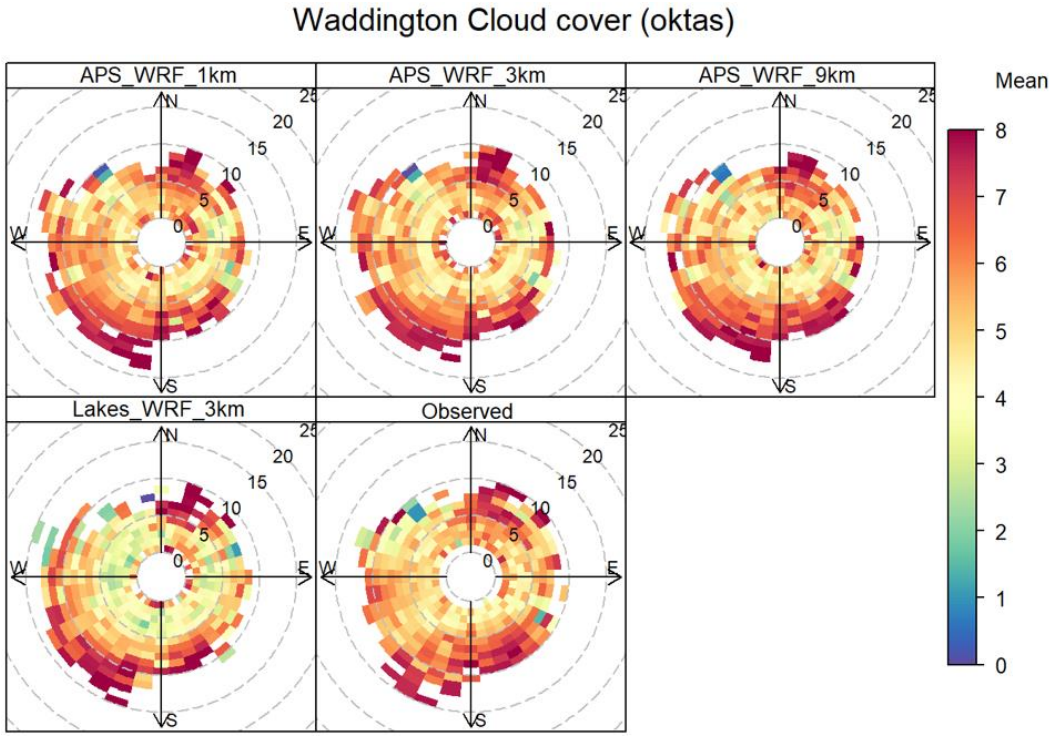

Figure 158 – Polar plots showing the mean cloud cover (indicated by the colour scale) associated with variation of wind speed (radial scale) and wind direction at Waddington. Combinations of wind speed and direction which occur for fewer than 3 hours per year are not displayed. Observed cloud cover values are plotted with observed wind speed and direction while modelled cloud cover values are plotted with the associated modelled wind data.

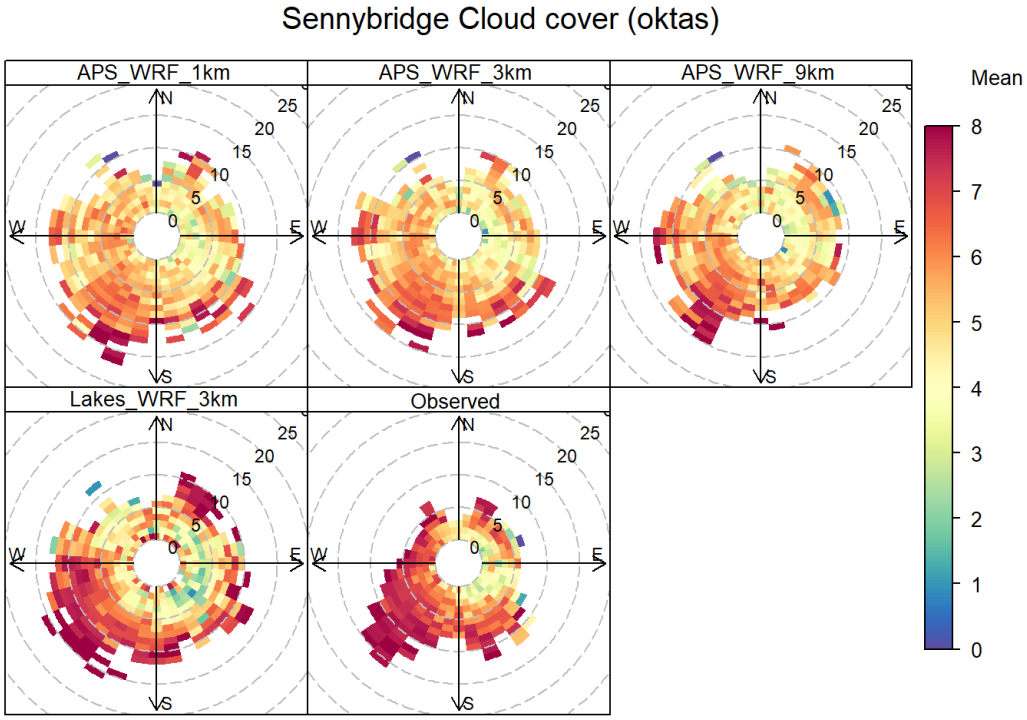

Figure 159 – Polar plots showing the mean cloud cover (indicated by the colour scale) associated with variation of wind speed (radial scale) and wind direction at Sennybridge. Combinations of wind speed and direction which occur for fewer than 3 hours per year are not displayed.

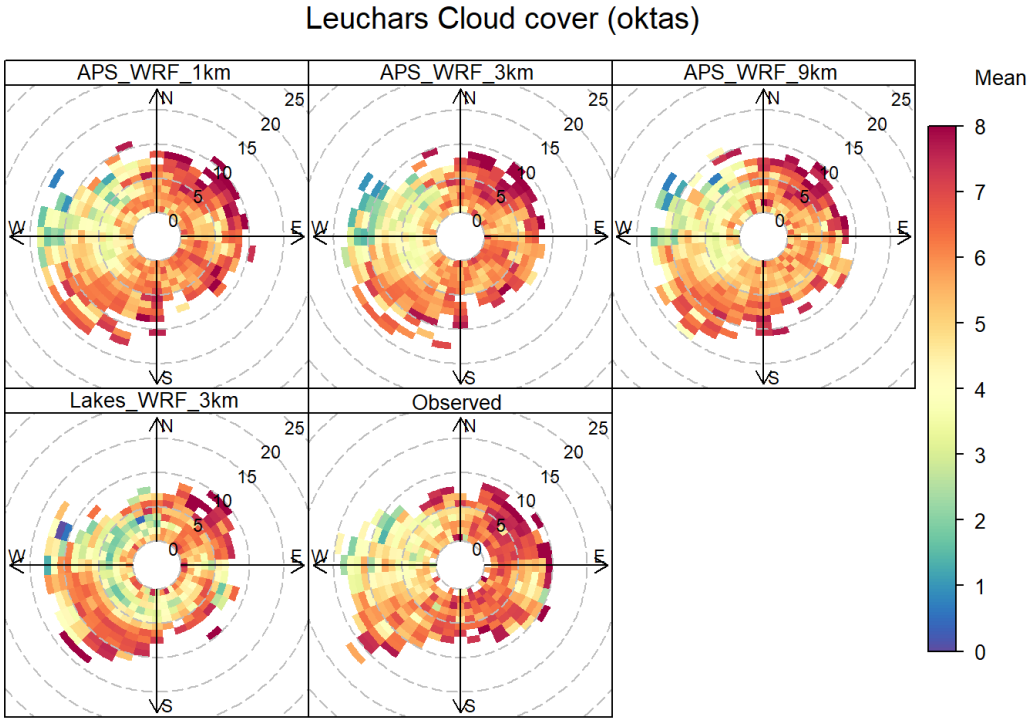

Figure 160 – Polar plots showing the mean cloud cover (indicated by the colour scale) associated with variation of wind speed (radial scale) and wind direction at Leuchars. Combinations of wind speed and direction which occur for fewer than 3 hours per year are not displayed.

B3 Secondary meteorological variables

Supplementary statistics and plots included in this section expand the comparison of secondary meteorological variables presented in Section 5.4.

B3.1 Solar radiation

This section gives additional plots of incoming solar radiation, supplementing those in Section 5.4.1.

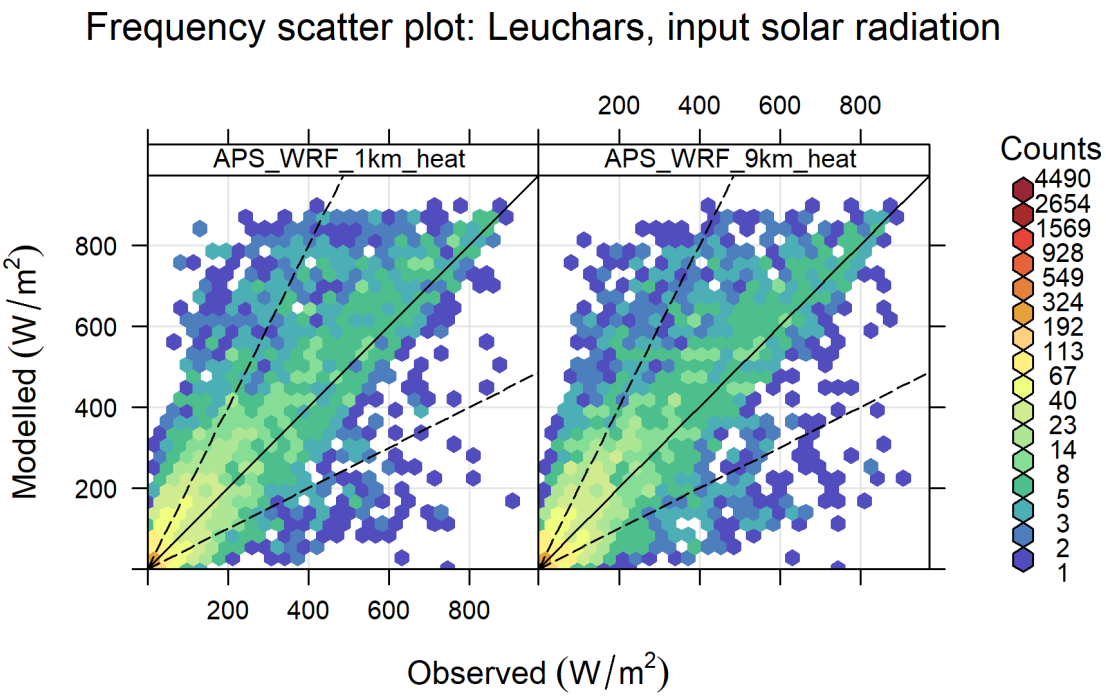

Figure 161 - Frequency scatter plots comparing hourly modelled and observed solar radiation in W/m² at Leuchars. Dashed lines indicate modelled values within a factor of 2 of observed values.

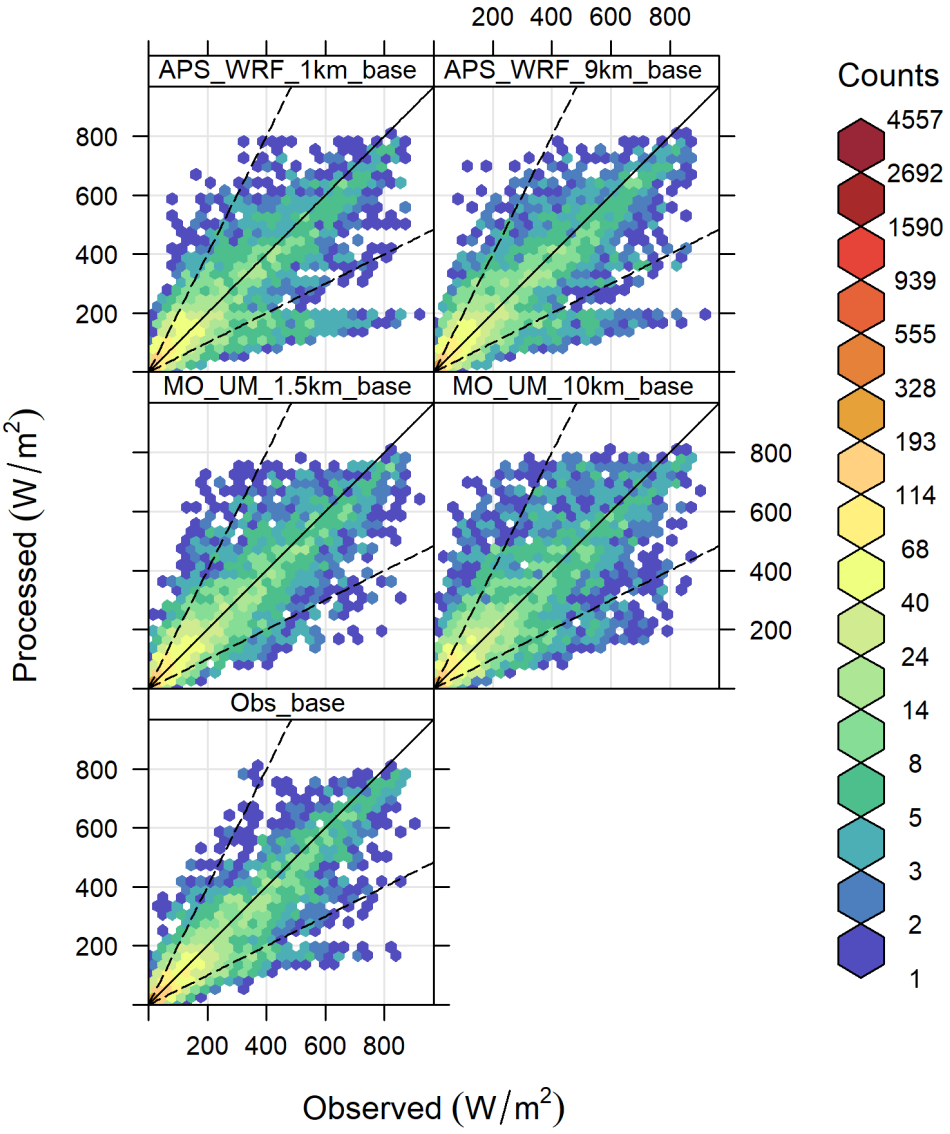

Figure 162 - Frequency scatter plots comparing hourly calculated (secondary) and observed (primary) solar radiation in W/m² at Leuchars. Dashed lines indicate modelled values within a factor of 2 of observed values.

B3.2 Surface sensible heat flux

This section gives additional plots and statistics for surface sensible heat flux, supplementing those in Section 5.4.2.

Table 63 – Statistics comparing surface sensible heat flux calculated by ADMS from observed 'base' input variables to surface sensible heat flux calculated from NWP 'base' input variables. Statistics calculated by site.

Site (terrain)	Model	Res. (km)	'Observed' mean (m)	MB	MGE	RMSE	R	IOA
				Ideal model value				
				0	0	0	1	1
Waddington (Flat)	APS_WRF	1	-5.7	-1.5	12.0	19.2	0.89	0.81
	APS_WRF	9		1.7	12.0	18.3	0.90	0.81
	MO_UM	1.5		3.6	10.9	16.5	0.92	0.83
	MO_UM	10		4.0	11.8	18.3	0.91	0.81
Northolt (Urban)	APS_WRF	1	1.1	-0.9	10.3	16.8	0.89	0.80
	APS_WRF	9		0.5	9.5	15.8	0.90	0.82
	MO_UM	1.5		0.7	9.2	14.8	0.92	0.82
	MO_UM	10		3.9	9.8	16.3	0.91	0.81
Sennybridge (Complex)	APS_WRF	1	-1.2	-6.3	19.1	28.7	0.81	0.60
	APS_WRF	9		-1.0	16.0	24.9	0.83	0.66
	MO_UM	1.5		1.6	13.5	22.5	0.83	0.71
	MO_UM	10		3.0	16.3	26.8	0.77	0.65
Leuchars (Coastal)	APS_WRF	1	-6.5	-0.6	13.7	21.6	0.86	0.76
	APS_WRF	9		-0.3	13.4	20.9	0.87	0.76
	MO_UM	1.5		3.7	12.5	20.4	0.88	0.78
	MO_UM	10		2.5	14.3	23.8	0.85	0.75

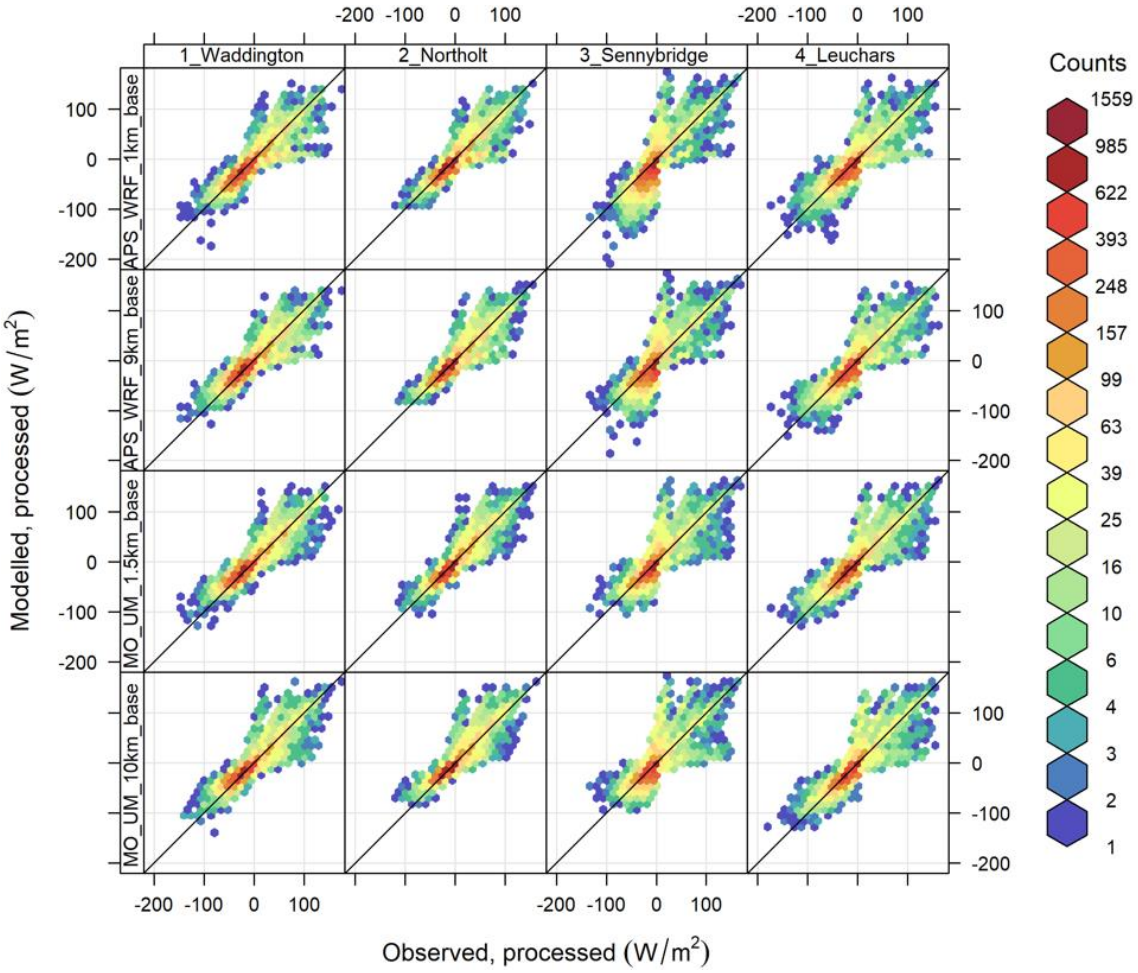

Figure 163 - Frequency scatter plots comparing hourly surface sensible heat flux in W/m², derived from base observations and model data at each site.

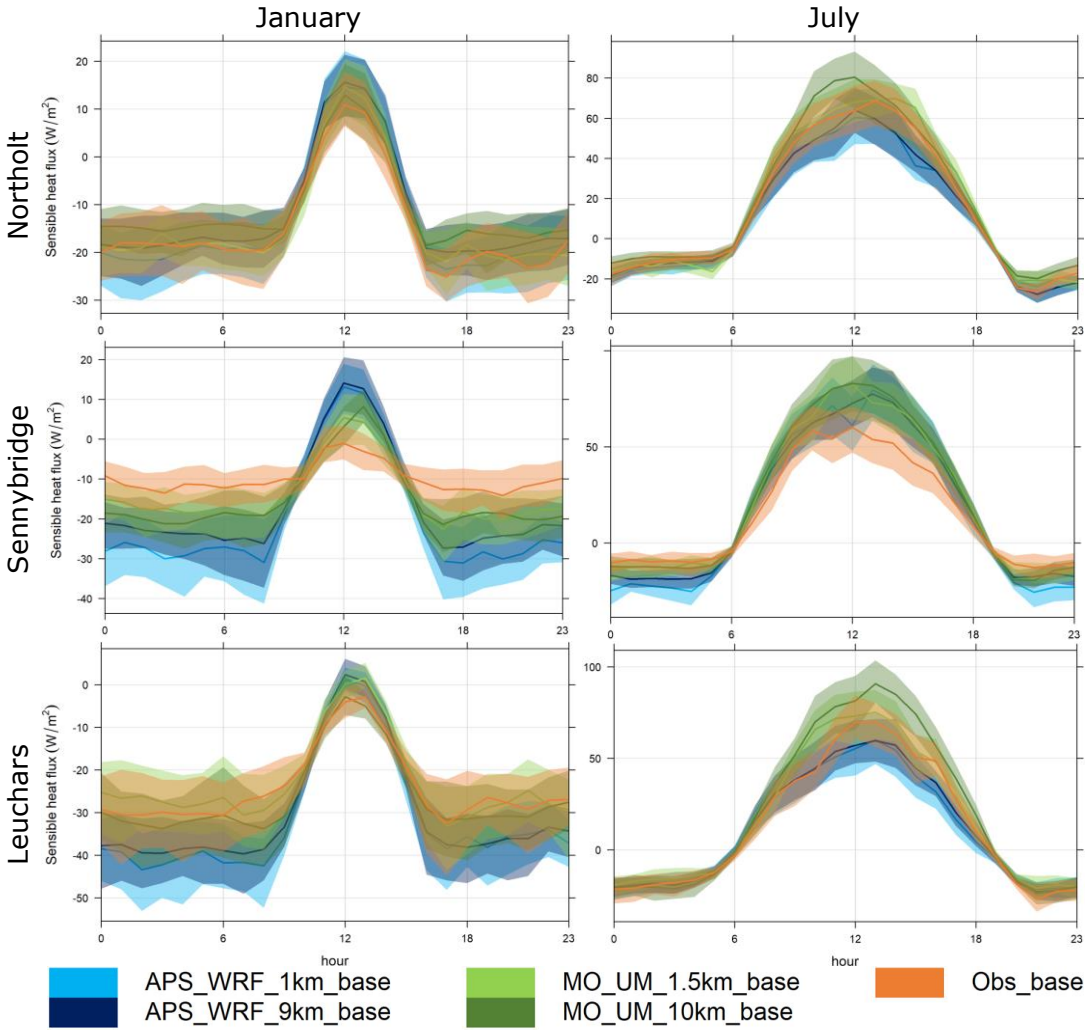

Figure 164 - Diurnal profiles of surface sensible heat flux in W/m^2 at Northolt, Sennybridge, and Leuchars, derived from observed and modelled base input variables, averaged for January (left) and July (right). The shaded areas show 95% confidence intervals around the mean.

Table 64 – Statistics comparing surface sensible heat flux calculated by ADMS from observed 'base' input variables to surface sensible heat flux extracted from NWP. Statistics calculated by site.

Site (terrain)	Model	Res. (km)	'Observed' mean (m)	MB	MGE	RMSE	R	IOA
				Ideal model value				
				0	0	0	1	1
Waddington (Flat)	APS_WRF	1	-5.7	9.2	23.6	33.8	0.78	0.62
	APS_WRF	9		8.0	23.0	32.4	0.77	0.64
	MO_UM	1.5		18.5	24.6	35.1	0.84	0.61
	MO_UM	10		12.4	20.4	30.4	0.87	0.68
Northolt (Urban)	APS_WRF	1	1.1	8.1	23.3	37.4	0.80	0.55
	APS_WRF	9		55.8	57.8	91.2	0.83	-0.11
	MO_UM	1.5		9.9	18.9	29.5	0.84	0.63
	MO_UM	10		17.9	24.1	38.3	0.79	0.53
Sennybridge (Complex)	APS_WRF	1	-1.2	13.3	29.8	47.7	0.73	0.37
	APS_WRF	9		14.8	28.0	46.4	0.74	0.41
	MO_UM	1.5		7.2	21.1	32.9	0.75	0.55
	MO_UM	10		10.4	21.5	33.6	0.78	0.54
Leuchars (Coastal)	APS_WRF	1	-6.5	25.9	33.5	60.8	0.79	0.40
	APS_WRF	9		12.9	28.2	46.9	0.79	0.50
	MO_UM	1.5		7.5	20.4	32.5	0.80	0.64
	MO_UM	10		6.0	18.8	27.6	0.81	0.67

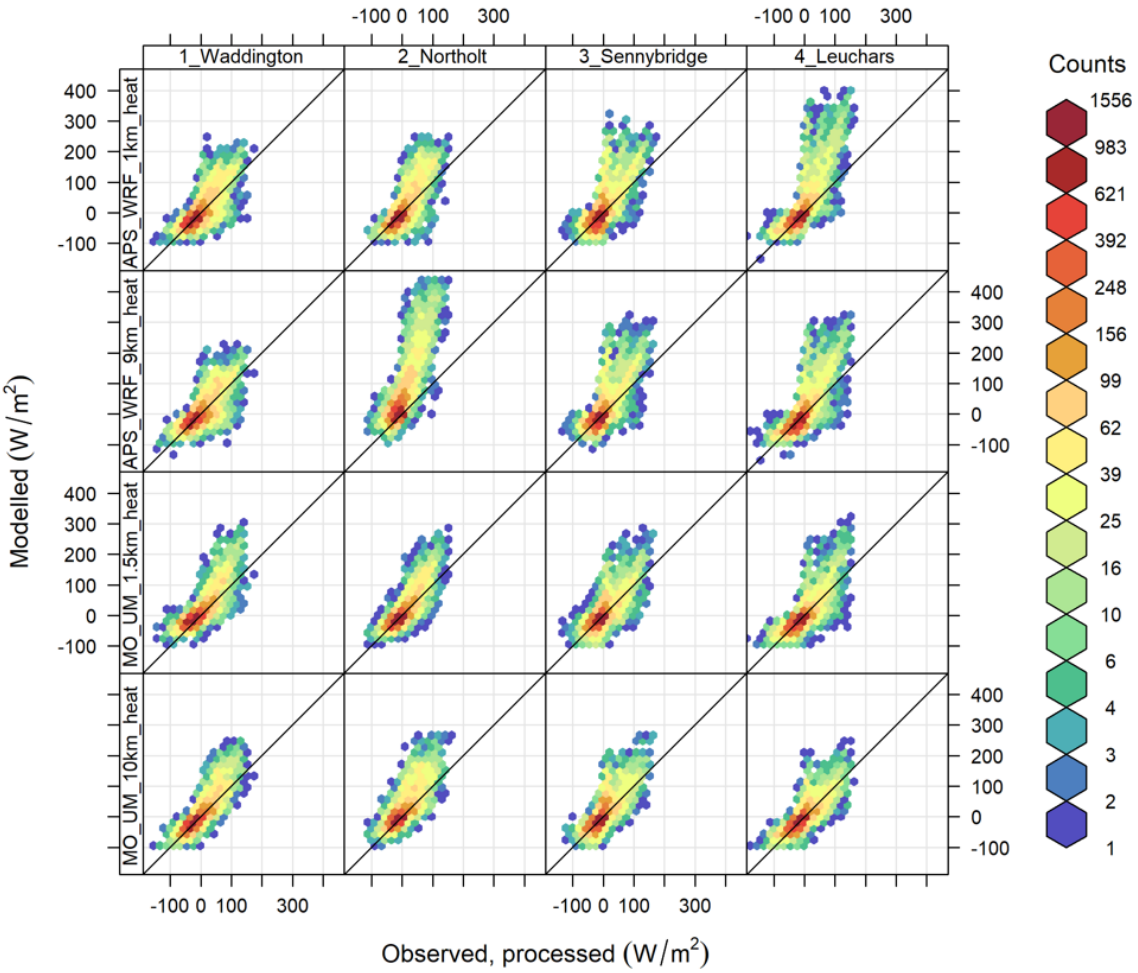

Figure 165 - Frequency scatter plots comparing hourly surface sensible heat flux in W/m², derived from base observations and extracted from NWP data at each site.

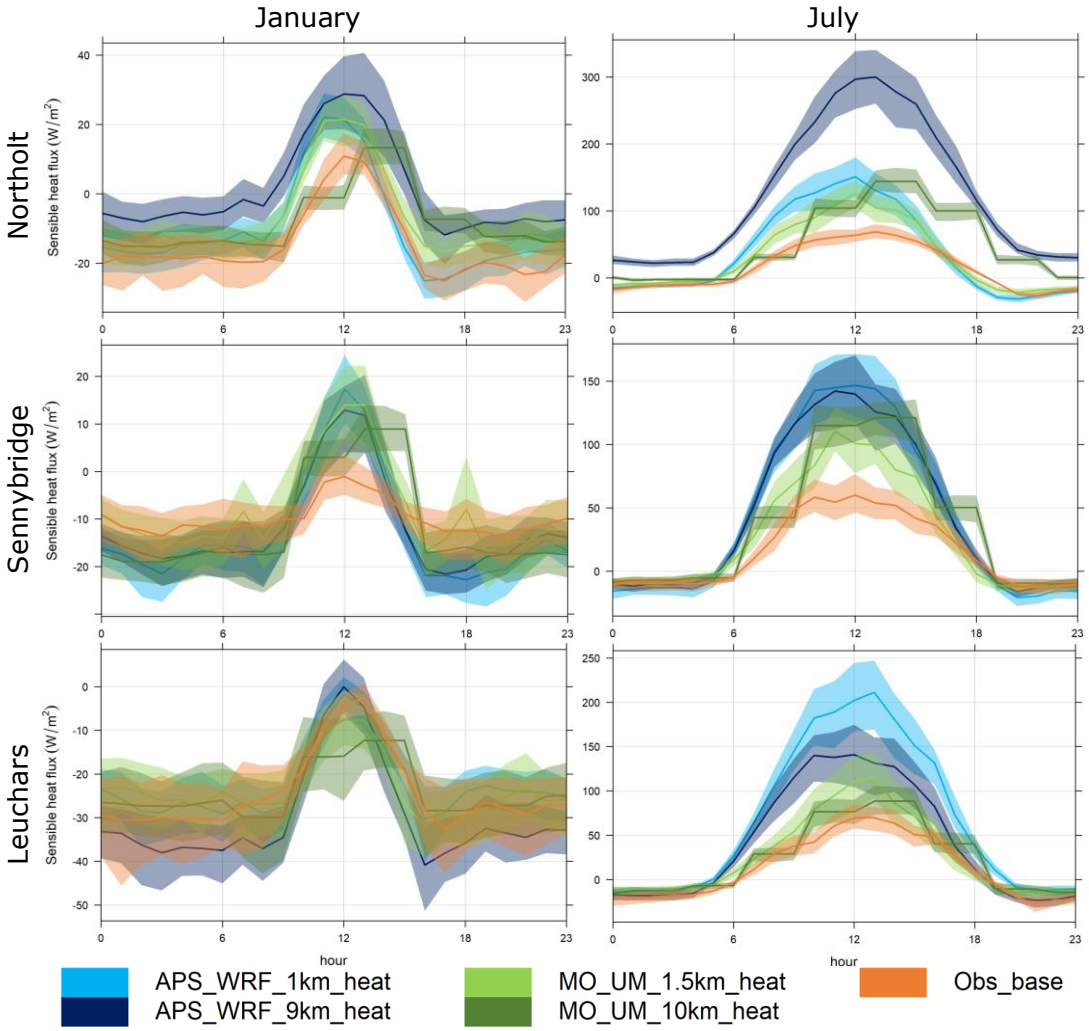

Figure 166 - Diurnal profiles of surface sensible heat flux in W/m² at Northolt, Sennybridge, and Leuchars, derived from base observations and extracted from NWP data, averaged for January (left) and July (right). The shaded areas show 95% confidence intervals around the mean.

B3.3 Boundary layer height

This section gives additional plots and statistics for boundary layer height, supplementing those in Section 5.4.3.

Table 65 – Statistics comparing boundary layer height calculated by ADMS from observed 'base' input variables to boundary layer height calculated from NWP 'base' input variables. Statistics calculated by site.

Site (terrain)	Model	Res. (km)	'Observed' mean (m)	MB	MGE	RMSE	R	IOA
				Ideal model value				
				0	0	0	1	1
Waddington (Flat)	APS_WRF	1	544.7	-27.6	116.2	186.0	0.91	0.84
	APS_WRF	9		-65.5	127.7	193.7	0.92	0.82
	MO_UM	1.5		-79.6	123.0	190.6	0.92	0.83
	MO_UM	10		-78.4	126.3	196.1	0.92	0.82
Northolt (Urban)	APS_WRF	1	441.3	-14.3	97.8	165.6	0.92	0.86
	APS_WRF	9		-41.8	97.1	159.1	0.93	0.86
	MO_UM	1.5		-14.2	85.9	142.1	0.94	0.87
	MO_UM	10		-83.1	109.7	178.5	0.93	0.84
Sennybridge (Complex)	APS_WRF	1	467.4	181.2	237.5	364.5	0.83	0.68
	APS_WRF	9		80.8	208.9	328.9	0.79	0.72
	MO_UM	1.5		24.1	166.0	277.0	0.83	0.78
	MO_UM	10		5.3	200.3	324.7	0.75	0.73
Leuchars (Coastal)	APS_WRF	1	512.3	-14.0	144.2	221.1	0.89	0.81
	APS_WRF	9		-10.3	138.6	208.9	0.90	0.82
	MO_UM	1.5		-53.3	133.0	207.3	0.91	0.83
	MO_UM	10		-21.4	130.8	206.6	0.90	0.83

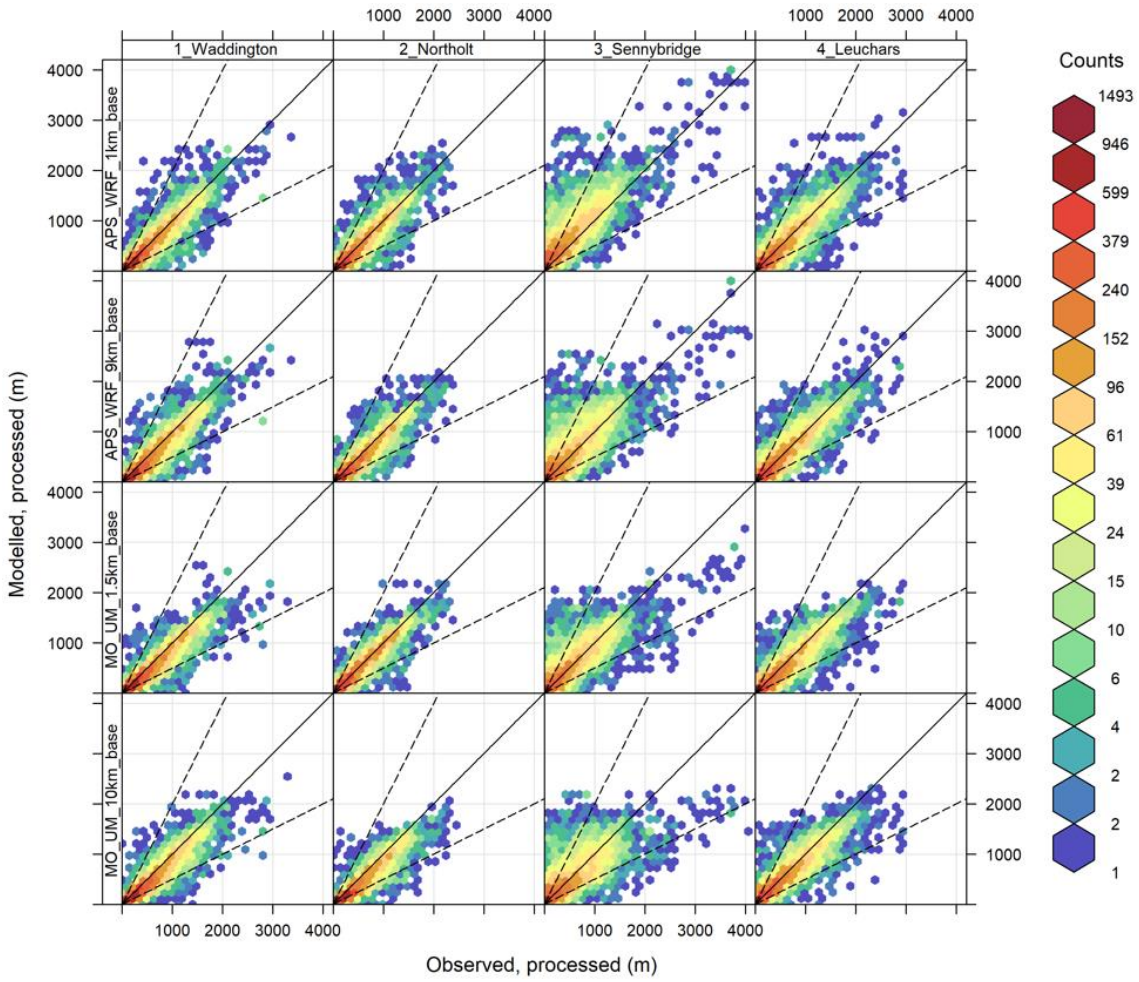

Figure 167 - Frequency scatter plots comparing hourly boundary layer heights in metres, derived from base observations and model data at each site. Dashed lines indicate modelled values within a factor of 2 of observed values.

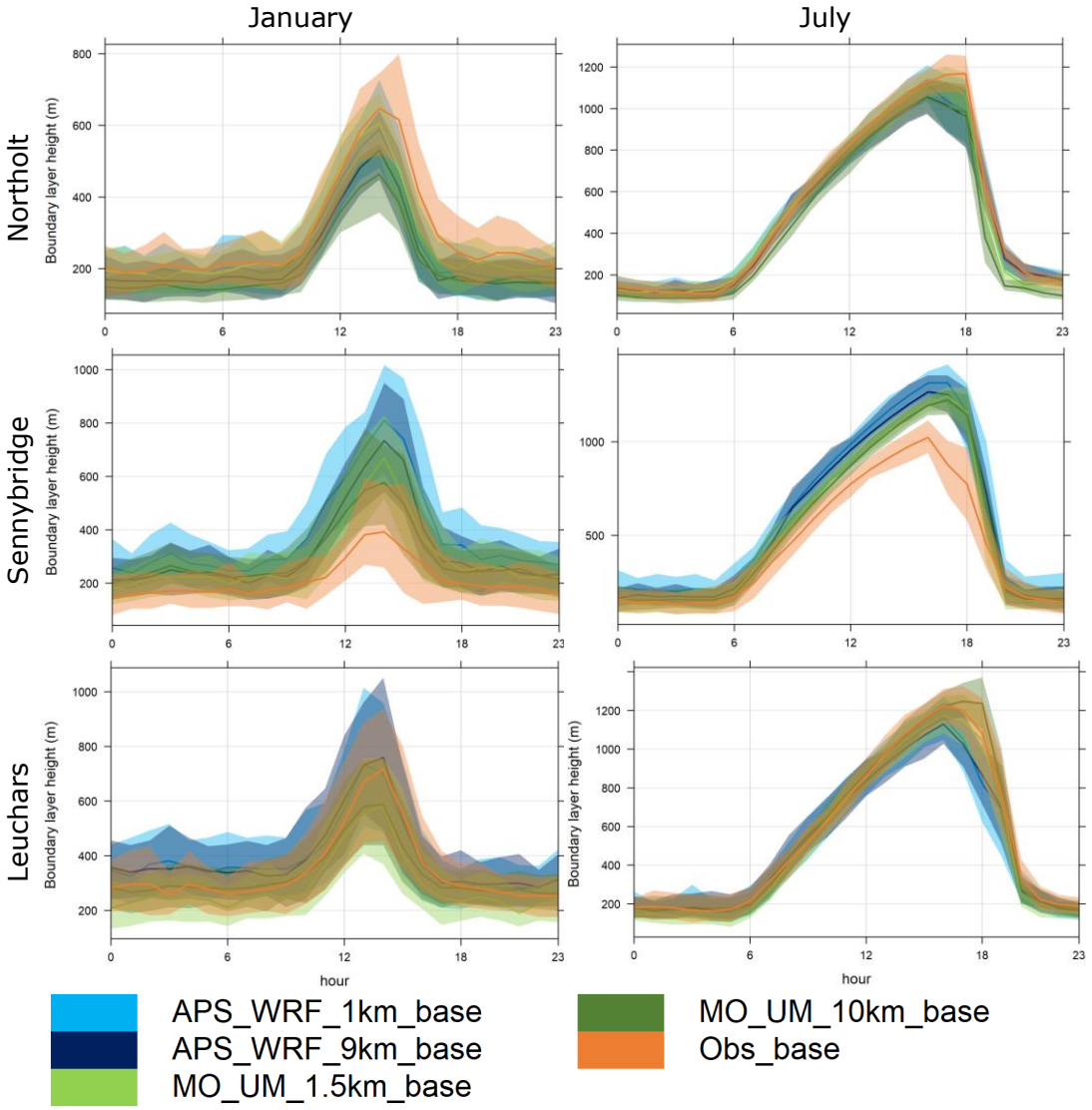

Figure 168 - Diurnal profiles of boundary layer height in m at Northolt, Sennybridge, and Leuchars, derived from observed and modelled base input variables, averaged for January (left) and July (right). The shaded areas show 95% confidence intervals around the mean.

Table 66 – Statistics comparing boundary layer height calculated by ADMS from observed 'base' input variables to boundary layer height extracted from NWP. Statistics calculated by site.

Site (terrain)	Model	Res. (km)	'Observed' mean (m)	MB	MGE	RMSE	R	IOA
				Ideal model value				
				0	0	0	1	1
Waddington (Flat)	APS_WRF	1	544.7	-126.8	248.4	379.1	0.62	0.65
	APS_WRF	9		-138.0	259.6	392.5	0.59	0.64
	MO_UM	1.5		-114.4	251.3	374.6	0.66	0.65
	MO_UM	10		138.9	295.2	399.2	0.63	0.59
Northolt (Urban)	APS_WRF	1	441.3	71.8	226.7	329.8	0.71	0.66
	APS_WRF	9		85.7	234.6	319.6	0.69	0.65
	MO_UM	1.5		30.4	216.1	334.4	0.69	0.68
	MO_UM	10		257.0	339.6	436.8	0.66	0.50
Sennybridge (Complex)	APS_WRF	1	467.4	-62.8	279.5	431.7	0.49	0.63
	APS_WRF	9		-91.0	267.2	417.7	0.54	0.64
	MO_UM	1.5		-36.8	279.0	433.6	0.52	0.63
	MO_UM	10		177.2	365.6	495.4	0.46	0.51
Leuchars (Coastal)	APS_WRF	1	512.3	-67.4	290.6	425.7	0.54	0.62
	APS_WRF	9		-89.4	278.8	416.5	0.54	0.63
	MO_UM	1.5		-181.0	285.0	440.6	0.55	0.63
	MO_UM	10		65.0	316.5	437.5	0.50	0.58

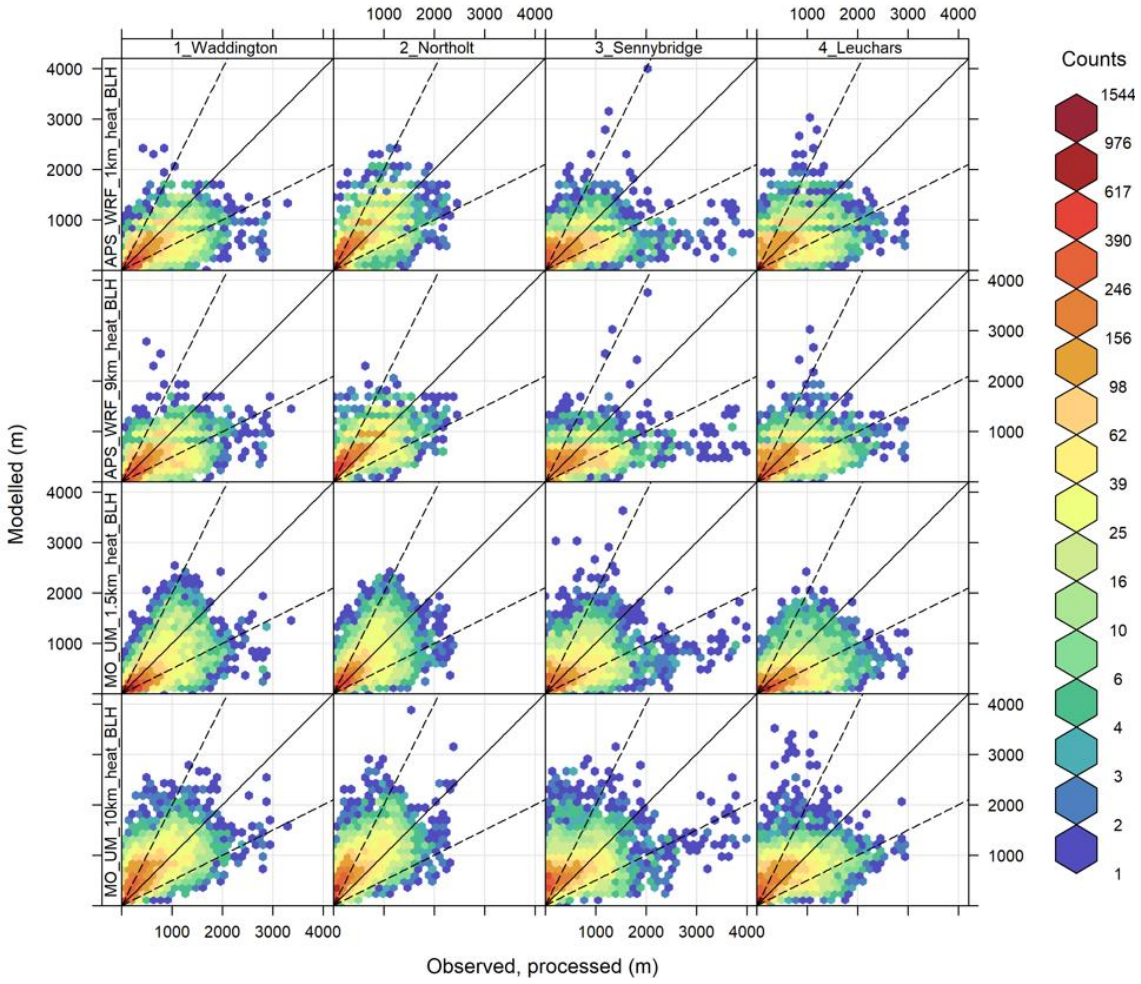

Figure 169 - Frequency scatter plots comparing hourly boundary layer heights in metres, derived from base observations and extracted from NWP data at each site. Dashed lines indicate modelled values within a factor of 2 of observed values.

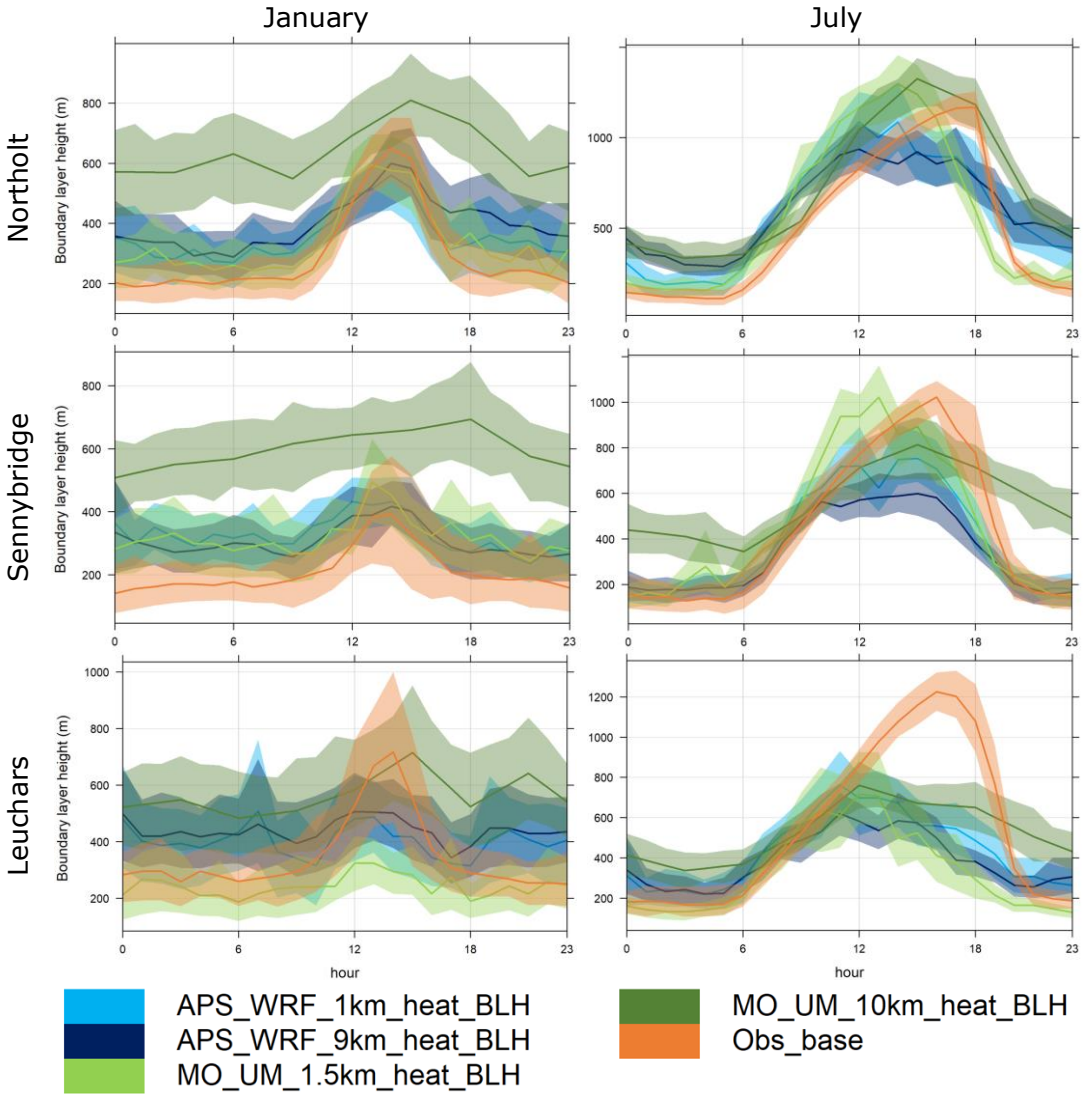

Figure 170 - Diurnal profiles of boundary layer height in m at Northolt, Sennybridge, and Leuchars, derived from base observations and extracted from NWP data, averaged for January (left) and July (right). The shaded areas show 95% confidence intervals around the mean.

B3.4 Stability

This section gives additional plots and statistics for atmospheric stability, supplementing those in Section 5.4.4.

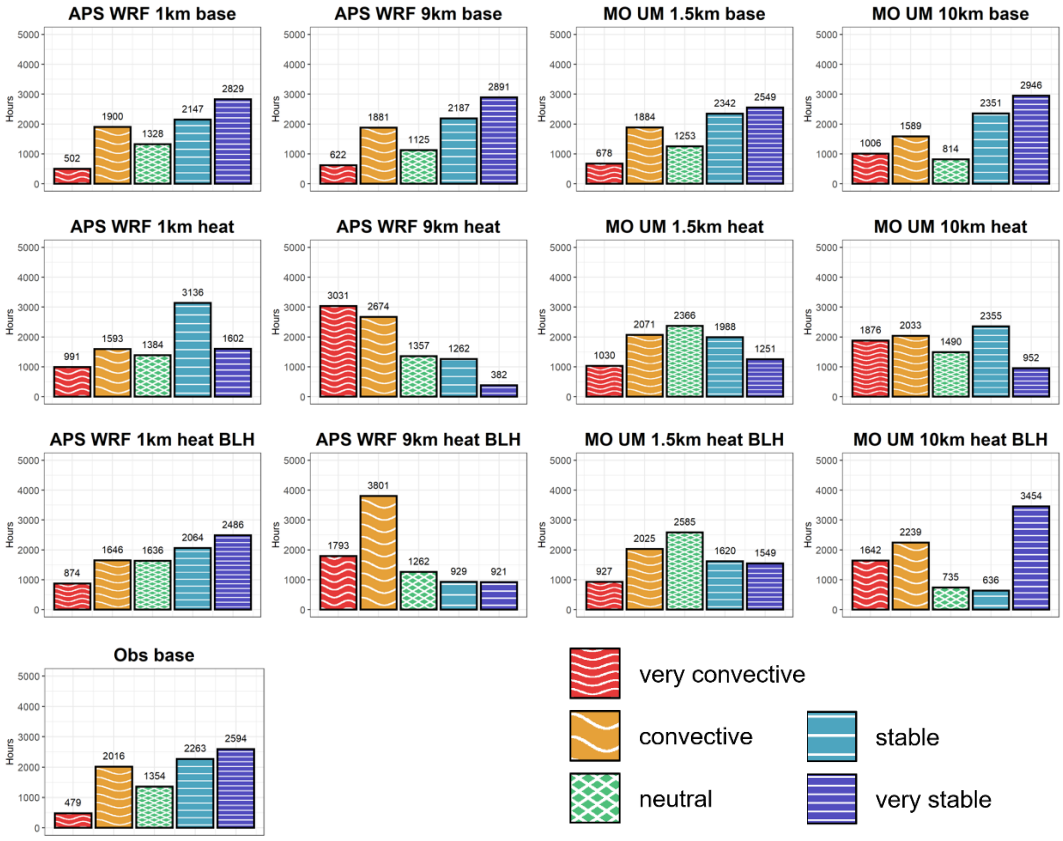

Figure 171 – Histograms showing number of hours in each stability category predicted by ADMS using observed and modelled input datasets with varying combinations of variables. Data for Northolt.

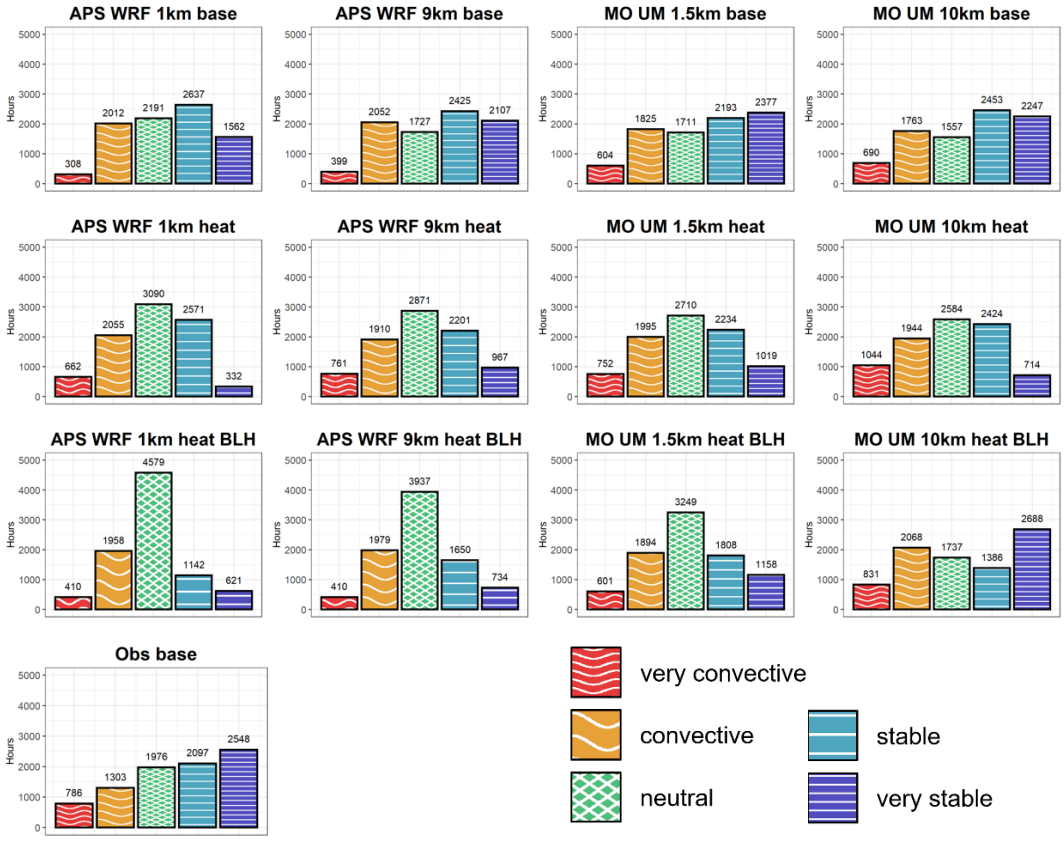

Figure 172 – Histograms showing number of hours in each stability category predicted by ADMS using observed and modelled input datasets with varying combinations of variables. Data for Sennybridge.

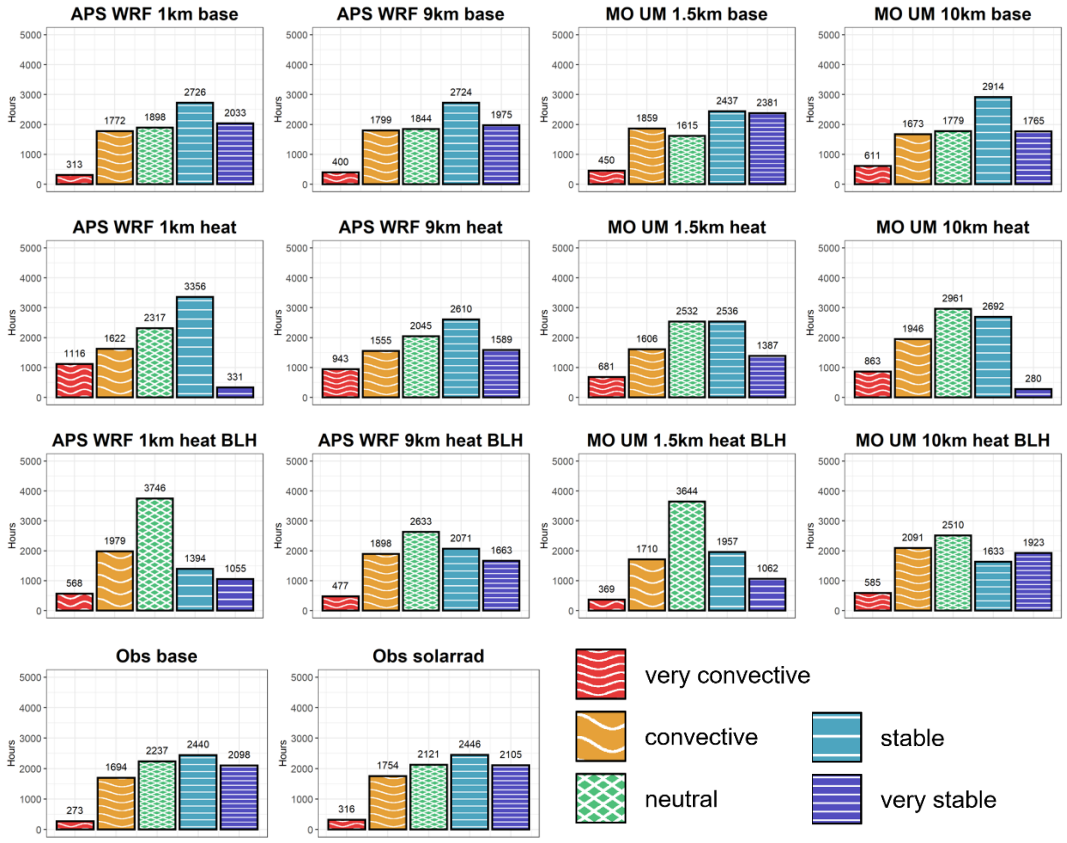

Figure 173 – Histograms showing number of hours in each stability category predicted by ADMS using observed and modelled input datasets with varying combinations of variables. Data for Leuchars.

APPENDIX C DISPERSION COMPARISON

Supplementary statistics and plots included in this section expand the comparison of dispersion results with different meteorological input datasets presented in Section 6.

C1 Concentration comparison

This section gives additional plots and statistics for modelled concentrations, supplementing those in Section 6. The concentration statistics considered are annual average (aa), 98th percentile (P98) and 100th percentile (P100).

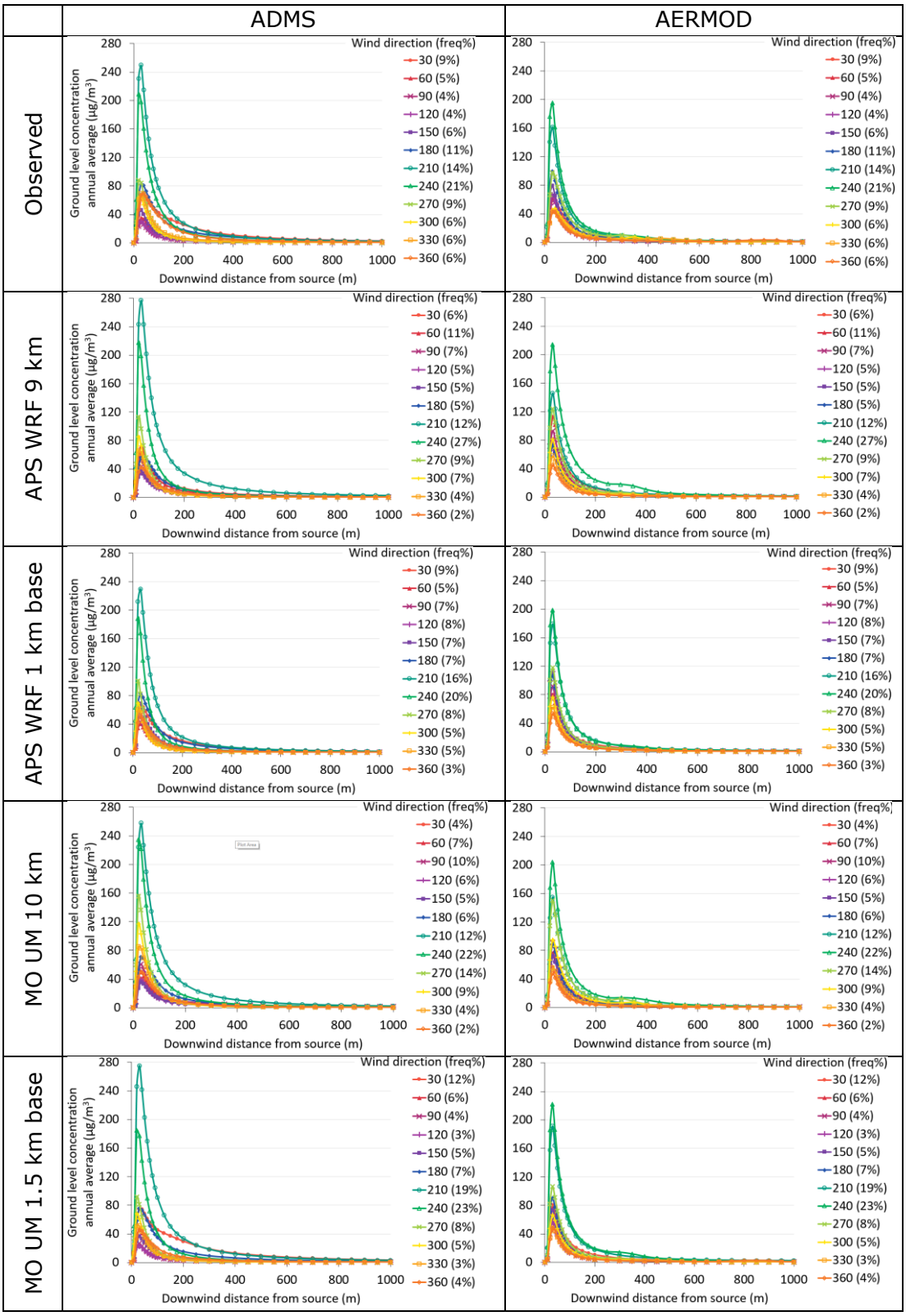

Figure 174 – Downwind profiles of annual average concentration for near-ground source at Sennybridge with varying wind direction, modelled with ADMS (left) and AERMOD (right), with observed or base NWP meteorological data.

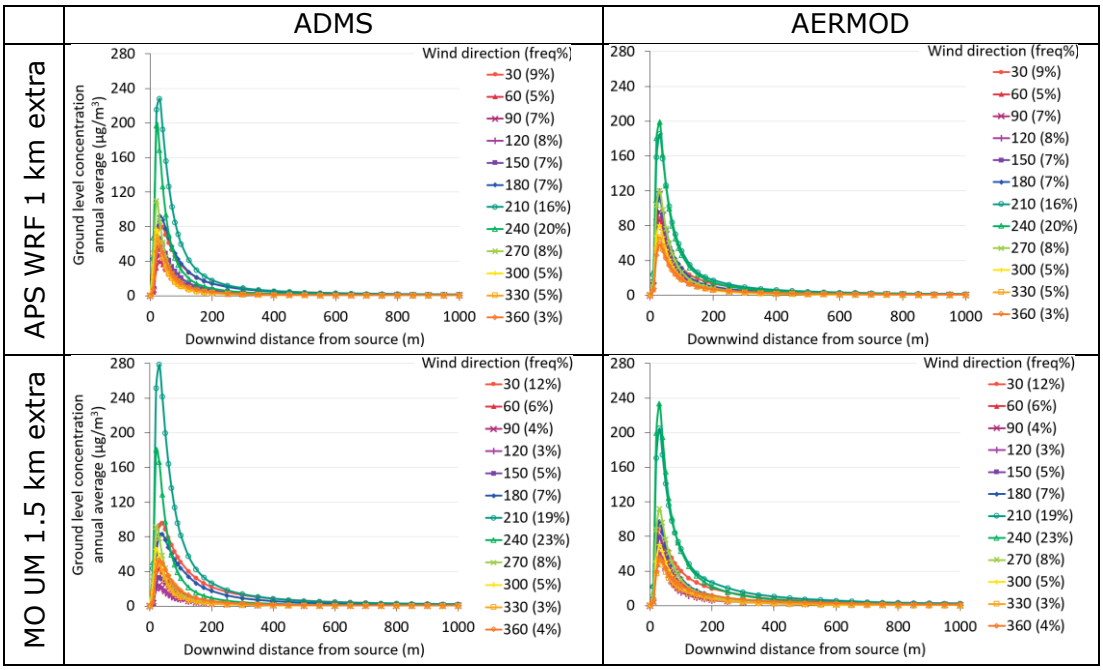

Figure 175 – Downwind profiles of annual average concentration for near-ground source at Sennybridge with varying wind direction, modelled with ADMS (left) and AERMOD (right), with extra NWP meteorological data.

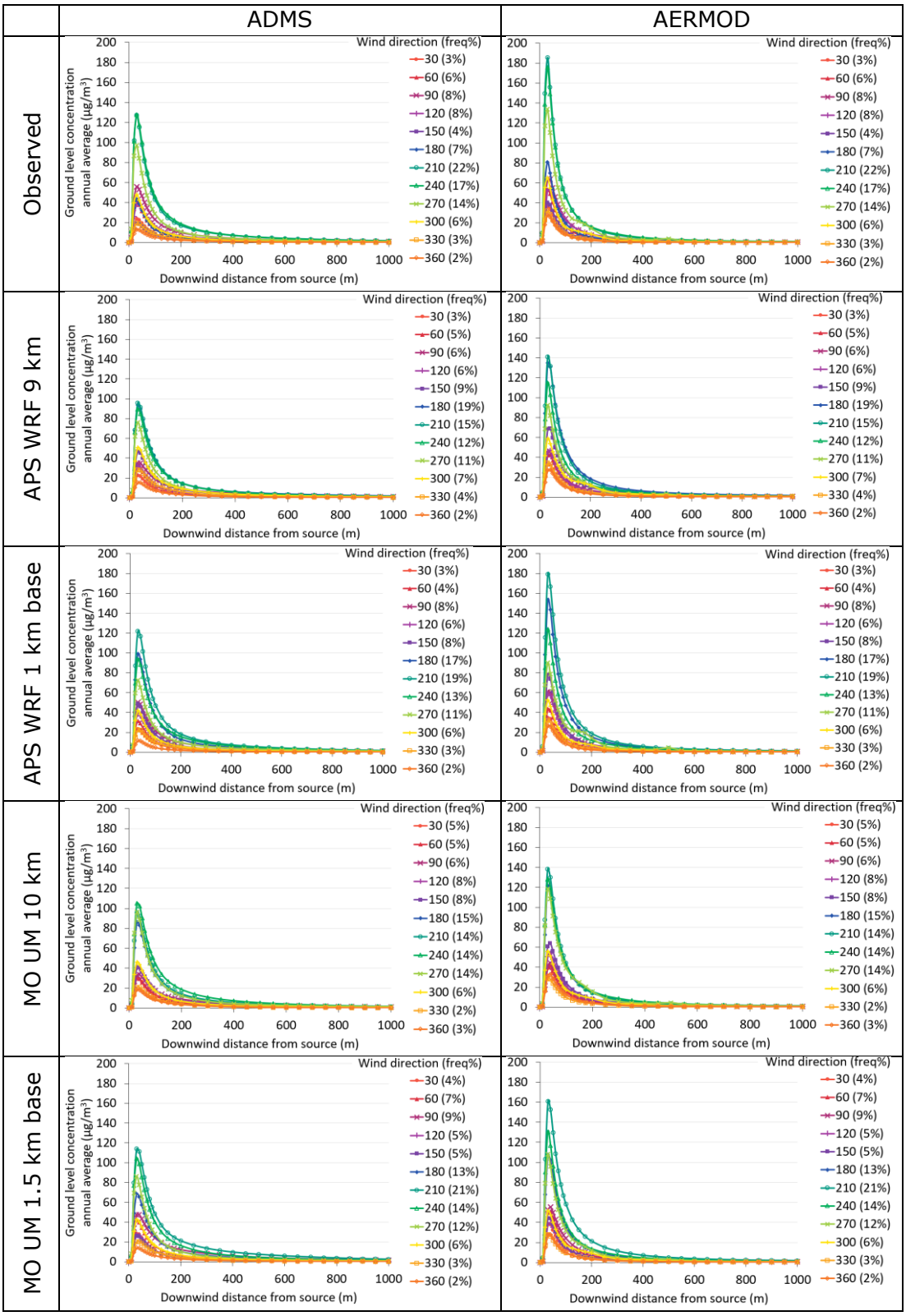

Figure 176 – Downwind profiles of annual average concentration for near-ground source at Drumalbin with varying wind direction, modelled with ADMS (left) and AERMOD (right), with observed or base NWP meteorological data.

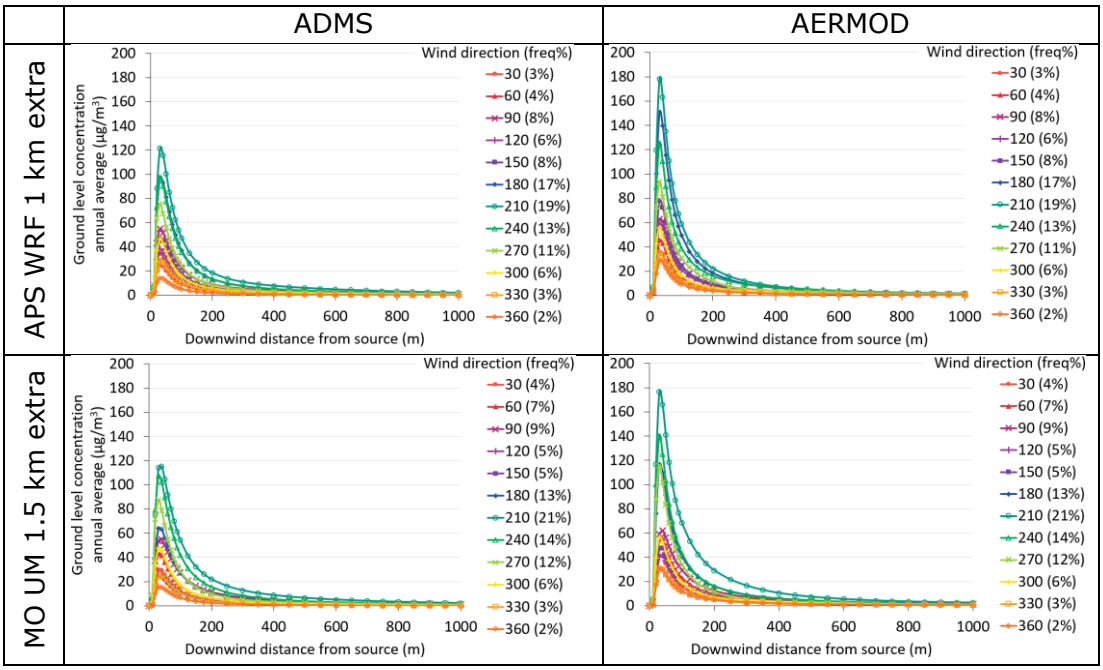

Figure 177 – Downwind profiles of annual average concentration for near-ground source at Drumalbin with varying wind direction, modelled with ADMS (left) and AERMOD (right), with extra NWP meteorological data.

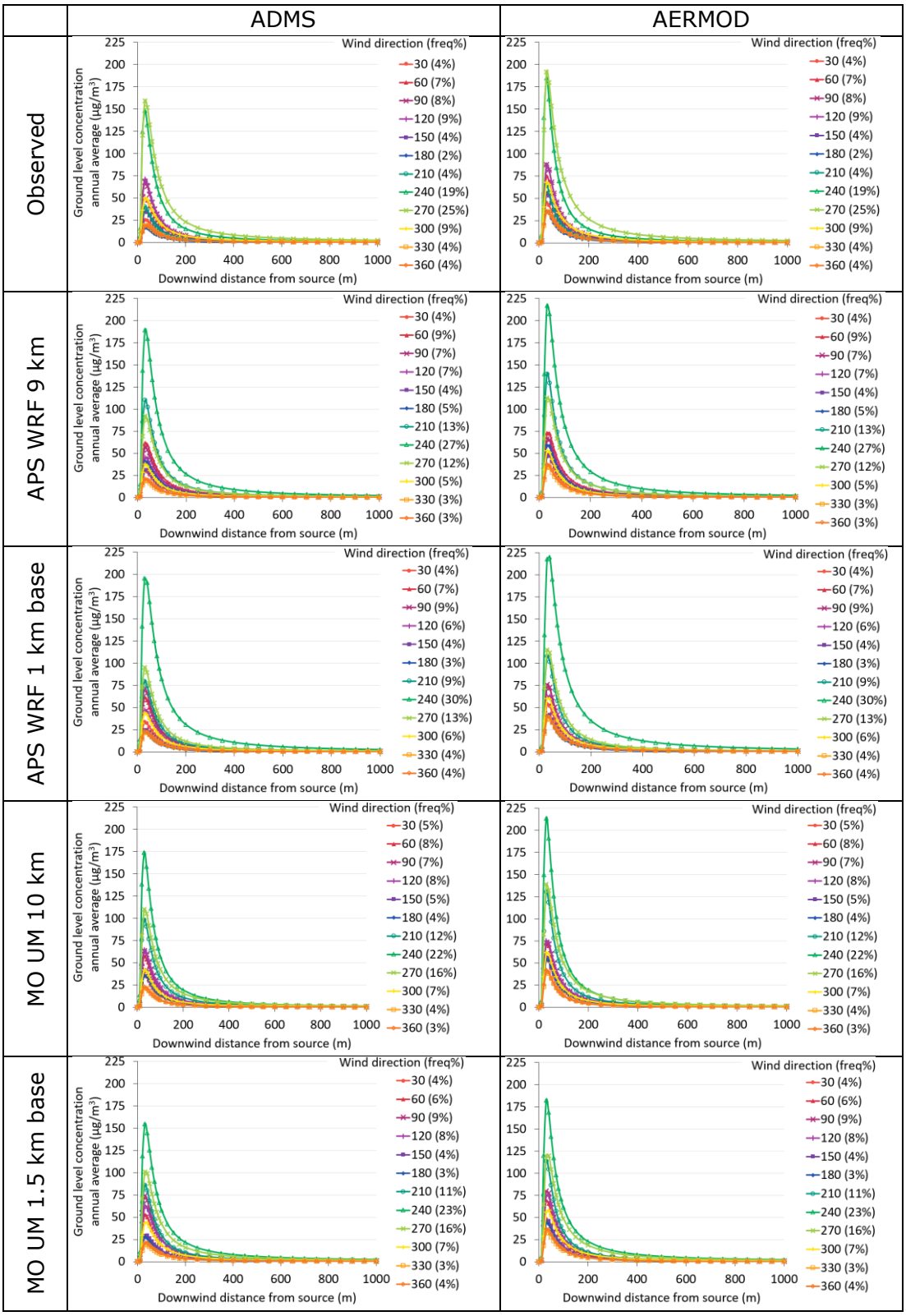

Figure 178 – Downwind profiles of annual average concentration for near-ground source at Leuchars with varying wind direction, modelled with ADMS (left) and AERMOD (right), with observed or base NWP meteorological data.

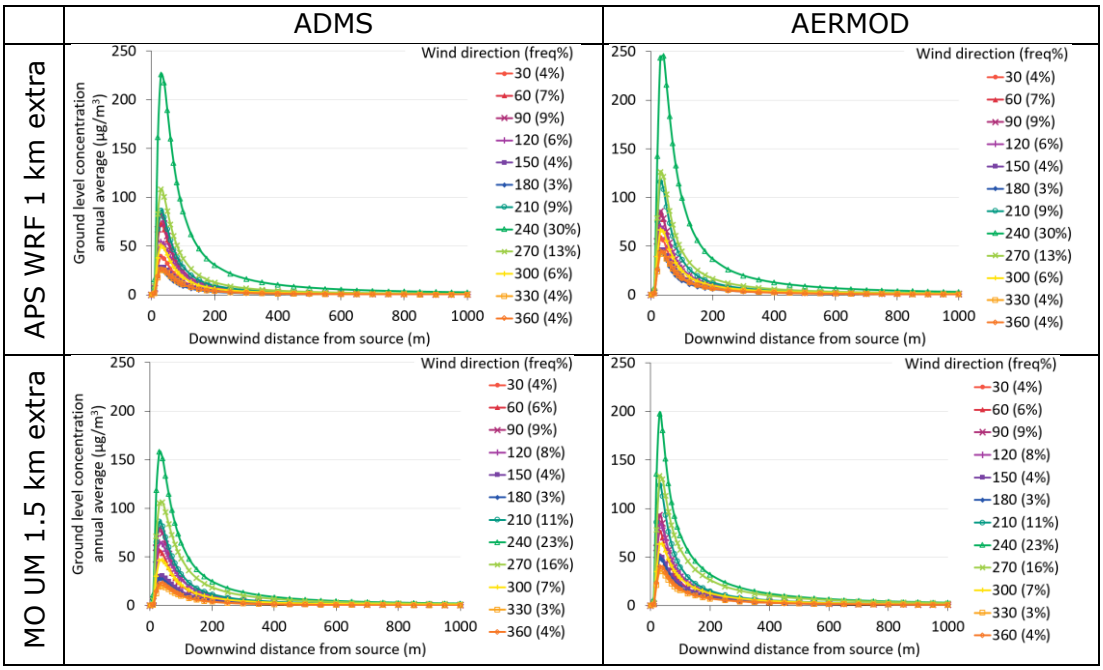

Figure 179 – Downwind profiles of annual average concentration for near-ground source at Leuchars with varying wind direction, modelled with ADMS (left) and AERMOD (right), with extra NWP meteorological data.

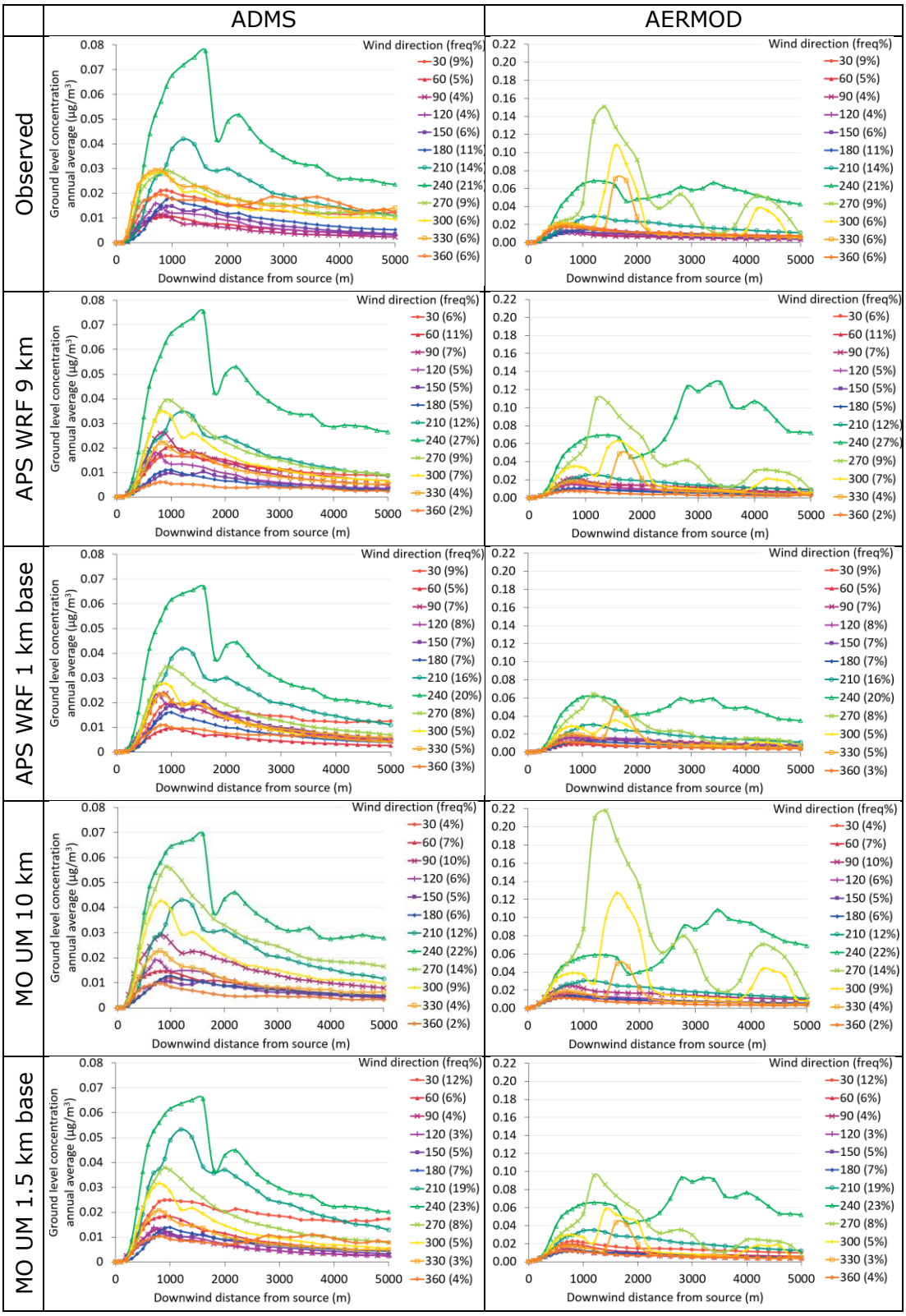

Figure 180 – Downwind profiles of annual average concentration for elevated source at Sennybridge with varying wind direction, modelled with ADMS (left) and AERMOD (right), with observed or base NWP meteorological data. Note different vertical scales are used for ADMS and AERMOD.

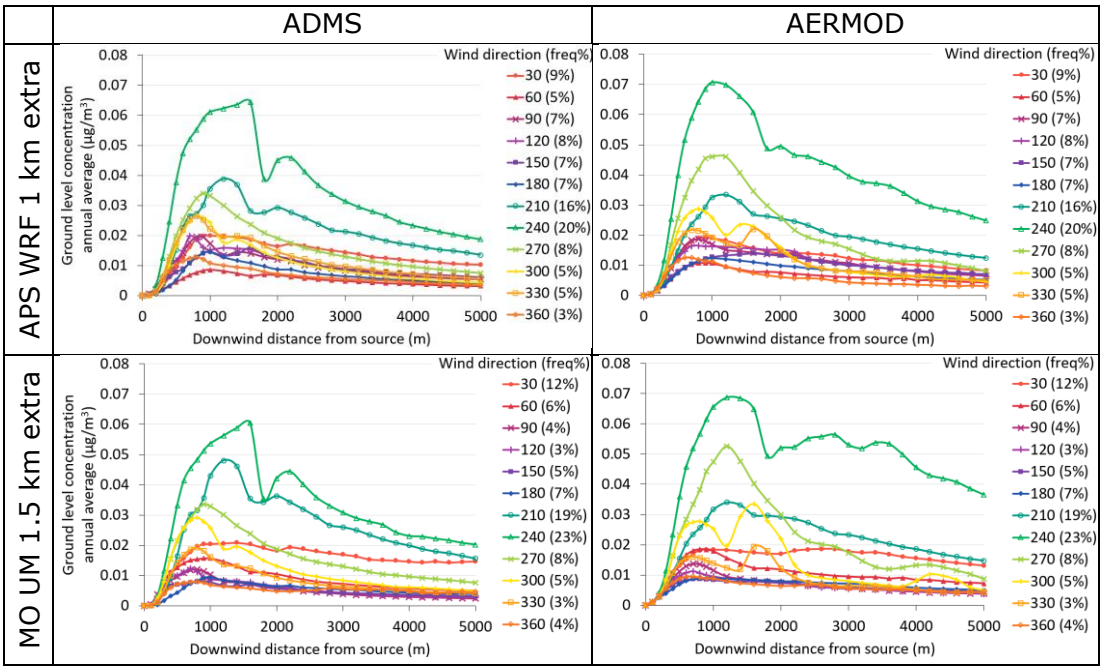

Figure 181 – Downwind profiles of annual average concentration for elevated source at Sennybridge with varying wind direction, modelled with ADMS (left) and AERMOD (right), with extra NWP meteorological data.

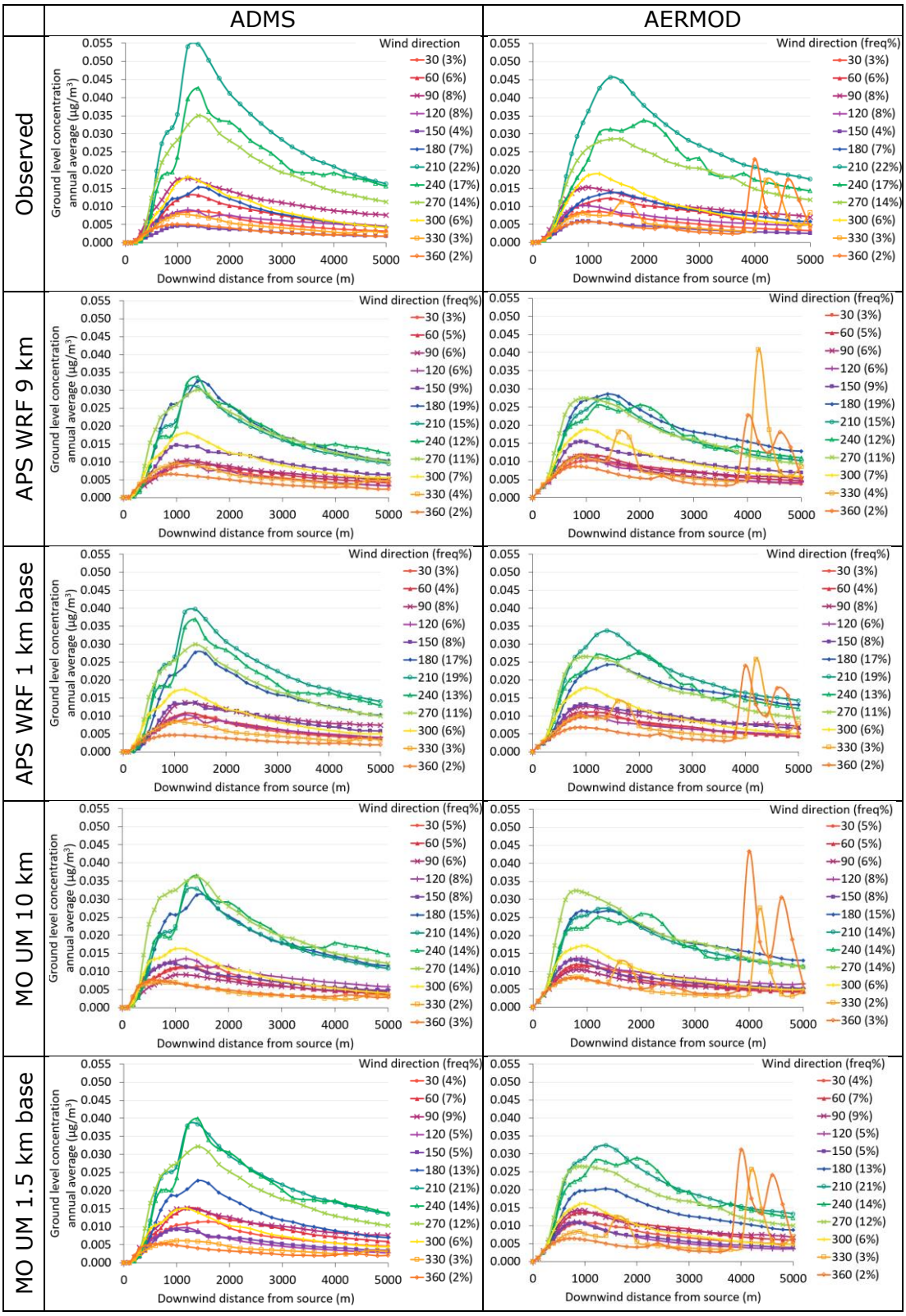

Figure 182 – Downwind profiles of annual average concentration for elevated source at Drumalbin with varying wind direction, modelled with ADMS (left) and AERMOD (right), with observed or base NWP meteorological data.

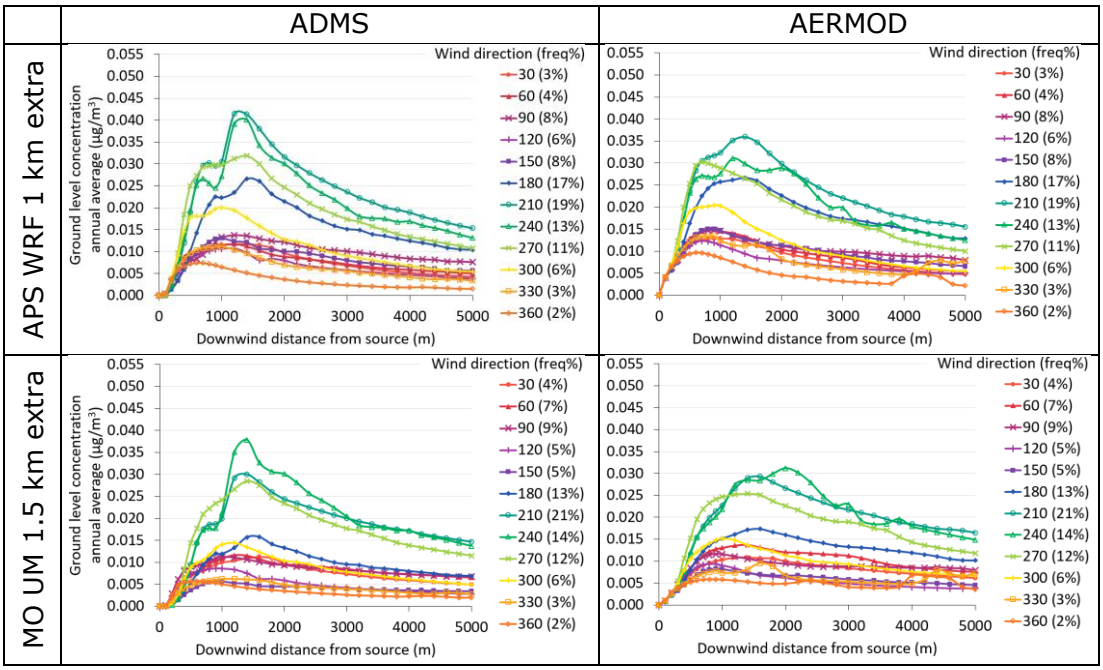

Figure 183 – Downwind profiles of annual average concentration for elevated source at Drumalbin with varying wind direction, modelled with ADMS (left) and AERMOD (right), with extra NWP meteorological data.

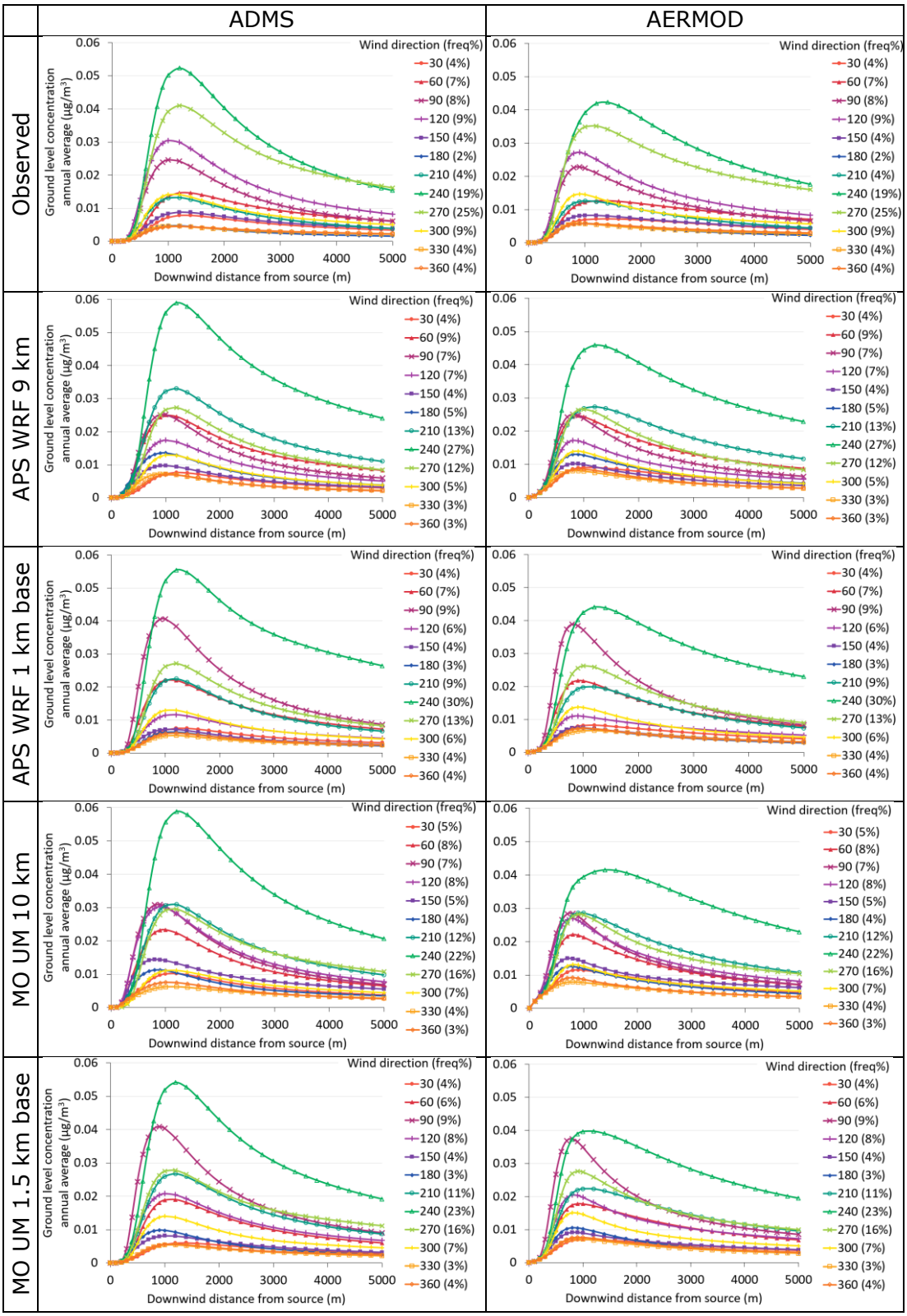

Figure 184 – Downwind profiles of annual average concentration for elevated source at Leuchars with varying wind direction, modelled with ADMS (left) and AERMOD (right), with observed or base NWP meteorological data.

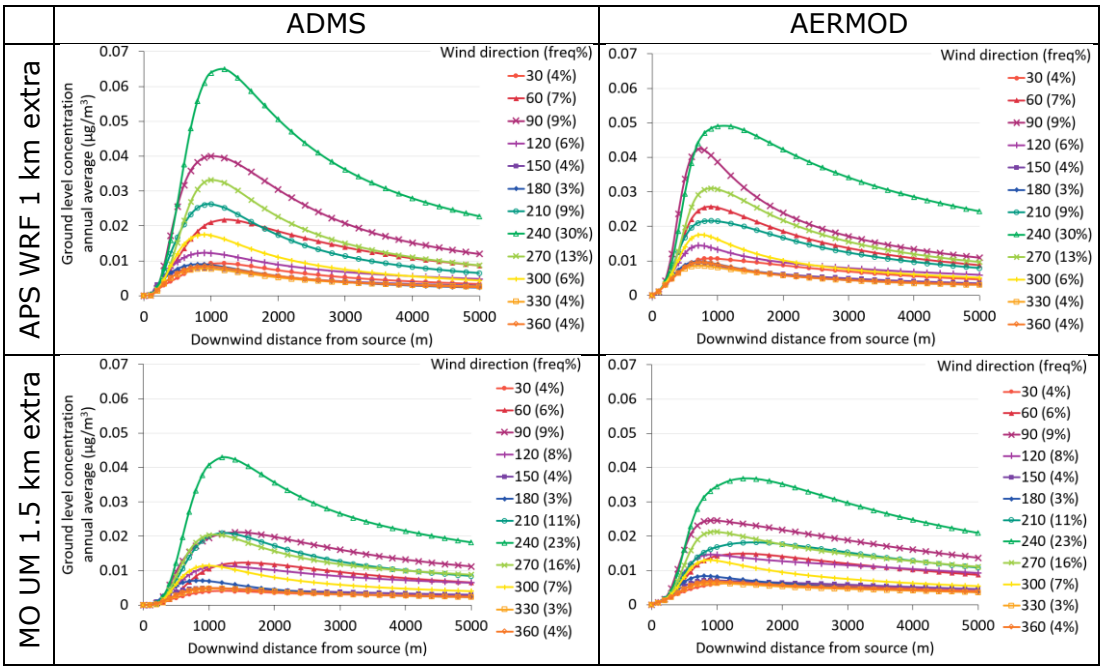

Figure 185 – Downwind profiles of annual average concentration for elevated source at Leuchars with varying wind direction, modelled with ADMS (left) and AERMOD (right), with extra NWP meteorological data.

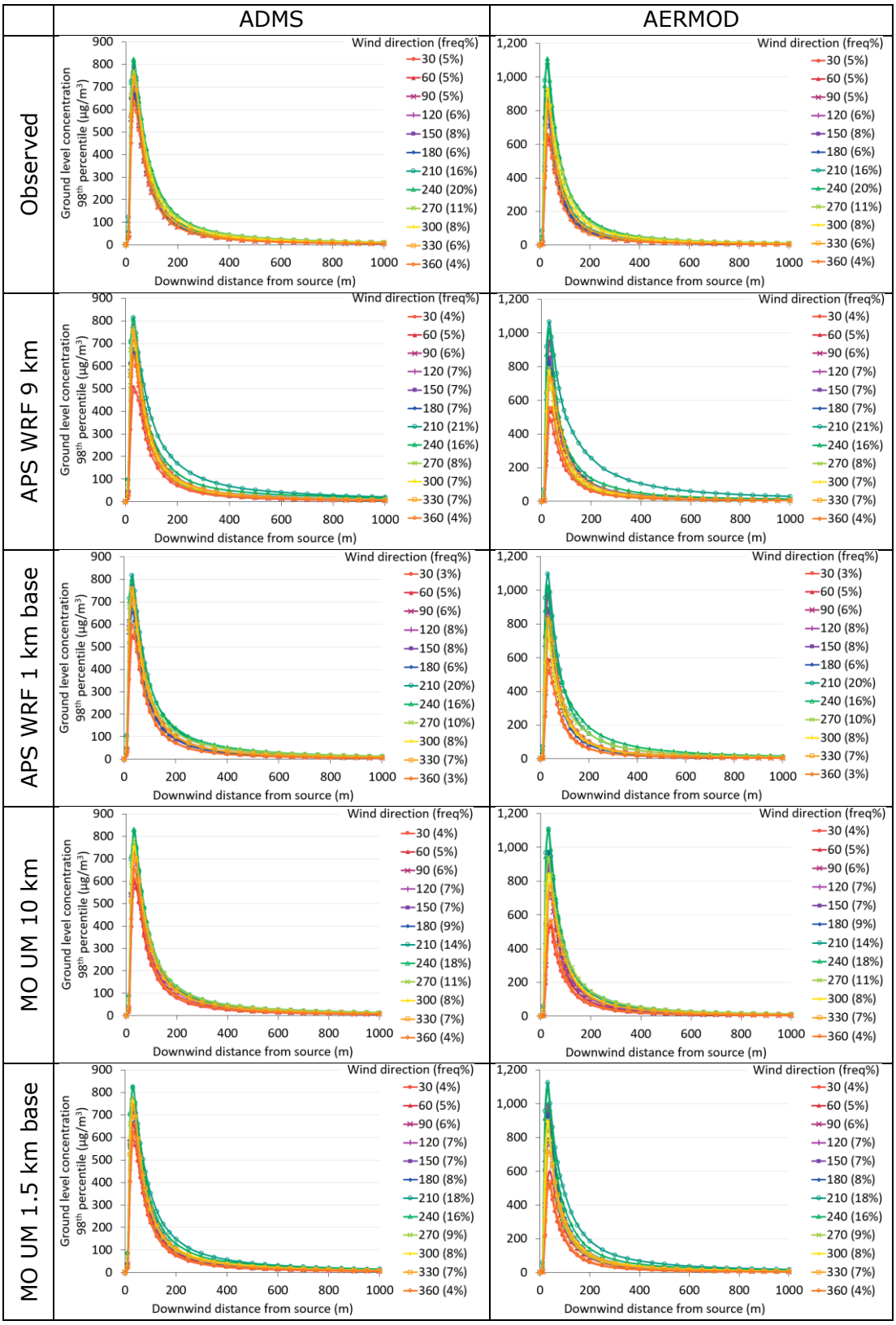

Figure 186 – Downwind profiles of 98th percentile concentration for near-ground source at Waddington with varying wind direction, modelled with ADMS (left) and AERMOD (right), with observed or base NWP meteorological data. Note different vertical scales are used for ADMS and AERMOD.

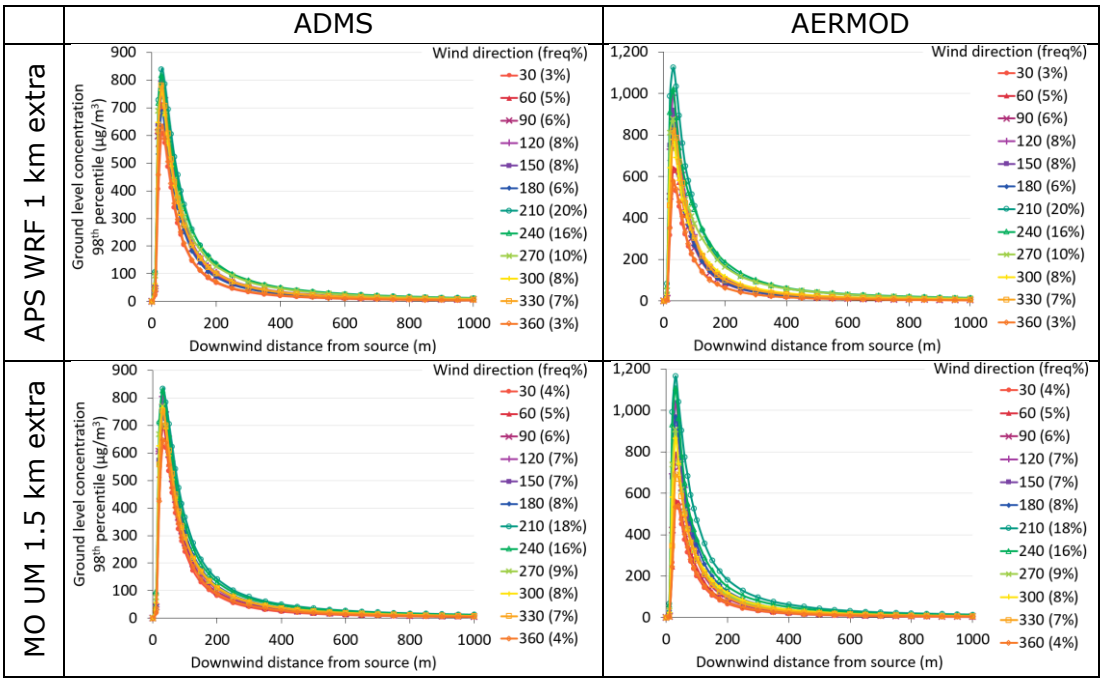

Figure 187 – Downwind profiles of 98th percentile concentration for near-ground source at Waddington with varying wind direction, modelled with ADMS (left) and AERMOD (right), with extra NWP meteorological data. Note different vertical scales are used for ADMS and AERMOD.

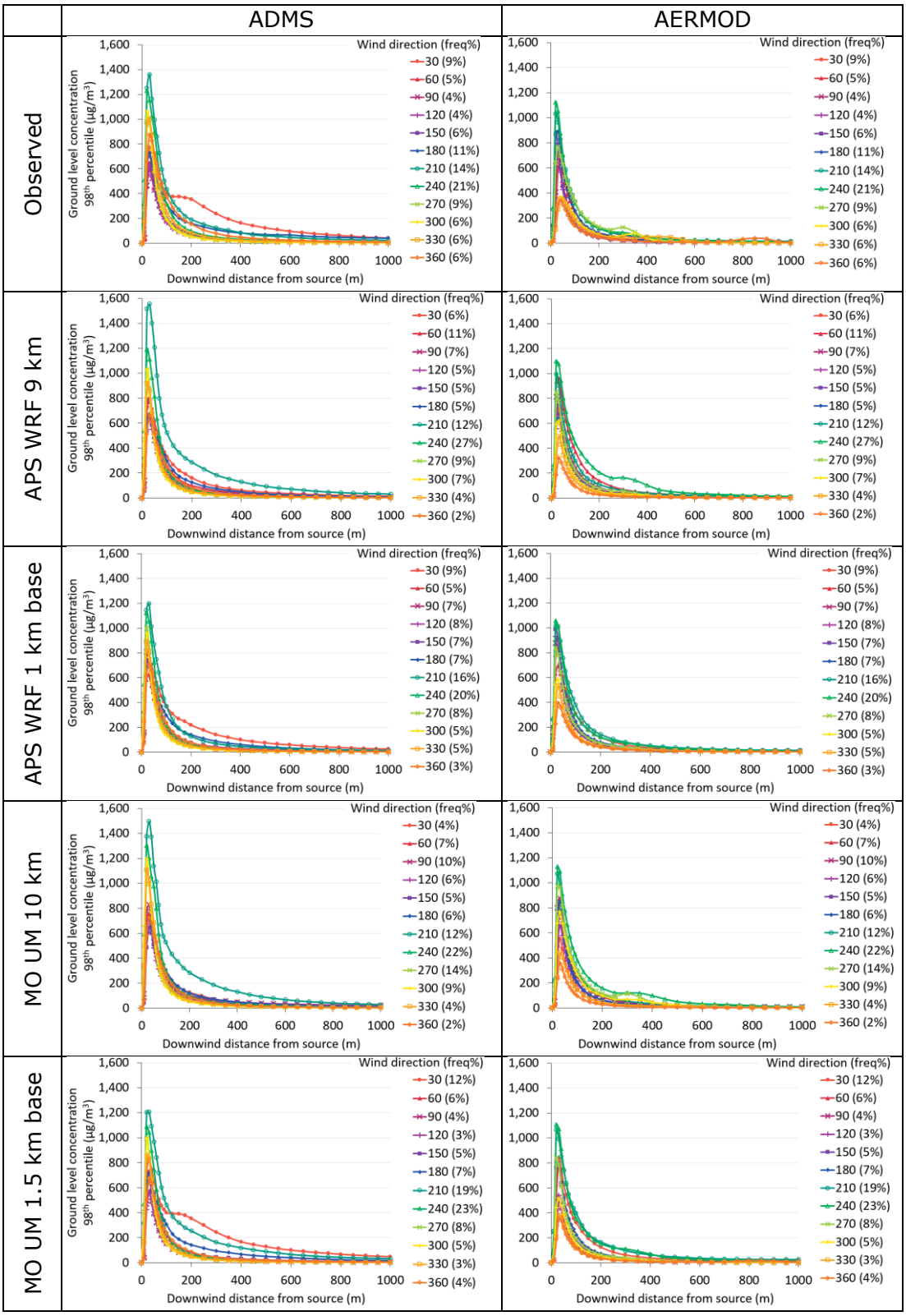

Figure 188 – Downwind profiles of 98th percentile concentration for near-ground source at Sennybridge with varying wind direction, modelled with ADMS (left) and AERMOD (right), with observed or base NWP meteorological data.

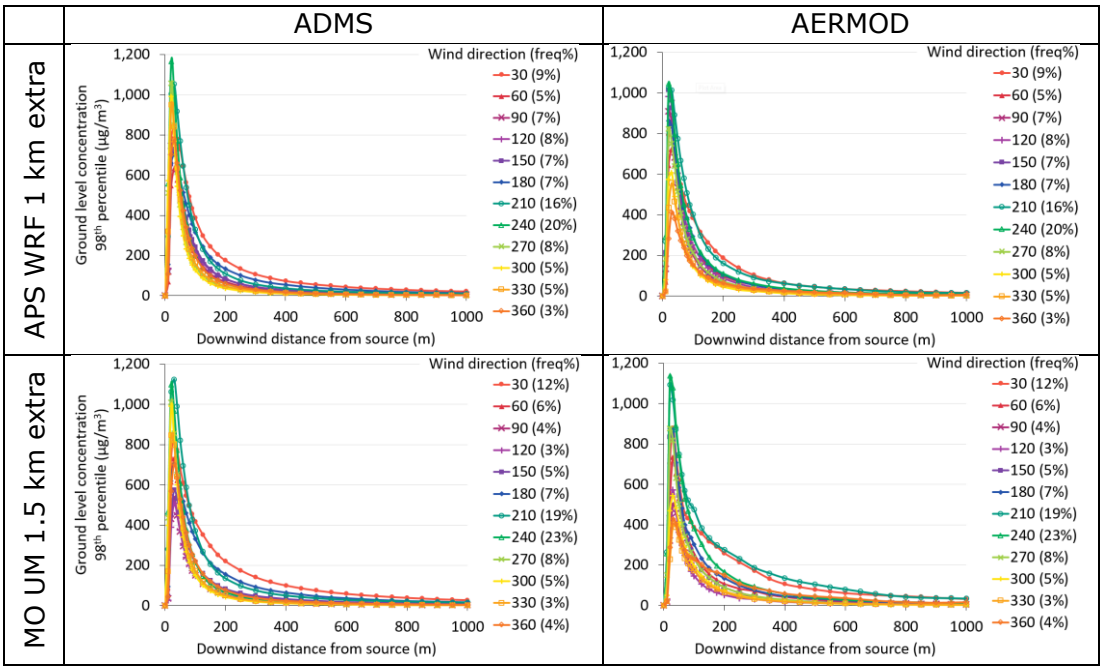

Figure 189 – Downwind profiles of 98th percentile concentration for near-ground source at Sennybridge with varying wind direction, modelled with ADMS (left) and AERMOD (right), with extra NWP meteorological data.

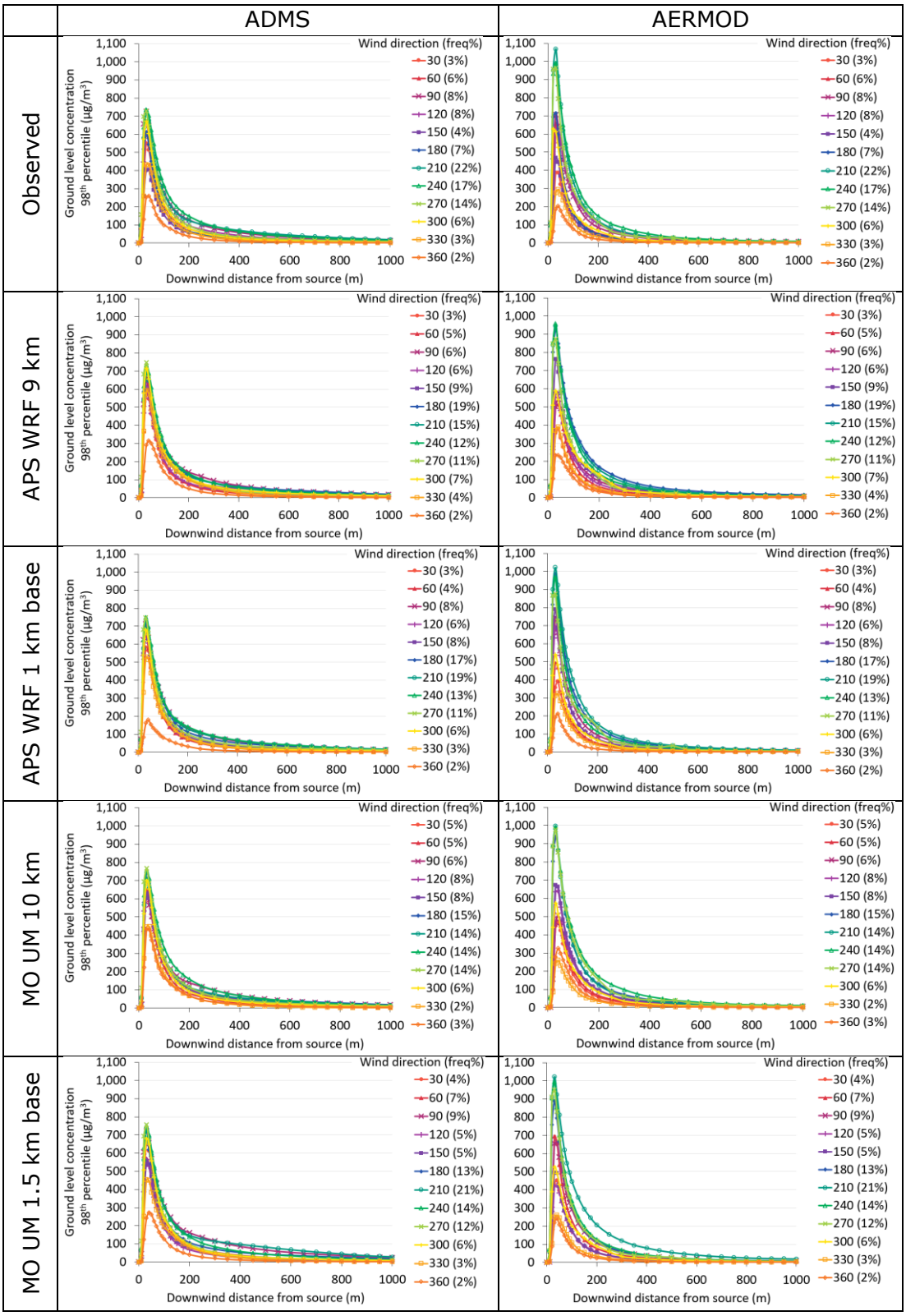

Figure 190 – Downwind profiles of 98th percentile concentration for near-ground source at Drumalbin with varying wind direction, modelled with ADMS (left) and AERMOD (right), with observed or base NWP meteorological data.

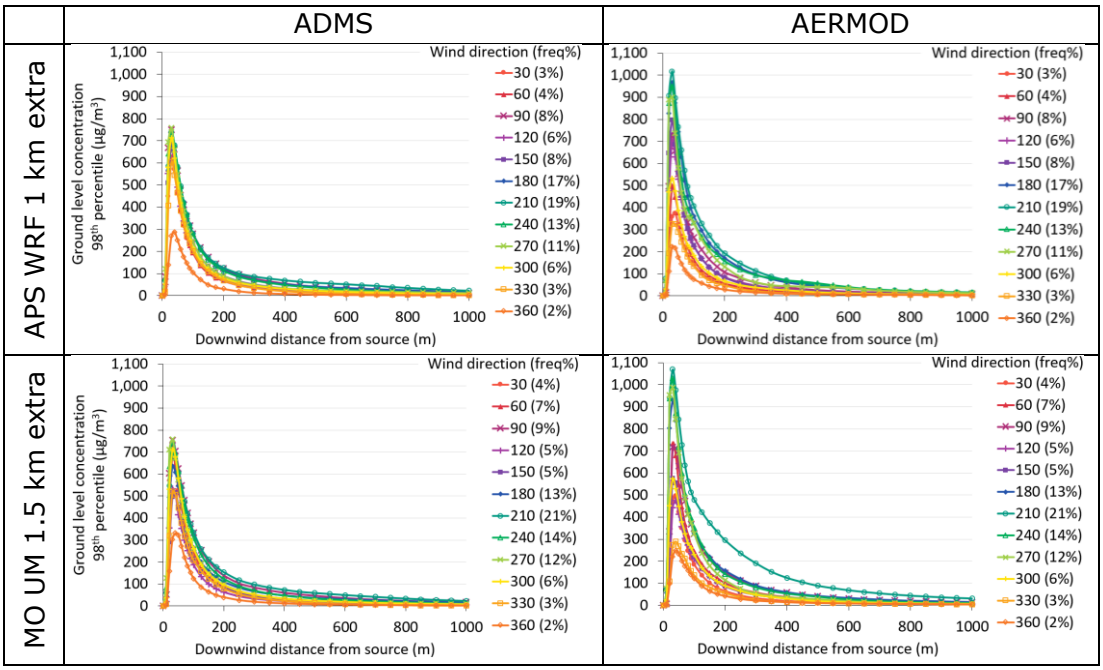

Figure 191 – Downwind profiles of 98th percentile concentration for near-ground source at Drumalbin with varying wind direction, modelled with ADMS (left) and AERMOD (right), with extra NWP meteorological data.

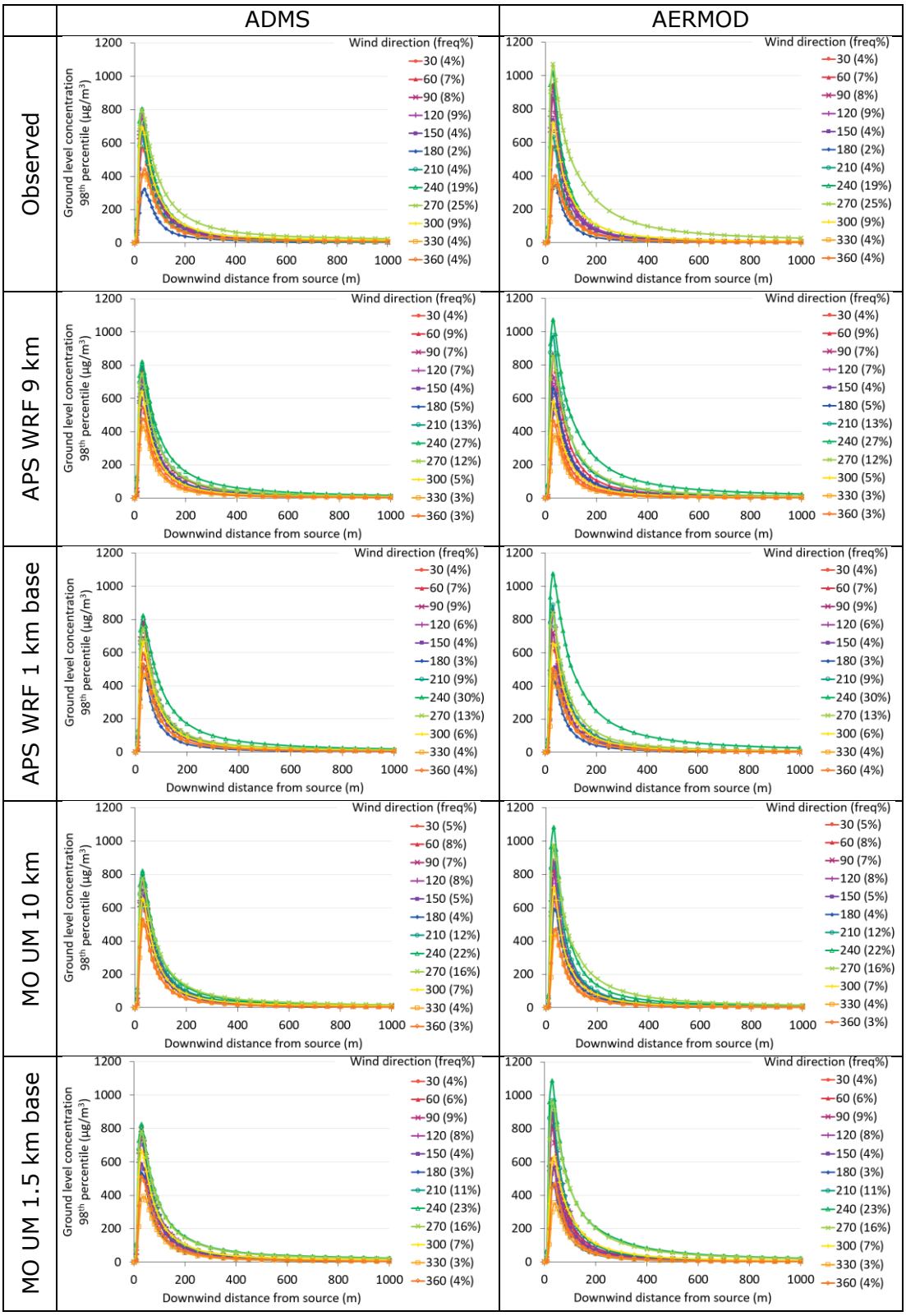

Figure 192 – Downwind profiles of 98th percentile concentration for near-ground source at Leuchars with varying wind direction, modelled with ADMS (left) and AERMOD (right), with observed or base NWP meteorological data.

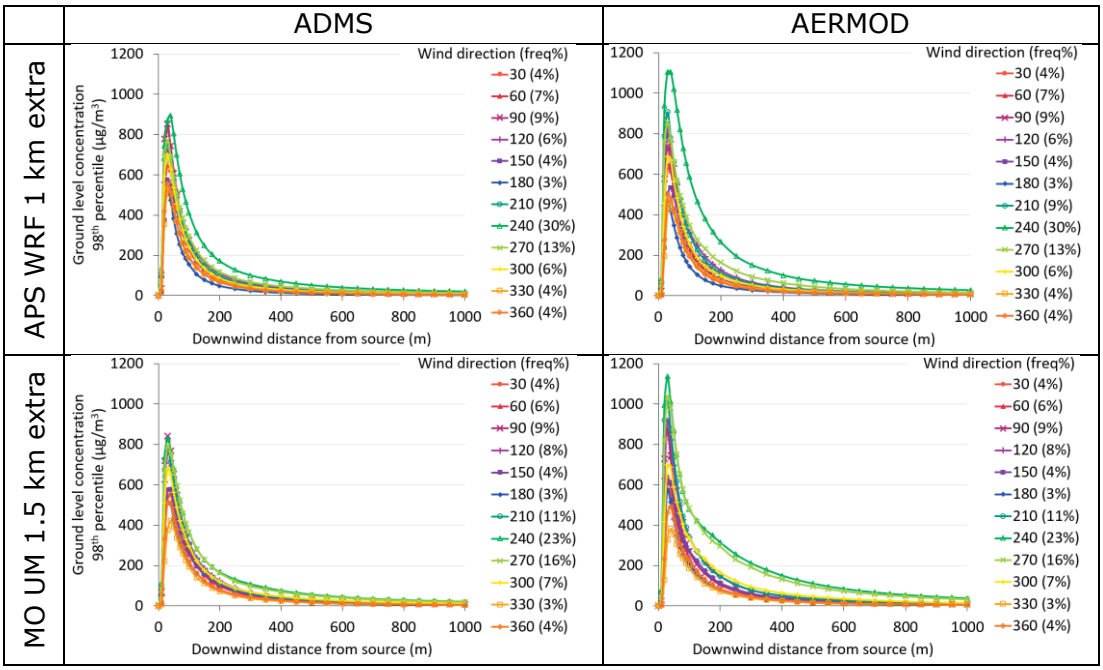

Figure 193 – Downwind profiles of 98th percentile concentration for near-ground source at Leuchars with varying wind direction, modelled with ADMS (left) and AERMOD (right), with extra NWP meteorological data.

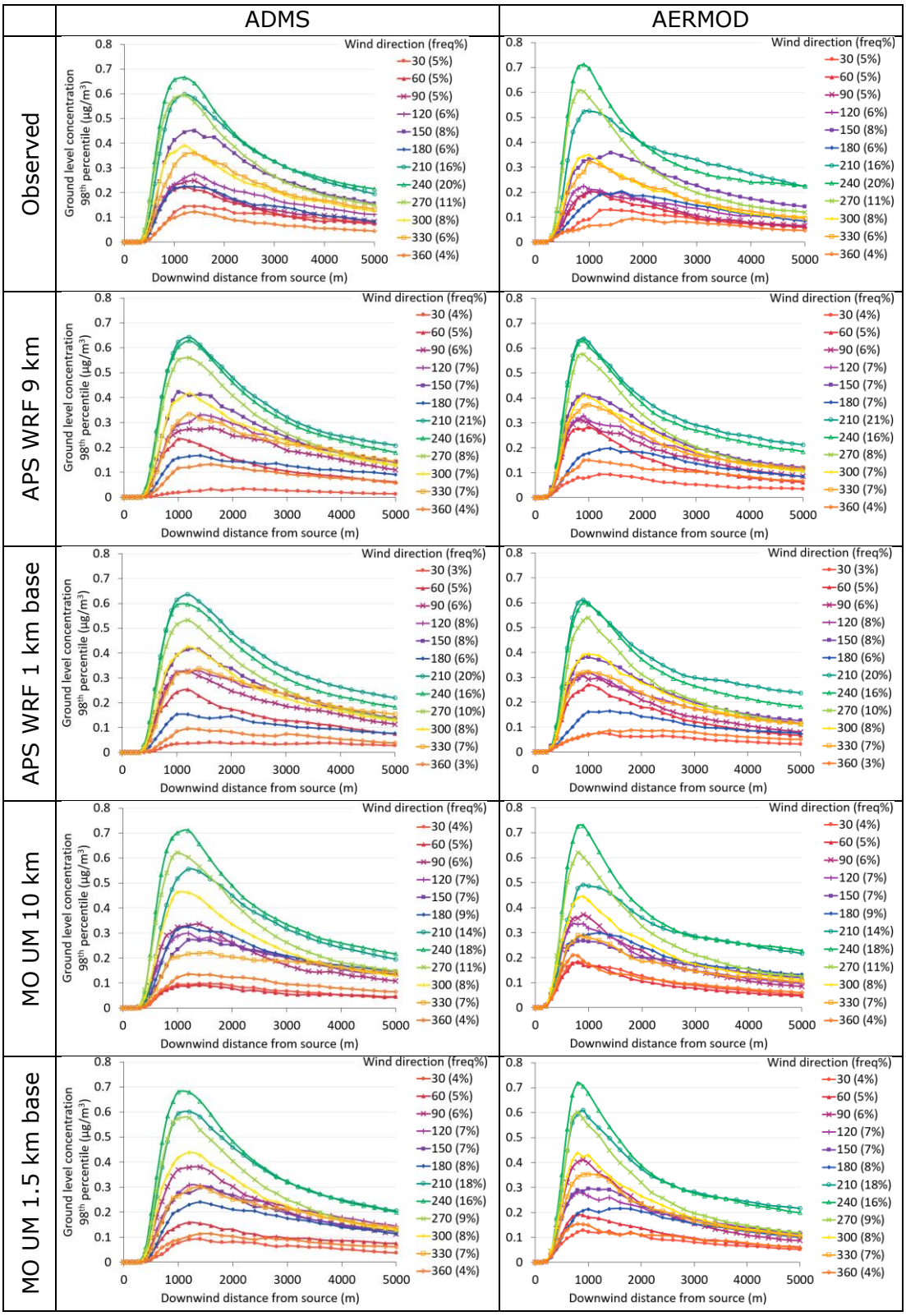

Figure 194 – Downwind profiles of 98th percentile concentration for elevated source at Waddington with varying wind direction, modelled with ADMS (left) and AERMOD (right), with observed or base NWP meteorological data.

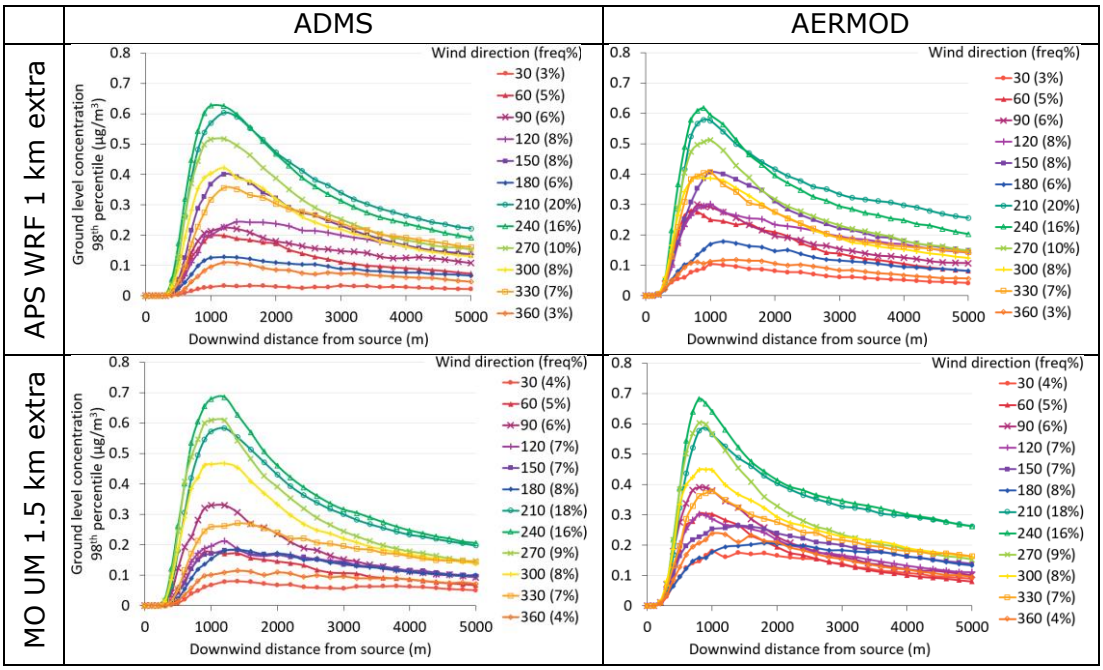

Figure 195 – Downwind profiles of 98th percentile concentration for elevated source at Waddington with varying wind direction, modelled with ADMS (left) and AERMOD (right), with extra NWP meteorological data.

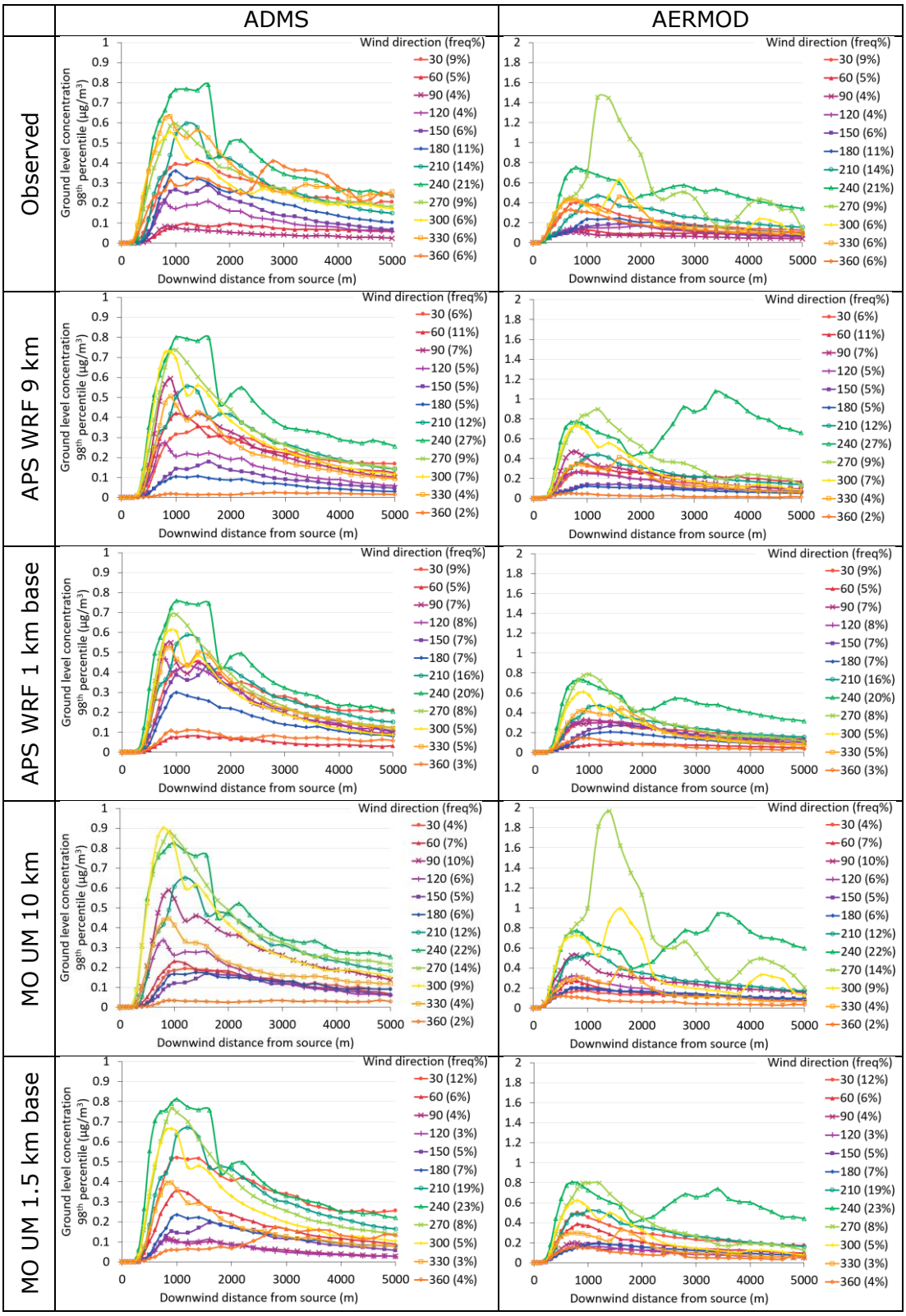

Figure 196 – Downwind profiles of 98th percentile concentration for elevated source at Sennybridge with varying wind direction, modelled with ADMS (left) and AERMOD (right), with observed or base NWP meteorological data. Note the different vertical scales used for ADMS and AERMOD.

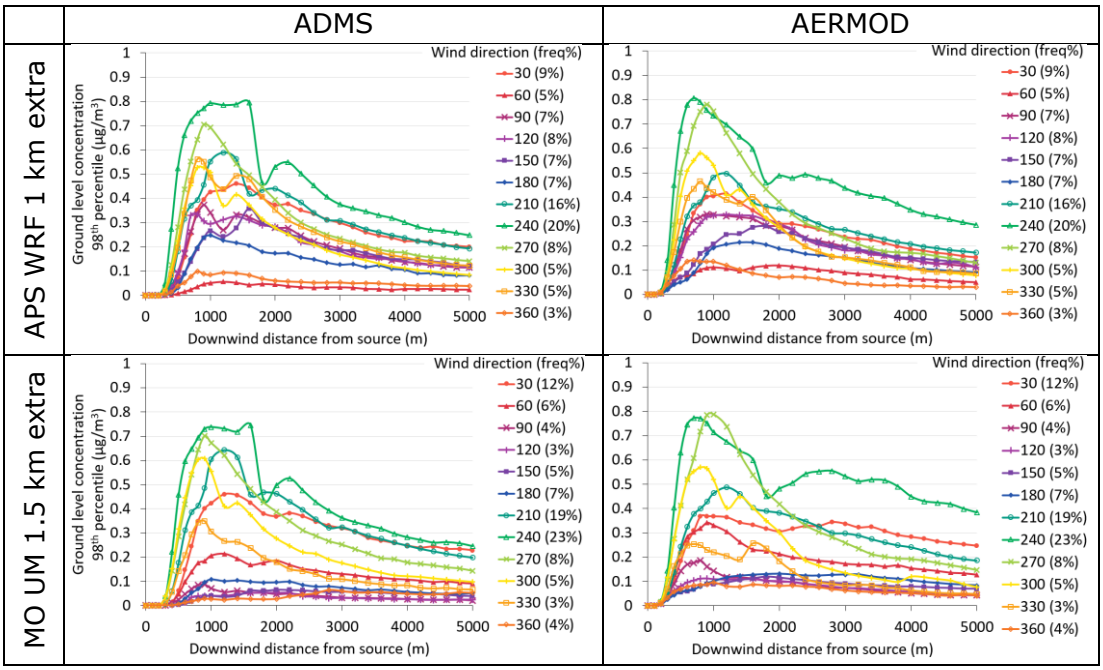

Figure 197 – Downwind profiles of 98th percentile concentration for elevated source at Sennybridge with varying wind direction, modelled with ADMS (left) and AERMOD (right), with extra NWP meteorological data.

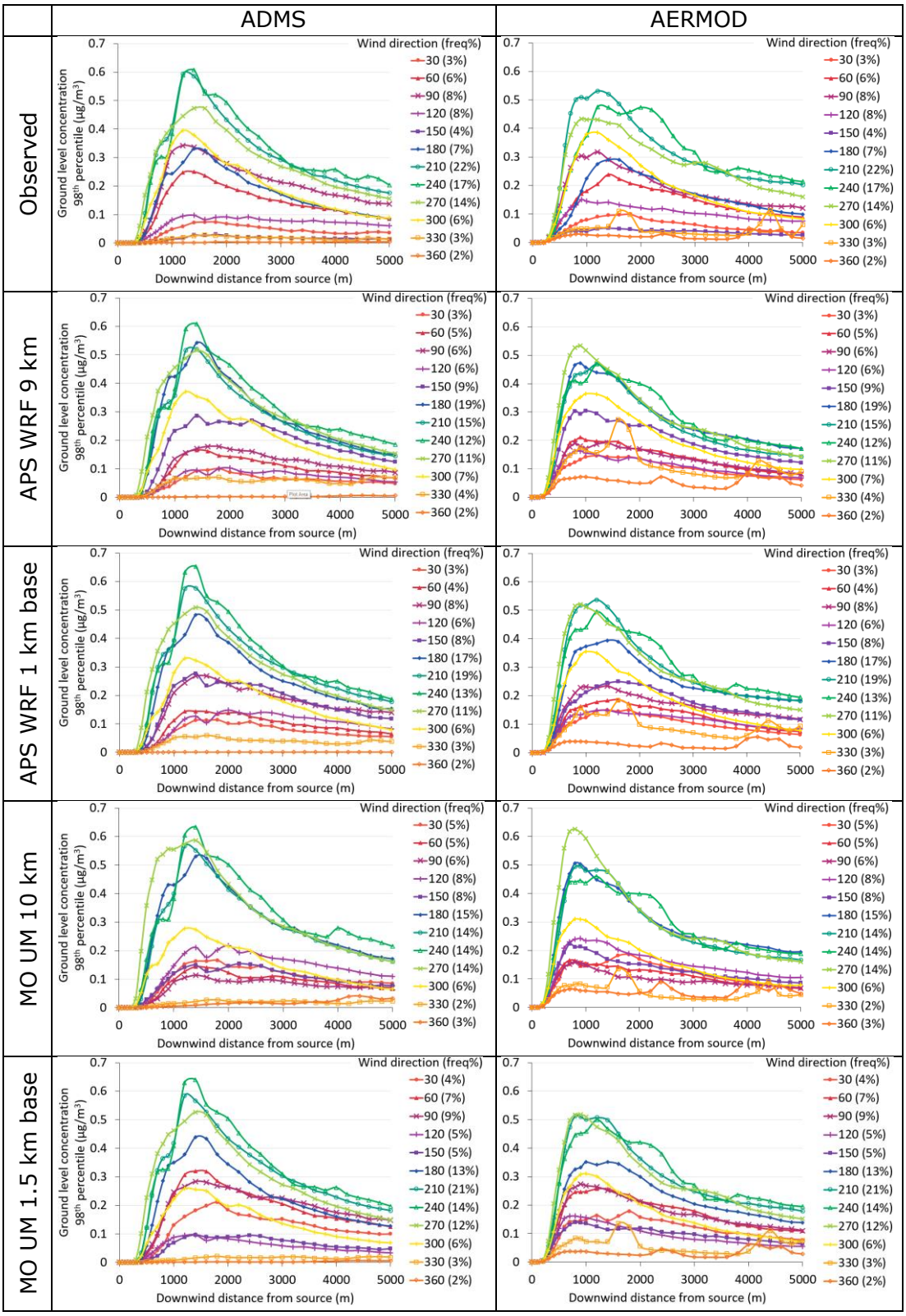

Figure 198 – Downwind profiles of 98th percentile concentration for elevated source at Drumalbin with varying wind direction, modelled with ADMS (left) and AERMOD (right), with observed or base NWP meteorological data.

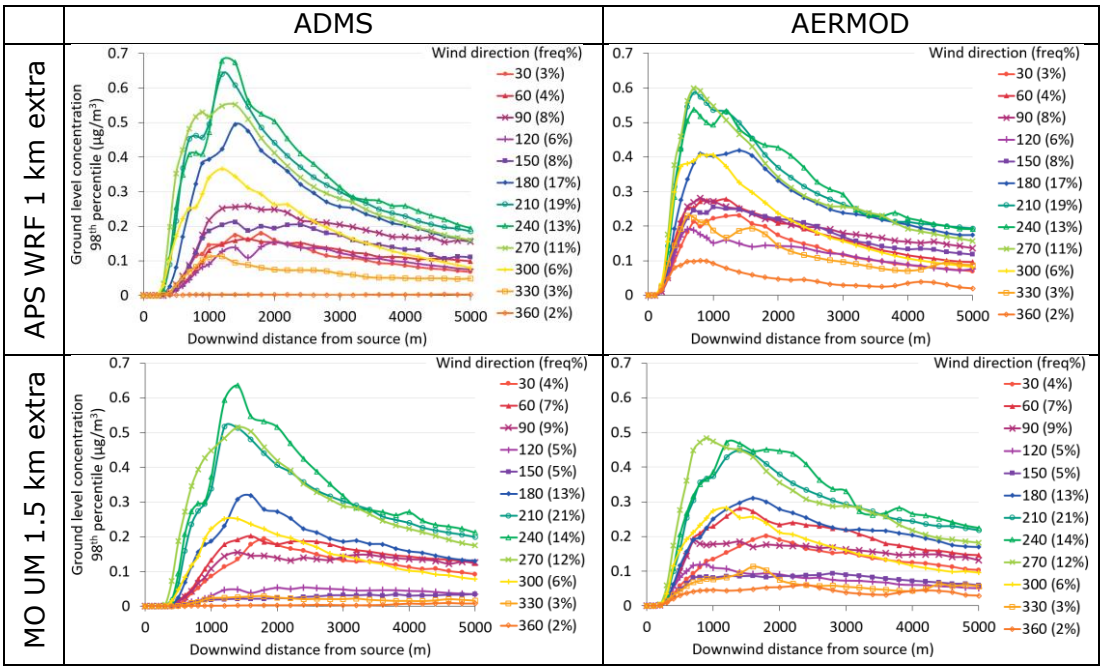

Figure 199 – Downwind profiles of 98th percentile concentration for elevated source at Drumalbin with varying wind direction, modelled with ADMS (left) and AERMOD (right), with extra NWP meteorological data.

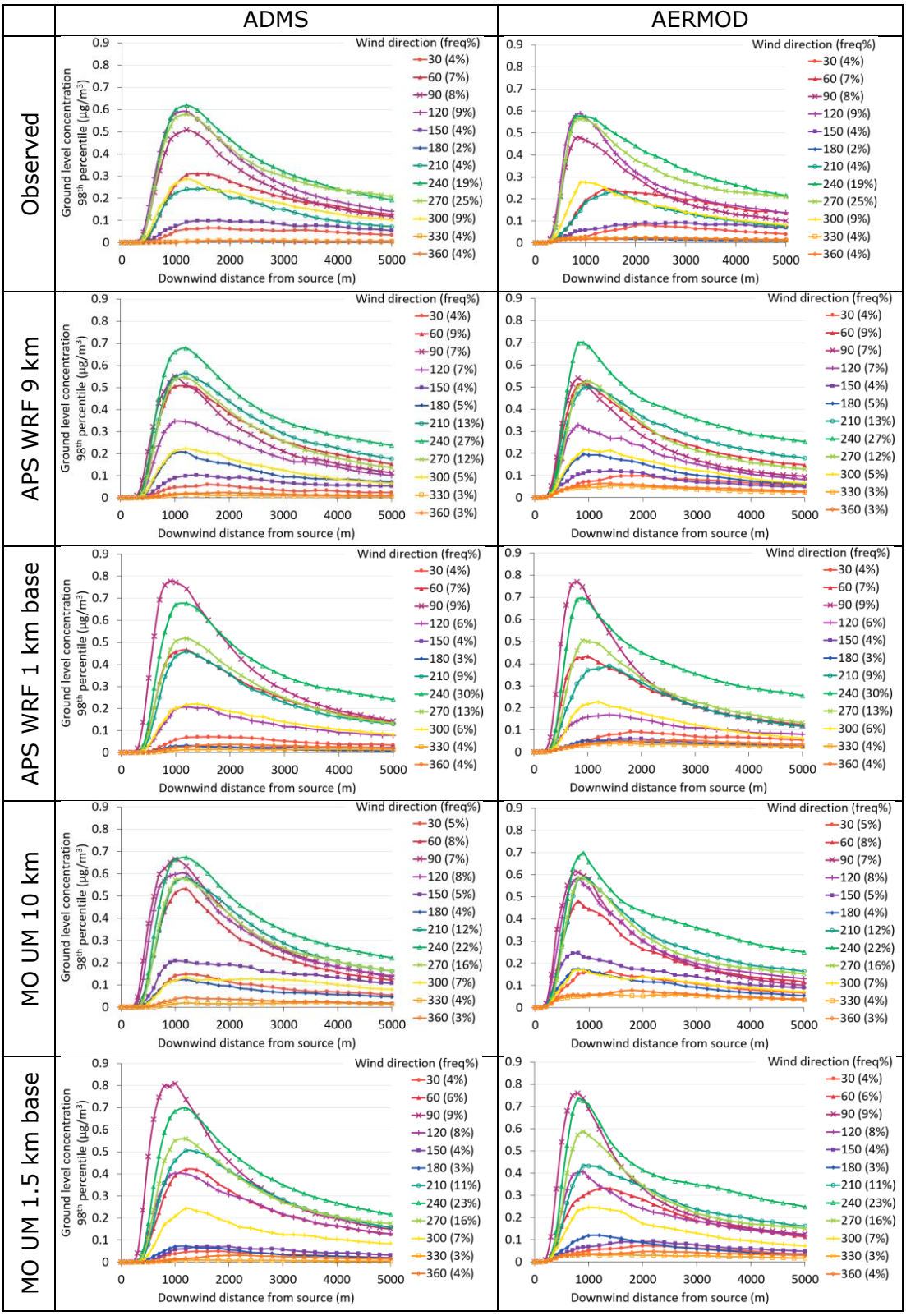

Figure 200 – Downwind profiles of 98th percentile concentration for elevated source at Leuchars with varying wind direction, modelled with ADMS (left) and AERMOD (right), with observed or base NWP meteorological data.

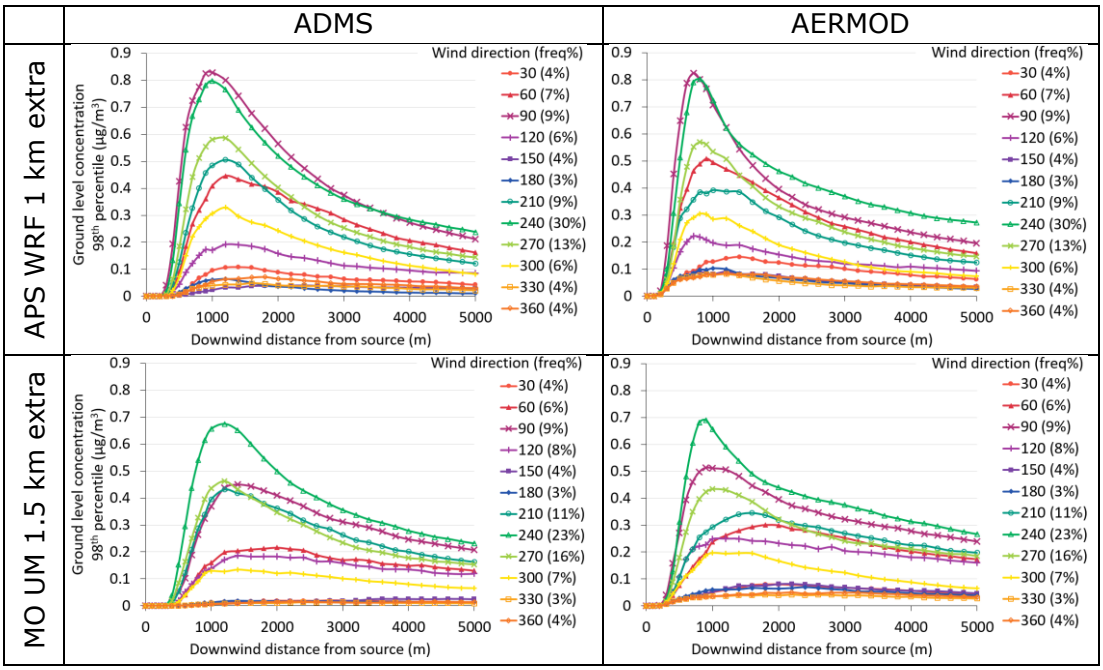

Figure 201 – Downwind profiles of 98th percentile concentration for elevated source at Leuchars with varying wind direction, modelled with ADMS (left) and AERMOD (right), with extra NWP meteorological data.

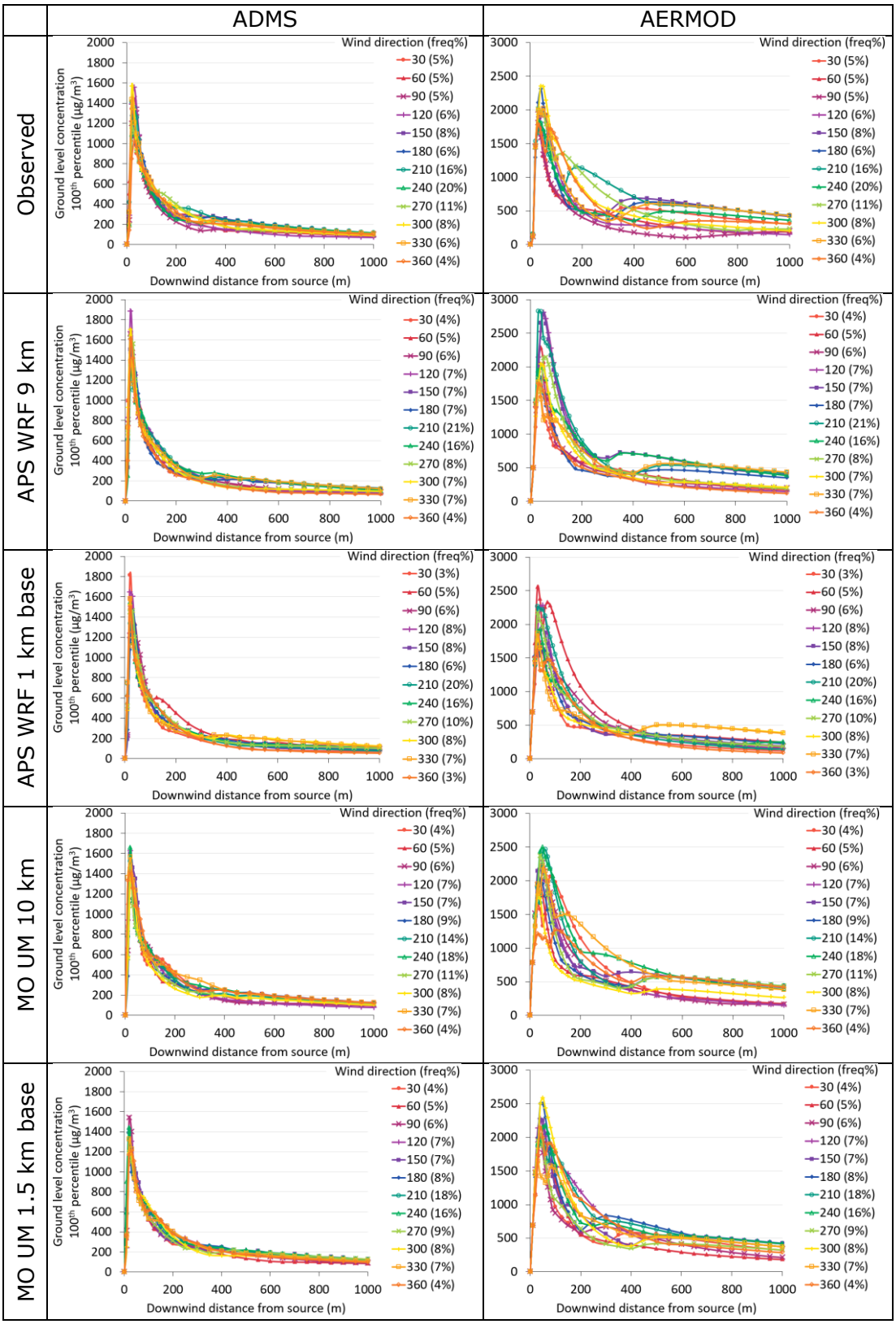

Figure 202 – Downwind profiles of 100th percentile concentration for near-ground source at Waddington with varying wind direction, modelled with ADMS (left) and AERMOD (right), with observed or base NWP meteorological data. Note different vertical scales are used for ADMS and AERMOD.

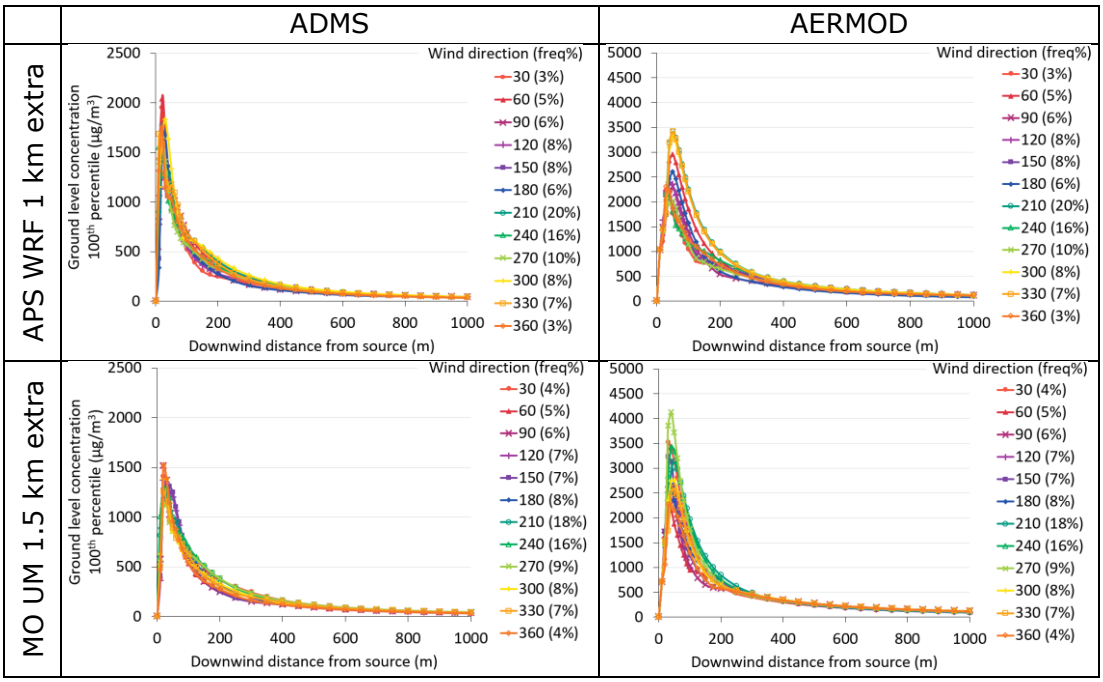

Figure 203 – Downwind profiles of 100th percentile concentration for near-ground source at Waddington with varying wind direction, modelled with ADMS (left) and AERMOD (right), with extra NWP meteorological data. Note different vertical scales are used for ADMS and AERMOD.

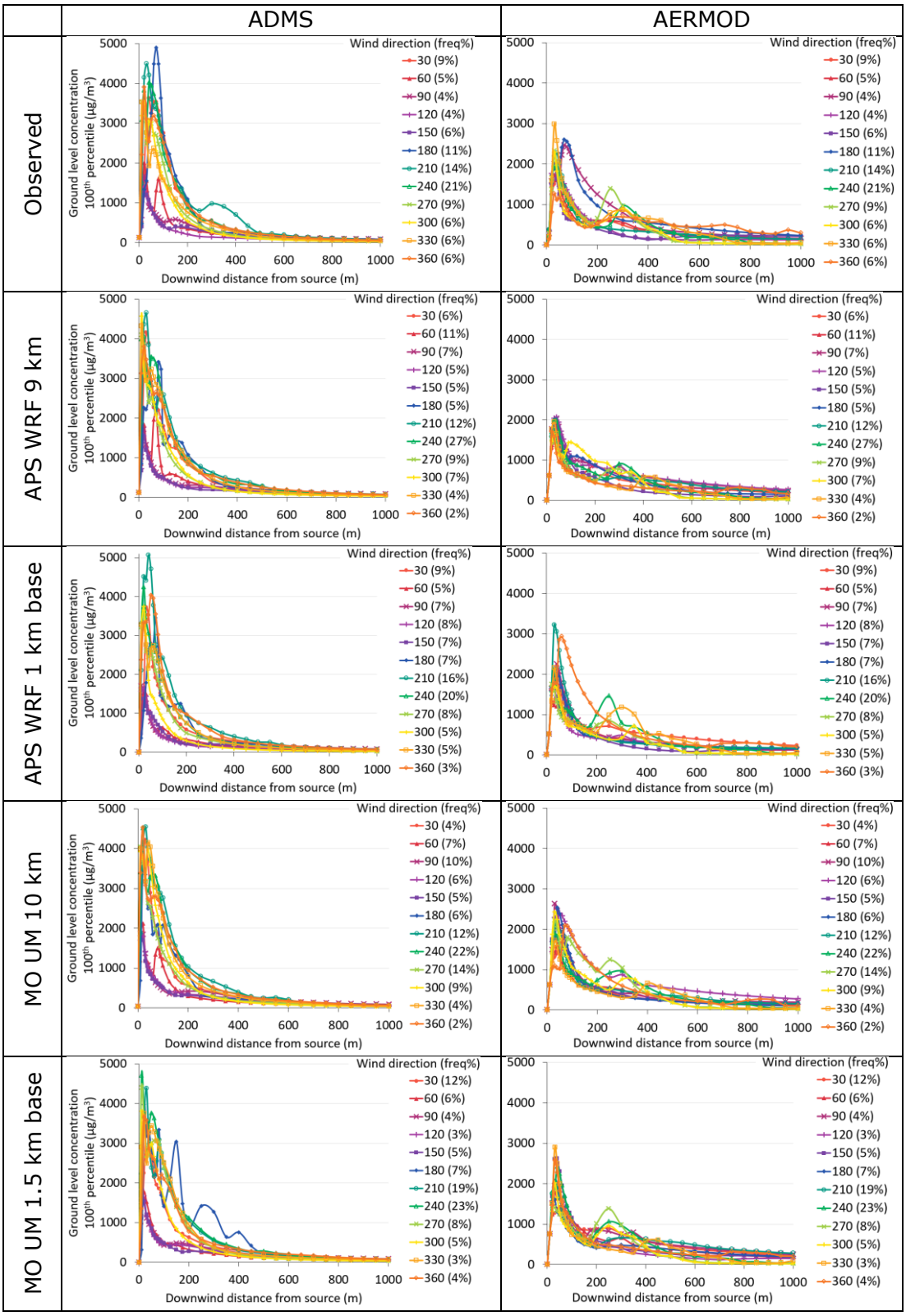

Figure 204 – Downwind profiles of 100th percentile concentration for near-ground source at Sennybridge with varying wind direction, modelled with ADMS (left) and AERMOD (right), with observed or base NWP meteorological data.

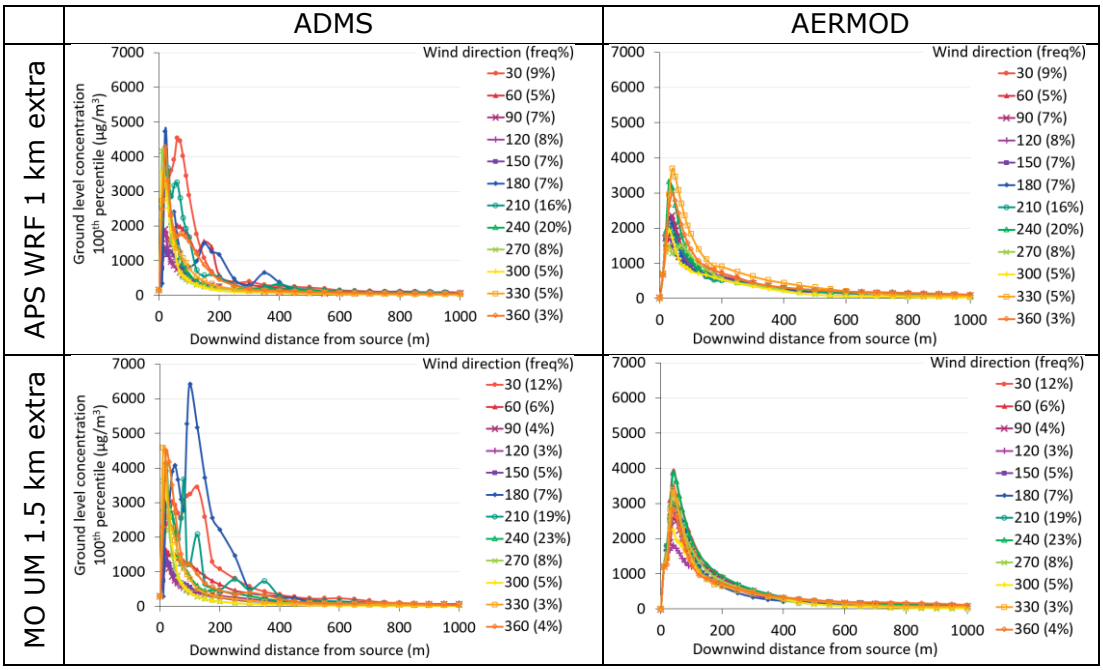

Figure 205 – Downwind profiles of 100th percentile concentration for near-ground source at Sennybridge with varying wind direction, modelled with ADMS (left) and AERMOD (right), with extra NWP meteorological data.

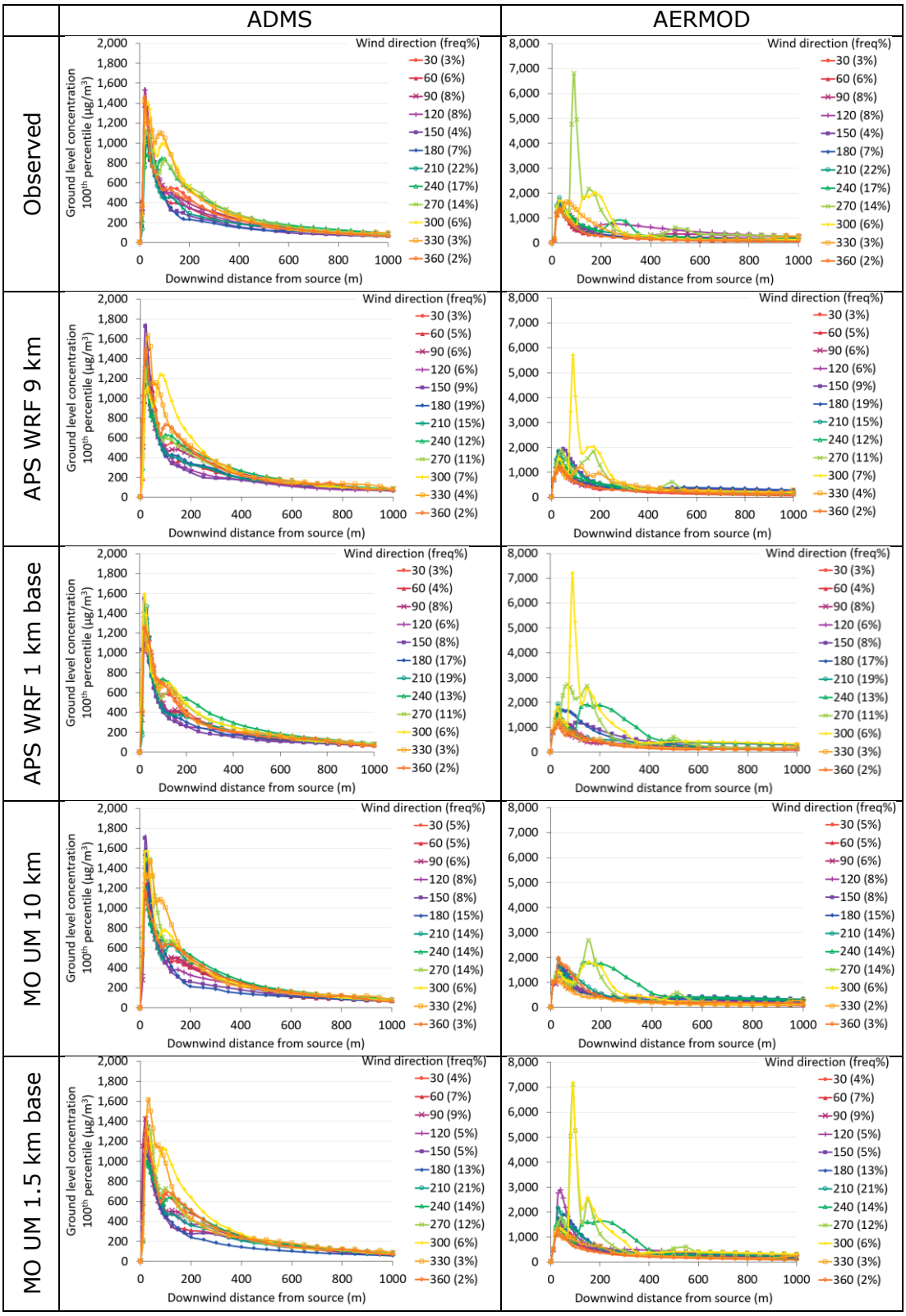

Figure 206 – Downwind profiles of 100th percentile concentration for near-ground source at Drumalbin with varying wind direction, modelled with ADMS (left) and AERMOD (right), with observed or base NWP meteorological data. Note different vertical scales are used for ADMS and AERMOD.

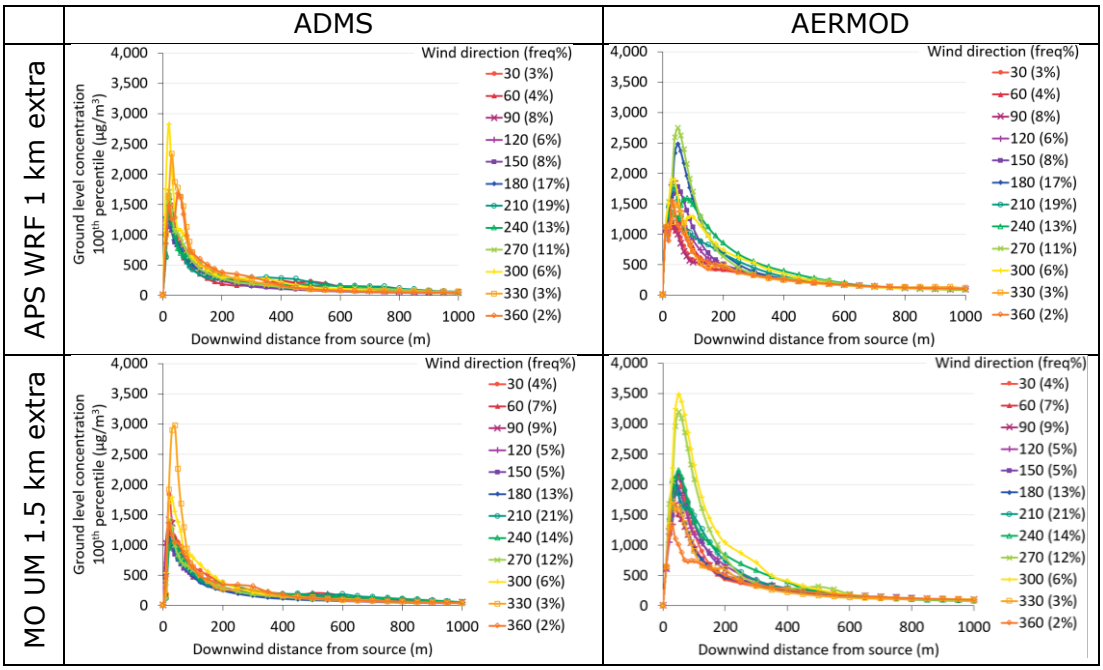

Figure 207 – Downwind profiles of 100th percentile concentration for near-ground source at Drumalbin with varying wind direction, modelled with ADMS (left) and AERMOD (right), with extra NWP meteorological data.

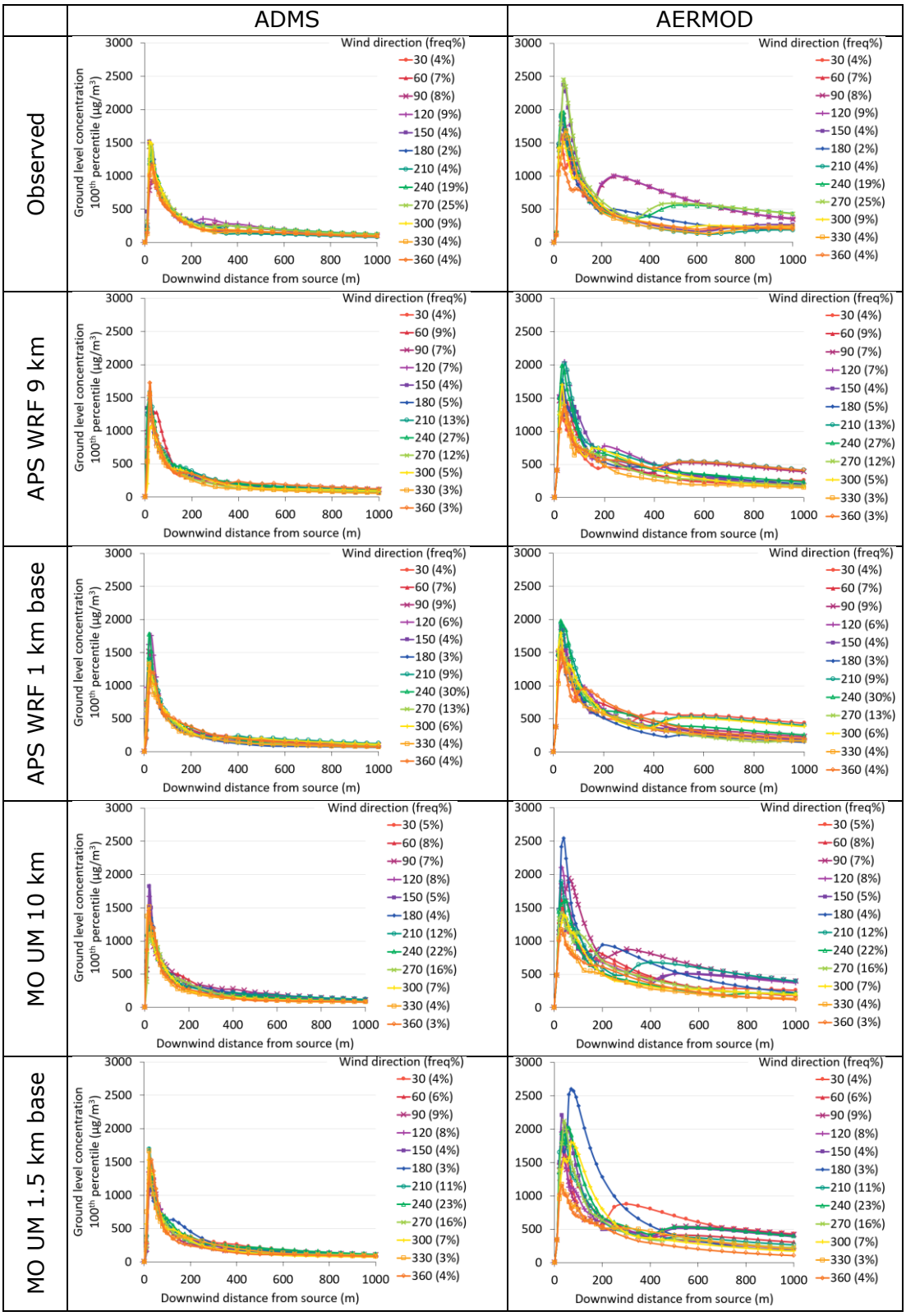

Figure 208 – Downwind profiles of 100th percentile concentration for near-ground source at Leuchars with varying wind direction, modelled with ADMS (left) and AERMOD (right), with observed or base NWP meteorological data.

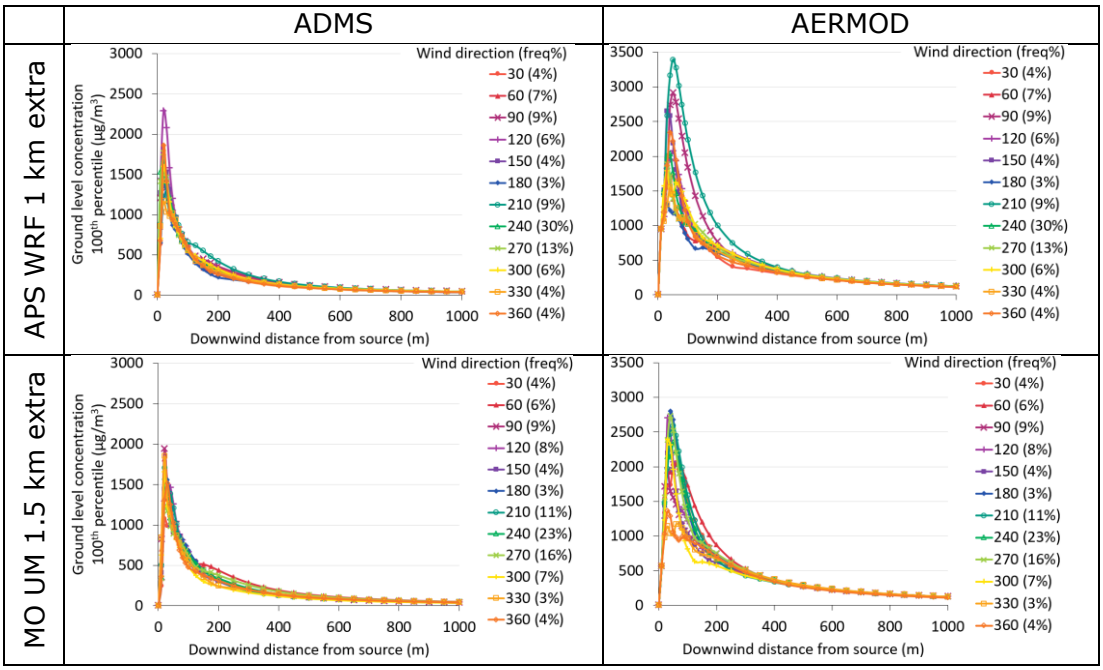

Figure 209 – Downwind profiles of 100th percentile concentration for near-ground source at Leuchars with varying wind direction, modelled with ADMS (left) and AERMOD (right), with extra NWP meteorological data. Note the different vertical scales used for ADMS and AERMOD.

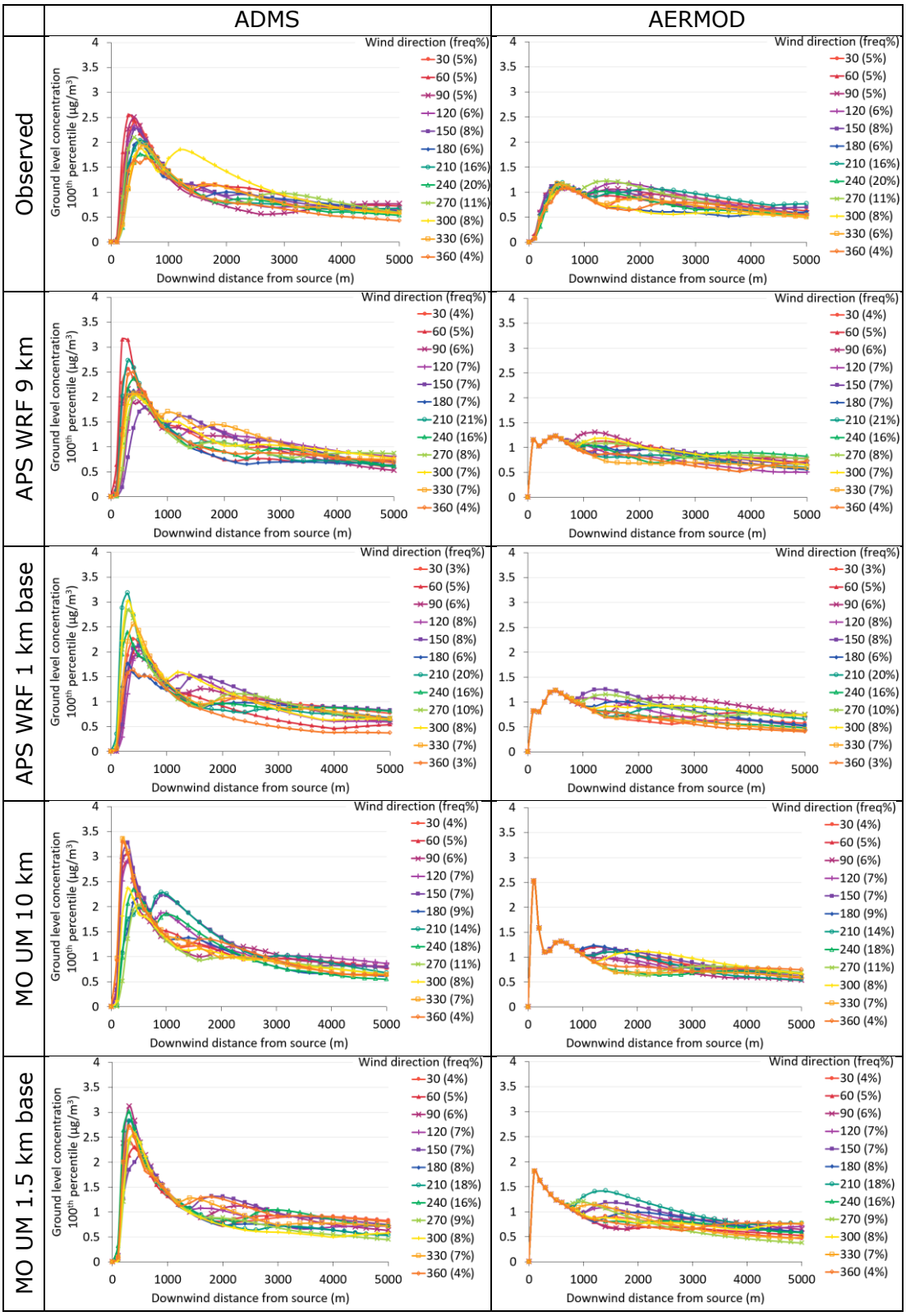

Figure 210 – Downwind profiles of 100th percentile concentration for elevated source at Waddington with varying wind direction, modelled with ADMS (left) and AERMOD (right), with observed or base NWP meteorological data.

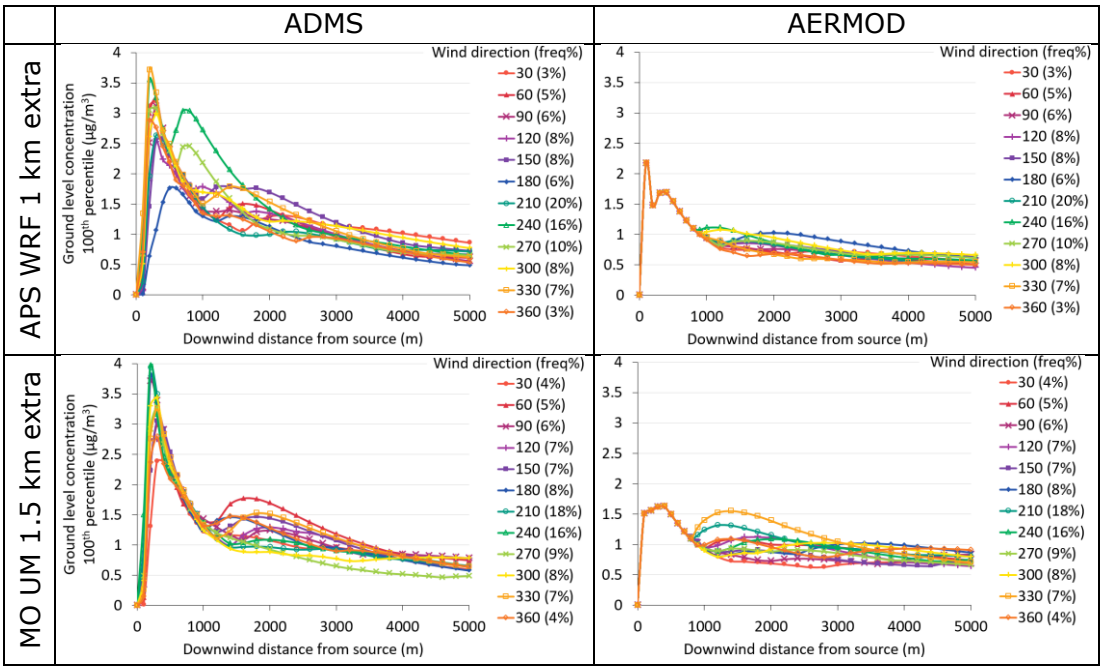

Figure 211 – Downwind profiles of 100th percentile concentration for elevated source at Waddington with varying wind direction, modelled with ADMS (left) and AERMOD (right), with extra NWP meteorological data.

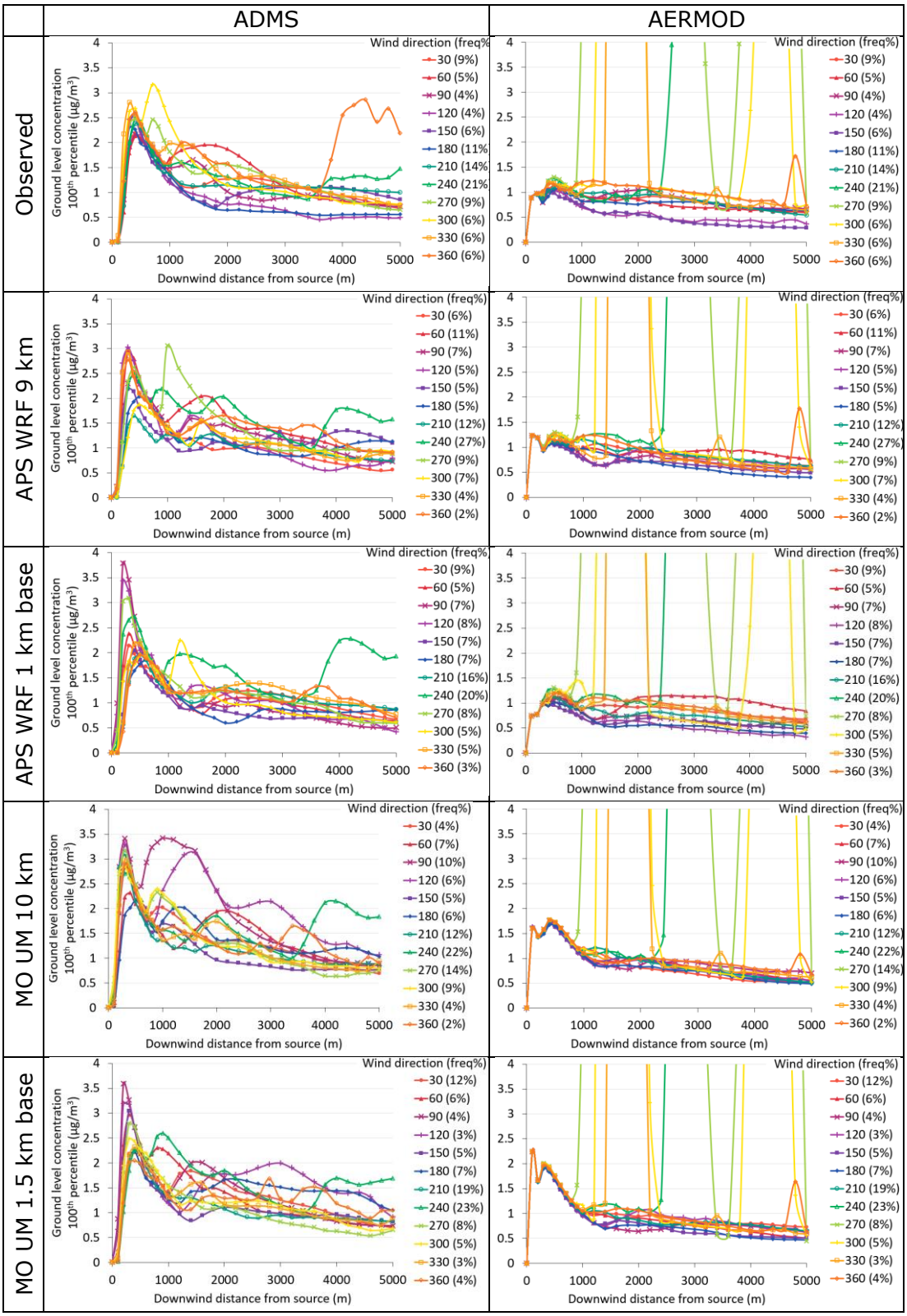

Figure 212 – Downwind profiles of 100th percentile concentration for elevated source at Sennybridge with varying wind direction, modelled with ADMS (left) and AERMOD (right), with observed or base NWP meteorological data.

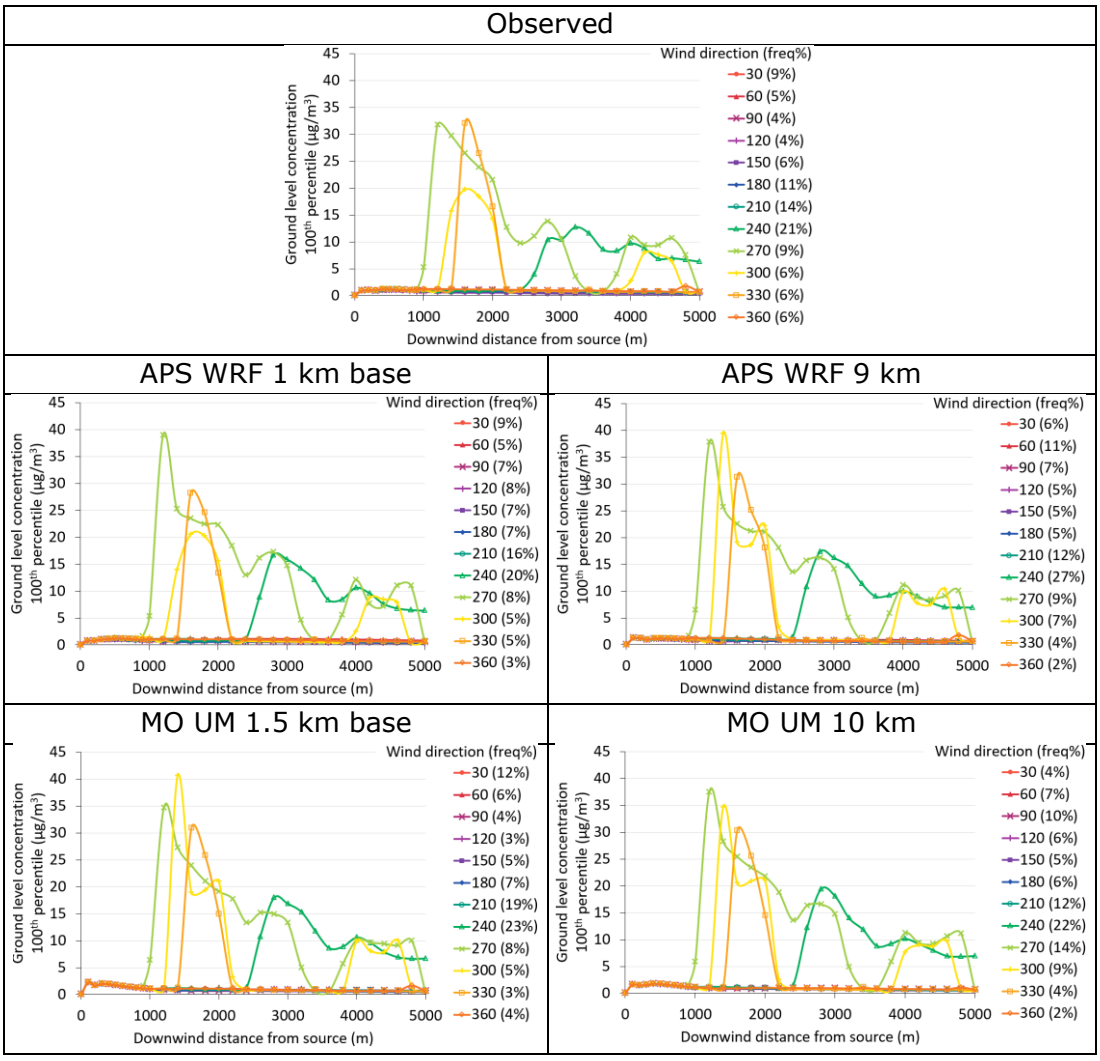

Figure 213 – Additional downwind profiles of 100th percentile concentration for elevated source at Sennybridge with varying wind direction, modelled with AERMOD, with observed or base NWP meteorological data. Increased scale to show high peaks from the westerly and northerly wind directions.

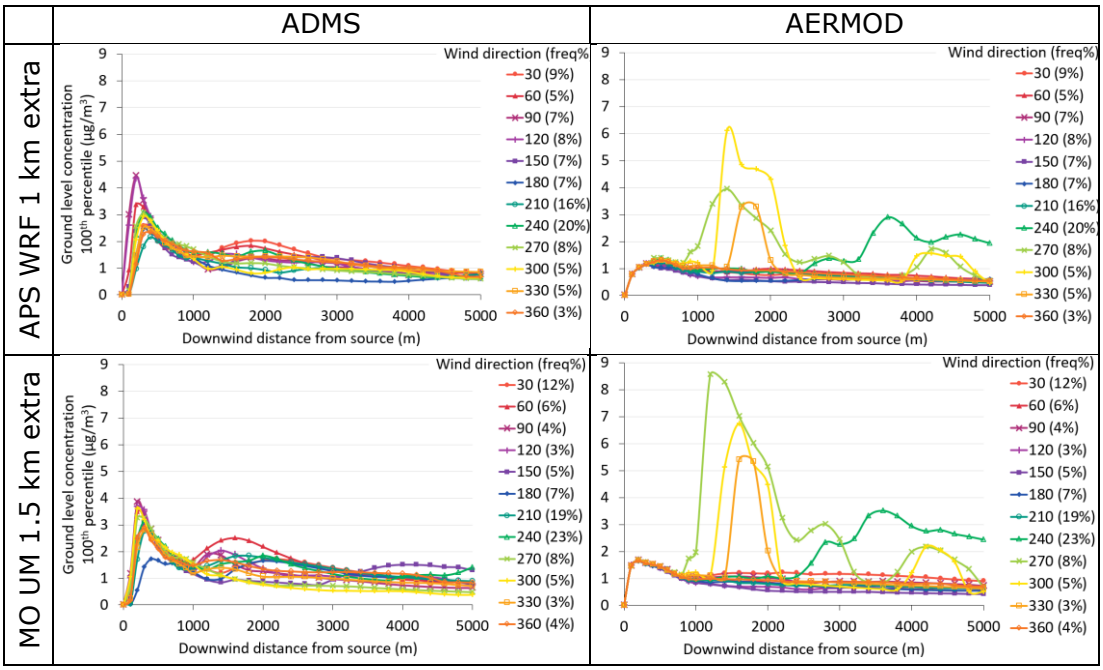

Figure 214 – Downwind profiles of 100th percentile concentration for elevated source at Sennybridge with varying wind direction, modelled with ADMS (left) and AERMOD (right), with extra NWP meteorological data.

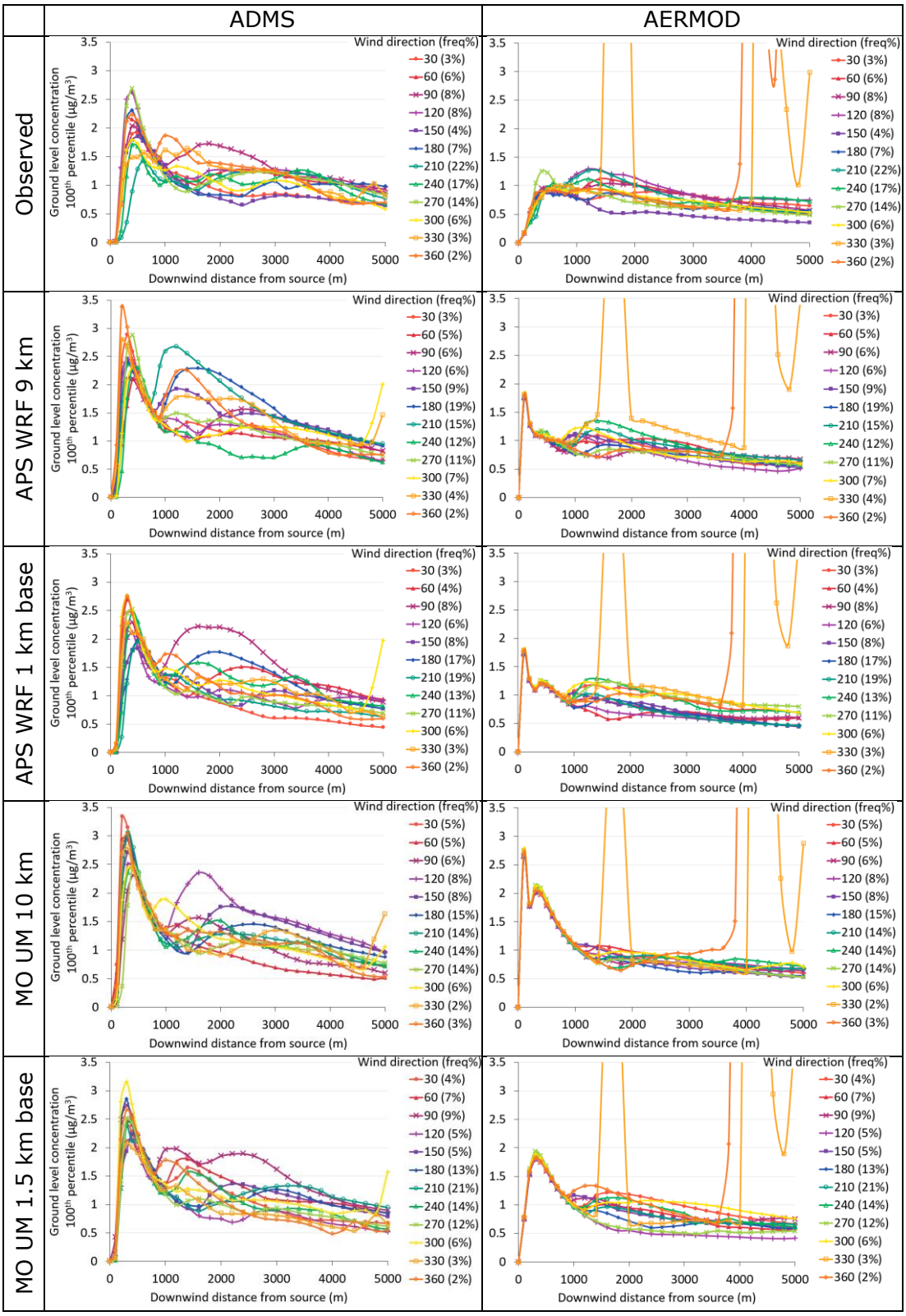

Figure 215 – Downwind profiles of 100th percentile concentration for elevated source at Drumalbin with varying wind direction, modelled with ADMS (left) and AERMOD (right), with observed or base NWP meteorological data.

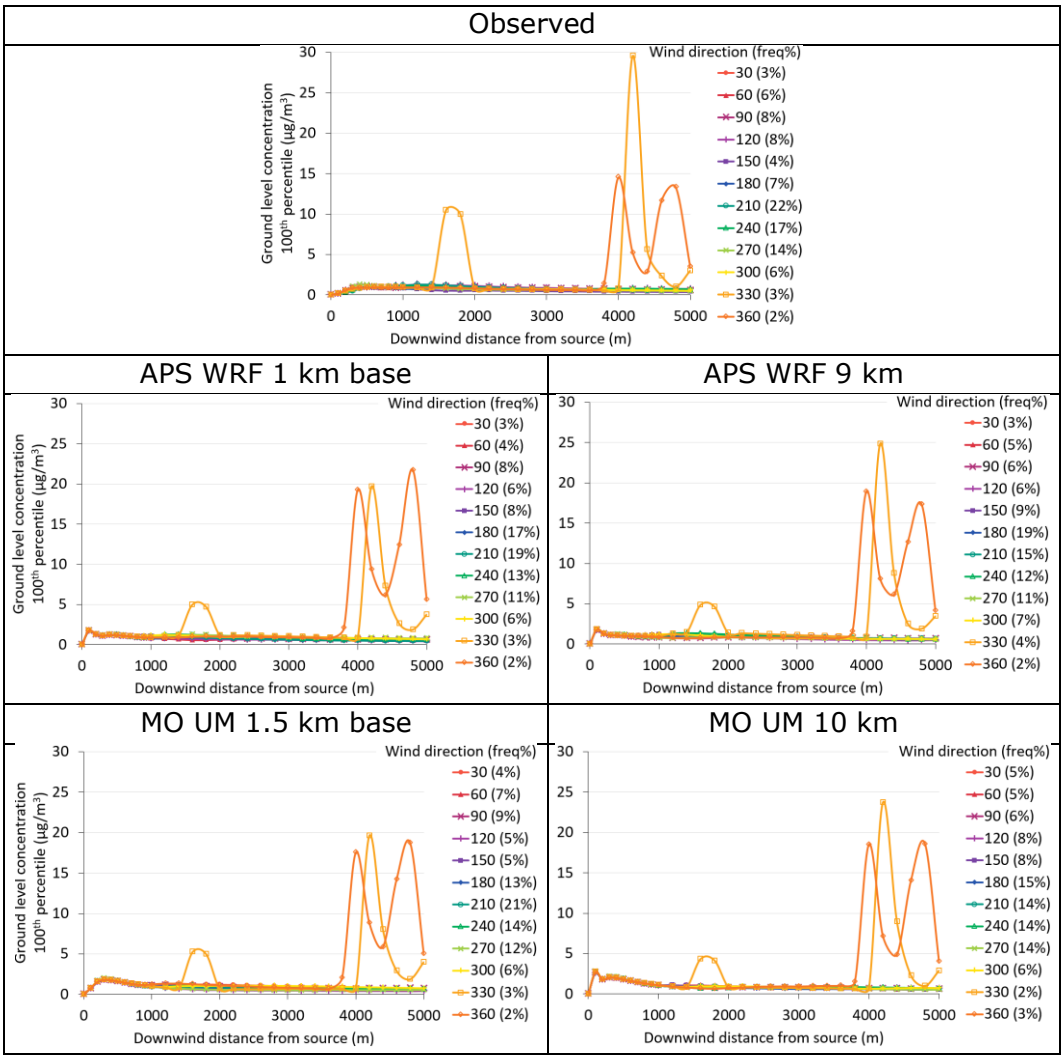

Figure 216 – Additional downwind profiles of 100th percentile concentration for elevated source at Drumalbin with varying wind direction, modelled with AERMOD, with observed or base NWP meteorological data. Increased scale to show high peaks from the northerly wind directions.

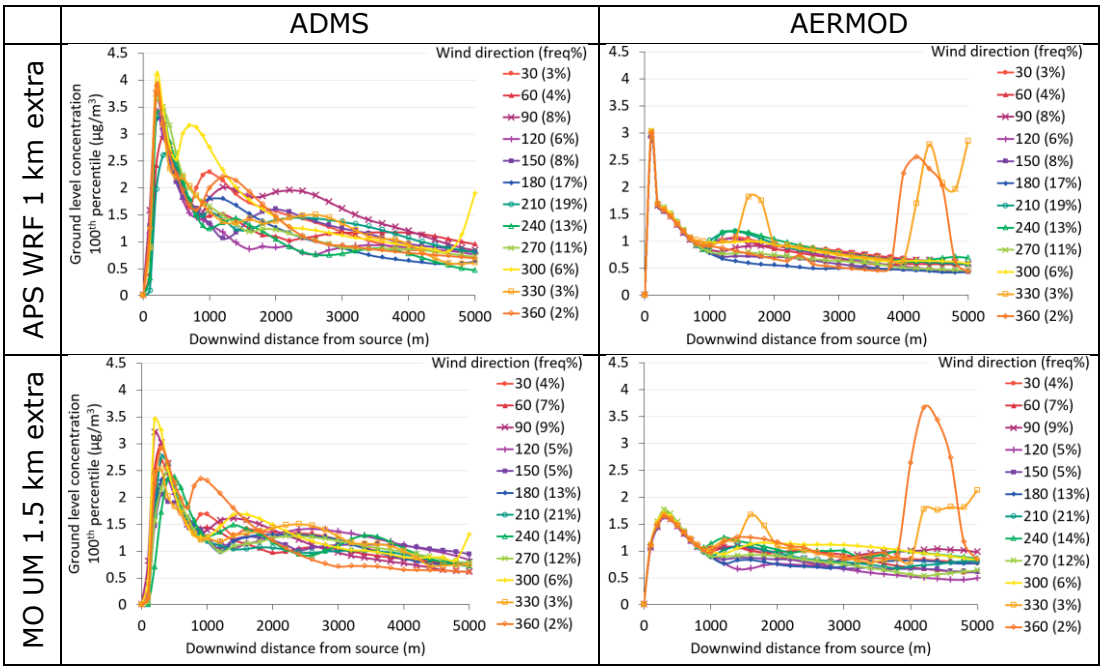

Figure 217 – Downwind profiles of 100th percentile concentration for elevated source at Drumalbin with varying wind direction, modelled with ADMS (left) and AERMOD (right), with extra NWP meteorological data.

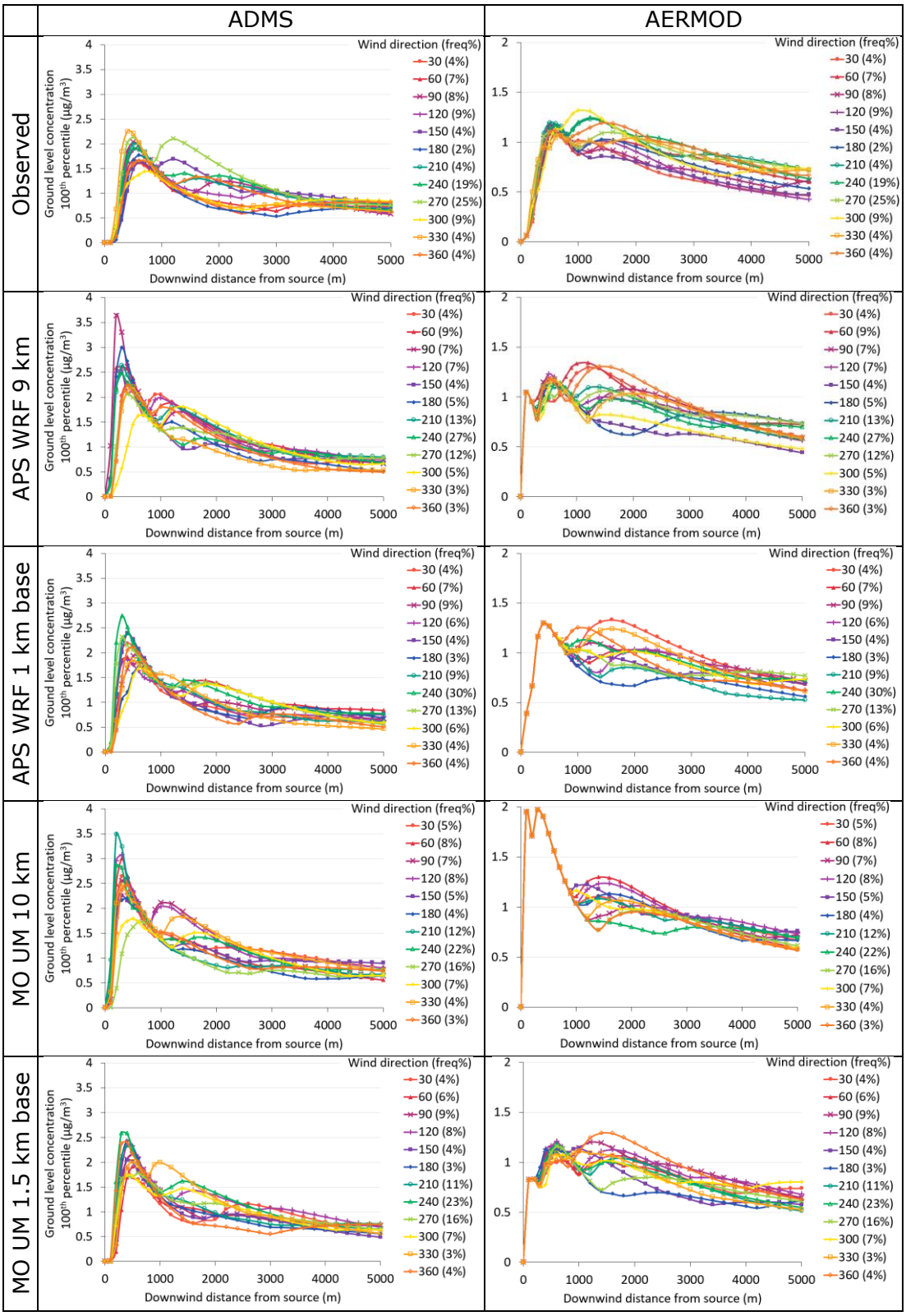

Figure 218 – Downwind profiles of 100th percentile concentration for elevated source at Leuchars with varying wind direction, modelled with ADMS (left) and AERMOD (right), with observed or base NWP meteorological data. Note the different vertical scales are used for ADMS and AERMOD.

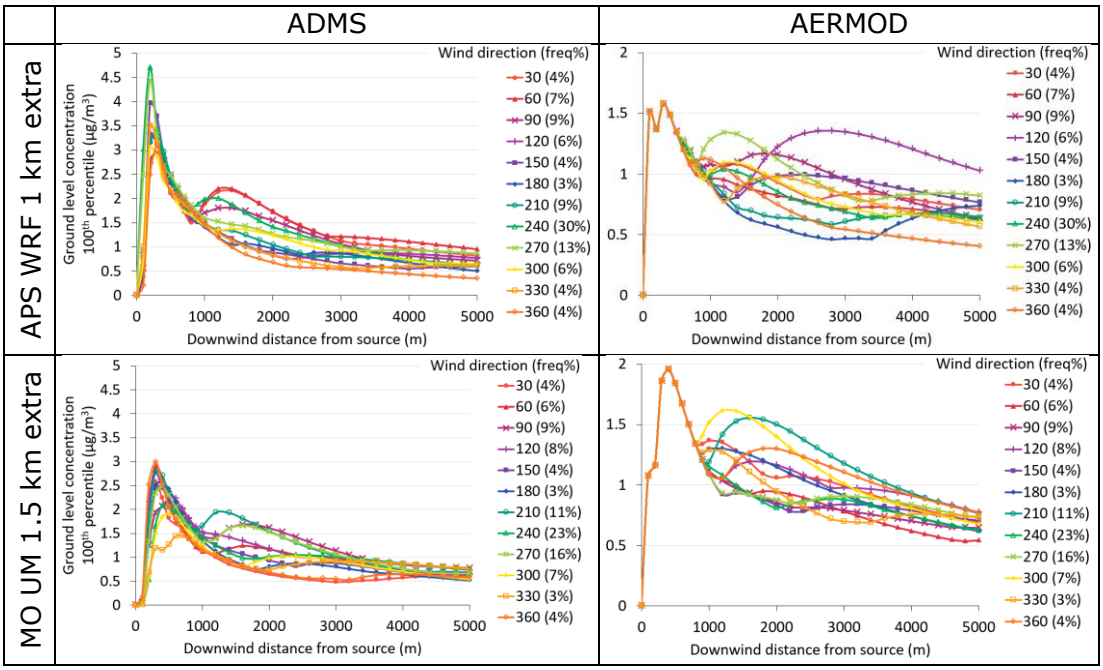

Figure 219 – Downwind profiles of 100th percentile concentration for elevated source at Leuchars with varying wind direction, modelled with ADMS (left) and AERMOD (right), with extra NWP meteorological data. Note the different vertical scales are used for ADMS and AERMOD.

Table 67 - Magnitudes and locations of maximum concentrations for each meteorological dataset and output statistic over the 2019 period for a near-ground source (G) at Waddington met site, as calculated by ADMS 6 and AERMOD dispersion models.

			Dispersion model									
			ADMS 6					AERMOD				
Met input	Source	Stat	Max (µg/m³)	X (m)	Y (m)	distance (m)	wind dir (°)	Max (µg/m³)	X (m)	Y (m)	distance (m)	wind dir (°)
Obs base	G	aa	158	26	15	30	240	201	26	15	30	240
APS WRF 1km base	G	aa	155	15	26	30	210	199	15	26	30	210
APS WRF 9km base	G	aa	140	15	26	30	210	170	15	26	30	210
MO UM 1.5km base	G	aa	133	15	26	30	210	173	15	26	30	210
MO UM 10km base	G	aa	142	26	15	30	240	180	26	15	30	240
APS WRF 1km extra	G	aa	163	15	26	30	210	210	15	26	30	210
MO UM 1.5km extra	G	aa	146	15	26	30	210	190	15	26	30	210
Obs base	G	P98	824	26	15	30	240	1109	26	15	30	240
APS WRF 1km base	G	P98	819	15	26	30	210	1098	15	26	30	210
APS WRF 9km base	G	P98	815	15	26	30	210	1067	15	26	30	210
MO UM 1.5km base	G	P98	825	15	26	30	210	1125	15	26	30	210
MO UM 10km base	G	P98	832	26	15	30	240	1110	15	26	30	210
APS WRF 1km extra	G	P98	839	15	26	30	210	1125	15	26	30	210
MO UM 1.5km extra	G	P98	833	15	26	30	210	1165	15	26	30	210
Obs base	G	P100	1568	17	-10	20	300	2350	35	-20	40	300
APS WRF 1km base	G	P100	1812	-10	-17	20	30	2553	-26	-15	30	60
APS WRF 9km base	G	P100	1884	-17	10	20	120	2832	15	26	30	210
MO UM 1.5km base	G	P100	1540	-20	0	20	90	2585	43	-25	50	300
MO UM 10km base	G	P100	1660	17	10	20	240	2497	43	25	50	240
APS WRF 1km extra	G	P100	2038	-17	-10	20	60	3414	25	43	50	210
MO UM 1.5km extra	G	P100	1522	0	-20	20	360	4123	40	0	40	270

Table 68 - Magnitudes and locations of maximum concentrations for each meteorological dataset and output statistic over the 2019 period for a near-ground source (G) at Leuchars met site, as calculated by ADMS 6 and AERMOD dispersion models.

			Dispersion model									
			ADMS 6					AERMOD				
Met input	Source	Stat	Max (µg/m³)	X (m)	Y (m)	distance (m)	wind dir (°)	Max (µg/m³)	X (m)	Y (m)	distance (m)	wind dir (°)
Obs base	G	aa	159	30	0	30	270	192	30	0	30	270
APS WRF 1km base	G	aa	196	26	15	30	240	220	35	20	40	240
APS WRF 9km base	G	aa	189	26	15	30	240	217	26	15	30	240
MO UM 1.5km base	G	aa	155	26	15	30	240	182	26	15	30	240
MO UM 10km base	G	aa	174	26	15	30	240	214	26	15	30	240
APS WRF 1km extra	G	aa	226	26	15	30	240	246	35	20	40	240
MO UM 1.5km extra	G	aa	158	26	15	30	240	198	26	15	30	240
Obs base	G	P98	806	26	15	30	240	1067	30	0	30	270
APS WRF 1km base	G	P98	823	26	15	30	240	1076	26	15	30	240
APS WRF 9km base	G	P98	822	26	15	30	240	1071	26	15	30	240
MO UM 1.5km base	G	P98	825	26	15	30	240	1087	26	15	30	240
MO UM 10km base	G	P98	821	26	15	30	240	1084	26	15	30	240
APS WRF 1km extra	G	P98	894	35	20	40	240	1105	35	20	40	240
MO UM 1.5km extra	G	P98	842	-30	0	30	90	1136	26	15	30	240
Obs base	G	P100	1515	17	-10	20	300	2457	40	0	40	270
APS WRF 1km base	G	P100	1773	17	10	20	240	1970	26	15	30	240
APS WRF 9km base	G	P100	1722	0	-20	20	360	2038	-35	20	40	120
MO UM 1.5km base	G	P100	1688	10	17	20	210	2603	0	70	70	180
MO UM 10km base	G	P100	1818	-10	17	20	150	2537	0	40	40	180
APS WRF 1km extra	G	P100	2283	-17	10	20	120	3396	25	43	50	210
MO UM 1.5km extra	G	P100	1939	-20	0	20	90	2795	0	40	40	180

Table 69 - Magnitudes and locations of maximum concentrations for each meteorological dataset and output statistic over the 2019 period for a near-ground source (G) at Sennybridge met site, as calculated by ADMS 6 and AERMOD dispersion models.

			Dispersion model									
			ADMS 6					AERMOD				
Met input	Source	Stat	Max (µg/m³)	X (m)	Y (m)	distance (m)	wind dir (°)	Max (µg/m³)	X (m)	Y (m)	distance (m)	wind dir (°)
Obs base	G	aa	250	15	26	30	210	195	26	15	30	240
APS WRF 1km base	G	aa	230	15	26	30	210	199	26	15	30	240
APS WRF 9km base	G	aa	277	15	26	30	210	215	26	15	30	240
MO UM 1.5km base	G	aa	275	15	26	30	210	222	26	15	30	240
MO UM 10km base	G	aa	258	15	26	30	210	204	26	15	30	240
APS WRF 1km extra	G	aa	228	15	26	30	210	199	26	15	30	240
MO UM 1.5km extra	G	aa	279	15	26	30	210	234	26	15	30	240
Obs base	G	P98	1362	15	26	30	210	1123	17	10	20	240
APS WRF 1km base	G	P98	1199	15	26	30	210	1056	17	10	20	240
APS WRF 9km base	G	P98	1556	15	26	30	210	1099	17	10	20	240
MO UM 1.5km base	G	P98	1207	15	26	30	210	1108	17	10	20	240
MO UM 10km base	G	P98	1498	15	26	30	210	1128	17	10	20	240
APS WRF 1km extra	G	P98	1166	17	10	20	240	1045	17	10	20	240
MO UM 1.5km extra	G	P98	1124	15	26	30	210	1137	17	10	20	240
Obs base	G	P100	4894	0	70	70	180	2981	15	-26	30	330
APS WRF 1km base	G	P100	5069	20	35	40	210	3218	15	26	30	210
APS WRF 9km base	G	P100	4649	15	26	30	210	2063	-35	20	40	120
MO UM 1.5km base	G	P100	4708	9	5	10	240	2900	15	-26	30	330
MO UM 10km base	G	P100	4555	15	26	30	210	2629	-30	0	30	90
APS WRF 1km extra	G	P100	4724	0	20	20	180	3688	20	-35	40	330
MO UM 1.5km extra	G	P100	6420	0	100	100	180	3944	-35	-20	40	60

Table 70 - Magnitudes and locations of maximum concentrations for each meteorological dataset and output statistic over the 2019 period for a near-ground source (G) at Drumalbin met site, as calculated by ADMS 6 and AERMOD dispersion models.

			Dispersion model									
			ADMS 6					AERMOD				
Met input	Source	Stat	Max (µg/m³)	X (m)	Y (m)	distance (m)	wind dir (°)	Max (µg/m³)	X (m)	Y (m)	distance (m)	wind dir (°)
Obs base	G	aa	128	26	15	30	240	185	15	26	30	210
APS WRF 1km base	G	aa	122	15	26	30	210	179	15	26	30	210
APS WRF 9km base	G	aa	96	15	26	30	210	141	15	26	30	210
MO UM 1.5km base	G	aa	114	15	26	30	210	161	15	26	30	210
MO UM 10km base	G	aa	105	26	15	30	240	138	15	26	30	210
APS WRF 1km extra	G	aa	121	15	26	30	210	178	15	26	30	210
MO UM 1.5km extra	G	aa	115	20	35	40	210	177	15	26	30	210
Obs base	G	P98	737	26	15	30	240	1068	15	26	30	210
APS WRF 1km base	G	P98	749	26	15	30	240	1022	15	26	30	210
APS WRF 9km base	G	P98	749	30	0	30	270	958	26	15	30	240
MO UM 1.5km base	G	P98	756	30	0	30	270	1024	15	26	30	210
MO UM 10km base	G	P98	767	30	0	30	270	998	15	26	30	210
APS WRF 1km extra	G	P98	758	30	0	30	270	1018	15	26	30	210
MO UM 1.5km extra	G	P98	758	30	0	30	270	1070	15	26	30	210
Obs base	G	P100	1530	-17	10	20	120	6795	90	0	90	270
APS WRF 1km base	G	P100	1589	17	-10	20	300	7195	78	-45	90	300
APS WRF 9km base	G	P100	1721	-10	17	20	150	5705	78	-45	90	300
MO UM 1.5km base	G	P100	1612	15	-26	30	330	7164	78	-45	90	300
MO UM 10km base	G	P100	1702	-10	17	20	150	2675	150	0	150	270
APS WRF 1km extra	G	P100	2824	17	-10	20	300	2740	50	0	50	270
MO UM 1.5km extra	G	P100	2976	20	-35	40	330	3476	43	-25	50	300

Table 71 - Magnitudes and locations of maximum concentrations for each meteorological dataset and output statistic over the 2019 period for an elevated source (E) at Waddington met site, as calculated by ADMS 6 and AERMOD dispersion models. *the maximum concentration is identical in all directions, due to effects of the AERMOD 'random plume' at low wind speeds.

			Dispersion model									
			ADMS 6					AERMOD				
Met input	Source	Stat	Max (µg/m³)	X (m)	Y (m)	distance (m)	wind dir (°)	Max (µg/m³)	X (m)	Y (m)	distance (m)	wind dir (°)
Obs base	E	aa	0.049	1039	600	1200	240	0.042	866	500	1000	240
APS WRF 1km base	E	aa	0.046	600	1039	1200	210	0.035	600	1039	1200	210
APS WRF 9km base	E	aa	0.040	600	1039	1200	210	0.035	500	866	1000	210
MO UM 1.5km base	E	aa	0.043	1039	600	1200	240	0.040	779	450	900	240
MO UM 10km base	E	aa	0.048	1039	600	1200	240	0.041	779	450	900	240
APS WRF 1km extra	E	aa	0.039	600	1039	1200	210	0.035	866	500	1000	240
MO UM 1.5km extra	E	aa	0.042	866	500	1000	240	0.040	866	500	1000	240
Obs base	E	P98	0.66	1039	600	1200	240	0.71	779	450	900	240
APS WRF 1km base	E	P98	0.64	600	1039	1200	210	0.61	450	779	900	210
APS WRF 9km base	E	P98	0.64	600	1039	1200	210	0.64	450	779	900	210
MO UM 1.5km base	E	P98	0.68	866	500	1000	240	0.72	693	400	800	240
MO UM 10km base	E	P98	0.71	1039	600	1200	240	0.73	779	450	900	240
APS WRF 1km extra	E	P98	0.63	866	500	1000	240	0.62	779	450	900	240
MO UM 1.5km extra	E	P98	0.69	1039	600	1200	240	0.68	693	400	800	240
Obs base	E	P100	2.5	-260	-150	300	60	1.2	1400	0	1400	270
APS WRF 1km base	E	P100	3.2	150	260	300	210	1.3	-700	1212	1400	150
APS WRF 9km base	E	P100	3.2	-173	-100	200	60	1.3	-1200	0	1200	90
MO UM 1.5km base	E	P100	3.1	-300	0	300	90	1.8	*	*	100	*
MO UM 10km base	E	P100	3.4	100	-173	200	330	2.5	*	*	100	*
APS WRF 1km extra	E	P100	3.7	100	-173	200	330	2.2	*	*	100	*
MO UM 1.5km extra	E	P100	4.0	173	100	200	240	1.6	*	*	400	*

Table 72 - Magnitudes and locations of maximum concentrations for each meteorological dataset and output statistic over the 2019 period for an elevated source (E) at Leuchars met site, as calculated by ADMS 6 and AERMOD dispersion models. *the maximum concentration is identical in all directions, due to effects of the AERMOD 'random plume' at low wind speeds.

			Dispersion model									
			ADMS 6					AERMOD				
Met input	Source	Stat	Max (µg/m³)	X (m)	Y (m)	distance (m)	wind dir (°)	Max (µg/m³)	X (m)	Y (m)	distance (m)	wind dir (°)
Obs base	E	aa	0.052	1039	600	1200	240	0.042	1212	700	1400	240
APS WRF 1km base	E	aa	0.055	1039	600	1200	240	0.044	1039	600	1200	240
APS WRF 9km base	E	aa	0.059	1039	600	1200	240	0.046	1039	600	1200	240
MO UM 1.5km base	E	aa	0.054	1039	600	1200	240	0.040	1039	600	1200	240
MO UM 10km base	E	aa	0.059	1039	600	1200	240	0.042	1212	700	1400	240
APS WRF 1km extra	E	aa	0.065	1039	600	1200	240	0.049	866	500	1000	240
MO UM 1.5km extra	E	aa	0.043	1039	600	1200	240	0.037	1212	700	1400	240
Obs base	E	P98	0.62	1039	600	1200	240	0.59	-779	450	900	120
APS WRF 1km base	E	P98	0.78	-900	0	900	90	0.77	-800	0	800	90
APS WRF 9km base	E	P98	0.68	1039	600	1200	240	0.70	779	450	900	240
MO UM 1.5km base	E	P98	0.81	-1000	0	1000	90	0.76	-800	0	800	90
MO UM 10km base	E	P98	0.67	1039	600	1200	240	0.70	779	450	900	240
APS WRF 1km extra	E	P98	0.83	-1000	0	1000	90	0.82	-700	0	700	90
MO UM 1.5km extra	E	P98	0.67	1039	600	1200	240	0.69	779	450	900	240
Obs base	E	P100	2.2	200	-346	400	330	1.3	866	-500	1000	300
APS WRF 1km base	E	P100	2.7	260	150	300	240	1.3	-800	-1386	1600	30
APS WRF 9km base	E	P100	3.6	-200	0	200	90	1.3	-1039	-600	1200	60
MO UM 1.5km base	E	P100	2.6	346	200	400	240	1.3	0	-1400	1400	360
MO UM 10km base	E	P100	3.5	100	173	200	210	2.0	*	*	300	*
APS WRF 1km extra	E	P100	4.7	173	100	200	240	1.6	*	*	300	*
MO UM 1.5km extra	E	P100	3.0	0	-300	300	360	2.0	*	*	400	*

Table 73 - Magnitudes and locations of maximum concentrations for each meteorological dataset and output statistic over the 2019 period for an elevated source (E) at Sennybridge met site, as calculated by ADMS 6 and AERMOD dispersion models.

			Dispersion model									
			ADMS 6					AERMOD				
Met input	Source	Stat	Max (µg/m³)	X (m)	Y (m)	distance (m)	wind dir (°)	Max (µg/m³)	X (m)	Y (m)	distance (m)	wind dir (°)
Obs base	E	aa	0.078	1386	800	1600	240	0.151	1400	0	1400	270
APS WRF 1km base	E	aa	0.067	1386	800	1600	240	0.064	1200	0	1200	270
APS WRF 9km base	E	aa	0.075	1386	800	1600	240	0.128	2944	1700	3400	240
MO UM 1.5km base	E	aa	0.066	1386	800	1600	240	0.096	1200	0	1200	270
MO UM 10km base	E	aa	0.069	1386	800	1600	240	0.218	1400	0	1400	270
APS WRF 1km extra	E	aa	0.064	1386	800	1600	240	0.071	866	500	1000	240
MO UM 1.5km extra	E	aa	0.060	1386	800	1600	240	0.069	1039	600	1200	240
Obs base	E	P98	0.79	1386	800	1600	240	1.45	1200	0	1200	270
APS WRF 1km base	E	P98	0.76	866	500	1000	240	0.79	1000	0	1000	270
APS WRF 9km base	E	P98	0.80	866	500	1000	240	1.08	2944	1700	3400	240
MO UM 1.5km base	E	P98	0.81	866	500	1000	240	0.80	606	350	700	240
MO UM 10km base	E	P98	0.90	693	-400	800	300	1.97	1400	0	1400	270
APS WRF 1km extra	E	P98	0.80	1386	800	1600	240	0.81	606	350	700	240
MO UM 1.5km extra	E	P98	0.75	1386	800	1600	240	0.79	1000	0	1000	270
Obs base	E	P100	3.2	606	-350	700	300	32.1	800	-1386	1600	330
APS WRF 1km base	E	P100	3.8	-200	0	200	90	39.0	1200	0	1200	270
APS WRF 9km base	E	P100	3.1	1000	0	1000	270	39.4	1212	-700	1400	300
MO UM 1.5km base	E	P100	3.6	-200	0	200	90	40.6	1212	-700	1400	300
MO UM 10km base	E	P100	3.4	-1000	0	1000	90	37.4	1200	0	1200	270
APS WRF 1km extra	E	P100	4.4	-200	0	200	90	6.1	1212	-700	1400	300
MO UM 1.5km extra	E	P100	3.9	-200	0	200	90	8.6	1200	0	1200	270

Table 74 - Magnitudes and locations of maximum concentrations for each meteorological dataset and output statistic over the 2019 period for an elevated source (E) at Drumalbin met site, as calculated by ADMS 6 and AERMOD dispersion models.

			Dispersion model									
			ADMS 6					AERMOD				
Met input	Source	Stat	Max (µg/m³)	X (m)	Y (m)	distance (m)	wind dir (°)	Max (µg/m³)	X (m)	Y (m)	distance (m)	wind dir (°)
Obs base	E	aa	0.055	700	1212	1400	210	0.046	700	1212	1400	210
APS WRF 1km base	E	aa	0.040	700	1212	1400	210	0.034	700	1212	1400	210
APS WRF 9km base	E	aa	0.034	1212	700	1400	240	0.041	2100	-3637	4200	330
MO UM 1.5km base	E	aa	0.040	1212	700	1400	240	0.032	700	1212	1400	210
MO UM 10km base	E	aa	0.036	1212	700	1400	240	0.043	0	-4000	4000	360
APS WRF 1km extra	E	aa	0.041	600	1039	1200	210	0.036	700	1212	1400	210
MO UM 1.5km extra	E	aa	0.038	1212	700	1400	240	0.031	1732	1000	2000	240
Obs base	E	P98	0.61	1212	700	1400	240	0.53	600	1039	1200	210
APS WRF 1km base	E	P98	0.65	1212	700	1400	240	0.54	600	1039	1200	210
APS WRF 9km base	E	P98	0.61	1212	700	1400	240	0.53	900	0	900	270
MO UM 1.5km base	E	P98	0.64	1212	700	1400	240	0.52	900	0	900	270
MO UM 10km base	E	P98	0.63	1212	700	1400	240	0.63	800	0	800	270
APS WRF 1km extra	E	P98	0.68	1039	600	1200	240	0.60	700	0	700	270
MO UM 1.5km extra	E	P98	0.64	1212	700	1400	240	0.48	900	0	900	270
Obs base	E	P100	2.7	400	0	400	270	29.6	2100	-3637	4200	330
APS WRF 1km base	E	P100	2.8	260	-150	300	300	21.7	0	-4800	4800	360
APS WRF 9km base	E	P100	3.4	0	-200	200	360	24.8	2100	-3637	4200	330
MO UM 1.5km base	E	P100	3.2	260	-150	300	300	19.6	2100	-3637	4200	330
MO UM 10km base	E	P100	3.3	-100	-173	200	30	23.7	2100	-3637	4200	330
APS WRF 1km extra	E	P100	4.1	173	-100	200	300	3.0	87	-50	100	300
MO UM 1.5km extra	E	P100	3.5	173	-100	200	300	3.7	0	-4200	4200	360

C2 Wet deposition comparison

This section gives additional plots and statistics for wet deposition, supplementing those in Section 6.4.

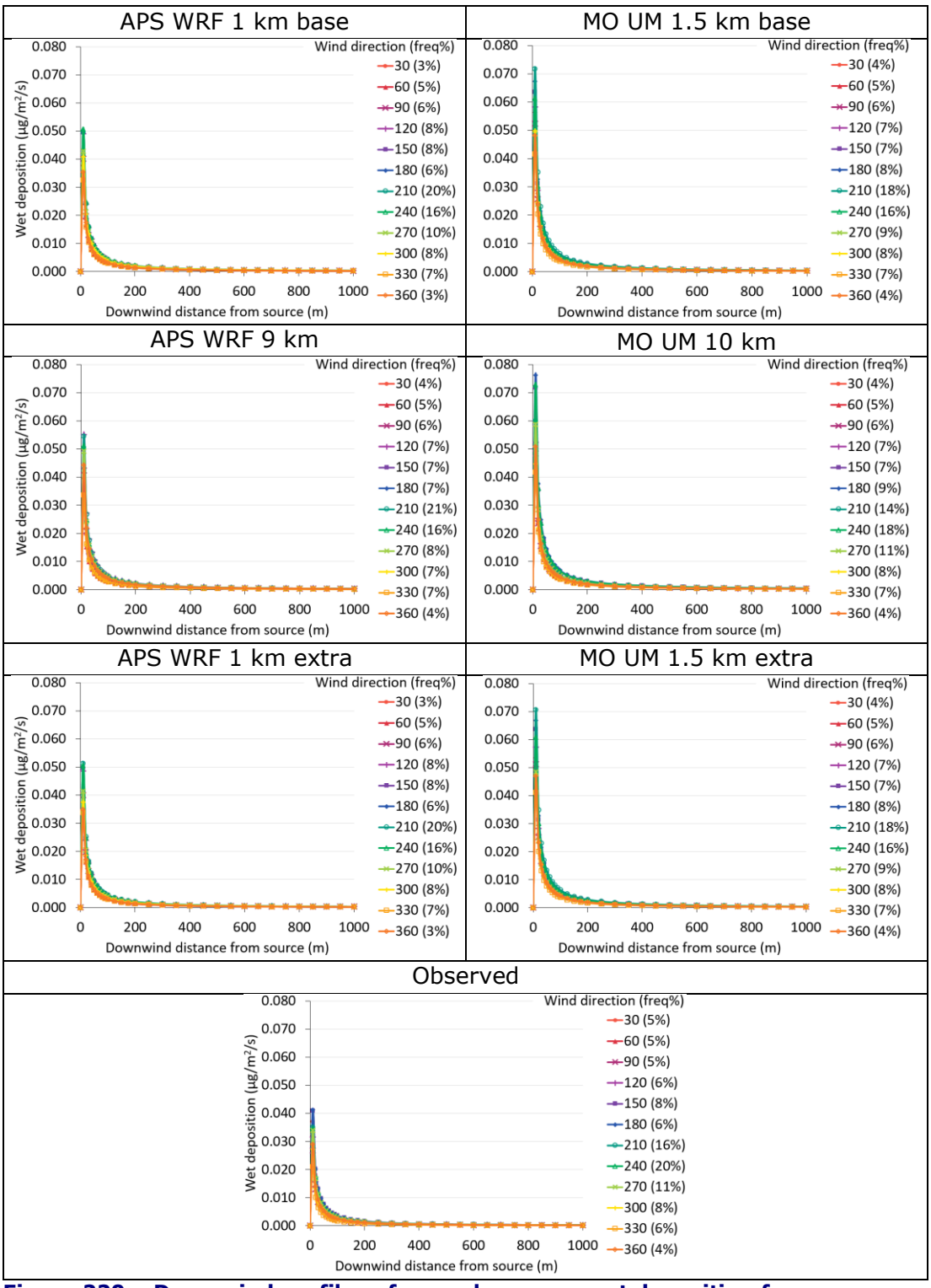

Figure 220 – Downwind profiles of annual average wet deposition for near-ground source at Waddington with varying wind direction, modelled with ADMS for all meteorological datasets.

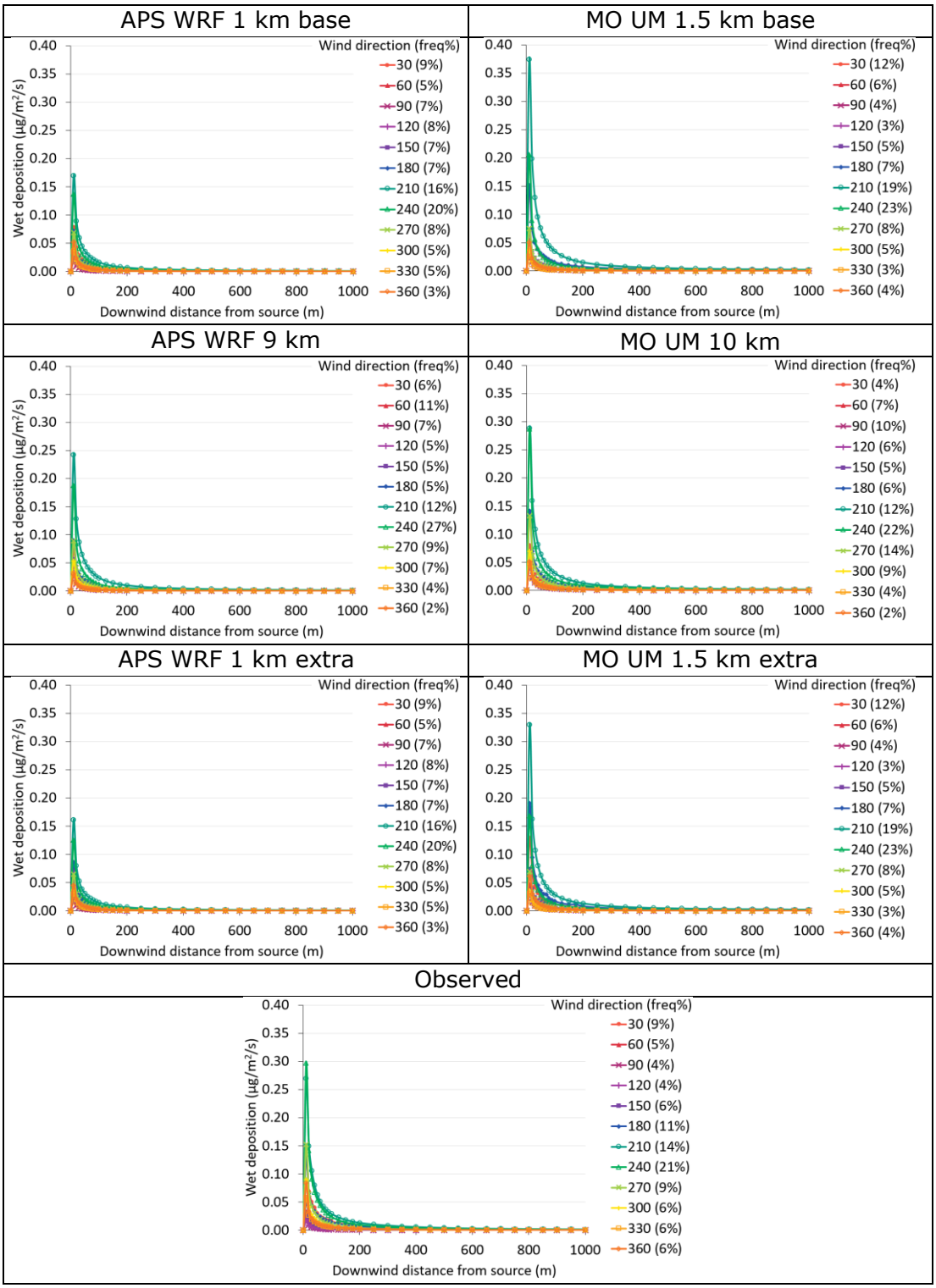

Figure 221 – Downwind profiles of annual average wet deposition for near-ground source at Sennybridge with varying wind direction, modelled with ADMS for all meteorological datasets.

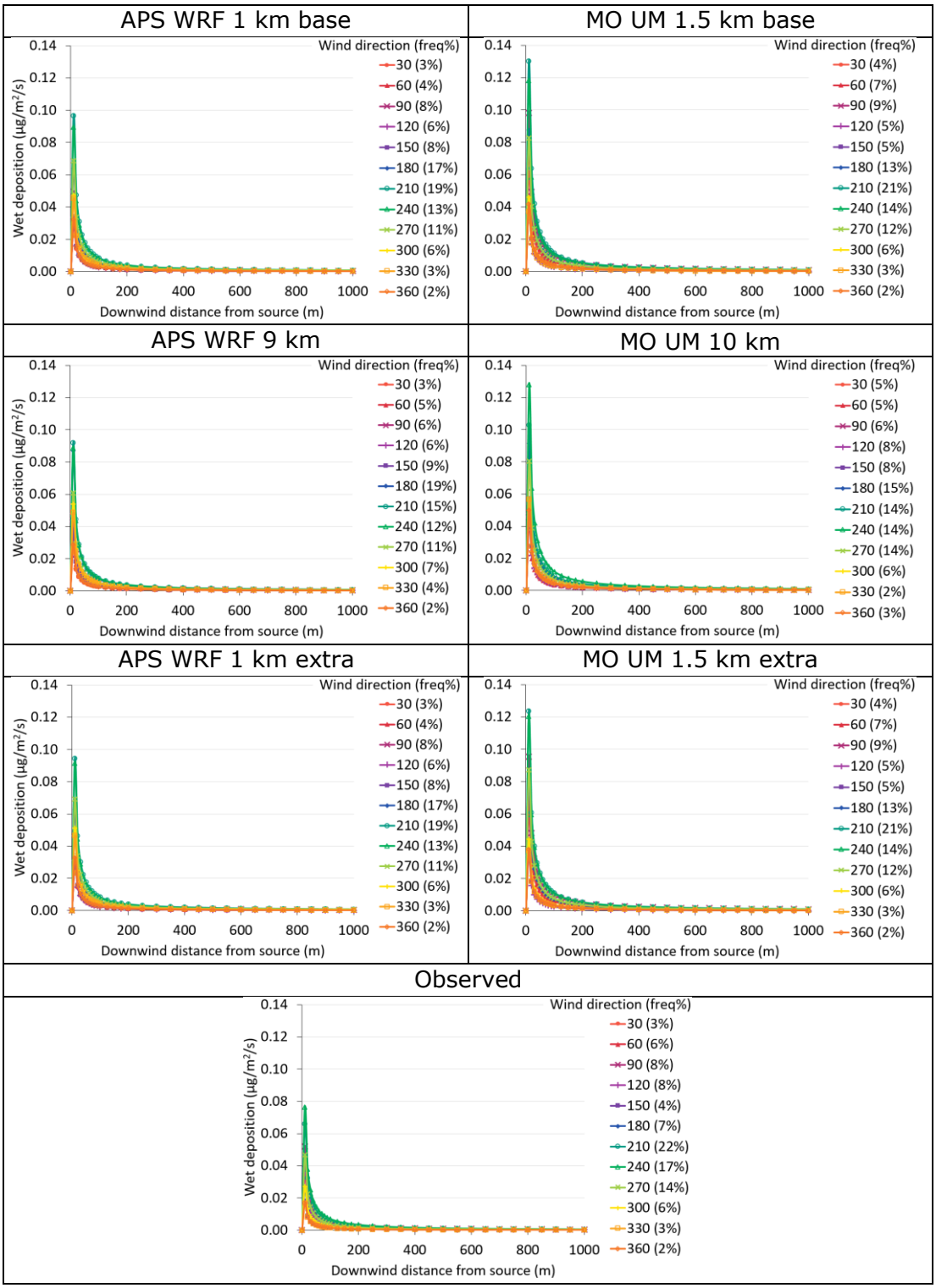

Figure 222 – Downwind profiles of annual average wet deposition for near-ground source at Drumalbin with varying wind direction, modelled with ADMS for all meteorological datasets.

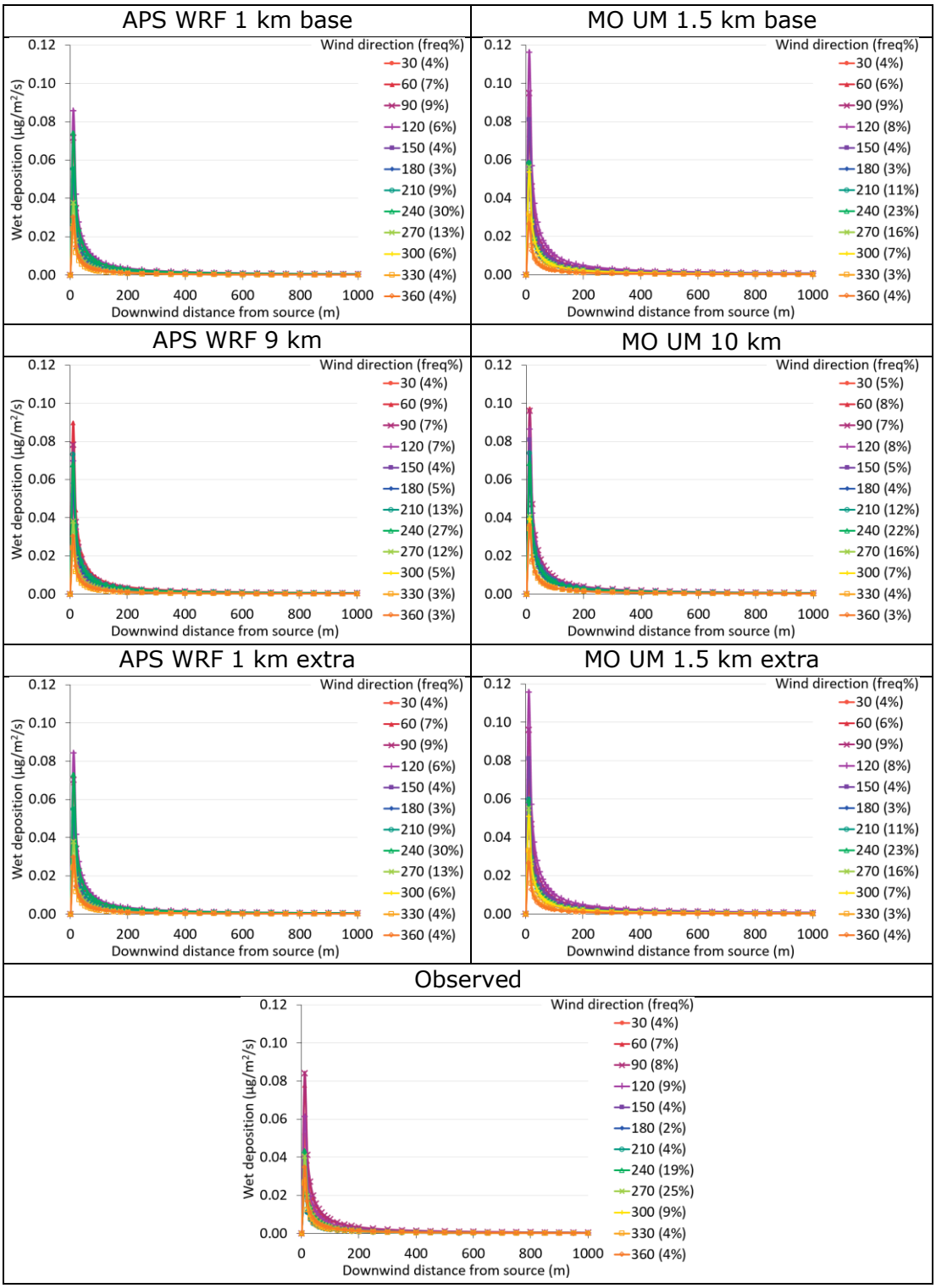

Figure 223 – Downwind profiles of annual average wet deposition for near-ground source at Leuchars with varying wind direction, modelled with ADMS for all meteorological datasets.

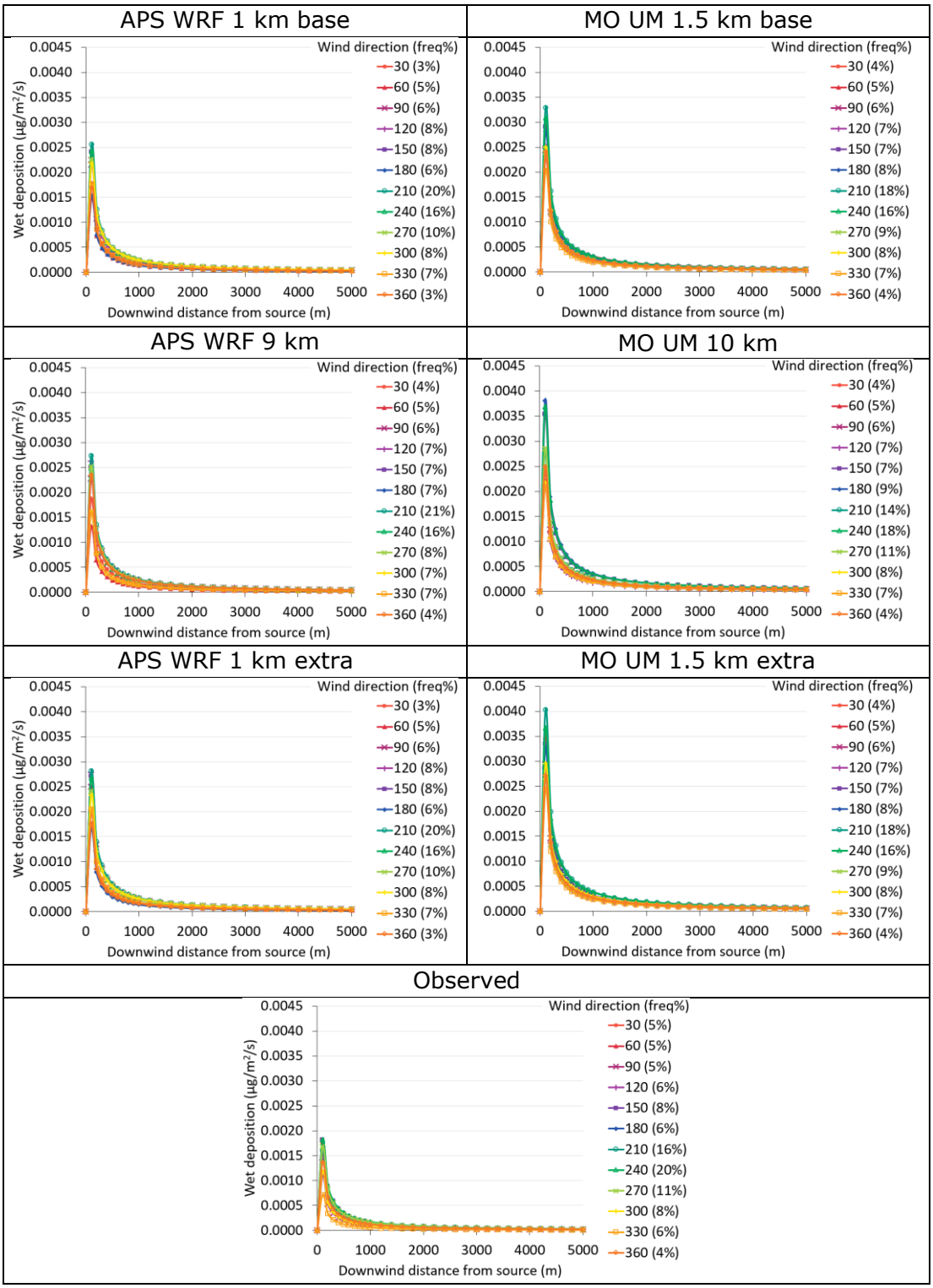

Figure 224 – Downwind profiles of annual average wet deposition for elevated source at Waddington with varying wind direction, modelled with ADMS for all meteorological datasets.

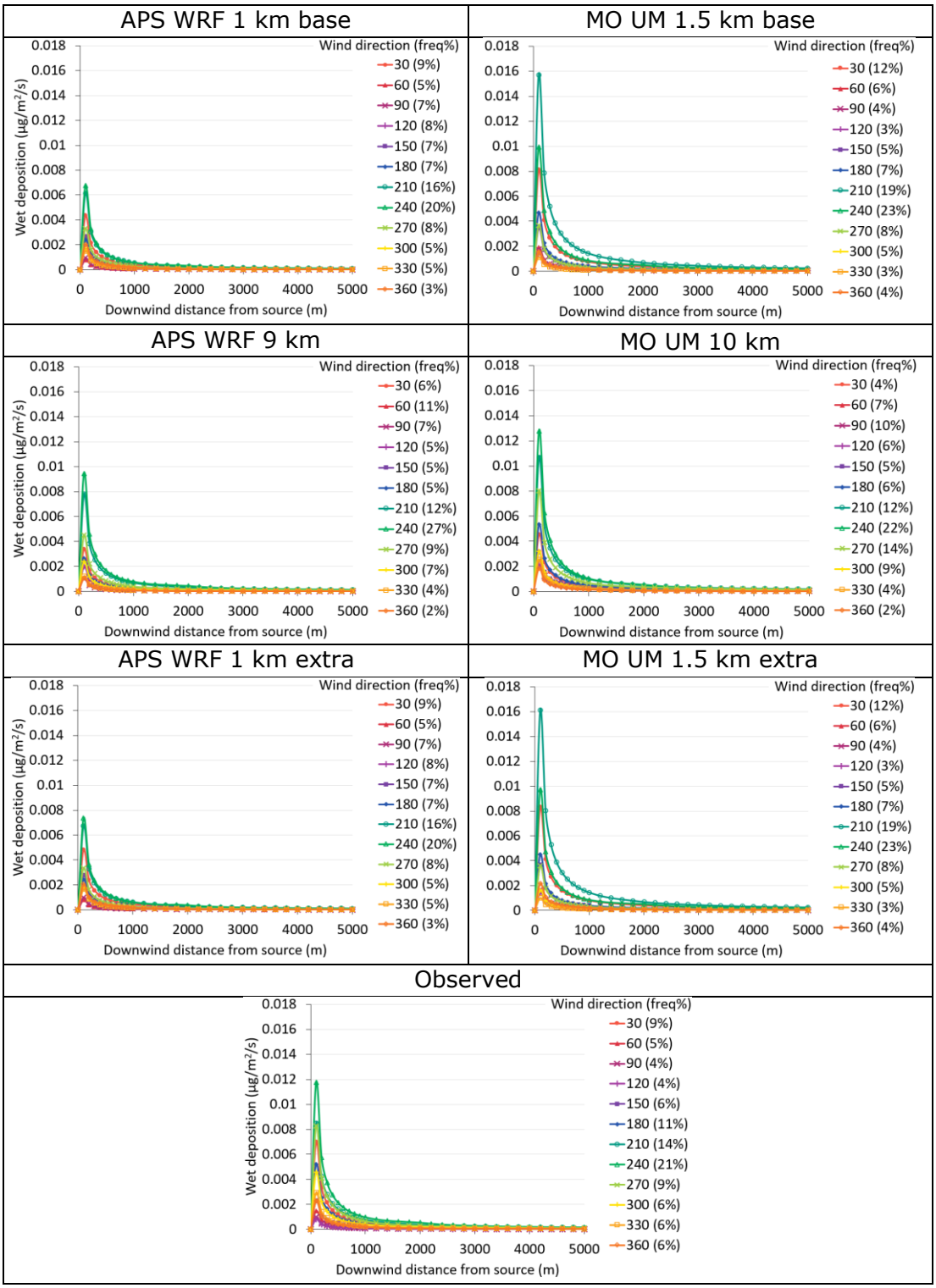

Figure 225 – Downwind profiles of annual average wet deposition for elevated source at Sennybridge with varying wind direction, modelled with ADMS for all meteorological datasets.

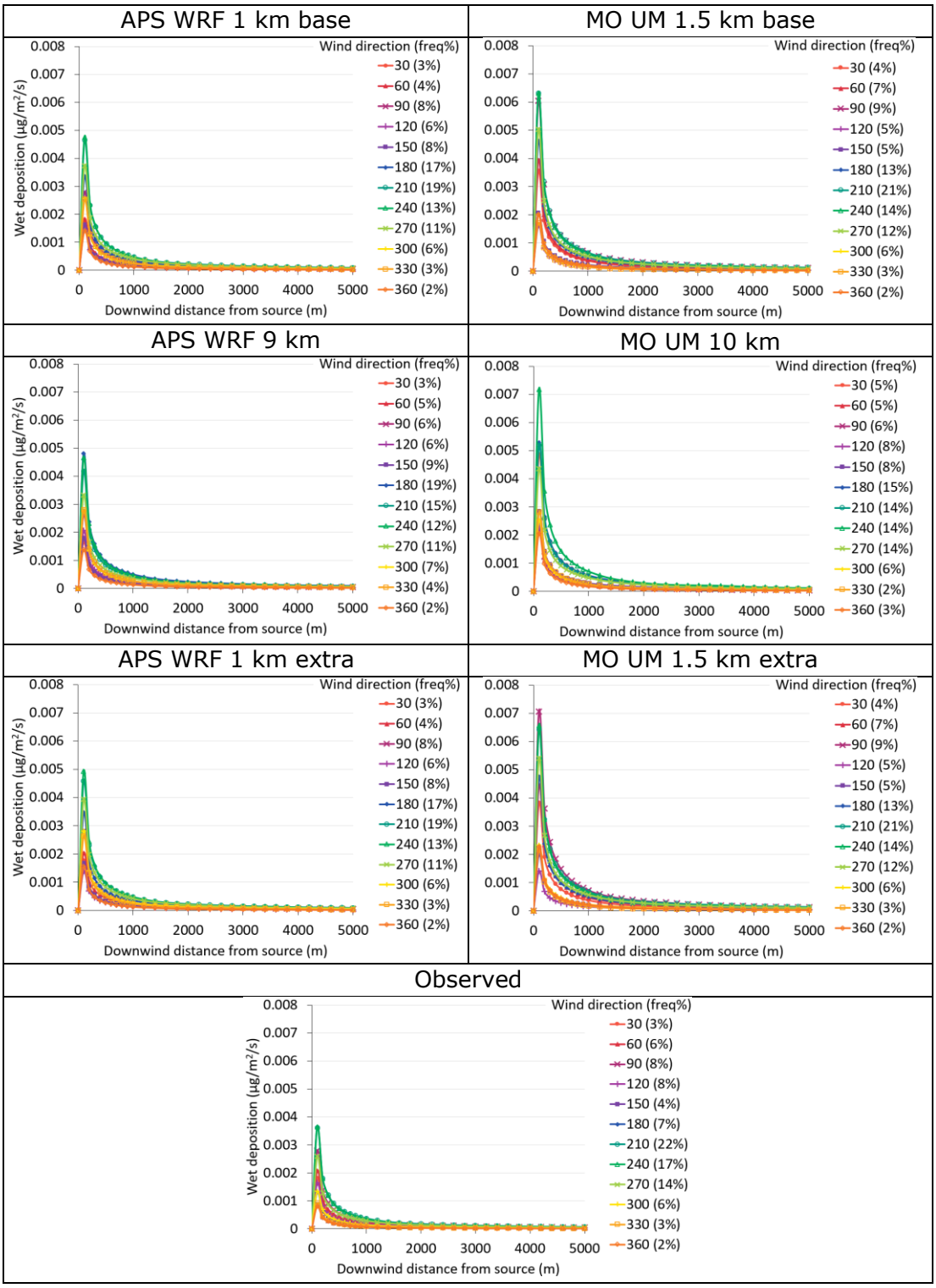

Figure 226 – Downwind profiles of annual average wet deposition for elevated source at Drumalbin with varying wind direction, modelled with ADMS for all meteorological datasets.

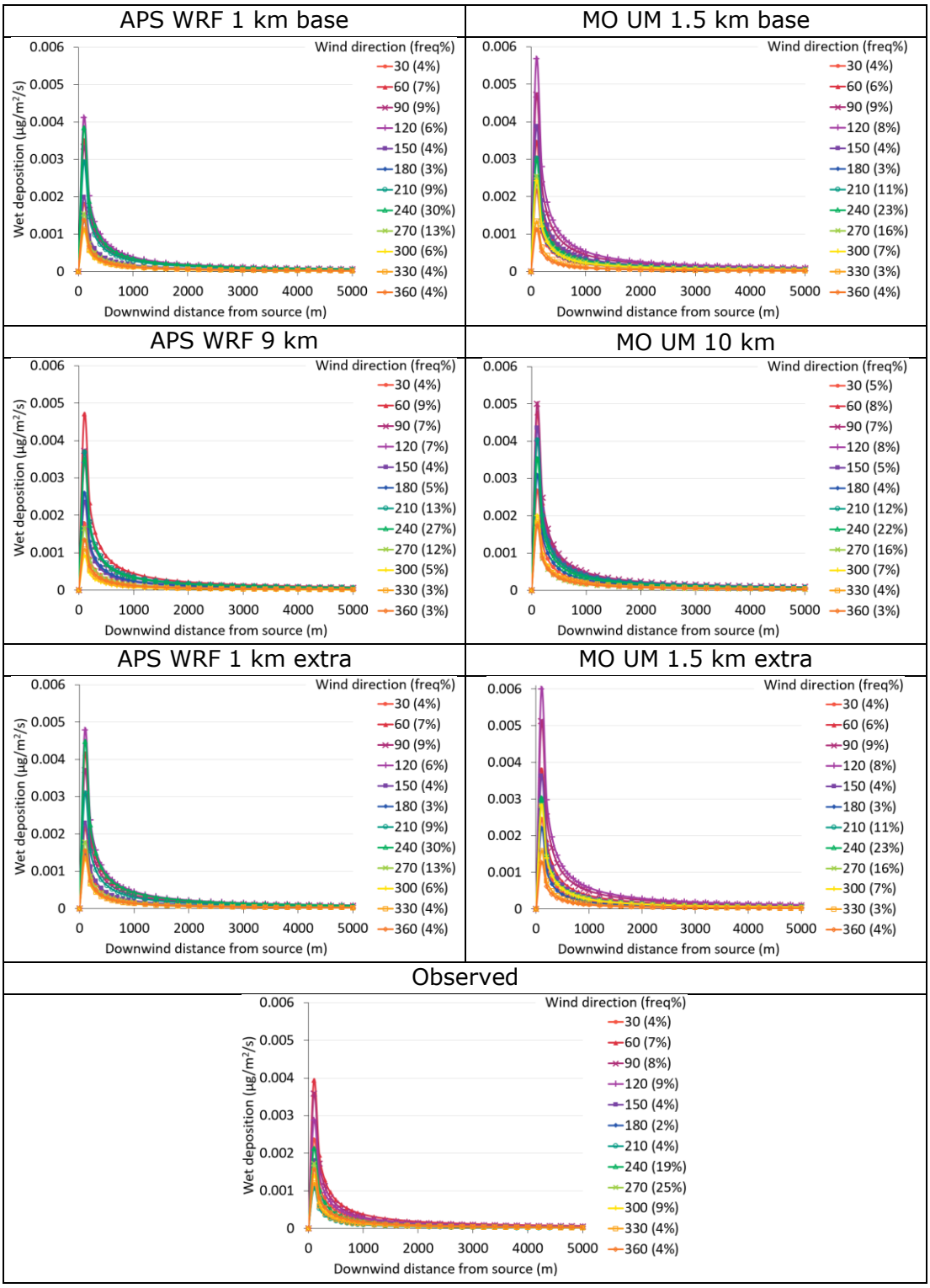

Figure 227 – Downwind profiles of annual average wet deposition for elevated source at Leuchars with varying wind direction, modelled with ADMS for all meteorological datasets.

Table 75 - Magnitudes and locations of maximum annual average wet deposition for each meteorological dataset and source height (near-ground, G, or elevated, E) over the 2019 period at Waddington met site, as calculated by ADMS 6.

			Dispersion model				
			ADMS 6				
Met input	Source	Stat	Max ($\mu g/m^2/s$)	X (m)	Y (m)	distance (m)	wind dir (°)
Obs base	G	wd	0.041	0	10	10	180
APS WRF 1km base	G	wd	0.051	9	5	10	240
APS WRF 9km base	G	wd	0.055	-9	5	10	120
MO UM 1.5km base	G	wd	0.072	5	9	10	210
MO UM 10km base	G	wd	0.076	0	10	10	180
APS WRF 1km extra	G	wd	0.051	5	9	10	210
MO UM 1.5km extra	G	wd	0.071	5	9	10	210
Obs base	E	wd	0.0018	87	50	100	240
APS WRF 1km base	E	wd	0.0026	50	87	100	210
APS WRF 9km base	E	wd	0.0027	50	87	100	210
MO UM 1.5km base	E	wd	0.0033	50	87	100	210
MO UM 10km base	E	wd	0.0038	0	100	100	180
APS WRF 1km extra	E	wd	0.0028	50	87	100	210
MO UM 1.5km extra	E	wd	0.0040	50	87	100	210

Table 76 - Magnitudes and locations of maximum annual average wet deposition for each meteorological dataset and source height (near-ground, G, or elevated, E) over the 2019 period at Leuchars met site, as calculated by ADMS 6.

			Dispersion model				
			ADMS 6				
Met input	Source	Stat	Max ($\mu g/m^2/s$)	X (m)	Y (m)	distance (m)	wind dir (°)
Obs base	G	wd	0.084	-10	0	10	90
APS WRF 1km base	G	wd	0.086	-9	5	10	120
APS WRF 9km base	G	wd	0.090	-9	-5	10	60
MO UM 1.5km base	G	wd	0.116	-9	5	10	120
MO UM 10km base	G	wd	0.097	-9	-5	10	60
APS WRF 1km extra	G	wd	0.084	-9	5	10	120
MO UM 1.5km extra	G	wd	0.116	-9	5	10	120
Obs base	E	wd	0.0039	-87	-50	100	60
APS WRF 1km base	E	wd	0.0041	-87	50	100	120
APS WRF 9km base	E	wd	0.0047	-87	-50	100	60
MO UM 1.5km base	E	wd	0.0057	-87	50	100	120
MO UM 10km base	E	wd	0.0050	-100	0	100	90
APS WRF 1km extra	E	wd	0.0048	-87	50	100	120
MO UM 1.5km extra	E	wd	0.0060	-87	50	100	120

Table 77 - Magnitudes and locations of maximum annual average wet deposition for each meteorological dataset and source height (near-ground, G, or elevated, E) over the 2019 period at Sennybridge met site, as calculated by ADMS 6.

			Dispersion model				
			ADMS 6				
Met input	Source	Stat	Max (µg/m²/s)	X (m)	Y (m)	distance (m)	wind dir (°)
Obs base	G	wd	0.297	9	5	10	240
APS WRF 1km base	G	wd	0.170	5	9	10	210
APS WRF 9km base	G	wd	0.243	5	9	10	210
MO UM 1.5km base	G	wd	0.374	5	9	10	210
MO UM 10km base	G	wd	0.289	5	9	10	210
APS WRF 1km extra	G	wd	0.162	5	9	10	210
MO UM 1.5km extra	G	wd	0.330	5	9	10	210
Obs base	E	wd	0.0118	87	50	100	240
APS WRF 1km base	E	wd	0.0068	87	50	100	240
APS WRF 9km base	E	wd	0.0095	87	50	100	240
MO UM 1.5km base	E	wd	0.0157	50	87	100	210
MO UM 10km base	E	wd	0.0128	87	50	100	240
APS WRF 1km extra	E	wd	0.0074	87	50	100	240
MO UM 1.5km extra	E	wd	0.0161	50	87	100	210

Table 78 - Magnitudes and locations of maximum annual average wet deposition for each meteorological dataset and source height (near-ground, G, or elevated, E) over the 2019 period at Drumalbin met site, as calculated by ADMS 6.

			Dispersion model				
			ADMS 6				
Met input	Source	Stat	Max (µg/m²/s)	X (m)	Y (m)	distance (m)	wind dir (°)
Obs base	G	wd	0.076	9	5	10	240
APS WRF 1km base	G	wd	0.097	5	9	10	210
APS WRF 9km base	G	wd	0.092	5	9	10	210
MO UM 1.5km base	G	wd	0.130	5	9	10	210
MO UM 10km base	G	wd	0.128	9	5	10	240
APS WRF 1km extra	G	wd	0.095	5	9	10	210
MO UM 1.5km extra	G	wd	0.124	5	9	10	210
Obs base	E	wd	0.0036	87	50	100	240
APS WRF 1km base	E	wd	0.0048	87	50	100	240
APS WRF 9km base	E	wd	0.0048	0	100	100	180
MO UM 1.5km base	E	wd	0.0063	50	87	100	210
MO UM 10km base	E	wd	0.0072	87	50	100	240
APS WRF 1km extra	E	wd	0.0049	87	50	100	240
MO UM 1.5km extra	E	wd	0.0071	-100	0	100	90

APPENDIX D DOUBLE-COUNTING TERRAIN EFFECTS

D1 Conversion of gridded NWP data

To aid in plotting the gridded NWP data using existing tools, a python script was written to convert the data into a format expected by the ADMS Flow field Plotter. For plotting individual hours, data was written out to *.W01* files, the format of which is described in Section 6.1.13 of the ADMS 6 User Guide. For plotting the long-term (annual) average NWP flow fields, the hourly gridded data were first time-averaged and then written out to *.wlt* files, the format of which is described in Section 6.1.14 of the ADMS 6 User Guide. The direction of the mean horizontal wind vector (degrees measured anticlockwise, 0° = wind from west) at a given grid cell was calculated as

$$\text{Angle (deg)} = \frac{180}{\pi}\,\text{atan2}(\bar{v}, \bar{u}),$$

where $\text{atan2}(y, x)$ is the 2-argument arctangent function, and $\bar{u}$ and $\bar{v}$ are the components of the mean wind velocity in west-east and south-north direction at that grid cell, respectively. The magnitude of the mean horizontal wind vector (m/s) at a given grid cell was calculated as

$$\text{Magnitude of mean horizontal wind vector } \left(\frac{\text{m}}{\text{s}}\right) = \sqrt{\bar{u}^2 + \bar{v}^2}.$$

It is this variable, along with the 'Angle', that the ADMS Flow Field Plotter uses to plot the mean wind vectors, and not the 'Mean horizontal wind speed (m/s)' ($= \overline{\sqrt{u^2 + v^2}}$).

D2 Short-term flow field plots for other wind sectors

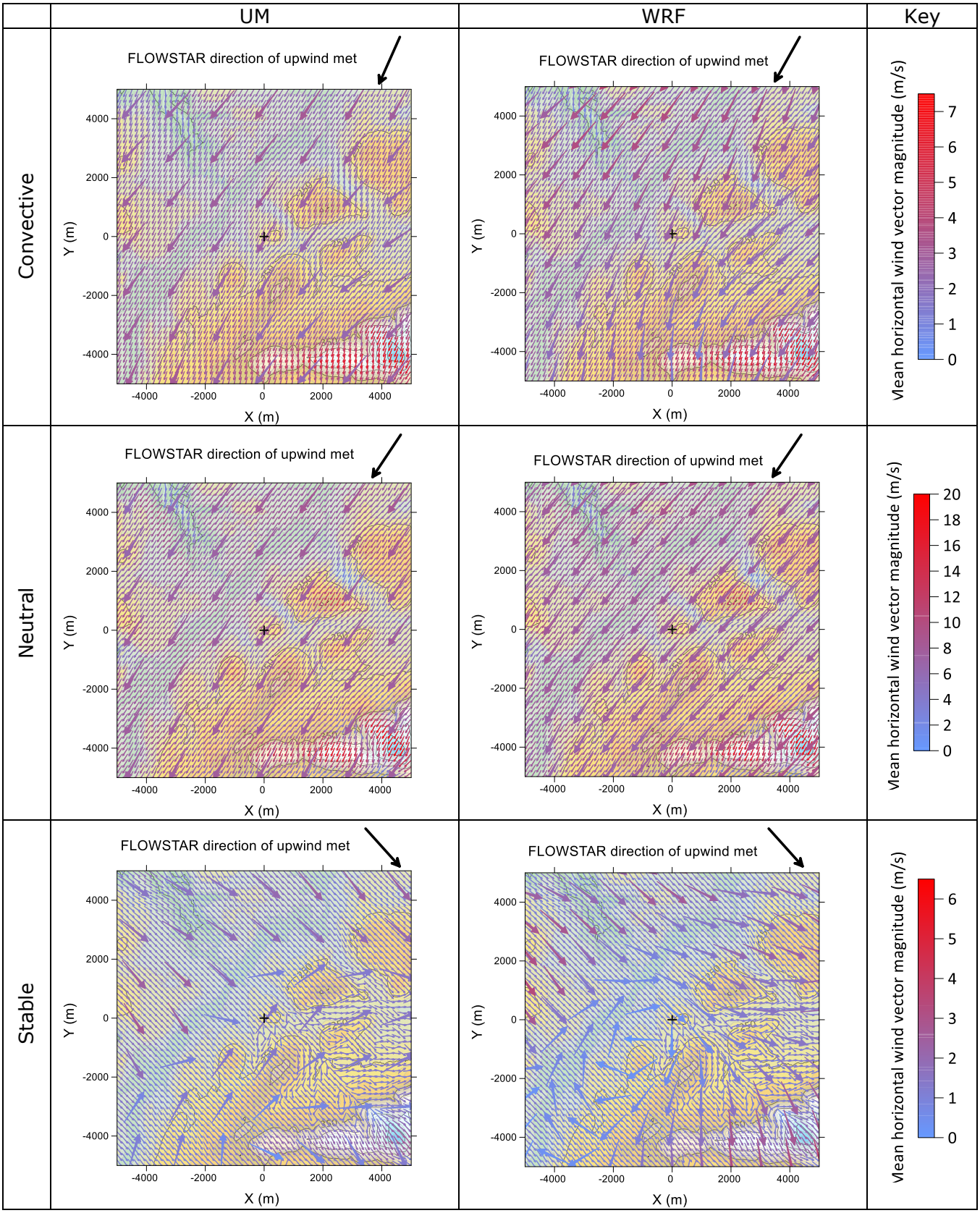

Figure 228 – Drumalbin 10 m agl horizontal wind vector fields for individual hours with a northerly wind direction and convective (top), neutral (middle) and stable (bottom) conditions. Large arrows show finest-resolution gridded NWP data, small arrows show equivalent FLOWSTAR run forced by coarsest-resolution NWP data; UM (left) and WRF (right).

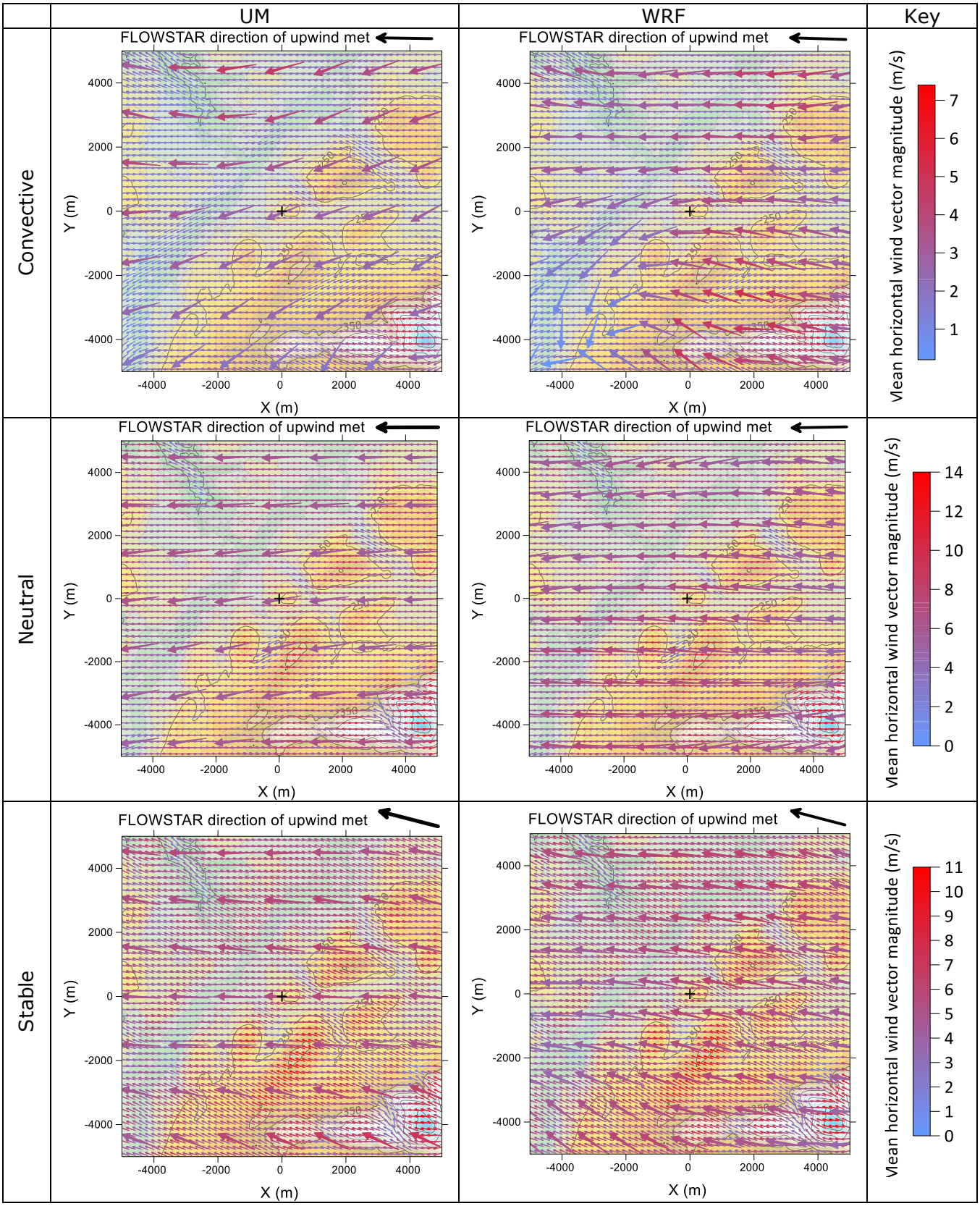

Figure 229 – As in Figure 228 but for an easterly wind direction at Drumalbin.

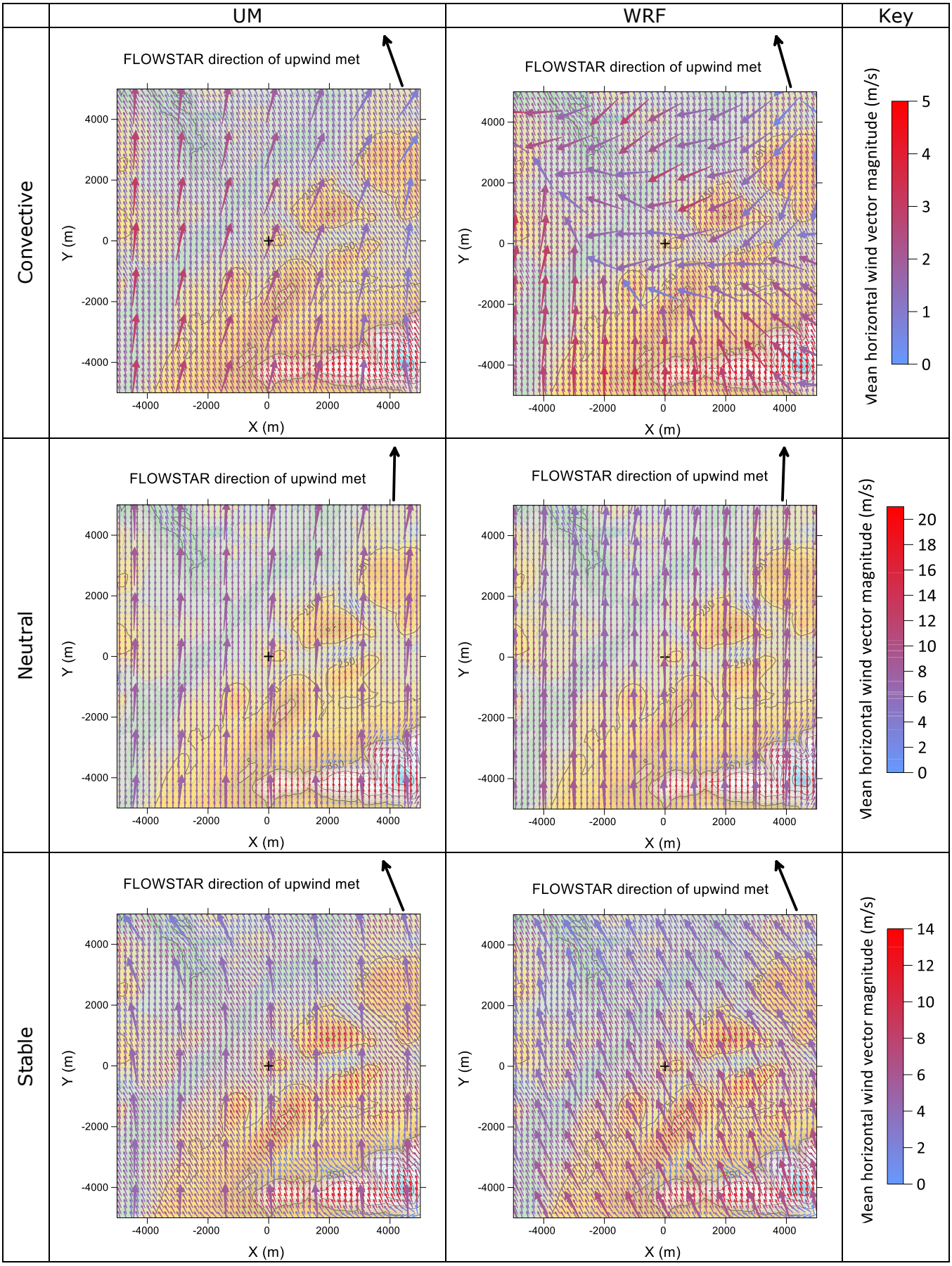

Figure 230 – As in Figure 228 but for a southerly wind direction at Drumalbin.

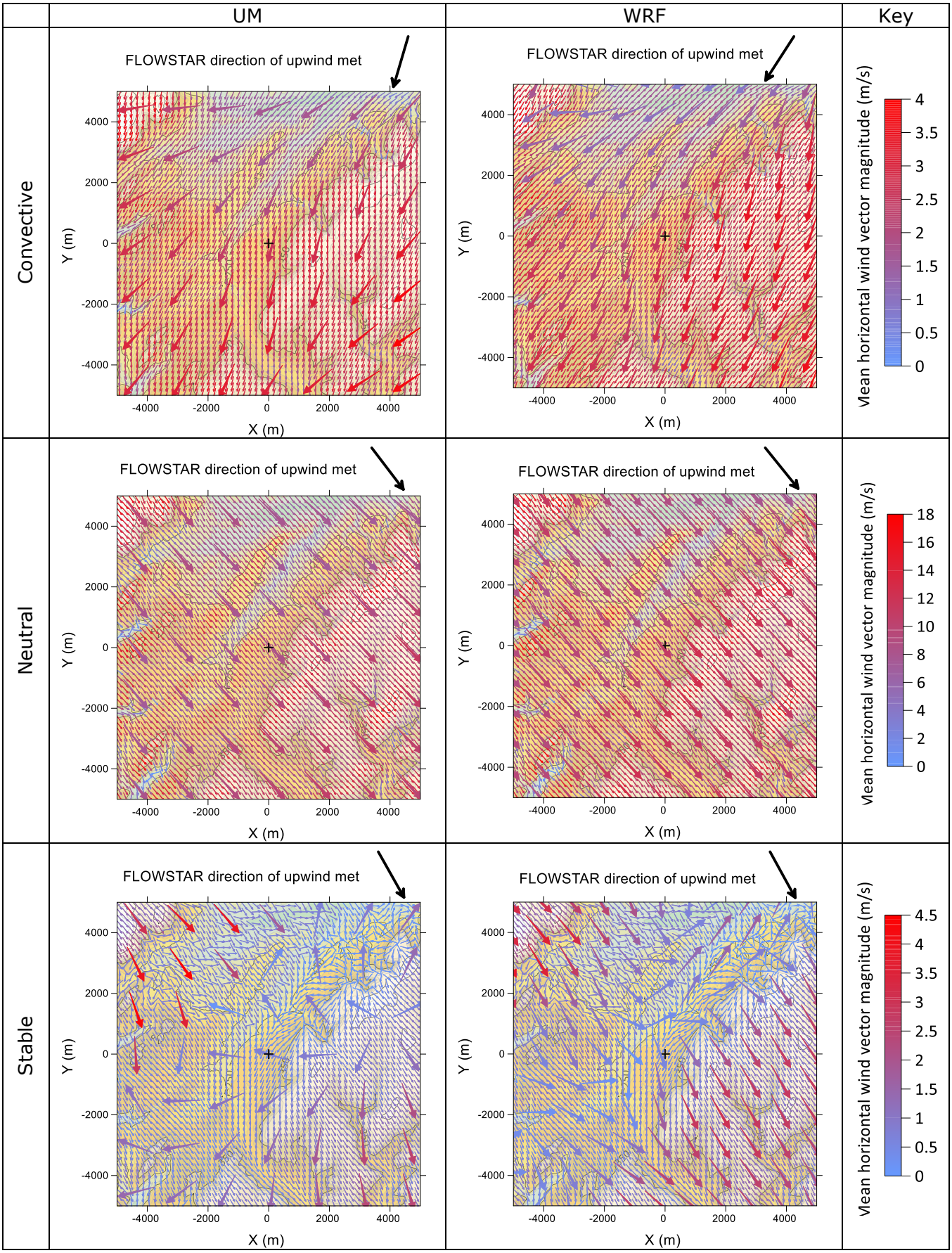

Figure 231 – As in Figure 228 but for a northerly wind direction at Sennybridge.

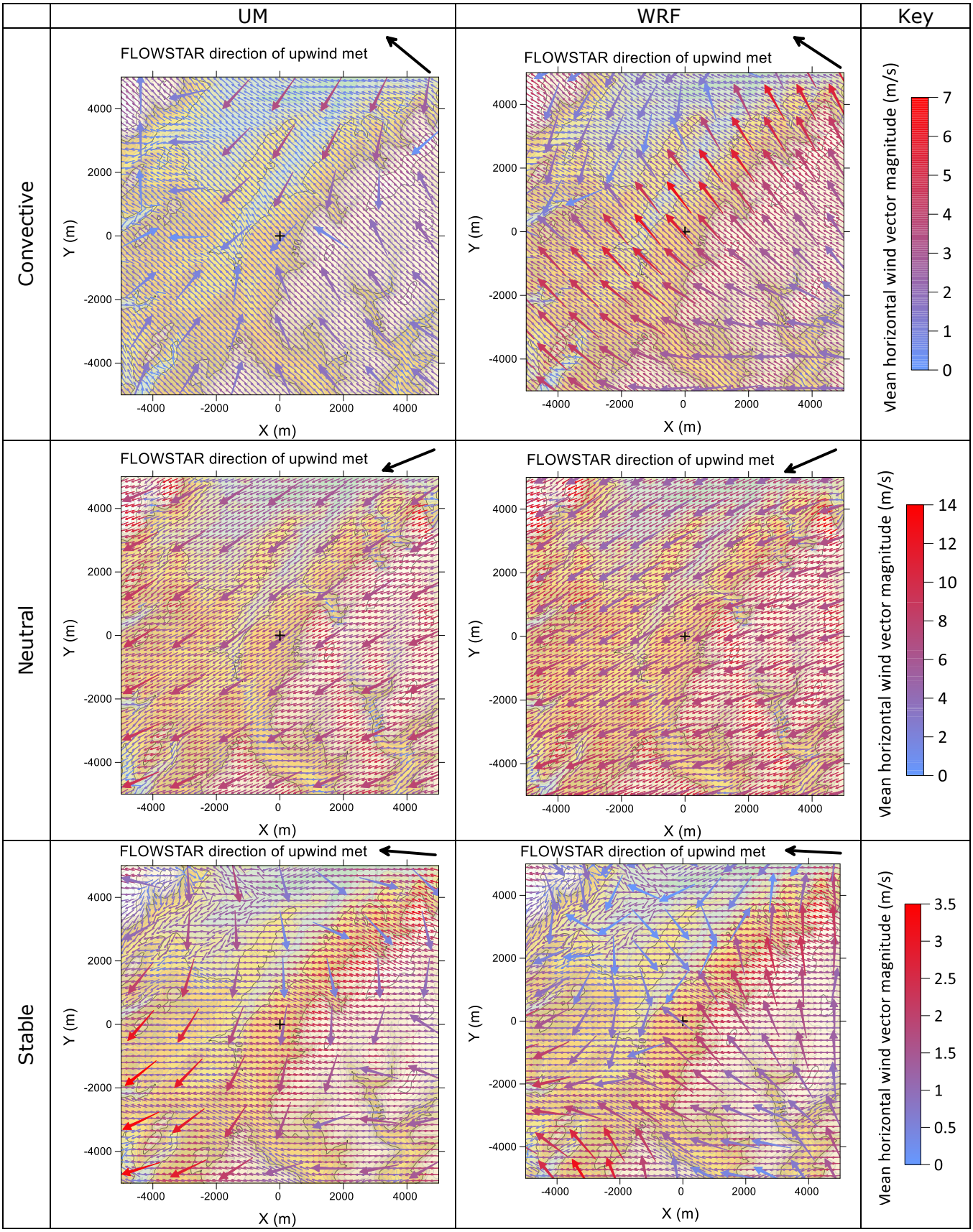

Figure 232 – As in Figure 228 but for a easterly wind direction at Sennybridge.

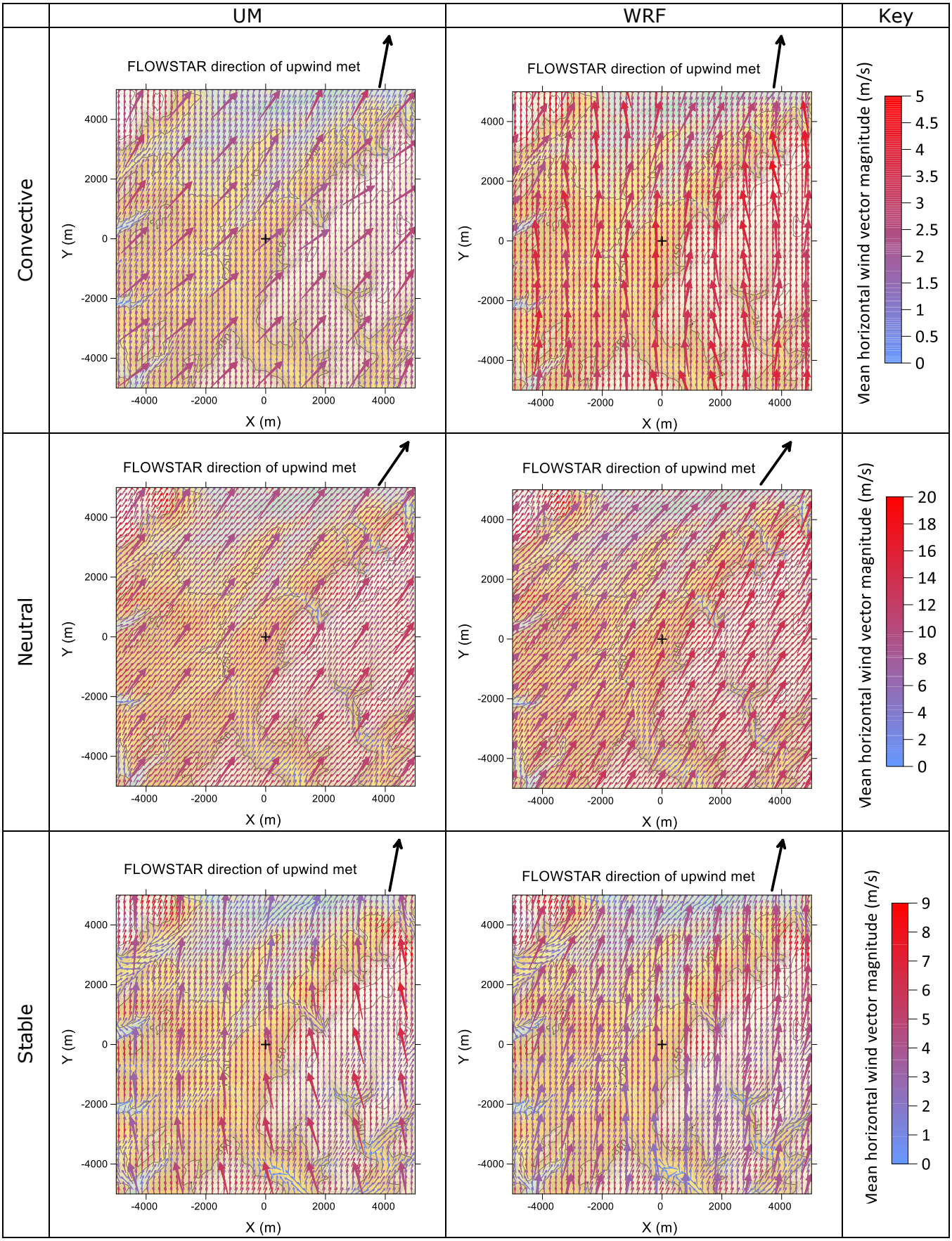

Figure 233 – As in Figure 228 but for a southerly wind direction at Sennybridge

D3 Spatially averaged gridded NWP data

To generate the spatially averaged NWP data at each site (Drumalbin and Sennybridge), the region of gridded 1.5 km-resolution UM data that covers most of, but is fully contained within, the ~13 x 13 km FLOWSTAR domain was spatially averaged. This meant averaging 7 x 7 grid cells covering a region of 10.5 x 10.5 km. We might instead have averaged over 9 x 9 grid cells covering a region of 13.5 x 13.5 km but the slightly smaller averaging area was chosen so that comparisons with results obtained using the 10 km resolution UM data could be made more easily. Figure ??? in Section ??? indicates that there is minimal double-counting when using the 10 km UM data. A python script was written to perform the spatial averaging and write the hourly values to an ADMS *.met* file for use with ADMS/FLOWSTAR. For a given hour, spatially averaged wind direction was calculated from the arithmetic mean u and v components over all 7 x 7 grid cells. For all other variables (wind speed, near-surface temperature, cloud cover, precipitation), the arithmetic mean values over all 7 x 7 grid cells were used directly.

D4 Long-term 98th percentile plots

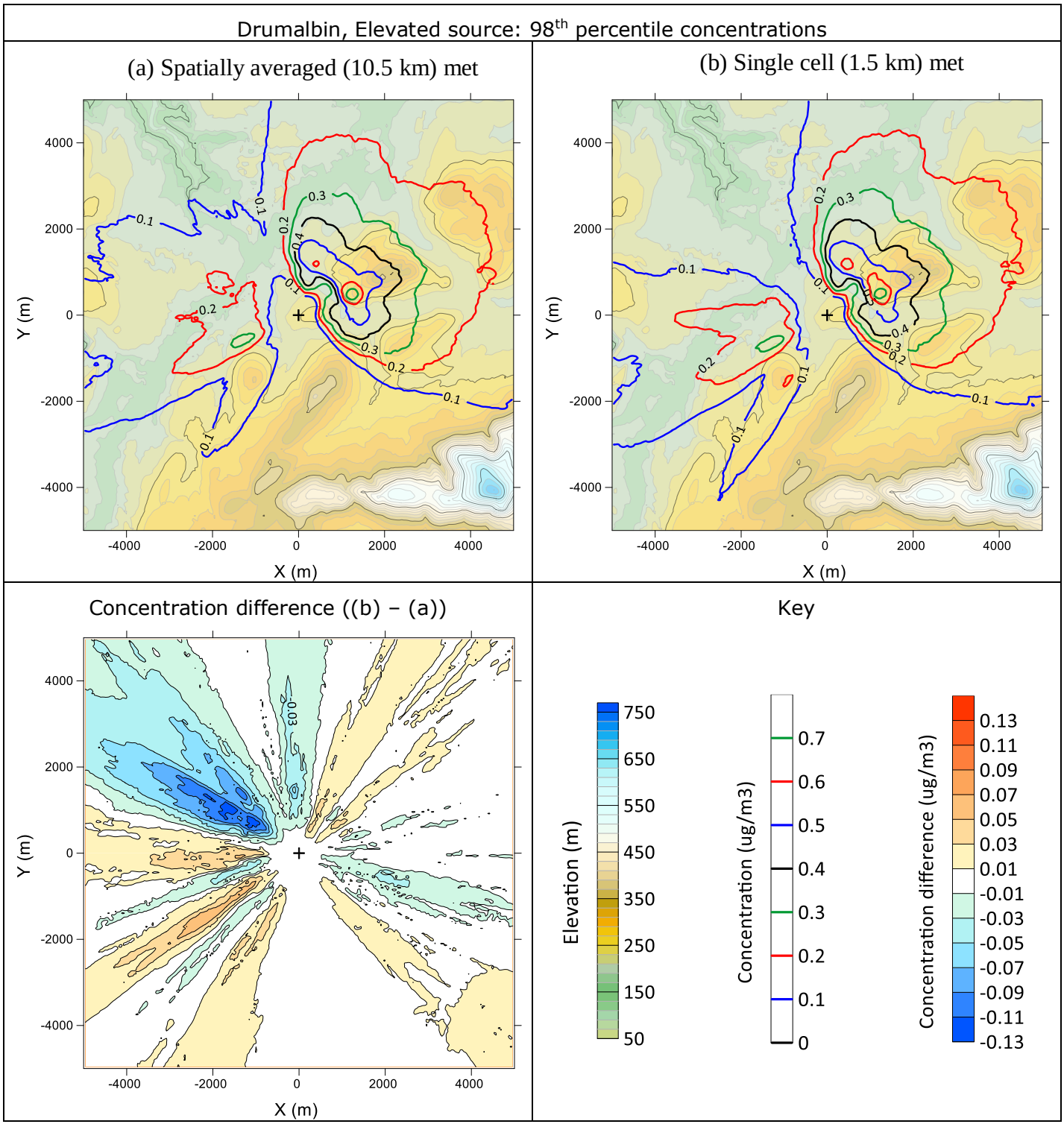

Figure 234 – Top: Drumalbin 98th percentile ground level concentrations (non-filled contours) for the elevated source from an ADMS/FLOWSTAR run forced by (a) spatially averaged (10.5 km) met and (b) single cell (1.5 km) met. Surface elevation shown by filled contours. Bottom left: Concentration difference (b) – (a).

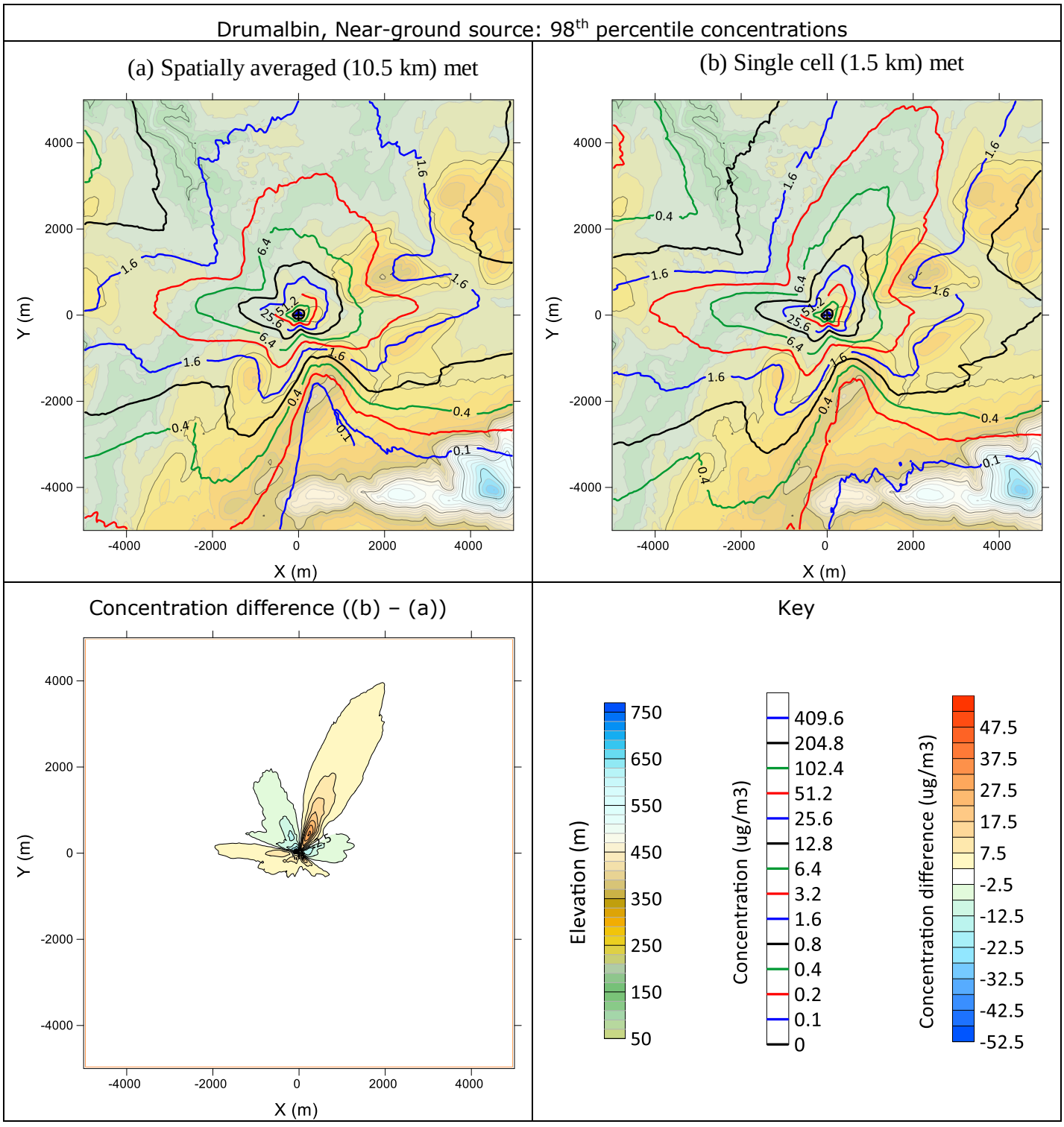

Figure 235 – As in Figure 234 but for the near-ground source at Drumalbin.

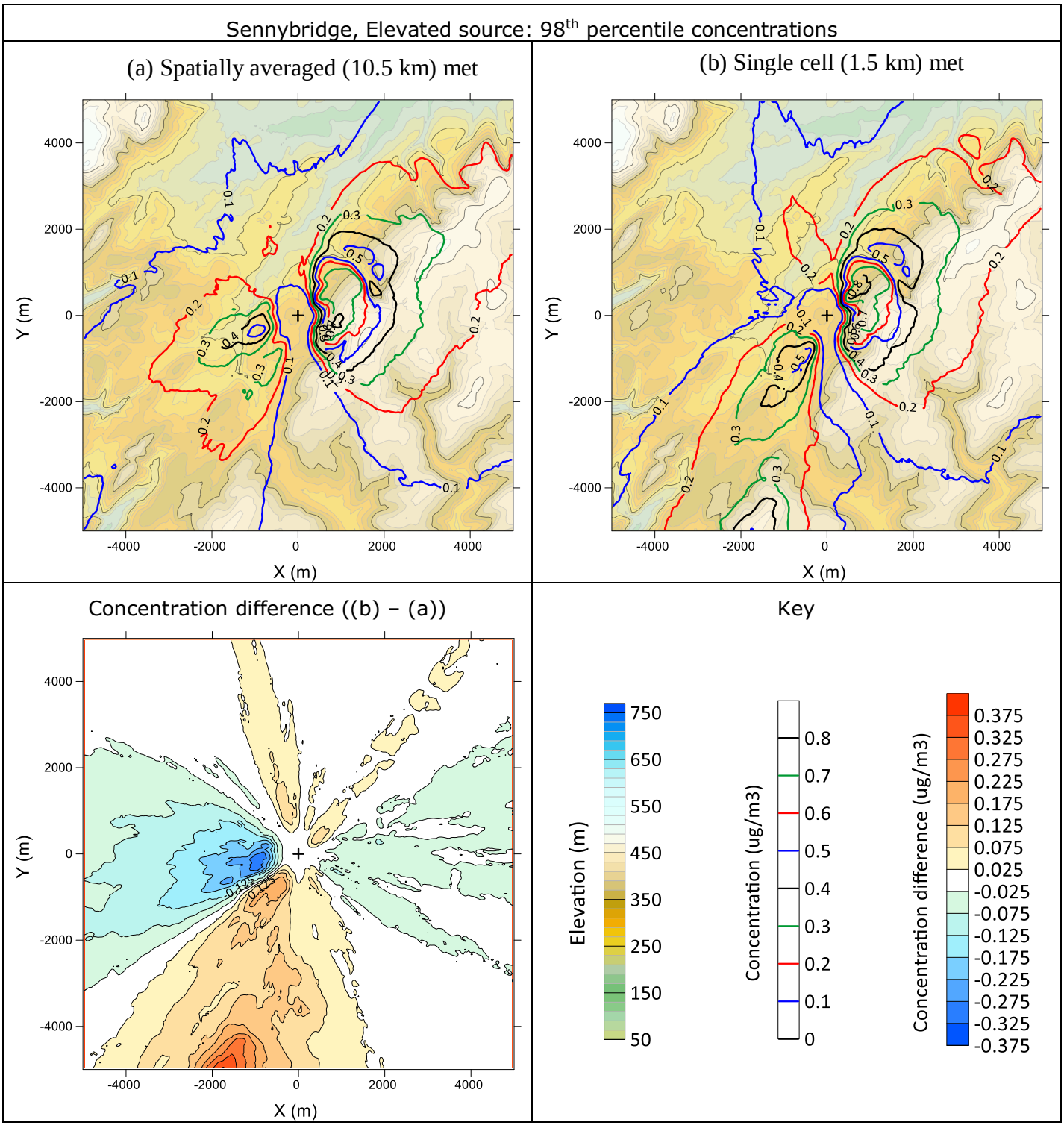

Figure 236 – As in Figure 234 but for the elevated source at Sennybridge.

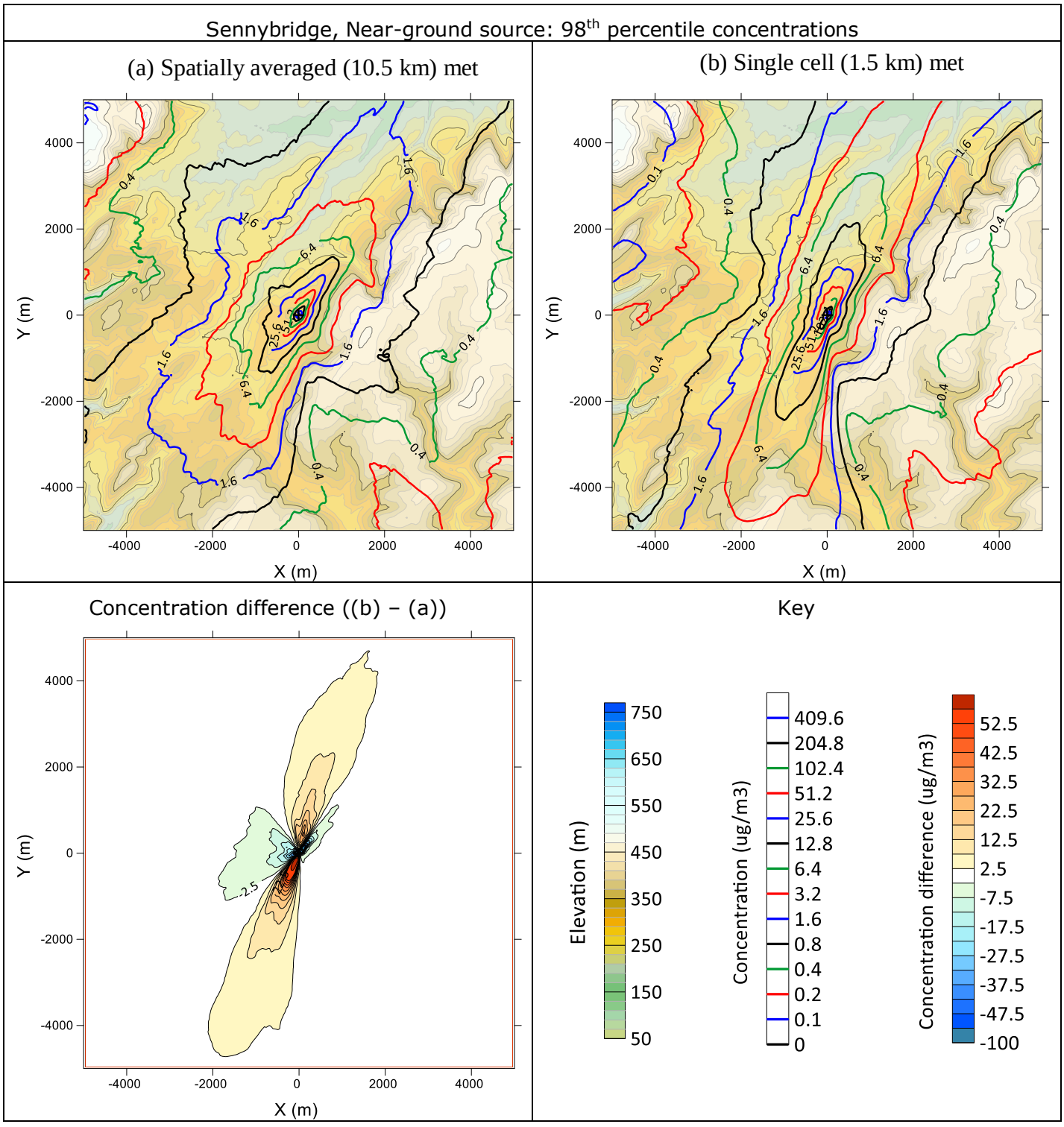

Figure 237 – As in Figure 234 but for the near-ground source at Sennybridge.

D5 FLOWSTAR code modifications

As part of this task, it was necessary to modify the FLOWSTAR source code. A new model option was implemented which is enabled via the ADMS additional input (*.aai*) file (keyword REMOVEWAVELENGTHS) and takes as input:

- A cut-off length scale, L_c, in metres
- A keyword set to either LONG or SHORT

When the keyword is set to LONG, the model removes spatial scales from the terrain height data that are longer than L_c. When the keyword is set to SHORT, the model removes spatial scales shorter than L_c. This is achieved as follows.

In its standard configuration, FLOWSTAR interpolates the user-supplied terrain data onto an (up)wind-aligned internal 2D grid with resolution defined by the user (typically 64×64, 128×128 or 256×256 points). It then performs a Fourier transform of this data, returning a complex 2D array representation of the terrain data in Fourier space, i.e. frequencies of individual wavenumber pairs.

When using the new option, a cut-off wavenumber k_c is calculated from the supplied cut-off length scale L_c as:

$$k_c = L_{xy}/L_c$$

where L_{xy} is the representative length-scale of the terrain extent (zeroth wavenumber in Fourier space) and is calculated as $L_{xy} = \frac{1}{\sqrt{2}}\sqrt{{L_x}^2 + {L_y}^2}$, where L_x and L_y are the west-east and south-north side lengths of the bounding box of the input terrain data respectively. Then any elements of the complex 2D array of Fourier-space terrain data with an 'overall' wavenumber k_{12} less than k_c (if removing scales longer than L_c) or greater than k_c (if removing scales shorter than L_c) are set to zero. Here, k_{12} is taken as $\sqrt{{k_1}^2 + {k_2}^2}$, where k_1 and k_2 are the along- and cross-wind wavenumbers respectively).

By performing the reverse Fourier transform on this modified Fourier-space terrain data, it is possible to retrieve the modified real-space terrain data, which can then be plotted to confirm that the relevant length-scales have been removed.

We first do this on an idealised terrain file that we know to contain only certain wavelengths. We define a terrain file with 64×64 points on a regular grid covering a 2 × 2 km region with height H (m) at grid point i,j given by:

$$H(i,j) = \left(10\sin\left(\frac{2\pi x_j}{2000}\right) + \sin\left(10\frac{2\pi x_j}{2000}\right)\right)\left(10\sin\left(\frac{2\pi y_i}{2000}\right) + \sin\left(10\frac{2\pi y_i}{2000}\right)\right)$$

i.e. a high-amplitude long-wavelength sine wave with a low-amplitude short-wavelength sine wave superimposed (in two dimensions). A 3D surface plot of this terrain file is shown in Figure 238, where the z-axis scale has been stretched to accentuate the height variation.

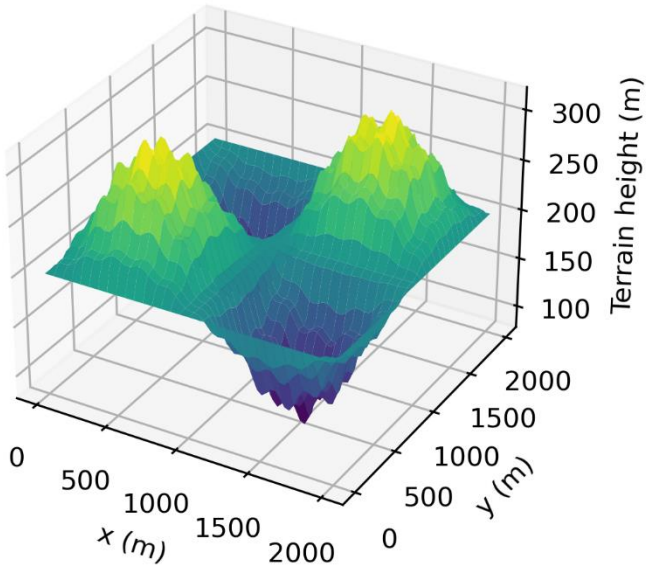

Figure 238 – 3D surface plot of idealised input terrain heights.

We first use the new option to remove the long wavelengths from the terrain data. Figure 239 shows the 3D surface plot of the resulting (real-space) terrain data as well as a 2D plot of terrain heights along a particular transect (y = 500 m) before and after the removal of the long wavelengths (L_c = 400 m). It is clear that the high-amplitude long-wavelength sine wave signal has successfully been removed from the terrain data.

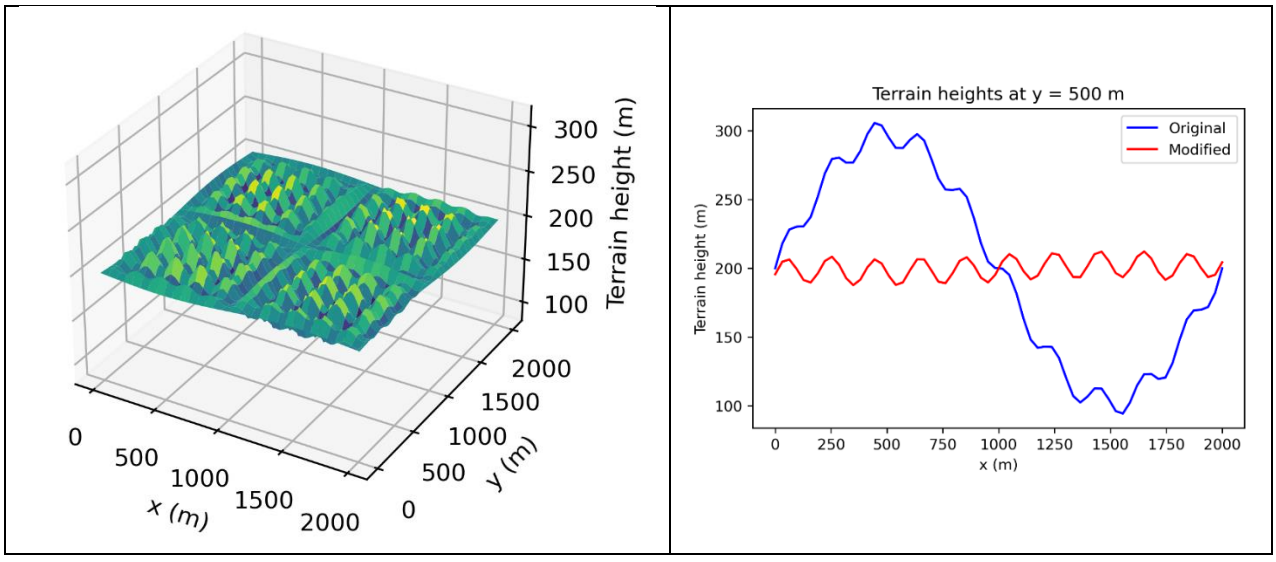

Figure 239 – 3D surface plot of idealised terrain with long wavelengths removed (left) and 2D plot showing terrain heights along the line y = 500 m before and after the removal of the long wavelengths (right).

Similarly, Figure 240 shows the same plots when the new option is used to remove the short wavelengths from the terrain data. Again, it is clear that the low-amplitude short-wavelength sine wave signal has successfully been removed from the terrain data.

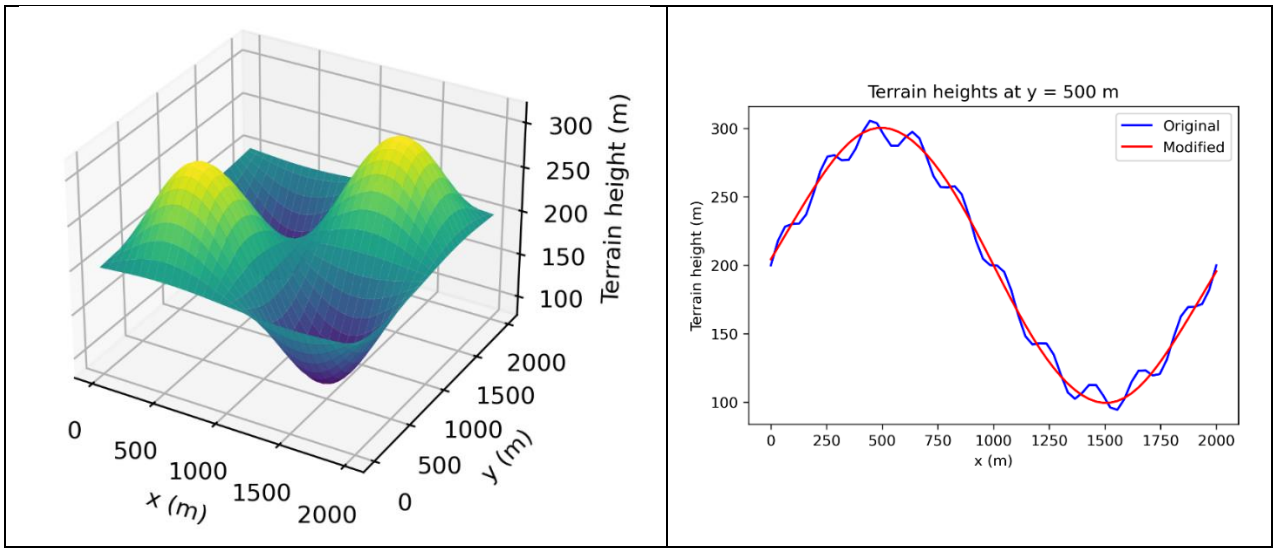

Figure 240 – As in Figure 239 but with short wavelengths removed.